Fuel for the Star Formation Engine: Dense Molecular Cloud Clumps in the Northern Galactic Plane

by

Erika Zetterlund

B.A., Augustana University, 2013

M.S., University of Colorado, 2016

A thesis submitted to the

Faculty of the Graduate School of the

University of Colorado in partial fulfillment

of the requirements for the degree of

Doctor of Philosophy

Department of Astrophysical and Planetary Sciences

2018

This thesis entitled:
Fuel for the Star Formation Engine: Dense Molecular Cloud Clumps in the Northern Galactic Plane
written by Erika Zetterlund
has been approved for the Department of Astrophysical and Planetary Sciences

Prof. Jason Glenn

Prof. Jeremy Darling

Prof. Benjamin Brown

Prof. Ann-Marie Madigan

Prof. Jem Corcoran

Date

The final copy of this thesis has been examined by the signatories, and we find that both the content and the form meet acceptable presentation standards of scholarly work in the above mentioned discipline.

Zetterlund, Erika (Ph.D., Astrophysics)

Fuel for the Star Formation Engine: Dense Molecular Cloud Clumps in the Northern Galactic Plane

Thesis directed by Prof. Jason Glenn

The interstellar medium (ISM) is a confusing, muddled place. It provides the fuel for star formation, but before that can occur, the ISM must cool and condense into molecular clouds. Even this is not enough, however. It is only the cores, contained within the clumps, contained within the clouds, which form stars. With all these nested structures, it takes an optically thin, yet still bright, tracer to uncover the processes which convert the molecular clouds into stars. Luckily, the ISM is dusty.

I use the *Herschel* infrared GALactic plane survey (Hi-GAL) to study molecular cloud clumps through their thermal dust emission at 500 μm. For adapting and testing the clump identification and distance techniques – developed for the Bolocam Galactic Plane Survey (BGPS) – I used six Hi-GAL maps at a representative sample of Galactic longitudes. I found many more clumps per square degree with Hi-GAL than were identified with BGPS, particularly at longitudes farther from the Galactic center, where Hi-GAL's increased sensitivity truly shines. Where I found the same clumps as BGPS, my distances and physical properties aligned well. Notably, clumps are slightly larger in Hi-GAL, where the diffuse edges are not overtaken by atmospheric noise, as was the case with BGPS.

The application of these techniques to $10° < \ell < 56°$ resulted in a catalog of 19,886 clumps, 10,124 of which have an associated velocity and therefore a kinematic distance, and 5,405 of which have their distances well constrained. From this dataset, I produced a face-on map of the Galactic Plane's dense molecular gas. Furthermore, I examined radial trends in clump physical properties and found that the average clump mass decreases with distance from the Galactic Center, although with a large degree of scatter.

Finally, with the addition of a catalog of clouds produced using the CO High Resolution

Survey (COHRS), I addressed molecular cloud clumps as fuel for star formation. I matched 3,674 clumps from my catalog to 473 clouds from the COHRS catalog, and found that the fraction of a cloud's mass contained in clumps is independent of cloud properties such as mass and virial parameter. As clouds grow, they linearly put more mass into clumps, producing both more clumps and more massive clumps. Star formation rates are dependent solely on cloud mass (or, equivalently, clump mass). This provides evidence for the soundness of star formation recipes used in numerical simulations of galaxy evolution, where a fixed fraction of gas mass is converted into star mass, once that gas meets conditions locating it inside a cloud.

Dedication

To all those who talked with me over tea/cocktails when things weren't going well.

Acknowledgements

> There is nothing like looking, if you want to find something (or so Thorin said to the young dwarves). You certainly usually find something, if you look, but it is not always quite the something you were after.
>
> - J.R.R. Tolkien, *The Hobbit*

First, thank you to Jason Glenn, for being my Thorin when plot after plot showed no correlation between variables. You were enthusiastic even when I was struggling to stay positive. Thank you for allowing me roam free, but also providing guidance and new directions when I was tapped out. I guess I also have to thank you for forcing to talk in front of people when that was the last thing in the world I desired. It helped.

Thank you as well to Erik Rosolowsky, for being the puppetmaster which enabled this project to exist. Between you and Jason, I was never lacking in ideas to pursue or motivation to run after them.

Finally, thank you to all the wonderful fools at West Gate Kung Fu. There is nothing like meticulous coordinations of limbs to distract you from your research problems. Not only have you forced me to take vital breaks, particularly in these last few months, but your friendships have been invaluable.

And of course, thank you to my family, for supporting and encouraging me when I chose to make my life more difficult than is necessary. I love you.

Contents

Chapter

1 Introduction **1**

1.1 How is the ISM structured? 1

1.1.1 Clouds, Clumps, and Cores 2

1.1.2 ISM Tracers 3

1.1.3 Galactic Observations 4

1.1.4 Extragalactic Observations 5

1.1.5 Simulations 6

1.2 Where and when do stars form? 7

1.2.1 In Simulations 7

1.2.2 Star Formation Tracers 8

1.2.3 Observations 8

1.3 Galactic Plane Surveys 9

1.3.1 Herschel infrared GALactic plane survey (Hi-GAL) 10

1.3.2 Bolocam Galactic Plane Survey (BGPS) 10

1.3.3 CO High Resolution Survey (COHRS) 11

1.3.4 Additional Surveys 11

1.4 Scope & Organization 12

2 Method and Initial Results Comparison with BGPS **14**

2.1 Introduction 15

2.2 Data 17

2.3 Method 19

2.3.1 Map Making 19

2.3.2 Filtering 19

2.3.3 Source Identification 21

2.3.4 Distance Determination 26

2.4 Results: Comparison to BGPS 28

2.4.1 Clump Densities on the Sky 31

2.4.2 Angular Sizes 32

2.4.3 Clump Masses 36

2.5 Discussion 39

2.6 Conclusions 41

3 Dense Gas Map and Environmental Trends **42**

3.1 Introduction 42

3.2 Data 46

3.3 Method 47

3.4 Results 50

3.4.1 Malmquist Bias 51

3.4.2 Trends with Galactocentric Radius 54

3.4.3 Surface Densities of Clumps 58

3.4.4 Mass Distributions 59

3.4.5 Dense Gas Distribution 65

3.5 Discussion 67

3.5.1 Mass Sensitivity 67

3.5.2 Density Profiles . . . 69
3.5.3 The Effects of GMCs . . . 69
3.5.4 Comparison to Literature . . . 70
3.6 Conclusions . . . 73

4 Clump and Star Formation within Clouds **74**
4.1 Introduction . . . 74
4.2 Data . . . 77
4.2.1 Hi-GAL clump catalog . . . 77
4.2.2 COHRS cloud catalog . . . 78
4.3 Method . . . 82
4.3.1 Matching Hi-GAL clumps to COHRS clouds . . . 82
4.3.2 Clump properties . . . 83
4.3.3 Cloud properties . . . 84
4.4 Results . . . 87
4.5 Clump Formation Efficiency . . . 89
4.5.1 CFE Distribution . . . 89
4.5.2 Relations with Physical Properties . . . 94
4.6 Star Formation Rates . . . 99
4.7 SFR Densities compared to the Kennicutt-Schmidt Law . . . 103
4.8 Virial Theorem . . . 106
4.9 Velocity Distributions and Spiral Arms . . . 109
4.10 Conclusions . . . 111

5 Concluding Thoughts **113**
5.1 Summary . . . 113
5.2 Future Work . . . 115
5.2.1 Complete Dense Gas Map . . . 115

5.2.2 CFE and SFR Radial Trends 116

5.2.3 Turbulence and its Effects on Clump and Star Formation 116

Bibliography **118**

Appendix

A Hi-GAL – BGPS matching catalog **124**

B Hi-GAL – COHRS matching catalog **137**

Tables

Table

1.1 ISM Phases 1

2.1 Distance statistics 31

2.2 Distance statistics for overlapping subregions 33

3.1 Cloud, clump, and core properties 44

3.2 Properties of mass distributions 61

A1 Hi-GAL – BGPS Catalog 124

B1 Hi-GAL – COHRS Catalog: COHRS Properties 138

B2 Hi-GAL – COHRS Catalog: Hi-GAL Properties 147

Figures

Figure

2.1 Example Hi-GAL maps 18

2.2 Attenuation of clump properties due to the use of a high-pass filter 20

2.3 Masking of Hi-GAL maps 22

2.4 PSDs of Hi-GAL maps 23

2.5 BOLOCAT source selection 25

2.6 Flux density comparison between filtered and unfiltered map objects 26

2.7 Example EMAF objects 29

2.8 Map comparison of Hi-GAL and BGPS clumps around $\ell = 11°$ 30

2.9 Distribution of angular sizes for Hi-GAL and BGPS objects 34

2.10 Angular radii comparison for clumps matched between Hi-GAL and BGPS 35

2.11 Mass comparison for clumps matched between Hi-GAL and BGPSs 37

2.12 Mass-Radius diagram for Hi-GAL clumps with well-constrained distances 38

3.1 Longitudinal clump distribution 50

3.2 Malmquist bias in clump masses 52

3.3 Mass and radius heliocentric distance trends 53

3.4 Clump mass vs Galactocentric radius in our minimal-bias sample 55

3.5 Face-on clump map showing normalized masses 56

3.6 Normalized mass vs Galactocentric radius 57

3.7 Mass surface density vs Galactocentric radius in minimal-bias sample 60

3.8 Mass distribution for all clumps in our minimal-bias sample 62

3.9 Mass distributions for clumps in equal-number bins in Galactocentric radius 63

3.10 Dense gas surface mass density map of the Galactic disk 66

3.11 Dense gas fraction map and radial distribution 68

3.12 Dense gas mass fraction map annotated with radial bins used in mass spectrum analysis 71

4.1 Cartoon demonstrating dendrogram approach to cloud identification 80

4.2 Sample COHRS mask and dendrogram 81

4.3 Sample clump-to-cloud matching. 88

4.4 Number densities of clouds and clumps 90

4.5 Clump mass fraction vs cloud mass 91

4.6 Clump mass fraction distributions 92

4.7 Clump mass fraction vs cloud properties 95

4.8 Clump frequency vs cloud mass 97

4.9 Clump masses vs cloud mass 98

4.10 SFR distribution 100

4.11 Clump mass fraction vs SFR 100

4.12 SFRs vs cloud and clump properties 102

4.13 SFRs vs cloud and clump number densities 104

4.14 Comparison to the Kennicutt-Schmidt law 105

4.15 Virial parameter vs cloud mass in full COHRS catalog 107

4.16 Velocities distributions for clouds and clumps 110

Chapter 1

Introduction

1.1 How is the ISM structured?

Although the interstellar medium (ISM) makes up only about 10% of the Milky Way's baryonic mass (Draine, 2011), it is the dominant component by volume. However, the ISM is not one diffuse fog which uniformly fills the space between stars. Instead, it varies by many orders of magnitude in both temperature and density. Traditionally, the ISM is broken down into several phases (Cox, 2005) (see Table 1.1). The hot ionized medium fills roughly half the Galaxy's volume with very diffuse ($n < 0.01$ cm^{-3}) and very hot ($T > 10^5$ K) ionized hydrogen and metals. Less tenuous are the warm ionized medium and warm neutral medium, both existing at densities of $n \sim 0.1 - 1$ cm^{-3} and temperatures of several thousand Kelvin. The cold neutral medium exists at densities of $n > 10$ cm^{-3} and temperatures of $T < 100$ K. Finally, in the coldest, densest phase, the hydrogen gas is molecular. At densities of $n > 30$ cm^{-3} and temperatures of $T \sim 10$ K, this is the ISM phase in which star formation occurs (Kennicutt & Evans, 2012).

Table 1.1: ISM Phases

Phase	n (cm^{-3})	T (K)
hot ionized	< 0.01	$> 10^5$
warm ionized	$0.1 - 1$	several 10^3
warm neutral	$0.1 - 1$	several 10^3
cold neutral	> 10	< 100
cold molecular	> 30	~ 10

1.1.1 Clouds, Clumps, and Cores

The dense molecular ISM can be divided into three categories of structures: clouds, clumps, and cores. Each of these structures is nested inside the previous structure type, with cores being the gravitationally bound precursors to individual stars or simple stellar systems. Typical radii are $R = 1 - 7.5$ pc for clouds, $R = 0.15 - 1.5$ pc for clumps, and $R = 0.015 - 0.1$ pc for cores. Meanwhile, as size decreases, H_2 densities increase, with typical densities being $n = 50 - 500$ cm^{-3} for clouds, $n = 10^3 - 10^4$ cm^{-3} for clumps, and $n = 10^4 - 10^5$ cm^{-3} for cores (Bergin & Tafalla, 2007). With observatories such as the *Herschel Space Observatory*, cores are only resolvable within ~ 1 kpc of the Sun. Clumps are detectable within ~ 7 kpc. Beyond this, we can only resolve entire clouds (Dunham et al., 2011). Note that this hierarchy was developed with the largest, most massive clouds in mind, the giant molecular clouds (GMCs). There also exist many smaller clouds, and these may contain only one clump and/or core. However, from a high-mass star formation perspective, it is the GMCs which are paramount (Zinnecker & Yorke, 2007). When the ISM is studied in external galaxies, dense molecular structures are resolvable only to GMC scales.

The initial mass function for molecular cloud clumps is not nearly as well studied as the stellar initial mass function. Depending on the physical process which dominates clump formation, the mass function is expected to follow either a power-law or lognormal distribution. A power-law mass function is predicted to indicate formation of clumps through gravitational collapse (e.g., Padoan & Nordlund, 2002). If instead clump formation is dominated by supersonic turbulence, a lognormal distribution is expected (e.g., Padoan et al., 1997). Supersonic turbulence is certainly present in molecular clouds, but whether it is the dominate driver of further concentration into clumps, is up for question. However, finding a lognormal distribution of clump masses is not sufficient evidence to conclude that the formation of those clumps was driven by turbulence, nor will gravitational collapse always result in a power-law distribution. Tassis et al. (2010) simulated clump formation in a variety of situations in which gravity dominated collapse, and produced lognormal distributions each time. Furthermore, they found that power-law tails emerge at late times. At these times, strong density peaks appear, as gravity dominates all opposing forces in concentrated structures. As with many such questions, the reality is likely not a binary choice between power-law and lognormal, but rather a combination of the two distributions (e.g., Hopkins, 2013; Offner et al., 2014; Basu et al., 2015). As the precursors to stars, it is important that we understand the molecular cloud clump mass distribution. Whereas individual stars form from molecular cloud cores, stellar clusters and OB associations form from clumps. Thus, the clump mass function is especially relevant when it comes to evaluating competing theories of high-mass star formation (e.g., Elmegreen, 1985; Ellsworth-Bowers et al., 2015b, for theoretical and observational descriptions respectively).

1.1.2 ISM Tracers

Molecular clouds are typically identified using emission from the lower rotational transitions in CO (e.g., Scoville & Solomon, 1975; Solomon et al., 1987). A cloud is defined by emission over a certain threshold, and velocity coherence is used to separate multiple clouds along the same line-of-sight. This tracer is only used for clouds, and not clumps or cores, due to the lowest-J transitions of CO being generally optically thick, which impedes our ability to identify the denser substructures and complicates the mass estimations of what we do identify. This problem can be somewhat mitigated by observing higher-J transitions of CO, or by observing the isotopologues of CO (^{13}CO and C^{18}O), but at the cost of weaker lines. The isotopologue approach is less dependable extragalactically than it is Galactically, since while we know the isotope ratios fairly well in the Milky Way, they are may differ substantially in other galaxies.

Further complications arise when using CO emission to find H_2 masses, since CO does not trace molecular hydrogen at a constant ratio. As the most diffuse molecular gas structures, the edges of molecular clouds transition into the neutral medium. In this transition zone, H_2 self-shields, but CO photodissociates (Wolfire et al., 2010), meaning that CO line surveys miss identifying this portion of the clouds. On the other end of the density spectrum, freeze-out dominates when densities exceed $\sim 3 \times 10^4$ cm^{-3} (Bacmann et al., 2002), meaning that CO-to-H_2 ratios will be low at clump scales. Finally, critical densities for CO line excitation are temperature dependent, leading to additional uncertainties in mass estimates.

In addition to CO, solid dust grains coexist with hydrogen gas, making up approximately 1% of the ISM by mass (Draine, 2003). There is evidence for grain growth in molecular clouds, making dust another useful tracer of molecular structures. This dust can be used in multiple manners. When colors are used to study the ISM, dust shows up as a reddening effect. At mid-IR wavelengths, such as 8 μm, dust reveals dense molecular gas through the extinction of diffuse Galactic background emission. Finally, at longer wavelengths (sub/millimeter) the energy that the dust absorbed at shorter wavelengths (causing the reddening and extinction mentioned above) is re-radiated as a thermal spectrum.

In this work, we are primarily concerned with thermal dust continuum surveys, particularly the *Herschel* infrared GALactic plane survey (Hi-GAL, see Section 1.3.1). The obvious disadvantage of using thermal dust emission as our dense gas tracer is that it lacks velocity information. This is particularly problematic towards the Galactic Center, where confusion levels are high. But, to our advantage, this emission is optically thin, allowing us to see through the entire Galactic disk. At wavelengths around 500 μm, we are observing close to the Rayleigh-Jeans limit for temperatures around 20 K. With a well agreed upon dust-to-gas ratio of 1% and dust opacities known to a factor of two (Ossenkopf & Henning, 1994), masses derived from dust can be well-constrained.

1.1.3 Galactic Observations

The past decade has produced numerous Galactic Plane surveys, allowing for detailed studies of the structure of our own Galaxy. These surveys provide data for both continuum dust emission, and CO line emission (see Section 1.3). However, despite the wealth of information made available by these surveys, very little has been conclusively determined about the overarching structure of the Milky Way. We have established that we are living in a barred spiral galaxy (Burton, 1988; Dame et al., 2001; Benjamin et al., 2005), but the number and configuration of the spiral arms is difficult to unravel, due to our location within the disk. The traditional approach to overcome our lack of a face-on view involves looking for structure within longitude-velocity ($\ell - v$) diagrams of

CO data (e.g., Dame & Thaddeus, 2011). A variety of other gas tracers have also been used (e.g., Vallée, 2008), as have trigonometric maser parallaxes (Reid et al., 2014).

On a smaller scale, CO line surveys have allowed for molecular clouds to be cataloged (e.g., Rice et al., 2016), and dust continuum surveys have allowed for their substructures, clumps and cores, to be likewise cataloged (e.g., Ginsburg et al., 2013). Through catalogs such as these, theories of star formation and galaxy evolution can be constrained (e.g., Kennicutt & Evans, 2012). Indeed, such studies of physical properties (e.g., Peretto & Fuller, 2010; Giannetti et al., 2013) and mass functions (e.g., Netterfield et al., 2009; Gómez et al., 2014; Ellsworth-Bowers et al., 2015a; Wienen et al., 2015) have already begun. However, consensus answers to questions concerning the evolution of dense molecular gas structures and their production of a universal stellar cluster mass function have not yet been reached. That is, a universal initial mass function not only for individual stars, but also for stellar clusters, has been observed (Fall & Zhang, 2001; Kroupa, 2002), but we do not know what processes within molecular cloud clumps lead to such a mass function (e.g., Dib et al., 2010, and references therein).

In addition to the physical properties of individual clouds and clumps, we can also study the distribution of these objects within the disk of the Galaxy. The radial distribution of GMCs has been investigated in the Milky Way (e.g., Scoville et al., 1987; Bronfman et al., 2000), finding a peak at intermediate Galactocentric radii, coinciding with the molecular ring. In the outer Galaxy, a precipitous drop in molecular gas surface density is seen at a distance from the Galactic Center of around 13.5 kpc (Kennicutt & Evans, 2012). In addition to radial distributions, the presence of dense molecular structures as the backbones to spiral arms is an area of active research (e.g., Wang et al., 2015).

1.1.4 Extragalactic Observations

Studying other galaxies can improve our understanding of our own Galaxy. Although they are farther away and thus not as well resolved, having a face-on view of these galaxises eases analysis. Much of what has been found in the Milky Way concerning radial trends is also seen in external galaxies, such as a decrease in GMCs with galactocentric radius after a peak at intermediate radii (e.g., Rosolowsky et al., 2007; Gratier et al., 2012; Freeman et al., 2017). Similarly, at larger kpc-scales, CO brightness peaks in the centers of galaxies or in rings at small galactocentric radii (Leroy et al., 2009; Utomo et al., 2017). Furthermore, Schruba et al. (2011) found that while H_2 surface density decreases with galactocentric radius, HI surface density does not, meaning that in the outer regions, galaxies are inefficient at converting atomic hydrogen into molecular hydrogen. Characteristic GMC masses are also seen to decrease with distance from the Galactic Center. However, the ratio of surface area located in spiral arms as opposed to the interarm region also decreases away from the Galactic Center. Therefore, it is up for debate as to whether the cause of this trend is galactocentric radius (Rosolowsky et al., 2007), or location with respect to the spiral arms (Stark & Lee, 2006; Colombo et al., 2014).

1.1.5 Simulations

In general, current simulations are more likely to comment on the distribution of baryonic mass as a whole, rather than specifically on the distribution of dense gas, or on GMCs as separate entities. The surface mass density of the gas component of spiral galaxy disks is often assumed to have an exponential profile with radius (e.g., Mo et al., 1998), a finding backed by N-body ΛCDM simulations of disk-halo interactions, but with a leveling off at small radii (Bauer et al., 2018). Distinguishing only between the warm and hot phases of the ISM, Guedes et al. (2011) simulated the formation of late-type spiral galaxies in a ΛCDM universe and found that number density of the ISM decreases with galactocentric radius, regardless of phase.

Fujimoto et al. (2014) studied the mass functions of GMCs in relation to their distance from the galactic center. By simulating a grand design barred spiral galaxy, they found that GMCs have mass distributions whose peaks are unaffected by environment, but whose tails show a higher prevalence of larger, more massive clouds nearer to the galactic center. Also with GMC resolutions, and with the addition of star formation and stellar feedback, Dobbs et al. (2011) simulated galaxy formation with and without the presence of spiral arms. They found that with spiral arms, galaxies form more massive GMCs. Only within these spiral arms can cloud masses exceed 3×10^5 $M_\odot$.

1.2 Where and when do stars form?

1.2.1 In Simulations

Given sufficient resolution, simulations could create stars when dense molecular cloud cores collapse to form them. However, this is outlandishly computationally intensive for entire-galaxy simulations. Instead, spiral galaxy simulations typically set a density threshold at which star-formation may occur. Provided that the dense region is also subject to converging flows and a cooling time which is shorter than the dynamical time, a set fraction of the gas mass is converted into stars. Density thresholds typically correspond to the neutral medium for single-galaxy simulations (e.g., Guedes et al., 2011; Dobbs et al., 2011), or even the hot ionized medium for larger cosmological simulations (e.g., Shull et al., 2012; Kim et al., 2014). Since GMCs form through colliding flows of warm neutral medium (Vázquez-Semadeni et al., 2011), the convergent flows criterion helps to ensure that this gas is in clouds, despite the low density threshold. Star formation efficiencies range from 1% to 10% per local dynamical time. This is in line with the findings of Krumholz & Tan (2007), who showed that star formation is slow on a large range of density scales, converting 1% of gas into stars per free-fall time.

Once star formation occurs in these simulations, feedback from the newly formed stars turns on. It is the inclusion and tuning of this feedback which has recently enabled the numerical modeling of long-lived spiral galaxies which reproduce observations (e.g., Katz et al., 1996; Kereš et al., 2009; Stinson et al., 2013). Because stellar feedback is driven by the formation of new stars, it is of the utmost importance that these star formation models be tested against reality.

However, numerical modeling of star formation in galaxies can do more than recreate what we see. It can also teach us about what happens if one process is removed. For example, Dobbs et al. (2011) found that while spiral arms form larger molecular clouds, they do not trigger star formation. The spiral arms merely gather gas that would have formed stars anyway. Again, the soundness of such claims is dependent on the truth of the premises. That is, on the truth of the star formation recipe.

1.2.2 Star Formation Tracers

The most direct method for tracing star formation is through the UV emission from the stars themselves (e.g., Hao et al., 2011; Murphy et al., 2011). The primary systematic effect to consider with such an approach is the attenuation of UV emission by interstellar dust. This is a serious disadvantage when looking through the dusty plane of the Milky Way. In this case, it is easier to observe the effects of the new stars on their surroundings. The very attenuation of UV light which causes problems for direct observation can be used to our advantage. It provides opportunities for indirect observations of star formation, such as emission-line tracers – the most famous of which is Hα (e.g., Hao et al., 2011; Murphy et al., 2011) – and continuum emission from the heated dust.

Whereas the cold gas of molecular cloud clumps has temperatures around 20 K, the gas and dust around newly formed stars have temperatures around 120 K, corresponding to a peak wavelength of 24 μm. This makes 24 μm thermal dust emission a popular tracer of ongoing star formation (e.g., Rieke et al., 2009). At longer wavelengths, cirrus emission becomes a more prominent contributor to the total monochromatic emission, but 70 μm emission is still frequently used as a tracer (e.g., Calzetti et al., 2010). Indeed it is preferred by some, due contamination by evolved stars at 24 μm (Svoboda et al., 2016).

1.2.3 Observations

When it comes to the observed conditions for star formation, perhaps the most famous relationship is the Kennicutt-Schmidt (KS) law. Derived using disk-averaged values, the KS law relates the surface density of star formation ($\Sigma_{\rm SFR}$) to the surface mass density of gas ($\Sigma_{\rm gas}$), as

$$\Sigma_{\rm SFR} \propto \Sigma_{\rm gas}^{N},$$

where $N = 1.4 \pm 0.15$ is the power-law exponent (Kennicutt, 1998). While this relationship is tight for disk-averaged values, the scatter increases greatly at subkiloparsec scales. At GMC scales (~ 80 pc), Onodera et al. (2010) claims that the KS law breaks down, due to the variety of evolutionary stages of the clouds, and the possibility of young clusters drifting away from their parent clouds.

On smaller scales, star-formation relations are less well known. It is generally agreed that stars form from the densest gas. That is, individual stars and simple stellar systems will form from molecular cloud cores. By the time the gas reaches this state, the core collapse efficiency is at least 25% (Enoch et al., 2008). Furthermore, Enoch et al. (2007) suggests that less than 10% of cloud mass is converted into cores, where it could potentially form stars. The fraction of clumps which are forming stars appears to be mildly affected by some environmental trend, so that there is a slight decline with Galactocentric radius (Ragan et al., 2016). However, spiral arms do not trigger star formation, although they do gather the molecular gas which will form stars (Eden et al., 2013; Ragan et al., 2016; Urquhart et al., 2018), in support of the simulations by Dobbs et al. (2011).

1.3 Galactic Plane Surveys

As our nearest galaxy, and therefore our best source of information on galaxy structure, a great deal of telescope time has been devoted to observing the Milky Way. Surveys of the Galactic Plane have been made at a wide variety of wavelengths using both photometric and spectroscopic instruments. The following surveys play major parts in the work presented in the proceeding chapters. Our primary survey is the *Herschel* infrared GALactic plane survey (Hi-GAL). In Chapter 2, we use the predecessor to Hi-GAL, the Bolocam Galactic Plane Survey (BGPS), as a point of comparison. In Chapter 4, we combine our results from Hi-GAL with the CO High Resolution Survey (COHRS) to learn about the structure of giant molecular clouds. The additional surveys described in Section 1.3.4 include supplementary surveys used in our analysis of Hi-GAL objects as well as other Galactic Plane surveys of note.

1.3.1 Herschel infrared GALactic plane survey (Hi-GAL)

The Hi-GAL science team originally planned to observe a 2° strip covering $|\ell| < 60°$, but this was extended to include the entire 360° of the Galactic Plane. By the time the entire plane was observed, the Hi-GAL survey was largest observing program taken on by *Herschel*. Observing with the SPIRE (Griffin et al., 2010) and PACS (Poglitsch et al., 2010) instruments in parallel, the *Herschel Space Observatory*, mapped the Galactic Plane in wavebands centered at 70, 160, 250, 350, and 500 μm. SPIRE (250, 350, and 500 μm) observed thermal emission from dust found within dense molecular gas clumps, while PACS (70 and 160 μm) observed comparatively warmer and more extended structures. The low optical depth of thermal dust in the submillimeter continuum allows Hi-GAL to reveal dense molecular gas structures throughout the Galactic disk.

The Hi-GAL survey has been used to advance the study of the physical properties (Elia et al., 2013) and mass functions (Olmi et al., 2013, 2014) of molecular cloud structures. The Hi-GAL team has published their first data release catalog of sources identified separately in all five of *Herschel's* photometric bands (Molinari et al., 2016). This data release covers the majority of the inner Galaxy, spanning longitudes of $-70° \leq \ell \leq 68°$. Distances to sources in a band-merged catalog were determined in Elia et al. (2017), where physical properties were also presented. In addition, this data release has been used to study the star forming fraction as a function of Galactocentric radius (Ragan et al., 2016), source clustering (Beuret et al., 2017), the Galactic bar as a star forming environment (Veneziani et al., 2017), and much more.

1.3.2 Bolocam Galactic Plane Survey (BGPS)

Similar to Hi-GAL, the Bolocam Galactic Plane Survey (BGPS) was a survey of thermal dust emission at $\lambda = 1.1$ mm. This survey was produced using the ground-based Caltech Submillimeter Observatory, and was released in two versions (Aguirre et al., 2011; Ginsburg et al., 2013), covering the longitudes $-10° < \ell < 90°$ and latitudes $|b| < 0.5°$, plus an additional 20 deg^2 of observations towards known GMC complexes. A catalog of 8,594 (Version 2) sources was produced, 20% of which have distances known to a precision of FWHM $\lesssim 2.3$ kpc. Even with its incomplete coverage of the Galactic Plane, a map of the BGPS catalog sources shows the emergence of spiral arms, as well as evidence for significant amounts of dense interarm gas (Ellsworth-Bowers et al., 2015a). In addition, the survey has been used to study topics such as the fragmentation of molecular cloud clumps (Heyer et al., 2018).

1.3.3 CO High Resolution Survey (COHRS)

The CO High Resolution Survey (COHRS; Dempsey et al., 2013) is a large-scale CO survey that imaged the inner Galactic Plane in ^{12}CO($J = 3 \rightarrow 2$) using the James Clerk Maxwell Telescope (JCMT). The survey mapped the Galactic Plane over a longitude range of $10^\circ.25 < \ell < 55^\circ.25$, with a width varying from $0^\circ.5 - 1^\circ$ of latitude, for a velocity range –30 km s^{-1} to 155 km s^{-1} with a resolution of 1 km s^{-1}. The ^{12}CO($J = 3 \rightarrow 2$) transition was chosen as being less optically thick that the $J = 2 \rightarrow 1$ and $J = 1 \rightarrow 0$ transitions. However, even this transition will be optically thick towards dense cores. The relatively diffuse material found between cores, however, will be well observed by this line. This line traces warm molecular gas (10-50 K) at moderate densities, and is therefore sensitive to GMCs with active star formation.

1.3.4 Additional Surveys

The BU-Galactic Ring Survey (GRS; Jackson et al., 2006) mapped the Galactic Plane in ^{13}CO(1-0) for longitudes $18^\circ < \ell < 56^\circ$ using the FCRAO 14-m telescope. The observations were made over the velocity range –5 to 85 km s^{-1} to a resolution of 0.212 km s^{-1}. By observing in ^{13}CO, GRS can be used to probe denser cloud substructures, where even the higher level transitions of ^{12}CO are optically thick. This survey has been used to study such topics as scaling relations within GMCs (Heyer et al., 2009), the dynamics of filamentary infrared dark clouds (Hernandez & Tan, 2011), and star formation differences in arm and inter-arm environments (Eden et al., 2013).

The Galactic Legacy Infrared Mid-Plane Survey Extraordinaire (GLIMPSE; Churchwell et al., 2009) observed the Galactic Plane in wavebands at 3.6, 4.5, 5.8, and 8.0 μm using the *Spitzer*

Space Telescope. This survey was done in parts, with GLIMPSE I imaging at longitudes of $10^{\circ}.25 < |\ell| < 70^{\circ}$, GLIMPSE II imaging $|\ell| < 70^{\circ}$ with a greater latitude range to account for the Galactic bulge, and GLIMPSE 3D increasing the latitude coverage around the central bar of the Galaxy. Furthermore, GLIMPSE 360 (Whitney et al., 2008) and Deep GLIMPSE (Whitney et al., 2011) completed the longitude coverage to include the entire Galactic Plane, but without the longest two wavebands, due to lack of the necessary coolant aboard *Spitzer*. The wavelengths observed by this survey are particularly useful in studying infrared dark clouds (IRDCs), young stellar objects (YSOs), and infrared bubbles. Thus, this survey shows its strength in the early stages of star formation, with IRDCs being the densest areas of molecular gas which are most likely to form stars, and infrared bubbles revealing O and B stars at ages of approximately 1 Myr.

Related to GLIMPSE, the MIPS Galactic Plane Survey (MIPSGAL; Carey et al., 2009) used the Multiband Infrared Photometer (MIPS; Rieke et al., 2004) aboard *Spitzer* to image the inner Galactic Plane at 24 and 70 μm. With wavebands falling between those of Hi-GAL and GLIMPSE, MIPSGAL was intended for the study of protostars and interstellar dust.

The APEX Telescope Large Area Survey of the Galaxy (ATLASGAL; Schuller et al., 2009; Csengeri et al., 2014, 2016) observed the Galactic Plane in 850 μm light using the Atacama Pathfinder Experiment (APEX). This was done over longitudes of $|\ell| \leq 60^{\circ}$, with a later extension to $\ell = -80^{\circ}$. This was the first systematic survey of the inner Galactic Plane in the submillimeter band, and has since been joined by BGPS and Hi-GAL. As such, it likewise looks at thermal dust emission from dense molecular cloud clumps. A catalog of sources has been produced by the ATLASGAL team (Contreras et al., 2013), which has been used in many publications, often in tandem with other similar catalogs (e.g., Deharveng et al., 2010; Urquhart et al., 2013).

1.4 Scope & Organization

This work builds on that of the BGPS team, in particular, that of Rosolowsky et al. (2010) and Ellsworth-Bowers et al. (2013, 2015a), who developed methods for molecular cloud clump identification and distance determination, respectively. I apply those methods to the new Hi-GAL data set. I then use the resulting catalog of molecular cloud clumps to investigate variations in physical properties with environment. When combined with the COHRS catalog of molecular clouds, this Hi-GAL clump catalog allows me to gain insight into what cloud properties influence the formation of molecular cloud clumps and stars. These conclusions provide an observational check for the star formation models utilized by numerical simulations of spiral galaxy evolution.

This thesis is composed of three articles prepared for peer-reviewed journals. Chapter 2 was published in the Astrophysical Journal (ApJ) and is cited in later chapters as Zetterlund et al. (2017). It details my methods of dense molecular cloud clump identification and distance determination. In addition, it compares my results from a subsample of Hi-GAL, to the results produced by the BGPS team. Chapter 3 was submitted for publication in Monthly Notices of the Royal Astronomical Society (MNRAS) and is cited as Zetterlund et al. (2018). In it, I produce a face-on dense gas map of the Galactic Plane for $10° < \ell < 56°$, and investigate environmental trends in clump properties. Chapter 4 is in preparation for submission. In it, I use the clump catalog from the previous chapter, along with the COHRS catalog of GMCs, to investigate which cloud properties affect their clump formation efficiency and star formation rate. Chapter 5 provides concluding thoughts and future directions in which this work may be taken. Appendices A and B provide the matched-object catalogs associated with Chapters 2 and 4, respectively.

My coauthors for Chapter 2 (Zetterlund et al., 2017) and Chapter 3 (Zetterlund et al., 2018) were Jason Glenn and Erik Rosolowsky. However, the work is largely mine and their role was one primarily of guidance. The exceptions are the interpretation of Figure 3.7 in Section 3.4.3, and the mass distribution fitting found in Section 3.4.4, which were the work of Erik Rosolowsky.

Chapter 2

Method and Initial Results Comparison with BGPS

As the precursors to stellar clusters, it is imperative that we understand the distribution and physical properties of dense molecular gas clouds and clumps. Such a study has been done with the ground-based Bolocam Galactic Plane Survey (BGPS). Now the *Herschel* infrared GALactic plane survey (Hi-GAL) allows us to do the same with higher quality data and complete coverage of the Galactic Plane. We have made a pilot study comparing dense molecular gas clumps identified in the Hi-GAL and BGPS surveys, using six $2^\circ \times 2^\circ$ regions centered at Galactic longitudes of $\ell = 11^\circ$, 30°, 41°, 50°, 202°, and 217°. We adopted the BGPS methodology for identifying clumps and estimating distances, leading to 6198 clumps being identified in our substudy, with 995 of those having well-constrained distances. These objects were evenly distributed with Galactic longitude, a consequence of Hi-GAL being source confusion limited. These clumps range in mass from 10^{-2} $M_\odot$ to 10^5 $M_\odot$, and have heliocentric distances of up to 16 kpc. When clumps found in both surveys are compared, we see that distances agree within 1 kpc and ratios of masses are of order unity. This serves as an external validation for BGPS and instills confidence as we move forward to cataloging the clumps from the entirety of Hi-GAL. In addition to the sources that were in common with BGPS, Hi-GAL found many additional sources, primarily due to the lack of atmospheric noise. We expect Hi-GAL to yield 2×10^5 clumps, with 20% having well-constrained distances, an order of magnitude above what was found in BGPS.

2.1 Introduction

Significant observational and theoretical progress has been made in the study of star formation. However, crucial aspects, such as why the stellar and star cluster initial mass functions appear uniform across many Galactic environments, remain unexplained. In order to understand stellar clusters and OB associations, it is critical to understand that from which they are formed. Thus the study of molecular cloud clumps has become a primary focus in the field of high-mass star formation (e.g., McKee & Ostriker, 2007). Large-scale studies of the Galactic dense molecular gas — its distribution and properties — are necessary in order to challenge models of galaxy evolution and reveal the origin of the stellar cluster initial mass function.

Such large-scale studies have recently become practical with the actualization of Galactic Plane dust continuum surveys at sub/millimeter wavelengths [BGPS: Aguirre et al. (2011); Ginsburg et al. (2013); ATLASGAL: Schuller et al. (2009); Csengeri et al. (2014, 2016); Hi-GAL: Molinari et al. (2010, 2016)]. These surveys have detected tens of thousands of molecular cloud clumps and cores, which can now be extracted and used to study physical properties of high-mass star formation regions. The census of Galactic dense molecular cloud structures enabled by these surveys will constrain star formation and galaxy evolution theories (e.g., Kennicutt & Evans, 2012). Such studies of physical properties (e.g., Peretto & Fuller, 2010; Giannetti et al., 2013; Elia et al., 2013) and mass distributions (e.g., Netterfield et al., 2009; Olmi et al., 2013, 2014; Gómez et al., 2014; Ellsworth-Bowers et al., 2015a; Wienen et al., 2015) have begun, but have yet to reveal a coherent story concerning the evolution of the dense interstellar medium and the uniformity of the stellar cluster mass function.

Fortunately, theoretical models of the dense interstellar medium are beginning to produce predictions robust enough to be used in conjunction with observational data to constrain the molecular cloud clump mass function (e.g., Donkov et al., 2012; Veltchev et al., 2013). This function is generally expected to take either a power-law or lognormal form, with each distribution corresponding to a different physical process in the molecular clouds. Gravitational collapse of dense structures would produce a power-law (e.g., Padoan & Nordlund, 2002). A lognormal density distribution can be produced by supersonic turbulence (e.g., Padoan et al., 1997), although such conditions are not necessary (Tassis et al., 2010). Likely, these processes are interacting within the dense molecular clouds, producing a mass function displaying a combination of these forms (e.g., Offner et al., 2014; Hopkins, 2013). Which mode dominates will have implications for the competing theories of high-mass star formation (Elmegreen, 1985).

On a grander scale, the distribution of dense molecular gas in the Milky Way has implications for using our Galaxy as the ground truth for studies of galaxy evolution. Until recently, numerical models had substantial difficulty generating long-lived spiral galaxies. This was due either to rapid depletion of gas before the disks could be sustained or the galaxies blowing themselves apart with an inadequate balance of gravity and stellar feedback. In the past two decades, remarkable progress has been made towards reproducing observed properties of galaxies (e.g., Katz et al., 1996; Kereš et al., 2009; Stinson et al., 2013). Currently, simulations that incorporate feedback into the interstellar medium from star formation and the late stages of massive stellar evolution can reliably create large spiral galaxies. However, the star formation, being unresolved in the simulations, uses prescriptive recipes tuned a posteriori. Typically, star formation is turned on at a fixed interstellar medium density threshold (e.g. 10^3 cm^{-3}), at which point $\sim 1\%$ of the gas mass is converted into stars (Kim et al., 2014). Unfortunately, numerical simulations have largely been unable to a priori produce the strong winds and inefficiency of star formation observed in galaxies (Hopkins et al., 2014). The dense molecular gas distribution is an observational key to probing the star formation efficiency on scales resolvable by simulations. Because the amount and rate of star formation drives feedback, it is imperative that these recipes are tested against reality.

We will use the *Herschel Space Observatory's* Hi-GAL survey, which provides complete coverage of the Galactic Plane in the far-infrared to submillimeter wavebands, to create such a map and test these explanations of clump mass functions and galaxy evolution models. This paper describes the method we will be using to identify Hi-GAL molecular cloud clumps and determine their heliocentric distances. It will furthermore compare the results of a number of representative test regions to BGPS, a well-vetted benchmark. However, we expect Hi-GAL to significantly supersede BGPS. Molinari et al. (2016) have independently begun cataloging the dense molecular cloud clumps found in the Hi-GAL survey. They have identified and extracted photometry for clumps found in the majority of the inner Galaxy in all five of *Herschel's* photometric bands. This work serves as a complement to the work of Molinari et al. (2016) through the use of a fundamentally different source identification technique. In addition, we go beyond their work in the determination of distances and physical properties of the clumps.

Dense molecular gas structures can be divided into three categories: clouds, clumps, and cores. Molecular clouds have denser substructures called molecular cloud clumps, which in turn have even denser substructures called molecular cloud cores. These cores are gravitationally bound and will form individual stars or simple stellar systems. Typical radii are clouds $R = 1 - 7.5$ pc, clumps $R = 0.15 - 1.5$ pc, and cores $R = 0.015 - 0.1$ pc. Typical densities are clouds $50 - 500$ cm^{-3}, clumps $10^3 - 10^4$ cm^{-3}, and cores $10^4 - 10^5$ cm^{-3} (Bergin & Tafalla, 2007). Cores are only resolvable within a couple kiloparsecs by single-dish telescopes. Clumps are detectable within ~ 7 kpc, beyond which the resolution is no longer sufficient for *Herschel*. Farther out we can only resolve entire clouds (Dunham et al., 2011).

2.2 Data

Previously, the Bolocam Galactic Plane Survey (BGPS) was made with the Caltech Submillimeter Observatory and was released in two versions (Aguirre et al., 2011; Ginsburg et al., 2013). BGPS was a $\lambda = 1.1$ mm survey over the longitudes $-10° < \ell < 90°$ and latitudes $|b| < 0.5°$, plus an additional 20 deg^2. From the survey, a catalog of 8,594 (Version 2) sources was produced, 20% of which have well constrained distances. Even with its incomplete coverage of the Galactic Plane, BGPS showed the emergence of spiral arms, as well as evidence for significant amounts of dense interarm gas (Ellsworth-Bowers et al., 2015a).

The *Herschel* infrared GALactic plane survey (Hi-GAL) (Molinari et al., 2010) originally planned to observe a 2° strip covering $|\ell| < 60°$, but was extended to include the entire 360°

of the Galactic Plane. Using the SPIRE (Griffin et al., 2010) and PACS (Poglitsch et al., 2010) instruments aboard the *Herschel Space Observatory* (HSO), this survey observed in wavebands at 70, 160, 250, 350, and 500 μm. SPIRE (250, 350, and 500 μm) observed thermal dust emission, which is concentrated in dense molecular gas clumps, whereas PACS (70 and 160 μm) observed dense gas and extended warm structures to a greater extent than the longer-wavelength SPIRE bands. Owing to the low optical depth of thermal dust in the submillimeter continuum, Hi-GAL allows us to view dense molecular gas throughout the entire Galactic disk. The flux density-limited gas mass sensitivity is 250 $M_\odot$ (5σ) at distances up to 20 kpc (corresponding with a 1σ RMS of 100 mJy at 250 μm, assuming a temperature of 20 K).

In this paper, we analyzed a representative sample of six Hi-GAL regions, centered at $\ell = 11°$, 30°, 41°, 50°, 202°, and 217°. This sample includes regions from both inner and outer portions of the Galaxy, and, with the exception of $\ell = 202°$, have a significant overlap with BGPS observations. Figure 2.1 shows the maps for the $\ell = 30°$ and 217° regions. Emission levels vary strongly depending on proximity to the Galactic Center, but there is extensive structure in all regions.

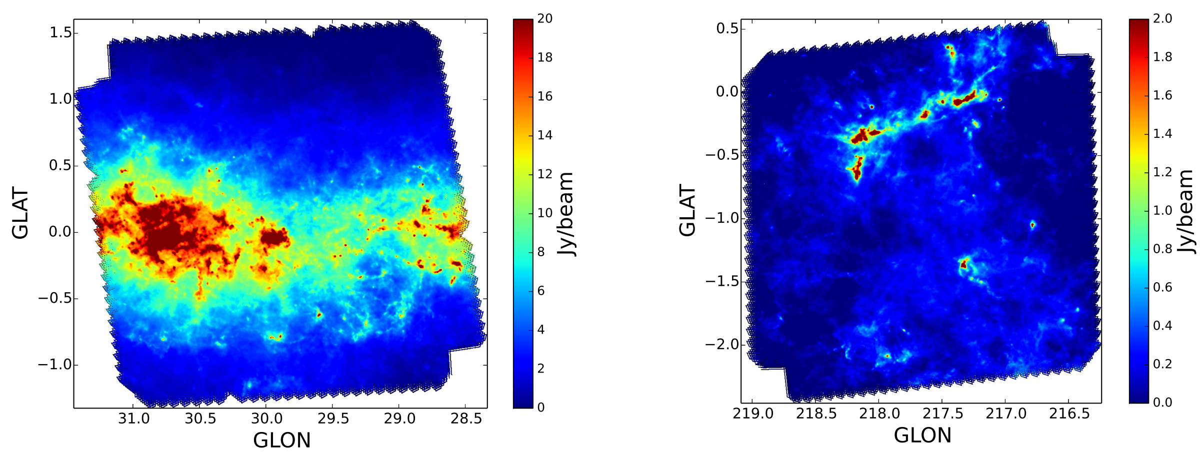

Figure 2.1: Example maps in SPIRE 500 μm from our representative sample of Hi-GAL — $\ell = 30°$ (*left*), which looks through the edge of the Galactic bar, and $\ell = 217°$ (*right*). Emission levels are significantly higher in the inner Galaxy than the outer Galaxy due both to the greater quantities of molecular gas, and to the longer optical path integrating more emission.

2.3 Method

2.3.1 Map Making

The Hi-GAL observations are stored in the Herschel Science Archive (HSA) and the Herschel Interactive Processing Environment (HIPE) allows users to access the data.[1] The tool UniHIPE was used to format the HSA data suitable to be input into the Hi-GAL mapping pipeline, Unimap (Piazzo et al., 2012, 2015a,b).

Each Hi-GAL observation is composed of two orthogonal scans. Unimap takes the time-ordered bolometer data from each scan and combines them to make a single astrophysical map, along with various evaluation maps. The pipeline begins by cleaning the time-ordered data. It removes the offset in the input data, then finds and removes signal jumps and glitches, both of which can be caused by cosmic rays. Finally, the drift, a low frequency signal due to slowly varying bolometer temperatures, is fit and removed. The time-ordered data are then made into a map, using an iterated Generalized Least Squares method. This method often leads to cross-like artifacts on bright sources, which are removed by Unimap's post-processing.

2.3.2 Filtering

The 500 μm SPIRE band has the lowest resolution of the bands, with a beam FWHM of $32''.2$, and so we convolved and rebinned all maps to 500 μm resolution to enable multiband photometry. Foreground cirrus clouds are present in all of the maps. Since this undesirable flux density is present on angular scales larger than that of molecular cloud clumps, the maps were high-pass filtered on the $3'$ scale to remove this flux density. The filtering was done in frequency-space using an inverted 2D Gaussian window with σ corresponding to $3'$. This scale was chosen for two reasons. Firs t, it is a larger angular scale than the largest of the BGPS clumps. Second, when the Hi-GAL maps were filtered on a larger scale of $\sigma = 5'$, nearly all of the clumps found were smaller than $3'$. Thus, this filtering scale removes as much extended emission as possible with minimal attenuation of

[1] `http://www.cosmos.esa.int/web/herschel/hipe-download`

molecular cloud clump sizes and flux densities (and therefore inferred masses).

Simulations were performed in order to quantify the effects of the high-pass filter. Synthetic Gaussian objects were inserted onto both the $\ell = 30^\circ$ map, and onto constant background maps. Synthetic sources were distributed randomly, but were restricted to have their centers no closer than three times the source FWHM. The maps were then filtered and objects identified by Bolocat (See Section 3.3) on the constant background map. These source masks were then used to calculate source properties on synthetic sources from the $\ell = 30^\circ$ background map. This was done for filtering scales of $\sigma = 2.4'$, $3.2'$, $4.1'$, and $4.8'$, and with various synthetic source sizes. For each combination of filtering scale and source size $\sim$1000 sources were generated, using multiple maps where necessary.

Figure 2.2 shows median attenuation factors (ratios of post-filtering recovered quantities to input quantities) for integrated flux density (S), peak flux density (S_{pk}), and FWHM. Our mean clump size corresponds most closely to the second smallest synthetic object size ($1.2'$), and 90% of our objects are smaller than the dashed line. Thus Hi-GAL clumps will have their integrated flux density attenuated by $(20 \pm 10)\%$ for our choice of a filtering scale of $\sigma = 3'$. Similarly, peak flux density will be attenuated by $< 1\%$, and FWHM will be attenuated by $(4 \pm 3)\%$.

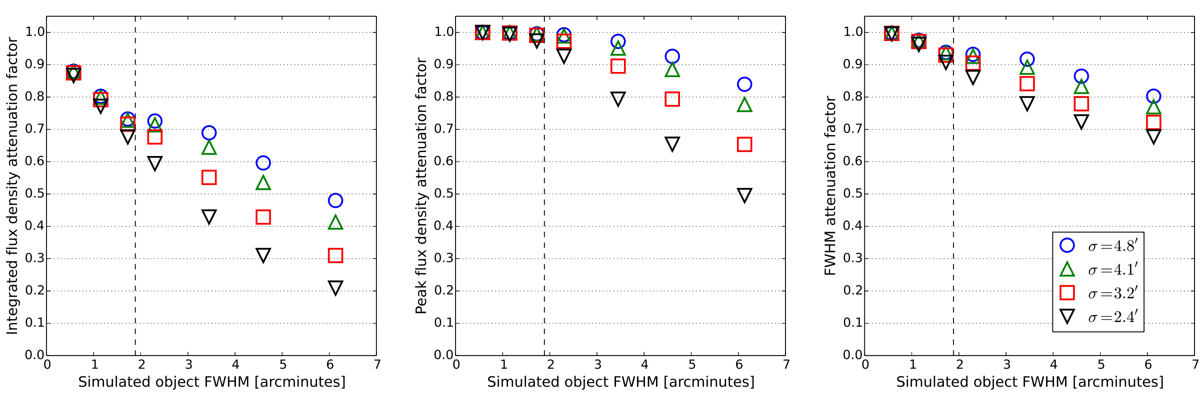

Figure 2.2: Attenuation factors for integrated flux density (*left*), peak flux density (*center*), and FWHM (*right*). Maps of simulated objects are filtered at various spatial scales. Plotted are the median attenuation factors of objects identified by Bolocat. The dashed line indicates the 90$^{\mathrm{th}}$ percentile in angular size for objects in our Hi-GAL substudy.

While the majority of the observation regions are covered by both of *Herschel's* orthogonal scans, the edges are not. We mask off the regions which are not covered by both scans to exclude these lower-quality data and to avoid confusing the clump-finding code with the original ragged map edges. This removed 29% of flux-containing pixels. We also masked off regions where the high-pass filter added flux density, as opposed to removing it. This was a consequence of the flux density on large scales being negative in these areas, and thus subtracting those negative values added flux density to the pixels. These areas were located at high galactic latitude, where flux density was low. This removed an additional $3-7\%$, depending on the field, of flux-containing pixels. The masking process is demonstrated in Figure 2.3.

2.3.3 Source Identification

Source identification was done on 500 μm SPIRE maps using Bolocat, a seeded watershed algorithm tool developed for BGPS (Rosolowsky et al., 2010). Clumps are found by first identifying regions of significant emission, where significance is determined in units of the local noise estimate. These regions of high significance are then expanded into adjacent lower significance areas, eliminating artificial small-scale structure. Finally, regions are split into multiple clumps, where appropriate, based on local maxima.

Hi-GAL is confusion limited by cirrus, large-scale structure, and source confusion that in BGPS were attenuated by an atmospheric subtraction algorithm. The flux density level of clumps which we can identify in each map is limited by the emission levels in the map. This is demonstrated in the power spectral densities (PSDs) in Figure 2.4. There is greater power along lines of sight with more interstellar medium (ISM), as well as greater power on larger scales, which may be due to source confusion or the sizes of GMCs themselves. A typical GMC with a radius of 10 pc (e.g. Solomon et al., 1987) would have to be > 23 kpc away in order to have a $3'$ extent.

With more overall emission in regions nearer the Galactic Center, sources in those regions must be brighter for us to detect them above the confusion noise. Therefore we used a constant-noise map for each region, with each "noise" map's value determined by the emission level in its

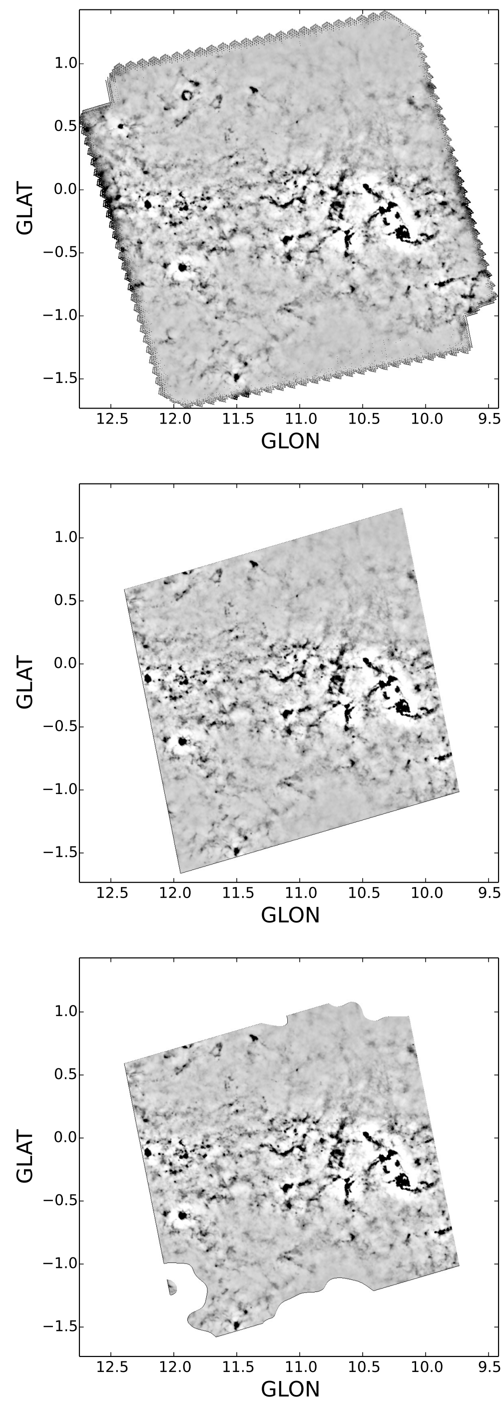

Figure 2.3: Masking the $\ell = 11^\circ$ region. *Top*: The complete high-pass filtered map. The two scan directions can be seen. *Middle*: Pixels not covered by both scans have been masked off. *Bottom*: Pixels to which the high-pass filter added flux density have been masked off.

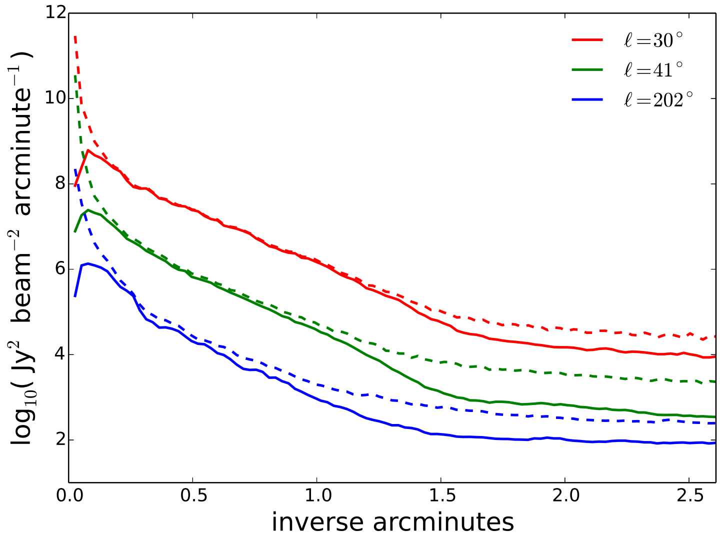

Figure 2.4: The PSDs for a representative sample of regions. Pre- and post-filtering are shown as dashed and solid lines, respectively. Emission levels on all spatial scales decrease with distance from the Galactic Center and lines of sight through the inner Galaxy have greater integrated flux density than towards the outer Galaxy.

respective emission map. This was done by fitting the distribution flux densities of pixels with positive emission to an exponential function. The noise value was taken to be proportional to the scale factor of the exponential fit, specifically 0.25λ, where λ is the scale factor. As an objective choice was not possible, this selection was made as it consistently produced object contours which matched our visual expectations across regions at widely varying Galactic longitudes. The specific value of 0.25λ for the noise was chosen after an exploration of Bolocat's parameter space, which was done using the $\ell = 41^{\circ}$ region as a test map.

The threshold for detection and the level down to which areas meeting the detection threshold were expanded were determined first. We chose to set the threshold at 3σ and to expand down to 1σ, where σ is the "noise" level. These values were chosen as they successfully included the flux density which had the appearance of real structure. A division criterion of 2σ was then decided upon. That is, if the saddle between two local maxima is different from the maxima by at least 2σ, then the clump is divided. This was chosen as it produced results consistent with what was seen in the flux density contours of the test map, a sample section of which can be seen in Figure 2.5. The initial threshold and division criterion were the same in BGPS, which only expanded down to 2σ.

Choosing a higher threshold would have decreased the number of sources found, as would have choosing a higher floor down to which to expand the regions, since clumps must be at least a beam in size. A higher expansion floor would have also decreased the size of clumps, particularly further from the mid-plane, where flux density is lower. Choosing a lower threshold for splitting clumps would also have led to smaller clumps, although clumps sizes would be limited by the requirement that local maxima must be separated by at least two beam widths. Our choices for these parameters were chosen to match our visual expectations in the test map, attempting to err on the side of a higher detection threshold and less clump division.

The high-pass filter also has associated systematic effects. A more aggressive filter would have resulted in smaller clumps. More significantly, the high-pass filter affects the flux densities of the identified clumps. Figure 2.6 compares high-pass filtered and unfiltered flux densities in the $\ell = 50^{\circ}$ region. Clumps were identified in the filtered map, with photometry re-calculated using the

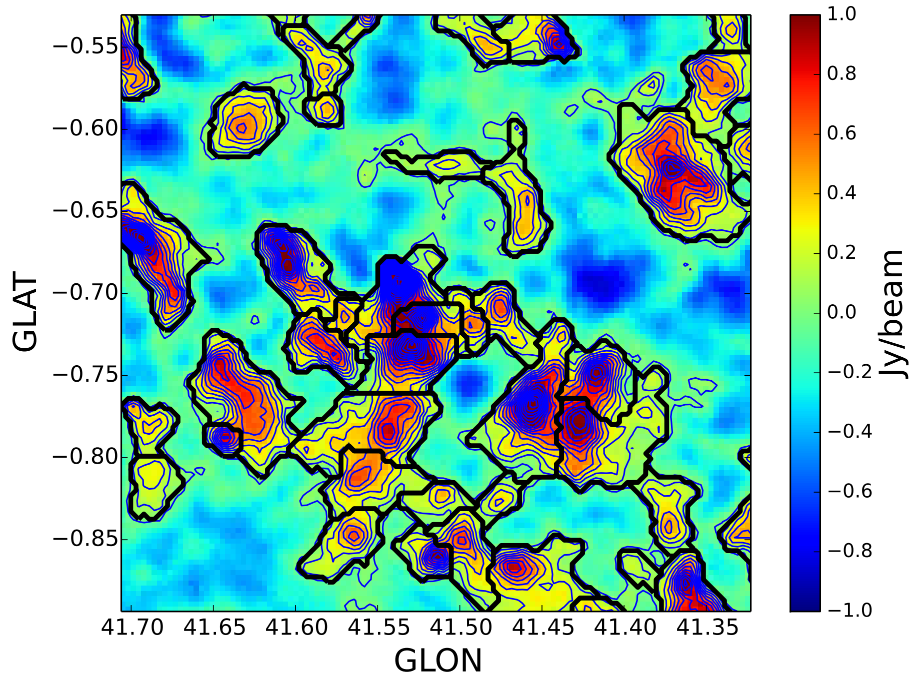

Figure 2.5: Subsection of the test map for determining Bolocat parameters. Thick black contours show object borders. Thin blue contours show flux density levels with a step size of 2σ, starting at zero.

unfiltered maps for the comparison. Photometry was done by summing the flux density found in the pixels within the source boundary, as opposed to background-subtracted aperture photometry. No clump exceeds a flux density ratio of unity by construction, as the small percentage of pixels where the filter added flux density were excluded from source finding.

There is a trend towards the clump containing a higher fraction of the total flux density along the line of sight for higher flux density clumps. On the other hand, the faintest clumps have a wide range of flux density ratios. These trends are seen in all of the regions in this substudy.

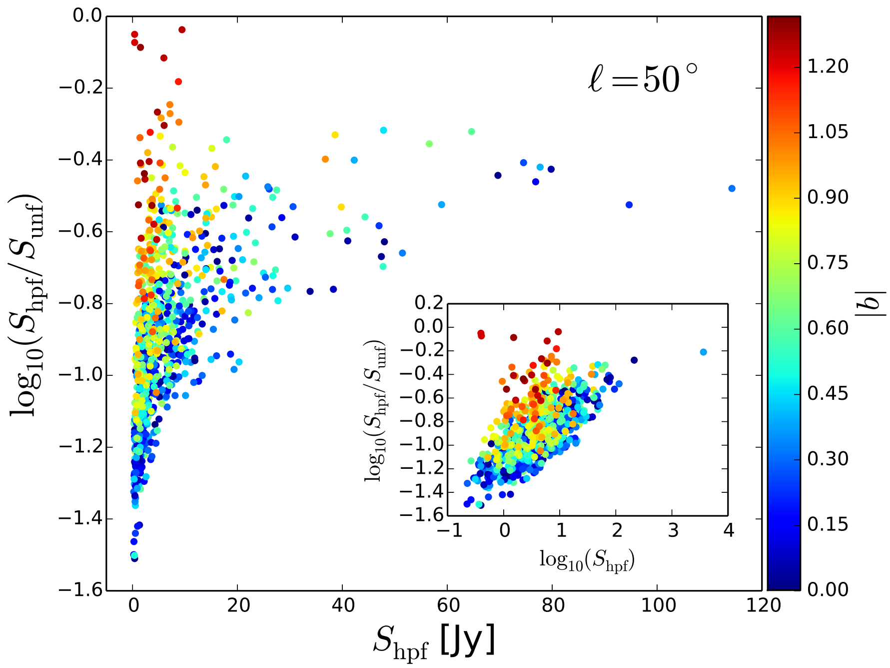

Figure 2.6: Comparison of high-pass filtered and unfiltered flux densities for the $\ell = 50^\circ$ region. $S_{\rm hpf}$ is the clump's total flux density, taken from the high-pass filtered map in which it was identified, and $S_{\rm unf}$ is the total flux density in the unfiltered map which lies within the clump's border. Colors correspond to absolute value of Galactic latitude.

2.3.4 Distance Determination

This distance determination method was developed for BGPS by Ellsworth-Bowers et al. (2013) and Ellsworth-Bowers et al. (2015a), and resulted in 1,710 well-constrained distances. Full details of the method are available in Ellsworth-Bowers et al. (2013, 2015a), and a summary is provided here. To construct a 3D map from the sources identified in Hi-GAL and to compute their physical properties, heliocentric distances must be determined. Every line of sight has a function $V_r(d_\odot)$, found from a Galactic rotation curve, describing radial velocity as a function of heliocentric distance. Kinematic distances can be determined by matching a clump's $v_{\rm LSR}$ to $V_r(d_\odot)$. However, within the inner Galaxy, this information results in two possible kinematic distances and an ambiguity as to which is the true distance. This ambiguity will be broken using probabilistic methods in a Bayesian framework. A unique distance probability density function (DPDF) will be calculated for each source. The posterior DPDF is found by

$$\mathrm{DPDF} = \mathcal{L}(d_\odot|\ell, b, v_{\rm LSR}) \prod_i P_i(d_\odot|\ell, b),$$

where $\mathcal{L}(d_\odot|\ell, b, v_{\rm LSR})$ is the kinematic distance likelihood, and the $P_i(d_\odot|\ell, b)$ are various Bayesian priors which will help determine which distance has the higher probability of being true. Once DPDFs are calculated, they can be drawn from in Monte Carlo simulations, even when distances are not well constrained, and thus cloud clump properties can be characterized, with robust uncertainties.

The rotation curve from the Reid et al. (2014) BeSSeL survey, derived from maser parallax measurements to sites of high-mass star forming regions ($-12^\circ \leq \ell \leq 240^\circ$), was paired with line-of-sight velocities derived from the ^{13}CO Galactic Ring Survey (GRS) to determine the kinematic distances to the molecular cloud clumps. Because there are often multiple velocity components in GRS spectra, each source spectrum is created by subtracting the spectrum of an off-source region from that of the on-source region. The off-source region is determined by creating a rind around the source mask, then excluding pixels associated with other Hi-GAL sources. In this way we eliminate the velocity components not associated with the clump from the clump's spectrum (see Ellsworth-Bowers et al., 2015a, Section 4). Dense gas tracer observations of specific sources, originally made for BGPS, were also utilized. These observations were associated with the new Hi-GAL sources through the object masks obtained from Bolocat. The most powerful P_i implemented in BGPS used absorption by the clumps of diffuse Galactic mid-infrared emission near $\lambda = 8$ μm. When the majority of this diffuse emission lies in the background, the molecular cloud clump is called an infrared dark cloud (IRDCs) (Perault et al., 1996; Simon et al., 2006; Peretto & Fuller, 2009; Battersby et al., 2011). Ellsworth-Bowers et al. (2013) defined the term 8 μm absorption feature to include molecular cloud clumps which exhibit any $\lambda = 8$ μm intensity decrement, thus allowing for absorption less pronounced than seen in IRDCs. The P_i developed to take advantage of this feature uses the Galactic infrared emission model of Robitaille et al. (2012) to simulate clumps at various heliocentric distances. These simulated images are then compared to the corresponding GLIMPSE (Churchwell et al., 2009) IRAC Band 4 image, using a χ^2 statistic, to generate the P_i.

The EMAF morphological matching of synthetic GLIMPSE based on Hi-GAL flux density and actual GLIMPSE maps works far better with high-pass filtered maps than with unfiltered maps. In the unfiltered maps, the presence of cirrus emission contributes too much flux to the clumps, causing them to be placed much further away than is plausible. Use of a $\sigma = 3'$ Gaussian high-pass filter removes the cirrus emission and remedies this problem. Two examples from the $\ell = 41^\circ$ region are shown in Figure 2.7.

Three additional P_is were developed by Ellsworth-Bowers et al. (2013). First, the molecular hydrogen (H_2) uses the small scale height of molecular gas in the disk to constrain clumps at high latitudes to be at their near kinematic distances. This is done using the three-dimensional model of the distribution of molecular gas in the disk of Wolfire et al. (2003). Second, the maser parallax P_i uses distances measured by the BeSSeL survey to precisely determine distances to its 100+ cataloged sources. Third, the known distances P_i associates molecular cloud clumps with giant molecular clouds (GMCs) found in the GRS catalog of Rathborne et al. (2009), and uses the GMC physical properties derived by Roman-Duval et al. (2010).

2.4 Results: Comparison to BGPS

A visual comparison of Hi-GAL and BGPS using the $\ell = 11^\circ$ region is seen in Figure 2.8. The Hi-GAL map is shown unfiltered and high-pass filtered, but the clumps were identified in the

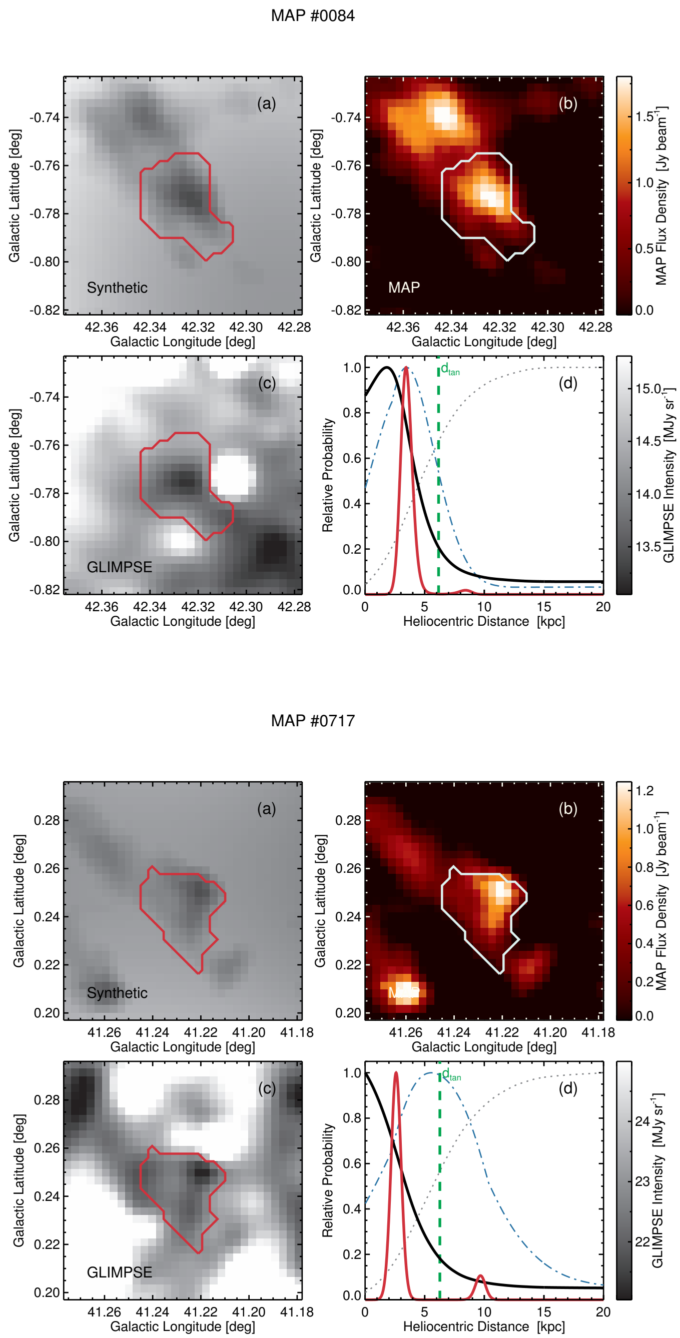

Figure 2.7: Two examples of EMAF morphological matching in the $\ell = 41^\circ$ region. Panels (a) on the left and right show the synthetic GLIMPSE map based on the SPIRE 500 μm map shown in the (b) panels. The synthetic maps shown are the best match to the GLIMPSE map shown in panels (c). Pixels with 8 μm emission instead of absorption were excluded from the morphological matching. DPDFs are shown in panels (d), with black and red corresponding to EMAF and posterior DPDFs, respectively.

filtered map. As is readily seen, there are many more clumps found in Hi-GAL than over the same region of BGPS. Furthermore, the clumps are larger in Hi-GAL than they were found to be in BGPS. Comparing the Hi-GAL clump borders with the BGPS maps shows that much of what looked like 1/f noise in BGPS was actually sources which failed to meet the detection criteria. Hi-GAL's higher sensitivity to slightly larger angular scales allows us to identify this flux as coming from clumps with greater confidence than was possible with BGPS. Conversely, BGPS identified almost nothing which was not identified in Hi-GAL, confirming the low false positive rate of BGPS, which was previously derived from simulations.

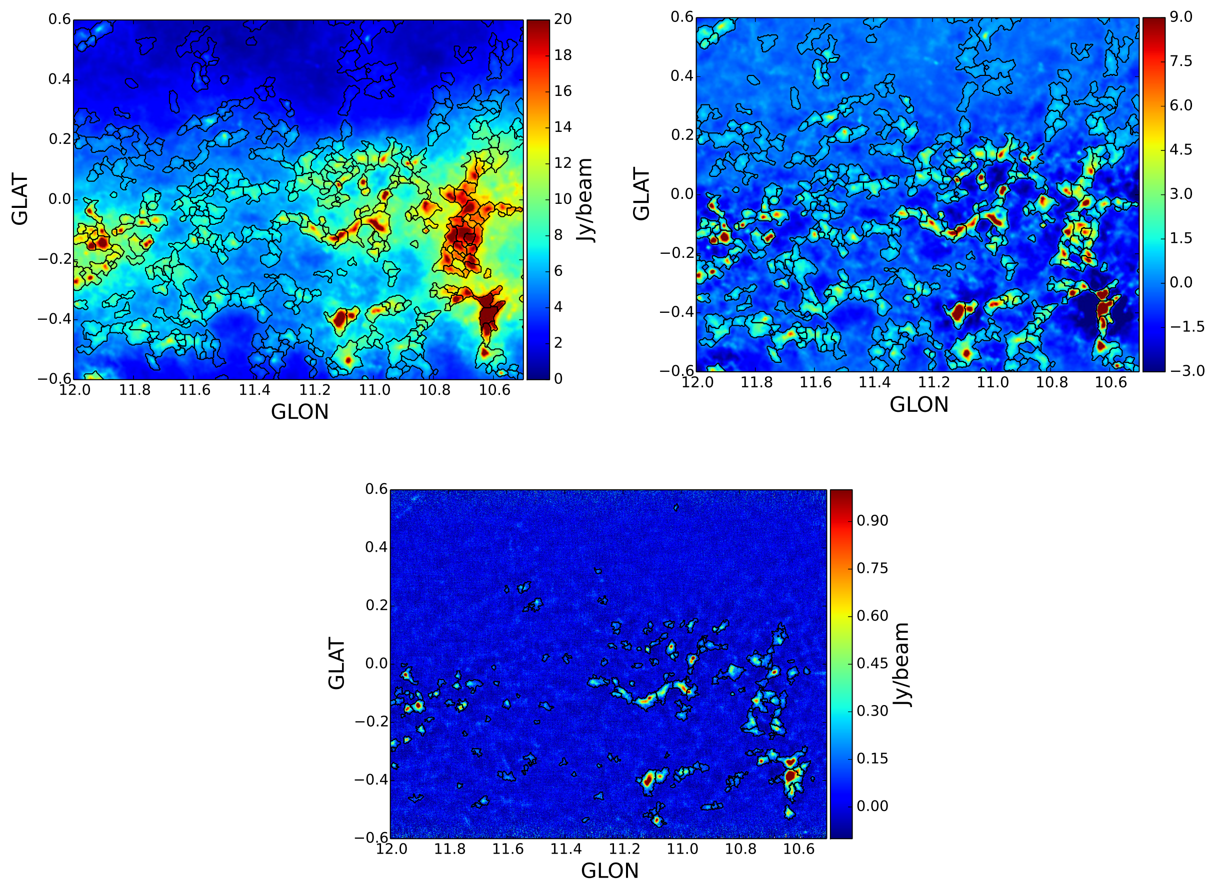

Figure 2.8: Comparison of molecular cloud clumps identified in the same $\ell = 11°$ region of Hi-GAL 500 μm (*upper*: unfiltered *left*, high-pass filtered *right*) and BGPS (*lower*). Hi-GAL's higher S/N and absence of atmospheric emission allow for more clumps to be identified than in the ground-based BGPS.

Table 2.1: Distance Statistics

Region*	Total Clumps	Some Distance Information	Well-constrained Distance
$\ell = 11°$	875	96	40
$\ell = 30°$	979	588	320
$\ell = 41°$	1027	567	243
$\ell = 50°$	923	582	392
$\ell = 202°$	1346	0	0
$\ell = 217°$	1048	0	0
sum	6198	1833	995
BGPS†	8594	3508	1710

*Each region is Hi-GAL unless otherwise specified, with Hi-GAL regions having dimensions of $2° \times 2°$.
†Data are for the entirety of BGPS.

2.4.1 Clump Densities on the Sky

Table 2.1 shows the number of clumps in a selection of complete Hi-GAL regions, as well as all of BGPS. Each region is $2° \times 2°$. Listed are the number of total clumps, the number of clumps with some distance information, and the number of clumps with well-constrained distances. Clumps were considered to have "well-constrained" distances if their DPDFs had a $\mathrm{FW}_{68} \leq 2.3$ kpc. That is, the isoprobability confidence region surrounding the distance of maximum likelihood which contains 68.3% of the total integrated probability has a full width less than 2.3 kpc. This was adopted from Ellsworth-Bowers et al. (2013), which found an empirical cut-off at this point such that clumps with $\mathrm{FW}_{68} \leq 2.3$ kpc either had 78% of the total integrated probability within the most likely kinematic peak, or were located at the tangent distance. Clumps with kinematic distances, regardless of whether the posterior DPDF met the well-constrained criteria, are considered to have some distance information. GRS observations are not available in $\ell = 11°, 202°,$ or $217°$, but there are directed observations of dense gas tracers in $\ell = 11°$. There is a slight tendency towards more clumps being identified in regions with lower levels of confusion, such as those in the outer galaxy.

Properties of clumps individually could only be compared where clumps identified in each survey aligned with one another. Therefore the overlapping subsections of each map pair were studied for such clumps. Table 2.2 compares the number of clumps found in these overlapping Hi-GAL and BGPS subregions. Listed are the number of total clumps, the number of clumps with some distance information, and the number of clumps with well-constrained distances. The reduction in number of Hi-GAL clumps in Table 2.2 as compared to Table 2.1 is primarily due to the smaller Galactic latitude range covered by BGPS as compared to Hi-GAL. Note that the regions are not consistently sized, and thus comparing numbers between regions is not a useful exercise. Information on the individual clumps being compared is listed in the Appendix.

In the $\ell = 11^\circ$ region, the numbers would indicate more clumps with distance information in BGPS than Hi-GAL. However, upon examination of the maps, it is apparent that this is only due to 5 single Hi-GAL clumps being split into two BGPS clumps each, and one single BGPS clump being split into two Hi-GAL clumps. Thus the numbers of clumps with distance information are equal in this region. There are no additional clumps with distance information in Hi-GAL for this region due to it not being covered by GRS. The only velocities are thus from directed observations of dense gas tracers done for BGPS. All additional distances are due to GRS. While the known distances prior, which associates nearby clumps with one another, was used, it did not provide any additional distances in this subset of Hi-GAL observations. The $\ell = 202^\circ$ and 217° regions has no distance information due to the lack of GRS observations in the outer Galaxy and a lack of directed observations.

2.4.2 Angular Sizes

The distributions of deconvolved angular radii is shown in Figure 2.9 for Hi-GAL (left) and BGPS (right). Rosolowsky et al. (2010) defined the deconvolved radius θ_R of a clump as the geometric mean of the deconvolved major and minor axes of the flux density distribution,

$$\theta_R = \eta[(\sigma_{\text{maj}}^2 - \sigma_{\text{beam}}^2)(\sigma_{\text{min}}^2 - \sigma_{\text{beam}}^2)]^{1/4}.$$

Table 2.2: Distance Statistics: Overlapping Subregions

Region	Area (deg^2)	Survey	Total Clumps	Some Distance Information	Well-constrained Distance
$\ell = 11^\circ$	1.80	Hi-GAL	376	53	30
		BGPS	190	57	34
$\ell = 30^\circ$	1.44	Hi-GAL	394	234	95
		BGPS	238	187	73
$\ell = 41^\circ$	2.64	Hi-GAL	650	383	107
		BGPS	63	55	20
$\ell = 50^\circ$	2.64	Hi-GAL	575	385	232
		BGPS	57	48	33
$\ell = 202^\circ$	0.85	Hi-GAL	171	0	0
		BGPS	10	0	0
$\ell = 217^\circ$	1.89	Hi-GAL	323	0	0
		BGPS	15	0	0

For Hi-GAL $\sigma_{\rm beam} = \theta_{\rm FWHM}/\sqrt{8 \ln 2} = 15''$, $\theta_{\rm FWHM} = 35''$, and $\eta = 2.4$ is a factor relating the rms size of the emission distribution to the true size of the source, which is adopted from Rosolowsky et al. (2010). Note that if $\sigma_{\rm min} < \sigma_{\rm beam}$ the deconvolved angular radius is non-real. This is the case for 14% of our sources, arising from finite S/N. Mean angular radii for Hi-GAL and BGPS sources are $71 \pm 33''$ and $51 \pm 24''$, respectively. Both follow log-normal distributions (with shape parameters of $\sigma = 0.34 \pm 0.02$ and $\sigma = 0.37 \pm 0.01$, respectively), shown in red. We expect that the lognormal distribution is a result of random processes in the observations (such as variations in clump distances and intrinsic sizes), an interpretation which is consistent with the central limit theorem. Thus, Figure 2.9 is intended to demonstrate the difference in typical sizes found in the two surveys.

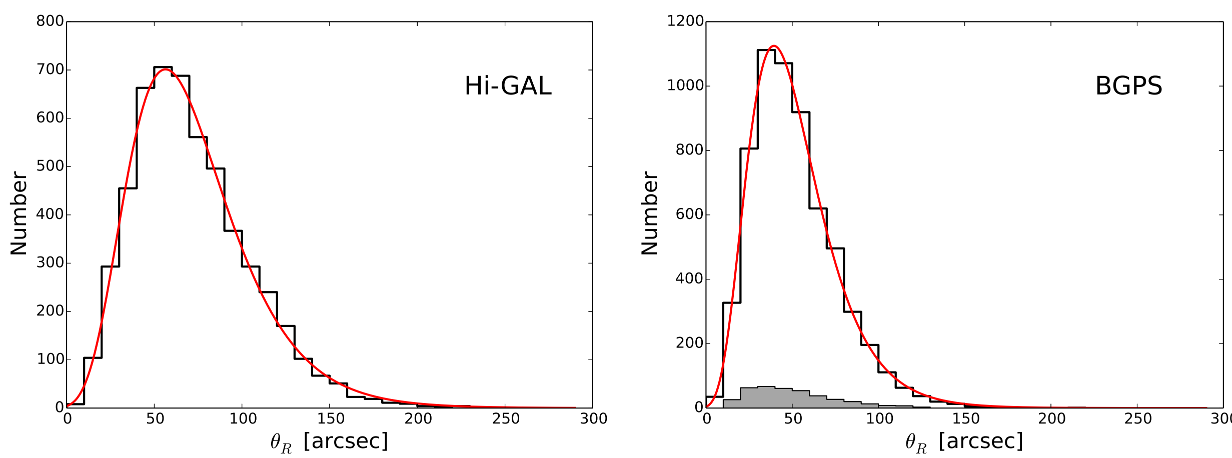

Figure 2.9: Distributions of deconvolved angular radii with log-normal fits in red. Hi-GAL is shown on the left, including clumps from all of the regions in this substudy, and has a shape parameter of $\sigma = 0.34$. BGPS is shown on the right (with all resolved sources included) and has a shape parameter of $\sigma = 0.37$. In grey is shown the subsample of BGPS clumps found in regions overlapping our Hi-GAL substudy.

A comparison of the angular radii of clumps matched between Hi-GAL and BGPS is seen in Figure 2.10. While we do not expect a consistent one-to-one ratio in angular radii, we do expect Hi-GAL clumps to be larger, and this is generally what we see, although less so with those clumps found in the $\ell = 30^\circ$ region. Dashed lines show a factor of 2 in slope on either side of the identity line and demonstrate the dearth of objects in the lower right of the plot, as compared to the upper left. Clumps can be significantly larger in Hi-GAL due to the dimmer edges of the clumps being above the noise in Hi-GAL, where they were not in BGPS. The $\ell = 30°$ region contains the edge of the Galactic bar, the bright emission and high confusion levels of which led to the high-pass filter creating more extensive negative bowls. This subtracted more flux than was ideal around the bright Galactic bar, and thus removed flux from the comparatively dim edges of the clumps in this region, to the extent that they were found to be smaller in Hi-GAL than in BGPS. Also of note are the clumps on the left edge of this plot. These are clumps which were unresolved in BGPS, but which we can now resolve with Hi-GAL because Hi-GAL detected faint, extended emission.

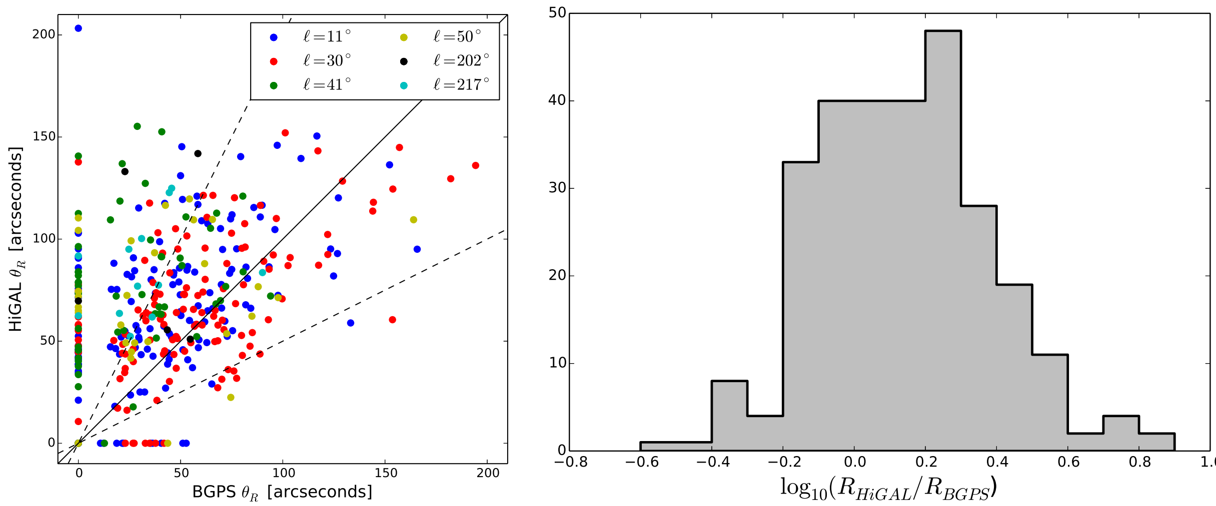

Figure 2.10: *Left*: Angular radius in Hi-GAL plotted against angular radius in BGPS, for clumps found in both surveys. Only those clumps which had well constrained distances in both surveys were used for this comparison. Colors correspond to the Hi-GAL region in which the clump was found. Note that in the line of unresolved BGPS clumps on the left of the plot, sources from the $\ell = 11°$ and $30°$ regions are covered by later regions, and not lacking. The solid line is where the radii are equal, while the dashed lines show a factor of two in either direction. *Right*: Hi-GAL to BGPS radius ratios of matching clumps, excluding those which are unresolved. The mean $\log_{10}(R_{\rm HiGAL}/R_{\rm BGPS})$ is 0.14, with a standard deviation of 0.24.

Figure 2.10 also shows the ratio of radii in the two surveys, for the same objects, but with unresolved objects excluded. The median and mean radius ratios are 1.37 and 1.61, respectively. This agrees with the difference in overall mean radii from the two surveys, as derived from Figure 2.9.

2.4.3 Clump Masses

Masses can be calculated for those clumps with well constrained distances using the high-pass filtered flux densities at 500 μm and the most probable distances from the clumps' DPDFs. The conversion from flux density to mass is

$$M = \frac{Rd_{\odot}^{2}}{\kappa_{500} B_{500}(T)} S_{500},$$

where $R = 100$ is the gas-to-dust mass ratio, $\kappa = 5.04$ cm^{2}g^{-1} is the opacity at 500 μm (Ossenkopf & Henning, 1994), $B_{500}(T)$ is the Planck function at 500 μm, $d_{\odot}$ is the heliocentric distance, and S_{500} is the integrated flux density. Battersby et al. (2011) used pixel-by-pixel modified blackbody fits of Hi-GAL data to determine that mid-infrared-dark molecular cloud clumps generally span the temperature range 15 K $\lesssim T \lesssim$ 25 K. Furthermore, Dunham et al. (2011) found an NH_3 gas kinetic temperature of $\langle T_K \rangle = 17.4 \pm 5.5$ K for a sample of 199 BGPS sources. For consistency with BGPS, and following these findings, we assume a clump temperature of 20 K.

So as not to limit ourselves to comparing only those clumps which have well constrained distances in both surveys, we calculate mass ratios while holding heliocentric distance constant. Figure 2.11 shows the ratio of clump masses in Hi-GAL to masses in BGPS, using those clumps listed in the Appendix. Where the ratio is significantly greater than one, the Hi-GAL clumps have much larger angular radii than their BGPS counterparts.

The median mass ratio for the 384 compared clumps is 1.60, and the mean is 2.02. Taken individually, each region had a mean mass ratio within one standard deviation of the other regions. Based on the difference in mean angular radii between the two surveys found in Section 4.2, we would expect this ratio to be 2.7 under the assumption that mass scales as the cube of the angular radius. The observed mass ratio scales as the angular radius squared, suggesting that the clumps are centrally concentrated.

With so few sources available for mass comparison, rather than the precise ratios, the meaningful results are that the median ratio of Hi-GAL mass to BGPS mass is of order unity, and that Hi-GAL masses are generally greater. The same can be said of radii, consistent with greater

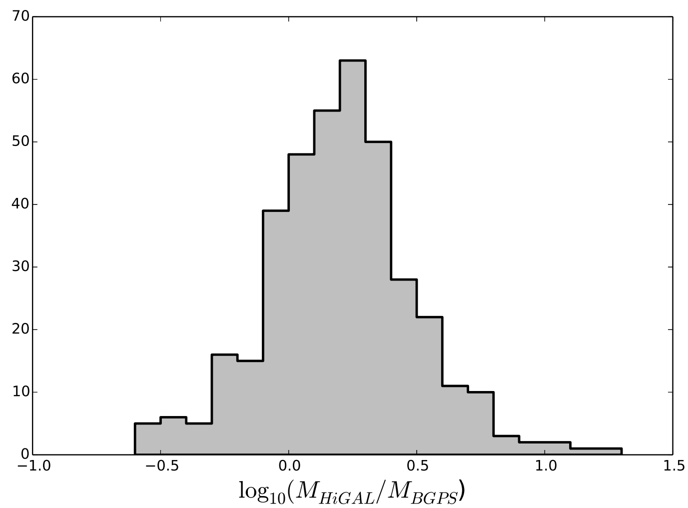

Figure 2.11: Hi-GAL to BGPS mass ratios of all matching clumps. The mean $\log_{10}(M_{\mathrm{HiGAL}}/M_{\mathrm{BGPS}})$ is 0.20, with a standard deviation of 0.29.

sensitivity to large-scale structure in Hi-GAL than BGPS, owing both to higher S/N and absence of atmospheric emission in Hi-GAL.

The distribution of masses against physical radii for all resolved Hi-GAL clumps with well-constrained distances is seen in Figure 2.12. Physical radii are calculated as $R = \theta_R d_\odot$, where θ_R is angular radius and $d_\odot$ is heliocentric distance. Points are colored by heliocentric distance, $d_\odot$. If mass scaled as radius cubed, as would happen if the clumps were of constant density, we would see a slope of 3. The figure shows a slope closer to 2 than to 3, thus indicating centrally concentrated masses. (The data are consistent with radial density profiles proportional to $1/R$; however, we caution against concluding a power-law profile in the absence of detailed modeling, including temperature profiles.) Malmquist bias is seen in that the smallest clumps are found at the nearest heliocentric distances, with the largest, most massive objects, being found distant to us.

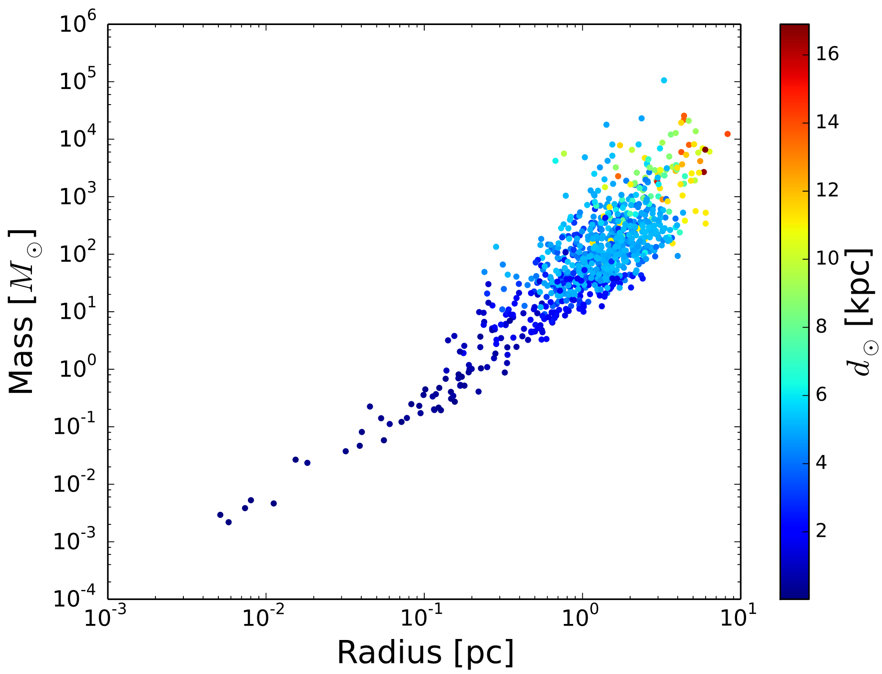

Figure 2.12: Mass plotted against physical radius for all resolved Hi-GAL sources with well-constrained distances. Colors correspond to heliocentric distance, $d_\odot$.

2.5 Discussion

Compared to BGPS, Hi-GAL detects more sources in all Galactic regions, due to the lack of atmospheric noise. It is especially true in the outer Galaxy, where most sources which are detected with Hi-GAL were lost below the atmospheric noise in BGPS. In BGPS the number of clumps dramatically decreased as observations moved further from the Galactic Center. Hi-GAL continues to see sources far from the Galactic Center, as well as at Galactic latitudes farther from the the mid-plane.

We identified a relatively constant number of clumps in each region, and, with a mean of 1033 clumps per $2^\circ \times 2^\circ$ region in our sample, we can expect nearly 2×10^5 clumps throughout the entire 360° of Hi-GAL. This is in excellent agreement with Molinari et al. (2016), who found 85,460 clumps in Hi-GAL at 500 μm between $\ell = -70^\circ$ and $\ell = 68^\circ$. When extrapolated linearly, this predicts 2.2×10^5 clumps in the entire Galactic Plane. In those regions where GRS is available, 59% of clumps had some distance information, and 33% had well-constrained distances. Thus, in the full $15^\circ \leq \ell \leq 56^\circ$ range covered by GRS, we can expect approximately 25,000 clumps with some distance information, and 14,000 clumps with well-constrained distances. We will be including other molecular line surveys in addition to GRS: MALT90 (Jackson et al., 2013), ThrUMMs (`http://www.astro.ufl.edu/~peterb/research/thrumms/`), and SEDIGISM (`http://colloques.lam.fr/GESF2014/S3/092_SCHULLE_Frederic.pdf`). Once these surveys and the lack of a kinematic distance ambiguity in the outer Galaxy are accounted for, we expect some distance information for 50% of clumps and well-constrained distances for 20% of clumps. This corresponds to 100,000 clumps and 40,000 clumps, respectively, providing a very large sample for investigating Galactic structure and physical properties of molecular cloud clumps.

BGPS used very different techniques for data reduction and large-scale structure removal than what we employed for Hi-GAL. Atmospheric emission was removed directly from the BGPS time-stream. In addition to removing atmospheric emission, this acted as an angular filter, allowing only emission on scales less than about $6'$ — which roughly corresponded with the array field of view of $7'.5$ — into the map. An iterative mapping algorithm then restored much of the structure removed in the sky subtraction (Aguirre et al., 2011). Since we had no need to remove atmospheric emission from Hi-GAL, we used a high-pass filter after the maps were made to remove large-scale, smooth dust emission. Despite these very different methods for large-scale structure removal, Hi-GAL and BGPS produce remarkably similar masses. The differences in masses, namely, that Hi-GAL produced generally higher masses, were expected. This is because Hi-GAL can see down to lower flux density levels and therefore can see down to the faint edges of clumps, where often BGPS could only see the brighter central regions.

Of the clumps matched between the two surveys, where the matched were one-to-one and both clumps had well-constrained distances, those distances agreed almost universally within 1 kpc. The one exception was placed at the near distance by BGPS using the HII Region Discovery Survey lookup table prior. In Hi-GAL, this prior was overridden by an EMAF not found by BGPS, which placed the clump at the far distance. Where a single clump in one survey was split in the other survey, distances for each member of the match agreed within 1 kpc, again with one exception. In this case, one Hi-GAL clumps combined two BGPS clumps, one of which had its placement at the tangent distance overridden by an EMAF placing it at the far distance.

The technique used by Molinari et al. (2016) to identify clumps in Hi-GAL was very different from our method. They used the CuTEx algorithm, which first identifies pixels above a curvature threshold. It then simultaneously fits elliptical Gaussian functions and a second-order background surface. Despite the disparate philosophies behind our clump identification techniques, our clump counts are impressively similar. Furthermore, we both see sources at all Galactic latitudes covered by Hi-GAL. Our clumps have slightly larger angular sizes, and once distances for the objects in the Molinari et al. (2016) catalog are determined, we can compare physical properties. That we found such similar results confirms that the objects we are finding are indeed clumps, thus validating both of our results.

The distribution of clumps found in our study of the $\ell = 217^{\circ}$ region correspond well visually with what Elia et al. (2013) found in their study of the same Hi-GAL region. The brighter filaments match up particularly well, and although we find more faint clumps, this is understandable, since their study was concerned only with objects for which there was a CO(1–0) velocity measurement. Although we do not yet have distances — and therefore masses and physical radii — for clumps in this outer Galaxy region, it can be noted that the masses and radii for our inner Galaxy clumps span a broader range than those of Elia et al. (2013). We find clumps down to smaller masses, as well as up to greater masses, and similarly for physical radii.

In future work we will extend beyond our sample of six regions and identify clumps in the entirety of Hi-GAL. We will also incorporate other molecular line surveys for the purpose of obtaining kinematic distances for clumps in areas of the Galactic Plane not covered by GRS. Furthermore, we will develop two additional priors. The first relies on molecular cloud clumps' absorption of starlight at short wavelengths and uses that to determine near-infrared extinction (NIREX) distances (Marshall et al., 2009). The second, H I self-absorption (HISA) and H I emission / absorption (HIE/A) techniques, was introduced by Roman-Duval et al. (2009) and Anderson & Bania (2009), and used on ATLASGAL clumps by Wienen et al. (2015).

2.6 Conclusions

We have made a pilot study with Hi-GAL, comparing dense molecular gas clumps in the Hi-GAL and BGPS surveys. When clumps found in both surveys are compared, derived distances agree within 1 kpc and masses are of order unity, with the mean Hi-GAL to BGPS mass ratio being 1.91. This serves as an external validation for BGPS and instills confidence as we move forward to cataloging the clumps from the entirety of Hi-GAL.

In addition to the sources which were in common with BGPS, Hi-GAL found many additional sources, primarily due to the lack of atmospheric noise. This is especially the case in the outer Galaxy. Being confusion limited, as opposed to atmospheric noise limited, means that we are able to detect clumps to lower flux densities in the outer Galaxy. Whereas BGPS produced a catalog of 8,594 clumps, 20% of which which have well-constrained distances, we expect Hi-GAL to yield 2×10^5 clumps, again with 20% having well-constrained distances.

Chapter 3

Dense Gas Map and Environmental Trends

In the quest to understand high-mass star formation, it is necessary to understand that from which the high-mass stars will form – the dense molecular gas clouds and clumps. The *Herschel* infrared GALactic plane survey (Hi-GAL) is a comprehensive survey of thermal dust emission that can be used to characterize the properties and Galactic distribution of molecular gas. We have analyzed the survey maps within the Galactic longitude range $10° < \ell < 56°$ and have transformed these 2D maps into a 3D dense gas map of the Galactic Plane using distance probability density functions. This range corresponds to the extent of the Galactic Ring Survey (GRS), which provided the majority of our line-of-sight velocities, and thus kinematic distances. In this section of Hi-GAL, we identify 19,886 clumps, out of which 10,124 have, at minimum, a kinematic distance, and 5,405 have their distances well constrained through Bayesian techniques. Of those with well-constrained distances, clump masses tend to decrease with Galactocentric radius, whereas clump radii are independent of Galactocentric radius.

3.1 Introduction

As it is the host of star formation, it is important that we understand the distribution and properties of molecular gas in our Galaxy. While much progress, theoretical and observational, has been made in the study of star formation, understanding the apparent uniformity of the initial mass functions for stars and star clusters (e.g. Kroupa, 2002) requires understanding their precursor material. However, not all molecular gas will form stars. Rather, it is *dense* molecular gas (Gao

& Solomon, 2004) that shows the closest connection to the star formation process. The correlation between the amount of dense molecular gas and the star formation rate appears linear on both global and local scales (Wu et al., 2007).

This linear relationship has been the basis for many effective models of star formation, especially in simulations of star formation and galaxy evolution. Current simulations use prescriptive recipes for star formation which are tuned such that the empirical relationship is produced, as opposed to using physically motivated parameter choices. A typical example has star formation turned on at a fixed interstellar medium density threshold (e.g. 10^3 cm^{-3}), at which point $\sim 1\%$ of the gas mass is converted into stars (e.g. Guedes et al., 2011; Kim et al., 2014; Dobbs, 2015). This route is taken because star formation is unresolved at the resolution of entire-galaxy simulations, but nevertheless, it presents a problem when these simulations cannot a priori reproduce the strong winds and star formation inefficiency observed in galaxies (Hopkins et al., 2014).

More recently, Usero et al. (2015) has suggested that this strictly linear relationship does not completely capture the complexities of star formation efficiency. Instead there is a dependency on galactocentric radius, with efficiency being lower nearer galaxy centres. Properties of the clouds as a whole, such as turbulence, may play a part.

With the presence of dense gas being the dominant factor in star formation efficiency, it is important that we understand how dense gas forms from the diffuse molecular clouds. Dense molecular gas structures can be roughly divided into three nested substructures: clouds, clumps, and cores. These structures increase with density at each level in this hierarchy, with cores being the gravitationally bound precursors to individual stars or simple stellar systems. Typical radii and densities are seen in Table 3.1. With *Herschel*, cores are only resolvable within ~ 1 kpc of the Sun. Clumps are resolvable within ~ 7 kpc. Beyond this, we can only resolve entire clouds (Dunham et al., 2011)

The molecular cloud clump mass function is expected to follow either a power-law or log-normal distribution function, depending on which physical process dominates clump formation. Gravitational collapse of dense structures is expected to produce a power-law distribution (e.g.,

Table 3.1: Cloud, Clump, and Core Properties

Parameter	Cloud	Clump	Core
R [pc]	$1-7.5$	$0.15-1.5$	$0.015-0.1$
n [cm^{-3}]	$50-500$	10^3-10^4	10^4-10^5

Padoan & Nordlund, 2002), whereas supersonic turbulence is expected to produce a lognormal density distribution (e.g., Padoan et al., 1997). However, supersonic turbulence is not necessary for a lognormal distribution (Tassis et al., 2010). As is the case with many such competing theories, it is likely that the answer lies in a combination of the two (e.g., Hopkins, 2013; Offner et al., 2014; Basu et al., 2015). Determining which of these processes dominates the molecular cloud clump formation is essential for evaluating competing theories of high-mass star formation (e.g., Elmegreen, 1985; Ellsworth-Bowers et al., 2015b, for theoretical and observational descriptions respectively).

In addition to mass functions, we can also study the physical distribution of the molecular cloud clumps. The radial distribution of GMCs has been investigated in the Milky Way (e.g., Scoville et al., 1987; Bronfman et al., 2000), and in external galaxies (e.g., Rosolowsky et al., 2007; Gratier et al., 2012; Freeman et al., 2017), generally finding a peak at intermediate galactocentric radii. A related question regards whether the GMC mass distribution is dependent on galactocentric radius (Rosolowsky et al., 2007), or location in a spiral arm vs. an interarm region (Stark & Lee, 2006; Colombo et al., 2014). While current simulations are more likely constrain the overall baryonic mass distribution than specifically on the spatial distribution of dense gas, those by Fujimoto et al. (2014) found that GMCs have mass distributions whose peaks are unaffected by environment. However, the tails of these distributions show a higher prevalence of larger, more massive clouds nearer to the galactic center.

Historically, the field used CO line surveys to trace the structure of the diffuse molecular gas (e.g., Scoville & Solomon, 1975; Solomon et al., 1987). However, the interpretation of CO line observations is complicated by a number of issues involving line excitation. In particular, critical densities are temperature dependent, leading to ambiguities in the mass being measured. Additionally, CO does not trace molecular hydrogen at a constant ratio, due to freeze-out and abundance variations. Freeze-out dominates when densities exceed $\sim 3 \times 10^4$ cm^{-3} (Bacmann et al., 2002), making it highly relevant to studies of dense molecular cloud clumps. Furthermore, there is an envelope in clouds where H_2 self-shields and dust is present, but CO is not (Wolfire et al., 2010). Finally, the lowest-J transitions of CO are generally optically thick, complicating mass estimations. Thermal dust continuum surveys provide a complementary view of star forming gas. While such maps do not provide the kinematic information that CO line surveys do, optically thin emission allows us to see through the entire Galactic disk. Furthermore, the dust opacities are known to a factor of two (Ossenkopf & Henning, 1994), allowing for well-constrained masses.

In recent years, dust continuum surveys have been performed covering much of the Galactic Plane, enabling the study of molecular cloud clumps across diverse Galactic environments. These have taken the form of dust continuum surveys of the Galactic Plane in the millimeter and submillimeter wavelengths [BGPS: Aguirre et al. (2011); Ginsburg et al. (2013); ATLASGAL: Schuller et al. (2009); Csengeri et al. (2014, 2016)]. Through these surveys, tens of thousands of molecular cloud clumps and cores have been detected, and their properties can now be analyzed. By extracting these sources and creating a census of molecular cloud structures, theories of star formation and galaxy evolution can be constrained (e.g., Kennicutt & Evans, 2012). Such studies of physical properties (e.g., Peretto & Fuller, 2010; Giannetti et al., 2013) and mass functions (e.g., Netterfield et al., 2009; Gómez et al., 2014; Ellsworth-Bowers et al., 2015a; Wienen et al., 2015) have already begun, but have not yet produced a consensus answer to questions concerning the evolution of these dense molecular gas structures and their production of a uniform stellar cluster mass function.

However, both BGPS and ATLASGAL suffer from low sensitivity due to being ground-based surveys. A great leap in sensitivity has been made recently with space-based Hi-GAL (Molinari et al., 2010, 2016). *Herschel Space Observatory's* Hi-GAL survey provides complete coverage of the Galactic Plane in the far-infrared to submillimeter wavebands. In this paper, we map the portion of Hi-GAL which overlaps with the Galactic Ring Survey (GRS) — the ^{13}CO(1-0) survey which provides our line-of-sight velocities — and investigate the distribution of dense molecular gas across this portion of the Milky Way, which should be representative of the inner Galaxy as a whole. Molinari et al. (2016) have independently begun cataloging the dense molecular cloud clumps found in the Hi-GAL survey. They have identified and extracted photometry for clumps found in the majority of the inner Galaxy in all five of *Herschel's* photometric bands. This work serves as a complement to the work of Molinari et al. (2016) through the use of a fundamentally different clump identification and distance determination techniques. Hi-GAL has also been used to advance the above studies of physical properties (Elia et al., 2013) and mass functions (Olmi et al., 2013, 2014).

Because of the excellent quality of the *Herschel* Hi-GAL survey, we have a new opportunity to explore the trends in molecular gas with respect to galactocentric radius. We build on the previous efforts of Zetterlund et al. (2017) which produced a catalog of compact emission structures over the Hi-GAL survey volume. From that work, we apply the distance determination methods used for the BGPS (Ellsworth-Bowers et al., 2013), yielding a broader survey of molecular cloud clump properties than was previously established. We then explore the trends in this clump catalog with respect to both heliocentric and galactocentric distances.

3.2 Data

The *Herschel* infrared GALactic plane survey (Hi-GAL) (Molinari et al., 2010) observed a $2°$ strip covering the entire $360°$ of longitude of the Galactic Plane. Using the SPIRE (Griffin et al., 2010) and PACS (Poglitsch et al., 2010) instruments aboard the *Herschel Space Observatory* (HSO), this survey observed in wavebands at 70, 160, 250, 350, and 500 μm. SPIRE (250, 350, and 500 μm) observed thermal dust emission which is concentrated in dense molecular gas clumps. Like SPIRE, PACS (70 and 160 μm) observed thermal dust emission from dense gas. However, PACS observed extended warm structures to a greater extent than SPIRE. Owing to the low optical depth of thermal dust in the submillimeter continuum, Hi-GAL allows us to view dense molecular gas throughout the entire Galactic disk.

In this paper, we analyzed Hi-GAL regions with Galactic longitudes $10° < \ell < 56°$. This range was chosen as corresponding to the limits of the ^{13}CO Galactic Ring Survey (GRS; Jackson et al., 2006) ($18^\circ < \ell < 56^\circ$), plus a few extra degrees near the Galactic Center. The expanded range allows us to match the coverage of the CO High-Resolution Survey (COHRS), which we will integrate into our analysis in a future paper. GRS probes dense gas in the Galactic Plane using the $J = 1 - 0$ transition in ^{13}CO for the velocity range –5 to 85 km s^{-1}. We have pointed observations of the $J = 3 - 2$ rotational transitions of HCO^+ and N_2H^+ made for BGPS clumps from Shirley et al. (2013) to provide velocities for this additional longitude not covered by GRS.

3.3 Method

Following Zetterlund et al. (2017), we apply an angular filter to the 500-μm Hi-GAL maps in $2^\circ \times 2^\circ$ tiles in order to remove large-scale flux density originating from cirrus clouds. We produce the maps using the pipeline Unimap (Piazzo et al., 2012, 2015a,b). We then apply a high-pass Gaussian filter with $\sigma = 3'$ to the maps. The orthogonal scanning used to produce Hi-GAL observations leaves each map with ragged edges not covered by both scan directions. Post-filtering, we mask off these edges, as well as a small number of pixels at high absolute Galactic latitudes. At these pixels, the large-scale flux density is negative, leading to the filter adding flux density as opposed to removing it.

We use Bolocat, a seeded watershed algorithm tool developed for BGPS (Rosolowsky et al., 2010), to identify sources in the processed maps. Bolocat identifies areas of significant emission and divides those areas into separate objects based on the difference in emission levels between local maxima and the saddle points between them. The thresholds to be considered significant emission and for dividing objects are based on the noise level of the map. Because Hi-GAL is confusion limited, the noise level of each map cannot usefully be defined by pixel statistics in dark areas of the map. Rather, we define the noise level by the distribution of flux density in the map as a whole. We take the flux density of all the positive flux density pixels in each map and fit their distribution to an exponential function. The various thresholds are set to values proportional to the scale factor of this fit. This method was chosen as it identifies objects consistent with what we would visually expect, over the large range of flux density levels found in maps at various longitudes (see Zetterlund et al., 2017).

With this clump catalog, we then determine clump distances using the method developed for BGPS by Ellsworth-Bowers et al. (2013) and Ellsworth-Bowers et al. (2015a). Most of the clump distances are based on their measured radial velocities; the distance ambiguity is resolved probabilistically. We determine the line-of-sight velocity with respect to the LSR using two methods. Many individual bright features have their velocities already determined through a suite of dense gas spectroscopy (e.g., Shirley et al., 2013). Targets without a specific dense gas measurement have their velocities established through morphologically matching the emission in the dust continuum to the emission from ^{13}CO(1-0) data in the BU-Galactic Ring Survey (Jackson et al., 2006). This is done by subtracting an off-source spectrum from an on-source spectrum for each clump and identifying a single peak in the resulting spectrum. The off-source spectrum is extracted by creating a rind around the source, excluding any pixels which belong to another clump. This method works remarkably well in both crowded and sparse environments, identifying a single velocity in approximately 50% of cases.

To determine whether each clump is located at the kinematic distance on the near or the far side of the Galactic Center, we employ probabilistic methods in a Bayesian framework. A distance probability density function (DPDF) is calculated for each clump. The posterior DPDF is found by,

$$\mathrm{DPDF} = \mathcal{L}(d_\odot|\ell, b, v_{\mathrm{LSR}}) \prod_i P_i(d_\odot|\ell, b),$$

where $\mathcal{L}(d_\odot|\ell, b, v_{\mathrm{LSR}})$ is the kinematic distance likelihood and the $P_i(d_\odot|\ell, b)$ are various Bayesian priors, which combine multiplicatively to create the posterior probability distribution for distance along the line of sight, often strongly favoring one v_{LSR} peak. The likelihood function is calculated by matching the line-of-sight velocities to the Galactic rotation curve from the BeSSeL survey (Reid et al., 2014) and equally weighting the near and far distances. For choosing between kinematic distances, the most powerful prior uses 8 μm absorption to place clumps with strong absorption features at the near kinematic distance. This method produces a continuous probability as a function of distance, not simply a discrimination between near and far locations. The methods of Ellsworth-Bowers et al. (2013, 2015a) use several other associations to constrain the DPDFs. These additional priors include using the small scale height of molecular hydrogen to constrain clumps found at high Galactic latitudes to be at their near kinematic distances. For a small number of objects, we have robust trigonometric maser parallaxes from the BeSSeL survey. These clumps' $(\ell, b, v_{\rm LSR})$ coordinates are matched to 6-dimensional (position, velocity) maser association volumes. Because these geometric distances are independent of the Galactic rotation curve and assumptions about the structure of the Galactic Plane, they offer the most robust of the distance measurements. Once DPDFs are calculated, we establish clump properties from Monte Carlo simulations over the distance distribution, which provides robust uncertainties for cloud clump properties.

Distances establish clump masses and radii, which are central to this study. Physical radii are given as $R = \theta_R d_\odot$, where θ_R is angular radius and $d_\odot$ is heliocentric distance. Our mass estimate uses the high-pass filtered flux densities at 500 μm. The conversion from flux density to mass is

$$M = \frac{\Gamma d_\odot^2}{\kappa_{500} B_{500}(T)} S_{500},$$

where $\Gamma = 100$ is the gas-to-dust mass ratio, $\kappa = 5.04$ cm^{2}g^{-1} is the opacity at 500 μm (Ossenkopf & Henning, 1994), $B_{500}(T)$ is the Planck function at 500 μm, $d_\odot$ is the heliocentric distance, and S_{500} is the clump-integrated flux density in the SPIRE PLW (500 μm) band. Battersby et al. (2011) used pixel-by-pixel modified blackbody fits of Hi-GAL data to determine that mid-infrared-dark molecular cloud clumps generally span the temperature range 15 K $\lesssim T \lesssim$ 25 K. Furthermore, Dunham et al. (2011) found an NH_3 gas kinetic temperature of $\langle T_K \rangle = 17.4 \pm 5.5$ K for a sample of 199 BGPS sources. Following these findings, we adopt a universal clump temperature of 20 K for this study.

While using a single *Herschel* band and a single representative temperature is not ideal, cirrus emission in the shorter wavelength bands make it impractical to use spectral energy distributions to extract individual clump temperatures. We therefore choose the 500 μm band, the longest of the

Herschel bands, to calculate masses. This band is as far as we can reach into the Rayleigh-Jeans limit, and thus as close to a $\mathbf{M} \propto \mathbf{T^{-1}}$ as is available. In this waveband, temperature difference of 5 K at a temperature of 20 K corresponds with a roughly 50% difference in mass.

3.4 Results

We identified 19 886 sources in total, 10 124 of which have some distance information, and 5 405 of which have well-constrained distances. The sources are spread evenly across the included Galactic longitudes, with a tendency towards lower flux densities at greater Galactic longitudes. Figure 3.1 shows the relatively constant number of clumps at each Galactic longitude, with a noticeable spike at $\ell = 30°$, due to the end of the Galactic bar. This constancy is caused by Hi-GAL being confusion-limited, as noted in Section 3.

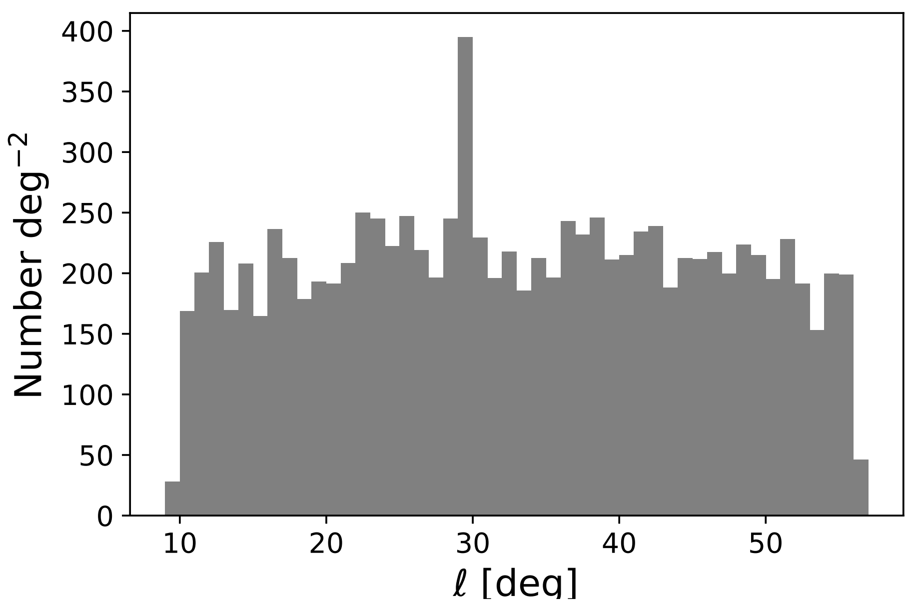

Figure 3.1: The distribution of sources with respect to Galactic longitude. The significant increase at $\ell \sim 30°$ shows the enhancement of source number and emission looking through the molecular ring toward the end of the Galactic bar.

Clumps were considered to have "well-constrained" distances if their DPDFs had a $\mathrm{FW}_{68} \leq$

2.3 kpc. That is, the isoprobability confidence region surrounding the distance of maximum likelihood which contains 68.3% of the total integrated probability has a full width less than 2.3 kpc. This was adopted from Ellsworth-Bowers et al. (2013), which found an empirical cut-off at this point such that clumps with $\mathrm{FW}_{68} \leq 2.3$ kpc either had 78% of the total integrated probability within the most likely kinematic peak, or were located at the tangent distance. Clumps with kinematic distances, regardless of whether the posterior DPDF met the well-constrained criterion, are considered to have some distance information.

3.4.1 Malmquist Bias

Due to the nature of the Hi-GAL survey and our subsequent angular filtering, we are subject to a form of Malmquist bias, identifying only larger, more massive objects at greater distances and smaller objects at nearer distances. This is demonstrated in Figure 3.2. The top panel shows a Mass-Radius diagram, coloured by heliocentric distance. There is a clear gradient with distance, showing nearby clumps having low masses and small radii, and distant clumps having high masses and larger radii. We attribute this relationship to a selection effect which is a product of our angular filtering process and the brightness levels that are required to be recognized as individual objects in our filtered maps. However, for larger clumps ($R > 0.3$ pc) there is a significant spread in the distances and surface densities probed. Over a four order-of-magnitude range in mass, there is a factor of $\sim$10 spread in surface density. Since most of the clumps are resolved and a range of masses are seen at all heliocentric distances, the slope of 2.08 ± 0.02 (where the uncertainty given is the standard deviation on the mean) in the mass-radius relationship suggests that spherical clumps would be centrally concentrated, as opposed to having constant densities as a function of radius (see §3.5.2).

The lower panel is a face-on map of the Galactic disk showing the positions of the clumps having well-constrained distances, coloured by clump mass. Again there is a clear gradient with less massive clumps near to our position, and more massive clumps farther away.

This bias can be seen more quantitatively in Figure 3.3. For each plot, clumps were separated

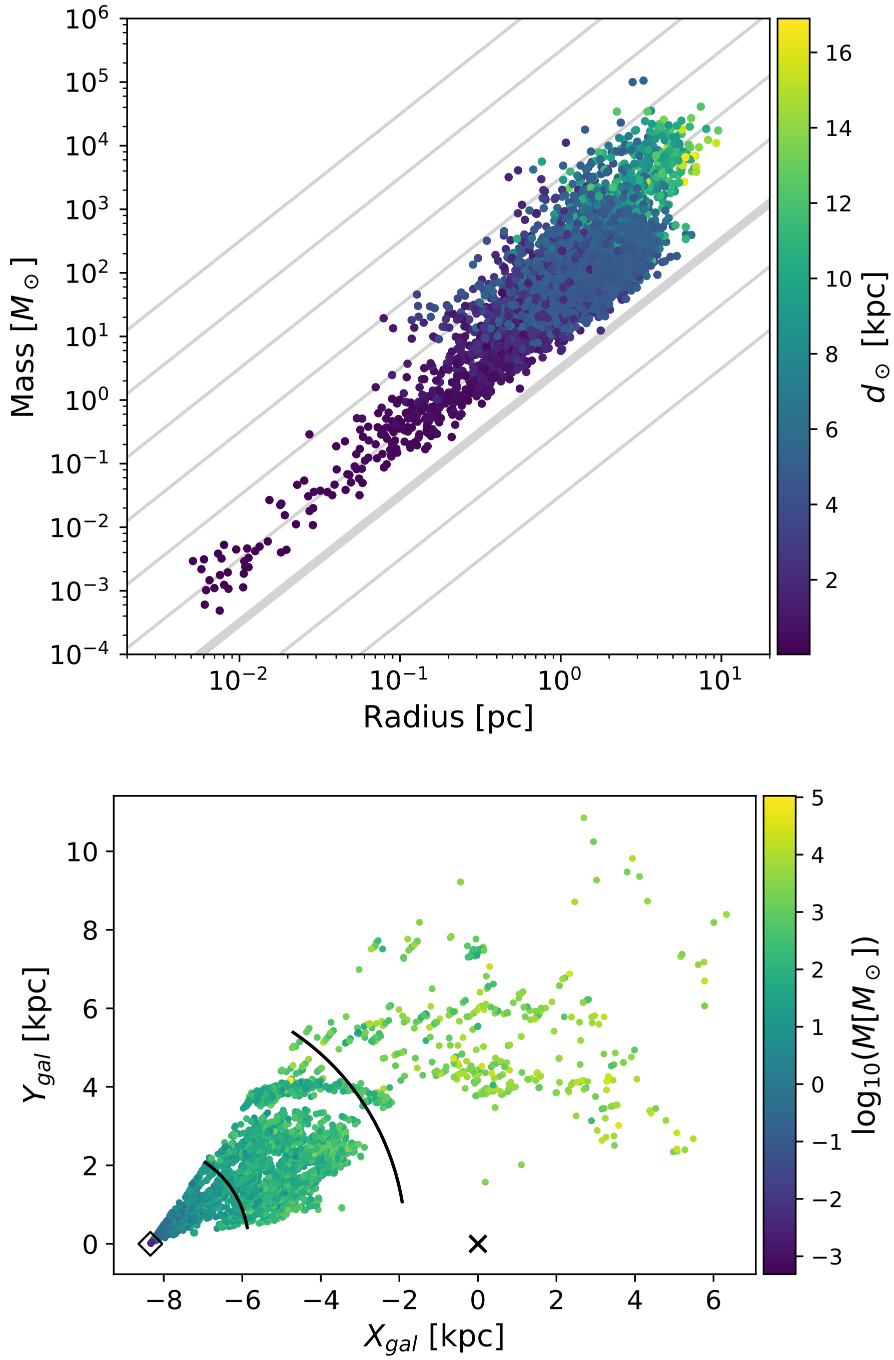

Figure 3.2: *Top*: Mass-Radius diagram for all clumps with well-constrained distances, with colours corresponding to heliocentric distances. Lines of constant surface density are shown in grey. The bold line is $\Sigma = 1$ $M_\odot$ pc^{-2}, and lines are separated by a factor of ten. *Bottom*: Map of the same clumps, with colours corresponding to clump masses. The solar position and Galactic Center are shown as a diamond and an $\times$, respectively. The effects of the Malmquist bias are apparent in both panels in the lack of sources with low mass at large distances. The black arcs indicate the bounds of our minumum-bias sample region, as determined from Figure 3.3.

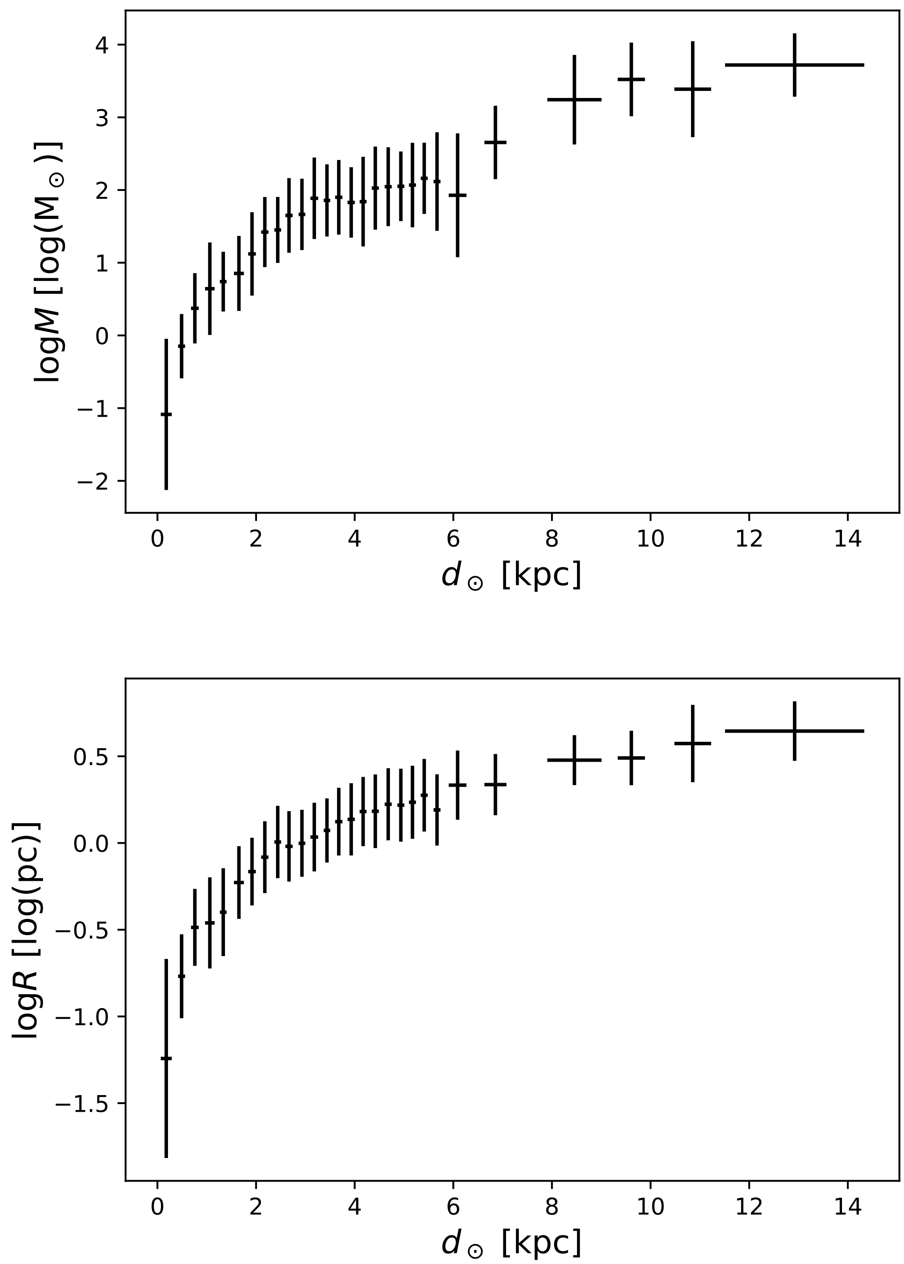

Figure 3.3: Mass and radius trends with heliocentric distance, more clearly shown. *Top*: Clumps separated by heliocentric distance into bins containing a minimum of 100 points and with a minimum width of 0.25 kpc. The mass distribution in each bin is fit to a log-normal, and the mode is plotted. Error bars represent the standard deviation on each axis. *Bottom*: As per the top panel, except for the radius distributions.

by heliocentric distance into bins containing a minimum of 100 points and with a minimum width of 0.25 kpc. The mass and radius distributions in each bin were fit to lognormal functions. The modes of the distributions are plotted, along with standard deviations in both mass/radius and distance. Over the range of 13 kpc, clump radii increase by more than an order of magnitude, and masses increase by roughly 4 orders of magnitude. However, most of the survey sources are found to lie in the range from $2.5 < d_{\odot}/\mathrm{kpc} < 6.5$. In this region, the distributions of mass as a function of distance do not show significant change and the effects of the Malmquist bias are minimized. For this part of the survey, we can probe a range of structures at different *galactocentric* radii, thereby assessing the evolution of the clump population with environment in the Galaxy.

3.4.2 Trends with Galactocentric Radius

Here, we select objects from the catalog with a heliocentric distance of 2.5 kpc – 6.5 kpc, where the distributions of clump mass and radius are minimally varying, as per Figure 3.3 (top). In this range, the effects of the Malmquist bias are significantly reduced, and it becomes possible to probe trends with galactocentric radius.

3.4.2.1 Mass Distribution with Radius

Figure 3.4 shows the trend of clump mass with Galactocentric radius within this slice of heliocentric distance. In this region, the clump mass appears to decrease moving outward from the molecular ring. The scatter in the cloud masses is large, but the median cloud mass decreases by nearly an order of magnitude over this range of radius. While source crowding may prevent the small clumps from being seen toward the molecular ring ($M < 10^2\ M_{\odot}$), the upper envelope of the trend indicates that higher mass clumps appear to be found in the molecule-rich region near $R_{\mathrm{gal}} \sim 4.5$ kpc.

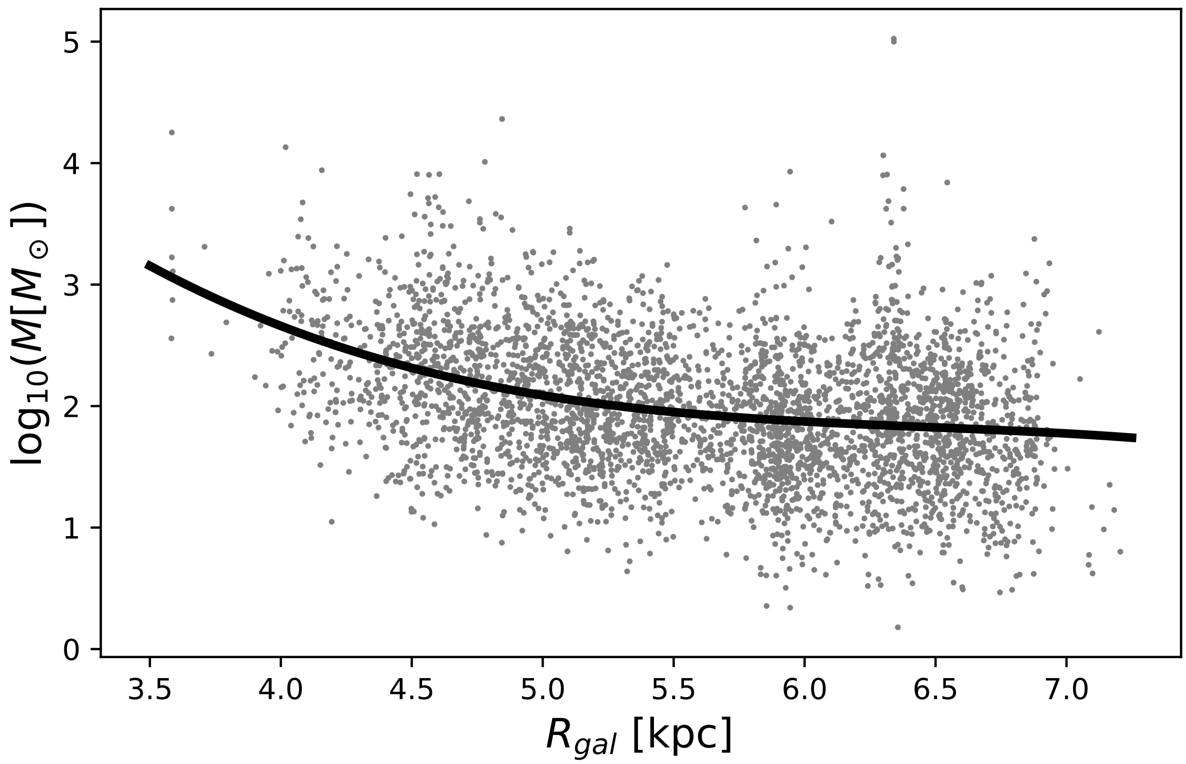

Figure 3.4: Clumps masses plotted against Galactocentric radius for those clumps in the heliocentric distance slice from 2.5 kpc – 6.5 kpc, where the Malmquist bias is minimized. The line shows a third degree polynomial fit, which represents the typical trend seen in the data and is meant merely as a guide for the eye, not a physical model. On average, our methods find higher mass clumps in the inner Galaxy compared to the outer Galaxy.

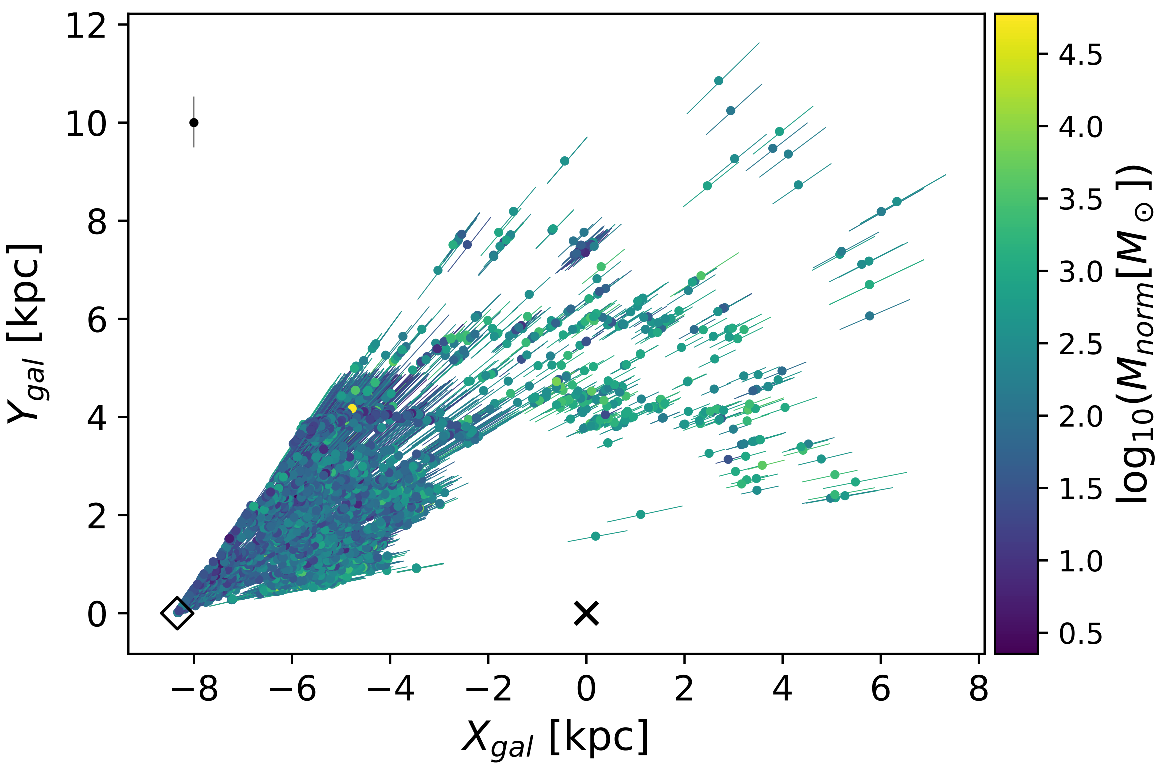

Figure 3.5: Map of clumps with well-constrained distances, as in Figure 3.2. colours correspond to clump masses which are normalized to the mass they would have if placed at the mean heliocentric distance of the clumps in our sample. Error bars show the uncertainty in heliocentric distance, and the black point shows representative error bars for clumps with $d_\odot < 5$kpc. The solar position and Galactic Center are shown as a diamond and an $\times$ respectively.

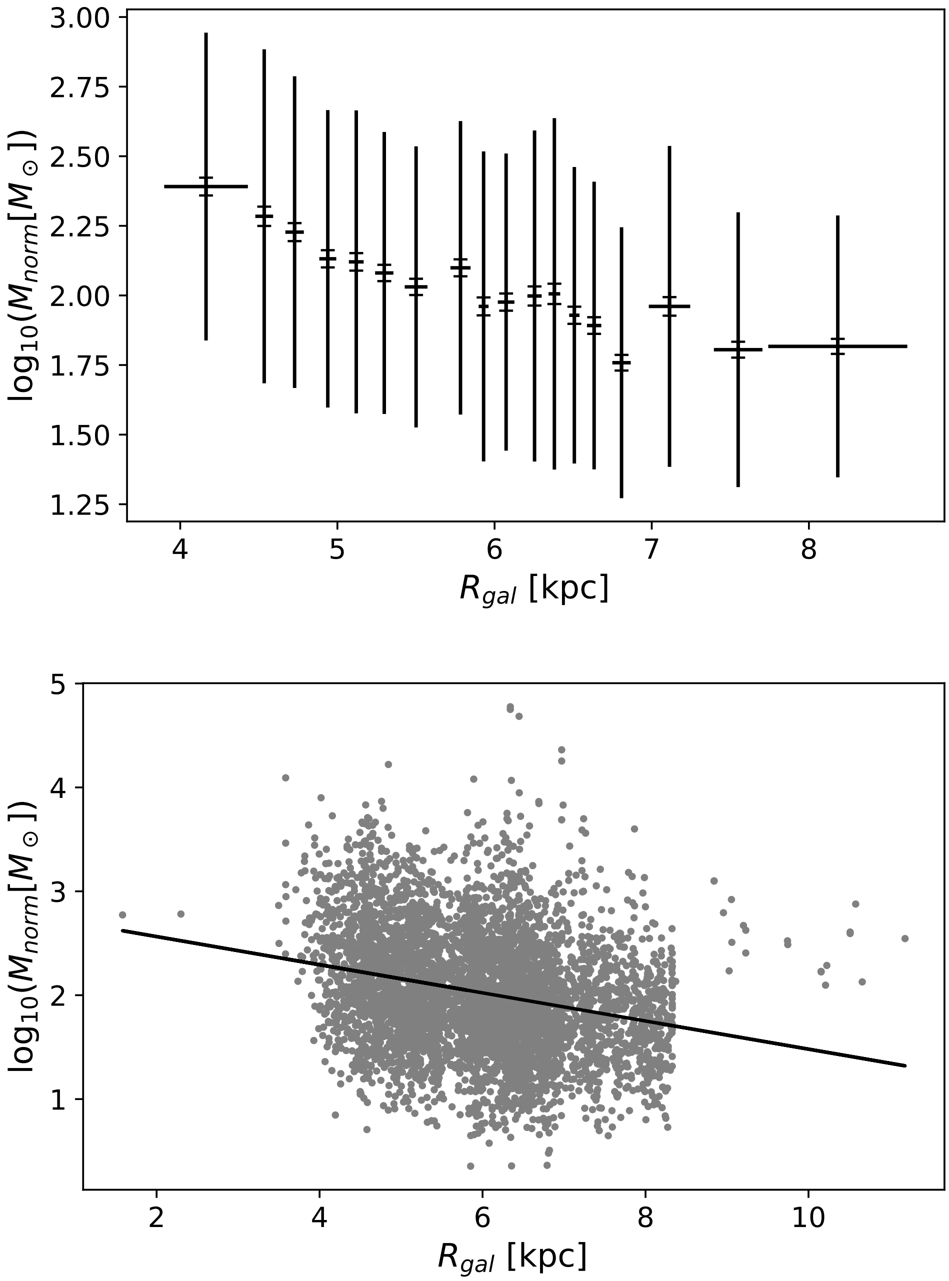

Figure 3.6: Normalized mass is negatively correlated with Galactocentric radius. *Top*: Clumps separated by Galactocentric radius into bins of N=300. Full error bars show standard deviations on both axes. Error bar caps show standard deviation on the mean for mass. *Bottom*: The same data un-binned and fit to a linear function. While there is a large spread in masses, there is also a clear negative trend. Note that the axis ranges in the two panels are different.

3.4.2.2 Normalized Masses

As an alternative strategy to mitigate the Malmquist bias, we can examine the clump population with distance-independent methods. Here, we consider the "normalized" clump mass, created by generating clump mass as if all the sources were located at the mean distance of the survey: $d_{\odot} = 4.12$ kpc. That is, Equation 4.3.2 is used as for true masses, but with $d_{\odot} = 4.12$ kpc for all clumps. This is tantamount to examining the distribution of clump-integrated flux densities, except we place those quantities on a common physical scale to guide our interpretation of the results. Figure 3.5 presents a normalized version of Figure 3.2 (bottom), now coloured by normalized mass, and with the addition of heliocentric distance error bars. The bias seen in Figure 3.2 is no longer present.

Using normalized masses allows us see if the negative trend in mass with Galactocentric radius from Figure 3.4 remains when the Malmquist bias is minimized using a second independent strategy. We show this trend of normalized mass ($\propto$ clump-integrated flux density) in Figure 3.6. Here we show that, on average, sources in the inner Galaxy have higher characteristic flux densities than those at large galactocentric radius. On the top, clumps were separated into bins of N=300 by $R_{\rm gal}$. On the bottom, the unbinned data were fit to a linear function. In both, a clear negative trend is seen, despite a wide spread in individual data points. Overall the flux densities of clumps are decreasing with galactocentric radius, consistent with the trend in the mass determinations seen in Figure 3.4.

3.4.3 Surface Densities of Clumps

Figure 3.7 shows the mean surface densities of clumps in the analysis. This property is particularly useful to study since it is proportional to the surface brightness of the emission and therefore independent of distance to the source. The typical (median) surface density of one of the clumps in this study is 20 $M_{\odot}$ pc^{-2}, similar to that seen other wide-area continuum studies (e.g. Kauffmann & Pillai, 2010). This average surface density is lower than the empirical minimum surface density for hosting massive star formation (typically about 250 $M_\odot$ pc^{-2}, Kauffmann & Pillai, 2010), but there are ample numbers of high surface density clumps in this sample volume. Furthermore, those clumps that don't appear star-forming at Hi-GAL's resolution may meet the surface density condition at higher resolutions.

The typical surface density of the clump appears to show an increase in the inner part of the Galaxy, coincident with the molecular ring. At least part of this effect arises from the difficulty of identifying low surface brightness sources against the bright background. However, the trend is also visible for $R_{\rm gal}$ in the vicinity of 4.5 kpc, where crowding is less significant. The increase in typical surface densities likely reflects the increasing pressure in the molecular medium changing its underlying structure (e.g., Ostriker et al., 2010).

3.4.4 Mass Distributions

We explore the mass distribution of the clumps identified in the survey following the approach of Freeman et al. (2017, hereafter F17). We restrict the cloud sample to heliocentric distances in the survey for which the Malmquist bias is minimized (2.5 to 6.5 kpc). For this sample, we complete a fit to the full population and then divide the sample into 6 bins of galactocentric radius with an equal number of clouds in each bin (126). For these binned mass distributions, we then fit the complementary cumulative distribution functions of the mass spectrum:

$$\mathrm{CCDF} = 1 - \frac{N(>M)}{N_{\rm tot}} = 1 - \frac{1}{N_{\rm tot}} \int_M^\infty \frac{dN}{dM'} dM'$$

with a functional form

$$\frac{dN}{dM} = M^\beta \exp\left(-\frac{M}{M_c}\right).$$

We consider two main models for this form of the mass distribution: a pure power-law (PL) where $M_c \to \infty$ and a truncated power-law (TPL) where the truncation mass (M_c) is determined through fit to the data. To analyze the mass distributions, we fit the CCDF using an Anderson-Darling goodness-of-fit metric as described in F17. To determine parameter uncertainties, we use the EMCEE

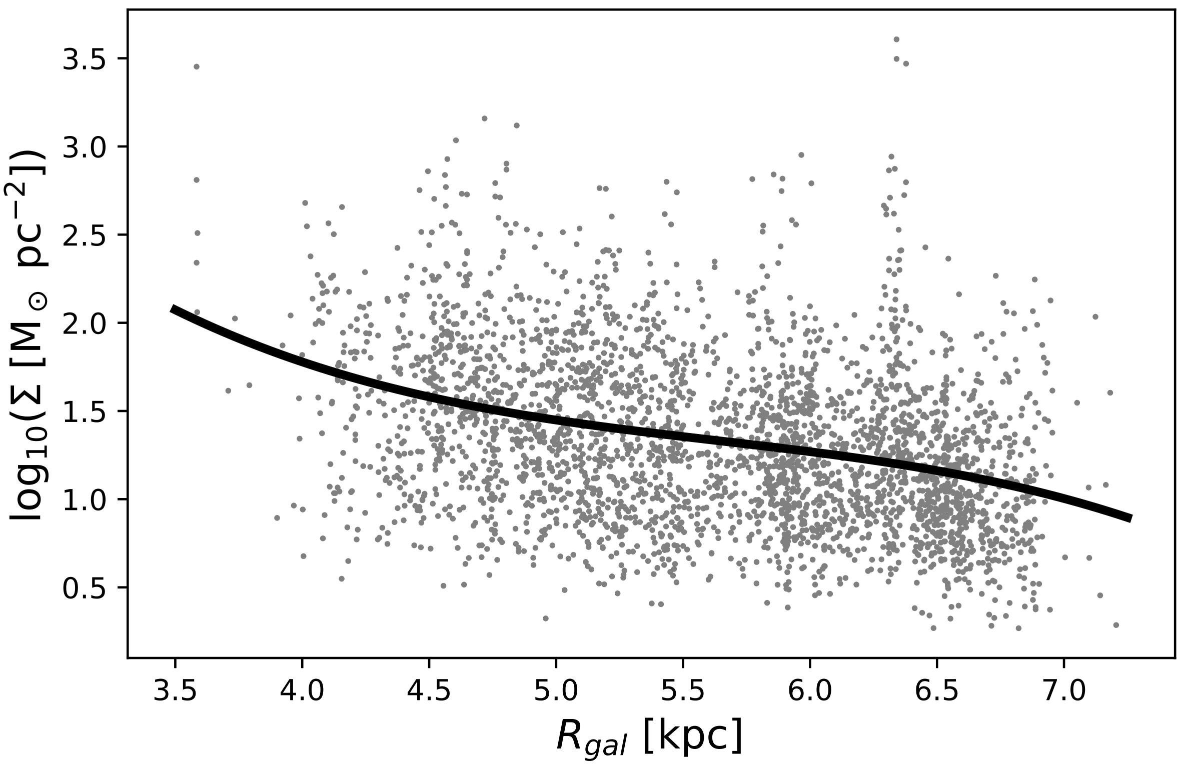

Figure 3.7: Clump surface density plotted against Galactocentric radius for those clumps in the heliocentric distance slice from 2.5 kpc – 6.5 kpc, where the Malmquist bias is minimized. The line represents a third degree polynomial fit, which represents the typical trend seen in the data and is meant merely as a guide for the eye, not a physical model.

Table 3.2: Properties of mass distributions

Property	Radial Bin (kpc) 3.6−7.0	3.6−4.5	4.5−4.8	4.8−5.1	5.1−5.5	5.5−6.3	6.3−7.0
Number of Clouds	756	126	126	126	126	126	126
M_{max} (10^3 $M_\odot$)	97.4	17.3	10.8	23.7	2.7	4.6	97.4
$\langle M\rangle_5$ ($10^3 M_\odot$)	28.0	7.7	7.6	4.6	2.3	2.8	16.0
β_{PL}	$-2.27^{+0.05}_{-0.05}$	$-1.96^{+0.09}_{-0.12}$	$-1.94^{+0.09}_{-0.11}$	$-2.29^{+0.12}_{-0.15}$	$-2.50^{+0.14}_{-0.18}$	$-3.09^{+0.19}_{-0.24}$	$-2.27^{+0.11}_{-0.12}$
β_{TPL}	$-2.23^{+0.05}_{-0.07}$	$-1.59^{+0.05}_{-0.38}$	$-1.55^{+0.10}_{-0.39}$	$-2.19^{+0.13}_{-0.18}$	$-0.57^{+0.57}_{-1.82}$	...	...
$M_{c,\mathrm{TPL}}$ ($10^3 M_\odot$)	$54.8^{+187.2}_{-0.1}$	$6.1^{+121.9}_{-0.1}$	$5.9^{+116.5}_{-0.1}$	$19.8^{+177.2}_{-0.1}$	$0.5^{+19.1}_{-0.1}$	...	...
$\log_{10} p_{\mathrm{PL}}$	−0.51	−0.97	−1.04	−0.46	−1.69	−0.24	−1.48
$\log_{10} p_{\mathrm{TPL}}$	−0.40	−0.32	−0.41	−0.42	−0.23	$-\infty$	$-\infty$

(Foreman-Mackey et al., 2013) package to sample the posterior probability density function of the fit parameters and report the errors as the difference between the median values and the 16th and 84th percentile of the value, which would correspond to -1σ and $+1\sigma$ respectively if the parameter were normally distributed. For each mass distribution, we restrict the fit to $M > 400\ M_\odot$ to study the population of massive clumps. Below this threshold, the distributions show some evidence for deviation from this model, but it is unclear as to whether this represents the effects of blending in the sample at far distances or a change in the functional form of the distribution (i.e., to the log-normal part of a Pareto-log-normal distribution Reed & Jorgensen 2004 such as that suggested by Brunt 2015; Basu et al. 2015). The large positive uncertainties in the truncation masses reflect a covariance in the fit parameters: high truncation masses can be compensated for in fitting by a steeper (more negative) power-law index, which is seen in the negative tail of the index uncertainties.

Table 3.2 summarizes the results of the mass distribution analysis for both the whole sample and individual radial bins. In particular, we report the maximum mass of clump found in the samples (M_{max}) as well as the geometric mean of the five most massive clumps ($\langle M\rangle_5$). There is not a clear trend in either of these properties with R_{gal}, mostly due to high mass structures associated with W51 in the last radial bin. With the exception of these data, there is a modest trend toward lower mass structures at larger R_{gal}. We also report the indices for the two functional models, β_{PL} and β_{TPL} respectively. For the TPL model, we report the characteristic mass of truncation and we compare the two models by reporting the peak log-probability associated with

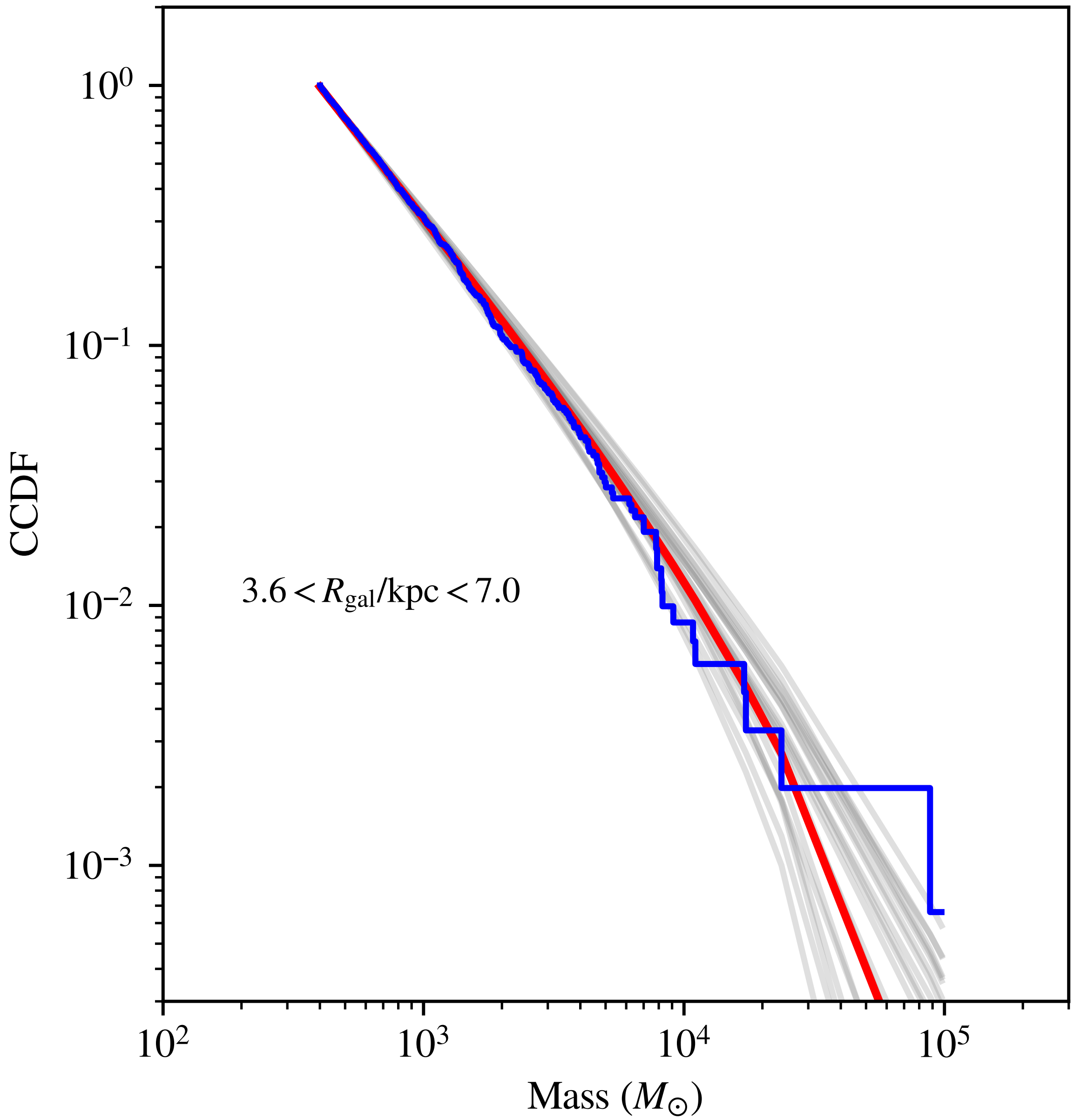

Figure 3.8: Mass distribution for clumps in our minimal-bias sample. The blue data show the complementary cumulative distribution function (CCDF) for clump mass and the red curve shows the truncated power-law fit to the CCDF. Grey curves show comparable models drawn from the posterior distributions of the fit parameters. The overall clump mass distribution function shows good agreement with a power-law model with index of $\beta = -2.27 \pm 0.05$ over the mass range with only weak evidence for a truncation at the high-mass end.

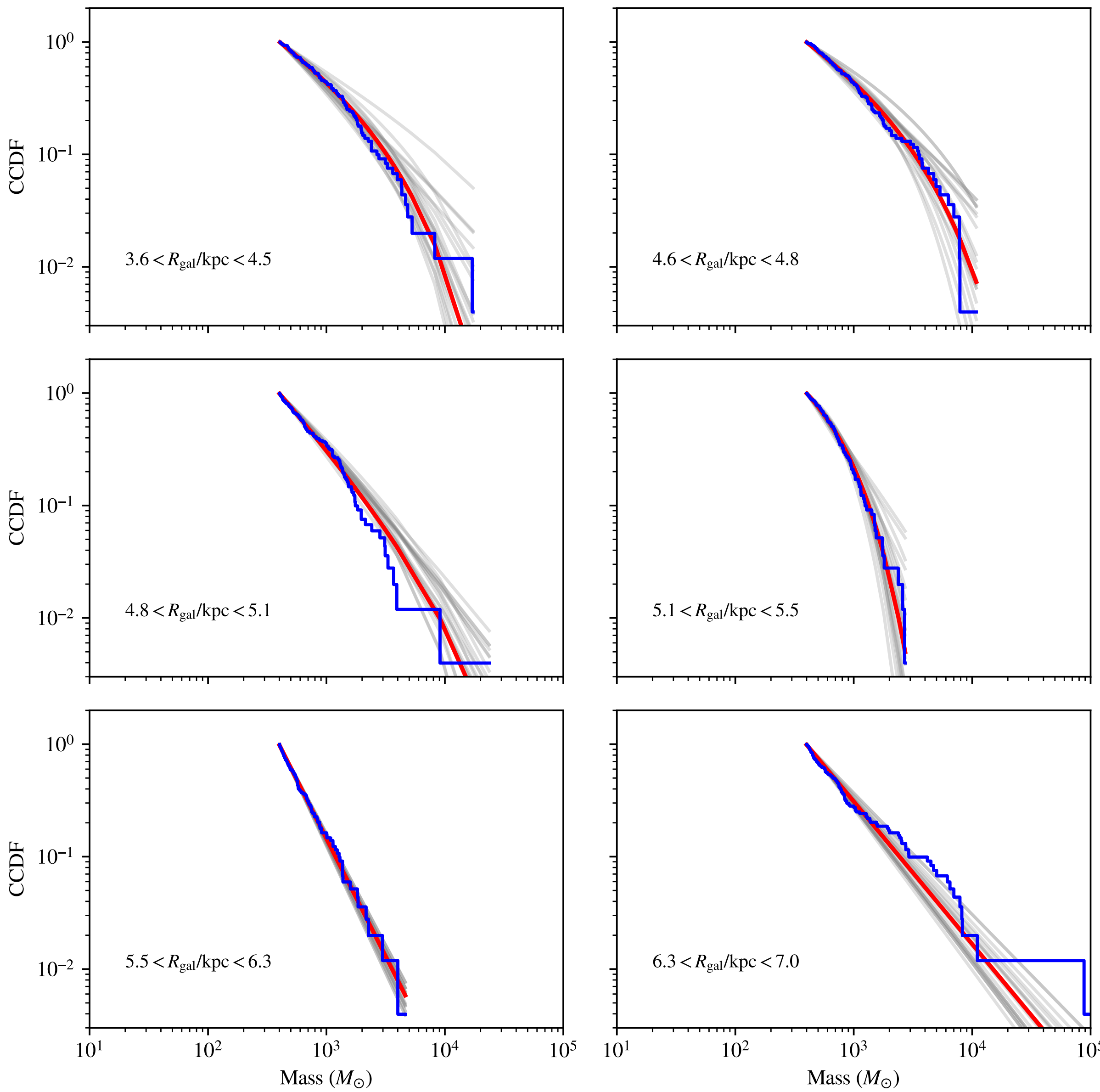

Figure 3.9: Mass Distributions for Clumps in Equal-Number bins of Galactocentric Radius. The curves show the complementary cumulative mass distribution functions (CCDFs) for clump masses in six equal bins of 126 objects. The red lines show power law fits to the CCDFs including truncations where they are detected, and the grey lines show 20 random draws from the posterior distribution of parameters.

the most credible model in the fit ($\log_{10} p$). This provides a discriminant for cases where one model provides a significantly better fit to the data than the other. In the large $R_{\rm gal}$ bins, there is no good model from the truncated power-law fit and we only report values for the power-law model. In most cases, both models provide good descriptions of the data and the clump mass distribution appears to have a power-law component with $\beta \sim 2$, though there is significant variation with $R_{\rm gal}$.

Figure 3.8 shows the mass distribution for all the clumps in this sample and the power-law fits to the results. The power-law models provide excellent fits to the data with a consistent index between TPL and PL fits of $\beta \approx -2.25 \pm 0.05$. There is very weak evidence for a truncation near $5 \times 10^4~M_\odot$, but this model is not clearly favoured, and the simpler PL model provides an equally good model for the results.

Despite this clear aggregate behaviour over the survey, separating the samples into bins of $R_{\rm gal}$ shows significantly different mass distributions in the different bins (see Figure 3.9). Notably, at small $R_{\rm gal}$ there is better evidence for a characteristic mass scale of $\sim 6\,000~M_\odot$, though this result is marginal. More strikingly, the mass distribution index for the PL fits shows a sharp decrease in the bin $5.5 < R_{\rm gal}/{\rm kpc} < 6.3$ where the index drops to $\beta_{\rm PL} = -3.1 \pm 0.2$ and is significantly different from the other bins. In contrast, the innermost bins also show the shallowest distributions $\beta_{\rm PL} > -2$. These variations are likely from sampling different parts of the galaxy. The steep mass distribution seems to arise because our mass distribution mostly samples the inter-arm regions of the galaxy at these radii. The shallower slopes appear associated with the molecular ring structures and a richer molecular ISM. What remains clear is that aggregation of these different populations over a large piece of the galaxy produces a single power-law mass distribution with index of $\beta \approx -2.25$. This emergent distribution reflects the typical gravitational fragmentation conditions over the inner galaxy, though there remains evidence that local conditions can produce significant variation.

3.4.5 Dense Gas Distribution

The dense gas mass surface density on the Galactic Plane is estimated by Monte Carlo sampling from the clump DPDFs. For each clump, we randomly draw from its DPDF 10^3 times. Each time we calculate its mass from its observed flux density and simulated distance, and place that mass in the appropriate location in a grid of 0.25 kpc $\times$ 0.25 kpc pixels representing the Galactic disk. The resulting map is shown in Figure 3.10. Spiral arm structure can be seen in two arcs roughly 4 kpc and 6 kpc from the Galactic Center. Much of $R_{\mathrm{gal}} \lesssim 3$ kpc was excluded due to significant radial streaming motion corrupting the circular motions, keeping only those clumps with robust trigonometric parallax measurements (see Ellsworth-Bowers et al., 2013). Sampling the entire DPDF results in some smearing effects along the line of sight, especially for sources more distant from the solar position, where the uncertainties tend to be larger, and the detected objects scarcer. We see little beyond $R_{\mathrm{gal}} = 8$ kpc. This is due to a combination of factors. On the near side of the Galactic Center, our longitude range limits our observable R_{gal} range. On the far side, we must first look through what is on the near side. Here our sensitivity at large heliocentric distances limits our ability to observe structures at large R_{gal}. As discussed in Section 1, at $d_{\odot} > 7$ kpc, we are only able to resolve entire clouds. On top of that, the amount of dense molecular gas drops off with increasing R_{gal}, so that where we can only resolve clouds, clouds are less likely to exist.

There is a marked, but unlabeled, region opposite the kinematic distance tangent point from the major GMC complex W43. It is possible that this region could be clumps which were mistakenly placed at the far kinematic distance, when they should be at the near distance within W43. There are many clumps with velocities putting them in one of these two regions, not all of which have had their kinematic distance ambiguity resolved. The Monte Carlo sampling of these unresolved DPDFs has contributed to the mirrored appearance of these two regions about the tangent point. However, this effect does not affect our conclusions about how clump properties vary with Galactocentric radius, nor about clump properties drawn from clumps with well-constrained distances, such as

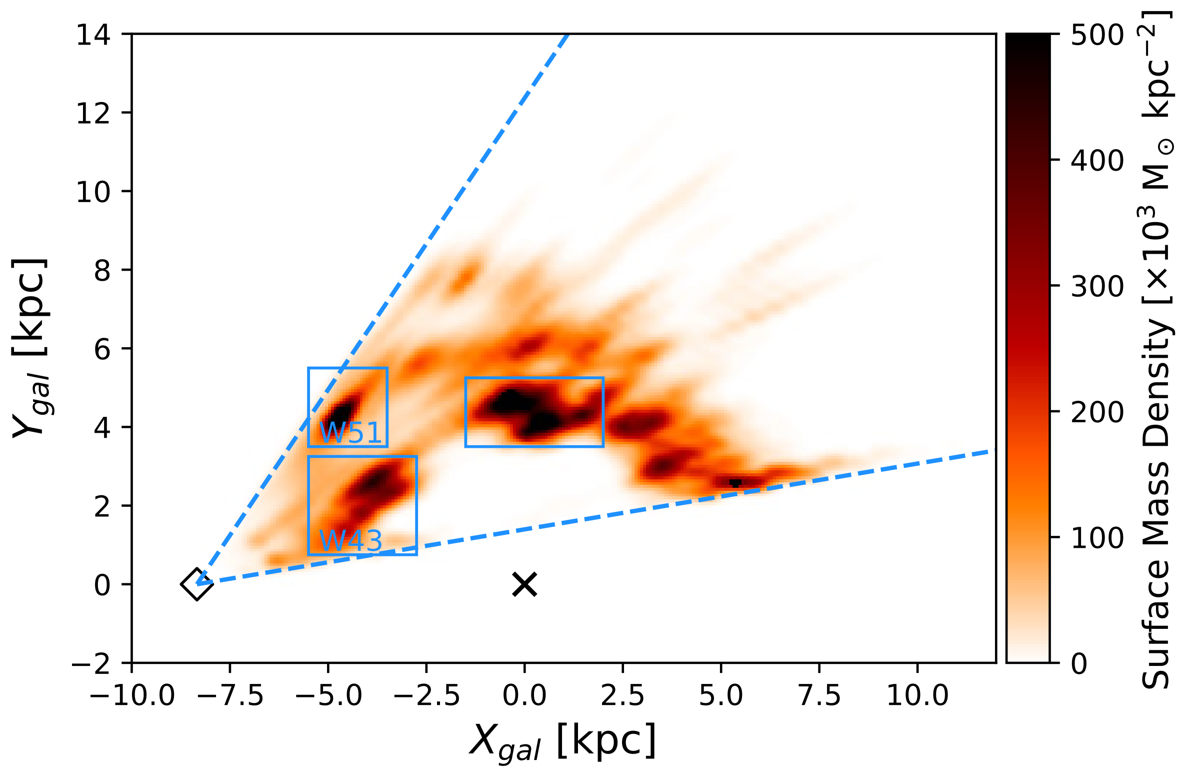

Figure 3.10: Dense gas mass surface density over the Galactic disk. Each object is drawn from its DPDF 10^3 times. For each draw, the mass of the clump is placed in a grid of 0.25 kpc pixels. The solar position and Galactic Center are shown as a diamond and an X, respectively. The three major GMCs are enclosed by blue rectangles, and the dashed lines indicate the longitude limits of this survey.

those in Figures 2, 3, 4, 5, and 6. There is also a significant number of clumps whose distances are well constrained in both regions, primarily due to 8 μm absorption features.

The azimuthally averaged H_2 model of Wolfire et al. (2003) was used to convert the dense gas mass surface density map in Figure 3.10 into a dense gas fraction map, seen in Figure 3.11 (a). Figure 3.11 (b) shows the dense gas fraction azimuthally averaged over the observed area. These panels show what may be spiral arms in arcs where the dense gas fraction is enhanced, and spikes corresponding to those arcs, respectively. As the map in Figure 3.10 includes H_2 at densities hardly above those considered in the Wolfire et al. (2003) model, we also include panels (c) and (d). These are the same as (a) and (b), respectively, but only considering clumps with number density $n \geq 10^3$ cm^{-3}. The spiral arms are again seen in the spikes around 4 kpc and 6 kpc. Note that the Wolfire et al. (2003) model does not include enhancements for spiral arms, so the dense gas fraction in these spikes is likely somewhat lower in reality.

3.5 Discussion

3.5.1 Mass Sensitivity

The Hi-GAL survey had a raw gas mass sensitivity limit of 250 $M_\odot$ (5σ) at distances up to 20 kpc (corresponding to a 1σ rms of 100 mJy at 250 μm, assuming a temperature of 20 K and a gas-to-dust conversion ratio of 100). However, because of source confusion, our actual sensitivity was about an order of magnitude worse. Figure 3.3 indicates that we can see clouds with masses of 3000 $M_\odot$ out to distances of 14 kpc. This decreased sensitivity impacts what we can detect on the far side of the Galactic Center, as discussed in Section 4.3. While, according to Figure 3.6, there should exist clumps of mass 100 $M_\odot$ at $R_{\rm gal} = 6$ kpc, it is evident in Figure 3.2 (bottom) and Figure 3.3 (top) that we do not see these clumps because of confusion.

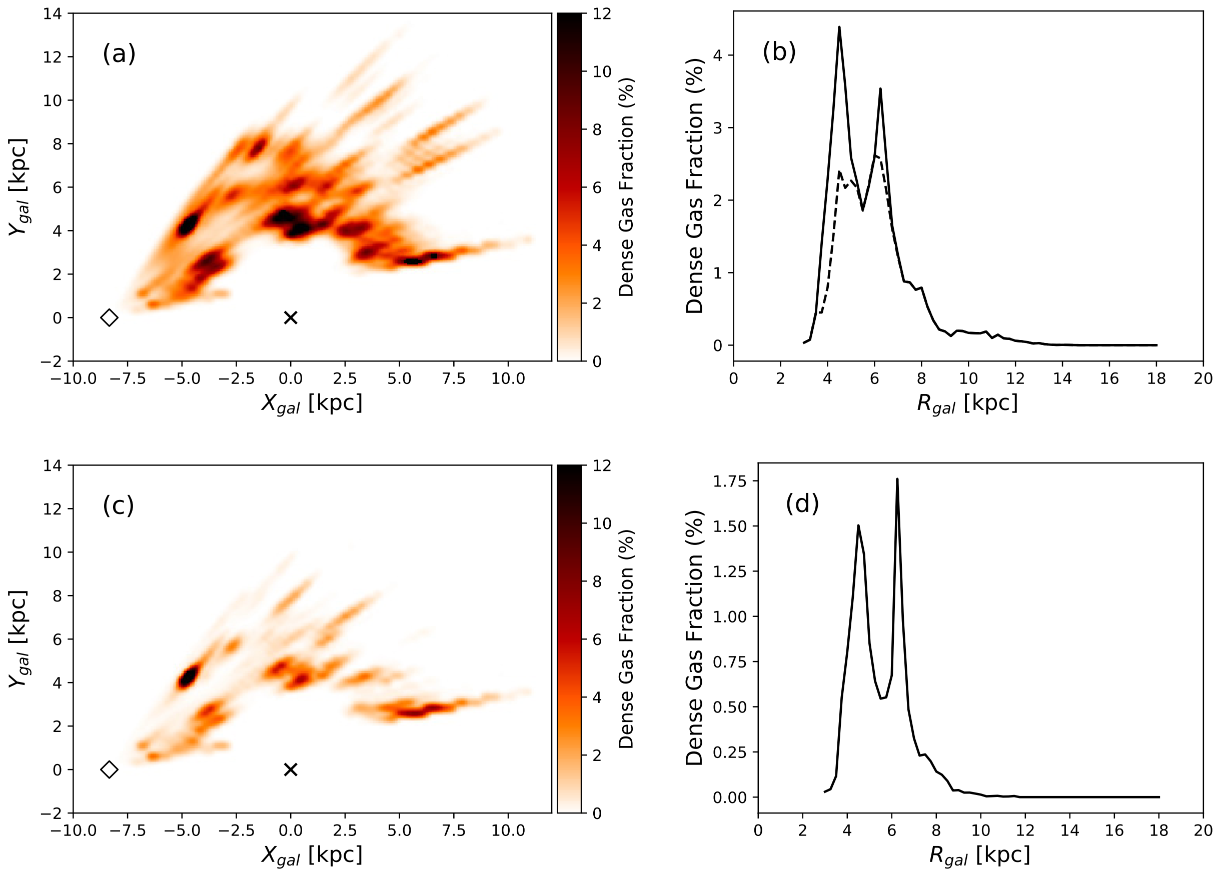

Figure 3.11: *(a)*: Map of the dense gas fraction in the Galactic Plane, made by dividing the dense gas distribution as in Figure 3.10 by the molecular hydrogen distribution from the model of Wolfire et al. (2003). The peak value is 47%. *(b)*: Dense gas fraction from (a) as a function of Galactocentric radius. The dashed line excludes the major GMCs indicated in Figure 3.10; the spikes at 4 kpc and 6 kpc remain, although they are less pronounced. *(c)*: As in (a), but only including structures with $n \geq 10^3$ cm^{-3}. The peak value is 44%. *(d)*: Azimuthally averaged dense gas fraction from (c) as a function of Galactocentric radius. Note that the Wolfire et al. (2003) model does not include enhancements for spiral arms, so the dense gas fraction in these spikes is likely somewhat lower in reality.

3.5.2 Density Profiles

Assuming spherical symmetry, a density profile of $\rho \propto r^{-\alpha}$ ($\alpha > 0$) leads to $M \propto R^{3-\alpha}$ for resolved clumps. In the mass-radius diagram of Figure 3.2 (top), we find that $M \propto R^{-(2.08\pm0.02)}$. This measured slope implies a density profile of roughly $\rho \propto r^{-1}$, although this proportionality is not well constrained. However, we do not expect all clumps to follow exactly the same density profile, and the variations in α and $\rho_\circ$ account for the main sources of the multiple order-of-magnitude scatter in Figure 3.2 (top). Note that such a density profile implies a density singularity. A Schuster density profile, $\rho(r) = \rho_\circ[1 + (r/r_\circ)^2]^{-\alpha/2}$ with $r_0 \ll R$, can be used to avoid this. However, we are observing on scales of $r \gg r_0$, such that the Schuster profile reduces to a power-law and $M \propto R^{3-\alpha}$ still holds. Simulations of star formation in clouds have shown that power-law density profiles such as $\rho \propto r^{-1.5}$ or $\rho \propto r^{-2}$ produce too many high-mass stars in proportion to low-mass stars. In comparison, top-hat and Bonnor-Ebert density profiles (constant for small r, $\propto r^{-2}$ for large r) more successfully replicate the observed IMF, although shifted to lower masses (Girichidis et al., 2011). The density profile we observe is a shallower power law than those simulated, and thus could represent a middle ground.

3.5.3 The Effects of GMCs

Considering Figure 3.10, it appears possible that the trend in normalized mass seen in Figure 3.6 and the structures seen in Figure 3.11 b and d may be dominated by the labeled GMCs. To test for the dominance of these GMCs, we removed the sources in the boxed regions from our analysis. The slope of the plot of normalized mass against Galactocentric radius is still negative when these sources are removed, and indeed slightly steeper. The steeper slope is most likely due to the removal of W51, which contributes high-mass objects at relatively large $R_{\rm gal}$ values. Since we are dealing with normalized, not true, masses, the slope is tracing the declining value of the typical flux density with Galactocentric radius.

Figure 3.11b also shows the radial dense gas fraction when the major GMCs are excluded.The two spikes around 4 kpc and 6 kpc are still present, although not as pronounced, due to the most massive regions being removed. This suggests that the decrease in dense gas and dense gas fraction with Galactocentric radius is not simply a result of a few massive GMC complexes.

The mass distribution analysis shows steeper mass distributions between 5.1 and 6.3 kpc. Figure 3.12 shows the locations of these radial bins in our selected survey region. These two bins are notable since they do not contain a significant fraction of the GMC structure in this region. There is a small portion of the W51 complex contained in this region but it does not appear to be enough to change the structure of the mass distributions. While this analysis lacks sufficient numbers of regions in the two categories, it is suggestive that regions with the large GMC complexes also show relatively top-heavy mass distributions for their global clump populations.

3.5.4 Comparison to Literature

3.5.4.1 Galactocentric Radius Trends

Our work is in general agreement with previous work on the trends of GMCs with Galactocentric radius using different tracers of dense gas. Scoville et al. (1987) found that GMCs peak in the molecular ring, located at $R_{\rm gal} = 4 - 7$ kpc. While we now consider the molecular ring to be nearer the Galactic Center and this range to include spiral arms, we do see a higher dense gas fraction in that range of Galactocentric radii (Figure 3.11). Later, Bronfman et al. (2000) found that the number of GMCs and $L_{\rm FIR}$ peak at $R_{\rm gal} = 4 - 5$ kpc. Indeed, we find that — while we exclude much that is nearer the Galactic Center than 4 kpc, due to the limitations of kinematic distance determinations — the typical mass of cloud clumps decreases moving outward from 4 kpc. The analysis of normalized masses suggests that this behaviour persists with a minimally biased sample.

Comparing to extragalactic work, where face-on views make for much easier mapping of GMCs, we also see agreement. On kpc-scales in galaxies, the brightness of CO typically peaks in the centres or in rings at small galactocentric radius (Leroy et al., 2009; Utomo et al., 2017). The result

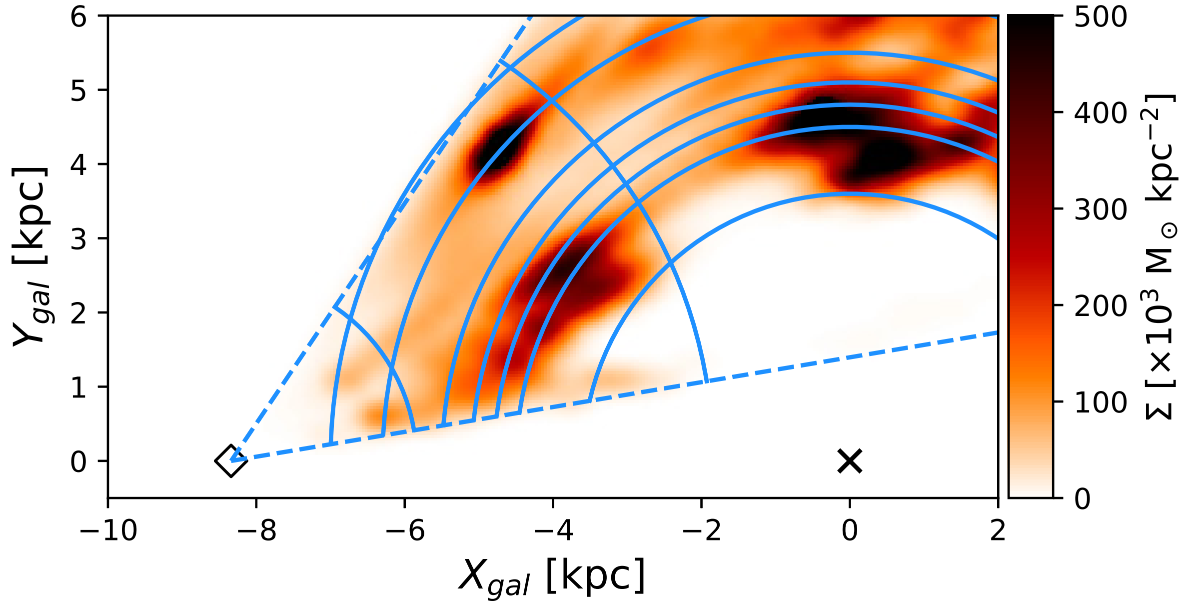

Figure 3.12: Dense gas mass fraction map annotated with radial bins used in mass spectrum analysis. Heliocentric arcs indicate the limits of the minimum-bias slice. This figure illustrates how the bins used in the mass distribution analysis relate to the dense gas structures seen in the Galaxy. The effects of the W51 region will be seen in the outer two radial bins.

holds at higher linear resolution where Gratier et al. (2012) found that CO brightness decreases with R_{gal} in M33, reflecting the same trend we see in Figures 3.6 and 3.4. Mass distribution analysis in Rosolowsky et al. (2007, Braine et al., submitted) shows that the characteristic mass of GMCs peaks at intermediate values of $R_{\mathrm{gal}} = 2 - 4$ kpc in M33 (noting the smaller size of the galaxy). As with our comparison to the Milky Way work of Bronfman et al. (2000) above, we exclude sources inside the 4 kpc ring for kinematic reasons, and therefore cannot conclude where the characteristic mass peaks, but we can conclude it falls off outside of 4 kpc, which is an intermediate R_{gal} value.

There are several possibilities for the cause of such an $M - R_{\mathrm{gal}}$ relation, the simplest explanation being that the decrease in gas surface density in the outer Galaxy means that clouds will accrue mass more slowly, leading to less massive clouds further from the Galactic Center. Blitz & Rosolowsky (2006) argued that hydrostatic pressure drives the conversion of HI into H_2, which is less efficient at larger radii. Meidt (2016) argued that the mass of dense gas cores is directly related to the cloud surface density, a property which is inherited from the environment. This would also lead to lower masses at larger radii.

Rosolowsky et al. (2007) additionally found that the mass distribution for GMCs in M33 is not different in the spiral arms vs. in the interarm regions. Contrarily, Colombo et al. (2014) found that, in M51, the mass distribution varies not by R_{gal}, but between arm and interarm regions, noting that the arm-to-interarm ratio decreases with R_{gal}. Unfortunately, while we do see interarm gas, we do not have enough of the Galactic Plane mapped to be definitive about the distribution of clumps within the interarm regions. For this reason, it is necessary to analyze the Southern Hemisphere and thus complete a map of the Galactic Plane.

3.5.4.2 Dense Gas Fraction

We calculated dense gas fraction in the same manner as Ellsworth-Bowers et al. (2015b) using the BGPS data. With Hi-GAL data, we find significantly higher dense gas mass fractions as compared with BGPS. We find that half of all non-zero pixels have >1% dense gas mass fraction, and that 10% of the non-zero pixels are >5% dense gas. Only a quarter of pixels above each limit remain when only structures with $n \geq 10^3$ cm^{-3} are considered. This compares with the finding by Ellsworth-Bowers et al. (2015b) that while there are pixels with >5% dense gas mass fraction, the vast majority of pixels have <1% dense gas. While we see higher dense gas fractions, due to our increased sensitivity, our results remain in agreement. Battisti & Heyer (2014) compared the masses found in BGPS sources to the masses of the parent GMCs in GRS, finding a mean fraction of $0.11^{+0.12}_{-0.06}$. Our work is consistent with this, finding only three pixels above their 1σ errors.

3.6 Conclusions

We have mapped the physical distribution of the dense molecular cloud clumps found in Hi-GAL within the Galactic longitude range $10° < \ell < 56°$. This range corresponds to the extent of the Galactic Ring Survey, which provided the majority of our line-of-sight velocities. These maps were made from 10 124 clumps which have, at minimum, a kinematic distance. Of these, 5 405 clumps had their distances well constrained through Bayesian techniques. Maps of the dense gas and dense gas fraction show features which are suggestive of spiral arms.

While the Malmquist bias impairs our ability to detect trends in clump mass and radius as a function of Galactocentric radius, we have analyzed these quantities over restricted heliocentric distances. This revealed that the mean clump mass decreases with distance from the Galactic Center, while the mean clump radius stays constant, indicating an additional decrease in mean clump density. Previous work concerning the distribution of clump masses, both Galactic and extragalactic, are in general agreement with our findings.

Chapter 4

Clump and Star Formation within Clouds

We investigate the physical properties of giant molecular clouds (GMCs) and their denser substructures. We trace clouds using the ^{12}CO(3-2) transition, as observed by the CO High Resolution Survey (COHRS). We identify their constituent clumps using thermal dust emission, as observed by the *Herschel* infrared GALactic plane survey (Hi-GAL). In total, we match 3,674 clumps to 473 clouds in the Galactic longitude range $10^{\circ} < \ell < 56^{\circ}$. We find a mean clump mass fraction of $0.08^{+0.05}_{-0.04}$. This mass fraction is independent of all cloud properties which we investigated: mass, surface mass density, and virial parameter. As clouds grow, they produce more clumps and more massive clumps. The star formation rate for clouds, as measured by 70 μm emission, is dependent solely on cloud mass (or, equivalently, clump mass). This provides evidence for the soundness of numerical models of galaxy evolution which convert a fixed fraction of GMC mass into star mass. There is still evidence for the Kennicutt-Schmidt law on GMC scales, although there is evidence for it beginning to break down. The virial theorem is a blunt instrument for predicting clump and star formation. Finally, in addition to supporting clouds against gravitational collapse, supersonic turbulence may play an important role in driving star formation.

4.1 Introduction

All stars form from molecular gas. However, not all molecular gas forms stars. Rather, the formation of stars is most closely tied to the presence of cold, dense molecular gas (Gao & Solomon, 2004). This dense gas is typically found in giant molecular clouds (GMCs), although smaller clouds do exist and form stars (e.g., Enoch et al., 2008). The amount of dense molecular gas and the star formation rate appear to be linearly correlated on both global and local scales (Wu et al., 2007).

This linear relationship is the basis for the integration of star formation into many numerical simulations of galaxy evolution. Current simulations use prescriptive recipes for star formation which are tuned such that the empirical relationship is produced, as opposed to using a priori selected parameter choices. Once some physical criteria are met, a set fraction of the gas mass is converted to stars, typically 1% to 10% per local dynamical time. The criteria for triggering star formation typically include a density threshold, the presence of converging flows, and a cooling time which is shorter than the dynamical time. This ensures that the gas is in GMCs, which are composed of cold, dense gas. While the density thresholds correspond to, at best, the neutral medium (e.g., 5 cm^{-3} in Guedes et al., 2011), GMCs are formed by colliding flows of warm neutral medium (e.g., Vázquez-Semadeni et al., 2011), which is the reasoning for having a converging flows criterion. This route is taken out of necessity, due to the resolution of galaxy-scale simulations.

However, this does not consider the complexities of a cloud's internal physics. Stars do not form randomly throughout GMCs. Rather, they form where the clouds in densest. We model this substructure with the concept of clumps embedded in clouds. Furthermore, these clumps contain cores, where star formation occurs. Cores are the gravitationally bound precursors to individual stars or simple stellar systems. Typical radii are $R = 1 - 7.5$ pc for clouds, $R = 0.15 - 1.5$ pc for clumps, and $R = 0.015 - 0.1$ pc for cores. Meanwhile, as size decreases $\mathrm{H_2}$ densities increase, with typical densities being $n = 50 - 500\ \mathrm{cm}^{-3}$ for clouds, $n = 10^3 - 10^4\ \mathrm{cm}^{-3}$ for clumps, and $n = 10^4 - 10^5\ \mathrm{cm}^{-3}$ for cores (Bergin & Tafalla, 2007). When optimized for resolution, entire-galaxy simulations are capable of resolving to cloud scales (e.g., Dobbs et al., 2011; Fujimoto et al., 2014). However, clump and core scales are not currently attainable.

Regardless of its necessity, a universal star formation efficiency which is activated at a universal density threshold is a very simplistic model for such an important process. Such a model ignores the conversion of relatively diffuse molecular gas in clouds to denser substructures. The fraction of gas mass converted to clumps and then to cores surely influences the number and mass of stars formed. Furthermore, clouds are turbulent, and this turbulence may be important in driving star formation (e.g., Padoan et al., 1997; Enoch et al., 2008), but is ignored in galaxy evolution simulations. Because of these simplifications, it is imperative that these star formation recipes be tested against reality.

Such a test requires observations of clouds and their substructures using the tracers best suited to each density level. Whole clouds are traditionally identified using emission from the lower rotational transitions in CO (e.g., Scoville & Solomon, 1975; Solomon et al., 1987). However, these transitions are generally optically thick, impeding our ability to detect denser substructures. This can be somewhat mitigated by observing higher-J transitions of CO or by observing the isotopologues of CO, most commonly ^{13}CO, but at the cost of weaker lines.

Dense cloud substructures are better traced by the solid dust grains found amongst the gas. Dust makes up approximately 1% of the ISM by mass (Draine, 2003) and there is evidence for grain growth within molecular clouds. This dust emits thermally in the millimeter and submillimeter regimes. Importantly, dust emission at these wavelengths is optically thin, allowing us to see through the entire Galactic disk, despite lacking velocity information.

Dust is also an effective tracer of recent star formation, if viewed at shorter wavelengths. Newly formed stars are still embedded in the dense gas from which they formed, making them difficult to observe directly. Instead, we observe the effects of the new stars on their environment. The heat from these stars can increase the temperature of the gas and dust from 20 K (a typical temperature for molecular cloud clumps) to around 120 K, corresponding to a peak wavelength of 24 μm. Naturally then, 24 μm is a popular waveband in which to view ongoing star formation (e.g., Rieke et al., 2009). At longer wavelengths, the emission revealing star formation becomes contaminated with cirrus emission. Nevertheless, 70 μm is another popular waveband for such work (e.g., Calzetti et al., 2010). In fact, it is preferred by some, as contamination from cirrus is easier to remove than the contamination from evolved stars found in 24 μm emission (Svoboda et al., 2016).

In this chapter, we use Galactic Plane surveys which trace molecular clouds, molecular cloud clumps, and ongoing star formation. We build on the previous efforts of Zetterlund et al. (2018), which produced a catalog of molecular cloud clumps using 500 μm thermal dust maps from the *Herschel* infrared GALactic plane survey (Hi-GAL) and the distance determination techniques of (Ellsworth-Bowers et al., 2013). The application of those methods to Hi-GAL is described in Zetterlund et al. (2017). We combine this molecular cloud clump catalog with the molecular cloud catalog of Colombo et al. (2018), made using CO High Resolution Survey (COHRS) data. Furthermore, we derive star formation rates from 70 μm Hi-GAL data. Using these catalogs, we investigate which cloud properties influence clump formation efficiencies and star formation rates in order to provide a check for galaxy evolution simulations.

4.2 Data

4.2.1 Hi-GAL clump catalog

The *Herschel* infrared GALactic plane survey (Hi-GAL) (Molinari et al., 2010) observed the entire 360° of the Galactic Plane in a 2° strip. Using the SPIRE (Griffin et al., 2010) and PACS (Poglitsch et al., 2010) instruments aboard the *Herschel Space Observatory* (HSO), this survey observed in wavebands centered at 70, 160, 250, 350, and 500 μm. In this chapter, we use SPIRE's 500 μm maps, which show thermal dust emission that is concentrated in dense molecular gas clumps. Owing to the low optical depth of thermal dust in the submillimeter continuum, Hi-GAL allows us to view this dense molecular gas throughout the entire Galactic disk. In addition, we use PACS's 70 μm maps in order to measure star formation rates as inferred by heated dust.

Molecular cloud clumps were extracted from the 500 μm maps in Zetterlund et al. (2018) (See Chapter 3). Each Hi-GAL map within the Galactic longitudes $10° < \ell < 56°$ was high-pass filtered to remove large-scale flux density originating from cirrus clouds. Source identification was done with Bolocat, a seeded watershed algorithm, on the processed maps (Rosolowsky et al., 2010).

Many line-of-sight clump velocities were known through pointed observations of the $J = 3-2$ rotational transitions of HCO^+ and N_2H^+ made for BGPS clumps from Shirley et al. (2013). Targets without a specific dense gas measurement had their velocities established through morphologically matching the emission in the dust continuum to the emission from ^{13}CO(1-0) data in the BU-Galactic Ring Survey (Jackson et al., 2006), using the algorithm developed by Ellsworth-Bowers et al. (2015a).

Using these velocities, distances were determined using the method developed for BGPS by Ellsworth-Bowers et al. (2013) and Ellsworth-Bowers et al. (2015a). This method probabilistically breaks the kinematic distance ambiguity using a Bayesian framework. A distance probability density function (DPDF) is calculated for each clump. The posterior DPDF is found by,

$$\mathrm{DPDF} = \mathcal{L}(d_\odot|\ell, b, v_\mathrm{LSR}) \prod_i P_i(d_\odot|\ell, b),$$

where $\mathcal{L}(d_\odot|\ell, b, v_\mathrm{LSR})$ is the kinematic distance likelihood, and the $P_i(d_\odot|\ell, b)$ are various Bayesian priors which will help determine which distance has the higher probability of being true. Parallax excluded, the most powerful prior morphologically matches 8 μm absorption features to the dust continuum emission, most often placing objects exhibiting significant absorption at their near kinematic distances. Using Bayesian statistics allows for a continuous distance probability function, as opposed to a simple near-far discrimination. Once DPDFs are calculated, distance estimates can be drawn in Monte Carlo fashion, and provide robust uncertainties for cloud clump properties.

4.2.2 COHRS cloud catalog

The CO High Resolution Survey (COHRS) (Dempsey et al., 2013) is a large-scale CO survey that imaged the inner Galactic Plane in $^{12}\mathrm{CO}(J = 3-2)$ using the James Clerk Maxwell Telescope (JCMT). The survey mapped the Galactic Plane over the longitude range $10^\circ.25 < \ell < 55^\circ.25$, with width varying from $0^\circ.5 - 1^\circ$ of latitude, for a velocity range $-30\,\mathrm{km\,s^{-1}} < v_{LSR} < 155\,\mathrm{km\,s^{-1}}$. This ^{12}CO line traces warm molecular gas (10-50 K) and moderate densities, and thus is sensitive to giant molecular clouds (GMCs) with active star formation.

Molecular gas clouds in COHRS were identified using the Spectral Clustering for Interstellar Molecular Emission Segmentation (SCIMES) algorithm (Colombo et al., 2015). This algorithm extracts a series of nested hierarchical sources in position-position-velocity (PPV) space, called a dendrogram, based on emission levels. The dendrograms consist of leaves, which correspond to local maxima and have no substructures; branches, which contain leaves and/or other branches; and a trunk, which is the superstructure which contains all other structures. These dendrograms are used to identify clouds using a graph theory framework. Dendrograms are converted into fully-connected graphs, which are then weighted based on properties of the isosurfaces connecting each pair of leaves. The weighted graphs, which can be represented as similarity matrices, are then used to identify coherent clouds. This is demonstrated in Figure 4.1. The similarity criteria utilized by SCIMES are based on the luminosities of the emission within the isosurface connecting two leaves, and the volumes of those isosurfaces. Higher similarity values are assigned to connections between leaves made by isosurfaces having more emission within smaller volumes. Leaves are separated into clusters which define clouds by globally maximizing intracluster similarity and minimizing intercluster similarity. Unlike algorithms such as BOLOCAT, SCIMES does not separate GMCs into their substructures, thus allowing us to compare properties of entire clouds (from COHRS) to those of their embedded clumps (from Hi-GAL). For details on the application of SCIMES to the COHRS dataset, see Colombo et al. (2018). A sample of the COHRS clouds identified by SCIMES is shown in Figure 4.2. The right shows a visual representation of the full dendrogram, whereas the left shows the ultimate mask selection.

Distances are assigned to COHRS clouds using the DPDFs from Zetterlund et al. (2018). Each Hi-GAL distance is assigned to a pixel in PPV space. The mean of any distance pixels falling within a cloud is assigned to that cloud. Clouds containing no distance pixels take on the distance of the nearest cloud within the dendrogram structure. Where this is not possible, as with isolated clouds, the nearest distance in PPV space is used. See further Colombo et al. (2018).

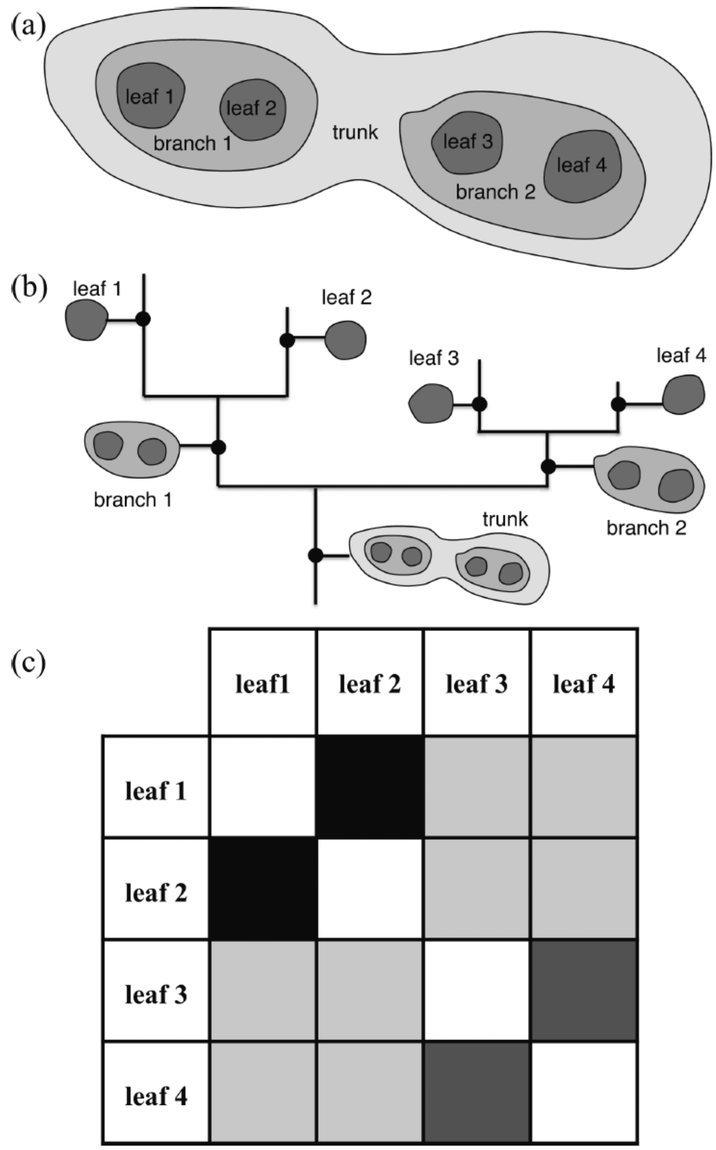

Figure 4.1: Nested substructures are identified from molecular line emission (a) and organized into a dendrogram (b). Leaves 1 and 2 are joined by branch 1, but these leaves are also joined to leaves 3 and 4 through the trunk at a lower hierarchical level. Since all leaves are connected to all other leaves, a fully-connected graph can be constructed, with the weights of the edges being shown in the similarity matrix (c), where darker colors indicate higher similarity. In this example, we consider the 'area' of the isosurface to weight the edges. Here the similarity between leaves 1 and 2 and between leaves 3 and 4 is much greater than between, for instance, leaves 1 and 4, due to the trunck having a greater area than either of the branches. Furthermore, leaves 1 and 2 have higher similarity than leaves 3 and 4, due to branch 1 having a slightly smaller area than branch 2. The optimal partition for the two clusters might provide the two objects identifiable with branches 1 and 2. (This figure from Colombo et al. 2015.)

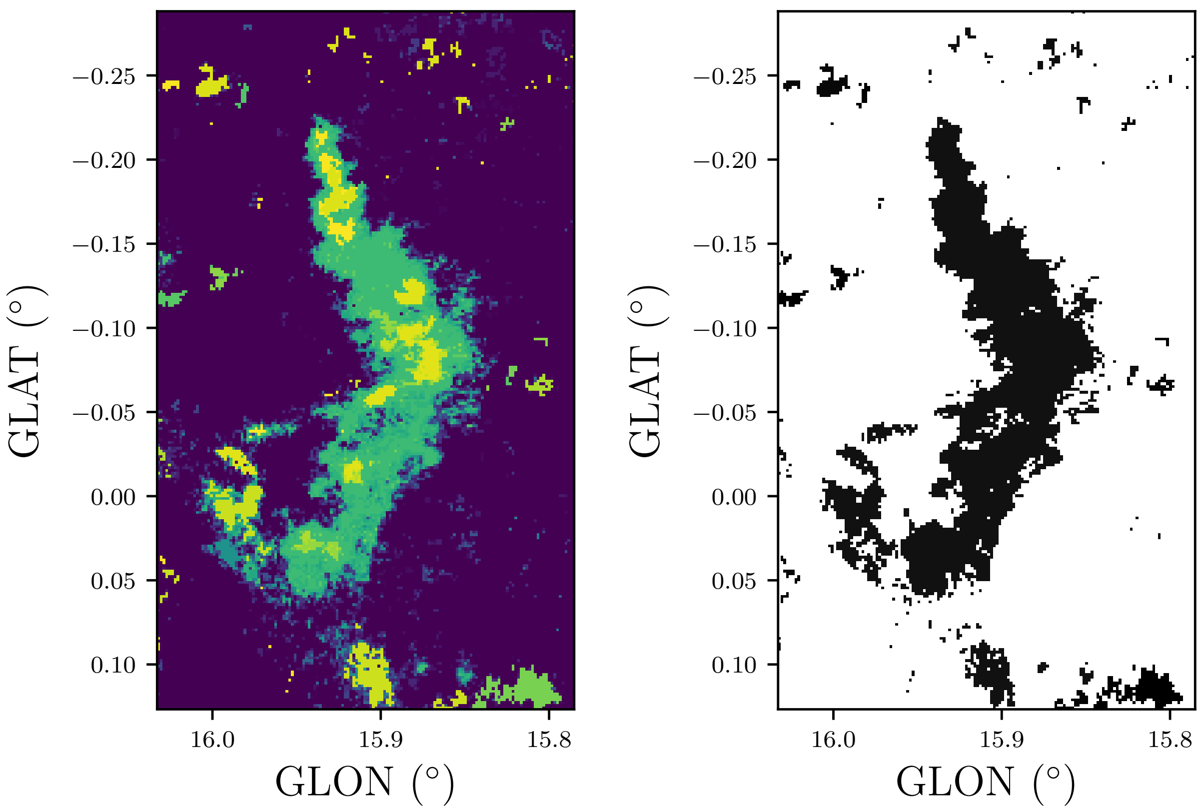

Figure 4.2: A sample image of the dendrogram structure underlying the COHRS clouds. *Left*: The full dendrogram structure for a sample region, represented as colored masks, with masks for smaller structures preferred to masks for the larger structures in which they are nested. Colors are assigned based on dendrogram structure number, and therefore more yellow pixels correspond to objects higher in the dendrogram hierarchy. *Right*: A binary view of the resulting COHRS cloud masks. In addition to the clouds on the right collapsing the dendrogram substructures, there are dendrogram levels lower than those chosen as COHRS objects, which were considered insignificant by the graph theory algorithm that made the separations into clusters.

4.3 Method

4.3.1 Matching Hi-GAL clumps to COHRS clouds

We match Hi-GAL clumps to their host COHRS clouds using the COHRS masks and Hi-GAL peak positions and velocities. For clumps with known velocities, matching is straightforward. Clumps which meet the local flux threshold are associated with whichever cloud's PPV mask they fall within. As the flux sensitivity of the maps varies by Galactic longitude (as discussed in Zetterlund et al., 2017), we set the integrated flux threshold to be equivalent to three beams' worth of emission at the clump identification threshold used in Bolocat. We chose this threshold as the value which minimizes dubious matches, while retaining as many likely matches as possible. So long as a cloud has at least one clump which lies within the cloud's PPV mask and meets the flux criterion, all of the cloud's velocity-matched clumps are kept, including those below the integrated flux density threshold. We also allow for secondary clumps to be associated to the cloud if their velocity is within 1σ of the cloud, but not strictly inside its mask. Each of these secondary match criteria account for fewer than 10% of matched clumps, and were included because they recover otherwise unmatched clumps which are clearly contained within clouds on visual inspection. We have determined that it is more likely that their inclusion avoids an underestimation of mass contained within clumps than causes an overestimation.

However, not all Hi-GAL clumps have known velocities. While we do not allow clouds to be matched solely to velocity-less clumps, we make additional matches based on the dendrograms from which the clouds were identified. To do this, we make a list of all the dendrogram structures at the peak clump (ℓ, b) position, collapsing the dendrogram object masks along the velocity axis. We then trace each dendrogram structure back to its parent cloud. If that dendrogram structure contains 4 or fewer leaves, contains 10% or fewer of the total number of leaves contained in the full cloud, and there is only one cloud which meets the prior two criteria, we associate the clump with the cloud. Since leaves in SCIMES are often smaller than a beam, it is not useful to require the clump be aligned with a dendrogram leaf. Since SCIMES only allows for binary mergers in its dendrograms, 4 leaves allows for the object to be two hierarchical levels down from a single leaf. However, not all clouds contain a large number of leaves, and therefore we use the $\leq$10% of total leaves criterion to ensure that the clump is aligned with a peak in the emission and not merely a small cloud. We found our cut-offs to simultaneously optimize for confidence in the match and number of matches found. Tighter requirements made for fewer matches, and for missing many matches that were obvious by eye. Loosening the requirements resulted in fewer matches at lower confidence, as more than one cloud along the line of sight could meet the criteria, leading to the clump not being matched to either cloud. The clump is also matched if there is exactly one cloud along the line of sight, regardless of leaf quantities.

4.3.2 Clump properties

Physical radii are given as $R = \theta_R d_\odot$, where θ_R is angular radius and $d_\odot$ is heliocentric distance. θ_R is calculated as the geometric mean of the deconvolved major and minor axes of the flux density distribution of the clump,

$$\theta_R = \eta[(\sigma^2_{\mathrm{maj}} - \sigma^2_{\mathrm{beam}})(\sigma^2_{\mathrm{min}} - \sigma^2_{\mathrm{beam}})]^{1/4},$$

where, for Hi-GAL PLW (500 μm), $\sigma_{\mathrm{beam}} = \theta_{\mathrm{FWHM}}/\sqrt{8\ln 2} = 15''$, $\theta_{\mathrm{FWHM}} = 35''$, and $\eta = 2.4$ is a factor relating the rms size of the emission distribution to the true size of the source, which is adopted from Rosolowsky et al. (2010).

Our clump mass estimates use high-pass filtered flux densities at 500 μm. The conversion from flux density to mass is

$$M = \frac{\Gamma d^2_\odot}{\kappa_{500} B_{500}(T)} S_{500},$$

where $\Gamma = 100$ is the gas-to-dust mass ratio, $\kappa = 5.04$ cm^{2}g^{-1} is the opacity at 500 μm (Ossenkopf & Henning, 1994), $B_{500}(T)$ is the Planck function at 500 μm, $d_\odot$ is the heliocentric distance, and S_{500} is the integrated flux density from 500 μm maps. Battersby et al. (2011) used pixel-by-pixel modified blackbody fits of Hi-GAL data to determine that mid-infrared-dark molecular cloud clumps generally span the temperature range 15 K $\lesssim T \lesssim$ 25 K. Following these findings, we adopt a constant clump temperature of 20 K for this study. Uncertainty in clump mass comes from two sources. First, photometric errors, which are relatively low, and arise from the confusion in the Hi-GAL maps. We calculate photometric errors by assuming the per-pixel confusion noise level can be estimated as the flux density level used for clump identification with Bolocat (see Zetterlund et al., 2017). Second, systematic errors arise from our assumption of a constant temperature, as well as uncertainty in the dust opacity. We estimate that due to these systematic factors, we know clump masses to a factor of two.

From the clump masses and radii, we calculate number densities as

$$n = \frac{3M}{4\pi\mu R^3}. \tag{4.1}$$

That is, by assuming a spherical geometry and a mean molecular mass of $\mu = 2.4$. Note that this results in mean number densities. However, we expect that the clumps are centrally concentrated, leading to greater densities near the middle.

4.3.3 Cloud properties

We define a cloud's clump formation efficiency as the fraction of the cloud's gas which was converted into dense clumps that may form stars. We estimate this quantity as our observed clump mass fraction,

$$\text{Clump Mass Fraction} = {}^{M_{\rm clump}}/_{M_{\rm GMC}} = \sum_i {}^{M_{{\rm clump},i}}/_{M_{\rm GMC}}. \tag{4.2}$$

That is, the sum of the clump masses contained in a cloud divided by the cloud mass, where i indexes the individual clumps.

Cloud properties derived from ^{12}CO(3-2) emission were calculated by Colombo et al. (2018) and are summarized here. The effective radius of a cloud is calculated from its gaussian fit axes as

$$R_{\rm eff} = \eta\sqrt{\sigma_{\rm maj}\sigma_{\rm min}},$$

where σ_{maj} and σ_{min} are the major and minor axes calculated as the intensity-weighted second moments along the two spatial dimensions of all of the pixels within the object mask. $\eta = 1.91$ is adopted as the scaling factor, following Rosolowsky & Leroy (2006) and Solomon et al. (1987). This η value is different than the one cited in Section 4.3.2 for determining clump radii. The $\eta = 2.4$ scaling factor used for clumps was calculated analytically for a spherical density profile of $\rho \propto r^{-1}$. The $\eta = 1.91$ value used for clouds includes an empirical correction calculated by Solomon et al. (1987), who studied GMCs using CO data.

We calculate the mass of a cloud using its ^{12}CO(3-2) luminosity. This so-called luminosity mass is calculated as

$$M_{\mathrm{lum}} = \frac{\alpha_{\mathrm{CO}}}{R_{31}} L_{\mathrm{CO}},$$

where L_{CO} is the ^{12}CO(3-2) luminosity. $R_{31} = 0.6$ is the CO(3-2)/CO(1-0) flux ratio, calculated using the ^{12}CO(1-0)/^{13}CO(1-0) flux ratio of 7.5 produced by Roman-Duval et al. (2016) in tandem with ^{12}CO(3-2)/^{13}CO(1-0) flux ratio 4.5, with a scatter of 40% calculated using GRS and COHRS data (Colombo et al., 2018). This ratio is less certain towards the low-mass end, which is fortunately not were our clouds generally lie. The Galactic ^{12}CO(1-0)-to-H_2 conversion factor is $\alpha_{\mathrm{CO}} = 4.35$ $\mathrm{M}_\odot$ pc^{-2} (K km $\mathrm{s}^{-1})^{-1}$, known to a precision of ± 0.1 dex, based on the aggregate of a variety of techniques (e.g., Bolatto et al., 2013). In the analysis that follows, cloud mass, M_{GMC}, is taken to be the cloud's mass derived from ^{12}CO(3-2) line luminosity, as defined in above. From this, we also calculate the surface mass densities as

$$\Sigma(\mathrm{M}_\odot\ \mathrm{pc}^{-2}) = \frac{M_{\mathrm{lum}}}{\pi R_{\mathrm{eff}}^2},$$

and number densities as in Equation 4.1.

In addition, the virial mass is calculated using the cloud's radius, R_{eff}, and velocity dispersion, σ_v, as

$$M_{\mathrm{vir}} = \frac{5\sigma_v^2 R_{\mathrm{eff}}}{G}, \tag{4.3}$$

where G is the gravitational constant, and σ_v is calculated as the intensity-weighted second moment along the velocity axis. This follows Bertoldi & McKee (1992) who assumed a constant cloud density profile. The two mass estimates are used to determine the virial parameter,

$$\alpha_{\rm vir} = \frac{M_{\rm vir}}{M_{\rm lum}}, \tag{4.4}$$

which measures deviations from virial equilibrium. In the absence of magnetism, $\alpha_{\rm vir} > 2$ indicates that the cloud is stable against collapse, whereas $\alpha_{\rm vir} \ll 2$ suggests that the random motions within the cloud are not great enough to support the cloud, which therefore may be collapsing (see Section 4.8).

The methods of Colombo et al. (2018) correct for the finite sensitivity of COHRS using the extrapolation techniques developed by Rosolowsky & Leroy (2006). These corrections are made by first determining the basic moments of the cloud ($\sigma_{\rm maj}$, $\sigma_{\rm min}$, σ_v, $F_{\rm CO}$) at various identification thresholds. The values at these thresholds are then linearly fit (quadratic polynomial fit for $F_{\rm CO}$) in order to determine the moments at infinite sensitivity (i.e. 0 K). Once these extrapolated moments are calculated, the beam width is deconvolved from the size of the cloud ($\sigma_{\rm maj}$, $\sigma_{\rm min}$, σ_v) by subtracting in quadrature. Note that these corrections have a more significant effect on smaller sources. As we are concerned with the largest clouds in the COHRS catalog, the effects on our data are minimal.

Star formation rates for clouds were calculated using Hi-GAL 70 μm images. This is the short wavelength limit for Hi-GAL and corresponds to dust that is heated by new stars. We relate star-formation rate to 70 μm luminosity using the calibration of Calzetti et al. (2010):

$$\mathrm{SFR}(\mathrm{M}_\odot\ \mathrm{yr}^{-1}) = \frac{L(70)(\mathrm{erg\ s}^{-1})}{1.7 \times 10^{43}}.$$

The scatter about this relation is ~ 0.2 dex, or about 60%. It should be noted that this calibration was developed using galaxy luminosity data, and therefore may not be as reliable for individual GMCs. At this wavelength, we are sensitive to stars of ages $0 - 100$ Myr, with a mean emission-contributing stellar age of 5 Myr.

In order to extract the flux densities required for conversion to SFRs, we integrate the flux density found within the velocity-collapsed COHRS mask. We account for background flux and cirrus emission by creating a rind around the mask with a width of 1 to 1.5 resolution elements. We fit a second-degree linear polynomial (i.e., a polynomial with the form $f(x) = c_0 + c_1x + c_2y + c_3xy$) to this rind and subtract the resulting background flux density from the the source flux density. Our main source of systematic uncertainty is due the superposition of multiple clouds along a single line-of-sight, although background subtraction mitigates much of this. We estimate our fractional SFR uncertainty as the fraction of CO flux along the line of sight which is not associated with the cloud. This accounts for uncertainties in our background subtraction, and asks the question, if all of the gas emitting in ^{12}CO(3-2) is equally forming stars, how much 70 μm emission did we mistakenly attribute to this cloud?

4.4 Results

We matched a total of 4,704 Hi-GAL clumps to 1,182 COHRS clouds. Of those 4,704 clumps, 3,157 were matched using their velocities (of which 423 did not meet the flux threshold, and 121 had velocities slightly outside the COHRS mask), and 1,124 were matched using the COHRS dendrograms. We are most concerned with clouds at size scales of $\sigma_{\rm major} > 3'$ (see Section 4.5.1). Using this cut, we retain a subset of the above containing 3,674 clumps matched to 473 clouds. Two sample clouds with their matched clumps are shown in Figure 4.3. Clouds (black contours) at large angular size scales typically have multiple clumps matched to them, using both velocity information (blue contours) and dendrogram structure (green contours) for those clumps without velocity information.

Although the COHRS catalog is extensive, containing 85,020 objects of widely varying sizes, only 724 of those are clouds that have angular sizes of $\sigma_{\rm major} > 3'$. We have matched clumps to 65% of these clouds. If we additionally require the clouds to have $M > 10^4$ M$_\odot$, we associate clumps with 75% of clouds, and 95% for $M > 10^5$ M$_\odot$. Of the 19,886 clumps in our Hi-GAL catalog, 7,362 lie within the narrower latitude coverage of COHRS. Of these, 64% were matched to COHRS clouds

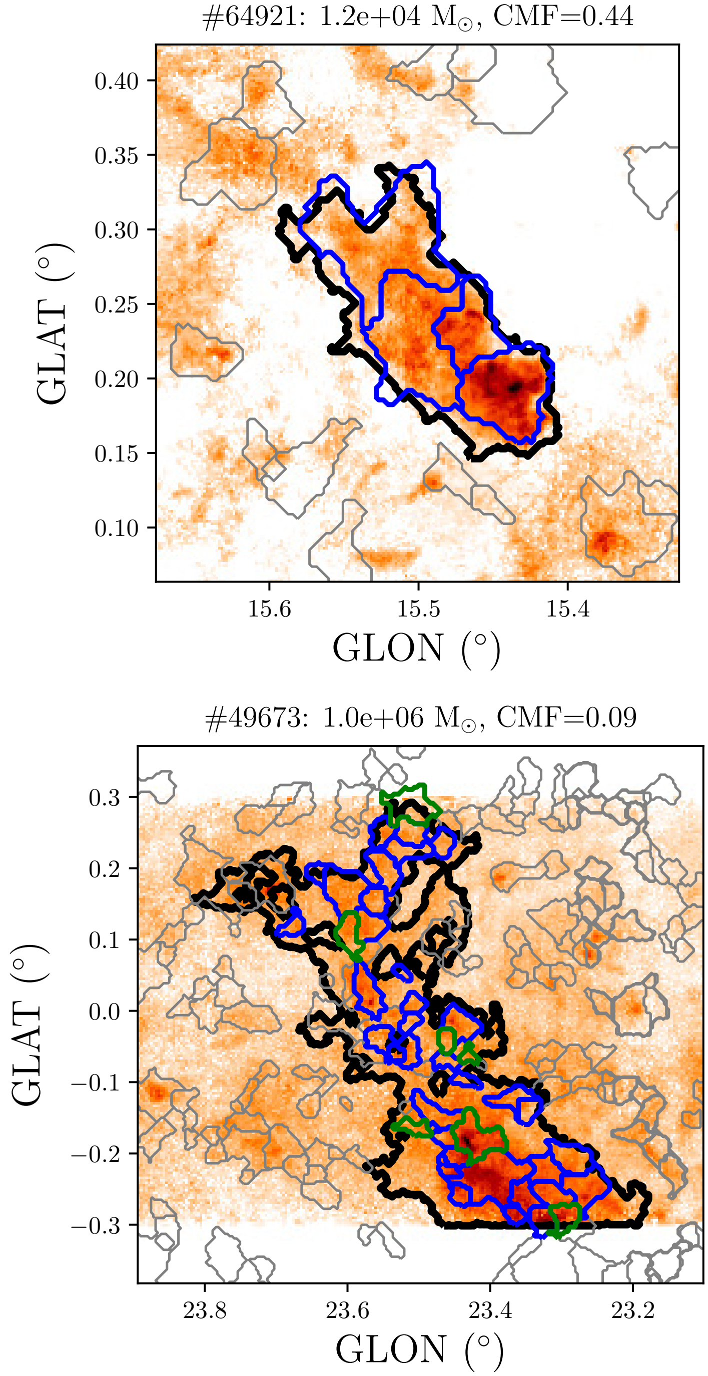

Figure 4.3: Sample clump-to-cloud matching, at two different size scales. ^{12}CO($J = 3-2$) emission is shown in orange, integrated over the velocity extent of the cloud. The thick black contour shows the COHRS cloud. Blue and green contours show Hi-GAL clumps matched to the cloud via velocity and dendrogram structure, respectively. Thin grey contours show other Hi-GAL clumps, which were not matched to the cloud contoured in the image. Emission (orange) outside of the black contour occurs in the same velocity range as the cloud shown, but is not associated with it, according to SCIMES. The COHRS catalog number, cloud mass, and clump mass fraction are found above each image.

(before instituting the angular size cut). Furthermore, 4,046 clumps both lie within the COHRS coverage and have known velocities. Our match rate for these known-velocity clumps is 78%.

In order to check that we are indeed probing denser regions with our Hi-GAL clump catalog than with our COHRS cloud catalog, we plot the number densities of individual clumps against those of their host clouds in Figure 4.4. Both our clouds and clumps are sparser than the nominal densities of $n_{\text{cloud}} = 50 - 500$ cm^{-3} and $n_{\text{clump}} = 10^3 - 10^4$ cm^{-3}. Despite this, nearly all of the points lie above the identity line, meaning that the clumps are denser than the cloud in which they are embedded. A handful of points lie below the identity line. These are likely a product of the substantial uncertainties on the density values. Clump densities appear to be dependent on cloud densities only in that clumps must be denser than clouds. No further correlation is seen. Mean cloud and clump densities are 58 cm^{-3} and 750 cm^{-3}, respectively. Density distributions for both structure types are well-described by lognormal functions. The parameters for these fits are $\mu = 3.6$, $\sigma = 0.02$ for clouds; and $\mu = 5.5$, $\sigma = 0.003$ for clumps. Free-fall times are shown as a grid of grey lines. The mean free-fall times for clouds and clumps are 6.1 Myr and 2.4 Myr respectively.

4.5 Clump Formation Efficiency

We calculate mass fractions using Equation 4.2. We expect these mass fractions to be reliable estimates of the clump formation efficiencies (CFEs). It is possible that some of our so-called clumps are not actually gravitationally bound, but instead are extended along the line-of-sight, artificially increasing the mass fraction by including gas mass which is less concentrated than a clump. In addition, there were likely clumps which did not meet our matching criteria, but should have been associated with a cloud in our catalog, thus artificially lowering our mass fractions.

4.5.1 CFE Distribution

Figure 4.5 (top) shows these mass fractions, plotted against cloud mass. The mass fractions span several orders of magnitude, with some points over unity. The Hi-GAL maps were high-pass filtered at a scale of $3'$ before clumps were identified. Due to this, at angular scales smaller than $3'$,

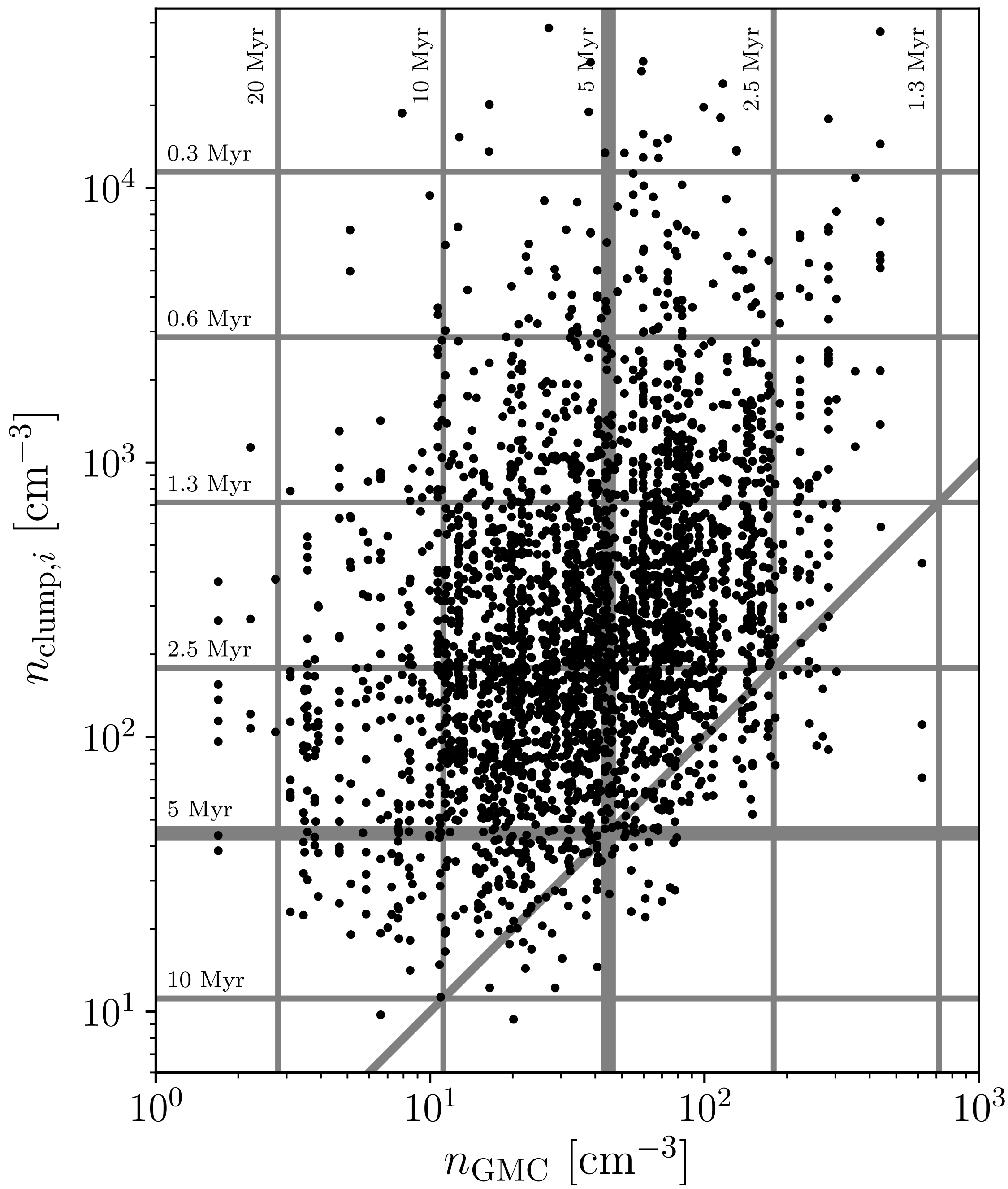

Figure 4.4: Number densities of individual clumps, plotted against their host clouds. Uncertainties (including systematic) are roughly an order-of-magnitude for clouds and a factor of 2 for clumps. The identity line is also shown in grey. Because of the large error bars, the handful of points below this line do not pose a problem. Horizontal and vertical lines correspond to free-fall times for clumps and clouds, respectively. The thick lines show $t_{\mathrm{ff}} = 5$ Myr, with additional lines being varying from their neighbors by a factor of 2. Note that we do not expect all GMCs to be collapsing.

we are prone to matching clouds and clumps at similar size scales, and is some cases even match clumps which are larger than their clouds. This leads to mass fractions greater than one.

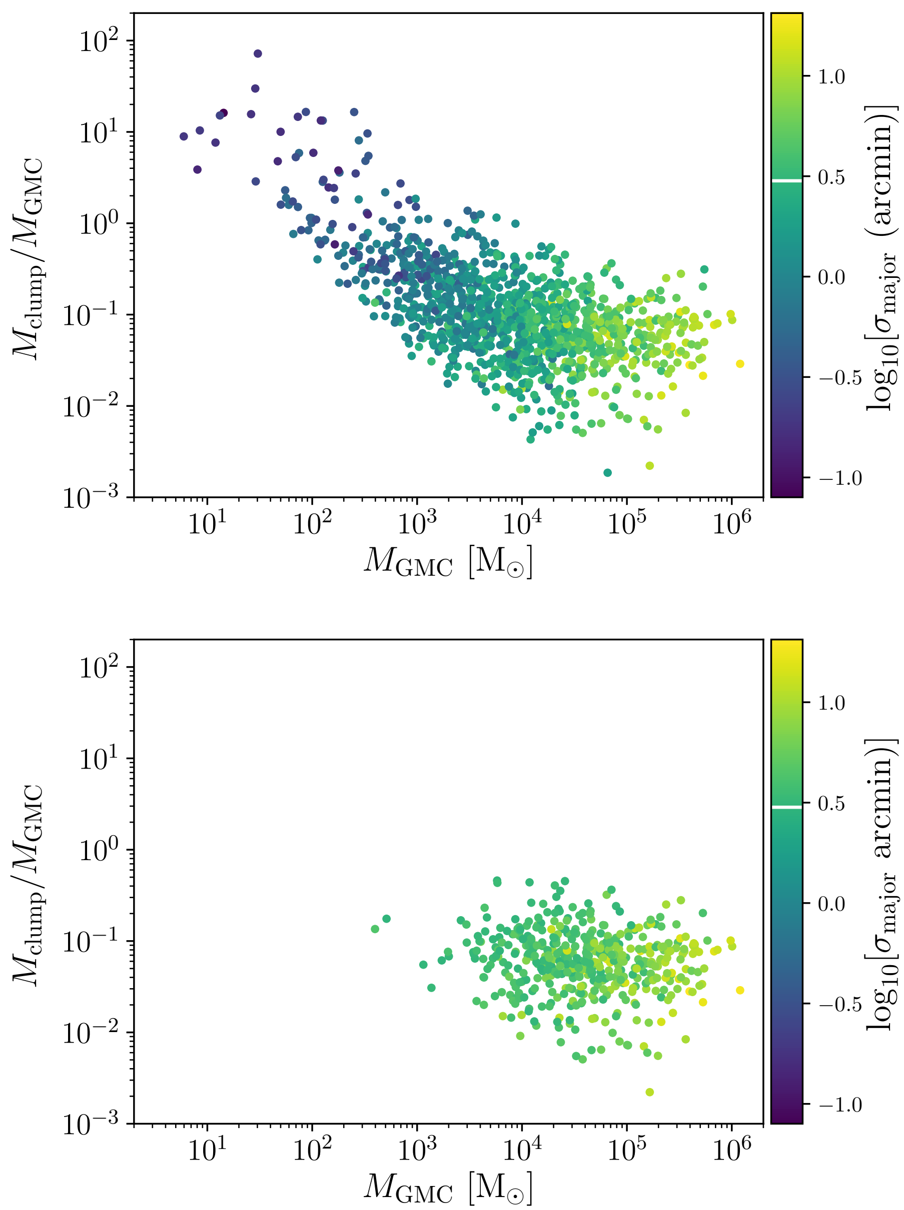

Figure 4.5: Clump mass fraction as a function of cloud mass. Points are colored by cloud major axis. The full sample is found in the upper panel. At size scales smaller than 3′ (marked with a white dash on the colorbar), Hi-GAL detects sources at similar angular sizes to COHRS, and thus similar mass levels in the clumps as the clouds, leading to clump mass fractions over unity. These clumps are excluded from our analysis, leaving only those clouds found in the lower panel.

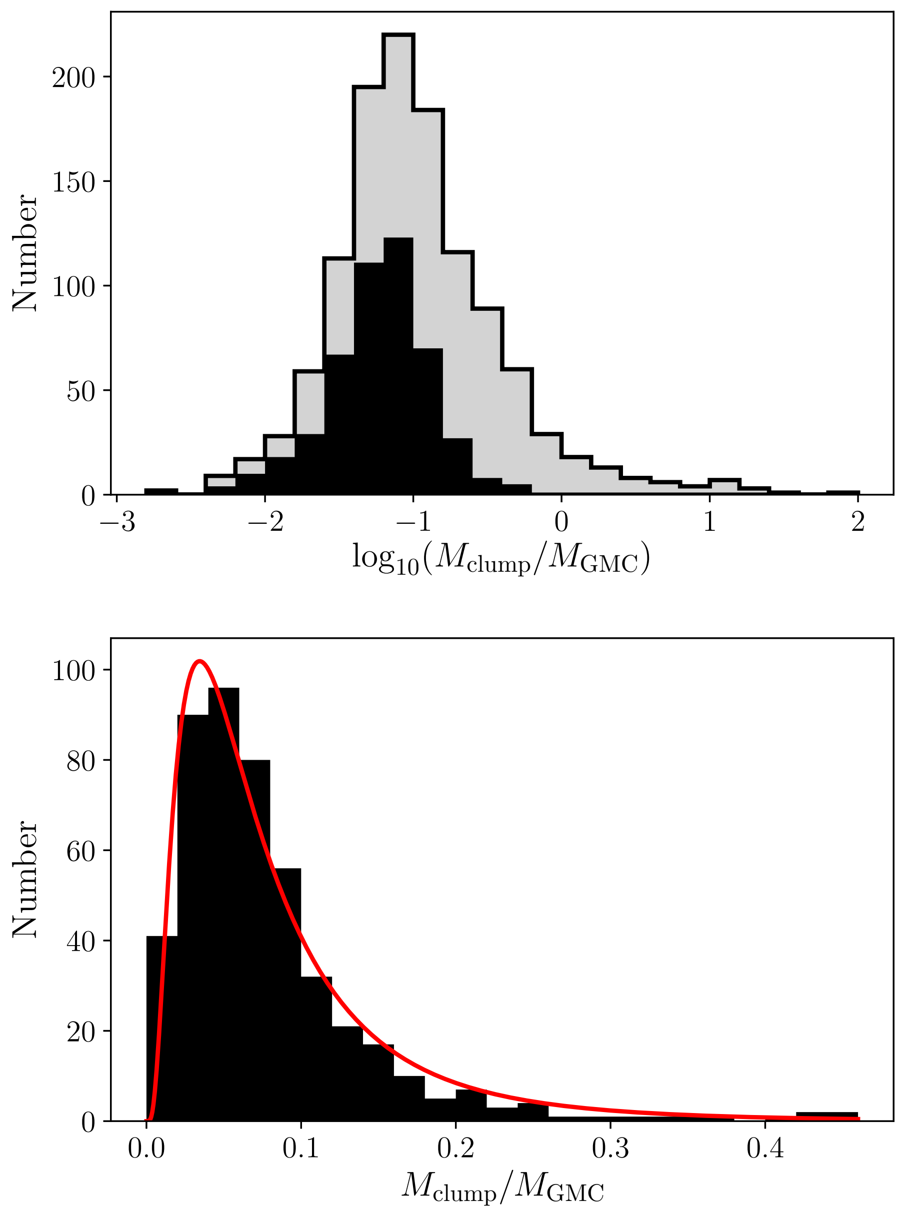

Figure 4.6: Distributions of clump mass fractions. *Upper*: Grey shows of the matched clouds. Black shows the subset which have $\sigma_{\rm major} > 3'$. *Lower*: The same subset of clouds with $\sigma_{\rm major} > 3'$, but with a linear horizontal axis. The red curve represents the lognormal fit to the data, with parameters $\mu = -2.7$ and $\sigma = 0.8$.

Because of this, we consider only the GMCs with $\sigma_{\rm major} > 3'$. This ensures that all clumps are smaller than the cloud which contains them. If we instead we accomplish this by checking the angular size of each clump against that of its host cloud, the distribution of mass fractions does not change significantly. Also notable is that the lower left-hand quadrant of this plot is empty. This is due to the mass sensitivity of Hi-GAL. The lower the cloud mass, the fainter its substructures, and thus the less likely we are to detect its clumps. Figure 4.5 (bottom) shows the distribution of mass fractions after the $\sigma_{\rm major} > 3'$ cut on cloud size was made.

The mass fractions seen in Figure 4.5 are shown in histogram form in Figure 4.6. The mean mass fraction above the $3'$ GMC size cut is $0.08^{+0.05}_{-0.04}$, where the error bars encompass 68% of the GMCs. This is consistent with the clump mass fraction of $0.11^{+0.12}_{-0.06}$ found by Battisti & Heyer (2014) using BGPS and GRS data. Clump mass fractions follow a single lognormal distribution, as seen in the lower panel. This fit well describes our observed tail of higher clump formation efficiencies. This suggests that the clouds in the tail of this distribution are a true part of a single well-sampled population, and not evidence for a separate population at a different evolutionary stage. This is supported by Urquhart et al. (2018), who observed that clumps form rapidly within clouds and do not continue to gain mass throughout their evolutionary lifecycle. Furthermore, this distribution is in agreement with the dense gas fraction map calculated produced by Zetterlund et al. (2018), using Hi-GAL clumps and the azimuthally averaged H_2 model of Wolfire et al. (2003). In this map, 8% was a fairly typical value, and the peak value was 44%.

Enoch et al. (2007) studied the molecular clouds Serpens, Perseus, and Ophiuchus, and found that, within visual extinction contours of $A_V = 2$, less than 5% of the clouds' mass was found in cores (2.7%, 3.8%, and 1.2%, respectively). For $A_V = 6$ contours, the core mass fraction was still less than 10% in all three clouds (4%, 7%, and 2%, respectively). The mean core mass fractions for these three clouds are 2.6% and 4.3% for extinction contours of extinction contours of $A_V = 2$ and $A_V = 6$, respectively. If we consider our clump mass fractions of $0.08^{+0.05}_{-0.04}$, and consider that cores are nested in clumps, this equates to a clump-to-core mass efficiency of approximately 50%. However, it should be noted that these clouds are only a few thousand solar masses large, and therefore on the low-mass end of our cloud sample.

In order to assess if our mass fractions could reasonably produce the observed star formation rate in the Milky Way given the cloud mass we see in COHRS, we estimate the clump formation efficiency required for a Galaxy-wide SFR of 1 $M_\odot$ yr^{-1} (e.g., Robitaille & Whitney, 2010), as

$$\sum_i M_{\mathrm{GMC},i} \times \mathrm{CFE} \times \varepsilon \times 1/t_{\mathrm{ff}} = 1\ \mathrm{M}_\odot\ \mathrm{yr}^{-1} \times f_{\mathrm{obs}}.$$

We use $\sum\limits_i M_{\mathrm{GMC},i} = 7.2 \times 10^7$ $M_\odot$, which is the sum of all GMCs ($M > 10^3$ $M_\odot$) in the COHRS catalog. We assume a clump-to-star mass efficiency of $\varepsilon = 10\%$ as an order-of-magnitude estimate consistent with a core-collapse efficiency of 25% (Enoch et al., 2008). As our timescale, we use the mean free-fall time of a GMC in the COHRS catalog, $t_{\mathrm{ff}} = \sqrt{3\pi/32G\rho} = 3.2 \times 10^6$ yr. COHRS observed longitudes $10^\circ.25 < \ell < 55^\circ.25$, which is 45° in total, or a fraction, $f_{\mathrm{obs}} = 1/8$, of the full 360° of the Galactic Plane. These values combine to give a necessary clump formation efficiency, CFE, of 0.06. Likely, this value should be slightly higher, due to $f_{\mathrm{obs}} = 1/8$ not taking into account that we observed a section of the Galactic Plane containing more mass than average. Moreover, the free-fall time is the lower limit on the time frame, with the upper limit being the lifetime of the cloud, $\tau = 10t_{\mathrm{ff}}$ (Kennicutt & Evans, 2012). Using the average lifetime puts the necessary clump formation efficiency at CFE = 0.6. Compared with our observed mass fractions, this range of CFEs is reasonable, especially considering that confusion in Hi-GAL likely leads to us underestimating the mass fractions. Most importantly, the entire range is less than unity. Given these CFE values, we find it more likely that we underestimated clump mass fractions from our data than overestimated, although the above analysis shouldn't be taken as more than an order-of-magnitude estimation.

4.5.2 Relations with Physical Properties

In order to determine what properties of a GMC influence its clump formation efficiency, we plot clump mass fractions of clouds against various physical properties (Figure 4.7). In examining cloud mass, surface mass density, and virial parameter we see no correlation between clump mass fraction and these cloud properties. A cloud having more mass does not influence its clump mass

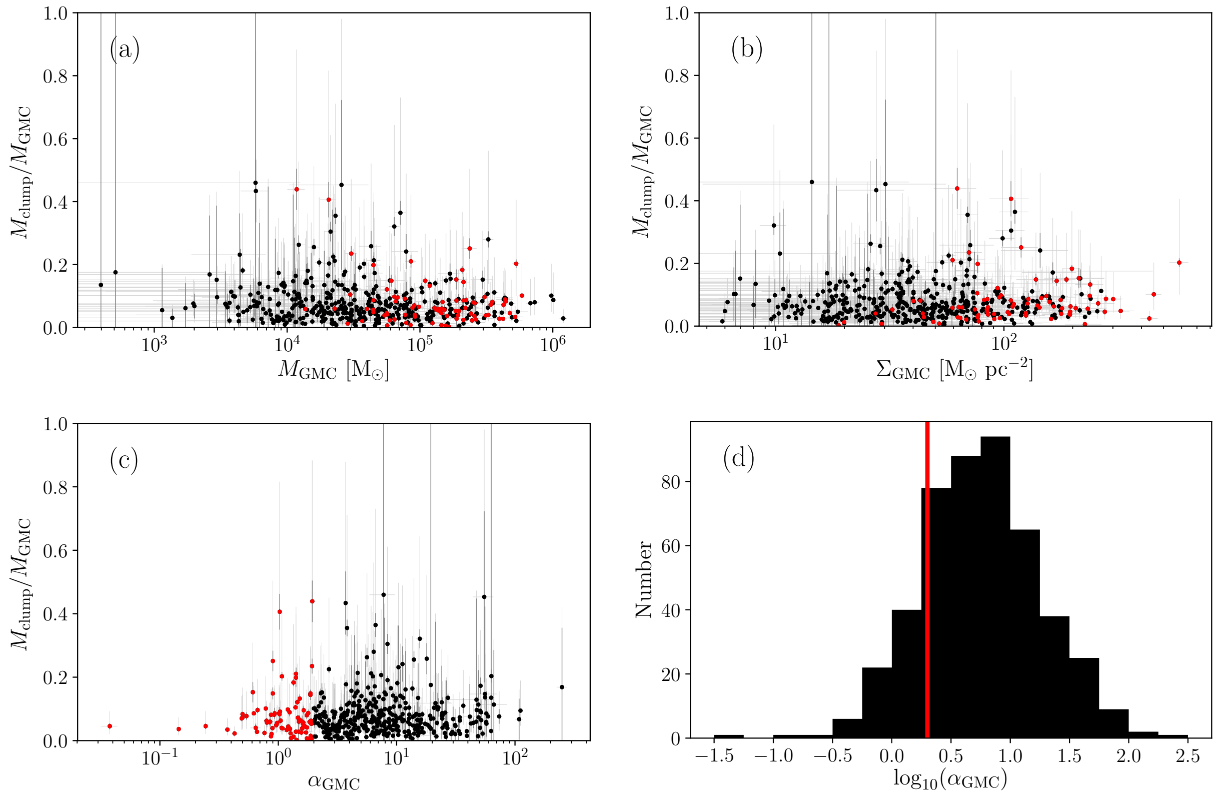

Figure 4.7: Clump mass fraction of the subset of clouds which have $\sigma_{\rm major} > 3'$, as a function of the following cloud properties: (a) mass, (b) surface mass density, and (c) virial parameter. Red points indicate clouds with virial parameters $\alpha_{\rm vir} < 2$. Panel (d) shows the distribution in virial parameters, with $\alpha = 2$ (below which clouds are unstable to collapse) marked by a red line.

fraction, nor does having more mass per projected area. In addition, a cloud's stability against collapse as a whole (see Section 4.8) does not influence the fraction of a cloud's mass which will collapse into denser clumps. This suggests that the clump formation efficiency is standard across clouds.

In these plots, red points correspond to non-virialized clouds ($\alpha_{\rm GMC} < 2$). That is, those unstable to gravitational collapse. This comprises $\sim 25\%$ of our sample. Panel (c) shows that the non-virialized clouds sample from the full distribution of clump mass fractions, as do virialized clouds. As seen in panels (a) and (b), these potentially collapsing clouds are more likely to have higher masses and surface mass densities. However, we know that lower mass clouds ($M \sim 10^3$ M$_\odot$) can collapse to form stars Enoch et al. (2008). These clouds are not absent from the COHRS catalog (see Section 4.8), but we are less likely to match Hi-GAL clumps to them. This may be due to the small clouds' clumps being too small for Hi-GAL to resolve, or too low mass to appear above the confusion noise. When we relax the $\sigma_{\rm major} > 3'$ size cut to GMCs and instead simply require the GMC to be larger than its constituent clumps (see Section 4.5.1), we recover some of these lower mass non-virialized clouds.

Clump mass fraction is not correlated with cloud mass or cloud surface mass density. There are two options for how this could come to be: (1) more massive clouds could have more clumps, or (2) they could have more massive clumps. The first option is investigated in Figure 4.8, which shows that more massive clouds have more clumps associated with them. They also have more COHRS dendrogram leaves, which correspond to local maxima in the CO(3-2) intensity, and serve as confirmation of the trend in number of Hi-GAL clumps. We find power law slopes of $\beta = 0.56 \pm 0.46$ and $\beta = 0.61 \pm 0.50$ relating cloud mass to number of clumps and number of dendrogram leaves, respectively. The 1σ dispersion for both data sets about their respective fits is 0.2 dex. Note that the large error bars make these fits statistically consistent with unity.

Figure 4.9 (upper) shows the mean clump mass for each cloud, plotted against the cloud mass. This demonstrates that more massive clouds also have more massive clumps, on average. This tendency could mean that the clump IMF is not universal, and instead favors more massive

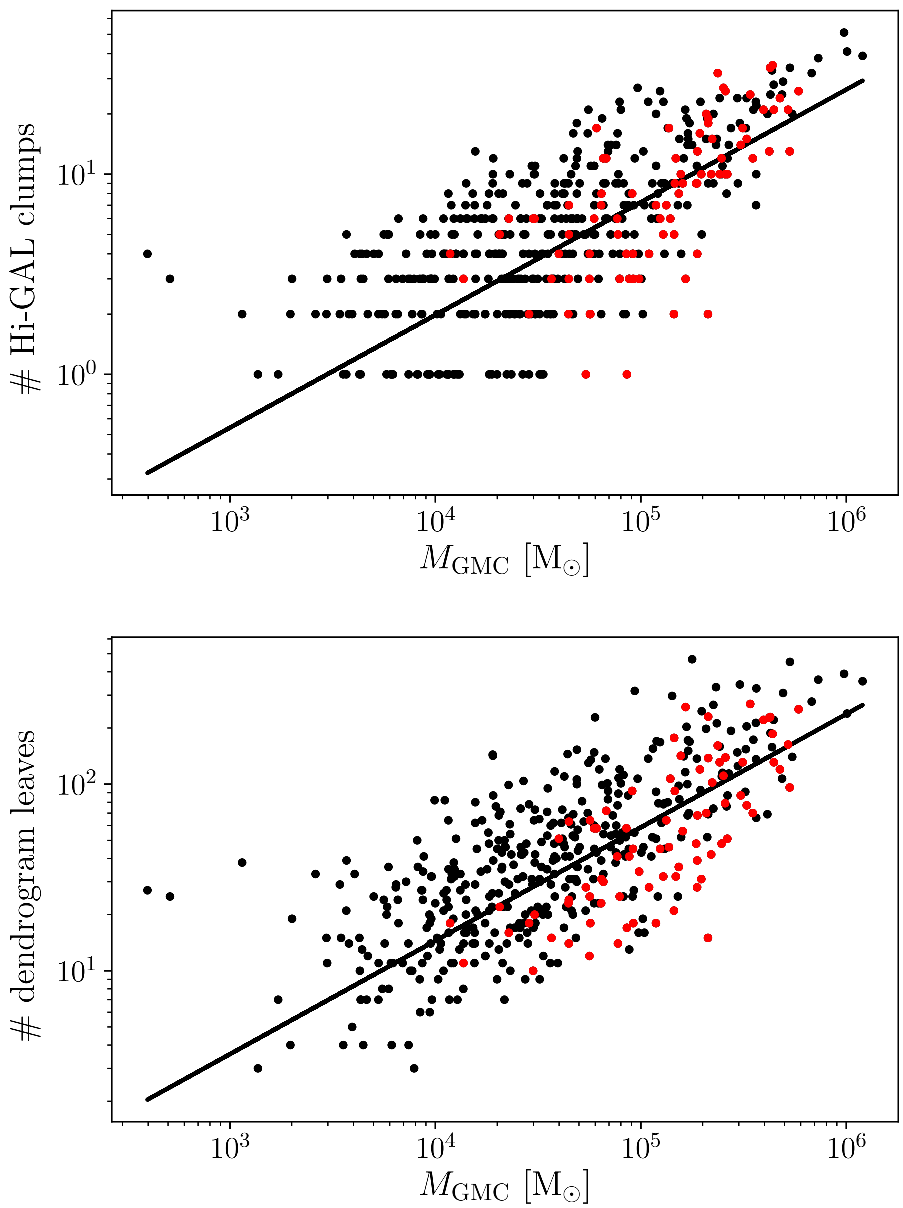

Figure 4.8: The number of clumps (top) and dendrogram leaves (bottom) in each cloud, as a function of cloud mass. The black lines represent power-law fits, both with slopes of 0.6 and 1σ dispersions of 0.2 dex.

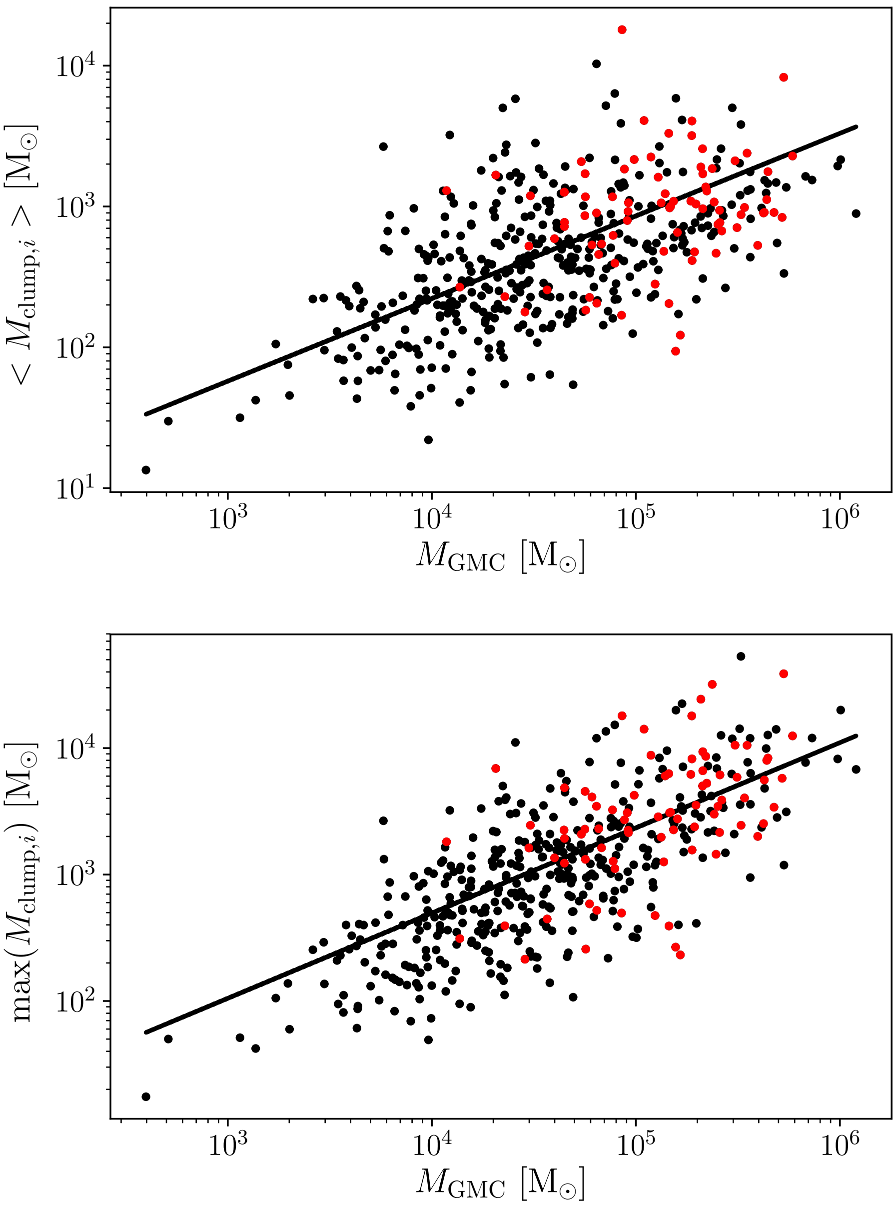

Figure 4.9: *Upper*: The mean clump mass in each cloud, as a function of cloud mass. Note that we find small-mass clumps in clouds of all sizes, but they are not plotted here; only the mean clump mass for each cloud is plotted. The black line represents a power-law fit with a slope of 0.6 and a 1σ dispersion of 0.3 dex. *Lower*: As above, except with maximum clump mass in each cloud. The black line represents a power-law fit with a slope of 0.7 and a 1σ dispersion of 0.3 dex.

clumps in more massive clouds. Note that we only plot the mean clump mass, not each individual clump mass, and thus the deficit of points in the lower right corner does not mean that we miss finding the massive clouds' small clumps.

We find a power-law slope of $\beta = 0.59 \pm 0.09$ relating mean clump mass to cloud mass and a 1σ dispersion about the fit of 0.3 dex. In addition, we plot maximum clump mass for each cloud, against cloud mass (Figure 4.9 lower). We see a similar power-law slope of $\beta = 0.67 \pm 0.09$, again with a 1σ dispersion of 0.3 dex. Note that we eliminated the intercept term for these two fits, which is the reason for the smaller slope uncertainties here, in comparison with the fits from Figure 4.8. These slopes are less than unity, and thus clump masses increase more slowly than cloud masses. Earlier we observed a universal clump mass fraction. The sum of the two effects (more clumps and more massive clumps) produces this linear scaling of total clump mass with cloud mass, within the uncertainties of the fits.

4.6 Star Formation Rates

Some fraction of the mass found in clumps goes on to collapse further and form stars. We examine the rate at which clumps embedded in our clouds are forming stars, by way of 70 μm Hi-GAL emission. We also investigate which of a cloud's properties influence its star formation rate. The median star formation rate in our sample of clouds is 1.1×10^{-5} $M_\odot$ yr^{-1}. The rms is nearly an order of magnitude, with the mean SFR in log-space being $\langle \log_{10}(\mathrm{SFR}) \rangle = -5.0 \pm 0.9$ $\log_{10}(M_\odot\ \mathrm{yr}^{-1})$. The total SFR for our cloud sample is 0.03 $M_\odot$ yr^{-1}. When extended to the whole Galactic Plane, this results in a SFR of 0.4 $M_\odot$ yr^{-1} for the Milky Way, which is low compared to more careful studies of this number (e.g., Robitaille & Whitney, 2010; Chomiuk & Povich, 2011), but within a factor of a few. The distribution of cloud SFRs is seen in Figure 4.10. There is no significant correlation with clump mass fraction, as seen in Figure 4.11. Thus, even if a cloud puts more of its mass in clumps, it does not necessarily form stars at a greater rate.

While clouds with greater M_{GMC} and M_{clump} form stars at higher rates (Figure 4.12 a and b), they do not have greater star formation rates per solar mass of cloud or clump mass, according

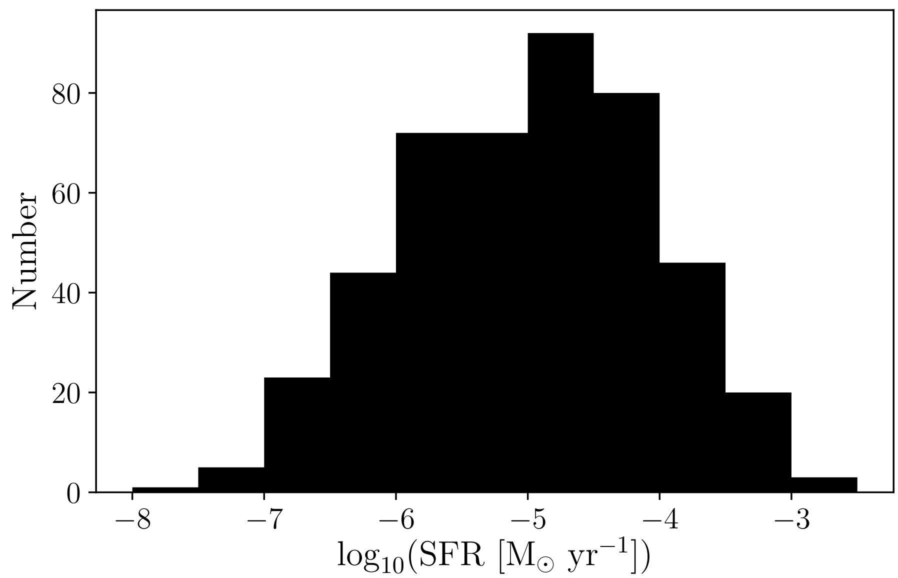

Figure 4.10: Distribution of star formation rates derived from Hi-GAL 70 μm emission. The mean and standard deviation in log-space are $-5.0 \pm 0.9\ \log_{10}(\mathrm{M}_\odot\ \mathrm{yr}^{-1})$.

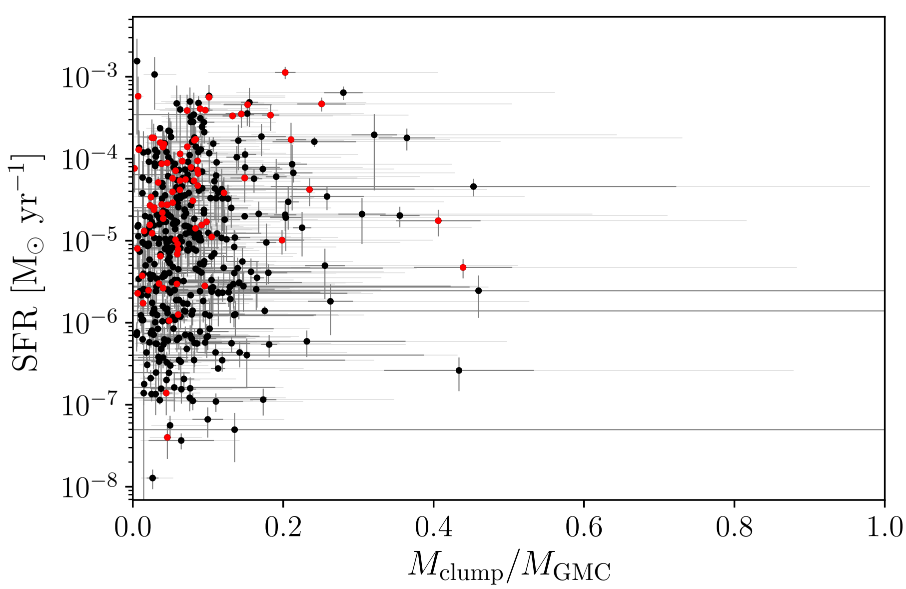

Figure 4.11: Star formation rate derived from Hi-GAL 70 μm emission as a function of clump mass fraction.

to Figure 4.12 panels (c) and (d), respectively. That is, star formation efficiencies do not change with M_{GMC} or M_{clump}. These plots show SFR normalized by M_{GMC} (M_{clump}), as a function of M_{GMC} (M_{clump}), for which there is no correlation. There is, however, a tightening to one universal value of SFR/M_{clump} as M_{clump} increases. This tightening is likely due to averaging of SFRs over more clumps as M_{clump} increases, as predicted by the Central Limit Theorem. With star formation happening in a greater number of clumps, fluctuations are absorbed into the mean, leading to a smaller spread in cloud-wide SFRs for more massive clouds. Clump masses in panels (b) and (d) are more tightly correlated with SFR than cloud masses in panels (a) and (c), particularly at the high-mass ends. This is in agreement with the work of Vutisalchavakul et al. (2016), who found that dense molecular gas is a better predictor of SFR than total molecular gas, and that the relationship is consistent with linear.

Alternately, panels (c) and (d) can be interpreted as inverse mass depletion times. We see that the mass depletion time for clouds is greater than that for clumps. This provides a consistency check on our model of clumps as substructures of clouds. Furthermore, while the depletion time in clumps is approximately 10 times shorter than in clouds, the free-fall times are only about a factor of 2.5 shorter (Figure 4.4). That star formation happens on timescales shorter than the free-fall time suggests that turbulence plays a significant role in driving star formation.

We consider the possibility that clouds with more massive clumps (Figure 4.12e) or with a greater number of clumps (Figure 4.12f) may have higher SFRs. Again, no correlation is seen, but the same tightening to a constant value for SFR/M_{clump} exists at higher clump masses and at greater clump numbers. Therefore to first order, on average in our sample, a cloud's SFR depends only on the mass in clumps, or equivalently, the mass of the GMC, since CFE appears to be universal. Thus spiral galaxy simulations which convert a fixed percentage of cloud mass into stars when a density threshold is met (e.g., Guedes et al., 2011; Shull et al., 2012) are not unduly simplifying the factors influencing star formation.

In order to test the density thresholds used by these simulations, we plot SFR against number densities across entire clouds, and the number densities in their constituent clumps (Figure 4.13).

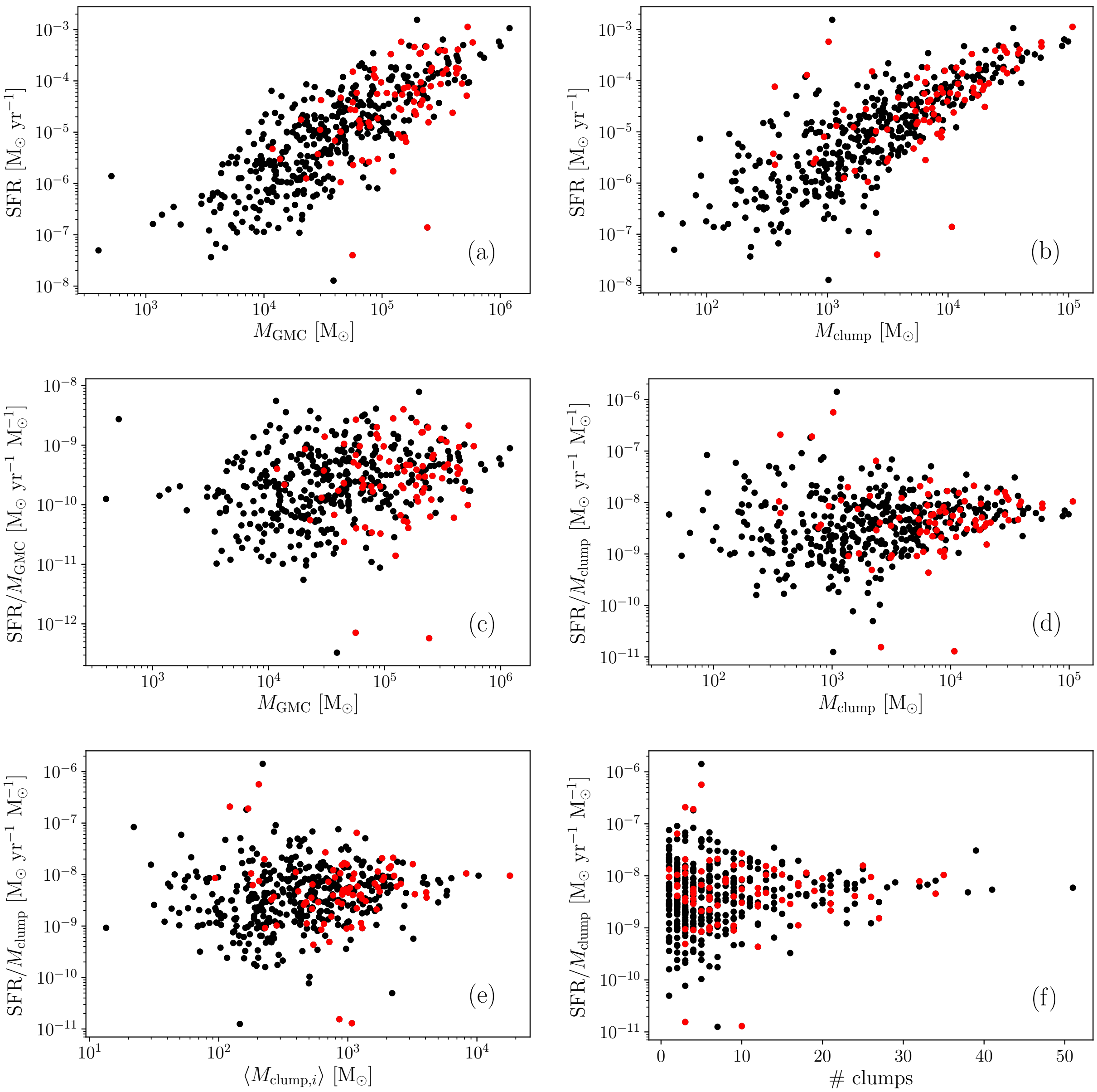

Figure 4.12: Star formation rates derived from Hi-GAL 70 μm emission, compared with cloud and clump masses. (a) and (b): SFR as a function of cloud mass and clump mass, respectively. (c) and (d): Same as above, but with SFRs normalized by the horizontal axis quantity. (e) SFR normalized by total clump mass, against mean clump mass. (f) SFR normalized by total clump mass, against number of clumps. Note that panel (a) is equivalent to the Kennicutt-Schmidt law, discussed in Section 4.7, without dividing by projected area. As in Figure 4.7, red points indicate clouds with virial parameters $\alpha_{\rm vir} < 2$.

We find SFR is correlated with number densities in clumps, but when the resolution of densities is decreased to the scale of whole clouds, this correlation is no longer present. However, the sub-parsec resolutions required to utilize clump-scale density information are far from feasible where whole-galaxies simulations are concerned. Thus, we recommend converting a fixed fraction of cloud mass into stars once densities indicate a GMC has formed, as per Figure 4.12 and adopting the observed dispersion.

4.7 SFR Densities compared to the Kennicutt-Schmidt Law

The Kennicutt-Schmidt (KS) law relates the SFR surface density ($\Sigma_{\rm SFR}$) to the surface mass density of gas ($\Sigma_{\rm gas}$) through,

$$\Sigma_{\rm SFR} = A\left(\frac{\Sigma_{\rm gas}}{1\ {\rm M}_\odot\ {\rm pc}^{-2}}\right)^N, \tag{4.5}$$

where $A = (2.5 \pm 0.7) \times 10^{-10}$ $\rm M_\odot\ yr^{-1}\ pc^{-2}$ and $N = 1.4 \pm 0.15$ is the power-law exponent (Kennicutt, 1998). In Figure 4.14, we compare our cloud data to the KS law (shown as a thick grey line). Our data fit the law remarkably well, although with a significant degree of dispersion. There are a few clouds with abnormally low $\Sigma_{\rm SFR}$ values. We find no other abnormalities in these clouds, and they fall within the overall scatter of star formation rates calculated using alternate calibrations from 24 μm emission (Rieke et al., 2009) and total infrared emission (Hao et al., 2011; Murphy et al., 2011).

While the KS law describes the data in this figure reasonably well by eye, we also fit Equation (4.5) to these data. We find parameters of $A = (0.9 \pm 4.3) \times 10^{-10}$ $\rm M_\odot\ yr^{-1}\ pc^{-2}$ and $N = 1.7 \pm 1.0$. The 1σ dispersion about this fit is 0.5 dex. Our fit is within 1σ of the KS law. There are caveats to applying the KS law here, however. First, Kennicutt (1998) derived this law from disk-averaged values of galaxies, not on a cloud-by-cloud basis. Onodera et al. (2010) showed that on GMC scales the scatter about the KS law increases so greatly that the relationship essentially breaks down. While we still see evidence for this relationship, it should not come as a surprise that the increased scatter at GMC scales would result in a poorly constrained slope. Second, the KS law

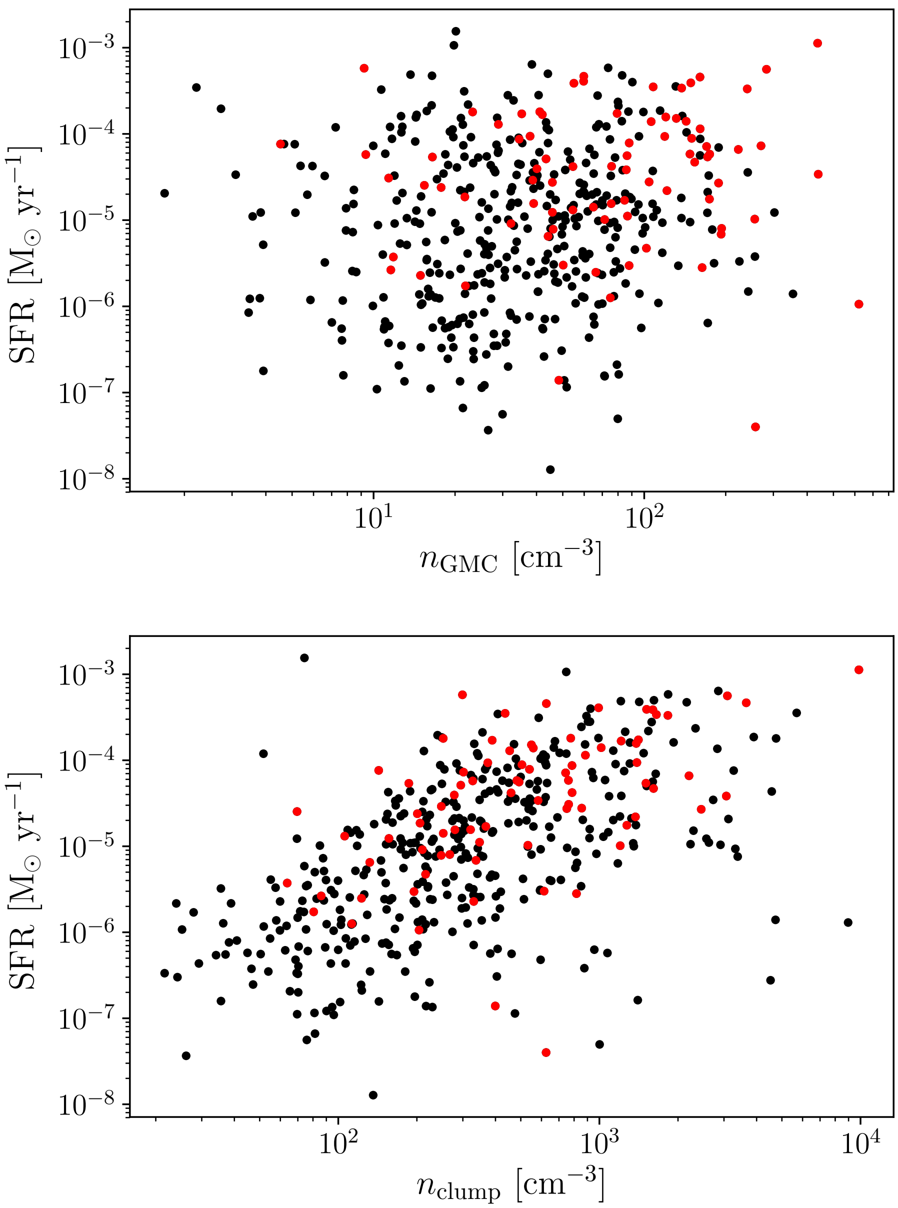

Figure 4.13: *Upper*: 70 μm star formation rates against the average number density across the entire cloud. *Lower*: Same as above, but for average number density for clumps within each cloud.

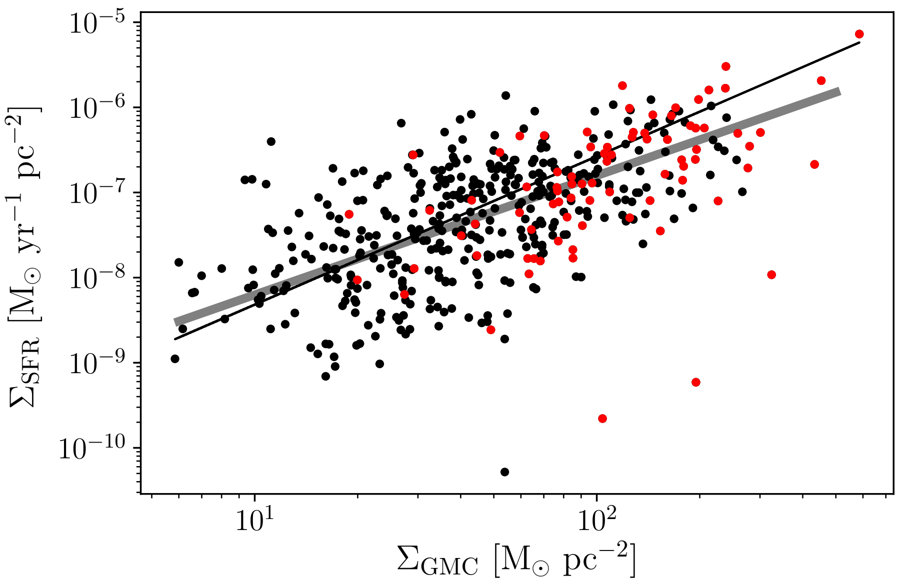

Figure 4.14: The Kennicutt-Schmidt law, compared to our star formation rate surface densities. The KS law (Equation 4.5) is shown as a thick grey line. Thin black line represents the power-law fit to the data, and has a slope of 1.7.

was derived using total gas mass (H I + H_2), whereas we are measuring only molecular gas. Using disk-averaged values, Leroy et al. (2013) studied this relationship with molecular gas, and found a slope of $N = 1 \pm 0.2$. That is, a linear relationship, which is also within 1σ of our fit slope.

4.8 Virial Theorem

The virial theorem says that, for a self-gravitating system, the total kinetic energy is twice the gravitational potential energy (with the opposite sign). The mass of such a system is therefore calculated as Equation 4.3. The virial parameter, α, is the ratio of this virial mass to the system's true mass (Equation 4.4). This can also be understood as describing the relative importance of kinetic and potential energy,

$$\alpha = \frac{2E_{\rm kin}}{|E_{\rm pot}|}.$$

A perfectly virialized system has $\alpha \equiv 1$ and is therefore self-gravitating, but supported by its motion and therefore not collapsing. This support is generally thought to come from internally generated turbulence (Bertoldi & McKee, 1992). A larger virial mass ($\alpha > 1$) suggests that the cloud is either pressure-confined or not bound. A smaller virial mass ($\alpha < 1$) suggests that the cloud cannot support itself and is unstable to gravitational collapse. In practice, this critical value is slightly higher to account for the wide range of possible shapes and density profiles. For non-magnetized clouds, we see critical values of $\alpha_{\rm cr} \gtrsim 2$ separating collapsing and supported clouds (Kauffmann et al., 2013).

In the majority of the plots above, those clouds which have $\alpha < 2$ – and are therefore unstable to collapse – are colored red. In Section 4.5.2 we noted that despite evidence elsewhere for star formation in clouds with masses of a few 10^3 $M_\odot$, none of our relatively low mass clouds have virial parameters which suggest gravitational collapse. However, this is not a matter of their lack of existence. Rather, they did not make our sample cut. Figure 4.15 shows the virial parameters and masses of all clouds in the COHRS catalog (grey), as well as those which were matched to Hi-GAL clumps, but did not meet our $3'$ cloud angular size requirement (black), and those used in

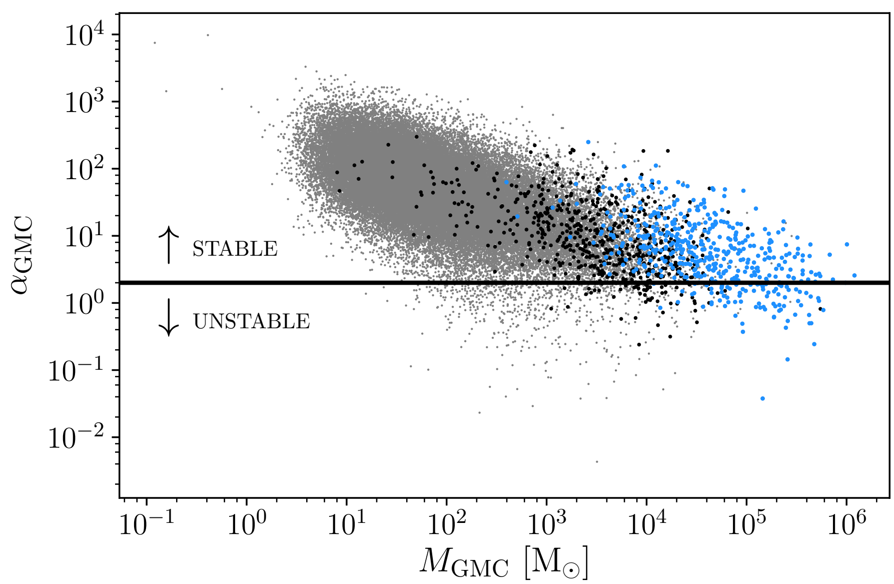

Figure 4.15: Virial parameters and masses of all clouds in the COHRS catalog (grey), as well as those which were matched to Hi-GAL clumps, but did not meet our $3'$ cloud angular size requirement (black), and those used in our analysis (blue). The black line denotes $\alpha = 2$, the nominal lower bound on stable clouds.

our analysis (blue). Potentially unstable clouds exist down to 10 $M_\odot$, and some with a few 10^3 $M_\odot$ were matched to Hi-GAL clumps but did not make our sample cut.

The vast majority of COHRS objects not containing clumps are stable against gravitational collapse. This is expected, since clouds undergoing collapse should have denser regions, which we would detect as clumps. The contrapositive is also true. Only a small portion of the clouds in the catalog have small virial parameters, and of those, we identify clumps in a fraction enhanced above the overall detection rate. Furthermore, the mean α value for clouds not matched to clumps is roughly an order of magnitude greater than the mean for those clouds containing clumps, suggesting that those without clumps are more stable against collapse.

Of those clouds containing clumps, both virialized and non-virialized clouds exist throughout the full range of clump mass fractions (e.g. Figure 4.7), cloud- and clump-mass-normalized SFRs (Figure 4.12), and SFR surface densities (Figure 4.14). For each of these quantities, the mean value for the virialized population is statistically indistinguishable from that of the non-virialized population. This is reasonable. All of these clouds contain clumps, and therefore are able to form stars, but that does not mean that they all are currently forming stars or even will form stars. Clouds can gravitationally collapse on clump scales, and yet still be virialized as a whole. Conversely, a cloud can have a low virial parameter and thus be unstable to gravitational collapse, and yet not currently be collapsing to form stars. We measured virial parameters on cloud scales, which are distant from the core scales on which star formation happens. However, even on clump scales, Traficante et al. (2018) found that the virial parameter is a poor indicator of clump dynamics. They found infalling motions in both virialized and non-virialized clumps, and the distributions of virial parameters for populations at various evolutionary stages were indistinguishable. Overall, the virial theorem is a blunt instrument, but it does have some merit in that clouds with small virial parameters are more likely to contain clumps.

4.9 Velocity Distributions and Spiral Arms

We examine velocity distributions in order to learn about the relative alignment of clouds and their clumps, as well as the sources of support in virialized clouds. Figure 4.16 shows the velocity distributions for the clouds and clumps therein. The upper panel shows the rms on the line-of-sight velocity for each cloud. The mean $v_{\rm RMS}$ is 3.9 ± 2.0 km s^{-1}. The sound speed in the ISM can be calculated as

$$c_s = \sqrt{\frac{kT}{\mu m_{\rm H}}},$$

where k is the Boltzmann constant, $T = 20$ K is our assumed clump temperature, $\mu = 2.4$ is the mean molecular mass in the molecular ISM, and $m_{\rm H}$ is the mass of a hydrogen atom. This results in a sound speed of 0.26 km s^{-1}. Comparing this to the distribution of cloud line widths, typical for molecular clouds, we see that velocities in all of our clouds are supersonic, and therefore turbulence plays a large role in the cloud stability. This turbulence could have its source in gravitational instabilities or in feedback from star formation (Krumholz, 2014). Furthermore, while it helps support the cloud on large scales, this same supersonic turbulence may help regulate star formation on smaller scales (Krumholz & McKee, 2005).

The middle panel shows the difference between the cloud's $v_{\rm LSR}$ and that of each of its constituent clumps. This is skewed slightly towards greater clump velocities, with a mean difference of -0.73 ± 0.08 km s^{-1}. The offset is present both when each clump is considered individually (as shown) and when the average clump velocity for each cloud is compared to the cloud velocity ($v_{\rm GMC} - \langle v_{{\rm clump},i} \rangle$). However, this is within the 1 km s^{-1} velocity resolution of COHRS. Furthermore, a similar distribution shape was found by Battisti & Heyer (2014), who did a similar analysis using GRS for clouds and BGPS for clumps. Since some of our velocity sources overlap, we cannot eliminate the possibility of biases in the surveys, but we can conclude that our matching algorithm is not at fault.

In the lower panel, we show these velocity differences normalized by the cloud line width. We find a smooth normal distribution with a mean and standard deviation of -0.2 and 0.8, respectively.

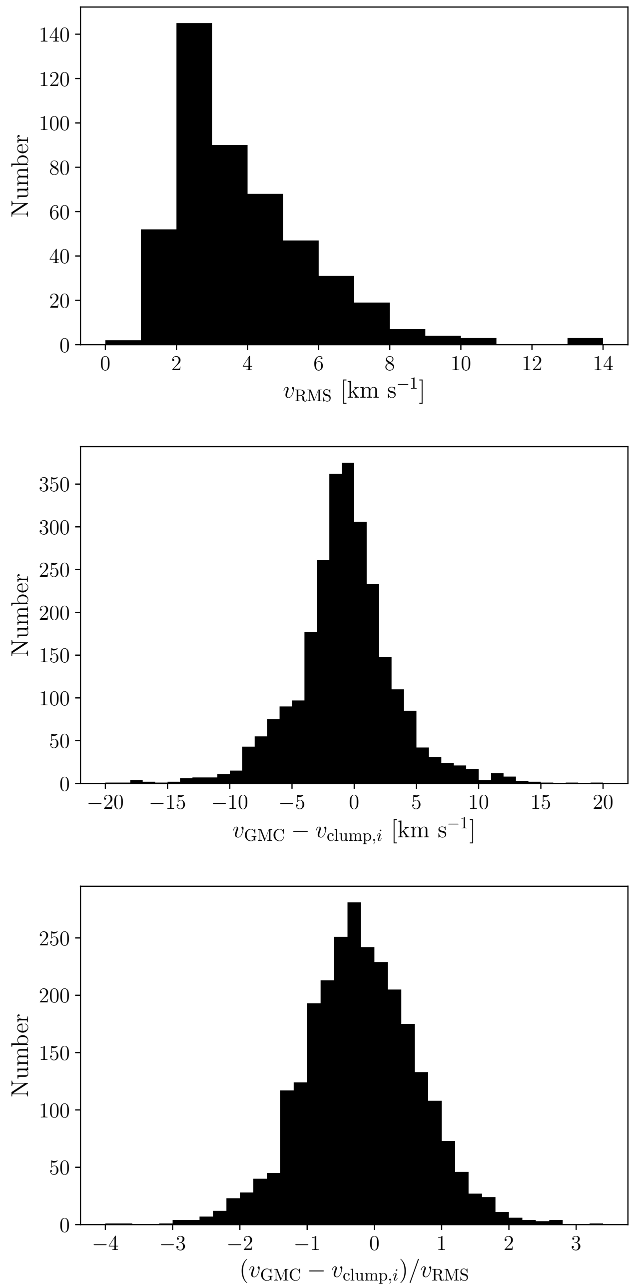

Figure 4.16: *Upper*: Distribution of the $v_{\rm LSR}$ rms for clouds. *Middle*: Distribution of the differences between cloud centroid velocity and velocities of each of its clumps. *Lower*: Same as middle panel, but normalized by cloud line width.

Negative values refer to greater line-of-sight velocities in clumps, which correspond to the inner edges of spiral arms for clouds on the near side of the Galactic Center (when observing in the fourth Galactic quadrant), where the majority of our clouds are located. This is in line with Vallée (2014), who found that ^{13}CO is found preferentially on the inner edge of spiral arms, as whereas ^{12}CO defines the mid-lane. Furthermore, 24 μm and 60 μm emission is found even closer to the inner edges. This suggest that denser gas is found toward the inner edges of spiral arms, in line with our velocity offsets.

4.10 Conclusions

We have paired our catalog of dust-identified molecular cloud clumps with the CO-identified molecular cloud catalog of Colombo et al. (2018). This took the form of matching clouds to their constituent clumps. Our final sample of matched objects consists of 3,674 clumps matched to 473 clouds. We draw a number of conclusions from the properties of these nested structures.

(1) The mean clump mass fraction is $0.08^{+0.05}_{-0.04}$. This is consistent with the findings of Battisti & Heyer (2014). When this clump mass fraction is combined with the core mass fractions of Enoch et al. (2007), we find a core-to-clump mass efficiency of approximately 50%.

(2) Clump formation efficiency is independent of cloud mass, cloud surface mass density, and the virial parameter of the cloud. That is, as clouds get more massive, they linearly put more mass into clumps.

(3) As clouds grow, they produce both more clumps, and more massive clumps. Both the number and mass of clumps grow at rates more shallow than linear. The power-law slopes for mean clump mass, maximum clump mass, and number of clumps, all as functions of cloud mass are $\beta = 0.59 \pm 0.09$, $\beta = 0.67 \pm 0.09$, and $\beta = 0.56 \pm 0.46$, respectively.

(4) A cloud's star formation rate is dependent solely on its mass (or equivalently, its clump mass, as the clump mass fraction is universal). This provides validation for star formation

models used in numerical simulations of galaxy evolution, where a set fraction of gas mass located in GMCs is converted into star mass.

(5) The star formation rate surface densities of our clouds follow the Kennicutt-Schmidt law within 1σ, although with a large degree of scatter. The linear relationship found by Leroy et al. (2013) is also within our 1σ error bars. While the KS law is still somewhat functional on GMC scales, it has broken down on clump scales.

(6) The virial parameter of a cloud is a poor predictor of clump and star formation. Both virialized and non-virialized clouds exist throughout the observed ranges of clump mass fractions, specific SFRs, and SFR surface densities. For each of these quantities, the difference in mean values for the $\alpha > 2$ and $\alpha < 2$ populations are statistically insignificant.

(7) Turbulence is a significant player in cloud physics. The depletion times in clumps are an order-of-magnitude shorter than in clouds, whereas the free-fall times are only shorter by a factor of 2.5. This suggests that turbulence plays a non-negligible role in star formation. The supersonic velocities seen in cloud line widths suggest turbulence also contributes to cloud stability.

Chapter 5

Concluding Thoughts

Yet trees are not 'trees', until so named and seen –
and never were so named, till those who had been
who speech's involuted breath unfurled,
faint echo and dim picture of the world

- J.R.R. Tolkien, *Mythopoeia*

5.1 Summary

In studying the ISM and the star formation therein, we try to make sense of the mess of structures by drawing boundaries and naming them clouds. Inside the clouds, we name clumps and cores, and draw yet fuzzier lines. Never has the nebulous nature of such definitions been clearer to me than when I sat down to pick the ideal parameters for clump identification. The *Herschel* infrared GALactic plane survey has enabled the study of dense molecular gas in the Milky Way in a powerful way. With a latitude width of 2° over the entire 360° longitude range, if there is a Galactic Plane survey you want to study, Hi-GAL has you covered with supplementary wavebands. What is more, the low optical depth of thermal dust emission allows Hi-GAL to see through the entire disk. *Herschel's* sensitivity when combined with the low optical depth of the dust it observes, means that the resulting maps, particularly toward the inner Galaxy, contain nothing but signal. The question is no longer, how can I get past the noise to the molecular cloud clumps? as was the case with BGPS. Now we ask, where in all this signal does the one clump end and the next begin?

Ultimately, decisions must be made. I drew lines delineating clumps, and determined their distances where possible. This was first done on a representative subsample of the Hi-GAL maps in Chapter 2. My results compared favorably with those of the BGPS team. My clumps were more extended than theirs, due primarily to the superior sensitivity of Hi-GAL revealing the diffuse clump edges where BGPS could not.

In Chapter 3, I applied this process to the portion of Hi-GAL at latitudes of $10° < \ell < 56°$, corresponding with a significant slice of the inner Galactic Plane. This resulted in a catalog of 19,886 clumps, 10,124 of which have an associated velocity and therefore a kinematic distance, and 5,405 of which have their distances well constrained. I sampled the distance probability density functions for these clumps in order to produce a face-on dense gas map of the Galaxy. This map was, once again, remarkably similar to the one produced using BGPS clump data. With the increased sensitivity, surface mass densities likewise increased, as did dense gas mass fractions. Working only with those clumps having well-constrained distances, I found that the mass of clumps in this catalog decrease with distance from the Galactic Center. Meanwhile, clump radius is unaffected by this environmental factor.

If a single catalog is instructive, then the intersection of two catalogs is more than doubly so. In Chapter 4, I combined my catalog of Hi-GAL clumps with a catalog of molecular clouds produced by Dario Colombo using COHRS data. I matched 3,674 clumps from my catalog to 473 clouds from the COHRS catalog. From this data set, I deduced that the clump formation efficiency of clouds is independent of cloud mass, surface mass density, and virial parameter. As they grow, clouds put mass into making more clumps, and into making more massive clumps, such that in total, they maintain a constant clump mass fraction. Furthermore, a cloud's star formation rate is dependent only on its mass (or, equivalently, on its clump mass). While average clump density and SFR are correlated, cloud density and SFR are not. Since numerical simulations of galaxy evolution cannot resolve more precisely than GMC scales, I concluded that the star formation recipes which convert a fixed fraction of GMC mass into star mass are not inconsistent with my results.

5.2 Future Work

5.2.1 Complete Dense Gas Map

The obvious direction to have gone following Chapter 3 was to extend the cataloging of Hi-GAL clumps over the entire Galactic Plane. This is still possible, and would result in an incredibly useful data set. However, it would not be as simple as running the same code set over additional Hi-GAL maps. While Hi-GAL spans the entire 360° of the Galactic Plane, that is not the case for all of our supplementary surveys. GRS provided the majority of our our line-of-sight velocities for the Northern Galactic Plane, but it does not extend to the Southern Galactic Plane. The molecular line surveys MALT90 (Jackson et al., 2013) and ThrUMMs (`http://www.astro.ufl.edu/~peterb/research/thrumms/`), however, cover these longitudes, and could be used to provide kinematic distances.

Our most powerful kinematic distance discriminator, 8 μm absorption, depends on GLIMPSE maps. These extend to longitudes $|\ell| < 70°$, thus covering the vast majority of the inner Galaxy. Fortunately, beyond the solar circle, there is no ambiguity in kinematic distances, and so GLIMPSE is not necessary. While our current techniques result in well-constrained distances for approximately 20% of clumps, we have plans to add two additional Bayesian priors which could increase this rate. The first, near infrared extinction, relies on a clumps' absorption of short-wavelength starlight (Marshall et al., 2009), and functions similarly to our 8 μm absorption techniques. The second, HI self-absorption and HI emission/absorption, are techniques which were introduced by Roman-Duval et al. (2009) and Anderson & Bania (2009), and used on ATLASGAL clumps by Wienen et al. (2015).

Considering that our current efforts have resulted in a catalog containing double the number of clumps as BGPS and triple the number of well-constrained distances, an effort to map the entire plane would dwarf existing molecular cloud clump catalogs. Such a catalog could be leveraged in many ways. For instance, it would be particularly useful in disentangling the effects of spiral arms and those of distance from the Galactic Center, over which there is considerable debate.

This work could be divided into several small projects for new graduate students. Writing each of the two proposed priors are self-contained projects, as is the expansion of the application of the whole package to Galactic longitudes $|\ell| < 70°$. A forth project could be the analysis of the map produced looking for the effects of spiral arms on clump properties.

5.2.2 CFE and SFR Radial Trends

Speaking of radial trends, we ran out of time to perform a careful analysis of the effects of Galactocentric radius on clump formation efficiencies and star formation rates. In Chapter 4 we determined that clump formation efficiency is independent of cloud mass, among other cloud properties. However, in Chapter 3, we found that average clump mass decreases with Galactocentric radius. Whether this means that CFE also decreases with distance to the Galactic Center is yet to be seen. I plan on including this analysis in the published version of Chapter 4.

5.2.3 Turbulence and its Effects on Clump and Star Formation

In our analysis of clump formation efficiencies and star formation rates (Chapter 4), we noted on several occasions that our observations suggest that turbulence plays a role in clump and star formation. This role warrants more careful analysis. As a first approach, we plan on following the methods of Battisti & Heyer (2014) for constraining the velocities of the colliding flows which form GMCs and their clumps. This is done by modeling the clump and cloud velocity differences which would be produced by ISM flows at various velocities and orientations, and comparing to observations.

A second, more thorough, approach to the role of turbulence will use the TurbuStat package (`http://turbustat.readthedocs.io`). This set of analysis tools calculates a suite of commonly applied turbulent statistics, and was developed for use on molecular cloud data by Koch et al. (2017), with additional characterization by Boyden et al. (2016). Mock ^{13}CO data, generated from magnetohydrodynamic simulations, show that various subsets of these 15 statistics are sensitive to five physical parameters: Mach number, plasma parameter, virial parameter, driving scales, and solenoidal driving fraction. Therefore, running this suite of statistics over our Hi-GAL and COHRS datasets could quantify the roles of turbulence and magnetic fields on clump and star formation. With the necessary catalogs and data cubes already in existence, the application of this package is well-suited to be a self-contained project for a new graduate student.

Bibliography

Aguirre, J. E., Ginsburg, A. G., Dunham, M. K., et al. 2011, ApJS, 192, 4

Anderson, L. D., & Bania, T. M. 2009, ApJ, 690, 706

Bacmann, A., Lefloch, B., Ceccarelli, C., et al. 2002, A&A, 389, L6

Basu, S., Gil, M., & Auddy, S. 2015, MNRAS, 449, 2413

Battersby, C., Bally, J., Ginsburg, A., et al. 2011, A&A, 535, A128

Battisti, A. J., & Heyer, M. H. 2014, ApJ, 780, 173

Bauer, J. S., Widrow, L. M., & Erkal, D. 2018, MNRAS, 476, 198

Benjamin, R. A., Churchwell, E., Babler, B. L., et al. 2005, ApJL, 630, L149

Bergin, E. A., & Tafalla, M. 2007, ARA&A, 45, 339

Bertoldi, F., & McKee, C. F. 1992, ApJ, 395, 140

Beuret, M., Billot, N., Cambrésy, L., et al. 2017, A&A, 597, A114

Blitz, L., & Rosolowsky, E. 2006, ApJ, 650, 933

Bolatto, A. D., Wolfire, M., & Leroy, A. K. 2013, ARA&A, 51, 207

Boyden, R. D., Koch, E. W., Rosolowsky, E. W., & Offner, S. S. R. 2016, ApJ, 833, 233

Bronfman, L., Casassus, S., May, J., & Nyman, L.-Å. 2000, A&A, 358, 521

Brunt, C. M. 2015, MNRAS, 449, 4465

Burton, W. B. 1988, The structure of our Galaxy derived from observations of neutral hydrogen (Springer), 295–358

Calzetti, D., Wu, S.-Y., Hong, S., et al. 2010, ApJ, 714, 1256

Carey, S. J., Noriega-Crespo, A., Mizuno, D. R., et al. 2009, PASP, 121, 76

Chomiuk, L., & Povich, M. S. 2011, AJ, 142, 197

Churchwell, E., Babler, B. L., Meade, M. R., et al. 2009, PASP, 121, 213

Colombo, D., Rosolowsky, E., Duarte-Cabral, A., Dempsey, J. T., & Currie, M. J. 2018, unpublished manuscript

Colombo, D., Rosolowsky, E., Ginsburg, A., Duarte-Cabral, A., & Hughes, A. 2015, MNRAS, 454, 2067

Colombo, D., Hughes, A., Schinnerer, E., et al. 2014, ApJ, 784, 3

Contreras, Y., Schuller, F., Urquhart, J. S., et al. 2013, A&A, 549, A45

Cox, D. P. 2005, ARA&A, 43, 337

Csengeri, T., Urquhart, J. S., Schuller, F., et al. 2014, A&A, 565, A75

Csengeri, T., Weiss, A., Wyrowski, F., et al. 2016, A&A, 585, A104

Dame, T. M., Hartmann, D., & Thaddeus, P. 2001, ApJ, 547, 792

Dame, T. M., & Thaddeus, P. 2011, ApJL, 734, L24

Deharveng, L., Schuller, F., Anderson, L. D., et al. 2010, A&A, 523, A6

Dempsey, J. T., Thomas, H. S., & Currie, M. J. 2013, ApJS, 209, 8

Dib, S., Shadmehri, M., Padoan, P., et al. 2010, MNRAS, 405, 401

Dobbs, C. L. 2015, MNRAS, 447, 3390

Dobbs, C. L., Burkert, A., & Pringle, J. E. 2011, MNRAS, 417, 1318

Donkov, S., Veltchev, T. V., & Klessen, R. S. 2012, MNRAS, 423, 889

Draine, B. T. 2003, ARA&A, 41, 241

—. 2011, Physics of the Interstellar and Intergalactic Medium (Princeton University Press)

Dunham, M. K., Rosolowsky, E., Evans, II, N. J., Cyganowski, C., & Urquhart, J. S. 2011, ApJ, 741, 110

Eden, D. J., Moore, T. J. T., Morgan, L. K., Thompson, M. A., & Urquhart, J. S. 2013, MNRAS, 431, 1587

Elia, D., Molinari, S., Fukui, Y., et al. 2013, ApJ, 772, 45

Elia, D., Molinari, S., Schisano, E., et al. 2017, MNRAS, 471, 100

Ellsworth-Bowers, T. P., Rosolowsky, E., Glenn, J., et al. 2015a, ApJ, 799, 29

Ellsworth-Bowers, T. P., Glenn, J., Rosolowsky, E., et al. 2013, ApJ, 770, 39

Ellsworth-Bowers, T. P., Glenn, J., Riley, A., et al. 2015b, ApJ, 805, 157

Elmegreen, B. G. 1985, in Birth and Infancy of Stars, ed. R. Lucas, A. Omont, & R. Stora, 257–277

Enoch, M. L., Evans, II, N. J., Sargent, A. I., et al. 2008, ApJ, 684, 1240

Enoch, M. L., Glenn, J., Evans, II, N. J., et al. 2007, ApJ, 666, 982

Fall, S. M., & Zhang, Q. 2001, ApJ, 561, 751

Foreman-Mackey, D., Hogg, D. W., Lang, D., & Goodman, J. 2013, PASP, 125, 306

Freeman, P., Rosolowsky, E., Kruijssen, J. M. D., Bastian, N., & Adamo, A. 2017, MNRAS, 468, 1769

Fujimoto, Y., Tasker, E. J., Wakayama, M., & Habe, A. 2014, MNRAS, 439, 936

Gao, Y., & Solomon, P. M. 2004, ApJ, 606, 271

Giannetti, A., Brand, J., Sánchez-Monge, Á., et al. 2013, A&A, 556, A16

Ginsburg, A., Glenn, J., Rosolowsky, E., et al. 2013, ApJS, 208, 14

Girichidis, P., Federrath, C., Banerjee, R., & Klessen, R. S. 2011, MNRAS, 413, 2741

Gómez, L., Wyrowski, F., Schuller, F., Menten, K. M., & Ballesteros-Paredes, J. 2014, A&A, 561, A148

Gratier, P., Braine, J., Rodriguez-Fernandez, N. J., et al. 2012, A&A, 542, A108

Griffin, M. J., Abergel, A., Abreu, A., et al. 2010, A&A, 518, L3

Guedes, J., Callegari, S., Madau, P., & Mayer, L. 2011, ApJ, 742, 76

Hao, C.-N., Kennicutt, R. C., Johnson, B. D., et al. 2011, ApJ, 741, 124

Hernandez, A. K., & Tan, J. C. 2011, ApJ, 730, 44

Heyer, M., Krawczyk, C., Duval, J., & Jackson, J. M. 2009, ApJ, 699, 1092

Heyer, M., Wilson, G. W., Gutermuth, R., et al. 2018, MNRAS, 473, 2222

Hopkins, P. F. 2013, MNRAS, 433, 170

Hopkins, P. F., Kereš, D., Oñorbe, J., et al. 2014, MNRAS, 445, 581

Jackson, J. M., Rathborne, J. M., Shah, R. Y., et al. 2006, ApJS, 163, 145

Jackson, J. M., Rathborne, J. M., Foster, J. B., et al. 2013, PASA, 30, e057

Katz, N., Weinberg, D. H., & Hernquist, L. 1996, ApJS, 105, 19

Kauffmann, J., & Pillai, T. 2010, ApJL, 723, L7

Kauffmann, J., Pillai, T., & Goldsmith, P. F. 2013, ApJ, 779, 185

Kennicutt, R. C., & Evans, N. J. 2012, ARA&A, 50, 531

Kennicutt, Jr., R. C. 1998, ApJ, 498, 541

Kereš, D., Katz, N., Davé, R., Fardal, M., & Weinberg, D. H. 2009, MNRAS, 396, 2332

Kim, J.-h., Abel, T., Agertz, O., et al. 2014, ApJS, 210, 14

Koch, E. W., Ward, C. G., Offner, S., Loeppky, J. L., & Rosolowsky, E. W. 2017, MNRAS, 471, 1506

Kroupa, P. 2002, Science, 295, 82

Krumholz, M. R. 2014, ??jnlPhR, 539, 49

Krumholz, M. R., & McKee, C. F. 2005, ApJ, 630, 250

Krumholz, M. R., & Tan, J. C. 2007, ApJ, 654, 304

Leroy, A. K., Walter, F., Bigiel, F., et al. 2009, AJ, 137, 4670

Leroy, A. K., Walter, F., Sandstrom, K., et al. 2013, AJ, 146, 19

Marshall, D. J., Joncas, G., & Jones, A. P. 2009, ApJ, 706, 727

McKee, C. F., & Ostriker, E. C. 2007, ARA&A, 45, 565

Meidt, S. E. 2016, ApJ, 818, 69

Mo, H. J., Mao, S., & White, S. D. M. 1998, MNRAS, 295, 319

Molinari, S., Swinyard, B., Bally, J., et al. 2010, PASP, 122, 314

Molinari, S., Schisano, E., Elia, D., et al. 2016, A&A, 591, A149

Murphy, E. J., Condon, J. J., Schinnerer, E., et al. 2011, ApJ, 737, 67

Netterfield, C. B., Ade, P. A. R., Bock, J. J., et al. 2009, ApJ, 707, 1824

Offner, S. S. R., Clark, P. C., Hennebelle, P., et al. 2014, Protostars and Planets VI, 53

Olmi, L., Anglés-Alcázar, D., Elia, D., et al. 2013, A&A, 551, A111

—. 2014, A&A, 564, A87

Onodera, S., Kuno, N., Tosaki, T., et al. 2010, ApJL, 722, L127

Ossenkopf, V., & Henning, T. 1994, A&A, 291, 943

Ostriker, E. C., McKee, C. F., & Leroy, A. K. 2010, ApJ, 721, 975

Padoan, P., & Nordlund, Å. 2002, ApJ, 576, 870

Padoan, P., Nordlund, A., & Jones, B. J. T. 1997, MNRAS, 288, 145

Perault, M., Omont, A., Simon, G., et al. 1996, A&A, 315, L165

Peretto, N., & Fuller, G. A. 2009, A&A, 505, 405

—. 2010, ApJ, 723, 555

Piazzo, L., Calzoletti, L., Faustini, F., et al. 2015a, MNRAS, 447, 1471

Piazzo, L., Ikhenaode, D., Natoli, P., et al. 2012, ITIP, 21, 3687

Piazzo, L., Panuzzo, P., & Pestalozzi, M. 2015b, Signal Processing, 108, 430

Poglitsch, A., Waelkens, C., Geis, N., et al. 2010, A&A, 518, L2

Ragan, S. E., Moore, T. J. T., Eden, D. J., et al. 2016, MNRAS, 462, 3123

Rathborne, J. M., Johnson, A. M., Jackson, J. M., Shah, R. Y., & Simon, R. 2009, ApJS, 182, 131

Reed, W. J., & Jorgensen, M. 2004, Communications in Statistics-Theory and Methods, 33, 1733

Reid, M. J., Menten, K. M., Brunthaler, A., et al. 2014, ApJ, 783, 130

Rice, T. S., Goodman, A. A., Bergin, E. A., Beaumont, C., & Dame, T. M. 2016, ApJ, 822, 52

Rieke, G. H., Alonso-Herrero, A., Weiner, B. J., et al. 2009, ApJ, 692, 556

Rieke, G. H., Young, E. T., Engelbracht, C. W., et al. 2004, ApJS, 154, 25

Robitaille, T. P., Churchwell, E., Benjamin, R. A., et al. 2012, A&A, 545, A39

Robitaille, T. P., & Whitney, B. A. 2010, ApJL, 710, L11

Roman-Duval, J., Heyer, M., Brunt, C. M., et al. 2016, ApJ, 818, 144

Roman-Duval, J., Jackson, J. M., Heyer, M., et al. 2009, ApJ, 699, 1153

Roman-Duval, J., Jackson, J. M., Heyer, M., Rathborne, J., & Simon, R. 2010, ApJ, 723, 492

Rosolowsky, E., Keto, E., Matsushita, S., & Willner, S. P. 2007, ApJ, 661, 830

Rosolowsky, E., & Leroy, A. 2006, PASP, 118, 590

Rosolowsky, E., Dunham, M. K., Ginsburg, A., et al. 2010, ApJS, 188, 123

Schruba, A., Leroy, A. K., Walter, F., et al. 2011, AJ, 142, 37

Schuller, F., Menten, K. M., Contreras, Y., et al. 2009, A&A, 504, 415

Scoville, N. Z., & Solomon, P. M. 1975, ApJL, 199, L105

Scoville, N. Z., Yun, M. S., Sanders, D. B., Clemens, D. P., & Waller, W. H. 1987, ApJS, 63, 821

Shirley, Y. L., Ellsworth-Bowers, T. P., Svoboda, B., et al. 2013, ApJS, 209, 2

Shull, J. M., Smith, B. D., & Danforth, C. W. 2012, ApJ, 759, 23

Simon, R., Jackson, J. M., Rathborne, J. M., & Chambers, E. T. 2006, ApJ, 639, 227

Solomon, P. M., Rivolo, A. R., Barrett, J., & Yahil, A. 1987, ApJ, 319, 730

Stark, A. A., & Lee, Y. 2006, ApJL, 641, L113

Stinson, G. S., Brook, C., Macciò, A. V., et al. 2013, MNRAS, 428, 129

Svoboda, B. E., Shirley, Y. L., Battersby, C., et al. 2016, ApJ, 822, 59

Tassis, K., Christie, D. A., Urban, A., et al. 2010, MNRAS, 408, 1089

Traficante, A., Duarte-Cabral, A., Elia, D., et al. 2018, ArXiv e-prints, arXiv:1803.08929

Urquhart, J. S., Thompson, M. A., Moore, T. J. T., et al. 2013, MNRAS, 435, 400

Urquhart, J. S., König, C., Giannetti, A., et al. 2018, MNRAS, 473, 1059

Usero, A., Leroy, A. K., Walter, F., et al. 2015, AJ, 150, 115

Utomo, D., Bolatto, A. D., Wong, T., et al. 2017, ApJ, 849, 26

Vallée, J. P. 2008, AJ, 135, 1301

—. 2014, AJ, 148, 5

Vázquez-Semadeni, E., Banerjee, R., Gómez, G. C., et al. 2011, MNRAS, 414, 2511

Veltchev, T. V., Donkov, S., & Klessen, R. S. 2013, MNRAS, 432, 3495

Veneziani, M., Schisano, E., Elia, D., et al. 2017, A&A, 599, A7

Vutisalchavakul, N., Evans, II, N. J., & Heyer, M. 2016, ApJ, 831, 73

Wang, K., Testi, L., Ginsburg, A., et al. 2015, MNRAS, 450, 4043

Whitney, B., Arendt, R., Babler, B., et al. 2008, GLIMPSE360: Completing the Spitzer Galactic Plane Survey, Spitzer Proposal

Whitney, B., Benjamin, R., Meade, M., et al. 2011, in Bulletin of the American Astronomical Society, Vol. 43, American Astronomical Society Meeting Abstracts #217, 241.16

Wienen, M., Wyrowski, F., Menten, K. M., et al. 2015, A&A, 579, A91

Wolfire, M. G., Hollenbach, D., & McKee, C. F. 2010, ApJ, 716, 1191

Wolfire, M. G., McKee, C. F., Hollenbach, D., & Tielens, A. G. G. M. 2003, ApJ, 587, 278

Wu, J., Evans, N., Gao, Y., et al. 2007, in Astronomical Society of the Pacific Conference Series, Vol. 375, From Z-Machines to ALMA: (Sub)Millimeter Spectroscopy of Galaxies, ed. A. J. Baker, J. Glenn, A. I. Harris, J. G. Mangum, & M. S. Yun, 291

Zetterlund, E., Glenn, J., & Rosolowsky, E. 2017, ApJ, 835, 203

—. 2018, submitted

Zinnecker, H., & Yorke, H. W. 2007, ARA&A, 45, 481

Appendix A

Hi-GAL – BGPS matching catalog

Table A1 lists the clumps matched between Hi-GAL and BGPS. Included are Galactic longitude and latitude (ℓ, b), integrated flux density (S, with subscripts denoting wavelength in μm), angular radius (θ_R), and heliocentric distance ($d_\odot$). Due to high-pass filtering, Hi-GAL integrated flux densities and angular radii are attenuated by $(20 \pm 10)\%$ and $(4 \pm 3)\%$, respectively, as seen in Figure 2. When a clump in one survey has multiple counterparts in the other survey, the additional counterparts are listed on the following lines.

Table A1: Hi-GAL – BGPS Catalog

Hi-GAL					BGPS					
ℓ (deg)	b (deg)	S_{500}[1] (Jy)	θ_R (arcsec)	$d_\odot$ (kpc)	Catalog #	ℓ (deg)	b (deg)	S_{1100} (Jy)	θ_R (arcsec)	$d_\odot$ (kpc)
11.32	-0.53	22.58 ± 0.19	95.2	$3.44^{+0.5}_{-0.7}$	2545	11.33	-0.53	0.37 ± 0.12	···	$3.50^{+0.6}_{-0.8}$
11.09	-0.53	142.56 ± 0.30	145.9	$3.30^{+0.4}_{-0.5}$	2508	11.06	-0.49	0.20 ± 0.08	···	···
···	···	···	···	···	2509	11.06	-0.54	0.15 ± 0.07	···	···
···	···	···	···	···	2511	11.08	-0.54	3.56 ± 0.32	59.4	$2.98^{+0.6}_{-0.7}$
···	···	···	···	···	2512	11.08	-0.49	0.38 ± 0.11	···	···
···	···	···	···	···	2514	11.09	-0.50	0.45 ± 0.14	37.9	···
···	···	···	···	···	2515	11.10	-0.52	0.17 ± 0.09	···	···
···	···	···	···	···	2523	11.12	-0.52	0.23 ± 0.09	···	···
10.63	-0.51	105.37 ± 0.24	109.0	···	2426	10.63	-0.51	2.89 ± 0.28	60.3	···
10.91	-0.50	57.76 ± 0.25	140.4	···	2471	10.88	-0.49	0.54 ± 0.13	39.9	···
···	···	···	···	···	2473	10.91	-0.49	0.84 ± 0.16	39.5	···
10.86	-0.49	20.20 ± 0.15	75.3	···	2468	10.87	-0.49	0.28 ± 0.11	18.9	···
11.69	-0.48	67.39 ± 0.25	131.1	···	2570	11.68	-0.47	1.02 ± 0.19	50.0	···
···	···	···	···	···	2571	11.70	-0.48	0.32 ± 0.10	···	···
···	···	···	···	···	2573	11.71	-0.48	0.12 ± 0.07	···	···

[1] Uncertainties on Hi-GAL integrated flux densities are photometric, and do not represent detection uncertainties.

Continuation of Table A1

Hi-GAL					BGPS					
ℓ (deg)	b (deg)	S_{500} (Jy)	θ_R (arcsec)	$d_\odot$ (kpc)	Catalog #	ℓ (deg)	b (deg)	S_{1100} (Jy)	θ_R (arcsec)	$d_\odot$ (kpc)
11.91	-0.46	29.88 ± 0.21	117.0	...	2589	11.91	-0.46	0.66 ± 0.16	58.5	...
11.28	-0.46	21.71 ± 0.18	85.8	$3.16^{+0.6}_{-0.7}$	2540	11.28	-0.45	0.76 ± 0.15	49.5	$3.20^{+0.6}_{-0.7}$
10.62	-0.44	70.88 ± 0.16	64.9	$4.96^{+0.5}_{-0.4}$	2421	10.62	-0.44	3.61 ± 0.28	63.2	$4.96^{+0.5}_{-0.4}$
10.84	-0.43	9.15 ± 0.10	44.5	...	2464	10.84	-0.43	0.27 ± 0.09	...	...
10.60	-0.42	11.60 ± 0.09	...	...	2419	10.60	-0.42	1.72 ± 0.18	51.1	...
11.77	-0.42	29.34 ± 0.18	88.2	...	2579	11.76	-0.42	0.38 ± 0.10	17.4	...
10.83	-0.41	9.26 ± 0.10	47.8	...	2463	10.84	-0.40	0.19 ± 0.07	...	...
11.11	-0.40	302.15 ± 0.24	95.2	...	2520	11.11	-0.40	14.90 ± 0.95	98.8	...
...	...	...	...	...	2524	11.14	-0.40	0.49 ± 0.11	24.6	...
10.82	-0.40	15.01 ± 0.13	66.1	...	2458	10.81	-0.40	0.80 ± 0.14	44.3	...
...	...	...	...	...	2460	10.83	-0.40	0.55 ± 0.14	40.0	...
11.60	-0.38	43.64 ± 0.22	115.5	...	2563	11.59	-0.39	1.15 ± 0.18	66.9	...
...	...	...	...	...	2566	11.62	-0.38	0.26 ± 0.09	18.9	...
11.07	-0.38	65.75 ± 0.15	67.8	...	2510	11.07	-0.38	4.63 ± 0.36	81.9	...
10.62	-0.38	756.01 ± 0.19	58.9	$4.96^{+0.5}_{-0.4}$	2418	10.60	-0.37	3.11 ± 0.23	52.7	$4.96^{+0.5}_{-0.4}$
...	...	...	...	...	2424	10.62	-0.39	42.63 ± 2.61	80.5	$4.96^{+0.5}_{-0.4}$
10.80	-0.38	10.44 ± 0.11	44.3	...	2457	10.80	-0.38	0.64 ± 0.15	43.8	...
...	...	...	...	...	2459	10.82	-0.39	0.11 ± 0.07	...	...
11.37	-0.38	17.61 ± 0.17	86.0	...	2546	11.37	-0.38	0.21 ± 0.08	...	...
10.99	-0.37	71.35 ± 0.20	95.0	...	2484	10.96	-0.36	0.69 ± 0.12	39.6	...
...	...	...	...	...	2487	10.98	-0.37	1.68 ± 0.18	50.8	...
...	...	...	...	...	2492	11.00	-0.37	1.25 ± 0.16	45.2	...
...	...	...	...	...	2494	11.01	-0.39	0.54 ± 0.12	30.1	...
9.95	-0.37	44.79 ± 0.15	71.3	$13.62^{+0.8}_{-0.6}$	2863	13.28	-0.39	0.25 ± 0.10	...	...
10.91	-0.36	14.34 ± 0.10	45.6	...	2477	10.92	-0.35	0.70 ± 0.14	50.6	...
10.93	-0.34	32.99 ± 0.18	99.7	...	...	...	...	...	...	...
11.54	-0.37	20.70 ± 0.17	90.7	...	2558	11.53	-0.35	0.23 ± 0.09	...	...
...	...	...	...	...	2559	11.54	-0.37	0.08 ± 0.06	...	...
11.98	-0.35	10.52 ± 0.12	47.2	...	2601	11.98	-0.35	0.53 ± 0.12	15.7	$4.14^{+0.5}_{-0.6}$
11.28	-0.35	6.41 ± 0.10	34.5	...	2541	11.28	-0.35	0.20 ± 0.07	...	...
10.58	-0.35	15.26 ± 0.09	...	$4.96^{+0.5}_{-0.4}$	2416	10.58	-0.35	1.57 ± 0.18	52.8	$4.96^{+0.5}_{-0.4}$
11.40	-0.33	26.77 ± 0.21	117.5	...	2549	11.40	-0.34	0.32 ± 0.11	42.2	...
10.62	-0.34	177.96 ± 0.16	59.9	$4.96^{+0.5}_{-0.4}$	2417	10.58	-0.29	0.36 ± 0.09	21.6	...
10.59	-0.30	7.31 ± 0.10	33.0	...	...	...	...	...	...	...
...	...	...	...	...	2425	10.62	-0.33	11.98 ± 0.79	105.2	$4.96^{+0.5}_{-0.4}$
10.72	-0.33	54.35 ± 0.13	46.8	$4.96^{+0.5}_{-0.4}$	2445	10.72	-0.33	3.33 ± 0.28	58.7	$4.96^{+0.5}_{-0.4}$
11.22	-0.32	9.54 ± 0.13	58.5	...	2536	11.23	-0.32	0.60 ± 0.14	51.0	...
11.25	-0.32	14.23 ± 0.14	60.9	...	...	...	...	...	...	...
12.16	-0.32	12.08 ± 0.16	83.8	...	2620	12.16	-0.32	0.67 ± 0.15	56.9	...
11.52	-0.33	40.83 ± 0.21	107.6	$4.36^{+0.4}_{-0.5}$	2554	11.51	-0.34	0.24 ± 0.09	...	...
...	...	...	...	...	2556	11.52	-0.32	0.87 ± 0.16	63.3	$4.22^{+0.4}_{-0.5}$
10.69	-0.31	31.58 ± 0.14	59.8	$4.96^{+0.5}_{-0.4}$	2437	10.69	-0.31	2.46 ± 0.26	71.7	$4.96^{+0.5}_{-0.4}$
10.76	-0.31	22.27 ± 0.16	81.5	...	2455	10.76	-0.30	0.33 ± 0.11	26.1	...

Continuation of Table A1

Hi-GAL					BGPS					
ℓ (deg)	b (deg)	S_{500} (Jy)	θ_R (arcsec)	$d_\odot$ (kpc)	Catalog #	ℓ (deg)	b (deg)	S_{1100} (Jy)	θ_R (arcsec)	$d_\odot$ (kpc)
11.70	-0.30	14.77 ± 0.14	62.6	···	2572	11.70	-0.30	0.65 ± 0.16	50.2	···
12.12	-0.29	17.33 ± 0.15	84.5	···	2616	12.11	-0.30	0.61 ± 0.14	27.5	···
10.74	-0.30	10.86 ± 0.11	42.6	···	2448	10.74	-0.30	0.41 ± 0.12	36.5	···
11.99	-0.27	66.45 ± 0.22	111.9	···	2602	11.99	-0.29	0.22 ± 0.08	···	···
···	···	···	···	···	2603	11.99	-0.27	1.76 ± 0.23	57.2	···
···	···	···	···	···	2605	12.02	-0.28	0.26 ± 0.09	18.0	···
12.06	-0.26	6.61 ± 0.08	···	···	2608	12.06	-0.26	0.48 ± 0.12	22.1	···
12.02	-0.26	23.15 ± 0.13	55.3	···	2604	12.02	-0.26	0.67 ± 0.14	29.1	···
11.94	-0.26	35.74 ± 0.18	69.4	···	2594	11.94	-0.26	1.26 ± 0.17	25.9	···
11.74	-0.24	8.28 ± 0.12	45.9	···	2577	11.74	-0.24	0.19 ± 0.08	···	···
10.69	-0.24	3.15 ± 0.08	···	···	2438	10.69	-0.24	0.14 ± 0.08	···	···
···	···	···	···	···	2439	10.69	-0.25	0.14 ± 0.07	···	···
11.90	-0.22	25.79 ± 0.18	83.6	···	2587	11.89	-0.22	1.34 ± 0.17	46.7	···
10.67	-0.22	45.02 ± 0.14	49.3	···	2434	10.67	-0.22	2.81 ± 0.25	62.8	···
12.02	-0.21	38.55 ± 0.18	72.7	···	2606	12.02	-0.21	1.60 ± 0.19	49.8	···
11.66	-0.20	10.06 ± 0.14	75.4	···	2569	11.66	-0.19	0.24 ± 0.09	16.1	···
10.67	-0.20	35.15 ± 0.13	58.0	···	2433	10.67	-0.20	1.95 ± 0.21	57.0	···
11.50	-0.19	8.77 ± 0.12	52.5	···	2553	11.50	-0.20	0.21 ± 0.08	···	···
11.86	-0.19	10.93 ± 0.12	44.3	···	2586	11.86	-0.19	0.40 ± 0.11	···	···
12.08	-0.18	38.19 ± 0.22	120.2	···	2609	12.07	-0.20	0.51 ± 0.13	38.7	···
···	···	···	···	···	2610	12.08	-0.18	0.51 ± 0.14	51.7	···
···	···	···	···	···	2613	12.10	-0.20	0.45 ± 0.12	36.8	···
11.00	-0.17	18.21 ± 0.12	59.4	···	2491	11.00	-0.17	1.47 ± 0.18	61.8	···
10.67	-0.16	20.74 ± 0.12	52.1	$3.22^{+0.5}_{-0.6}$	2432	10.67	-0.17	1.04 ± 0.17	45.5	$3.20^{+0.6}_{-0.8}$
11.94	-0.15	51.08 ± 0.12	41.1	···	2592	11.94	-0.15	2.73 ± 0.25	44.4	···
11.75	-0.14	50.71 ± 0.14	55.1	···	2576	11.75	-0.14	1.31 ± 0.17	43.9	···
···	···	···	···	···	2578	11.76	-0.15	1.34 ± 0.15	31.6	···
10.98	-0.15	14.94 ± 0.13	64.5	···	2488	10.98	-0.15	0.73 ± 0.15	50.0	···
11.47	-0.14	27.49 ± 0.19	86.6	···	2550	11.46	-0.14	0.90 ± 0.16	53.5	···
11.90	-0.14	142.13 ± 0.18	66.0	$13.70^{+0.4}_{-0.7}$	2590	11.90	-0.14	6.46 ± 0.45	65.7	···
12.15	-0.14	3.09 ± 0.07	···	···	2619	12.15	-0.14	0.60 ± 0.13	40.6	···
11.60	-0.13	20.55 ± 0.14	57.3	···	2565	11.60	-0.13	0.87 ± 0.14	41.8	···
11.79	-0.14	21.15 ± 0.19	98.7	···	2582	11.80	-0.13	0.58 ± 0.13	39.8	···
11.01	-0.13	2.74 ± 0.08	25.1	···	2493	11.01	-0.13	0.39 ± 0.11	32.4	···
12.11	-0.13	16.73 ± 0.09	···	···	2615	12.11	-0.13	0.83 ± 0.12	10.8	···
11.13	-0.13	57.02 ± 0.14	66.1	$2.86^{+0.6}_{-0.6}$	2519	11.12	-0.12	8.56 ± 0.59	108.9	$3.02^{+0.6}_{-0.7}$
11.11	-0.12	75.43 ± 0.16	73.4	$3.28^{+0.5}_{-0.7}$	···	···	···	···	···	···
11.98	-0.13	20.10 ± 0.15	66.2	$12.08^{+0.4}_{-0.4}$	2599	11.97	-0.12	0.76 ± 0.15	47.3	$12.10^{+0.4}_{-0.4}$
···	···	···	···	···	2600	11.99	-0.13	0.51 ± 0.11	22.8	$12.12^{+0.4}_{-0.3}$
10.68	-0.13	39.80 ± 0.12	60.1	$3.04^{+0.6}_{-0.6}$	2436	10.68	-0.12	1.62 ± 0.18	54.4	$3.22^{+0.6}_{-0.7}$
10.65	-0.12	32.68 ± 0.16	77.7	$3.02^{+0.8}_{-1.1}$	2427	10.65	-0.12	1.46 ± 0.20	69.9	$3.10^{+0.9}_{-1.3}$
12.20	-0.12	221.80 ± 0.19	81.9	···	2623	12.20	-0.12	7.82 ± 0.51	63.2	···
···	···	···	···	···	2625	12.21	-0.12	5.36 ± 0.37	53.1	···

Continuation of Table A1

Hi-GAL					BGPS					
ℓ (deg)	b (deg)	S_{500} (Jy)	θ_R (arcsec)	$d_\odot$ (kpc)	Catalog #	ℓ (deg)	b (deg)	S_{1100} (Jy)	θ_R (arcsec)	$d_\odot$ (kpc)
...	...	...	...	...	2627	12.22	-0.16	0.23 ± 0.09	8.6	...
11.93	-0.11	7.90 ± 0.10	21.1	...	2591	11.93	-0.11	0.33 ± 0.10	...	...
11.56	-0.11	18.25 ± 0.16	75.8	...	2562	11.56	-0.11	0.12 ± 0.06	...	...
11.86	-0.11	5.40 ± 0.07	...	...	2585	11.86	-0.10	0.36 ± 0.09	...	...
12.21	-0.10	215.54 ± 0.13	40.9	...	2624	12.21	-0.10	12.88 ± 0.82	53.5	...
11.97	-0.09	9.21 ± 0.10	45.8	...	2598	11.97	-0.09	0.63 ± 0.14	51.1	...
11.90	-0.10	22.42 ± 0.13	38.6	...	2588	11.90	-0.11	0.85 ± 0.15	...	...
11.84	-0.10	22.45 ± 0.13	46.9	...	2584	11.84	-0.10	0.95 ± 0.14	27.9	...
10.82	-0.10	5.29 ± 0.06	...	...	2461	10.82	-0.10	0.24 ± 0.08	...	...
10.70	-0.11	74.00 ± 0.19	109.9	...	2443	10.70	-0.10	2.05 ± 0.22	74.5	...
...	...	...	...	...	2447	10.71	-0.12	0.30 ± 0.07	...	...
11.94	-0.10	11.11 ± 0.11	45.9	...	2593	11.94	-0.10	0.29 ± 0.09	...	...
11.06	-0.10	63.86 ± 0.20	104.7	$2.92^{+0.6}_{-0.7}$	2507	11.06	-0.09	4.69 ± 0.37	96.2	$3.00^{+0.6}_{-0.7}$
11.20	-0.10	71.16 ± 0.21	110.8	$3.22^{+0.5}_{-0.6}$	2530	11.19	-0.10	3.02 ± 0.29	78.3	$3.18^{+0.6}_{-0.7}$
...	...	...	...	...	2531	11.22	-0.10	0.96 ± 0.14	10.7	$3.18^{+0.6}_{-0.7}$
10.98	-0.08	158.98 ± 0.28	136.4	$3.24^{+0.5}_{-0.6}$	2485	10.97	-0.09	3.16 ± 0.28	70.1	$3.58^{+0.5}_{-0.6}$
...	...	...	...	...	2486	10.98	-0.05	0.20 ± 0.08	...	...
...	...	...	...	...	2489	11.00	-0.08	5.71 ± 0.41	82.1	$2.92^{+0.6}_{-0.7}$
11.77	-0.07	30.30 ± 0.14	56.1	...	2581	11.77	-0.07	1.01 ± 0.14	35.1	...
10.81	-0.08	6.79 ± 0.11	44.6	...	2456	10.79	-0.09	0.25 ± 0.09	...	...
11.17	-0.07	7.24 ± 0.08	...	...	2527	11.17	-0.07	0.38 ± 0.10	12.3	...
10.72	-0.07	15.34 ± 0.13	67.3	...	2446	10.72	-0.06	0.84 ± 0.16	58.6	...
11.72	-0.07	40.58 ± 0.18	83.2	...	2574	11.72	-0.09	0.15 ± 0.07	...	...
...	...	...	...	...	2575	11.72	-0.07	1.80 ± 0.23	74.0	...
11.63	-0.06	2.58 ± 0.07	...	...	2567	11.63	-0.06	0.26 ± 0.09	...	...
11.23	-0.07	14.84 ± 0.12	57.6	$3.24^{+0.6}_{-0.7}$	2533	11.23	-0.06	0.76 ± 0.14	28.2	$3.24^{+0.6}_{-0.8}$
11.82	-0.06	13.21 ± 0.14	53.7	...	2583	11.82	-0.06	0.52 ± 0.13	44.5	...
10.88	-0.05	5.28 ± 0.08	...	...	2469	10.88	-0.05	0.53 ± 0.11	36.4	...
12.16	-0.04	0.86 ± 0.04	...	...	2621	12.16	-0.04	0.21 ± 0.08	...	...
11.76	-0.04	14.15 ± 0.13	52.7	...	2580	11.77	-0.04	0.60 ± 0.12	24.4	...
11.05	-0.04	5.71 ± 0.09	...	$3.20^{+0.6}_{-0.8}$	2504	11.05	-0.04	0.47 ± 0.11	18.8	$3.16^{+0.6}_{-0.8}$
10.86	-0.04	5.23 ± 0.10	43.0	...	2462	10.82	-0.02	4.66 ± 0.40	116.7	...
10.82	-0.02	78.09 ± 0.23	107.5	...	...	...	...	...	...	...
...	...	...	...	...	2466	10.85	-0.05	0.09 ± 0.06	...	...
12.20	-0.03	58.95 ± 0.16	52.4	...	2622	12.20	-0.03	3.56 ± 0.32	72.8	...
12.12	-0.03	11.59 ± 0.12	43.4	...	2617	12.12	-0.03	0.65 ± 0.12	30.7	...
11.94	-0.04	52.62 ± 0.17	86.3	...	2595	11.94	-0.04	4.02 ± 0.34	82.0	...
12.03	-0.03	36.93 ± 0.18	79.0	$9.66^{+0.8}_{-0.7}$	2607	12.03	-0.03	1.42 ± 0.19	49.2	$9.66^{+0.8}_{-0.7}$
12.15	-0.03	4.41 ± 0.10	41.0	...	2618	12.15	-0.02	0.26 ± 0.09	...	...
11.03	-0.03	3.64 ± 0.08	...	...	2499	11.03	-0.03	0.15 ± 0.06	...	...
10.68	-0.03	89.46 ± 0.19	73.7	...	2435	10.68	-0.03	3.82 ± 0.32	64.3	...
10.62	-0.03	29.28 ± 0.17	72.4	...	2420	10.62	-0.03	1.82 ± 0.20	64.3	...
...	...	...	...	...	2423	10.62	-0.06	0.27 ± 0.09	33.4	...

Continuation of Table A1

Hi-GAL					BGPS					
ℓ (deg)	b (deg)	S_{500} (Jy)	θ_R (arcsec)	$d_\odot$ (kpc)	Catalog #	ℓ (deg)	b (deg)	S_{1100} (Jy)	θ_R (arcsec)	$d_\odot$ (kpc)
10.97	-0.02	10.25 ± 0.12	52.0	⋯	2483	10.97	-0.02	0.35 ± 0.10	20.9	⋯
10.57	-0.02	15.29 ± 0.13	51.8	⋯	2415	10.57	-0.02	0.50 ± 0.11	29.6	⋯
11.65	-0.01	6.50 ± 0.10	42.0	⋯	2568	11.64	-0.01	0.19 ± 0.07	⋯	⋯
12.25	-0.00	7.99 ± 0.10	25.1	⋯	2634	12.25	-0.00	0.65 ± 0.14	30.1	⋯
11.15	-0.01	12.12 ± 0.16	82.7	⋯	2526	11.15	-0.00	0.39 ± 0.11	23.9	⋯
11.95	0.00	1.73 ± 0.07	⋯	⋯	2597	11.95	-0.00	0.17 ± 0.08	⋯	⋯
11.27	0.01	4.94 ± 0.11	46.1	⋯	2539	11.26	0.01	0.42 ± 0.12	33.8	⋯
11.40	0.03	29.16 ± 0.19	103.2	⋯	2547	11.39	0.03	0.15 ± 0.07	⋯	⋯
⋯	⋯	⋯	⋯	⋯	2548	11.40	0.02	0.40 ± 0.11	⋯	⋯
11.10	0.01	6.35 ± 0.12	50.7	⋯	2513	11.09	0.01	0.38 ± 0.10	29.7	⋯
⋯	⋯	⋯	⋯	⋯	2516	11.10	0.01	0.15 ± 0.07	⋯	⋯
10.75	0.02	48.56 ± 0.17	80.7	⋯	2451	10.74	0.04	0.11 ± 0.06	⋯	⋯
⋯	⋯	⋯	⋯	⋯	2452	10.74	0.01	3.35 ± 0.30	82.8	⋯
10.96	0.02	74.57 ± 0.15	50.6	⋯	2481	10.96	0.02	4.48 ± 0.34	59.0	⋯
10.70	0.01	54.17 ± 0.18	95.2	⋯	2442	10.70	-0.00	0.42 ± 0.10	⋯	⋯
⋯	⋯	⋯	⋯	⋯	2444	10.71	0.01	1.74 ± 0.23	77.4	⋯
11.03	0.03	10.40 ± 0.09	18.1	⋯	2496	11.02	0.03	0.29 ± 0.08	⋯	⋯
⋯	⋯	⋯	⋯	⋯	2498	11.03	0.03	0.62 ± 0.10	17.8	⋯
12.24	0.04	5.57 ± 0.10	35.4	⋯	2628	12.24	0.04	0.23 ± 0.08	⋯	⋯
10.69	0.04	28.37 ± 0.16	85.0	⋯	2441	10.69	0.05	0.52 ± 0.13	37.0	⋯
11.11	0.05	18.21 ± 0.09	⋯	⋯	2521	11.11	0.05	0.81 ± 0.12	⋯	⋯
11.15	0.05	6.45 ± 0.10	38.7	⋯	2525	11.14	0.05	0.22 ± 0.07	⋯	⋯
10.93	0.05	5.42 ± 0.09	⋯	⋯	2476	10.92	0.05	0.57 ± 0.12	35.4	⋯
⋯	⋯	⋯	⋯	⋯	2479	10.94	0.04	0.23 ± 0.08	⋯	⋯
11.03	0.06	40.47 ± 0.13	37.0	⋯	2500	11.03	0.06	2.98 ± 0.27	55.8	⋯
10.85	0.06	16.60 ± 0.17	90.8	⋯	2465	10.85	0.06	0.34 ± 0.10	26.9	⋯
11.23	0.06	30.43 ± 0.20	102.9	⋯	2535	11.24	0.06	0.45 ± 0.12	⋯	⋯
11.19	0.07	18.93 ± 0.16	80.1	⋯	2528	11.18	0.06	0.49 ± 0.12	35.6	⋯
⋯	⋯	⋯	⋯	⋯	2529	11.19	0.07	0.31 ± 0.10	⋯	⋯
10.90	0.07	9.84 ± 0.10	29.0	⋯	2472	10.90	0.07	1.46 ± 0.20	65.3	⋯
11.09	0.07	18.25 ± 0.13	46.4	⋯	2517	11.09	0.07	0.64 ± 0.13	18.2	⋯
10.93	0.07	6.78 ± 0.09	38.7	⋯	2478	10.93	0.07	0.62 ± 0.13	43.7	⋯
10.67	0.10	72.81 ± 0.22	116.6	⋯	2430	10.67	0.09	2.70 ± 0.27	89.9	$2.48^{+0.8}_{-1.2}$
10.92	0.09	2.67 ± 0.08	⋯	⋯	2474	10.92	0.09	0.17 ± 0.07	⋯	⋯
⋯	⋯	⋯	⋯	⋯	2475	10.92	0.10	0.09 ± 0.05	⋯	⋯
11.06	0.10	6.28 ± 0.09	23.6	⋯	2505	11.06	0.10	0.40 ± 0.10	25.5	⋯
⋯	⋯	⋯	⋯	⋯	2506	11.07	0.09	0.13 ± 0.06	⋯	⋯
12.09	0.11	1.95 ± 0.07	⋯	⋯	2612	12.09	0.11	0.25 ± 0.09	21.5	⋯
11.12	0.12	19.38 ± 0.16	73.5	⋯	2522	11.12	0.12	0.38 ± 0.10	37.7	⋯
10.86	0.13	28.11 ± 0.19	82.4	⋯	2467	10.86	0.13	1.38 ± 0.19	46.6	⋯
10.96	0.15	64.78 ± 0.21	121.0	$14.08^{+1.0}_{-0.7}$	2482	10.96	0.14	1.48 ± 0.20	58.0	⋯
12.21	0.14	53.89 ± 0.21	94.9	$3.54^{+0.4}_{-0.5}$	2626	12.22	0.14	2.65 ± 0.26	70.6	$3.52^{+0.5}_{-0.5}$
11.22	0.13	38.45 ± 0.20	105.1	⋯	2532	11.22	0.11	0.35 ± 0.10	18.9	⋯

Continuation of Table A1

Hi-GAL					BGPS					
ℓ (deg)	b (deg)	S_{500} (Jy)	θ_R (arcsec)	$d_\odot$ (kpc)	Catalog #	ℓ (deg)	b (deg)	S_{1100} (Jy)	θ_R (arcsec)	$d_\odot$ (kpc)
...	...	...	...	...	2534	11.22	0.13	0.79 ± 0.15	50.7	...
11.11	0.14	10.80 ± 0.12	42.4	...	2518	11.11	0.14	0.33 ± 0.09	...	...
11.04	0.14	34.76 ± 0.17	77.7	...	2501	11.03	0.14	0.42 ± 0.09	20.6	...
...	...	...	...	...	2502	11.05	0.14	0.46 ± 0.11	25.6	...
11.00	0.15	30.20 ± 0.18	91.5	...	2490	10.99	0.14	0.22 ± 0.08	...	...
11.54	0.19	3.19 ± 0.08	...	...	2557	11.53	0.19	0.24 ± 0.08	...	...
11.50	0.21	27.87 ± 0.18	86.4	...	2552	11.49	0.21	1.26 ± 0.18	65.0	...
...	...	...	...	...	2555	11.51	0.20	0.24 ± 0.08	28.3	...
11.27	0.22	16.92 ± 0.17	84.8	...	2537	11.27	0.22	0.49 ± 0.13	53.1	...
12.29	0.24	24.92 ± 0.21	115.2	...	2639	12.30	0.25	0.41 ± 0.12	29.5	...
11.60	0.26	10.38 ± 0.15	73.5	$3.02^{+0.6}_{-0.7}$	2564	11.60	0.26	0.23 ± 0.09	...	$3.04^{+0.6}_{-0.7}$
11.55	0.26	28.43 ± 0.18	85.1	$3.14^{+0.4}_{-0.5}$	2560	11.53	0.27	0.74 ± 0.15	40.1	$3.16^{+0.5}_{-0.6}$
...	...	...	...	...	2561	11.55	0.26	0.60 ± 0.12	34.9	$3.06^{+0.5}_{-0.6}$
11.29	0.32	6.86 ± 0.12	43.6	...	2542	11.28	0.32	0.34 ± 0.10	20.1	...
12.24	0.35	7.41 ± 0.12	54.9	...	2629	12.24	0.34	0.34 ± 0.10	22.8	...
...	...	...	...	...	2632	12.24	0.36	0.10 ± 0.06	...	...
12.36	0.51	3.15 ± 0.08	27.0	$2.06^{+0.6}_{-0.8}$	2647	12.37	0.51	0.69 ± 0.14	42.7	$2.42^{+0.6}_{-0.7}$
11.00	0.56	28.21 ± 0.31	203.3	...	2495	11.02	0.54	0.30 ± 0.10	...	...
29.90	-0.81	34.60 ± 0.11	58.2	$4.58^{+0.3}_{-0.3}$	5075	29.90	-0.80	1.12 ± 0.30	41.8	$4.58^{+0.4}_{-0.4}$
29.96	-0.78	88.38 ± 0.18	116.5	$4.58^{+0.4}_{-0.4}$	5088	29.95	-0.79	1.88 ± 0.42	51.8	$4.58^{+0.4}_{-0.4}$
...	...	...	...	...	5089	29.96	-0.78	1.16 ± 0.34	37.2	$4.62^{+0.4}_{-0.4}$
29.89	-0.78	94.77 ± 0.20	117.6	$4.52^{+0.4}_{-0.4}$	5069	29.88	-0.78	1.43 ± 0.37	34.9	$4.54^{+0.4}_{-0.4}$
...	...	...	...	...	5071	29.90	-0.78	0.75 ± 0.29	...	$4.54^{+0.4}_{-0.4}$
29.60	-0.62	154.57 ± 0.21	128.4	$4.24^{+0.5}_{-0.5}$	5028	29.60	-0.61	5.94 ± 0.57	83.9	$4.26^{+0.4}_{-0.4}$
...	...	...	...	...	5030	29.61	-0.58	0.76 ± 0.18	45.3	$4.20^{+0.4}_{-0.4}$
30.45	-0.50	9.66 ± 0.07	36.5	...	5196	30.46	-0.50	0.74 ± 0.16	53.1	...
30.46	-0.49	17.59 ± 0.10	65.0	...	...	...	...	...	...	...
29.87	-0.50	12.58 ± 0.10	65.3	$3.86^{+0.3}_{-0.3}$	5065	29.86	-0.49	0.27 ± 0.09	29.2	$3.90^{+0.3}_{-0.3}$
30.37	-0.48	5.05 ± 0.08	52.3	$2.88^{+0.3}_{-0.4}$	5173	30.38	-0.48	0.48 ± 0.12	47.8	$2.94^{+0.5}_{-0.5}$
29.88	-0.47	15.49 ± 0.14	95.1	...	5068	29.88	-0.47	0.46 ± 0.12	48.6	...
29.84	-0.48	8.93 ± 0.08	34.6	$3.80^{+0.3}_{-0.3}$	5062	29.84	-0.48	0.51 ± 0.10	22.7	$3.82^{+0.3}_{-0.3}$
30.39	-0.47	4.29 ± 0.07	36.6	...	5180	30.40	-0.46	0.24 ± 0.09	22.9	$2.88^{+0.4}_{-0.4}$
29.64	-0.44	18.02 ± 0.14	93.1	...	5038	29.65	-0.44	0.55 ± 0.12	41.2	...
29.47	-0.43	5.24 ± 0.08	43.5	...	5006	29.47	-0.42	0.44 ± 0.12	46.7	...
29.98	-0.42	45.76 ± 0.17	107.6	$4.06^{+0.4}_{-0.3}$	5091	29.98	-0.42	1.93 ± 0.24	81.4	...
29.63	-0.38	10.59 ± 0.11	73.7	...	5036	29.63	-0.38	0.40 ± 0.10	38.1	...
30.44	-0.38	10.58 ± 0.07	...	...	5191	30.44	-0.38	0.76 ± 0.13	26.7	...
29.55	-0.36	14.44 ± 0.12	77.8	$4.94^{+0.4}_{-0.4}$	5019	29.54	-0.35	0.23 ± 0.08	...	...
...	...	...	...	...	5020	29.56	-0.36	0.12 ± 0.06	...	$4.94^{+0.4}_{-0.4}$
30.26	-0.33	29.34 ± 0.15	95.6	...	5141	30.26	-0.33	0.85 ± 0.15	62.0	...
...	...	...	...	...	5142	30.27	-0.31	0.12 ± 0.06	...	...
30.36	-0.33	18.71 ± 0.12	65.6	...	5165	30.36	-0.36	0.08 ± 0.05	...	...

Continuation of Table A1

Hi-GAL					BGPS					
ℓ (deg)	b (deg)	S_{500} (Jy)	θ_R (arcsec)	$d_\odot$ (kpc)	Catalog #	ℓ (deg)	b (deg)	S_{1100} (Jy)	θ_R (arcsec)	$d_\odot$ (kpc)
...	...	...	...	...	5166	30.36	-0.33	0.94 ± 0.14	56.3	...
29.91	-0.30	34.19 ± 0.15	113.7	...	5072	29.90	-0.30	0.37 ± 0.10	42.0	...
...	...	...	...	...	5073	29.90	-0.28	0.24 ± 0.08	18.9	...
...	...	...	...	...	5077	29.91	-0.33	0.53 ± 0.13	44.0	...
...	...	...	...	...	5078	29.92	-0.28	0.39 ± 0.11	39.1	...
29.76	-0.32	5.83 ± 0.10	44.7	...	5049	29.77	-0.31	0.32 ± 0.09	...	$4.98^{+0.4}_{-0.4}$
30.43	-0.30	17.93 ± 0.10	57.3	$8.68^{+0.5}_{-0.7}$	5189	30.43	-0.30	1.21 ± 0.15	56.8	$8.70^{+0.5}_{-0.7}$
29.97	-0.31	10.00 ± 0.11	67.9	...	5086	29.96	-0.30	0.43 ± 0.11	37.3	$5.00^{+0.4}_{-0.4}$
30.40	-0.30	22.48 ± 0.10	50.2	$8.72^{+0.5}_{-0.7}$	5184	30.40	-0.30	2.06 ± 0.21	68.2	$8.72^{+0.5}_{-0.7}$
29.93	-0.29	9.25 ± 0.09	57.7	...	5082	29.93	-0.29	0.31 ± 0.09	...	...
30.31	-0.30	38.48 ± 0.17	121.4	...	5150	30.30	-0.29	1.31 ± 0.19	65.8	$5.34^{+0.6}_{-0.5}$
30.27	-0.29	15.78 ± 0.10	60.3	...	5137	30.25	-0.29	0.14 ± 0.07	13.1	...
...	...	...	...	...	5139	30.27	-0.29	0.91 ± 0.14	57.4	...
30.09	-0.28	8.63 ± 0.09	50.5	...	5109	30.09	-0.28	0.35 ± 0.09	35.1	$5.20^{+0.4}_{-0.4}$
30.05	-0.28	8.66 ± 0.08	40.0	...	5105	30.05	-0.28	0.35 ± 0.10	26.9	$5.10^{+0.4}_{-0.4}$
30.34	-0.28	14.14 ± 0.11	76.2	...	5157	30.34	-0.29	0.15 ± 0.06	...	...
...	...	...	...	...	5164	30.35	-0.27	0.81 ± 0.14	52.9	...
30.01	-0.27	173.40 ± 0.22	118.0	$9.08^{+0.6}_{-0.9}$	5096	30.01	-0.27	8.46 ± 0.58	91.5	$5.52^{+0.5}_{-0.5}$
...	...	...	...	...	5104	30.04	-0.26	1.09 ± 0.15	52.9	...
29.58	-0.27	4.20 ± 0.07	...	...	5025	29.58	-0.27	0.54 ± 0.10	23.0	...
29.83	-0.26	2.15 ± 0.05	...	$5.10^{+0.4}_{-0.3}$	5059	29.83	-0.26	0.14 ± 0.07	...	...
29.78	-0.27	20.95 ± 0.11	58.3	...	5052	29.78	-0.27	1.60 ± 0.17	57.8	$9.06^{+0.3}_{-0.4}$
...	...	...	...	...	5053	29.78	-0.30	0.11 ± 0.06	...	...
30.10	-0.26	20.68 ± 0.11	64.0	...	5113	30.11	-0.26	1.04 ± 0.15	48.0	...
29.76	-0.24	55.67 ± 0.18	136.1	...	5047	29.75	-0.24	3.29 ± 0.30	118.7	...
...	...	...	...	...	5048	29.78	-0.23	1.55 ± 0.19	75.7	...
29.60	-0.26	22.60 ± 0.17	121.4	...	5029	29.60	-0.25	0.70 ± 0.14	61.1	...
29.91	-0.25	5.85 ± 0.08	60.9	...	5074	29.90	-0.23	3.80 ± 0.34	117.2	$5.42^{+0.6}_{-0.5}$
29.89	-0.22	37.51 ± 0.14	82.3	$5.46^{+0.6}_{-0.5}$	...	...	...	...	...	...
29.46	-0.25	26.42 ± 0.16	110.7	$4.24^{+0.3}_{-0.4}$	5005	29.46	-0.24	0.31 ± 0.10	27.6	$4.20^{+0.4}_{-0.4}$
...	...	...	...	...	5011	29.48	-0.25	0.40 ± 0.10	35.4	$4.24^{+0.4}_{-0.4}$
30.43	-0.23	171.53 ± 0.17	87.2	$8.56^{+0.5}_{-0.8}$	5187	30.43	-0.23	13.97 ± 0.91	117.5	$8.58^{+0.5}_{-0.7}$
29.70	-0.22	9.20 ± 0.10	62.8	...	5042	29.70	-0.22	0.40 ± 0.11	41.4	...
29.46	-0.21	14.31 ± 0.10	62.5	...	5008	29.47	-0.21	0.40 ± 0.10	31.7	...
30.30	-0.22	103.83 ± 0.18	124.5	...	5144	30.27	-0.23	0.73 ± 0.11	38.5	$7.20^{+1.0}_{-1.0}$
...	...	...	...	...	5149	30.30	-0.22	6.21 ± 0.46	115.3	...
29.83	-0.19	9.30 ± 0.11	68.4	$4.84^{+0.4}_{-0.4}$	5057	29.83	-0.19	1.15 ± 0.18	76.9	...
29.68	-0.20	7.60 ± 0.09	50.6	$5.06^{+0.4}_{-0.4}$	5040	29.68	-0.20	0.11 ± 0.06	...	...
...	...	...	...	...	5041	29.68	-0.19	0.13 ± 0.07	...	...
30.22	-0.18	161.42 ± 0.18	102.3	...	5125	30.22	-0.18	12.16 ± 0.81	122.0	...
29.49	-0.18	56.39 ± 0.16	96.1	...	5012	29.49	-0.18	2.82 ± 0.26	81.6	...
29.44	-0.17	25.24 ± 0.11	44.6	...	5003	29.44	-0.17	0.70 ± 0.13	...	...
30.00	-0.15	19.50 ± 0.09	47.5	...	5094	29.99	-0.17	0.50 ± 0.10	29.1	...

Continuation of Table A1

Hi-GAL					BGPS						
ℓ (deg)	b (deg)	S_{500} (Jy)	θ_R (arcsec)	$d_\odot$ (kpc)	Catalog #	ℓ (deg)	b (deg)	S_{1100} (Jy)	θ_R (arcsec)	$d_\odot$ (kpc)
...	...	...	...	...	5095	30.00	-0.15	1.23 ± 0.17	54.9	...
30.31	-0.15	16.95 ± 0.10	55.7	$6.04^{+1.2}_{-0.6}$	5153	30.32	-0.15	1.66 ± 0.20	71.2	$6.06^{+1.3}_{-0.6}$
30.37	-0.14	14.28 ± 0.07	35.4	$7.12^{+1.0}_{-1.0}$	5170	30.38	-0.14	2.78 ± 0.23	76.1	$7.12^{+1.0}_{-1.0}$
30.07	-0.14	15.67 ± 0.13	102.9	$4.94^{+0.5}_{-0.5}$	5107	30.07	-0.14	0.95 ± 0.15	74.9	...
...	...	...	...	...	5108	30.08	-0.15	0.12 ± 0.05	...	...
30.20	-0.12	27.46 ± 0.13	85.3	...	5120	30.17	-0.13	0.20 ± 0.07	...	...
...	...	...	...	...	5121	30.20	-0.12	2.71 ± 0.27	93.3	...
30.01	-0.13	12.81 ± 0.07	30.3	$5.18^{+0.5}_{-0.5}$	5097	30.01	-0.12	1.17 ± 0.14	44.5	$5.24^{+0.5}_{-0.5}$
30.43	-0.11	43.20 ± 0.12	70.7	...	5190	30.43	-0.11	4.80 ± 0.36	99.7	...
30.35	-0.12	55.93 ± 0.14	90.9	...	5160	30.34	-0.12	5.21 ± 0.39	103.6	$7.12^{+1.0}_{-1.0}$
30.39	-0.11	116.72 ± 0.14	87.0	...	5179	30.39	-0.11	9.42 ± 0.62	102.6	$7.12^{+1.0}_{-1.0}$
29.66	-0.10	7.57 ± 0.10	72.4	...	5039	29.67	-0.10	0.46 ± 0.12	58.5	...
29.84	-0.10	9.56 ± 0.07	27.2	$5.56^{+0.5}_{-0.4}$	5061	29.84	-0.10	1.50 ± 0.18	68.2	$5.56^{+0.5}_{-0.4}$
29.82	-0.09	9.22 ± 0.07	...	$5.52^{+0.5}_{-0.4}$	5058	29.82	-0.09	0.88 ± 0.13	37.8	...
30.21	-0.09	6.99 ± 0.08	52.8	...	5127	30.21	-0.09	1.32 ± 0.19	79.8	...
29.47	-0.09	10.64 ± 0.10	60.0	...	5009	29.47	-0.09	0.40 ± 0.11	33.0	...
30.14	-0.07	20.68 ± 0.10	57.9	$4.66^{+0.5}_{-0.5}$	5116	30.14	-0.07	1.89 ± 0.22	68.3	$4.68^{+0.5}_{-0.4}$
...	...	...	...	...	5117	30.14	-0.04	0.10 ± 0.06	...	...
30.11	-0.07	10.05 ± 0.09	49.2	$4.76^{+0.5}_{-0.5}$	5112	30.11	-0.07	0.90 ± 0.16	55.0	...
29.55	-0.08	15.58 ± 0.14	103.1	...	5022	29.56	-0.07	0.48 ± 0.12	38.9	...
29.94	-0.06	186.72 ± 0.10	59.4	$5.36^{+0.5}_{-0.4}$	5079	29.92	-0.06	65.12 ± 3.96	157.1	$5.44^{+0.5}_{-0.4}$
29.92	-0.05	283.15 ± 0.14	85.5	$5.46^{+0.6}_{-0.4}$	...	...	...	...	...	...
30.40	-0.05	2.28 ± 0.05	...	$6.93^{+0.9}_{-0.9}$	5183	30.40	-0.05	0.40 ± 0.10	34.9	$6.12^{+1.1}_{-0.6}$
29.86	-0.05	83.02 ± 0.10	43.7	$5.60^{+0.5}_{-0.4}$	5067	29.86	-0.05	11.67 ± 0.74	88.8	$5.60^{+0.5}_{-0.4}$
29.42	-0.05	8.66 ± 0.09	60.8	$5.10^{+0.5}_{-0.5}$	5002	29.42	-0.05	0.57 ± 0.16	40.1	...
29.84	-0.04	15.12 ± 0.08	31.4	$5.54^{+0.5}_{-0.4}$	5063	29.84	-0.04	3.69 ± 0.28	70.2	$5.54^{+0.5}_{-0.4}$
30.45	-0.03	19.79 ± 0.10	54.2	$11.40^{+0.4}_{-0.4}$	5192	30.45	-0.03	2.39 ± 0.26	85.1	$11.40^{+0.4}_{-0.4}$
29.53	-0.02	27.42 ± 0.17	120.3	...	5017	29.53	-0.01	1.06 ± 0.17	76.4	...
30.29	-0.03	4.27 ± 0.07	45.1	...	5145	30.28	-0.03	0.24 ± 0.09	...	...
...	...	...	...	...	5147	30.29	-0.02	0.67 ± 0.14	52.0	...
29.96	-0.02	304.84 ± 0.13	60.5	$5.26^{+0.3}_{-0.3}$	5087	29.96	-0.01	35.71 ± 2.19	119.3	$5.30^{+0.3}_{-0.3}$
29.94	0.02	4.88 ± 0.06	...	$5.26^{+0.3}_{-0.3}$	...	...	...	...	...	...
...	...	...	...	...	5093	29.99	-0.01	2.08 ± 0.15	34.3	...
29.62	-0.00	14.56 ± 0.13	88.0	...	5032	29.62	-0.00	0.80 ± 0.16	72.6	...
30.42	-0.01	5.38 ± 0.08	51.3	...	5186	30.42	-0.00	0.56 ± 0.13	48.4	...
30.38	-0.01	6.37 ± 0.06	16.2	...	5175	30.38	-0.00	0.43 ± 0.09	23.8	...
29.89	-0.01	56.18 ± 0.11	60.5	...	5070	29.89	-0.00	11.85 ± 0.75	93.0	$5.36^{+0.4}_{-0.4}$
29.85	0.00	14.21 ± 0.08	31.8	$5.40^{+0.4}_{-0.4}$	5064	29.85	-0.00	4.00 ± 0.30	77.4	$5.42^{+0.4}_{-0.4}$
29.47	0.01	21.85 ± 0.12	75.7	...	5010	29.47	0.02	1.26 ± 0.19	70.9	...
30.38	0.02	9.93 ± 0.09	50.7	...	5172	30.38	0.03	0.77 ± 0.12	46.1	...
30.22	0.02	4.28 ± 0.06	21.0	...	5126	30.22	0.02	0.61 ± 0.12	38.4	...
29.41	0.04	38.28 ± 0.18	137.8	...	5004	29.44	0.03	0.14 ± 0.07	...	...
29.86	0.03	25.63 ± 0.09	43.0	$5.74^{+0.6}_{-0.5}$	5066	29.87	0.03	4.53 ± 0.34	80.2	$5.74^{+0.6}_{-0.5}$

Continuation of Table A1

Hi-GAL					BGPS						
ℓ (deg)	b (deg)	S_{500} (Jy)	θ_R (arcsec)	$d_\odot$ (kpc)	Catalog #	ℓ (deg)	b (deg)	S_{1100} (Jy)	θ_R (arcsec)	$d_\odot$ (kpc)
30.35	0.04	10.39 ± 0.10	57.9	...	5161	30.35	0.04	0.97 ± 0.17	60.6	...
...	...	...	...	...	5177	30.38	0.04	0.10 ± 0.04	...	...
30.29	0.05	36.48 ± 0.09	49.8	...	5148	30.29	0.05	2.96 ± 0.25	66.7	...
30.26	0.04	54.52 ± 0.13	77.6	...	5136	30.26	0.04	3.76 ± 0.31	80.8	...
29.96	0.06	2.75 ± 0.06	...	...	5083	29.93	0.08	0.10 ± 0.06	...	...
29.94	0.07	2.48 ± 0.07	36.1	...	...	...	...	...	...	...
...	...	...	...	...	5084	29.95	0.06	1.48 ± 0.20	73.3	...
29.57	0.06	5.95 ± 0.09	47.7	...	5023	29.57	0.05	0.16 ± 0.07	...	...
...	...	...	...	...	5024	29.58	0.05	0.16 ± 0.06	...	...
29.74	0.07	5.80 ± 0.09	46.1	...	5046	29.75	0.07	0.25 ± 0.08	26.8	...
30.32	0.07	65.97 ± 0.14	92.2	$11.34^{+0.5}_{-0.4}$	5154	30.32	0.07	4.43 ± 0.35	95.3	...
30.10	0.08	15.35 ± 0.08	36.7	...	5111	30.10	0.08	1.18 ± 0.15	47.9	...
29.77	0.09	7.59 ± 0.10	64.0	...	5051	29.77	0.09	0.69 ± 0.14	60.4	...
29.91	0.09	2.06 ± 0.05	...	...	5076	29.91	0.09	0.51 ± 0.12	41.9	...
30.06	0.10	30.63 ± 0.11	65.1	...	5106	30.06	0.10	1.87 ± 0.20	66.9	...
30.37	0.11	98.56 ± 0.15	92.5	...	5167	30.36	0.11	5.62 ± 0.41	86.8	...
...	...	...	...	...	5178	30.39	0.12	0.96 ± 0.13	35.2	$7.14^{+1.0}_{-1.0}$
30.03	0.10	69.04 ± 0.14	89.1	...	5103	30.03	0.10	3.93 ± 0.33	90.7	...
29.63	0.11	17.77 ± 0.11	65.6	...	5034	29.62	0.09	0.23 ± 0.08	...	...
...	...	...	...	...	5035	29.63	0.11	0.87 ± 0.15	51.4	...
30.32	0.12	87.11 ± 0.19	129.6	...	5152	30.32	0.17	1.06 ± 0.18	76.1	...
...	...	...	...	...	5156	30.32	0.12	5.06 ± 0.38	106.1	...
29.61	0.13	10.82 ± 0.11	74.6	...	5031	29.61	0.12	0.14 ± 0.07	...	...
29.70	0.11	10.24 ± 0.12	73.0	$16.52^{+0.9}_{-0.8}$	5043	29.70	0.10	0.18 ± 0.07	...	$16.42^{+0.9}_{-0.7}$
...	...	...	...	...	5044	29.70	0.12	0.46 ± 0.12	39.9	$16.50^{+0.9}_{-0.8}$
30.41	0.14	6.07 ± 0.08	...	$5.10^{+0.5}_{-0.4}$	5185	30.41	0.14	0.35 ± 0.11	27.3	...
29.95	0.15	4.82 ± 0.05	...	...	5085	29.95	0.15	0.31 ± 0.09	...	...
30.21	0.18	29.50 ± 0.16	110.1	...	5123	30.20	0.17	1.23 ± 0.18	72.7	...
...	...	...	...	...	5128	30.22	0.20	0.20 ± 0.08	24.2	...
29.55	0.18	35.34 ± 0.16	105.1	$4.40^{+0.4}_{-0.4}$	5018	29.53	0.18	0.22 ± 0.06	...	...
...	...	...	...	...	5021	29.55	0.19	1.14 ± 0.15	47.5	$4.34^{+0.4}_{-0.3}$
29.50	0.18	12.46 ± 0.11	63.9	...	5015	29.50	0.19	0.46 ± 0.12	33.2	...
29.80	0.19	33.63 ± 0.14	95.5	...	5054	29.80	0.19	1.50 ± 0.19	80.0	...
30.28	0.21	10.35 ± 0.11	71.1	...	5146	30.29	0.20	0.28 ± 0.10	37.2	...
30.31	0.21	2.01 ± 0.07	...	...	5151	30.31	0.21	0.24 ± 0.09	32.8	...
29.60	0.21	6.05 ± 0.07	31.6	$4.36^{+0.5}_{-0.5}$	5027	29.60	0.21	0.38 ± 0.10	20.4	...
29.77	0.21	23.99 ± 0.12	72.8	$16.90^{+1.1}_{-0.9}$	5050	29.77	0.21	1.06 ± 0.15	51.9	...
29.46	0.22	7.45 ± 0.11	61.9	...	5007	29.46	0.22	0.15 ± 0.07	...	...
...	...	...	...	...	5013	29.48	0.24	0.11 ± 0.06	...	...
...	...	...	...	...	5014	29.49	0.25	0.15 ± 0.08	...	...
29.60	0.23	4.85 ± 0.08	45.3	...	5026	29.59	0.24	0.38 ± 0.09	42.2	...
30.25	0.24	20.14 ± 0.12	73.0	...	5134	30.25	0.25	0.94 ± 0.15	51.5	...
29.62	0.25	22.43 ± 0.13	74.1	$4.24^{+0.4}_{-0.4}$	5033	29.62	0.25	1.16 ± 0.17	61.0	$4.24^{+0.4}_{-0.4}$

Continuation of Table A1

Hi-GAL					BGPS					
ℓ (deg)	b (deg)	S_{500} (Jy)	θ_R (arcsec)	$d_\odot$ (kpc)	Catalog #	ℓ (deg)	b (deg)	S_{1100} (Jy)	θ_R (arcsec)	$d_\odot$ (kpc)
30.37	0.29	5.50 ± 0.06	17.2	...	5168	30.37	0.29	0.31 ± 0.09	19.2	...
30.32	0.29	18.77 ± 0.12	62.2	$6.86^{+0.9}_{-0.9}$	5155	30.32	0.29	1.42 ± 0.20	66.2	$6.06^{+1.1}_{-0.6}$
...	...	...	...	...	5159	30.35	0.30	0.12 ± 0.07	...	...
30.20	0.31	8.48 ± 0.06	10.7	...	5122	30.20	0.31	0.33 ± 0.09	...	...
30.40	0.32	4.21 ± 0.05	...	...	5181	30.40	0.32	0.17 ± 0.07	...	...
30.37	0.32	10.04 ± 0.10	58.1	...	5169	30.37	0.33	0.35 ± 0.09	...	...
29.72	0.34	7.50 ± 0.09	53.4	...	5045	29.72	0.33	0.32 ± 0.09	22.9	...
30.26	0.34	12.72 ± 0.12	78.8	...	5133	30.24	0.34	0.07 ± 0.05	...	...
...	...	...	...	...	5135	30.26	0.34	0.42 ± 0.10	36.5	$4.04^{+0.4}_{-0.4}$
...	...	...	...	...	5138	30.27	0.35	0.10 ± 0.06	...	...
...	...	...	...	...	5140	30.27	0.34	0.15 ± 0.07	...	...
30.38	0.35	14.69 ± 0.10	62.9	...	5174	30.38	0.35	0.47 ± 0.11	35.2	...
30.40	0.37	21.85 ± 0.13	89.6	$6.94^{+0.9}_{-0.9}$	5176	30.38	0.37	0.17 ± 0.07	...	$6.14^{+1.9}_{-0.3}$
...	...	...	...	...	5182	30.40	0.37	0.18 ± 0.08	32.5	$6.12^{+2.0}_{-0.3}$
29.64	0.37	8.07 ± 0.10	50.3	...	5037	29.64	0.38	0.18 ± 0.07	17.3	...
29.50	0.39	20.16 ± 0.14	83.4	...	5016	29.50	0.39	0.80 ± 0.14	44.7	$4.48^{+0.4}_{-0.4}$
30.35	0.39	48.35 ± 0.14	80.3	...	5162	30.35	0.39	1.86 ± 0.21	62.0	...
30.21	0.43	5.86 ± 0.09	48.4	...	5124	30.21	0.43	0.23 ± 0.08	21.7	...
30.42	0.46	99.58 ± 0.23	152.1	$1.06^{+0.7}_{-0.8}$	5188	30.42	0.47	3.90 ± 0.38	101.2	$1.08^{+0.6}_{-0.7}$
30.37	0.48	21.80 ± 0.10	43.7	$1.20^{+0.6}_{-0.7}$	5171	30.37	0.48	0.82 ± 0.15	23.0	$1.20^{+0.6}_{-0.7}$
30.33	0.52	7.94 ± 0.08	43.7	$1.12^{+0.6}_{-0.6}$	5158	30.34	0.52	0.58 ± 0.16	41.6	$1.18^{+0.6}_{-0.6}$
30.35	0.52	9.48 ± 0.08	44.1	$1.04^{+0.6}_{-0.7}$	5163	30.35	0.52	0.39 ± 0.12	21.5	$1.06^{+0.6}_{-0.7}$
30.28	0.52	6.10 ± 0.09	55.2	...	5143	30.27	0.53	0.26 ± 0.11	...	...
41.18	-0.50	16.80 ± 0.09	96.3	...	6646	41.17	-0.49	0.21 ± 0.08	...	...
42.44	-0.46	28.96 ± 0.11	112.5	$3.66^{+0.7}_{-0.6}$	6684	42.44	-0.46	0.19 ± 0.09	...	...
42.11	-0.45	44.63 ± 0.08	63.4	$8.66^{+0.6}_{-0.8}$	6676	42.11	-0.45	1.80 ± 0.21	39.8	$8.66^{+0.6}_{-0.8}$
40.81	-0.42	13.85 ± 0.08	73.2	$6.10^{+1.1}_{-1.1}$	6628	40.81	-0.41	0.32 ± 0.10	...	$6.10^{+1.1}_{-1.1}$
42.30	-0.30	28.45 ± 0.07	52.2	...	6681	42.30	-0.30	2.03 ± 0.25	57.9	...
42.43	-0.27	113.31 ± 0.13	121.1	$4.26^{+0.9}_{-0.7}$	6683	42.43	-0.26	4.86 ± 0.41	80.5	$4.26^{+0.9}_{-0.7}$
41.94	-0.26	13.14 ± 0.07	55.3	...	6670	41.94	-0.26	0.44 ± 0.12	22.2	...
41.04	-0.25	53.60 ± 0.09	105.3	...	6632	41.04	-0.24	2.17 ± 0.24	64.7	...
40.91	-0.25	20.88 ± 0.07	63.4	$1.78^{+0.5}_{-0.6}$	6630	40.91	-0.25	1.07 ± 0.17	37.6	$1.78^{+0.6}_{-0.6}$
41.10	-0.24	40.23 ± 0.07	68.2	$8.66^{+0.6}_{-0.7}$	6635	41.08	-0.24	0.34 ± 0.10	14.4	$8.68^{+0.5}_{-0.6}$
...	...	...	...	...	6637	41.10	-0.24	1.77 ± 0.20	52.9	$8.66^{+0.6}_{-0.7}$
42.16	-0.25	34.86 ± 0.13	152.6	...	6678	42.16	-0.23	0.65 ± 0.15	40.8	...
40.88	-0.23	15.56 ± 0.07	77.0	...	6629	40.88	-0.23	0.15 ± 0.07	...	...
41.13	-0.23	69.17 ± 0.08	84.0	$8.68^{+0.6}_{-0.6}$	6640	41.13	-0.23	3.04 ± 0.29	80.6	$8.68^{+0.6}_{-0.6}$
42.33	-0.21	8.07 ± 0.06	47.2	...	6682	42.33	-0.21	0.38 ± 0.11	...	...
42.64	-0.20	3.87 ± 0.03	...	...	6685	42.64	-0.20	0.26 ± 0.10	...	...
41.23	-0.21	30.33 ± 0.07	69.9	...	6651	41.23	-0.20	1.27 ± 0.18	45.8	...
...	...	...	...	...	6653	41.24	-0.22	0.31 ± 0.10	23.7	...
41.13	-0.19	24.48 ± 0.06	51.5	$8.58^{+0.6}_{-0.7}$	6641	41.13	-0.19	0.80 ± 0.14	38.1	$8.58^{+0.6}_{-0.7}$

Continuation of Table A1

Hi-GAL					BGPS					
ℓ (deg)	b (deg)	S_{500} (Jy)	θ_R (arcsec)	$d_\odot$ (kpc)	Catalog #	ℓ (deg)	b (deg)	S_{1100} (Jy)	θ_R (arcsec)	$d_\odot$ (kpc)
41.33	-0.20	13.02 ± 0.05	17.8	...	6657	41.33	-0.19	0.66 ± 0.12	...	...
...	...	...	...	...	6658	41.34	-0.22	0.31 ± 0.10	26.8	...
41.16	-0.18	85.11 ± 0.11	112.7	...	6645	41.16	-0.19	1.88 ± 0.23	67.7	...
41.31	-0.17	32.96 ± 0.07	63.2	...	6656	41.31	-0.17	1.23 ± 0.18	40.5	$3.58^{+0.8}_{-0.7}$
42.82	-0.14	21.01 ± 0.08	84.0	...	6688	42.83	-0.14	0.34 ± 0.13	...	...
41.51	-0.16	26.47 ± 0.13	155.2	...	6662	41.51	-0.14	0.41 ± 0.11	28.8	...
41.16	-0.14	12.25 ± 0.05	45.5	...	6644	41.16	-0.14	0.34 ± 0.11	...	...
41.34	-0.14	11.67 ± 0.06	41.7	...	6659	41.35	-0.14	0.41 ± 0.10	...	...
40.63	-0.14	107.38 ± 0.10	76.8	...	6625	40.62	-0.14	4.63 ± 0.38	58.5	...
...	...	...	...	...	6626	40.65	-0.13	0.25 ± 0.11	13.6	...
40.70	-0.13	26.87 ± 0.09	87.0	...	6627	40.70	-0.13	0.95 ± 0.18	50.7	...
42.03	-0.12	41.60 ± 0.12	136.9	...	6674	42.05	-0.12	0.43 ± 0.13	21.5	...
41.08	-0.12	28.38 ± 0.07	72.1	...	6634	41.08	-0.12	1.38 ± 0.20	53.8	...
...	...	...	...	...	6636	41.08	-0.15	0.21 ± 0.08	...	...
...	...	...	...	...	6638	41.10	-0.12	0.65 ± 0.14	40.3	...
42.69	-0.11	62.43 ± 0.11	110.9	...	6686	42.68	-0.11	1.24 ± 0.21	52.6	...
...	...	...	...	...	6687	42.69	-0.13	0.26 ± 0.10	...	$6.06^{+1.1}_{-1.1}$
41.12	-0.11	13.89 ± 0.06	54.4	...	6639	41.12	-0.11	0.54 ± 0.12	19.3	...
41.06	-0.10	6.36 ± 0.05	33.6	...	6633	41.06	-0.09	0.35 ± 0.10	...	...
40.58	-0.08	4.41 ± 0.04	...	...	6624	40.58	-0.08	0.31 ± 0.10	...	...
42.17	-0.09	21.31 ± 0.10	109.4	$9.68^{+0.5}_{-0.5}$	6679	42.17	-0.08	0.38 ± 0.11	15.7	$9.68^{+0.5}_{-0.5}$
41.14	-0.07	17.11 ± 0.08	78.7	...	6643	41.15	-0.08	0.34 ± 0.10	...	...
41.76	-0.05	4.65 ± 0.04	...	...	6667	41.76	-0.05	0.50 ± 0.14	12.8	...
41.72	-0.01	20.70 ± 0.09	90.7	...	6665	41.72	-0.00	0.72 ± 0.16	49.8	...
41.71	0.04	20.22 ± 0.09	99.6	...	6664	41.71	0.04	0.44 ± 0.13	35.3	...
41.38	0.03	26.59 ± 0.08	66.8	$3.70^{+0.7}_{-0.6}$	6661	41.38	0.04	1.06 ± 0.16	39.5	$3.70^{+0.7}_{-0.6}$
41.18	0.05	5.04 ± 0.04	...	...	6647	41.18	0.05	0.24 ± 0.09	...	...
41.74	0.10	25.78 ± 0.08	72.1	$11.36^{+0.5}_{-0.5}$	6666	41.74	0.10	0.99 ± 0.16	18.5	$11.36^{+0.5}_{-0.5}$
41.19	0.12	14.57 ± 0.07	66.8	$2.38^{+0.6}_{-0.6}$	6648	41.19	0.12	0.53 ± 0.14	42.1	...
41.13	0.13	8.27 ± 0.07	82.1	...	6642	41.13	0.13	0.18 ± 0.07	...	...
41.59	0.16	5.65 ± 0.04	27.7	$11.04^{+0.5}_{-0.5}$	6663	41.59	0.16	0.18 ± 0.08	...	$11.04^{+0.5}_{-0.5}$
41.23	0.17	16.24 ± 0.07	78.9	...	6652	41.23	0.16	0.14 ± 0.07	...	...
...	...	...	...	...	6654	41.24	0.17	0.27 ± 0.10	...	...
42.04	0.19	14.13 ± 0.05	37.7	$11.00^{+0.5}_{-0.5}$	6672	42.04	0.19	0.44 ± 0.10	...	...
42.05	0.20	21.75 ± 0.09	91.4	$11.04^{+0.5}_{-0.5}$	6673	42.04	0.21	1.00 ± 0.18	40.5	$11.04^{+0.5}_{-0.5}$
42.24	0.34	8.21 ± 0.06	40.2	$15.24^{+0.8}_{-0.7}$	6680	42.24	0.34	0.33 ± 0.10	...	$15.24^{+0.8}_{-0.7}$
42.01	0.35	25.23 ± 0.12	127.3	...	6671	42.02	0.34	0.49 ± 0.13	32.8	...
42.10	0.36	21.52 ± 0.09	72.8	...	6675	42.10	0.36	0.94 ± 0.16	31.1	...
41.22	0.36	30.06 ± 0.11	140.7	$4.58^{+0.9}_{-0.6}$	6649	41.22	0.36	0.23 ± 0.09	...	$4.60^{+0.9}_{-0.6}$
41.27	0.37	25.16 ± 0.09	91.3	...	6655	41.27	0.38	0.68 ± 0.15	40.8	...
41.23	0.40	31.38 ± 0.12	118.6	$4.54^{+0.8}_{-0.6}$	6650	41.23	0.40	0.40 ± 0.12	20.4	$4.52^{+0.9}_{-0.6}$
41.35	0.41	11.41 ± 0.07	56.2	$11.32^{+0.7}_{-0.6}$	6660	41.35	0.40	0.41 ± 0.11	...	$11.32^{+0.7}_{-0.6}$
41.87	0.49	20.13 ± 0.09	83.8	$1.32^{+0.7}_{-0.7}$	6668	41.88	0.49	0.48 ± 0.14	...	$1.32^{+0.7}_{-0.7}$

Continuation of Table A1

Hi-GAL					BGPS					
ℓ (deg)	b (deg)	S_{500} (Jy)	θ_R (arcsec)	$d_\odot$ (kpc)	Catalog #	ℓ (deg)	b (deg)	S_{1100} (Jy)	θ_R (arcsec)	$d_\odot$ (kpc)
42.12	0.52	10.98 ± 0.08	73.7	$2.04^{+0.7}_{-0.7}$	6677	42.12	0.52	0.40 ± 0.14	...	...
49.42	-0.48	27.72 ± 0.07	62.2	$5.28^{+0.7}_{-0.7}$	6876	49.41	-0.46	0.81 ± 0.20	22.2	$5.29^{+0.7}_{-0.7}$
...	...	...	...	...	6878	49.42	-0.48	1.40 ± 0.29	62.7	...
49.71	-0.46	19.44 ± 0.07	66.7	$5.16^{+0.7}_{-0.7}$	6906	49.72	-0.46	0.34 ± 0.15	...	$5.26^{+0.7}_{-0.7}$
49.67	-0.46	47.85 ± 0.07	49.1	$5.26^{+0.8}_{-0.8}$	6905	49.67	-0.46	2.01 ± 0.29	27.6	$5.26^{+0.8}_{-0.8}$
50.27	-0.45	19.25 ± 0.07	65.0	...	6917	50.27	-0.44	0.41 ± 0.15	...	...
50.40	-0.40	77.71 ± 0.11	119.7	$2.40^{+0.5}_{-0.5}$	6920	50.40	-0.41	1.72 ± 0.33	54.3	$2.74^{+0.8}_{-0.7}$
50.38	-0.41	21.56 ± 0.06	49.8	$3.08^{+1.0}_{-0.8}$	6919	50.38	-0.42	0.84 ± 0.23	34.0	...
50.29	-0.39	42.27 ± 0.08	49.2	...	6918	50.29	-0.39	1.83 ± 0.27	23.3	...
49.40	-0.31	114.28 ± 0.06	22.5	$6.19^{+0.9}_{-0.9}$	6870	49.39	-0.31	15.66 ± 1.01	74.6	$6.20^{+0.9}_{-0.9}$
49.56	-0.27	74.55 ± 0.07	53.7	$5.29^{+1.3}_{-1.3}$	6902	49.56	-0.27	5.55 ± 0.50	72.6	$5.29^{+1.3}_{-1.3}$
49.60	-0.25	26.59 ± 0.07	41.6	$5.30^{+1.1}_{-1.1}$	6904	49.60	-0.25	1.41 ± 0.24	25.7	$5.30^{+1.1}_{-1.1}$
49.48	-0.23	7.93 ± 0.04	...	...	6894	49.48	-0.21	0.23 ± 0.12	...	...
...	...	...	...	...	6895	49.48	-0.23	0.85 ± 0.20	43.7	...
49.40	-0.22	94.68 ± 0.08	76.7	$7.02^{+0.8}_{-1.1}$	6872	49.40	-0.22	7.18 ± 0.57	88.0	$7.02^{+0.8}_{-1.1}$
50.99	-0.21	10.45 ± 0.06	44.7	$5.16^{+1.1}_{-1.1}$	6925	50.99	-0.21	0.69 ± 0.19	25.9	$5.16^{+1.1}_{-1.1}$
49.38	-0.18	6.18 ± 0.03	...	$7.00^{+0.7}_{-1.0}$	6869	49.38	-0.18	0.50 ± 0.13	...	$7.12^{+0.8}_{-1.1}$
49.99	-0.13	76.85 ± 0.12	109.6	...	6911	49.98	-0.14	1.06 ± 0.21	29.3	...
...	...	...	...	...	6912	50.00	-0.13	1.08 ± 0.23	36.3	...
49.45	-0.07	30.98 ± 0.07	71.3	...	6888	49.44	-0.08	0.68 ± 0.20	47.5	...
...	...	...	...	...	6890	49.45	-0.06	1.08 ± 0.20	50.2	...
49.41	-0.05	41.03 ± 0.09	88.0	...	6880	49.41	-0.06	0.16 ± 0.09	...	...
...	...	...	...	...	6881	49.42	-0.04	0.62 ± 0.17	30.8	...
...	...	...	...	...	6883	49.42	-0.05	0.39 ± 0.12	31.0	...
49.44	-0.04	22.13 ± 0.06	63.9	...	6886	49.43	-0.05	0.29 ± 0.12	...	...
...	...	...	...	...	6889	49.44	-0.04	0.24 ± 0.13	...	...
49.41	-0.01	48.02 ± 0.10	104.3	$5.98^{+0.8}_{-0.8}$	6875	49.41	-0.01	0.43 ± 0.14	...	$5.36^{+1.0}_{-1.0}$
...	...	...	...	...	6882	49.42	-0.02	0.30 ± 0.11	...	$5.36^{+1.0}_{-1.0}$
51.38	-0.02	212.78 ± 0.13	109.5	$5.82^{+0.9}_{-0.9}$	6926	51.37	-0.05	0.89 ± 0.21	35.4	$5.74^{+0.8}_{-0.8}$
...	...	...	...	...	6927	51.37	-0.03	6.71 ± 0.60	79.5	$5.82^{+0.9}_{-0.9}$
...	...	...	...	...	6928	51.38	-0.00	3.92 ± 0.39	49.0	$5.82^{+0.9}_{-0.9}$
49.73	-0.01	69.67 ± 0.11	93.3	...	6907	49.72	-0.01	2.13 ± 0.31	37.3	...
50.05	0.05	79.81 ± 0.12	116.5	$5.29^{+1.2}_{-1.2}$	6914	50.04	0.07	0.44 ± 0.17	...	$5.29^{+1.1}_{-1.1}$
...	...	...	...	...	6916	50.06	0.06	1.85 ± 0.35	42.6	$6.98^{+0.7}_{-1.0}$
50.77	0.15	28.46 ± 0.08	71.9	...	6922	50.77	0.15	0.84 ± 0.20	...	...
50.92	0.24	13.65 ± 0.08	74.4	...	6924	50.92	0.24	0.42 ± 0.16	...	...
50.05	0.27	30.60 ± 0.10	99.2	$5.22^{+1.2}_{-1.2}$	6913	50.04	0.27	0.67 ± 0.19	25.8	$5.22^{+1.2}_{-1.2}$
...	...	...	...	...	6915	50.05	0.25	0.22 ± 0.12	...	$5.23^{+1.2}_{-1.2}$
50.65	0.29	25.33 ± 0.11	110.4	...	6921	50.65	0.29	0.32 ± 0.13	...	...
49.42	0.33	25.79 ± 0.08	72.4	$12.14^{+0.6}_{-0.6}$	6879	49.42	0.33	0.94 ± 0.18	23.8	$12.14^{+0.6}_{-0.6}$
49.92	0.37	20.28 ± 0.08	57.9	...	6910	49.92	0.37	0.72 ± 0.20	20.8	...
49.84	0.38	58.92 ± 0.13	109.4	$10.16^{+0.6}_{-0.6}$	6908	49.83	0.37	1.41 ± 0.25	31.2	$10.18^{+0.6}_{-0.6}$

Continuation of Table A1											
Hi-GAL					BGPS						
ℓ (deg)	b (deg)	S_{500} (Jy)	θ_R (arcsec)	$d_\odot$ (kpc)	Catalog #	ℓ (deg)	b (deg)	S_{1100} (Jy)	θ_R (arcsec)	$d_\odot$ (kpc)
...	...	...	...	...	6909	49.84	0.39	0.35 ± 0.15	25.1	$10.08^{+0.6}_{-0.6}$
201.36	0.29	39.02 ± 0.02	141.9	...	8245	201.34	0.29	1.15 ± 0.21	24.1	...
...	...	...	...	...	8246	201.36	0.28	1.28 ± 0.24	34.4	...
201.42	0.49	8.86 ± 0.01	69.7	...	8248	201.41	0.49	0.33 ± 0.12	...	...
201.54	0.53	33.16 ± 0.01	133.1	...	8252	201.54	0.53	0.29 ± 0.12	...	...
...	...	...	...	...	8253	201.55	0.55	0.43 ± 0.16	22.8	...
201.61	0.54	13.67 ± 0.01	51.0	...	8254	201.61	0.54	3.32 ± 0.35	54.7	...
201.63	0.57	14.95 ± 0.01	55.5	...	8256	201.64	0.57	1.87 ± 0.26	43.5	...
...	...	...	...	...	8257	201.66	0.57	0.20 ± 0.11	...	...
218.14	-0.52	10.79 ± 0.02	95.0	...	8590	218.14	-0.52	0.62 ± 0.23	24.7	...
218.19	-0.38	29.06 ± 0.02	100.3	...	8594	218.20	-0.39	1.14 ± 0.30	30.9	...
218.10	-0.36	22.63 ± 0.01	52.3	...	8589	218.10	-0.36	1.83 ± 0.32	25.4	...
218.05	-0.32	12.02 ± 0.01	63.6	...	8587	218.04	-0.32	1.35 ± 0.31	20.1	...
218.02	-0.32	25.49 ± 0.02	91.7	...	8586	218.02	-0.32	1.32 ± 0.29	...	...
217.64	-0.19	33.94 ± 0.02	124.9	...	8585	217.63	-0.19	1.82 ± 0.36	45.6	...
218.05	-0.11	16.50 ± 0.02	61.8	...	8588	218.05	-0.11	1.96 ± 0.37	36.1	...
217.37	-0.08	98.91 ± 0.02	83.6	...	8583	217.38	-0.08	13.96 ± 1.16	90.1	...
217.49	-0.07	13.80 ± 0.02	76.9	...	8584	217.49	-0.07	1.19 ± 0.30	29.0	...
217.30	-0.05	34.60 ± 0.02	77.5	...	8582	217.30	-0.05	2.56 ± 0.42	39.2	...
217.04	-0.06	10.94 ± 0.02	62.4	...	8580	217.04	-0.05	0.72 ± 0.23	...	...
217.26	-0.02	33.38 ± 0.02	122.8	...	8581	217.26	-0.03	1.82 ± 0.38	44.5	...
End of Table										

Appendix B

Hi-GAL – COHRS matching catalog

Table B1 lists COHRS cloud properties for those clouds with associated Hi-GAL clumps and $\sigma_{\rm maj} > 3'$. For each cloud, its catalog number is listed first. The # clumps refers to the total number of Hi-GAL clumps matched to the given cloud, using either line-of-sight velocities or dendrogram structure. Information on each of these clumps can be found in Table B2. The quantities $(\ell, b, v_{\rm LSR})$ locate the centroid of the cloud's emission in PPV space, using Galactic coordinates. The quantities $\sigma_{\rm maj}$, $\sigma_{\rm min}$, and $v_{\rm RMS}$ are the cloud dimensions in PPV space, calculated as the intensity-weighted second moments for each axis. The heliocentric distance, $d_\odot$, is derived using the distances of Hi-GAL clumps, as discussed in Section 4.2.2. CFE is the clump formation efficiency, estimated as the ratio of of the mass in clumps to the cloud mass, as discussed in Sections 4.3.3 and 4.5. The next five columns contain physical properties of the clouds: M is the mass derived from the cloud's CO(3-2) luminosity, n is the number density, R is the effective radius, Σ is the surface mass density, and $\alpha_{\rm vir}$ is the virial parameter. Finally SFR is the star formation rate, as calculated using 70 μm Hi-GAL emission. See Section 4.3.3 for physical property and star formation rate calculations.

Table B1: Hi-GAL – COHRS Catalog: COHRS Properties

COHRS catalog #	# clumps	ℓ (deg)	b (deg)	$v_{\rm LSR}$ (km s^{-1})	$\sigma_{\rm maj}$ (arcmin)	$\sigma_{\rm min}$ (arcmin)	$v_{\rm RMS}$ (km s^{-1})	$d_{\odot}$ (kpc)	CFE	M (M$_{\odot}$)	n (cm^{-3})	R (pc)	Σ (M$_{\odot}$ pc^{-2})	$\alpha_{\rm vir}$	SFR (M$_{\odot}$ yr^{-1})
32	7	54.87	+0.20	39	12.4	1.6	1.9	4.9 ± 2.0	0.10	(1.2 ± 1.0)E+4	(0.0 ± 2.8)E+2	24 ± 10	7 ± 8	8.8 ± 0.5	(8.5 ± 1.4)E-7
48	5	54.41	−0.45	36	7.6	2.0	1.9	5.0 ± 1.4	0.05	(2.1 ± 1.2)E+4	(0.2 ± 5.3)E+2	15 ± 4	28 ± 23	2.9 ± 0.1	(2.4 ± 0.4)E-7
52	14	54.79	−0.39	39	13.2	2.7	3.1	4.9 ± 2.0	0.03	(6.9 ± 5.7)E+4	(0.0 ± 1.5)E+3	26 ± 11	33 ± 38	4.1 ± 0.3	(1.3 ± 0.2)E-6
531	9	54.34	−0.26	40	4.7	3.3	6.8	5.0 ± 1.5	0.05	(1.9 ± 1.1)E+4	(0.6 ± 6.9)E+2	11 ± 3	49 ± 41	31 ± 1	(2.5 ± 0.6)E-6
552	4	54.80	+0.07	36	5.7	1.8	4.0	4.9 ± 2.0	0.04	(4.3 ± 3.6)E+3	(0.1 ± 2.1)E+2	12 ± 5	10 ± 12	51 ± 3	(3.8 ± 1.0)E-7
555	2	55.12	+0.32	34	5.2	2.5	3.2	4.9 ± 0.2	0.03	(7.7 ± 0.7)E+3	(2.4 ± 4.2)E+1	11.0 ± 0.5	20 ± 3	16.9 ± 0.2	(1.8 ± 0.4)E-6
574	4	54.41	−0.02	36	4.8	2.0	5.2	6.4 ± 1.8	0.09	(1.6 ± 0.9)E+4	(0.3 ± 4.6)E+2	13 ± 4	29 ± 24	26 ± 2	(1.0 ± 0.1)E-5
704	2	55.13	+0.47	10	9.7	2.0	3.4	4.9 ± 0.2	0.02	(6.6 ± 0.6)E+3	(0.4 ± 2.1)E+1	18.9 ± 0.8	5.8 ± 0.7	39.3 ± 0.3	(1.8 ± 0.5)E-7
708	5	54.45	+0.43	10	5.2	3.0	3.2	4.9 ± 1.4	0.04	(1.0 ± 0.6)E+4	(0.3 ± 3.3)E+2	12 ± 3	23 ± 19	14.3 ± 0.6	(1.1 ± 0.1)E-7
768	6	54.61	+0.03	41	3.6	2.7	6.1	4.9 ± 2.0	0.06	(6.6 ± 5.4)E+3	(0.4 ± 4.2)E+2	9 ± 4	28 ± 32	57 ± 3	···
770	8	55.15	−0.28	39	8.5	3.4	2.8	4.6 ± 1.3	0.04	(4.2 ± 2.3)E+4	(0.4 ± 9.5)E+2	17 ± 5	49 ± 38	3.6 ± 0.1	(8.0 ± 0.9)E-6
801	3	54.40	+0.25	35	3.3	2.2	2.6	5.0 ± 1.4	0.07	(2.0 ± 1.2)E+3	(0.2 ± 1.0)E+2	8 ± 2	11 ± 9	30 ± 1	···
870	5	54.74	−0.07	37	3.7	2.1	5.8	4.9 ± 2.0	0.09	(5.6 ± 4.6)E+3	(0.4 ± 3.8)E+2	8 ± 3	27 ± 32	57 ± 4	(5.6 ± 1.3)E-7
875	6	55.14	+0.14	35	6.6	3.3	3.6	4.9 ± 0.2	0.06	(2.6 ± 0.2)E+4	(0.4 ± 1.1)E+2	14.0 ± 0.6	42 ± 5	8.01 ± 0.06	(3.3 ± 1.0)E-6
913	4	54.93	−0.23	38	6.2	2.8	2.3	4.9 ± 2.1	0.07	(1.3 ± 1.1)E+4	(0.2 ± 5.4)E+2	13 ± 6	23 ± 28	6.2 ± 0.4	(1.7 ± 0.4)E-6
931	6	55.13	−0.13	34	8.5	3.0	4.9	4.6 ± 1.3	0.04	(1.7 ± 0.9)E+4	(0.1 ± 3.8)E+2	17 ± 5	20 ± 15	27 ± 1	(1.0 ± 0.3)E-6
963	4	54.12	−0.32	56	5.6	1.7	2.6	5.0 ± 1.3	0.10	(4.0 ± 2.2)E+3	(0.1 ± 1.3)E+2	11 ± 3	10 ± 8	22.3 ± 0.9	(6.7 ± 3.0)E-7
988	3	54.26	−0.09	51	5.8	3.2	3.0	5.7 ± 0.7	0.01	(3.8 ± 1.0)E+4	(0.5 ± 4.4)E+2	15 ± 2	55 ± 20	4.2 ± 0.1	(7.1 ± 2.7)E-7
1084	1	54.22	+0.39	18	3.3	0.7	2.4	5.0 ± 2.4	0.03	(1.4 ± 1.3)E+3	(0.2 ± 1.3)E+2	7 ± 3	10 ± 13	33 ± 2	(2.5 ± 0.8)E-7
1105	2	54.22	−0.29	37	4.6	1.6	2.4	5.7 ± 0.7	0.03	(6.4 ± 1.7)E+3	(0.2 ± 1.0)E+2	11 ± 1	17 ± 6	11.7 ± 0.4	···
1146	5	54.23	+0.31	37	4.6	3.8	5.9	5.0 ± 2.4	0.11	(9.5 ± 9.0)E+3	(0.2 ± 5.2)E+2	12 ± 6	22 ± 30	49 ± 4	(2.3 ± 0.7)E-6
1220	8	54.13	−0.08	39	6.1	3.0	2.6	5.7 ± 0.7	0.06	(1.5 ± 0.4)E+5	(0.2 ± 1.7)E+3	15 ± 2	206 ± 75	0.80 ± 0.02	(7.1 ± 0.4)E-5
1223	3	54.19	+0.28	−4	4.4	2.9	2.6	5.0 ± 2.4	0.04	(4.3 ± 4.1)E+3	(0.2 ± 2.7)E+2	10 ± 5	13 ± 18	19 ± 1	(1.6 ± 0.9)E-6
1707	4	53.68	+0.46	24	9.3	2.6	2.8	5.7 ± 0.5	0.08	(2.0 ± 0.3)E+4	(0.1 ± 1.1)E+2	22 ± 2	13 ± 3	9.7 ± 0.2	(1.4 ± 0.4)E-5
1743	1	53.39	+0.20	6	3.1	0.7	1.5	5.1 ± 3.3	0.06	(1.7 ± 2.2)E+3	(0.3 ± 2.4)E+2	6 ± 4	14 ± 26	10 ± 1	(3.5 ± 0.9)E-7
1758	5	54.06	+0.36	28	6.7	4.0	6.0	5.0 ± 2.4	0.07	(5.9 ± 5.7)E+3	(0.1 ± 2.5)E+2	15 ± 7	8 ± 11	108 ± 8	(3.2 ± 0.8)E-6
1809	3	53.28	+0.03	23	8.2	3.0	1.2	5.7 ± 0.5	0.03	(9.2 ± 1.6)E+4	(0.5 ± 5.5)E+2	19 ± 2	77 ± 19	0.37 ± 0.01	(3.0 ± 0.6)E-6
1821	10	53.59	+0.05	23	8.2	4.2	1.2	5.7 ± 0.5	0.04	(2.6 ± 0.4)E+5	(0.1 ± 1.5)E+3	21 ± 2	195 ± 48	0.144 ± 0.003	(1.6 ± 0.1)E-4
1872	11	53.64	+0.30	36	7.8	6.0	7.4	5.7 ± 0.5	0.07	(5.7 ± 1.0)E+4	(0.2 ± 3.0)E+2	22 ± 2	37 ± 9	24.3 ± 0.4	(7.4 ± 1.3)E-5
2012	3	54.08	+0.13	−6	3.5	1.6	1.7	5.0 ± 2.4	0.13	(4.5 ± 4.3)E+3	(0.4 ± 3.8)E+2	8 ± 4	24 ± 33	5.5 ± 0.4	(2.4 ± 0.8)E-6
2388	6	54.11	+0.14	32	5.1	1.7	1.8	5.7 ± 0.5	0.09	(1.1 ± 0.2)E+4	(0.3 ± 1.1)E+2	12 ± 1	24 ± 6	4.28 ± 0.08	(5.2 ± 1.4)E-6
2630	4	53.82	+0.14	50	5.7	3.8	4.5	5.7 ± 0.5	0.01	(1.4 ± 0.2)E+4	(0.2 ± 1.0)E+2	15 ± 1	18 ± 5	26.0 ± 0.5	(1.1 ± 0.3)E-6
2812	1	53.44	+0.01	42	3.9	1.2	1.7	5.1 ± 3.5	0.14	(6.2 ± 8.6)E+3	(0.5 ± 7.2)E+2	8 ± 6	30 ± 60	4.4 ± 0.5	(4.6 ± 1.6)E-6
2964	11	53.81	−0.13	44	12.7	2.3	3.8	5.7 ± 0.5	0.02	(1.2 ± 0.2)E+5	(0.2 ± 4.8)E+2	29 ± 2	46 ± 11	4.01 ± 0.07	(9.2 ± 1.4)E-6
3011	3	53.19	+0.18	5	4.2	3.1	2.9	7.3 ± 0.8	0.07	(9.8 ± 2.2)E+4	(1.2 ± 9.7)E+2	15 ± 2	140 ± 44	1.51 ± 0.05	(9.3 ± 1.3)E-5
3021	6	53.27	−0.17	43	8.8	4.5	1.8	7.3 ± 0.8	0.01	(1.2 ± 0.3)E+5	(0.2 ± 6.5)E+2	28 ± 3	49 ± 15	0.87 ± 0.04	(1.7 ± 0.5)E-6
3045	11	53.22	−0.26	62	15.3	3.1	4.1	7.3 ± 0.8	0.04	(1.9 ± 0.4)E+5	(0.1 ± 6.2)E+2	45 ± 5	30 ± 9	4.8 ± 0.2	(2.2 ± 0.6)E-5
3050	1	53.48	−0.10	44	5.1	1.5	2.3	7.3 ± 0.8	0.01	(3.3 ± 0.7)E+4	(0.4 ± 3.2)E+2	15 ± 2	45 ± 14	2.8 ± 0.2	(7.6 ± 2.5)E-7
3059	2	53.12	+0.06	22	6.9	4.3	0.4	7.3 ± 0.8	0.05	(1.4 ± 0.3)E+5	(0.5 ± 9.2)E+2	23 ± 3	84 ± 26	0.038 ± 0.006	(2.7 ± 0.8)E-5
3118	1	52.16	+0.11	55	3.8	1.2	2.1	5.2 ± 1.8	0.06	(3.6 ± 2.4)E+3	(0.3 ± 2.0)E+2	8 ± 3	17 ± 16	11.5 ± 0.7	(3.7 ± 0.8)E-8
3121	4	52.77	−0.05	56	6.8	1.6	5.0	9.2 ± 1.5	0.03	(9.1 ± 3.0)E+4	(0.2 ± 8.0)E+2	25 ± 4	46 ± 21	7.9 ± 0.8	(8.0 ± 2.7)E-7
3137	2	52.12	+0.42	54	3.3	2.3	3.9	5.2 ± 3.6	0.08	(3.4 ± 4.7)E+3	(0.3 ± 3.9)E+2	8 ± 6	16 ± 32	42 ± 5	(1.2 ± 0.4)E-7
3278	5	53.01	−0.24	23	7.9	2.4	1.2	9.2 ± 1.5	0.04	(7.7 ± 2.5)E+4	(0.1 ± 5.7)E+2	30 ± 5	27 ± 13	0.64 ± 0.06	(2.6 ± 1.1)E-6
3400	3	52.99	+0.27	3	10.2	1.5	4.2	9.2 ± 1.5	0.08	(4.9 ± 1.6)E+4	(0.0 ± 2.9)E+2	37 ± 6	11 ± 5	15 ± 1	(1.2 ± 0.3)E-5
3405	10	53.00	+0.05	4	11.6	3.6	2.5	9.2 ± 1.5	0.05	(2.0 ± 0.6)E+5	(0.1 ± 9.8)E+2	44 ± 7	32 ± 15	1.6 ± 0.1	(5.8 ± 1.6)E-5
3547	2	52.75	+0.12	59	3.7	2.2	4.5	9.2 ± 1.5	0.02	(2.9 ± 1.0)E+4	(0.3 ± 4.1)E+2	16 ± 3	38 ± 17	13 ± 1	(2.2 ± 0.9)E-6
3565	3	52.21	−0.01	54	8.4	2.3	3.1	5.2 ± 1.8	0.03	(2.6 ± 1.8)E+4	(0.2 ± 6.6)E+2	18 ± 6	26 ± 25	7.8 ± 0.4	(5.6 ± 1.3)E-7
3636	6	52.85	+0.20	45	9.9	3.4	2.6	9.2 ± 1.5	0.03	(1.1 ± 0.4)E+5	(0.1 ± 6.5)E+2	38 ± 6	25 ± 12	2.5 ± 0.2	(1.5 ± 0.7)E-5
3638	1	52.32	+0.32	47	3.9	3.4	2.8	5.2 ± 3.6	0.12	(0.8 ± 1.1)E+4	(0.3 ± 7.1)E+2	11 ± 7	23 ± 45	12 ± 1	(3.5 ± 1.0)E-7
3682	4	52.43	+0.03	49	4.5	2.2	4.4	5.2 ± 1.7	0.07	(1.1 ± 0.8)E+4	(0.4 ± 5.0)E+2	10 ± 3	35 ± 33	20 ± 1	(7.1 ± 1.9)E-7
3694	1	52.75	+0.04	44	5.2	1.8	2.3	9.2 ± 1.5	0.11	(2.0 ± 0.7)E+4	(0.1 ± 2.2)E+2	20 ± 3	16 ± 7	6.3 ± 0.6	(1.1 ± 0.3)E-7
3733	1	51.94	+0.25	49	3.2	1.6	5.1	5.2 ± 0.6	0.11	(6.1 ± 1.3)E+3	(0.6 ± 1.2)E+2	7.3 ± 0.8	36 ± 11	36.6 ± 0.7	(4.3 ± 1.5)E-7
3745	6	52.08	+0.31	46	11.6	2.1	2.3	5.2 ± 3.5	0.10	(1.2 ± 1.7)E+4	(0.0 ± 4.6)E+2	24 ± 16	7 ± 13	12 ± 1	(1.2 ± 0.6)E-6
3898	3	51.83	−0.09	62	5.1	0.8	2.1	5.8 ± 0.6	0.05	(6.9 ± 1.4)E+3	(1.8 ± 8.2)E+1	12 ± 1	16 ± 5	8.9 ± 0.2	(3.3 ± 1.1)E-7
3976	3	51.92	−0.35	59	4.3	2.6	3.1	5.8 ± 0.6	0.01	(2.2 ± 0.5)E+4	(0.6 ± 2.7)E+2	11 ± 1	55 ± 16	5.6 ± 0.2	(2.2 ± 0.6)E-6
4013	3	51.88	−0.22	62	3.9	1.9	3.7	5.8 ± 0.6	0.05	(1.6 ± 0.3)E+4	(0.7 ± 2.2)E+2	10 ± 1	52 ± 15	10.0 ± 0.2	(1.1 ± 0.2)E-6

Continuation of Table B1

COHRS catalog #	# clumps	ℓ (deg)	b (deg)	$v_{\rm LSR}$ (km s^{-1})	$\sigma_{\rm maj}$ (arcmin)	$\sigma_{\rm min}$ (arcmin)	$v_{\rm RMS}$ (km s^{-1})	$d_\odot$ (kpc)	CFE	M (M$_\odot$)	n (cm^{-3})	R (pc)	Σ (M$_\odot$ pc^{-2})	$\alpha_{\rm vir}$	SFR (M$_\odot$ yr^{-1})
4638	3	51.31	+0.32	53	6.1	1.2	3.4	5.8 ± 0.6	0.04	(7.6 ± 1.5)E+3	(1.1 ± 7.3)E+1	14 ± 1	12 ± 3	24.4 ± 0.5	(5.4 ± 0.7)E−7
4685	3	51.99	+0.21	7	3.5	1.6	2.0	5.2 ± 0.6	0.07	(3.5 ± 0.8)E+3	(2.8 ± 6.5)E+1	8.0 ± 0.9	17 ± 5	10.7 ± 0.2	(4.8 ± 1.2)E−7
4806	10	51.64	−0.34	43	8.8	3.7	4.1	5.8 ± 0.6	0.07	(3.0 ± 0.6)E+4	(0.1 ± 1.9)E+2	22 ± 2	21 ± 6	13.7 ± 0.3	(9.1 ± 0.8)E−6
4861	18	51.81	+0.37	3	10.5	3.0	2.7	5.3 ± 0.6	0.06	(4.9 ± 1.0)E+4	(0.2 ± 3.1)E+2	23 ± 2	31 ± 9	3.84 ± 0.07	(3.0 ± 0.6)E−5
4962	6	51.22	−0.42	56	4.2	2.3	2.3	5.8 ± 0.6	0.02	(1.5 ± 0.3)E+4	(0.5 ± 2.0)E+2	11 ± 1	42 ± 12	4.2 ± 0.1	(3.1 ± 0.6)E−7
4993	17	51.48	−0.04	55	21.3	3.5	2.4	5.8 ± 0.6	0.08	(1.4 ± 0.3)E+5	(0.0 ± 3.8)E+2	49 ± 5	18 ± 5	2.42 ± 0.06	(7.6 ± 0.3)E−5
5087	2	52.00	−0.16	58	5.1	1.2	2.9	5.8 ± 0.6	0.02	(5.5 ± 1.1)E+3	(1.3 ± 6.3)E+1	12 ± 1	12 ± 4	20.6 ± · · ·	(1.3 ± 0.3)E−7
5253	2	51.69	−0.45	48	3.7	1.5	1.3	5.8 ± 0.6	0.10	(3.9 ± 0.8)E+3	(2.1 ± 6.0)E+1	9.1 ± 0.9	15 ± 4	4.8 ± 0.2	(6.6 ± 2.7)E−8
5281	6	51.91	+0.12	53	7.2	2.9	3.0	5.8 ± 0.6	0.07	(1.7 ± 0.3)E+4	(0.1 ± 1.3)E+2	18 ± 2	17 ± 5	11.0 ± 0.2	(2.1 ± 0.5)E−7
5359	9	51.58	+0.26	54	7.1	3.4	3.0	5.8 ± 0.6	0.05	(2.8 ± 0.6)E+4	(0.2 ± 2.1)E+2	18 ± 2	28 ± 8	6.9 ± 0.2	(6.1 ± 1.3)E−7
5423	7	50.99	+0.23	44	5.8	2.0	2.6	4.5 ± 0.8	0.15	(1.4 ± 0.5)E+4	(0.4 ± 3.2)E+2	11 ± 2	38 ± 20	6.1 ± 0.1	(2.0 ± 0.2)E−5
5428	23	50.76	+0.11	44	9.8	6.8	2.6	4.5 ± 0.8	0.06	(7.9 ± 2.9)E+4	(0.3 ± 9.1)E+2	21 ± 4	56 ± 29	2.03 ± 0.05	(3.3 ± 0.5)E−5
5451	4	50.84	−0.12	49	4.3	2.1	4.6	4.5 ± 0.8	0.04	(1.1 ± 0.4)E+4	(0.7 ± 3.2)E+2	9 ± 2	48 ± 25	19.4 ± 0.5	(1.6 ± 0.5)E−7
5634	5	51.01	−0.32	55	8.9	1.9	2.9	4.5 ± 0.8	0.02	(2.2 ± 0.8)E+4	(0.2 ± 3.3)E+2	16 ± 3	27 ± 14	7.1 ± 0.2	(7.4 ± 1.3)E−7
5637	27	51.06	−0.10	56	14.3	10.1	2.8	4.5 ± 0.8	0.03	(9.6 ± 3.5)E+4	(0.1 ± 7.6)E+2	31 ± 6	32 ± 17	2.91 ± 0.07	(1.1 ± 0.2)E−5
5703	6	50.50	−0.42	63	12.4	2.0	2.7	4.5 ± 0.7	0.01	(2.3 ± 0.7)E+4	(0.1 ± 2.1)E+2	22 ± 3	15 ± 6	8.3 ± 0.2	(2.6 ± 9.5)E−6
5838	1	50.57	+0.09	59	4.8	1.6	2.3	4.5 ± 0.7	0.02	(4.3 ± 1.3)E+3	(2.5 ± 9.9)E+1	9 ± 1	17 ± 7	12.9 ± 0.3	· · ·
5850	4	50.04	−0.26	62	3.4	1.5	2.0	4.5 ± 0.7	0.10	(5.3 ± 1.6)E+3	(0.8 ± 1.7)E+2	6 ± 1	40 ± 17	5.6 ± 0.1	(3.3 ± 0.6)E−6
6127	2	50.30	−0.20	46	3.3	1.9	5.9	4.5 ± 0.7	0.06	(5.3 ± 1.6)E+3	(0.7 ± 1.6)E+2	7 ± 1	38 ± 16	52 ± 1	(1.5 ± 0.5)E−7
6275	7	50.48	−0.15	55	6.9	5.1	5.9	4.5 ± 0.7	0.03	(3.9 ± 1.2)E+4	(0.5 ± 5.2)E+2	15 ± 2	54 ± 23	15.8 ± 0.3	(1.3 ± 0.3)E−8
6349	3	50.57	+0.19	55	5.4	2.1	7.4	4.5 ± 0.7	0.08	(8.7 ± 2.6)E+3	(0.3 ± 1.7)E+2	10 ± 2	27 ± 12	74 ± 1	(7.0 ± 2.3)E−7
6377	3	50.29	−0.42	15	3.3	2.4	2.2	1.1 ± 3.1	0.18	(0.5 ± 2.9)E+3	(0.4 ± 2.3)E+3	2 ± 5	50 ± 398	19.5 ± 0.4	(1.4 ± 0.2)E−6
6403	2	50.26	+0.46	23	3.8	0.8	1.2	5.4 ± 0.2	0.11	(3.8 ± 0.3)E+3	(2.6 ± 2.5)E+1	8.4 ± 0.3	17 ± 2	3.8 ± · · ·	(2.8 ± 0.2)E−7
6427	5	49.95	+0.18	9	5.3	2.0	1.5	5.5 ± 0.3	0.12	(8.4 ± 0.8)E+3	(1.9 ± 4.4)E+1	12.1 ± 0.6	18 ± 2	3.98 ± 0.04	(2.3 ± 0.5)E−6
6440	10	50.49	+0.42	5	12.5	2.9	3.0	5.4 ± 2.2	0.13	(1.9 ± 1.5)E+4	(0.0 ± 3.8)E+2	27 ± 11	8 ± 9	15 ± 1	(1.2 ± 0.4)E−6
6538	3	50.34	+0.30	43	5.1	1.4	3.3	5.4 ± 0.2	0.08	(5.9 ± 0.5)E+3	(1.6 ± 2.8)E+1	11.4 ± 0.5	15 ± 2	24.4 ± 0.2	(1.1 ± 0.3)E−7
6589	2	50.66	−0.34	51	3.1	1.1	8.9	5.4 ± 3.0	0.17	(2.6 ± 2.9)E+3	(0.3 ± 2.8)E+2	7 ± 4	17 ± 26	250 ± 25	· · ·
6694	3	49.89	−0.17	48	4.6	1.6	1.6	4.5 ± 0.7	0.01	(7.9 ± 2.4)E+3	(0.5 ± 1.9)E+2	9 ± 1	34 ± 15	3.17 ± 0.07	(1.4 ± 0.4)E−7
6709	5	50.09	+0.25	55	5.3	1.9	2.0	4.5 ± 0.7	0.08	(1.2 ± 0.4)E+4	(0.5 ± 2.5)E+2	10 ± 1	40 ± 17	3.62 ± 0.07	(2.2 ± 0.2)E−6
6744	12	50.37	+0.08	63	11.6	3.8	3.6	4.5 ± 0.7	0.05	(1.9 ± 0.6)E+4	(0.1 ± 1.8)E+2	22 ± 3	13 ± 6	17.4 ± 0.3	(1.2 ± 0.2)E−6
6990	4	49.95	+0.04	44	6.7	2.3	1.5	4.5 ± 0.7	0.01	(9.6 ± 2.9)E+3	(0.2 ± 1.6)E+2	12 ± 2	20 ± 9	3.44 ± 0.07	(7.4 ± 4.3)E−6
7046	3	50.72	−0.22	59	3.6	2.5	5.0	4.5 ± 0.7	0.02	(8.8 ± 2.6)E+3	(0.8 ± 2.3)E+2	8 ± 1	48 ± 20	25.6 ± 0.5	(2.1 ± 0.5)E−7
7055	9	50.03	−0.02	53	7.7	3.9	3.8	4.5 ± 0.7	0.08	(5.0 ± 1.5)E+4	(0.6 ± 6.7)E+2	15 ± 2	69 ± 30	5.01 ± 0.09	(2.7 ± 0.3)E−5
7119	7	50.34	−0.43	40	7.3	3.7	4.2	4.5 ± 0.7	0.06	(4.4 ± 1.3)E+4	(0.6 ± 6.2)E+2	14 ± 2	68 ± 29	6.7 ± 0.1	(2.6 ± 2.3)E−5
7466	4	49.77	+0.10	61	7.2	1.2	1.9	6.5 ± 0.4	0.06	(1.1 ± 0.1)E+4	(0.7 ± 4.7)E+1	18 ± 1	10 ± 2	6.9 ± 0.1	(6.5 ± 1.8)E−7
7632	11	49.73	−0.03	47	8.4	3.8	3.6	6.5 ± 0.4	0.09	(5.9 ± 0.7)E+4	(0.2 ± 2.0)E+2	23 ± 1	35 ± 6	5.85 ± 0.09	(4.4 ± 1.3)E−5
8017	3	49.28	−0.04	57	4.4	2.6	9.5	6.3 ± 0.3	0.05	(8.8 ± 0.8)E+4	(1.8 ± 4.1)E+2	12.6 ± 0.5	177 ± 22	14.9 ± 0.2	(7.8 ± 1.2)E−6
8079	10	49.44	−0.25	53	10.3	2.7	6.0	6.3 ± 0.3	0.04	(3.6 ± 0.3)E+5	(0.8 ± 8.1)E+2	26 ± 1	167 ± 20	3.04 ± 0.03	(2.4 ± 0.2)E−4
8099	4	49.05	−0.12	54	5.6	3.6	7.1	6.3 ± 0.3	0.01	(7.3 ± 0.6)E+4	(0.7 ± 2.6)E+2	16.4 ± 0.7	87 ± 11	13.1 ± 0.1	(2.4 ± 0.6)E−6
8191	10	48.97	+0.12	56	10.5	5.3	4.9	6.3 ± 0.3	0.03	(7.8 ± 0.7)E+4	(0.1 ± 1.6)E+2	29 ± 1	29 ± 4	10.3 ± 0.1	(2.1 ± 0.6)E−5
8289	6	48.71	−0.43	64	3.1	2.8	4.8	5.6 ± 3.3	0.05	(1.9 ± 2.3)E+4	(0.1 ± 1.7)E+3	9 ± 5	73 ± 122	13 ± 1	(8.2 ± 1.8)E−6
8330	4	49.16	−0.24	65	7.0	2.4	4.3	6.3 ± 0.3	0.08	(1.3 ± 0.1)E+5	(0.9 ± 4.2)E+2	18.2 ± 0.8	125 ± 15	2.99 ± 0.03	(1.8 ± 0.2)E−4
8393	3	49.39	−0.08	51	6.5	1.1	2.7	6.3 ± 0.3	0.01	(2.2 ± 0.2)E+4	(2.0 ± 7.8)E+1	16.2 ± 0.7	26 ± 3	6.4 ± 0.1	(6.3 ± 0.9)E−7
8526	1	48.98	−0.10	16	5.0	2.4	2.9	5.6 ± 0.2	0.02	(8.2 ± 0.6)E+3	(1.8 ± 3.5)E+1	12.2 ± 0.5	18 ± 2	14.1 ± 0.1	(5.9 ± 3.1)E−6
8761	3	48.65	−0.13	15	6.2	2.6	1.9	8.8 ± 0.9	0.03	(3.0 ± 0.6)E+4	(0.1 ± 1.8)E+2	23 ± 2	18 ± 5	3.1 ± 0.2	(1.0 ± 0.3)E−6
8801	2	48.63	+0.35	37	3.6	1.4	2.6	2.5 ± 3.1	0.06	(1.1 ± 2.8)E+3	(0.8 ± 5.3)E+2	4 ± 5	25 ± 85	26 ± 1	(1.6 ± 0.8)E−7
9226	3	49.58	+0.17	63	3.8	3.7	1.5	6.3 ± 0.3	0.02	(3.7 ± 0.3)E+4	(0.7 ± 1.6)E+2	13.1 ± 0.6	68 ± 8	0.88 ± 0.02	(2.5 ± 1.1)E−6
9428	11	48.65	+0.13	51	10.0	4.3	3.5	3.3 ± 1.2	0.02	(3.1 ± 2.2)E+4	(0.0 ± 1.1)E+3	14 ± 5	49 ± 50	6.7 ± 0.2	(1.5 ± 0.8)E−5
9429	3	48.62	−0.26	57	10.3	2.8	2.4	3.3 ± 1.2	0.02	(9.9 ± 7.2)E+3	(0.1 ± 3.5)E+2	14 ± 5	16 ± 17	9.3 ± 0.2	(9.1 ± 3.7)E−6
9444	12	48.65	+0.25	9	7.9	5.6	4.1	8.8 ± 0.9	0.04	(2.6 ± 0.6)E+5	(0.0 ± 1.1)E+3	33 ± 3	75 ± 22	2.5 ± 0.1	(1.5 ± 0.4)E−4
9446	9	48.61	+0.03	17	3.9	2.9	2.4	8.8 ± 0.9	0.15	(1.9 ± 0.4)E+5	(0.2 ± 1.6)E+3	17 ± 2	213 ± 63	0.61 ± 0.03	(4.6 ± 0.7)E−4
9450	13	48.59	−0.32	34	7.6	3.1	2.9	3.3 ± 1.2	0.06	(1.6 ± 1.1)E+4	(0.5 ± 7.1)E+2	11 ± 4	43 ± 44	6.8 ± 0.2	(9.9 ± 2.8)E−6
9452	4	48.61	−0.46	31	4.5	1.9	2.2	3.3 ± 1.2	0.05	(5.0 ± 3.6)E+3	(0.8 ± 3.9)E+2	6 ± 2	39 ± 40	6.9 ± 0.2	(2.5 ± 0.7)E−6
10122	2	47.17	−0.27	64	3.7	0.9	2.1	5.8 ± 0.1	0.05	(4.7 ± 0.2)E+3	(3.0 ± 1.7)E+1	8.6 ± 0.2	20 ± 1	9.5 ± 0.3	(5.6 ± 1.7)E−8
10353	2	46.99	+0.12	41	4.2	1.4	3.2	5.8 ± 0.1	0.08	(2.0 ± 0.1)E+3	(7.7 ± 6.7)E+0	10.1 ± 0.3	6.2 ± 0.4	59 ± 1	(1.6 ± 0.6)E−7
10427	4	46.77	+0.20	13	3.0	1.3	2.3	5.8 ± 0.2	0.18	(4.6 ± 0.3)E+3	(4.2 ± 2.4)E+1	7.6 ± 0.2	25 ± 2	10.13 ± 0.09	(5.4 ± 1.6)E−7
10433	10	46.76	−0.08	16	9.0	3.9	4.1	5.8 ± 2.0	0.04	(3.0 ± 2.1)E+4	(0.1 ± 6.4)E+2	22 ± 8	19 ± 19	15 ± 1	(4.0 ± 1.5)E−6
10443	5	46.53	+0.21	7	5.4	2.7	2.4	5.9 ± 2.0	0.10	(1.2 ± 0.8)E+4	(0.2 ± 4.0)E+2	14 ± 5	20 ± 19	8.0 ± 0.6	(6.8 ± 2.2)E−7

Continuation of Table B1

COHRS catalog #	# clumps	ℓ (deg)	b (deg)	$v_{\rm LSR}$ (km s^{-1})	$\sigma_{\rm maj}$ (arcmin)	$\sigma_{\rm min}$ (arcmin)	$v_{\rm RMS}$ (km s^{-1})	$d_\odot$ (kpc)	CFE	M (M$_\odot$)	n (cm^{-3})	R (pc)	Σ (M$_\odot$ pc^{-2})	$\alpha_{\rm vir}$	SFR (M$_\odot$ yr^{-1})
10606	19	46.94	+0.18	57	20.9	9.2	2.7	4.7 ± 0.7	0.06	(6.5 ± 1.9)E+4	(0.0 ± 3.1)E+2	42 ± 6	12 ± 5	5.5 ± 0.1	(1.1 ± 0.2)E−5
10699	3	46.32	+0.06	58	6.2	2.0	2.4	4.7 ± 0.7	0.03	(8.4 ± 2.5)E+3	(0.2 ± 1.4)E+2	12 ± 2	19 ± 8	9.9 ± 0.2	(3.4 ± 0.5)E−7
10924	21	46.38	−0.21	54	9.7	2.6	3.1	4.7 ± 0.7	0.07	(8.0 ± 2.4)E+4	(0.5 ± 8.6)E+2	18 ± 3	75 ± 31	2.51 ± 0.05	(3.8 ± 0.4)E−5
10942	6	46.78	−0.01	47	6.7	4.8	1.6	4.7 ± 0.7	0.04	(1.9 ± 0.6)E+4	(0.2 ± 2.5)E+2	15 ± 2	27 ± 11	2.37 ± 0.05	(6.3 ± 2.7)E−7
11021	6	46.54	+0.00	50	4.8	2.7	7.3	4.7 ± 0.7	0.06	(1.4 ± 0.4)E+4	(0.6 ± 2.8)E+2	10 ± 1	44 ± 18	44.5 ± 0.9	(1.1 ± 0.2)E−6
11178	13	46.12	−0.03	60	9.2	5.1	2.9	4.7 ± 0.7	0.01	(4.9 ± 1.5)E+4	(0.3 ± 5.3)E+2	20 ± 3	41 ± 18	3.84 ± 0.09	(4.0 ± 1.4)E−6
11195	6	45.78	+0.20	22	9.4	3.1	5.2	10.3 ± 4.9	0.02	(8.1 ± 7.7)E+4	(0.0 ± 1.3)E+3	40 ± 19	16 ± 22	15 ± 5	(1.2 ± 0.6)E−5
11202	13	45.89	−0.15	14	8.0	4.3	2.6	10.3 ± 4.9	0.03	(1.9 ± 1.8)E+5	(0.0 ± 3.3)E+3	37 ± 17	45 ± 60	1.5 ± 0.5	(2.5 ± 0.8)E−5
11203	1	46.21	−0.10	17	4.6	1.7	2.2	10.3 ± 4.9	0.09	(3.2 ± 3.1)E+4	(0.0 ± 1.0)E+3	20 ± 9	26 ± 35	4 ± 1	(1.2 ± 0.4)E−5
11207	6	46.08	−0.14	50	3.7	3.2	3.0	4.7 ± 0.7	0.08	(1.8 ± 0.5)E+4	(1.0 ± 4.1)E+2	9 ± 1	68 ± 30	5.4 ± 0.1	(1.4 ± 0.5)E−6
11504	5	45.23	−0.14	56	4.0	3.6	3.4	6.4 ± 0.3	0.06	(1.6 ± 0.2)E+4	(2.6 ± 7.9)E+1	13.6 ± 0.7	28 ± 4	11.3 ± 0.2	(1.9 ± 0.6)E−6
11516	3	45.54	−0.28	50	4.8	1.2	2.5	6.4 ± 0.3	0.14	(9.4 ± 0.9)E+3	(1.9 ± 5.0)E+1	12.5 ± 0.6	19 ± 3	9.3 ± 0.3	(4.3 ± 1.5)E−7
11577	3	45.31	−0.32	56	3.9	3.2	4.4	6.4 ± 0.3	0.06	(1.8 ± 0.2)E+4	(3.6 ± 9.6)E+1	12.6 ± 0.6	36 ± 5	15.9 ± 0.3	···
11618	3	45.08	−0.08	64	3.8	2.3	5.1	6.0 ± 1.5	0.05	(7.4 ± 3.8)E+3	(0.3 ± 2.4)E+2	11 ± 3	21 ± 15	42 ± 2	(8.5 ± 3.0)E−7
11626	14	45.46	+0.06	58	6.4	4.7	3.0	6.4 ± 0.3	0.10	(3.1 ± 0.3)E+5	(0.1 ± 1.0)E+3	20 ± 1	238 ± 34	0.67 ± 0.01	(3.9 ± 0.1)E−4
11627	7	45.13	+0.13	59	4.5	2.1	3.5	6.4 ± 0.3	0.13	(1.2 ± 0.1)E+5	(2.4 ± 6.3)E+2	12.6 ± 0.6	238 ± 34	1.52 ± 0.02	(3.3 ± 0.1)E−4
11822	2	45.51	−0.36	60	4.4	2.3	3.8	6.4 ± 0.3	0.06	(2.4 ± 0.2)E+4	(0.5 ± 1.3)E+2	12.7 ± 0.6	48 ± 7	8.6 ± 0.2	(1.9 ± 0.5)E−6
11911	3	45.55	−0.48	58	5.4	1.1	3.4	6.4 ± 0.3	0.04	(2.1 ± 0.2)E+4	(0.3 ± 1.0)E+2	13.9 ± 0.7	35 ± 5	8.7 ± 0.2	(2.0 ± 0.4)E−7
11938	8	45.62	+0.32	17	4.3	2.2	6.7	6.0 ± 1.3	0.09	(1.2 ± 0.5)E+4	(0.3 ± 2.9)E+2	11 ± 2	29 ± 17	52 ± 2	(7.8 ± 2.6)E−7
12064	4	45.22	+0.09	21	11.1	3.7	8.1	6.4 ± 0.3	0.01	(4.7 ± 0.5)E+4	(0.1 ± 1.1)E+2	30 ± 1	17 ± 2	48.7 ± 0.7	(1.2 ± 1.0)E−4
12071	4	45.60	−0.05	7	4.7	2.7	2.5	11.0 ± 1.9	0.11	(7.9 ± 2.7)E+4	(0.2 ± 7.6)E+2	24 ± 4	45 ± 22	2.2 ± 0.3	(5.3 ± 1.7)E−5
12231	15	45.75	−0.27	53	7.3	3.6	5.9	6.4 ± 0.3	0.06	(1.5 ± 0.2)E+5	(0.7 ± 5.0)E+2	21 ± 1	114 ± 16	5.49 ± 0.08	(1.7 ± 0.4)E−5
12462	3	45.77	+0.03	68	4.5	2.1	2.9	6.4 ± 0.3	0.02	(1.2 ± 0.1)E+4	(2.4 ± 6.2)E+1	12.6 ± 0.6	23 ± 3	10.3 ± 0.2	(4.3 ± 1.5)E−7
12981	3	45.83	+0.27	62	3.3	1.0	···	6.4 ± 0.3	0.17	(8.6 ± 0.9)E+3	(5.2 ± 6.6)E+1	8.8 ± 0.4	36 ± 5	···	(1.2 ± 0.4)E−7
13109	9	44.96	+0.19	66	7.1	3.9	2.0	6.4 ± 0.3	0.03	(3.8 ± 0.4)E+4	(0.2 ± 1.2)E+2	21 ± 1	28 ± 4	2.59 ± 0.05	(1.2 ± 0.3)E−6
13159	2	44.52	−0.03	41	7.2	4.4	1.2	6.4 ± 0.6	0.01	(2.9 ± 0.5)E+4	(0.1 ± 1.7)E+2	21 ± 2	20 ± 5	1.35 ± 0.04	(3.7 ± 2.2)E−6
13183	8	44.38	+0.07	17	18.0	5.5	4.4	6.1 ± 2.0	0.05	(3.8 ± 2.4)E+4	(0.0 ± 3.7)E+2	45 ± 14	6 ± 5	27 ± 2	(2.0 ± 1.2)E−5
13267	16	44.69	−0.10	56	7.7	3.4	5.4	6.4 ± 0.6	0.03	(7.7 ± 1.5)E+4	(0.3 ± 4.6)E+2	21 ± 2	54 ± 15	9.2 ± 0.2	(8.4 ± 2.7)E−7
13614	6	44.12	+0.11	58	4.5	2.4	3.2	6.9 ± 0.5	0.05	(4.9 ± 0.7)E+4	(0.7 ± 3.6)E+2	14 ± 1	82 ± 17	3.3 ± 0.1	(4.8 ± 1.4)E−6
13648	2	44.00	−0.02	65	3.4	1.2	2.3	6.9 ± 0.5	0.14	(2.4 ± 0.4)E+4	(1.1 ± 2.5)E+2	9.7 ± 0.7	82 ± 18	2.43 ± 0.06	(1.1 ± 0.2)E−5
13723	4	43.95	+0.19	58	3.6	1.4	2.2	6.9 ± 0.5	0.06	(1.8 ± 0.3)E+4	(0.7 ± 1.8)E+2	10.4 ± 0.8	54 ± 11	3.3 ± 0.2	(6.2 ± 1.8)E−7
13761	7	43.70	−0.44	61	5.7	2.7	3.0	6.9 ± 0.5	0.07	(1.8 ± 0.3)E+4	(0.1 ± 1.1)E+2	17 ± 1	20 ± 4	10.1 ± 0.2	(1.4 ± 0.2)E−6
14044	1	43.61	−0.39	64	3.2	2.9	2.6	6.9 ± 0.5	0.05	(9.2 ± 1.4)E+3	(2.3 ± 8.0)E+1	11.6 ± 0.9	21 ± 5	9.8 ± 0.3	(3.0 ± 0.6)E−7
14251	21	44.39	−0.14	62	12.5	5.2	3.8	6.9 ± 0.5	0.03	(5.2 ± 0.8)E+5	(0.0 ± 1.4)E+3	36 ± 3	125 ± 27	1.18 ± 0.03	(5.1 ± 0.9)E−5
14266	3	43.92	−0.22	63	4.5	2.6	3.4	6.9 ± 0.5	0.05	(4.3 ± 0.6)E+4	(0.6 ± 3.1)E+2	14 ± 1	69 ± 15	4.5 ± 0.1	(4.0 ± 0.8)E−6
14326	9	43.70	+0.22	69	5.6	2.3	4.6	6.9 ± 0.5	0.05	(2.7 ± 0.4)E+4	(0.2 ± 1.6)E+2	16 ± 1	32 ± 7	15.4 ± 0.4	(5.8 ± 1.8)E−6
14529	8	43.64	+0.33	13	8.0	3.9	5.0	6.9 ± 0.5	0.06	(2.0 ± 0.3)E+4	(0.6 ± 8.5)E+1	24 ± 2	11 ± 2	34.2 ± 0.8	(1.2 ± 0.4)E−6
14531	3	43.43	+0.21	12	5.2	1.8	4.4	6.2 ± 1.7	0.10	(6.4 ± 3.5)E+3	(0.1 ± 1.8)E+2	13 ± 4	11 ± 9	48 ± 3	(1.3 ± 0.8)E−6
14584	1	43.65	−0.21	16	4.4	1.4	3.9	6.2 ± 1.6	0.02	(3.7 ± 1.9)E+3	(0.1 ± 1.2)E+2	11 ± 3	10 ± 7	53 ± 3	(5.8 ± 2.4)E−7
14587	8	43.70	+0.11	13	13.1	3.9	4.3	6.9 ± 0.5	0.03	(4.9 ± 0.7)E+4	(0.0 ± 1.3)E+2	37 ± 3	11 ± 2	16.3 ± 0.4	(5.2 ± 2.1)E−6
15030	6	43.82	−0.10	53	6.0	3.5	10.4	6.9 ± 0.5	0.17	(4.6 ± 0.7)E+4	(0.3 ± 2.5)E+2	19 ± 1	42 ± 9	51 ± 1	(7.5 ± 1.2)E−5
15167	7	43.45	+0.29	56	6.0	4.7	6.6	6.9 ± 0.5	0.03	(3.5 ± 0.5)E+4	(0.2 ± 1.7)E+2	21 ± 2	26 ± 6	29.6 ± 0.7	(1.4 ± 0.5)E−6
15380	6	44.46	+0.07	68	3.3	2.2	1.7	6.9 ± 0.5	0.06	(2.3 ± 0.3)E+4	(0.7 ± 2.2)E+2	10.7 ± 0.8	63 ± 14	1.49 ± 0.04	(1.3 ± 0.4)E−6
15544	5	43.07	+0.11	63	8.0	4.3	4.0	9.5 ± 1.3	0.01	(2.0 ± 0.5)E+5	(0.0 ± 1.0)E+3	34 ± 4	54 ± 20	3.2 ± 0.2	(1.5 ± 1.4)E−3
15615	17	43.33	−0.35	61	6.3	2.9	2.0	9.5 ± 1.3	0.06	(1.4 ± 0.4)E+5	(0.3 ± 9.4)E+2	26 ± 3	66 ± 24	0.85 ± 0.07	(9.1 ± 1.4)E−6
15717	5	43.52	−0.12	56	7.5	2.4	3.9	9.5 ± 1.3	0.06	(5.4 ± 1.4)E+4	(0.1 ± 3.3)E+2	29 ± 4	20 ± 7	9.6 ± 0.7	(2.5 ± 0.9)E−6
16267	3	43.09	−0.18	42	13.4	4.4	2.0	9.5 ± 1.3	0.00	(1.7 ± 0.4)E+5	(0.0 ± 5.5)E+2	53 ± 7	19 ± 7	1.4 ± 0.1	(7.6 ± 3.7)E−5
16500	6	42.55	−0.16	65	4.9	1.9	3.4	8.4 ± 1.3	0.07	(4.3 ± 1.3)E+4	(0.3 ± 5.1)E+2	18 ± 3	45 ± 20	5.5 ± 0.4	(2.4 ± 0.4)E−5
16541	9	42.06	−0.06	59	6.6	2.5	2.9	8.4 ± 1.3	0.06	(1.5 ± 0.5)E+5	(0.0 ± 1.3)E+3	23 ± 4	85 ± 37	1.6 ± 0.1	(7.8 ± 2.6)E−6
16562	1	42.04	−0.22	64	3.1	1.7	5.0	8.4 ± 1.3	0.01	(2.9 ± 0.9)E+4	(0.7 ± 5.0)E+2	12 ± 2	65 ± 28	12.0 ± 0.9	(1.1 ± 0.3)E−6
16587	19	42.80	−0.16	62	8.6	3.8	4.6	8.4 ± 1.3	0.06	(2.1 ± 0.6)E+5	(0.0 ± 1.4)E+3	31 ± 5	69 ± 30	3.6 ± 0.3	(3.6 ± 0.8)E−5
16598	9	42.74	+0.20	63	5.3	2.7	3.0	8.4 ± 1.3	0.09	(4.2 ± 1.3)E+4	(0.2 ± 4.4)E+2	20 ± 3	35 ± 15	4.8 ± 0.3	(4.1 ± 1.0)E−6
16950	8	42.31	−0.05	57	4.8	4.0	3.7	8.4 ± 1.3	0.03	(1.2 ± 0.4)E+5	(0.1 ± 1.2)E+3	21 ± 3	90 ± 39	2.7 ± 0.2	(3.4 ± 0.9)E−6
16971	4	42.41	−0.26	63	5.1	1.2	3.6	8.4 ± 1.3	0.15	(5.9 ± 1.8)E+4	(0.4 ± 7.0)E+2	18 ± 3	61 ± 27	4.5 ± 0.3	(7.8 ± 1.6)E−5
17346	6	42.95	−0.03	8	3.8	2.4	2.9	8.4 ± 1.3	0.05	(4.7 ± 1.4)E+4	(0.6 ± 6.5)E+2	15 ± 2	66 ± 29	3.0 ± 0.2	(8.5 ± 3.3)E−6
17437	8	42.33	−0.23	26	5.6	3.2	3.8	6.3 ± 2.7	0.07	(1.8 ± 1.6)E+4	(0.2 ± 6.7)E+2	16 ± 7	23 ± 28	15 ± 2	(3.5 ± 2.3)E−5
17862	6	41.69	−0.18	62	5.4	2.7	4.2	6.3 ± 0.9	0.02	(4.9 ± 1.4)E+4	(0.6 ± 6.5)E+2	15 ± 2	70 ± 29	6.3 ± 0.2	(3.9 ± 0.9)E−6
17887	12	41.81	+0.07	16	7.1	2.6	1.8	11.2 ± 0.4	0.08	(1.5 ± 0.1)E+5	(0.2 ± 2.0)E+2	33 ± 1	43 ± 4	0.87 ± 0.03	(5.4 ± 1.5)E−5

Continuation of Table B1

COHRS catalog #	# clumps	ℓ (deg)	b (deg)	$v_{\rm LSR}$ (km s^{-1})	$\sigma_{\rm maj}$ (arcmin)	$\sigma_{\rm min}$ (arcmin)	$v_{\rm RMS}$ (km s^{-1})	$d_\odot$ (kpc)	CFE	M (M$_\odot$)	n (cm^{-3})	R (pc)	Σ (M$_\odot$ pc^{-2})	$\alpha_{\rm vir}$	SFR (M$_\odot$ yr^{-1})
18040	5	41.51	−0.17	62	5.5	2.3	3.0	6.1 ± 0.5	0.08	(2.3 ± 0.4)E+4	(0.3 ± 1.8)E+2	14 ± 1	36 ± 9	6.3 ± 0.1	(1.4 ± 0.4)E–5
18143	4	41.05	−0.17	38	8.3	4.6	2.0	6.1 ± 0.5	0.01	(8.5 ± 1.4)E+4	(0.3 ± 4.2)E+2	23 ± 2	52 ± 12	1.28 ± 0.04	(1.3 ± 0.9)E–4
18295	8	41.25	+0.14	40	5.9	4.5	2.3	6.1 ± 0.5	0.03	(6.4 ± 1.1)E+4	(0.5 ± 4.1)E+2	18 ± 2	64 ± 15	1.72 ± 0.04	(1.2 ± 0.7)E–5
18347	16	40.82	−0.20	24	6.0	3.5	4.3	6.1 ± 0.5	0.13	(4.7 ± 0.8)E+4	(0.4 ± 3.2)E+2	17 ± 1	54 ± 13	7.7 ± 0.2	(2.5 ± 1.1)E–5
18359	9	40.76	+0.09	19	5.5	2.2	3.0	6.4 ± 1.9	0.14	(1.4 ± 0.8)E+4	(0.2 ± 3.7)E+2	15 ± 4	20 ± 17	10.8 ± 0.8	(3.1 ± 0.8)E–6
18403	7	41.10	+0.11	16	10.3	2.8	3.0	6.1 ± 0.5	0.05	(3.5 ± 0.6)E+4	(0.1 ± 1.5)E+2	26 ± 2	17 ± 4	7.5 ± 0.1	(7.3 ± 3.3)E–6
18462	2	40.61	−0.14	25	3.7	1.5	8.6	10.4 ± 3.1	0.45	(2.6 ± 1.5)E+4	(0.2 ± 6.2)E+2	16 ± 5	30 ± 25	55 ± 11	(4.6 ± 1.1)E–5
18629	5	41.54	+0.02	62	3.5	1.5	4.1	6.1 ± 0.5	0.12	(2.7 ± 0.5)E+4	(1.4 ± 3.3)E+2	9.3 ± 0.8	100 ± 24	6.7 ± 0.1	(1.8 ± 0.6)E–5
18631	12	41.30	+0.07	60	4.9	4.6	1.9	6.1 ± 0.5	0.08	(6.6 ± 1.1)E+4	(0.6 ± 4.7)E+2	16 ± 1	82 ± 20	1.03 ± 0.02	(1.4 ± 0.5)E–5
18865	23	41.18	−0.20	59	8.2	4.7	4.3	6.1 ± 0.5	0.09	(2.0 ± 0.3)E+5	(0.7 ± 9.8)E+2	23 ± 2	121 ± 29	2.46 ± 0.05	(1.3 ± 0.3)E–4
19020	4	41.00	+0.03	72	3.4	2.7	3.9	6.4 ± 2.1	0.03	(1.3 ± 0.8)E+4	(0.4 ± 5.1)E+2	11 ± 3	34 ± 32	15 ± 1	(1.5 ± 0.7)E–6
19174	4	40.71	+0.23	47	4.3	1.6	1.8	6.5 ± 1.8	0.23	(4.4 ± 2.5)E+3	(0.1 ± 1.4)E+2	12 ± 3	10 ± 8	10.4 ± 0.8	(5.9 ± 2.1)E–7
19208	2	40.42	+0.22	81	3.6	1.9	1.8	6.5 ± 1.6	0.07	(5.7 ± 2.8)E+3	(0.2 ± 1.8)E+2	10 ± 3	17 ± 12	7.0 ± 0.5	···
19241	5	40.40	−0.05	72	4.7	2.2	6.2	7.7 ± 0.8	0.04	(4.8 ± 1.0)E+4	(0.5 ± 4.5)E+2	16 ± 2	62 ± 19	14.7 ± 0.6	(6.8 ± 2.0)E–6
19251	2	40.19	−0.27	63	5.0	2.4	2.0	7.7 ± 0.8	0.01	(3.2 ± 0.7)E+4	(0.3 ± 2.8)E+2	17 ± 2	36 ± 11	2.5 ± 0.1	(1.2 ± 0.3)E–6
19544	4	39.41	−0.18	65	5.3	1.9	4.8	4.6 ± 0.6	0.10	(1.2 ± 0.3)E+4	(0.4 ± 2.2)E+2	10 ± 1	36 ± 14	22.5 ± 0.4	(6.4 ± 1.8)E–6
19604	1	40.03	−0.12	83	3.6	1.9	3.7	4.6 ± 0.6	0.08	(6.1 ± 1.7)E+3	(0.6 ± 1.5)E+2	7 ± 1	35 ± 14	19.2 ± 0.4	(1.3 ± 0.4)E–6
19910	5	38.93	−0.25	43	5.3	1.9	3.7	4.6 ± 0.6	0.05	(2.0 ± 0.6)E+4	(0.8 ± 3.7)E+2	10 ± 1	62 ± 24	7.9 ± 0.1	(1.3 ± 0.5)E–6
20135	7	38.95	+0.02	18	4.3	1.1	2.0	11.5 ± 5.3	0.08	(2.5 ± 2.3)E+4	(0.1 ± 7.7)E+2	20 ± 9	20 ± 26	4 ± 1	(3.5 ± 1.1)E–7
20221	4	39.22	−0.07	21	6.8	2.5	3.1	11.2 ± 0.6	0.15	(1.6 ± 0.2)E+5	(0.2 ± 3.3)E+2	32 ± 2	49 ± 7	2.29 ± 0.09	(1.1 ± 0.2)E–4
20288	8	39.57	−0.20	60	6.3	2.3	5.7	4.6 ± 0.6	0.08	(4.1 ± 1.1)E+4	(0.9 ± 6.3)E+2	12 ± 2	89 ± 35	11.2 ± 0.2	(4.5 ± 1.2)E–6
20469	12	39.88	−0.22	58	6.6	2.8	3.0	4.6 ± 0.6	0.05	(4.2 ± 1.2)E+4	(0.8 ± 6.0)E+2	13 ± 2	80 ± 31	3.15 ± 0.06	(6.3 ± 1.1)E–6
20640	8	38.62	−0.20	66	4.1	1.9	2.6	4.5 ± 1.2	0.16	(1.5 ± 0.8)E+4	(1.2 ± 6.5)E+2	8 ± 2	74 ± 54	4.1 ± 0.1	(4.2 ± 1.9)E–6
20881	18	38.29	−0.19	60	9.3	3.4	6.9	7.0 ± 0.3	0.06	(1.7 ± 0.2)E+5	(0.3 ± 4.2)E+2	27 ± 1	74 ± 10	8.6 ± 0.1	(4.5 ± 1.8)E–5
20979	13	37.92	+0.19	44	15.9	3.8	3.1	7.0 ± 0.3	0.06	(6.9 ± 0.7)E+4	(0.0 ± 1.0)E+2	45 ± 2	11 ± 2	7.1 ± 0.1	(3.4 ± 1.4)E–5
21042	7	37.52	+0.05	40	6.0	4.8	2.7	7.0 ± 0.3	0.05	(8.3 ± 0.8)E+4	(0.4 ± 2.6)E+2	21 ± 1	59 ± 8	2.17 ± 0.04	(7.8 ± 4.3)E–5
21151	15	38.48	+0.15	26	8.5	5.2	6.8	11.2 ± 2.5	0.06	(2.1 ± 0.9)E+5	(0.0 ± 1.4)E+3	44 ± 10	34 ± 21	11 ± 2	(7.3 ± 3.0)E–5
21387	2	38.02	−0.26	62	3.2	1.5	3.6	7.0 ± 0.3	0.09	(2.0 ± 0.2)E+4	(0.9 ± 1.4)E+2	9.8 ± 0.5	66 ± 9	7.2 ± 0.2	(1.8 ± 0.8)E–6
21395	6	37.43	−0.06	56	4.1	1.2	2.1	7.0 ± 0.3	0.23	(3.0 ± 0.3)E+4	(0.8 ± 1.7)E+2	11.7 ± 0.6	70 ± 10	1.93 ± 0.03	(4.2 ± 1.6)E–5
21672	2	37.75	−0.23	55	3.9	2.1	6.0	7.0 ± 0.3	0.09	(8.4 ± 0.8)E+4	(1.9 ± 4.7)E+2	12.2 ± 0.6	181 ± 26	6.1 ± 0.1	(7.0 ± 1.8)E–5
21685	20	37.77	−0.09	49	11.8	3.1	4.6	7.0 ± 0.3	0.14	(1.2 ± 0.1)E+5	(0.1 ± 2.4)E+2	34 ± 2	34 ± 5	7.1 ± 0.1	(1.0 ± 0.4)E–4
22111	1	38.51	−0.02	22	3.4	2.7	4.9	11.3 ± 5.1	0.02	(1.9 ± 1.7)E+4	(0.1 ± 5.9)E+2	19 ± 9	16 ± 20	29 ± 10	(8.8 ± 5.2)E–6
22317	2	38.65	+0.14	80	4.1	2.2	2.6	7.0 ± 0.3	0.04	(3.1 ± 0.3)E+4	(0.6 ± 1.6)E+2	12.7 ± 0.6	61 ± 9	3.2 ± 0.1	(3.6 ± 2.0)E–6
22474	4	37.93	+0.20	5	3.9	2.3	6.7	6.7 ± 6.3	0.15	(1.1 ± 2.1)E+4	(0.0 ± 1.2)E+3	12 ± 11	25 ± 67	56 ± 14	(2.8 ± 1.4)E–6
22490	5	37.60	+0.02	18	10.8	9.6	2.3	7.0 ± 0.3	0.01	(1.5 ± 0.1)E+5	(0.1 ± 2.4)E+2	40 ± 2	29 ± 4	1.74 ± 0.03	(5.8 ± 4.2)E–4
23387	5	38.53	+0.04	79	6.7	2.6	2.7	7.0 ± 0.3	0.04	(5.9 ± 0.6)E+4	(0.3 ± 2.0)E+2	20 ± 1	48 ± 7	2.76 ± 0.06	···
23448	8	38.18	−0.09	83	5.8	2.3	6.6	7.0 ± 0.3	0.13	(3.2 ± 0.3)E+4	(0.3 ± 1.3)E+2	17.2 ± 0.9	35 ± 5	27.2 ± 0.5	(4.0 ± 2.3)E–6
23617	7	38.32	−0.14	83	10.6	3.6	3.8	7.0 ± 0.3	0.12	(8.7 ± 0.9)E+4	(0.1 ± 1.9)E+2	31 ± 2	29 ± 4	5.9 ± 0.1	(3.3 ± 2.0)E–5
23816	21	37.81	+0.05	84	13.0	5.4	4.2	7.0 ± 0.3	0.09	(1.6 ± 0.2)E+5	(0.1 ± 2.9)E+2	39 ± 2	35 ± 5	4.8 ± 0.1	(1.2 ± 0.7)E–4
23933	5	37.29	−0.24	38	4.3	1.5	3.6	8.0 ± 0.5	0.21	(4.5 ± 0.5)E+4	(0.6 ± 2.5)E+2	14.2 ± 0.8	71 ± 12	4.7 ± 0.1	(6.7 ± 1.6)E–5
23935	10	37.52	+0.22	85	7.8	1.9	2.4	8.0 ± 0.5	0.06	(2.2 ± 0.3)E+5	(0.5 ± 7.0)E+2	25 ± 2	109 ± 18	0.80 ± 0.03	(4.2 ± 1.6)E–5
24101	7	37.25	−0.11	43	5.4	2.1	2.8	8.0 ± 0.5	0.04	(5.9 ± 0.7)E+4	(0.4 ± 2.6)E+2	18 ± 1	57 ± 10	2.89 ± 0.07	(4.6 ± 1.3)E–5
24119	13	37.29	+0.06	88	12.3	3.0	4.7	8.0 ± 0.5	0.13	(1.0 ± 0.1)E+5	(0.1 ± 2.1)E+2	40 ± 2	21 ± 3	9.8 ± 0.3	(3.3 ± 1.6)E–5
24187	2	36.25	+0.13	54	4.1	2.1	4.3	6.9 ± 3.9	0.02	(8.6 ± 9.9)E+3	(0.2 ± 5.3)E+2	12 ± 7	18 ± 29	31 ± 5	···
24211	21	36.43	−0.13	53	17.4	5.0	3.3	6.3 ± 0.5	0.03	(4.0 ± 0.6)E+5	(0.2 ± 8.7)E+2	45 ± 3	63 ± 13	1.41 ± 0.03	(2.4 ± 1.1)E–5
24457	1	36.19	−0.22	38	4.3	1.8	2.1	6.9 ± 1.7	0.03	(9.4 ± 4.6)E+3	(0.2 ± 2.5)E+2	13 ± 3	19 ± 13	7.1 ± 0.5	···
24513	11	36.93	+0.16	54	5.9	3.1	7.0	6.8 ± 1.5	0.07	(2.9 ± 1.3)E+4	(0.2 ± 5.0)E+2	18 ± 4	29 ± 19	34 ± 2	(7.6 ± 2.7)E–6
24528	5	36.35	−0.09	29	7.1	4.8	2.4	6.3 ± 0.5	0.03	(5.3 ± 0.8)E+4	(0.2 ± 2.4)E+2	21 ± 2	37 ± 8	2.77 ± 0.06	···
24881	3	36.67	−0.23	80	3.8	3.0	2.1	6.3 ± 0.5	0.03	(2.5 ± 0.4)E+4	(0.6 ± 2.1)E+2	12.0 ± 0.9	56 ± 12	2.42 ± 0.07	(1.3 ± 0.8)E–6
24892	5	36.25	−0.12	81	3.9	3.1	2.5	6.3 ± 0.5	0.04	(3.5 ± 0.5)E+4	(0.8 ± 2.9)E+2	12.2 ± 0.9	75 ± 16	2.48 ± 0.06	···
25264	3	36.68	+0.09	60	6.2	2.7	1.6	6.3 ± 0.5	0.07	(2.6 ± 0.4)E+4	(0.2 ± 1.5)E+2	17 ± 1	29 ± 6	2.05 ± 0.04	(1.4 ± 0.4)E–6
25514	27	36.74	−0.14	78	17.4	4.8	2.9	6.3 ± 0.5	0.08	(2.5 ± 0.4)E+5	(0.1 ± 5.6)E+2	45 ± 3	40 ± 8	1.74 ± 0.06	(3.1 ± 1.0)E–5
25555	5	36.17	+0.12	77	4.3	2.9	4.1	6.3 ± 0.5	0.06	(2.7 ± 0.4)E+4	(0.5 ± 2.1)E+2	13 ± 1	52 ± 11	9.3 ± 0.2	···
25866	17	35.41	+0.16	79	14.1	4.6	3.6	5.7 ± 0.4	0.04	(3.1 ± 0.4)E+5	(0.3 ± 8.9)E+2	33 ± 2	90 ± 18	1.59 ± 0.03	(8.7 ± 4.0)E–5
25964	6	35.38	−0.27	52	4.7	1.3	2.3	5.7 ± 0.4	0.18	(1.4 ± 0.2)E+4	(0.4 ± 1.2)E+2	10.9 ± 0.8	38 ± 8	4.62 ± 0.09	(4.1 ± 1.1)E–6
25983	8	35.72	−0.05	50	5.5	2.8	2.3	5.7 ± 0.4	0.09	(2.1 ± 0.3)E+4	(0.3 ± 1.4)E+2	14 ± 1	35 ± 7	3.87 ± 0.06	(2.2 ± 0.4)E–5
26017	24	35.54	−0.08	50	8.8	6.4	5.0	5.7 ± 0.4	0.08	(2.9 ± 0.4)E+5	(0.1 ± 1.1)E+3	24 ± 2	159 ± 31	2.36 ± 0.03	(1.4 ± 0.3)E–4
26268	1	34.88	−0.01	49	5.6	1.7	1.5	5.8 ± 0.3	0.02	(9.4 ± 1.0)E+3	(1.6 ± 5.2)E+1	13.4 ± 0.7	17 ± 3	3.65 ± 0.08	(3.4 ± 1.9)E–6

Continuation of Table B1																
COHRS catalog #	# clumps	ℓ (deg)	b (deg)	$v_{\rm LSR}$ (km s^{-1})	$\sigma_{\rm maj}$ (arcmin)	$\sigma_{\rm min}$ (arcmin)	$v_{\rm RMS}$ (km s^{-1})	$d_\odot$ (kpc)	CFE	M (M$_\odot$)	n (cm^{-3})	R (pc)	Σ (M$_\odot$ pc^{-2})	$\alpha_{\rm vir}$	SFR (M$_\odot$ yr^{-1})
26370	4	35.22	−0.25	60	5.4	2.2	2.6	5.8 ± 0.3	0.03	(1.8 ± 0.2)E+4	(0.3 ± 1.0)E+2	13.4 ± 0.7	33 ± 5	5.7 ± 0.1	(3.8 ± 2.4)E−7
26608	2	35.38	+0.09	53	3.2	1.8	4.9	5.8 ± 0.3	0.03	(3.7 ± 0.4)E+4	(2.6 ± 3.3)E+2	8.3 ± 0.5	168 ± 27	6.27 ± 0.08	(3.8 ± 2.3)E−6
26964	5	35.34	−0.04	91	6.9	3.8	7.1	5.8 ± 0.3	0.06	(4.8 ± 0.5)E+4	(0.3 ± 2.0)E+2	18 ± 1	46 ± 7	21.9 ± 0.3	(1.6 ± 0.9)E−5
27150	18	34.68	−0.08	81	7.8	6.0	7.5	5.8 ± 0.3	0.03	(3.0 ± 0.3)E+5	(0.1 ± 1.0)E+3	22 ± 1	191 ± 30	4.84 ± 0.06	(3.7 ± 1.7)E−5
27530	1	34.47	+0.11	61	5.4	1.7	2.7	5.8 ± 0.3	0.01	(2.3 ± 0.3)E+4	(0.4 ± 1.4)E+2	13.0 ± 0.7	44 ± 7	4.61 ± 0.07	(3.4 ± 1.9)E−6
27741	1	34.91	+0.01	28	4.0	1.6	1.4	5.8 ± 0.3	0.09	(7.4 ± 0.8)E+3	(3.1 ± 5.7)E+1	9.8 ± 0.5	24 ± 4	2.95 ± 0.06	(1.0 ± 0.8)E−5
27779	7	34.27	−0.04	89	9.9	7.8	6.0	5.8 ± 0.3	0.03	(1.1 ± 0.1)E+5	(0.2 ± 3.0)E+2	29 ± 2	44 ± 7	10.4 ± 0.1	(1.1 ± 0.7)E−4
28338	2	35.02	−0.20	87	3.4	2.4	5.0	5.8 ± 0.3	0.05	(1.5 ± 0.2)E+4	(0.7 ± 1.2)E+2	9.6 ± 0.5	53 ± 8	18.3 ± 0.3	(2.3 ± 1.8)E−6
28618	3	34.04	+0.12	36	3.3	2.4	3.8	5.8 ± 0.3	0.05	(3.0 ± 0.3)E+4	(1.5 ± 2.4)E+2	9.3 ± 0.5	109 ± 17	5.25 ± 0.07	(9.5 ± 3.2)E−6
29052	34	34.83	−0.06	45	18.5	9.6	5.1	5.8 ± 0.3	0.02	(5.3 ± 0.6)E+5	(0.2 ± 8.3)E+2	48 ± 3	74 ± 12	2.73 ± 0.03	(9.2 ± 4.5)E−5
29208	23	33.66	−0.18	51	9.0	4.3	3.9	6.3 ± 0.3	0.06	(1.3 ± 0.1)E+5	(0.3 ± 3.2)E+2	25 ± 1	68 ± 9	3.35 ± 0.04	(4.4 ± 1.8)E−5
29247	2	33.77	+0.22	56	10.1	0.8	1.9	6.3 ± 0.3	0.01	(5.7 ± 0.5)E+4	(0.1 ± 1.4)E+2	25 ± 1	29 ± 4	1.8 ± ···	(2.3 ± 1.3)E−6
29256	7	33.95	−0.02	58	4.2	4.1	6.0	6.3 ± 0.3	0.08	(6.6 ± 0.6)E+4	(0.9 ± 2.8)E+2	14.4 ± 0.7	101 ± 13	9.2 ± 0.1	(1.8 ± 1.0)E−5
29302	4	33.95	−0.22	10	9.3	3.8	1.6	7.1 ± 4.3	0.05	(3.1 ± 3.7)E+4	(0.1 ± 8.9)E+2	28 ± 17	13 ± 21	2.6 ± 0.5	(2.0 ± 1.5)E−5
29322	2	33.67	−0.00	35	3.7	2.9	2.2	6.3 ± 0.3	0.05	(1.7 ± 0.2)E+4	(4.6 ± 9.3)E+1	11.5 ± 0.5	42 ± 5	3.74 ± 0.07	(1.0 ± 0.8)E−5
29325	24	34.24	+0.10	55	11.1	7.1	7.5	6.3 ± 0.3	0.28	(3.3 ± 0.3)E+5	(0.4 ± 6.2)E+2	32 ± 1	99 ± 13	6.40 ± 0.08	(6.4 ± 1.2)E−4
29360	21	33.59	+0.01	105	11.1	3.0	2.6	6.3 ± 0.3	0.08	(4.4 ± 0.4)E+5	(0.8 ± 9.7)E+2	28 ± 1	177 ± 23	0.50 ± 0.03	(1.7 ± 0.7)E−4
29361	9	33.70	+0.20	41	7.1	2.7	3.1	6.3 ± 0.3	0.11	(4.4 ± 0.4)E+4	(0.3 ± 1.5)E+2	18.8 ± 0.9	40 ± 5	4.86 ± 0.06	(4.3 ± 2.5)E−5
29368	9	33.61	−0.04	88	16.8	4.4	3.0	6.3 ± 0.3	0.01	(2.1 ± 0.2)E+5	(0.1 ± 3.1)E+2	43 ± 2	37 ± 5	2.03 ± 0.05	(5.9 ± 3.5)E−5
29435	2	33.95	−0.18	90	3.0	3.4	2.1	6.3 ± 0.3	0.04	(1.1 ± 0.1)E+4	(3.1 ± 5.9)E+1	11.2 ± 0.5	27 ± 4	5.5 ± 0.1	(4.8 ± 2.7)E−7
29444	3	33.70	+0.20	93	10.0	3.3	2.5	6.3 ± 0.3	0.01	(6.2 ± 0.6)E+4	(0.1 ± 1.5)E+2	26 ± 1	29 ± 4	3.01 ± 0.08	(9.6 ± 5.6)E−6
29561	3	33.04	+0.06	83	3.7	1.1	2.7	6.7 ± 0.2	0.36	(2.3 ± 0.2)E+4	(0.9 ± 1.1)E+2	10.3 ± 0.4	69 ± 7	3.8 ± 0.1	(2.0 ± 0.6)E−5
29564	2	33.02	+0.16	73	5.5	2.8	3.5	6.7 ± 0.2	0.06	(3.6 ± 0.3)E+4	(0.3 ± 1.1)E+2	16.4 ± 0.6	43 ± 4	6.26 ± 0.08	(4.5 ± 1.8)E−6
29629	12	32.48	−0.09	77	5.5	5.2	5.1	6.7 ± 0.2	0.04	(9.3 ± 0.7)E+4	(0.5 ± 2.3)E+2	20.0 ± 0.7	74 ± 8	6.39 ± 0.08	(1.7 ± 0.8)E−5
29740	2	32.92	+0.27	32	4.1	0.5	1.3	7.1 ± 5.6	0.15	(3.0 ± 4.6)E+3	(0.1 ± 2.7)E+2	12 ± 9	7 ± 15	8 ± 2	(4.0 ± 2.4)E−7
29806	5	32.56	−0.24	46	3.8	1.7	3.2	2.7 ± 0.6	0.08	(3.7 ± 1.5)E+3	(1.7 ± 2.5)E+2	4.4 ± 0.9	60 ± 35	14.2 ± 0.1	(6.4 ± 2.9)E−7
29832	20	32.47	+0.18	44	6.1	3.0	6.4	8.5 ± 1.0	0.08	(2.3 ± 0.5)E+5	(0.1 ± 1.5)E+3	23 ± 3	140 ± 45	4.7 ± 0.2	(5.3 ± 1.1)E−5
29908	5	33.35	+0.10	11	9.4	4.7	3.2	13.0 ± 6.4	0.08	(8.4 ± 8.3)E+4	(0.0 ± 1.0)E+3	54 ± 26	9 ± 13	8 ± 4	(3.5 ± 2.9)E−4
29910	3	32.76	+0.19	19	3.6	1.6	7.6	8.5 ± 1.0	0.24	(7.9 ± 1.8)E+4	(1.4 ± 9.2)E+2	13 ± 2	144 ± 47	11.2 ± 0.6	(1.6 ± 0.2)E−4
29959	8	32.78	−0.07	36	8.3	5.0	3.6	11.5 ± 2.4	0.08	(2.6 ± 1.1)E+5	(0.0 ± 1.7)E+3	44 ± 9	44 ± 26	2.5 ± 0.4	(1.6 ± 1.0)E−4
30096	9	33.35	−0.01	73	12.1	3.3	4.1	6.7 ± 0.2	0.14	(1.3 ± 0.1)E+5	(0.1 ± 2.0)E+2	33 ± 1	38 ± 4	5.05 ± 0.06	(1.7 ± 0.9)E−4
30821	29	32.80	−0.02	94	10.6	5.0	6.0	6.7 ± 0.2	0.03	(4.9 ± 0.4)E+5	(0.7 ± 7.9)E+2	31 ± 1	163 ± 17	2.64 ± 0.05	(1.2 ± 0.5)E−4
30901	4	33.17	+0.23	97	4.6	1.6	5.8	6.7 ± 0.2	0.14	(9.1 ± 0.7)E+3	(1.7 ± 3.5)E+1	12.9 ± 0.5	17 ± 2	56 ± 1	(1.3 ± 0.6)E−6
30971	4	33.39	+0.15	84	5.9	2.1	2.5	6.7 ± 0.2	0.12	(2.9 ± 0.2)E+4	(2.5 ± 8.5)E+1	16.7 ± 0.6	33 ± 3	4.36 ± 0.07	(1.1 ± 0.6)E−5
31071	10	32.74	−0.26	89	10.6	1.8	4.5	6.7 ± 0.2	0.08	(4.6 ± 0.3)E+4	(0.8 ± 8.0)E+1	29 ± 1	18 ± 2	14.7 ± 0.2	(7.6 ± 2.8)E−6
31380	9	31.98	−0.20	97	7.4	3.6	4.4	6.2 ± 0.2	0.05	(8.2 ± 0.6)E+4	(0.4 ± 2.2)E+2	20.1 ± 0.8	65 ± 7	5.44 ± 0.06	(6.1 ± 2.2)E−5
31384	17	31.87	+0.10	98	15.9	3.1	8.1	6.2 ± 0.2	0.11	(3.2 ± 0.3)E+5	(0.2 ± 4.3)E+2	40 ± 2	66 ± 7	9.4 ± 0.1	(1.5 ± 0.3)E−4
31417	2	31.50	−0.00	105	5.5	3.3	4.7	6.2 ± 0.2	0.01	(1.0 ± 0.1)E+5	(1.1 ± 3.4)E+2	15.7 ± 0.6	133 ± 15	3.98 ± 0.08	(1.5 ± 0.8)E−5
31476	6	32.25	−0.17	43	3.6	2.6	2.6	4.3 ± 1.0	0.03	(8.7 ± 3.9)E+3	(0.8 ± 3.5)E+2	8 ± 2	49 ± 31	6.8 ± 0.2	(2.8 ± 1.0)E−6
31505	6	32.12	−0.08	45	3.9	3.1	5.2	4.3 ± 1.0	0.06	(2.8 ± 1.2)E+4	(1.8 ± 9.8)E+2	9 ± 2	122 ± 77	9.8 ± 0.3	(3.2 ± 1.2)E−6
31508	6	32.23	+0.12	82	5.8	3.0	2.7	6.2 ± 0.2	0.02	(3.3 ± 0.3)E+4	(0.3 ± 1.1)E+2	15.9 ± 0.6	41 ± 5	4.16 ± 0.06	(8.6 ± 3.5)E−6
31567	9	31.54	−0.13	42	6.9	4.7	4.2	6.3 ± 0.2	0.04	(1.3 ± 0.1)E+5	(0.6 ± 2.8)E+2	20.6 ± 0.7	94 ± 9	3.29 ± 0.03	(2.0 ± 0.9)E−5
31930	2	30.83	−0.18	52	3.7	3.1	2.7	6.3 ± 0.2	0.04	(5.7 ± 0.4)E+4	(1.3 ± 2.1)E+2	12.0 ± 0.4	125 ± 12	1.75 ± 0.02	(1.5 ± 0.7)E−4
32092	25	31.11	+0.04	40	9.9	6.4	3.8	6.3 ± 0.2	0.07	(3.4 ± 0.2)E+5	(0.5 ± 5.3)E+2	29 ± 1	127 ± 12	1.46 ± 0.01	(3.9 ± 2.2)E−4
32180	4	30.91	+0.17	107	5.2	2.0	2.3	6.3 ± 0.2	0.12	(5.6 ± 0.4)E+4	(0.9 ± 1.9)E+2	13.8 ± 0.5	94 ± 9	1.45 ± 0.02	(3.8 ± 2.1)E−5
32327	2	31.28	−0.16	23	4.3	2.4	3.0	6.3 ± 0.2	0.21	(1.7 ± 0.1)E+4	(4.0 ± 6.6)E+1	12.1 ± 0.4	38 ± 4	7.40 ± 0.08	(3.0 ± 1.6)E−5
32345	3	31.38	+0.21	17	3.9	1.6	3.5	6.3 ± 0.2	0.04	(9.6 ± 0.6)E+3	(3.4 ± 4.2)E+1	10.4 ± 0.4	28 ± 3	15.1 ± 0.2	(1.6 ± 1.0)E−5
32439	2	31.84	−0.16	38	9.7	2.6	2.5	6.3 ± 0.2	0.03	(4.7 ± 0.3)E+4	(1.2 ± 8.6)E+1	24.9 ± 0.8	24 ± 2	3.77 ± 0.04	(1.7 ± 0.9)E−5
32932	13	30.79	−0.05	94	5.9	3.6	5.4	6.3 ± 0.2	0.20	(5.3 ± 0.4)E+5	(0.4 ± 1.4)E+3	17.0 ± 0.6	586 ± 56	1.07 ± 0.01	(1.1 ± 0.2)E−3
33035	3	31.08	−0.24	103	4.1	1.5	2.9	6.3 ± 0.2	0.07	(2.2 ± 0.1)E+4	(7.1 ± 9.3)E+1	10.7 ± 0.4	60 ± 6	4.73 ± 0.06	(7.8 ± 4.1)E−6
33079	4	31.28	+0.08	106	4.4	3.3	3.6	6.3 ± 0.2	0.15	(1.1 ± 0.1)E+5	(1.7 ± 3.7)E+2	13.6 ± 0.5	188 ± 18	1.87 ± 0.02	(5.8 ± 2.9)E−5
33232	9	31.11	+0.23	102	4.4	2.5	5.1	6.3 ± 0.2	0.04	(1.1 ± 0.1)E+5	(2.4 ± 4.2)E+2	12.4 ± 0.4	236 ± 23	3.34 ± 0.06	(3.6 ± 1.7)E−5
33263	6	31.70	−0.17	103	6.0	2.5	2.1	6.3 ± 0.2	0.09	(7.7 ± 0.5)E+4	(0.8 ± 2.2)E+2	16.0 ± 0.5	95 ± 9	1.04 ± 0.03	(1.6 ± 0.6)E−5
33391	6	31.42	−0.24	90	4.2	3.3	5.4	6.3 ± 0.2	0.16	(3.8 ± 0.3)E+4	(0.7 ± 1.3)E+2	13.3 ± 0.5	69 ± 7	11.9 ± 0.1	(5.7 ± 1.9)E−5
33476	2	31.56	−0.08	81	10.4	4.5	2.8	6.3 ± 0.2	0.04	(8.2 ± 0.6)E+4	(0.1 ± 1.3)E+2	28 ± 1	33 ± 3	3.01 ± 0.06	(1.9 ± 1.3)E−5
33502	1	30.87	+0.06	75	4.9	1.8	2.0	6.3 ± 0.2	0.04	(5.4 ± 0.4)E+4	(1.0 ± 1.9)E+2	12.8 ± 0.4	105 ± 10	1.09 ± 0.03	(2.8 ± 1.9)E−5
33530	7	31.16	−0.09	82	12.2	4.7	5.1	6.3 ± 0.2	0.01	(3.6 ± 0.2)E+5	(0.4 ± 5.1)E+2	32 ± 1	111 ± 11	2.68 ± 0.03	(1.4 ± 0.8)E−4
33772	2	31.20	−0.27	94	5.4	1.2	7.2	6.3 ± 0.2	0.03	(1.3 ± 0.1)E+4	(2.1 ± 4.4)E+1	13.7 ± 0.5	23 ± 2	63 ± 1	(1.3 ± 0.6)E−7

Continuation of Table B1

COHRS catalog #	# clumps	ℓ (deg)	b (deg)	$v_{\rm LSR}$ (km s^{-1})	$\sigma_{\rm maj}$ (arcmin)	$\sigma_{\rm min}$ (arcmin)	$v_{\rm RMS}$ (km s^{-1})	$d_\odot$ (kpc)	CFE	M (M$_\odot$)	n (cm^{-3})	R (pc)	Σ (M$_\odot$ pc^{-2})	$\alpha_{\rm vir}$	SFR (M$_\odot$ yr^{-1})
33826	4	30.58	+0.15	93	6.6	2.6	6.4	6.3 ± 0.2	0.02	(9.8 ± 0.7)E+4	(0.7 ± 2.5)E+2	17.6 ± 0.6	101 ± 10	8.6 ± 0.2	(1.9 ± 1.3)E−5
34131	1	30.32	+0.08	110	3.2	2.4	2.3	7.3 ± 0.2	0.06	(3.4 ± 0.2)E+4	(0.9 ± 1.2)E+2	11.5 ± 0.3	81 ± 7	2.01 ± 0.04	(1.8 ± 1.1)E−5
34159	21	30.47	+0.06	43	10.7	6.4	4.2	7.3 ± 0.2	0.08	(3.5 ± 0.2)E+5	(0.3 ± 4.0)E+2	36 ± 1	88 ± 8	2.11 ± 0.03	(2.8 ± 1.4)E−4
34198	2	30.34	+0.04	94	3.7	2.3	3.3	7.3 ± 0.2	0.02	(2.1 ± 0.1)E+5	(4.4 ± 6.9)E+2	12.5 ± 0.4	433 ± 38	0.77 ± 0.03	(3.4 ± 2.1)E−5
34216	4	30.28	−0.22	104	4.2	2.6	2.7	7.3 ± 0.2	0.09	(1.9 ± 0.1)E+5	(2.7 ± 5.4)E+2	14.1 ± 0.4	301 ± 26	0.62 ± 0.01	(7.3 ± 1.6)E−5
34249	3	30.40	−0.05	109	2.7	2.1	4.1	7.3 ± 0.2	0.11	(3.9 ± 0.2)E+4	(1.7 ± 1.7)E+2	9.7 ± 0.3	133 ± 11	4.7 ± 0.1	(3.3 ± 1.8)E−5
34614	14	29.41	−0.14	97	6.8	4.3	4.3	6.5 ± 0.2	0.04	(1.7 ± 0.1)E+5	(0.8 ± 3.1)E+2	20.5 ± 0.6	128 ± 10	2.57 ± 0.03	(1.7 ± 0.7)E−5
34629	4	29.47	+0.03	27	5.8	1.8	3.7	6.5 ± 0.2	0.03	(1.9 ± 0.1)E+4	(2.1 ± 4.7)E+1	15.6 ± 0.4	26 ± 2	12.7 ± 0.2	(7.1 ± 4.4)E−7
34703	6	29.55	+0.17	33	4.9	3.3	7.6	6.5 ± 0.2	0.03	(4.9 ± 0.3)E+4	(0.6 ± 1.2)E+2	15.1 ± 0.4	68 ± 5	20.7 ± 0.2	(1.1 ± 0.6)E−5
35524	6	29.95	+0.12	38	5.7	3.5	3.1	11.9 ± 5.0	0.05	(1.2 ± 1.0)E+5	(0.0 ± 2.2)E+3	31 ± 13	39 ± 46	3 ± 1	(1.8 ± 1.0)E−4
35552	5	29.86	−0.25	99	4.9	2.1	4.7	6.5 ± 0.2	0.07	(4.2 ± 0.2)E+4	(0.6 ± 1.1)E+2	13.8 ± 0.4	70 ± 6	8.6 ± 0.1	(2.0 ± 0.6)E−5
35564	3	28.85	+0.11	47	5.8	3.9	7.9	6.5 ± 0.2	0.02	(3.7 ± 0.2)E+4	(2.6 ± 7.8)E+1	17.9 ± 0.5	37 ± 3	34.4 ± 0.3	(5.5 ± 3.6)E−5
35719	1	28.84	−0.16	30	4.6	1.8	2.7	6.5 ± 0.2	0.04	(1.0 ± 0.1)E+4	(2.1 ± 3.1)E+1	12.6 ± 0.3	21 ± 2	10.2 ± 0.1	(2.2 ± 1.7)E−5
35752	4	29.75	+0.12	42	3.6	1.4	5.1	7.4 ± 9.1	0.13	(0.7 ± 1.8)E+4	(0.0 ± 1.1)E+3	11 ± 14	18 ± 65	47 ± 20	(2.7 ± 1.5)E−6
35844	4	29.53	−0.02	48	6.6	1.6	3.0	6.5 ± 0.2	0.17	(2.0 ± 0.1)E+4	(1.6 ± 4.4)E+1	17.3 ± 0.5	22 ± 2	8.9 ± 0.1	(3.5 ± 2.0)E−6
36382	2	29.84	+0.19	83	6.2	1.7	2.1	6.5 ± 0.2	0.04	(3.5 ± 0.2)E+4	(3.1 ± 7.9)E+1	16.6 ± 0.5	41 ± 3	2.48 ± 0.04	(3.7 ± 1.7)E−6
36544	26	29.94	−0.02	99	6.7	4.2	4.4	6.5 ± 0.2	0.10	(5.9 ± 0.3)E+5	(0.3 ± 1.1)E+3	20.3 ± 0.6	453 ± 36	0.78 ± 0.01	(5.6 ± 0.6)E−4
37312	3	29.46	−0.18	77	6.1	3.5	2.7	6.5 ± 0.2	0.02	(7.9 ± 0.4)E+4	(0.5 ± 1.6)E+2	18.0 ± 0.5	77 ± 6	1.88 ± 0.04	(1.3 ± 0.8)E−5
37387	12	29.42	+0.18	79	11.1	3.0	1.8	6.5 ± 0.2	0.02	(2.5 ± 0.1)E+5	(0.4 ± 3.1)E+2	29.4 ± 0.8	91 ± 7	0.43 ± 0.01	(1.6 ± 0.7)E−5
37849	28	28.15	−0.04	98	12.1	6.9	5.4	6.9 ± 0.2	0.09	(4.4 ± 0.3)E+5	(0.3 ± 5.5)E+2	38 ± 1	98 ± 10	2.88 ± 0.04	(2.4 ± 1.2)E−4
38663	32	28.86	+0.09	100	23.0	4.1	6.9	6.9 ± 0.2	0.08	(6.8 ± 0.5)E+5	(0.1 ± 5.1)E+2	64 ± 2	54 ± 5	5.24 ± 0.06	(3.3 ± 1.3)E−4
39046	14	28.31	+0.03	38	11.7	7.9	8.1	6.9 ± 0.2	0.06	(2.3 ± 0.2)E+5	(0.2 ± 2.9)E+2	38 ± 1	50 ± 5	12.5 ± 0.1	(4.7 ± 3.1)E−4
39731	23	28.77	−0.22	89	12.0	4.5	6.2	6.9 ± 0.2	0.11	(3.6 ± 0.3)E+5	(0.3 ± 4.9)E+2	35 ± 1	95 ± 9	4.29 ± 0.06	(9.0 ± 3.1)E−5
39826	6	28.80	+0.20	81	5.6	4.2	3.8	6.9 ± 0.2	0.02	(1.2 ± 0.1)E+5	(0.7 ± 3.1)E+2	18.9 ± 0.7	108 ± 11	2.60 ± 0.04	(1.2 ± 0.7)E−4
40422	6	27.69	−0.21	43	10.9	2.5	2.9	7.4 ± 0.3	0.06	(5.2 ± 0.4)E+4	(0.6 ± 7.7)E+1	33 ± 1	15 ± 2	6.2 ± 0.1	(4.2 ± 2.7)E−5
40478	2	27.98	+0.17	103	5.5	1.3	2.9	7.4 ± 0.3	0.03	(2.8 ± 0.2)E+4	(2.5 ± 8.3)E+1	16.5 ± 0.6	33 ± 3	5.6 ± 0.1	(2.4 ± 1.3)E−6
41092	7	28.19	+0.21	87	4.7	1.6	2.1	7.4 ± 0.3	0.10	(6.4 ± 0.5)E+4	(0.8 ± 2.2)E+2	14.5 ± 0.5	97 ± 10	1.20 ± 0.03	(1.7 ± 0.7)E−5
41160	4	27.04	−0.16	100	3.7	3.5	4.4	7.4 ± 0.3	0.04	(6.3 ± 0.5)E+4	(0.8 ± 2.0)E+2	15.0 ± 0.5	89 ± 9	5.34 ± 0.09	(3.3 ± 1.9)E−5
41990	2	27.38	−0.27	103	5.6	1.4	6.4	7.4 ± 0.3	0.09	(1.6 ± 0.1)E+4	(1.3 ± 4.5)E+1	16.8 ± 0.6	18 ± 2	50.8 ± 0.7	(5.2 ± 2.1)E−6
42120	3	27.81	−0.25	101	3.4	1.8	2.8	7.4 ± 0.3	0.18	(2.7 ± 0.2)E+4	(0.8 ± 1.2)E+2	11.3 ± 0.4	69 ± 7	3.7 ± 0.2	(9.5 ± 6.6)E−6
43140	5	27.11	−0.10	49	8.6	2.0	8.9	7.4 ± 0.3	0.03	(6.0 ± 0.4)E+4	(0.1 ± 1.1)E+2	25.7 ± 0.9	29 ± 3	39.2 ± 0.5	(8.2 ± 6.0)E−5
43337	1	27.82	−0.19	16	3.7	2.4	9.6	7.4 ± 0.3	0.09	(1.2 ± 0.1)E+4	(2.3 ± 4.7)E+1	13.0 ± 0.5	23 ± 2	111 ± 1	(2.4 ± 1.8)E−5
43455	2	28.44	+0.05	−13	7.1	2.5	4.4	15.4 ± 0.7	0.32	(6.4 ± 0.6)E+4	(0.3 ± 8.9)E+1	46 ± 2	10 ± 1	16 ± 1	(2.0 ± 1.5)E−4
43988	9	27.21	+0.15	30	6.7	3.5	6.0	7.4 ± 0.3	0.11	(1.4 ± 0.1)E+5	(0.5 ± 3.1)E+2	22.2 ± 0.8	92 ± 9	6.52 ± 0.08	(6.2 ± 2.7)E−5
44021	15	27.78	+0.17	40	12.9	5.0	9.0	7.4 ± 0.3	0.04	(2.3 ± 0.2)E+5	(0.1 ± 2.8)E+2	40 ± 1	46 ± 5	16.4 ± 0.2	(1.6 ± 0.7)E−4
44031	4	27.63	−0.12	76	8.2	3.1	2.2	7.4 ± 0.3	0.04	(9.2 ± 0.7)E+4	(0.2 ± 1.7)E+2	25.7 ± 0.9	44 ± 5	1.61 ± 0.08	(1.9 ± 0.9)E−5
44090	12	28.29	−0.02	78	8.4	7.1	2.9	7.4 ± 0.3	0.08	(3.5 ± 0.3)E+5	(0.4 ± 5.3)E+2	32 ± 1	107 ± 11	0.92 ± 0.03	(1.7 ± 1.1)E−4
44151	2	27.75	+0.19	81	5.3	1.7	2.6	7.4 ± 0.3	0.10	(1.6 ± 0.1)E+4	(1.4 ± 4.6)E+1	16.4 ± 0.6	18 ± 2	8.6 ± 0.2	···
44337	2	28.38	−0.27	42	7.8	1.2	6.6	7.4 ± 0.3	0.05	(3.8 ± 0.3)E+4	(1.3 ± 8.0)E+1	22.9 ± 0.8	23 ± 2	31.2 ± 0.4	(5.3 ± 3.2)E−6
44587	38	27.44	+0.02	93	13.2	5.3	5.8	7.4 ± 0.3	0.08	(7.3 ± 0.5)E+5	(0.4 ± 8.6)E+2	42 ± 2	134 ± 14	2.23 ± 0.05	(2.8 ± 1.3)E−4
44699	1	27.06	−0.01	82	5.8	1.0	2.7	7.4 ± 0.3	0.02	(1.8 ± 0.1)E+4	(1.4 ± 5.2)E+1	17.2 ± 0.6	20 ± 2	7.8 ± 0.1	(1.3 ± 0.8)E−5
44901	4	27.21	−0.13	25	4.6	3.5	3.9	7.4 ± 0.3	0.19	(3.5 ± 0.3)E+4	(0.3 ± 1.0)E+2	17.0 ± 0.6	39 ± 4	8.4 ± 0.1	(6.0 ± 3.9)E−5
45016	2	26.93	−0.09	−14	8.3	2.2	4.0	7.6 ± 8.2	0.12	(2.2 ± 4.8)E+4	(0.0 ± 1.3)E+3	25 ± 28	11 ± 33	21 ± 8	(4.3 ± 3.3)E−5
45022	9	26.77	−0.10	74	9.5	3.1	7.4	7.8 ± 0.4	0.03	(1.5 ± 0.1)E+5	(0.2 ± 3.1)E+2	31 ± 1	52 ± 7	12.6 ± 0.2	(1.3 ± 0.8)E−4
45091	2	26.13	−0.03	27	4.0	2.3	2.9	7.8 ± 0.4	0.21	(2.3 ± 0.2)E+4	(3.2 ± 9.9)E+1	14.2 ± 0.7	36 ± 5	6.1 ± 0.1	(8.6 ± 6.2)E−5
45156	22	26.63	+0.05	26	12.6	7.4	6.0	7.8 ± 0.4	0.05	(3.6 ± 0.3)E+5	(0.2 ± 5.0)E+2	45 ± 2	58 ± 8	5.10 ± 0.09	(2.1 ± 1.0)E−4
45225	15	26.68	−0.01	98	6.5	3.8	3.6	7.8 ± 0.4	0.04	(3.3 ± 0.3)E+5	(1.1 ± 8.7)E+2	23 ± 1	194 ± 25	1.07 ± 0.03	(1.4 ± 0.9)E−4
45264	5	26.05	−0.24	108	3.9	1.3	3.3	6.8 ± 0.2	0.04	(4.6 ± 0.3)E+4	(1.4 ± 2.1)E+2	11.1 ± 0.4	120 ± 12	3.07 ± 0.07	(1.1 ± 0.4)E−5
45483	11	25.72	+0.23	106	8.1	3.2	6.9	6.8 ± 0.2	0.09	(2.5 ± 0.2)E+5	(0.8 ± 5.3)E+2	23.2 ± 0.9	147 ± 15	5.17 ± 0.06	(2.1 ± 0.6)E−4
45506	7	26.57	−0.27	106	4.9	1.6	3.9	6.8 ± 0.2	0.20	(3.8 ± 0.3)E+4	(0.6 ± 1.4)E+2	13.7 ± 0.5	65 ± 7	6.3 ± 0.1	(2.1 ± 0.8)E−5
45622	7	26.41	+0.18	104	5.9	2.2	4.6	6.8 ± 0.2	0.06	(9.2 ± 0.7)E+4	(0.8 ± 2.7)E+2	16.7 ± 0.6	105 ± 11	4.5 ± 0.1	(8.2 ± 3.5)E−6
45919	6	26.34	−0.10	112	3.9	1.6	1.8	6.8 ± 0.2	0.10	(3.0 ± 0.2)E+4	(0.9 ± 1.3)E+2	11.2 ± 0.4	76 ± 8	1.40 ± 0.04	(1.1 ± 0.4)E−5
45974	3	26.19	+0.17	69	6.1	4.3	3.8	6.8 ± 0.2	0.01	(1.0 ± 0.1)E+5	(0.5 ± 2.5)E+2	20.0 ± 0.7	80 ± 8	3.38 ± 0.05	(1.1 ± 0.7)E−5
46051	25	25.63	−0.16	94	12.6	4.2	5.0	6.8 ± 0.2	0.08	(4.9 ± 0.4)E+5	(0.4 ± 6.8)E+2	35 ± 1	123 ± 13	2.08 ± 0.03	(5.0 ± 2.4)E−4
46449	20	26.22	+0.04	103	6.6	5.3	5.9	6.8 ± 0.2	0.05	(4.1 ± 0.3)E+5	(1.4 ± 9.0)E+2	22.6 ± 0.8	256 ± 27	2.23 ± 0.04	(1.0 ± 0.5)E−4
47282	5	25.61	−0.22	116	5.0	2.2	3.8	6.8 ± 0.2	0.06	(1.3 ± 0.1)E+5	(1.7 ± 4.4)E+2	14.5 ± 0.5	196 ± 20	1.89 ± 0.04	(5.4 ± 2.7)E−5
47343	1	25.44	+0.05	−13	3.1	1.5	2.2	15.6 ± 0.7	0.21	(8.6 ± 0.8)E+4	(0.4 ± 2.6)E+2	21 ± 1	60 ± 8	1.4 ± 0.1	(1.7 ± 1.0)E−4
47571	6	25.70	+0.11	29	7.5	4.1	5.9	6.8 ± 0.2	0.05	(6.7 ± 0.5)E+4	(0.2 ± 1.4)E+2	23.0 ± 0.8	41 ± 4	13.8 ± 0.2	(2.2 ± 1.5)E−4

Continuation of Table B1

COHRS catalog #	# clumps	ℓ (deg)	b (deg)	$v_{\rm LSR}$ (km s^{-1})	$\sigma_{\rm maj}$ (arcmin)	$\sigma_{\rm min}$ (arcmin)	$v_{\rm RMS}$ (km s^{-1})	$d_{\odot}$ (kpc)	CFE	M (M$_{\odot}$)	n (cm^{-3})	R (pc)	Σ (M$_{\odot}$ pc^{-2})	$\alpha_{\rm vir}$	SFR (M$_{\odot}$ yr^{-1})
47799	15	25.41	−0.16	61	13.3	3.7	4.3	6.8 ± 0.2	0.16	(1.7 ± 0.1)E+5	(0.1 ± 2.3)E+2	37 ± 1	40 ± 4	4.67 ± 0.06	(4.9 ± 2.4)E−4
47871	2	25.90	+0.18	66	4.8	2.9	6.0	6.8 ± 0.2	0.01	(4.6 ± 0.3)E+4	(0.5 ± 1.5)E+2	15.0 ± 0.6	65 ± 7	13.6 ± 0.2	(1.5 ± 0.9)E−5
47974	4	26.36	+0.09	56	4.6	4.1	5.3	6.8 ± 0.2	0.07	(4.3 ± 0.3)E+4	(0.4 ± 1.3)E+2	16.5 ± 0.6	50 ± 5	12.7 ± 0.2	(3.6 ± 2.4)E−5
48215	4	25.40	+0.21	39	6.2	1.4	2.8	6.8 ± 0.2	0.17	(2.7 ± 0.2)E+4	(2.2 ± 7.7)E+1	17.1 ± 0.6	29 ± 3	5.74 ± 0.08	(2.1 ± 0.9)E−5
48361	6	25.18	+0.10	47	5.2	3.1	6.8	6.8 ± 0.2	0.10	(4.1 ± 0.3)E+4	(0.4 ± 1.3)E+2	16.0 ± 0.6	51 ± 5	20.7 ± 0.3	(3.3 ± 1.9)E−5
48386	39	24.57	−0.08	48	22.8	6.6	6.5	6.7 ± 0.2	0.03	(1.2 ± 0.1)E+6	(0.2 ± 8.2)E+2	63 ± 2	98 ± 9	2.57 ± 0.03	(1.1 ± 0.7)E−3
48393	14	25.28	+0.13	104	11.6	3.3	5.3	6.7 ± 0.2	0.06	(1.7 ± 0.1)E+5	(0.2 ± 2.3)E+2	32 ± 1	54 ± 5	5.98 ± 0.08	(5.4 ± 2.6)E−5
48404	8	25.05	+0.01	102	5.9	3.0	4.3	6.7 ± 0.2	0.04	(8.7 ± 0.6)E+4	(0.7 ± 2.1)E+2	17.4 ± 0.6	92 ± 8	4.36 ± 0.09	(2.1 ± 1.0)E−5
48409	20	24.76	+0.07	107	5.6	4.1	3.6	6.7 ± 0.2	0.18	(2.1 ± 0.1)E+5	(1.4 ± 4.8)E+2	18.3 ± 0.6	198 ± 18	1.34 ± 0.03	(3.4 ± 1.2)E−4
48878	4	23.90	−0.20	56	5.6	2.4	2.4	6.5 ± 0.2	0.12	(4.5 ± 0.2)E+4	(0.5 ± 1.0)E+2	15.7 ± 0.4	58 ± 4	2.30 ± 0.04	(3.4 ± 2.2)E−5
49673	41	23.44	−0.13	91	13.6	4.4	13.3	6.5 ± 0.2	0.09	(1.0 ± 0.1)E+6	(0.1 ± 1.0)E+3	37 ± 1	240 ± 19	7.46 ± 0.07	(4.8 ± 1.0)E−4
50188	7	23.31	+0.05	82	3.9	1.9	5.9	6.5 ± 0.2	0.11	(1.0 ± 0.1)E+5	(3.0 ± 3.4)E+2	11.1 ± 0.3	266 ± 21	4.40 ± 0.08	(1.2 ± 0.4)E−5
50208	10	24.06	+0.01	85	8.9	6.4	7.4	6.5 ± 0.2	0.08	(2.5 ± 0.1)E+5	(0.4 ± 3.2)E+2	28.2 ± 0.8	99 ± 8	7.29 ± 0.08	(1.1 ± 0.6)E−4
50299	3	24.27	−0.25	87	3.4	1.6	6.4	6.5 ± 0.2	0.04	(2.4 ± 0.1)E+4	(1.1 ± 0.9)E+2	9.5 ± 0.3	84 ± 6	18.9 ± 0.2	(1.3 ± 0.7)E−5
50336	17	24.63	−0.19	91	8.6	4.0	7.9	6.5 ± 0.2	0.06	(3.2 ± 0.2)E+5	(0.9 ± 4.9)E+2	24.4 ± 0.7	174 ± 13	5.43 ± 0.05	(4.0 ± 2.0)E−4
51146	51	24.28	+0.14	112	13.0	6.9	6.7	6.5 ± 0.2	0.10	(9.7 ± 0.5)E+5	(0.7 ± 9.5)E+2	38 ± 1	219 ± 17	2.00 ± 0.04	(5.8 ± 2.1)E−4
51220	1	23.86	−0.25	94	2.7	1.3	4.5	6.5 ± 0.2	0.06	(2.7 ± 0.1)E+4	(2.2 ± 1.3)E+2	7.8 ± 0.2	139 ± 11	7.0 ± 0.2	(3.3 ± 1.8)E−6
51607	1	23.87	+0.08	38	4.1	1.5	2.2	6.5 ± 0.2	0.23	(2.2 ± 0.1)E+4	(6.5 ± 7.4)E+1	11.1 ± 0.3	57 ± 4	2.68 ± 0.03	(1.4 ± 0.8)E−5
51644	10	23.43	−0.04	53	10.4	4.8	3.5	6.5 ± 0.2	0.03	(2.6 ± 0.1)E+5	(0.4 ± 3.3)E+2	29.6 ± 0.8	96 ± 7	1.57 ± 0.05	(1.8 ± 1.2)E−4
52418	2	23.06	−0.10	102	5.2	2.1	2.9	6.0 ± 0.3	0.06	(3.1 ± 0.3)E+4	(0.5 ± 1.6)E+2	13.2 ± 0.7	56 ± 8	4.11 ± 0.09	(1.4 ± 0.8)E−5
52427	9	23.05	+0.18	105	5.0	3.0	3.3	6.0 ± 0.3	0.06	(7.5 ± 0.8)E+4	(1.2 ± 3.8)E+2	13.8 ± 0.7	127 ± 19	2.35 ± 0.04	(9.3 ± 3.8)E−6
52494	1	23.19	+0.26	82	3.2	0.9	5.6	6.0 ± 0.3	0.01	(1.3 ± 0.1)E+4	(1.1 ± 1.2)E+2	7.8 ± 0.4	69 ± 10	21.7 ± 0.6	(1.1 ± 0.5)E−6
52918	4	22.78	−0.25	71	3.9	2.7	3.9	6.0 ± 0.3	0.07	(5.5 ± 0.6)E+4	(1.6 ± 3.5)E+2	11.1 ± 0.6	142 ± 21	3.57 ± 0.05	(5.6 ± 2.9)E−5
53025	3	23.09	−0.10	66	3.6	1.8	2.9	6.0 ± 0.3	0.05	(5.6 ± 0.6)E+4	(2.6 ± 4.1)E+2	9.6 ± 0.5	195 ± 29	1.67 ± 0.03	(4.0 ± 1.8)E−8
53035	9	23.02	−0.22	70	7.1	2.7	5.9	6.0 ± 0.3	0.03	(2.3 ± 0.2)E+5	(1.6 ± 8.9)E+2	17.8 ± 0.9	226 ± 33	3.24 ± 0.04	(8.8 ± 2.6)E−5
53168	4	21.68	+0.15	114	3.7	1.5	3.5	6.8 ± 0.3	0.14	(1.4 ± 0.1)E+4	(4.6 ± 8.9)E+1	10.6 ± 0.5	39 ± 6	10.8 ± 0.2	(3.1 ± 2.0)E−6
54855	9	21.74	+0.03	22	6.3	4.9	3.9	6.8 ± 0.3	0.11	(6.6 ± 0.7)E+4	(0.3 ± 2.1)E+2	21 ± 1	47 ± 7	5.80 ± 0.09	(3.9 ± 2.2)E−5
55007	4	22.34	+0.23	15	4.9	1.3	2.8	1.4 ± 6.5	0.14	(0.4 ± 3.8)E+3	(0.1 ± 1.2)E+3	3 ± 13	17 ± 230	63 ± 3	(5.0 ± 3.0)E−8
55153	5	21.66	−0.10	103	7.0	4.1	13.2	6.8 ± 0.3	0.06	(9.3 ± 1.0)E+4	(0.4 ± 3.0)E+2	21 ± 1	64 ± 9	47.0 ± 0.7	(2.9 ± 1.6)E−5
55611	6	22.02	+0.17	50	7.2	5.7	3.1	6.8 ± 0.3	0.05	(1.4 ± 0.1)E+5	(0.4 ± 3.9)E+2	24 ± 1	75 ± 11	1.91 ± 0.04	(2.9 ± 1.4)E−5
55828	4	22.39	−0.14	42	3.8	1.8	10.1	6.8 ± 0.3	0.20	(2.1 ± 0.2)E+4	(0.6 ± 1.3)E+2	11.1 ± 0.6	54 ± 8	63 ± 1	(1.9 ± 1.2)E−5
55855	6	22.46	−0.02	114	3.6	2.8	5.9	6.8 ± 0.3	0.07	(7.5 ± 0.8)E+4	(1.7 ± 4.3)E+2	12.1 ± 0.6	164 ± 24	6.4 ± 0.1	(1.2 ± 0.6)E−5
56137	1	21.50	+0.14	45	3.3	1.2	7.8	7.9 ± 6.0	0.11	(1.1 ± 1.7)E+4	(0.0 ± 1.1)E+3	11 ± 8	31 ± 67	66 ± 19	(2.3 ± 1.4)E−6
56420	16	22.31	−0.01	82	6.6	4.2	7.4	6.8 ± 0.3	0.06	(1.7 ± 0.2)E+5	(0.7 ± 5.6)E+2	21 ± 1	123 ± 18	7.9 ± 0.1	(8.6 ± 3.5)E−5
56572	6	22.71	−0.22	106	6.7	2.6	2.6	6.8 ± 0.3	0.10	(7.6 ± 0.8)E+4	(0.4 ± 2.7)E+2	19 ± 1	66 ± 10	2.04 ± 0.04	(1.2 ± 0.7)E−4
56737	4	21.95	+0.09	75	4.2	2.2	5.9	6.8 ± 0.3	0.07	(3.3 ± 0.3)E+4	(0.7 ± 1.8)E+2	12.6 ± 0.6	67 ± 10	15.2 ± 0.4	(9.8 ± 6.2)E−6
56817	7	22.55	−0.21	78	4.6	2.2	2.9	6.8 ± 0.3	0.06	(1.3 ± 0.1)E+5	(2.2 ± 6.8)E+2	13.5 ± 0.7	233 ± 34	0.98 ± 0.02	···
56827	3	22.96	+0.21	73	2.2	1.1	2.4	6.8 ± 0.3	0.05	(4.5 ± 0.5)E+4	(6.2 ± 4.7)E+2	6.6 ± 0.3	324 ± 47	0.96 ± 0.04	(1.1 ± 0.6)E−6
56934	7	22.77	−0.05	71	6.6	3.7	5.4	6.8 ± 0.3	0.03	(1.5 ± 0.2)E+5	(0.7 ± 5.2)E+2	20 ± 1	119 ± 17	4.4 ± 0.1	(9.2 ± 4.1)E−6
56950	4	21.55	+0.24	79	5.0	1.6	4.1	6.8 ± 0.3	0.10	(2.1 ± 0.2)E+4	(0.3 ± 1.0)E+2	14.1 ± 0.7	34 ± 5	12.8 ± 0.3	(2.6 ± 1.2)E−6
57240	4	21.40	−0.22	89	2.3	1.9	4.4	6.8 ± 0.3	0.30	(2.1 ± 0.2)E+4	(1.7 ± 1.9)E+2	7.9 ± 0.4	107 ± 16	8.4 ± 0.3	(2.1 ± 1.2)E−5
57409	14	21.92	−0.21	79	6.1	2.3	5.0	6.8 ± 0.3	0.07	(7.6 ± 0.8)E+4	(0.6 ± 3.0)E+2	17.3 ± 0.9	81 ± 12	6.5 ± 0.1	(2.2 ± 0.7)E−5
57439	3	21.70	−0.25	67	4.2	0.9	4.5	6.8 ± 0.3	0.11	(1.2 ± 0.1)E+4	(3.4 ± 7.4)E+1	11.3 ± 0.6	30 ± 4	21.8 ± 0.5	(2.7 ± 1.4)E−6
57792	18	20.76	−0.10	57	5.6	3.7	4.1	7.6 ± 0.4	0.14	(2.1 ± 0.2)E+5	(1.1 ± 8.1)E+2	20 ± 1	170 ± 27	1.87 ± 0.04	(3.5 ± 1.1)E−4
57819	9	21.59	−0.05	68	8.3	3.2	2.4	7.6 ± 0.4	0.05	(1.9 ± 0.2)E+5	(0.4 ± 5.3)E+2	27 ± 2	84 ± 13	0.97 ± 0.03	(3.9 ± 2.4)E−5
57885	6	21.29	+0.19	26	4.8	2.8	7.2	6.0 ± 1.7	0.09	(3.2 ± 1.8)E+4	(0.6 ± 9.4)E+2	13 ± 4	61 ± 49	24 ± 2	(4.3 ± 1.9)E−6
57988	1	21.19	−0.12	65	3.9	1.1	2.2	7.6 ± 0.4	0.26	(1.2 ± 0.1)E+4	(2.7 ± 7.6)E+1	12.2 ± 0.7	26 ± 4	5.6 ± 0.3	(1.8 ± 1.1)E−6
58032	9	21.30	+0.01	74	7.1	4.0	2.7	7.6 ± 0.4	0.04	(1.6 ± 0.2)E+5	(0.4 ± 5.0)E+2	24 ± 1	85 ± 14	1.26 ± 0.05	(6.5 ± 2.6)E−6
58080	2	21.22	−0.14	92	3.7	2.2	4.5	7.6 ± 0.4	0.13	(2.6 ± 0.3)E+4	(0.5 ± 1.5)E+2	12.8 ± 0.7	50 ± 8	11.4 ± 0.5	(8.4 ± 5.1)E−6
58292	8	20.49	−0.14	54	4.5	2.2	13.0	7.8 ± 0.4	0.07	(6.1 ± 0.6)E+4	(0.7 ± 2.8)E+2	15.2 ± 0.8	84 ± 12	49 ± 1	(1.5 ± 0.6)E−5
58875	5	19.66	−0.24	41	3.9	2.6	5.3	7.8 ± 0.4	0.36	(7.1 ± 0.7)E+4	(1.0 ± 3.5)E+2	14.2 ± 0.7	112 ± 16	6.6 ± 0.2	(1.8 ± 0.5)E−4
59293	14	20.87	−0.06	33	12.0	4.8	5.6	7.8 ± 0.4	0.04	(1.8 ± 0.2)E+5	(0.1 ± 3.1)E+2	39 ± 2	36 ± 5	8.2 ± 0.2	(8.8 ± 5.5)E−5
60338	4	20.83	+0.14	58	4.0	1.7	3.8	7.8 ± 0.4	0.26	(1.6 ± 0.2)E+4	(2.7 ± 8.3)E+1	13.3 ± 0.7	29 ± 4	14.0 ± 0.5	(5.0 ± 3.0)E−6
60612	14	20.45	+0.03	77	14.0	3.2	5.4	7.8 ± 0.4	0.04	(2.7 ± 0.3)E+5	(0.1 ± 4.2)E+2	44 ± 2	44 ± 6	5.4 ± 0.1	(1.2 ± 0.8)E−4
61310	25	19.83	−0.12	63	12.4	6.7	6.5	7.8 ± 0.4	0.09	(4.3 ± 0.4)E+5	(0.2 ± 6.9)E+2	43 ± 2	73 ± 11	5.0 ± 0.1	(3.1 ± 1.3)E−4
61476	1	19.32	−0.18	37	5.1	1.5	3.1	7.0 ± 0.5	0.08	(1.3 ± 0.2)E+4	(1.7 ± 8.8)E+1	15 ± 1	19 ± 4	12.8 ± 0.4	(5.7 ± 2.8)E−7
61609	13	19.44	+0.05	25	13.9	6.4	2.4	7.0 ± 0.5	0.03	(4.2 ± 0.6)E+5	(0.0 ± 1.0)E+3	42 ± 3	77 ± 16	0.66 ± 0.02	(1.8 ± 0.9)E−4
62233	3	18.33	−0.30	65	5.4	2.1	2.5	5.7 ± 0.4	0.06	(8.8 ± 1.3)E+4	(1.6 ± 6.7)E+2	13 ± 1	165 ± 35	1.05 ± 0.02	(1.1 ± 0.9)E−4

Continuation of Table B1

COHRS catalog #	# clumps	ℓ (deg)	b (deg)	$v_{\rm LSR}$ (km s^{-1})	$\sigma_{\rm maj}$ (arcmin)	$\sigma_{\rm min}$ (arcmin)	$v_{\rm RMS}$ (km s^{-1})	$d_\odot$ (kpc)	CFE	M (M$_\odot$)	n (cm^{-3})	R (pc)	Σ (M$_\odot$ pc^{-2})	$\alpha_{\rm vir}$	SFR (M$_\odot$ yr^{-1})
62313	4	18.68	−0.40	65	3.5	2.3	2.6	5.7 ± 0.4	0.06	(4.0 ± 0.6)E+4	(1.9 ± 4.2)E+2	9.4 ± 0.7	143 ± 30	1.84 ± 0.06	(6.9 ± 2.1)E−6
62708	4	17.91	+0.06	41	4.7	2.7	6.3	8.1 ± 3.9	0.12	(3.3 ± 3.1)E+4	(0.0 ± 1.2)E+3	17 ± 8	35 ± 48	24 ± 5	(4.7 ± 2.0)E−6
62744	6	17.61	+0.06	39	5.4	2.6	5.2	8.1 ± 3.9	0.04	(6.9 ± 6.6)E+4	(0.0 ± 2.3)E+3	19 ± 9	59 ± 80	9 ± 2	(2.3 ± 0.8)E−5
62785	11	18.16	+0.02	50	4.7	3.1	3.3	5.7 ± 0.4	0.10	(4.8 ± 0.7)E+4	(0.9 ± 3.7)E+2	12.8 ± 0.9	94 ± 20	3.39 ± 0.06	(1.2 ± 0.4)E−5
62805	7	18.64	−0.27	42	5.4	2.6	2.0	5.7 ± 0.4	0.20	(4.5 ± 0.7)E+4	(0.7 ± 3.3)E+2	14 ± 1	77 ± 16	1.41 ± 0.03	(1.0 ± 0.3)E−5
62885	35	18.21	−0.29	48	13.0	4.5	3.9	5.7 ± 0.4	0.09	(4.4 ± 0.6)E+5	(0.1 ± 1.4)E+3	31 ± 2	146 ± 31	1.25 ± 0.02	(4.1 ± 0.7)E−4
62971	1	18.91	−0.41	24	3.5	1.2	1.6	8.1 ± 5.9	0.07	(1.2 ± 1.7)E+4	(0.3 ± 9.7)E+2	12 ± 9	27 ± 55	3.0 ± 0.9	(6.4 ± 4.0)E−5
63606	33	18.91	−0.28	60	12.4	4.3	9.7	5.7 ± 0.4	0.09	(4.3 ± 0.6)E+5	(0.1 ± 1.5)E+3	30 ± 2	157 ± 33	7.4 ± 0.1	(2.8 ± 0.6)E−4
63718	7	17.79	−0.14	49	3.4	1.8	3.2	5.7 ± 0.4	0.13	(1.6 ± 0.2)E+4	(1.0 ± 1.8)E+2	8.6 ± 0.6	66 ± 14	6.4 ± 0.1	(5.6 ± 1.3)E−7
63783	24	17.21	−0.21	44	8.9	4.7	5.8	6.4 ± 0.6	0.07	(2.4 ± 0.5)E+5	(0.1 ± 1.3)E+3	25 ± 3	121 ± 34	4.1 ± 0.1	(4.6 ± 1.5)E−5
63972	24	16.94	+0.34	22	7.5	5.6	2.1	6.4 ± 0.6	0.05	(4.8 ± 1.0)E+5	(0.1 ± 2.7)E+3	23 ± 2	277 ± 78	0.244 ± 0.006	(8.9 ± 1.2)E−5
64017	19	17.60	+0.22	21	9.7	5.9	2.5	6.4 ± 0.6	0.09	(2.1 ± 0.4)E+5	(0.0 ± 1.0)E+3	28 ± 3	85 ± 24	0.93 ± 0.02	(9.4 ± 1.8)E−5
64271	10	15.88	−0.06	23	7.8	3.2	3.0	5.5 ± 0.4	0.15	(2.3 ± 0.3)E+4	(0.2 ± 1.3)E+2	18 ± 1	22 ± 5	8.1 ± 0.1	(5.6 ± 2.6)E−6
64385	1	16.62	+0.27	44	4.7	1.2	1.0	5.5 ± 0.4	0.06	(4.3 ± 0.6)E+3	(1.5 ± 4.1)E+1	10.5 ± 0.8	12 ± 3	2.68 ± 0.07	(3.3 ± 1.8)E−7
64405	23	16.11	+0.39	21	9.9	3.9	5.4	5.5 ± 0.4	0.08	(1.1 ± 0.2)E+5	(0.4 ± 4.7)E+2	23 ± 2	65 ± 14	7.1 ± 0.1	(1.1 ± 0.2)E−5
64461	1	16.86	−0.45	46	3.9	0.8	1.7	5.5 ± 0.4	0.02	(1.0 ± 0.2)E+4	(0.6 ± 1.2)E+2	8.7 ± 0.6	44 ± 9	2.68 ± 0.05	(7.6 ± 2.6)E−7
64896	26	16.46	−0.28	45	9.7	4.1	2.3	5.5 ± 0.4	0.08	(2.6 ± 0.4)E+5	(0.1 ± 1.1)E+3	23 ± 2	158 ± 33	0.54 ± 0.01	(7.9 ± 2.0)E−5
64921	4	15.48	+0.23	47	3.4	1.2	1.6	5.5 ± 0.4	0.44	(1.2 ± 0.2)E+4	(1.0 ± 1.5)E+2	7.8 ± 0.6	62 ± 13	1.94 ± 0.03	(4.7 ± 1.2)E−6
64989	2	16.84	−0.29	40	4.3	1.1	2.5	5.5 ± 0.4	0.10	(1.0 ± 0.2)E+4	(0.5 ± 1.1)E+2	9.6 ± 0.7	35 ± 7	6.7 ± 0.1	(2.4 ± 1.5)E−6
65090	2	16.87	+0.09	51	6.8	2.4	8.6	5.5 ± 0.4	0.05	(2.3 ± 0.3)E+4	(0.3 ± 1.5)E+2	15 ± 1	31 ± 6	57.4 ± 0.8	(1.6 ± 0.8)E−5
65257	2	15.65	+0.40	48	3.2	2.4	1.9	5.5 ± 0.4	0.07	(8.6 ± 1.3)E+3	(0.5 ± 1.0)E+2	8.6 ± 0.6	37 ± 8	4.41 ± 0.07	(1.7 ± 0.6)E−6
65332	5	16.46	+0.34	33	5.3	3.7	4.9	5.5 ± 0.4	0.05	(2.7 ± 0.4)E+4	(0.4 ± 1.9)E+2	14 ± 1	45 ± 9	14.5 ± 0.2	(1.5 ± 0.6)E−6
65506	3	16.58	−0.10	36	4.6	1.2	3.6	5.5 ± 0.4	0.16	(1.2 ± 0.2)E+4	(0.4 ± 1.1)E+2	10.3 ± 0.8	35 ± 7	13.6 ± 0.2	(2.6 ± 1.1)E−6
65666	4	15.53	−0.42	39	5.7	3.0	2.9	5.5 ± 0.4	0.07	(4.1 ± 0.6)E+4	(0.6 ± 3.0)E+2	14 ± 1	68 ± 14	3.41 ± 0.06	(1.3 ± 0.8)E−5
66032	9	16.30	−0.40	20	9.6	6.4	4.9	5.5 ± 0.4	0.09	(7.8 ± 1.2)E+4	(0.2 ± 3.1)E+2	25 ± 2	40 ± 8	8.8 ± 0.1	(4.1 ± 2.0)E−5
66707	1	17.12	+0.03	70	3.4	1.1	1.8	8.1 ± 4.8	0.46	(5.8 ± 6.8)E+3	(0.2 ± 4.1)E+2	11 ± 7	14 ± 24	8 ± 2	(2.5 ± 1.3)E−6
66998	2	16.84	−0.06	68	6.6	1.8	1.6	5.5 ± 0.4	0.09	(1.4 ± 0.2)E+4	(1.7 ± 9.4)E+1	15 ± 1	20 ± 4	3.03 ± 0.06	(2.4 ± 1.6)E−6
67240	1	15.50	+0.21	27	3.0	3.4	2.5	5.5 ± 0.4	0.02	(1.2 ± 0.2)E+4	(0.5 ± 1.2)E+2	9.7 ± 0.7	39 ± 8	6.1 ± 0.1	(5.0 ± 2.7)E−6
67670	12	16.84	−0.26	24	7.7	5.0	3.8	5.5 ± 0.4	0.01	(1.6 ± 0.2)E+5	(0.8 ± 8.1)E+2	20 ± 1	130 ± 27	2.07 ± 0.03	(3.8 ± 1.9)E−5
68082	3	16.25	+0.01	24	3.4	2.1	1.1	5.5 ± 0.4	0.06	(1.4 ± 0.2)E+4	(0.9 ± 1.6)E+2	8.6 ± 0.6	59 ± 13	0.85 ± 0.06	(3.0 ± 1.6)E−6
68117	3	16.60	−0.06	57	5.4	2.8	3.1	5.5 ± 0.4	0.12	(3.1 ± 0.5)E+4	(0.6 ± 2.4)E+2	13 ± 1	58 ± 12	4.82 ± 0.08	(1.0 ± 0.5)E−5
69018	5	15.93	+0.22	28	11.8	3.7	2.9	5.5 ± 0.4	0.03	(3.6 ± 0.5)E+4	(0.1 ± 1.4)E+2	27 ± 2	16 ± 3	7.4 ± 0.1	(5.5 ± 1.7)E−7
69166	4	16.77	+0.05	29	3.9	2.0	4.5	5.5 ± 0.4	0.11	(2.0 ± 0.3)E+4	(1.0 ± 2.2)E+2	9.4 ± 0.7	73 ± 15	10.6 ± 0.2	(7.0 ± 3.0)E−6
69546	5	16.17	−0.30	41	3.4	1.5	3.2	4.9 ± 0.6	0.04	(2.2 ± 0.5)E+4	(2.4 ± 4.8)E+2	7.1 ± 0.8	136 ± 44	3.93 ± 0.07	(1.5 ± 0.5)E−6
69572	3	15.44	−0.08	48	4.7	1.5	2.4	4.9 ± 0.6	0.13	(9.5 ± 2.2)E+3	(0.5 ± 1.6)E+2	9 ± 1	35 ± 11	6.4 ± 0.1	(1.9 ± 1.0)E−6
69761	26	15.75	−0.32	52	13.1	4.9	10.1	4.9 ± 0.6	0.05	(1.2 ± 0.3)E+5	(0.3 ± 7.2)E+2	27 ± 3	56 ± 18	25.5 ± 0.4	(7.6 ± 2.3)E−6
69835	5	15.24	−0.17	15	4.0	1.7	1.5	4.9 ± 0.6	0.43	(5.8 ± 1.3)E+3	(0.4 ± 1.1)E+2	8.2 ± 0.9	28 ± 9	3.71 ± 0.06	(2.6 ± 1.2)E−7
69836	5	15.25	−0.45	19	5.1	2.2	1.9	4.9 ± 0.6	0.09	(4.5 ± 1.0)E+4	(1.5 ± 6.5)E+2	11 ± 1	128 ± 42	1.02 ± 0.02	(4.7 ± 1.4)E−5
70160	3	15.32	+0.22	20	4.4	0.9	· · ·	4.9 ± 0.6	0.10	(3.0 ± 0.7)E+3	(1.9 ± 5.4)E+1	9 ± 1	13 ± 4	· · ·	(5.7 ± 1.5)E−7
70493	21	14.52	+0.34	19	10.8	3.8	6.2	4.5 ± 0.3	0.08	(5.6 ± 0.7)E+4	(0.3 ± 2.3)E+2	20 ± 1	43 ± 8	16.5 ± 0.1	(1.4 ± 0.2)E−5
70825	17	13.89	+0.24	47	5.6	3.6	2.0	4.5 ± 0.3	0.15	(6.1 ± 0.8)E+4	(1.5 ± 4.4)E+2	11.8 ± 0.8	138 ± 25	0.899 ± 0.008	(5.8 ± 1.0)E−5
71144	16	14.05	−0.43	19	10.0	3.0	2.8	4.5 ± 0.3	0.04	(1.9 ± 0.2)E+5	(1.2 ± 8.9)E+2	19 ± 1	178 ± 32	0.894 ± 0.009	(2.2 ± 0.4)E−5
71167	2	13.98	−0.15	17	5.5	1.7	1.7	4.5 ± 0.3	0.04	(1.4 ± 0.2)E+4	(0.5 ± 1.2)E+2	10.2 ± 0.6	43 ± 8	2.53 ± 0.04	(5.0 ± 3.6)E−5
71532	6	14.61	−0.06	38	4.7	3.9	2.4	4.5 ± 0.3	0.02	(5.9 ± 0.8)E+4	(1.9 ± 4.7)E+2	10.8 ± 0.7	161 ± 29	1.27 ± 0.02	(2.7 ± 1.2)E−5
72525	34	14.23	−0.16	39	12.2	3.9	2.8	4.5 ± 0.3	0.07	(4.3 ± 0.5)E+5	(0.1 ± 1.6)E+3	23 ± 1	258 ± 46	0.498 ± 0.005	(1.4 ± 0.3)E−4
72909	12	14.67	−0.31	59	8.9	4.8	2.2	4.5 ± 0.3	0.10	(4.9 ± 0.6)E+4	(0.3 ± 2.3)E+2	18 ± 1	48 ± 9	2.09 ± 0.03	(5.6 ± 2.9)E−6
74066	9	14.66	−0.41	20	8.9	5.0	3.3	4.5 ± 0.3	0.08	(6.7 ± 0.9)E+4	(0.5 ± 3.2)E+2	18 ± 1	65 ± 12	3.44 ± 0.03	(8.0 ± 3.4)E−6
74969	5	14.51	−0.05	63	15.4	2.2	4.5	4.5 ± 0.3	0.08	(2.7 ± 0.3)E+4	(0.5 ± 8.3)E+1	28 ± 2	11 ± 2	24.1 ± 0.2	(7.6 ± 5.2)E−5
74998	14	14.92	−0.01	26	6.3	5.2	3.1	4.5 ± 0.3	0.07	(7.2 ± 0.9)E+4	(1.0 ± 4.2)E+2	14.5 ± 0.9	109 ± 20	2.25 ± 0.02	(1.5 ± 0.6)E−5
75133	32	12.78	−0.20	35	14.0	5.9	2.7	4.2 ± 0.3	0.25	(2.4 ± 0.3)E+5	(0.6 ± 8.1)E+2	25 ± 2	119 ± 22	0.900 ± 0.007	(4.7 ± 0.9)E−4
75161	17	13.44	−0.03	14	18.5	8.9	4.7	4.2 ± 0.3	0.02	(2.7 ± 0.4)E+5	(0.3 ± 7.0)E+2	34 ± 2	75 ± 14	3.14 ± 0.02	(2.0 ± 0.6)E−5
75162	10	13.68	−0.27	15	7.9	4.3	4.2	4.2 ± 0.3	0.01	(1.6 ± 0.2)E+5	(1.9 ± 9.1)E+2	15 ± 1	226 ± 41	1.91 ± 0.02	(8.0 ± 3.6)E−6
75208	8	12.82	+0.41	18	9.1	3.6	1.5	4.2 ± 0.3	0.07	(9.1 ± 1.2)E+4	(0.9 ± 4.9)E+2	16 ± 1	110 ± 20	0.491 ± 0.004	(5.6 ± 1.5)E−5
75322	12	13.30	−0.33	38	6.1	3.8	2.8	4.2 ± 0.3	0.10	(6.8 ± 0.9)E+4	(1.6 ± 5.0)E+2	11.9 ± 0.8	153 ± 28	1.64 ± 0.02	(2.8 ± 1.4)E−6
75375	15	13.11	−0.07	51	8.8	3.7	4.6	4.2 ± 0.3	0.09	(2.2 ± 0.3)E+5	(0.2 ± 1.2)E+3	16 ± 1	280 ± 51	1.79 ± 0.01	(6.6 ± 2.1)E−5
75384	6	12.21	−0.23	50	4.8	2.1	4.9	4.5 ± 0.3	0.07	(1.3 ± 0.2)E+4	(0.7 ± 1.3)E+2	9.3 ± 0.6	49 ± 10	19.5 ± 0.2	(1.5 ± 0.8)E−5
76716	6	12.22	+0.01	47	6.5	3.3	2.6	4.5 ± 0.3	0.09	(2.6 ± 0.4)E+4	(0.5 ± 1.9)E+2	13.0 ± 0.9	49 ± 10	3.84 ± 0.04	(1.1 ± 0.6)E−5
77060	2	12.86	−0.01	50	4.3	2.5	2.6	4.5 ± 0.3	0.06	(4.4 ± 0.6)E+4	(2.6 ± 4.7)E+2	8.9 ± 0.6	179 ± 35	1.63 ± 0.03	(1.0 ± 0.4)E−5

Continuation of Table B1

COHRS catalog #	# clumps	ℓ (deg)	b (deg)	$v_{\rm LSR}$ (km s^{-1})	$\sigma_{\rm maj}$ (arcmin)	$\sigma_{\rm min}$ (arcmin)	$v_{\rm RMS}$ (km s^{-1})	$d_{\odot}$ (kpc)	CFE	M (M$_{\odot}$)	n (cm^{-3})	R (pc)	Σ (M$_{\odot}$ pc^{-2})	$\alpha_{\rm vir}$	SFR (M$_{\odot}$ yr^{-1})
78512	5	12.94	+0.43	32	3.7	2.4	1.5	4.5 ± 0.3	0.41	(2.1 ± 0.3)E+4	(1.7 ± 2.5)E+2	7.8 ± 0.5	107 ± 21	1.03 ± 0.01	(1.8 ± 0.6)E–5
78679	3	12.20	+0.14	38	3.5	1.4	3.5	4.5 ± 0.3	0.13	(9.6 ± 1.3)E+3	(1.3 ± 1.4)E+2	6.6 ± 0.5	70 ± 14	9.89 ± 0.09	(3.0 ± 1.5)E–6
80328	3	12.66	−0.29	11	5.6	2.9	3.4	4.5 ± 0.3	0.05	(3.5 ± 0.5)E+4	(1.0 ± 2.9)E+2	11.2 ± 0.8	88 ± 17	4.31 ± 0.04	(1.1 ± 0.5)E–5
82207	19	11.85	−0.19	45	14.8	4.9	7.1	5.0 ± 0.6	0.07	(1.7 ± 0.4)E+5	(0.2 ± 8.8)E+2	31 ± 4	56 ± 19	10.8 ± 0.2	(9.2 ± 3.6)E–5
82236	16	11.49	+0.22	31	9.3	3.6	2.4	5.0 ± 0.6	0.05	(5.5 ± 1.3)E+4	(0.3 ± 4.5)E+2	20 ± 2	45 ± 15	2.46 ± 0.05	(3.1 ± 1.2)E–6
82293	11	11.86	−0.13	9	9.7	6.9	5.9	5.0 ± 0.6	0.07	(5.9 ± 1.4)E+4	(0.2 ± 4.1)E+2	24 ± 3	34 ± 12	16.1 ± 0.3	(5.8 ± 3.9)E–5
82671	7	10.44	+0.01	67	6.1	3.8	7.2	6.4 ± 0.6	0.17	(1.7 ± 0.3)E+5	(0.1 ± 1.2)E+3	18 ± 2	164 ± 44	6.5 ± 0.2	(1.9 ± 0.8)E–4
83048	10	11.09	−0.35	33	8.2	7.0	3.0	6.4 ± 0.6	0.04	(2.4 ± 0.5)E+5	(0.0 ± 1.1)E+3	27 ± 3	104 ± 28	1.21 ± 0.04	(1.4 ± 0.6)E–7
84131	9	10.34	−0.18	12	6.7	4.9	5.3	6.4 ± 0.6	0.15	(3.0 ± 0.6)E+5	(0.1 ± 1.8)E+3	21 ± 2	216 ± 58	2.34 ± 0.06	(3.6 ± 1.0)E–4
84734	20	10.71	−0.06	31	10.7	3.5	6.4	6.4 ± 0.6	0.05	(5.5 ± 1.0)E+5	(0.1 ± 2.4)E+3	28 ± 3	215 ± 57	2.51 ± 0.07	(9.4 ± 4.8)E–5
84999	9	10.98	+0.01	23	4.8	2.7	6.9	6.4 ± 0.6	0.26	(4.3 ± 0.8)E+4	(0.7 ± 3.9)E+2	14 ± 1	71 ± 19	18.0 ± 0.5	(3.5 ± 1.1)E–5

End of Table

Table B2 shows Hi-GAL clump properties. The first column lists the COHRS cloud catalog number to which the clump – whose catalog number is listed in the second column – is associated. Only the first instance of each cloud is listed. All subsequent clumps are matched to the same cloud until a new COHRS catalog number is given. The quantities (ℓ, b) locate the centroid of the clump's gaussian profile fit, in Galactic coordinates. $v_{\rm LSR}$ are velocities extracted from ^{13}CO(1-0) using GRS, or from pointed observations of other dense gas tracers, originally made for BGPS. Where a $v_{\rm LSR}$ is listed, the clumps was matched to the cloud using velocities. Where there is no velocity, the COHRS dendrograms were used. See Section 4.3.1 for more details on our matching methods. The angular radii $\theta_{\rm R}$ also come from the gaussian profile fit, deconvolved from the beam. The remaining columns contain physical properties of the clumps: M is the mass derived from integrated flux density at 500 μm, n is the number density, and R is the effective radius. Instead of using individual clump distances to calculate these properties, the host cloud's distance is used. In this way, clump mass fractions are distance-independent. Uncertainties given for M and n refer only to photometric errors. We estimate systematic uncertainties of a factor of two. See Section 4.3.2 for more information on physical property calculations.

Table B2: Hi-GAL – COHRS Catalog: Hi-GAL Properties

COHRS catalog #	Hi-GAL catalog #	ℓ (deg)	b (deg)	$v_{\rm LSR}$ (km s^{-1})	$\theta_{\rm R}$ (arcmin)	M (M$_\odot$)	n (cm^{-3})	R (pc)
32	19442	54.99	+0.15	39	2.3	(3.63 ± 0.02)E+2	(4.15 ± 0.02)E+1	3.3
···	19458	54.86	+0.19	39	2.5	(3.44 ± 0.02)E+2	(3.19 ± 0.02)E+1	3.5
···	19467	54.95	+0.20	38	1.4	(1.13 ± 0.01)E+2	(5.31 ± 0.06)E+1	2.0
···	19468	54.81	+0.21	39	1.6	(1.67 ± 0.02)E+2	(5.29 ± 0.05)E+1	2.3
···	19477	54.76	+0.24	40	2.0	(1.25 ± 0.02)E+2	(2.25 ± 0.03)E+1	2.8
···	19488	54.73	+0.24	40	0.6	(1.82 ± 0.07)E+1	(9.3 ± 0.4)E+1	0.9
···	19455	54.99	+0.18	···	1.1	(9.0 ± 0.1)E+1	(8.9 ± 0.1)E+1	1.6
48	19141	54.35	−0.50	34	1.5	(1.28 ± 0.01)E+2	(5.13 ± 0.05)E+1	2.2
···	19144	54.37	−0.48	34	0.6	(5.27 ± 0.07)E+1	(2.87 ± 0.04)E+2	0.9
···	19152	54.45	−0.46	35	2.0	(1.07 ± 0.02)E+2	(1.69 ± 0.02)E+1	2.9
···	19153	54.48	−0.46	36	0.4	(7.1 ± 0.6)E+1	(1.9 ± 0.2)E+2	0.5
···	19167	54.38	−0.43	36	2.5	(7.17 ± 0.02)E+2	(6.18 ± 0.02)E+1	3.6
52	19140	54.65	−0.49	37	0.3	(1.87 ± 0.05)E+1	(7.0 ± 0.2)E+2	0.5
···	19158	54.74	−0.44	38	1.2	(2.34 ± 0.01)E+2	(1.800 ± 0.009)E+2	1.7
···	19170	54.77	−0.42	38	1.0	(9.99 ± 0.09)E+1	(1.52 ± 0.01)E+2	1.4
···	19173	54.83	−0.41	41	1.1	(1.57 ± 0.01)E+2	(1.77 ± 0.01)E+2	1.5
···	19186	54.75	−0.39	40	2.1	(6.77 ± 0.02)E+2	(9.49 ± 0.03)E+1	3.1
···	19196	54.86	−0.34	41	···	(4.5 ± 0.4)E+0	···	···
···	19211	54.89	−0.31	38	0.6	(1.80 ± 0.06)E+1	(1.07 ± 0.04)E+2	0.9
···	19148	54.69	−0.47	···	1.6	(3.25 ± 0.02)E+2	(1.103 ± 0.005)E+2	2.3
···	19147	54.65	−0.47	···	···	(1.65 ± 0.05)E+1	···	···
···	19156	54.62	−0.47	···	2.1	(1.83 ± 0.02)E+2	(2.83 ± 0.03)E+1	3.0
···	19174	54.71	−0.42	···	0.8	(1.178 ± 0.009)E+2	(3.46 ± 0.03)E+2	1.1
···	19203	54.84	−0.32	···	1.0	(1.38 ± 0.01)E+2	(1.89 ± 0.01)E+2	1.4
···	19206	54.97	−0.32	···	···	(1.03 ± 0.05)E+1	···	···
···	19207	54.95	−0.32	···	0.3	(1.06 ± 0.05)E+1	(4.8 ± 0.2)E+2	0.4
531	19201	54.36	−0.33	35	0.7	(4.65 ± 0.08)E+1	(1.88 ± 0.03)E+2	1.0
···	19204	54.33	−0.34	36	1.5	(1.21 ± 0.01)E+2	(4.49 ± 0.05)E+1	2.2
···	19252	54.34	−0.25	37	1.9	(2.43 ± 0.02)E+2	(4.99 ± 0.03)E+1	2.7
···	19254	54.28	−0.23	37	0.7	(5.00 ± 0.08)E+1	(1.90 ± 0.03)E+2	1.0

Continuation of Table B2

COHRS catalog #	Hi-GAL catalog #	ℓ (deg)	b (deg)	$v_{\rm LSR}$ (km s^{-1})	$\theta_{\rm R}$ (arcmin)	M ($M_\odot$)	n (cm^{-3})	R (pc)
···	19256	54.30	−0.23	36	0.7	(3.67 ± 0.08)E+1	(1.24 ± 0.03)E+2	1.1
···	19261	54.34	−0.22	37	1.3	(2.05 ± 0.01)E+2	(1.286 ± 0.008)E+2	1.9
···	19262	54.40	−0.22	39	1.2	(1.00 ± 0.01)E+2	(7.13 ± 0.08)E+1	1.8
···	19273	54.37	−0.21	39	0.9	(4.92 ± 0.09)E+1	(9.0 ± 0.2)E+1	1.3
···	19244	54.39	−0.25	···	···	(2.92 ± 0.06)E+1	···	···
552	19387	54.84	+0.04	31	0.9	(4.15 ± 0.08)E+1	(8.8 ± 0.2)E+1	1.2
···	19394	54.77	+0.06	38	0.7	(1.88 ± 0.07)E+1	(6.2 ± 0.2)E+1	1.1
···	19397	54.80	+0.07	37	1.7	(6.1 ± 0.1)E+1	(1.66 ± 0.04)E+1	2.5
···	19411	54.74	+0.08	39	1.5	(5.1 ± 0.1)E+1	(1.93 ± 0.05)E+1	2.2
555	19538	55.12	+0.34	33	1.5	(1.86 ± 0.01)E+2	(7.15 ± 0.05)E+1	2.2
···	19568	55.14	+0.38	33	···	(1.16 ± 0.06)E+1	···	···
574	19355	54.44	−0.04	29	0.8	(6.3 ± 0.1)E+1	(7.9 ± 0.2)E+1	1.5
···	19356	54.39	−0.04	38	1.5	(1.112 ± 0.003)E+3	(2.217 ± 0.005)E+2	2.7
···	19375	54.44	+0.01	23	1.5	(1.45 ± 0.02)E+2	(2.76 ± 0.04)E+1	2.8
···	19408	54.45	+0.07	43	1.4	(5.8 ± 0.2)E+1	(1.22 ± 0.04)E+1	2.7
704	19605	55.11	+0.47	9	1.1	(8.3 ± 0.1)E+1	(9.6 ± 0.1)E+1	1.5
···	19597	55.21	+0.44	···	0.4	(1.58 ± 0.06)E+1	(3.0 ± 0.1)E+2	0.6
708	19572	54.47	+0.39	8	1.1	(1.15 ± 0.01)E+2	(1.27 ± 0.01)E+2	1.5
···	19583	54.37	+0.42	11	0.8	(1.32 ± 0.01)E+2	(3.72 ± 0.03)E+2	1.1
···	19599	54.51	+0.45	5	1.4	(9.0 ± 0.1)E+1	(4.22 ± 0.06)E+1	2.0
···	19621	54.40	+0.48	11	···	(1.28 ± 0.06)E+1	···	···
···	19613	54.51	+0.48	···	0.2	(8.4 ± 0.6)E+0	(1.36 ± 0.09)E+3	0.3
768	19352	54.60	−0.04	41	1.7	(1.17 ± 0.01)E+2	(3.56 ± 0.04)E+1	2.4
···	19390	54.57	+0.04	38	0.9	(3.38 ± 0.08)E+1	(6.8 ± 0.2)E+1	1.3
···	19402	54.60	+0.08	36	2.4	(1.47 ± 0.02)E+2	(1.45 ± 0.02)E+1	3.4
···	19367	54.59	+0.00	···	1.2	(5.4 ± 0.1)E+1	(4.38 ± 0.08)E+1	1.7
···	19389	54.64	+0.04	···	0.9	(1.82 ± 0.08)E+1	(3.5 ± 0.2)E+1	1.3
···	19395	54.63	+0.06	···	0.4	(1.77 ± 0.06)E+1	(4.4 ± 0.2)E+2	0.5
770	19192	55.06	−0.37	37	2.4	(2.00 ± 0.02)E+2	(2.24 ± 0.02)E+1	3.3
···	19197	55.10	−0.34	37	0.8	(1.032 ± 0.008)E+2	(3.43 ± 0.03)E+2	1.1
···	19218	55.15	−0.30	41	1.5	(1.235 ± 0.002)E+3	(5.669 ± 0.007)E+2	2.1
···	19226	55.23	−0.29	39	···	(1.48 ± 0.04)E+1	···	···
···	19251	55.18	−0.23	37	1.1	(4.12 ± 0.08)E+1	(4.57 ± 0.09)E+1	1.5
···	19269	55.22	−0.21	37	1.4	(1.40 ± 0.01)E+2	(8.63 ± 0.07)E+1	1.9
···	19223	55.04	−0.30	···	1.6	(6.9 ± 0.1)E+1	(2.56 ± 0.05)E+1	2.2
···	19250	55.24	−0.24	···	···	(9.4 ± 0.4)E+0	···	···
801	19513	54.37	+0.29	36	1.4	(6.0 ± 0.1)E+1	(2.91 ± 0.06)E+1	2.0
···	19479	54.41	+0.23	···	1.3	(3.1 ± 0.1)E+1	(1.97 ± 0.07)E+1	1.9
···	19480	54.37	+0.23	···	1.0	(4.5 ± 0.1)E+1	(6.6 ± 0.1)E+1	1.4
870	19323	54.72	−0.10	47	···	(4.3 ± 0.5)E+0	···	···
···	19337	54.69	−0.08	41	0.6	(4.68 ± 0.07)E+1	(3.68 ± 0.06)E+2	0.8
···	19345	54.75	−0.07	30	1.7	(2.30 ± 0.01)E+2	(6.38 ± 0.04)E+1	2.4
···	19346	54.68	−0.06	41	0.8	(5.64 ± 0.08)E+1	(1.72 ± 0.02)E+2	1.1
···	19319	54.77	−0.12	···	1.8	(1.42 ± 0.01)E+2	(3.54 ± 0.03)E+1	2.5
875	19417	55.09	+0.10	35	1.9	(1.96 ± 0.01)E+2	(4.21 ± 0.03)E+1	2.7
···	19433	55.07	+0.14	35	1.7	(1.81 ± 0.01)E+2	(5.16 ± 0.04)E+1	2.4
···	19445	55.22	+0.16	39	1.3	(6.7 ± 0.1)E+1	(4.80 ± 0.08)E+1	1.8
···	19447	55.15	+0.17	38	2.7	(8.50 ± 0.02)E+2	(6.17 ± 0.02)E+1	3.8
···	19475	55.17	+0.22	39	1.7	(1.79 ± 0.01)E+2	(4.75 ± 0.04)E+1	2.5
···	19418	55.17	+0.11	···	1.1	(8.0 ± 0.1)E+1	(9.4 ± 0.1)E+1	1.5
913	19227	54.93	−0.28	38	1.4	(7.7 ± 0.1)E+1	(4.09 ± 0.06)E+1	2.0
···	19253	54.94	−0.24	37	2.5	(4.76 ± 0.02)E+2	(4.40 ± 0.02)E+1	3.5
···	19257	55.01	−0.22	35	0.8	(6.40 ± 0.09)E+1	(1.74 ± 0.02)E+2	1.1
···	19302	54.86	−0.15	···	2.1	(2.31 ± 0.02)E+2	(3.60 ± 0.03)E+1	3.0
931	19275	55.08	−0.19	34	1.7	(9.6 ± 0.1)E+1	(3.22 ± 0.04)E+1	2.3
···	19304	55.09	−0.13	33	1.6	(6.2 ± 0.1)E+1	(2.48 ± 0.04)E+1	2.2
···	19326	55.05	−0.09	29	0.5	(2.97 ± 0.06)E+1	(3.88 ± 0.08)E+2	0.7
···	19333	55.09	−0.09	30	1.0	(5.04 ± 0.09)E+1	(7.5 ± 0.1)E+1	1.4
···	19298	55.18	−0.14	···	2.6	(3.56 ± 0.02)E+2	(3.24 ± 0.02)E+1	3.5
···	19328	55.15	−0.09	···	1.7	(7.0 ± 0.1)E+1	(2.37 ± 0.04)E+1	2.3
963	19193	54.18	−0.34	59	0.8	(4.00 ± 0.09)E+1	(9.8 ± 0.2)E+1	1.2
···	19200	54.20	−0.33	60	0.5	(8.7 ± 0.6)E+0	(8.3 ± 0.6)E+1	0.8
···	19224	54.12	−0.29	54	···	(2.12 ± 0.06)E+1	···	···
···	19208	54.06	−0.33	···	1.7	(3.28 ± 0.02)E+2	(8.68 ± 0.04)E+1	2.5
988	19270	54.25	−0.20	48	0.9	(1.39 ± 0.01)E+2	(2.00 ± 0.02)E+2	1.4
···	19277	54.27	−0.19	50	···	(1.01 ± 0.06)E+1	···	···
···	19325	54.25	−0.10	52	0.4	(4.25 ± 0.08)E+1	(4.60 ± 0.09)E+2	0.7
1084	19582	54.25	+0.41	18	1.1	(4.2 ± 0.1)E+1	(4.7 ± 0.1)E+1	1.5
1105	19220	54.25	−0.29	36	1.5	(1.52 ± 0.02)E+2	(4.35 ± 0.05)E+1	2.4
···	19247	54.21	−0.25	···	0.6	(2.44 ± 0.09)E+1	(8.6 ± 0.3)E+1	1.0
1146	19491	54.23	+0.26	32	1.7	(3.92 ± 0.02)E+2	(1.062 ± 0.004)E+2	2.5
···	19529	54.22	+0.33	37	1.7	(3.70 ± 0.02)E+2	(9.58 ± 0.04)E+1	2.5
···	19533	54.25	+0.32	36	0.7	(2.75 ± 0.07)E+1	(1.06 ± 0.03)E+2	1.0
···	19553	54.20	+0.36	44	1.4	(1.92 ± 0.01)E+2	(8.45 ± 0.06)E+1	2.1
···	19563	54.29	+0.39	44	1.4	(9.5 ± 0.1)E+1	(4.80 ± 0.06)E+1	2.0
1220	19290	54.09	−0.17	40	0.7	(9.2 ± 0.1)E+1	(2.22 ± 0.03)E+2	1.2
···	19307	54.04	−0.13	40	1.0	(2.10 ± 0.01)E+2	(2.13 ± 0.01)E+2	1.6
···	19316	54.22	−0.12	37	1.9	(7.73 ± 0.02)E+2	(1.003 ± 0.003)E+2	3.1
···	19334	54.11	−0.09	39	1.3	(2.258 ± 0.002)E+3	(9.598 ± 0.007)E+2	2.1
···	19341	54.10	−0.07	40	0.8	(8.89 ± 0.01)E+2	(1.758 ± 0.002)E+3	1.3
···	19344	54.13	−0.07	41	1.4	(2.035 ± 0.002)E+3	(6.253 ± 0.005)E+2	2.4
···	19350	54.08	−0.05	38	0.9	(8.87 ± 0.01)E+2	(1.265 ± 0.002)E+3	1.4
···	19351	54.11	−0.04	39	1.2	(1.568 ± 0.002)E+3	(7.960 ± 0.008)E+2	2.0
1223	19492	54.16	+0.26	−4	1.3	(5.6 ± 0.1)E+1	(3.80 ± 0.08)E+1	1.8

Continuation of Table B2

COHRS catalog #	Hi-GAL catalog #	ℓ (deg)	b (deg)	$v_{\rm LSR}$ (km s^{-1})	$\theta_{\rm R}$ (arcmin)	M (M$_\odot$)	n (cm^{-3})	R (pc)
···	19539	54.18	+0.32	−3	1.2	(9.1 ± 0.1)E+1	(7.9 ± 0.1)E+1	1.7
···	19511	54.18	+0.28	···	0.5	(2.58 ± 0.06)E+1	(2.70 ± 0.06)E+2	0.7
1707	18720	53.73	+0.44	23	1.0	(2.07 ± 0.02)E+2	(1.69 ± 0.01)E+2	1.7
···	18730	53.76	+0.48	24	2.5	(1.272 ± 0.004)E+3	(7.31 ± 0.02)E+1	4.1
···	18739	53.71	+0.50	24	···	(4.64 ± 0.08)E+1	···	···
···	18721	53.52	+0.45	···	···	(2.5 ± 0.1)E+1	···	···
1743	18594	53.42	+0.20	6	1.3	(1.05 ± 0.02)E+2	(5.40 ± 0.08)E+1	2.0
1758	19522	53.98	+0.28	24	1.7	(3.9 ± 0.1)E+1	(9.7 ± 0.3)E+0	2.5
···	19536	54.05	+0.33	34	1.8	(1.61 ± 0.02)E+2	(3.59 ± 0.04)E+1	2.6
···	19594	54.08	+0.42	34	1.9	(9.9 ± 0.1)E+1	(1.93 ± 0.03)E+1	2.7
···	19608	54.12	+0.47	35	0.9	(3.87 ± 0.08)E+1	(6.3 ± 0.1)E+1	1.4
···	19623	54.11	+0.49	35	1.2	(6.2 ± 0.1)E+1	(5.00 ± 0.09)E+1	1.7
1809	18521	53.32	+0.02	22	1.4	(7.76 ± 0.02)E+2	(2.515 ± 0.007)E+2	2.3
···	18534	53.30	+0.04	25	0.6	(2.71 ± 0.01)E+2	(1.324 ± 0.007)E+3	0.9
···	18535	53.24	+0.05	24	1.9	(2.144 ± 0.003)E+3	(2.663 ± 0.004)E+2	3.2
1821	18516	53.74	+0.01	24	1.3	(8.11 ± 0.02)E+2	(3.310 ± 0.009)E+2	2.1
···	18517	53.64	+0.01	24	1.9	(1.831 ± 0.003)E+3	(2.385 ± 0.004)E+2	3.1
···	18526	53.62	+0.03	23	1.2	(2.125 ± 0.002)E+3	(1.052 ± 0.001)E+3	2.0
···	18527	53.55	+0.03	24	1.0	(9.45 ± 0.02)E+2	(7.37 ± 0.01)E+2	1.7
···	18533	53.51	+0.04	23	0.8	(1.79 ± 0.01)E+2	(3.40 ± 0.03)E+2	1.3
···	18540	53.57	+0.05	24	1.8	(2.152 ± 0.002)E+3	(3.426 ± 0.004)E+2	2.9
···	18543	53.50	+0.06	22	0.5	(1.09 ± 0.01)E+2	(7.12 ± 0.08)E+2	0.9
···	18544	53.48	+0.06	22	0.5	(5.5 ± 0.1)E+1	(4.7 ± 0.1)E+2	0.8
···	18550	53.59	+0.07	26	1.2	(1.050 ± 0.002)E+3	(4.96 ± 0.01)E+2	2.0
···	18558	53.60	+0.10	24	0.2	(1.25 ± 0.01)E+2	(9.11 ± 0.08)E+3	0.4
1872	18600	53.63	+0.21	36	0.7	(7.02 ± 0.01)E+2	(1.883 ± 0.004)E+3	1.1
···	18617	53.62	+0.24	37	1.2	(9.46 ± 0.02)E+2	(5.35 ± 0.01)E+2	1.9
···	18625	53.64	+0.27	36	1.7	(6.93 ± 0.02)E+2	(1.355 ± 0.005)E+2	2.7
···	18626	53.60	+0.27	40	1.4	(5.68 ± 0.02)E+2	(1.756 ± 0.007)E+2	2.4
···	18629	53.57	+0.27	40	1.0	(3.74 ± 0.02)E+2	(2.89 ± 0.01)E+2	1.7
···	18638	53.72	+0.28	27	···	(9.4 ± 0.7)E+0	···	···
···	18658	53.76	+0.32	24	1.8	(1.53 ± 0.02)E+2	(2.44 ± 0.04)E+1	2.9
···	18674	53.61	+0.38	42	···	(2.7 ± 0.1)E+1	···	···
···	18689	53.63	+0.41	46	···	(8.5 ± 0.1)E+1	···	···
···	18693	53.66	+0.41	···	0.9	(1.03 ± 0.01)E+2	(1.23 ± 0.02)E+2	1.5
···	18706	53.64	+0.43	···	1.6	(3.06 ± 0.02)E+2	(6.60 ± 0.05)E+1	2.7
2012	19416	54.09	+0.10	−5	1.0	(2.27 ± 0.01)E+2	(3.10 ± 0.01)E+2	1.4
···	19464	54.06	+0.20	−4	1.2	(3.5 ± 0.1)E+1	(2.96 ± 0.08)E+1	1.7
···	19430	54.07	+0.13	···	1.4	(3.06 ± 0.01)E+2	(1.322 ± 0.006)E+2	2.1
2388	19415	54.12	+0.10	32	···	(2.42 ± 0.07)E+1	···	···
···	19424	54.03	+0.12	33	0.5	(4.64 ± 0.08)E+1	(3.25 ± 0.06)E+2	0.8
···	19434	54.10	+0.14	31	1.1	(2.23 ± 0.01)E+2	(1.580 ± 0.009)E+2	1.8
···	19436	54.18	+0.15	30	0.7	(5.8 ± 0.1)E+1	(1.38 ± 0.03)E+2	1.2
···	19437	54.13	+0.14	32	1.0	(2.30 ± 0.01)E+2	(2.26 ± 0.01)E+2	1.6
···	19449	54.15	+0.16	33	1.1	(3.97 ± 0.02)E+2	(2.52 ± 0.01)E+2	1.9
2630	18556	53.78	+0.11	51	1.1	(2.6 ± 0.1)E+1	(1.9 ± 0.1)E+1	1.8
···	18563	53.80	+0.13	52	0.4	(1.8 ± 0.1)E+1	(1.8 ± 0.1)E+2	0.7
···	18568	53.83	+0.15	52	1.4	(9.5 ± 0.2)E+1	(3.18 ± 0.07)E+1	2.3
···	18582	53.81	+0.17	52	0.7	(2.3 ± 0.1)E+1	(6.7 ± 0.3)E+1	1.1
2812	18508	53.45	+0.01	42	2.1	(8.66 ± 0.03)E+2	(1.252 ± 0.004)E+2	3.0
2964	18408	53.78	−0.19	47	···	(3.03 ± 0.09)E+1	···	···
···	18410	53.84	−0.19	46	···	(4.05 ± 0.08)E+1	···	···
···	18417	53.81	−0.17	47	1.5	(5.53 ± 0.02)E+2	(1.515 ± 0.006)E+2	2.5
···	18436	53.67	−0.12	43	1.4	(2.84 ± 0.02)E+2	(8.86 ± 0.07)E+1	2.3
···	18439	53.79	−0.12	49	1.3	(3.92 ± 0.02)E+2	(1.788 ± 0.009)E+2	2.1
···	18441	53.74	−0.11	46	0.9	(1.38 ± 0.02)E+2	(1.66 ± 0.02)E+2	1.5
···	18452	53.80	−0.10	46	0.5	(1.51 ± 0.01)E+2	(9.14 ± 0.07)E+2	0.9
···	18464	53.66	−0.08	43	···	(2.8 ± 0.1)E+1	···	···
···	18467	53.71	−0.08	42	1.0	(2.87 ± 0.02)E+2	(2.25 ± 0.01)E+2	1.7
···	18473	53.82	−0.07	44	0.6	(5.31 ± 0.02)E+2	(2.446 ± 0.007)E+3	1.0
···	18432	53.70	−0.12	···	···	(5.3 ± 0.1)E+1	···	···
3011	18587	53.18	+0.17	6	1.6	(4.235 ± 0.004)E+3	(4.102 ± 0.004)E+2	3.5
···	18601	53.19	+0.21	1	1.2	(1.456 ± 0.004)E+3	(3.731 ± 0.009)E+2	2.5
···	18604	53.16	+0.21	3	1.0	(7.73 ± 0.03)E+2	(3.38 ± 0.01)E+2	2.1
3021	18356	53.17	−0.30	43	1.2	(2.74 ± 0.03)E+2	(7.42 ± 0.08)E+1	2.5
···	18419	53.19	−0.16	40	0.6	(4.9 ± 0.2)E+1	(1.14 ± 0.04)E+2	1.2
···	18431	53.35	−0.12	43	2.2	(4.74 ± 0.04)E+2	(1.79 ± 0.02)E+1	4.7
···	18433	53.30	−0.12	43	1.2	(3.90 ± 0.03)E+2	(1.035 ± 0.008)E+2	2.5
···	18373	53.27	−0.26	···	1.5	(2.09 ± 0.03)E+2	(2.80 ± 0.04)E+1	3.1
···	18434	53.21	−0.13	···	0.9	(2.90 ± 0.03)E+2	(1.45 ± 0.01)E+2	2.0
3045	18338	53.31	−0.33	58	0.3	(3.0 ± 0.2)E+1	(7.3 ± 0.4)E+2	0.5
···	18350	53.44	−0.31	58	1.8	(1.004 ± 0.005)E+3	(6.99 ± 0.03)E+1	3.9
···	18360	53.41	−0.29	57	2.3	(1.583 ± 0.006)E+3	(5.63 ± 0.02)E+1	4.8
···	18371	53.35	−0.26	58	1.9	(4.40 ± 0.04)E+2	(2.55 ± 0.03)E+1	4.1
···	18381	53.16	−0.24	61	1.4	(2.284 ± 0.004)E+3	(3.773 ± 0.007)E+2	2.9
···	18388	53.13	−0.22	61	0.6	(1.81 ± 0.02)E+2	(2.87 ± 0.03)E+2	1.4
···	18420	52.96	−0.16	59	0.5	(6.3 ± 0.2)E+1	(1.95 ± 0.06)E+2	1.1
···	18409	53.11	−0.20	···	1.1	(2.70 ± 0.03)E+2	(8.21 ± 0.09)E+1	2.4
···	18336	53.36	−0.34	···	2.1	(3.95 ± 0.05)E+2	(1.82 ± 0.02)E+1	4.4
···	18382	53.21	−0.24	···	2.0	(1.058 ± 0.005)E+3	(5.68 ± 0.03)E+1	4.2
···	18421	52.86	−0.17	···	1.7	(1.54 ± 0.03)E+2	(1.41 ± 0.03)E+1	3.5
3050	18446	53.46	−0.11	42	1.3	(1.81 ± 0.03)E+2	(3.82 ± 0.07)E+1	2.7
3059	18499	53.06	−0.01	22	1.0	(3.37 ± 0.03)E+2	(1.33 ± 0.01)E+2	2.2
···	18546	53.14	+0.07	21	1.2	(6.274 ± 0.004)E+3	(1.3673 ± 0.0009)E+3	2.6

Continuation of Table B2

COHRS catalog #	Hi-GAL catalog #	ℓ (deg)	b (deg)	v_{LSR} (km s^{-1})	θ_{R} (arcmin)	M ($\mathrm{M}_{\odot}$)	n (cm^{-3})	R (pc)
3118	18567	52.18	+0.12	54	2.2	(2.29 ± 0.02)E+2	(2.61 ± 0.03)E+1	3.3
3121	18447	52.74	−0.11	54	1.3	(3.45 ± 0.05)E+2	(3.42 ± 0.05)E+1	3.4
···	18477	52.72	−0.06	53	1.4	(4.15 ± 0.05)E+2	(3.32 ± 0.04)E+1	3.7
···	18481	52.77	−0.06	···	1.1	(5.16 ± 0.05)E+2	(7.23 ± 0.07)E+1	3.1
···	18486	52.83	−0.05	···	2.1	(1.053 ± 0.007)E+3	(2.38 ± 0.02)E+1	5.6
3137	18691	52.11	+0.41	50	1.4	(2.09 ± 0.02)E+2	(9.67 ± 0.09)E+1	2.1
···	18710	52.17	+0.43	51	0.9	(5.0 ± 0.1)E+1	(8.4 ± 0.2)E+1	1.3
3278	18367	53.00	−0.26	23	1.2	(1.274 ± 0.005)E+3	(1.450 ± 0.006)E+2	3.3
···	18370	52.97	−0.27	23	1.3	(8.28 ± 0.05)E+2	(8.01 ± 0.05)E+1	3.5
···	18393	53.09	−0.23	24	1.0	(1.58 ± 0.04)E+2	(3.56 ± 0.08)E+1	2.6
···	18401	53.04	−0.22	24	1.1	(3.69 ± 0.05)E+2	(5.23 ± 0.07)E+1	3.1
···	18414	53.13	−0.17	23	1.0	(4.87 ± 0.04)E+2	(1.17 ± 0.01)E+2	2.6
3400	18612	53.01	+0.23	7	···	(8.5 ± 0.3)E+1	···	···
···	18637	53.03	+0.27	5	2.1	(3.767 ± 0.009)E+3	(8.97 ± 0.02)E+1	5.5
···	18613	52.85	+0.23	···	0.8	(1.35 ± 0.04)E+2	(4.9 ± 0.1)E+1	2.2
3405	18422	52.75	−0.17	1	2.0	(9.39 ± 0.07)E+2	(2.64 ± 0.02)E+1	5.2
···	18511	52.90	+0.01	5	0.9	(3.70 ± 0.04)E+2	(1.05 ± 0.01)E+2	2.4
···	18541	53.03	+0.06	6	1.4	(2.143 ± 0.006)E+3	(1.576 ± 0.004)E+2	3.8
···	18551	53.01	+0.08	5	0.5	(6.44 ± 0.03)E+2	(1.089 ± 0.005)E+3	1.3
···	18554	53.08	+0.09	4	···	(2.41 ± 0.03)E+2	···	···
···	18555	53.03	+0.08	4	0.8	(1.175 ± 0.004)E+3	(4.74 ± 0.02)E+2	2.2
···	18559	53.03	+0.11	5	1.0	(3.538 ± 0.005)E+3	(7.45 ± 0.01)E+2	2.7
···	18562	53.00	+0.12	4	1.1	(8.43 ± 0.05)E+2	(1.419 ± 0.008)E+2	2.9
···	18501	53.02	−0.01	···	0.5	(9.5 ± 0.3)E+1	(1.49 ± 0.05)E+2	1.4
···	18502	52.87	−0.01	···	1.2	(4.22 ± 0.05)E+2	(5.74 ± 0.06)E+1	3.1
3547	18547	52.78	+0.07	44	0.9	(2.04 ± 0.04)E+2	(5.0 ± 0.1)E+1	2.5
···	18574	52.76	+0.15	59	1.4	(3.67 ± 0.05)E+2	(2.73 ± 0.04)E+1	3.8
3565	18503	52.14	−0.00	57	2.2	(6.67 ± 0.03)E+2	(7.21 ± 0.03)E+1	3.3
···	18532	52.21	+0.04	54	1.4	(6.4 ± 0.2)E+1	(2.53 ± 0.06)E+1	2.2
···	18545	52.18	+0.07	55	1.1	(6.6 ± 0.1)E+1	(5.4 ± 0.1)E+1	1.7
3636	18589	52.76	+0.19	47	1.1	(3.50 ± 0.05)E+2	(5.58 ± 0.08)E+1	2.9
···	18611	52.77	+0.22	47	0.8	(3.24 ± 0.04)E+2	(1.15 ± 0.01)E+2	2.2
···	18621	52.78	+0.24	46	0.5	(2.27 ± 0.03)E+2	(3.65 ± 0.05)E+2	1.4
···	18639	52.78	+0.27	45	1.6	(8.92 ± 0.06)E+2	(4.98 ± 0.03)E+1	4.2
···	18591	52.98	+0.19	···	2.0	(1.150 ± 0.007)E+3	(3.12 ± 0.02)E+1	5.3
···	18603	52.87	+0.21	···	0.8	(1.82 ± 0.03)E+2	(8.8 ± 0.2)E+1	2.0
3638	18655	52.34	+0.32	47	1.8	(9.70 ± 0.03)E+2	(1.804 ± 0.005)E+2	2.8
3682	18507	52.37	−0.00	41	0.7	(8.2 ± 0.1)E+1	(2.70 ± 0.03)E+2	1.1
···	18512	52.39	+0.00	41	0.8	(9.4 ± 0.1)E+1	(1.84 ± 0.02)E+2	1.3
···	18519	52.43	+0.02	50	0.9	(1.47 ± 0.01)E+2	(2.25 ± 0.02)E+2	1.4
···	18524	52.48	+0.03	49	1.6	(4.68 ± 0.02)E+2	(1.248 ± 0.006)E+2	2.5
3694	18536	52.74	+0.05	44	1.7	(2.206 ± 0.007)E+3	(9.61 ± 0.03)E+1	4.5
3733	18618	51.96	+0.26	46	3.0	(6.68 ± 0.03)E+2	(2.93 ± 0.01)E+1	4.5
3745	18627	52.16	+0.27	45	···	(4.61 ± 0.07)E+1	···	···
···	18632	52.08	+0.26	45	1.1	(1.77 ± 0.02)E+2	(1.50 ± 0.01)E+2	1.7
···	18640	52.09	+0.29	46	1.2	(2.27 ± 0.02)E+2	(1.47 ± 0.01)E+2	1.8
···	18645	52.18	+0.29	45	1.6	(4.79 ± 0.02)E+2	(1.273 ± 0.006)E+2	2.5
···	18650	52.04	+0.31	47	1.6	(1.39 ± 0.02)E+2	(3.81 ± 0.05)E+1	2.5
···	18657	52.01	+0.33	47	1.6	(1.85 ± 0.02)E+2	(4.95 ± 0.05)E+1	2.5
3898	18443	51.86	−0.11	61	···	(5.5 ± 0.1)E+1	···	···
···	18463	51.82	−0.09	62	1.6	(1.42 ± 0.02)E+2	(3.03 ± 0.04)E+1	2.7
···	18460	51.87	−0.09	···	1.0	(1.17 ± 0.02)E+2	(1.10 ± 0.01)E+2	1.6
3976	18332	51.95	−0.35	58	···	(1.51 ± 0.09)E+1	···	···
···	18337	51.91	−0.34	57	1.5	(9.4 ± 0.2)E+1	(2.21 ± 0.04)E+1	2.6
···	18335	51.88	−0.36	···	1.7	(1.45 ± 0.02)E+2	(2.58 ± 0.04)E+1	2.8
4013	18374	51.89	−0.25	62	1.2	(1.87 ± 0.02)E+2	(8.68 ± 0.09)E+1	2.1
···	18390	51.97	−0.22	···	1.8	(2.99 ± 0.03)E+2	(4.68 ± 0.04)E+1	3.0
···	18398	51.87	−0.22	···	1.7	(2.51 ± 0.02)E+2	(4.57 ± 0.04)E+1	2.8
4638	17804	51.21	+0.28	49	2.1	(1.18 ± 0.03)E+2	(1.13 ± 0.03)E+1	3.5
···	17818	51.27	+0.31	···	0.9	(5.6 ± 0.2)E+1	(6.9 ± 0.2)E+1	1.5
···	17827	51.36	+0.33	···	1.7	(1.34 ± 0.03)E+2	(2.21 ± 0.05)E+1	2.9
4685	18571	51.98	+0.13	8	1.8	(9.5 ± 0.2)E+1	(1.93 ± 0.04)E+1	2.7
···	18597	51.97	+0.21	7	0.8	(6.8 ± 0.1)E+1	(1.28 ± 0.02)E+2	1.3
···	18615	52.02	+0.23	7	1.2	(8.6 ± 0.1)E+1	(5.9 ± 0.1)E+1	1.8
4806	17467	51.58	−0.39	43	1.3	(4.19 ± 0.03)E+2	(1.81 ± 0.01)E+2	2.1
···	17482	51.53	−0.37	44	1.2	(1.16 ± 0.02)E+2	(5.4 ± 0.1)E+1	2.1
···	17486	51.64	−0.34	42	1.9	(6.45 ± 0.03)E+2	(8.59 ± 0.05)E+1	3.1
···	18311	51.62	−0.42	44	···	(2.9 ± 0.1)E+1	···	···
···	18322	51.60	−0.37	43	1.5	(4.02 ± 0.02)E+2	(9.70 ± 0.05)E+1	2.6
···	18327	51.61	−0.35	43	0.6	(1.78 ± 0.01)E+2	(5.79 ± 0.04)E+2	1.1
···	18351	51.73	−0.31	41	1.0	(1.21 ± 0.02)E+2	(9.0 ± 0.1)E+1	1.8
···	18352	51.70	−0.30	41	0.7	(7.1 ± 0.1)E+1	(1.53 ± 0.03)E+2	1.2
···	18354	51.81	−0.30	40	0.5	(1.28 ± 0.01)E+2	(1.02 ± 0.01)E+3	0.8
···	18358	51.76	−0.29	41	0.8	(1.63 ± 0.02)E+2	(2.59 ± 0.03)E+2	1.4
4861	18643	52.01	+0.29	6	···	(5.46 ± 0.07)E+1	···	···
···	18662	51.95	+0.33	6	1.9	(2.11 ± 0.02)E+2	(3.50 ± 0.03)E+1	2.9
···	18669	51.75	+0.37	5	1.5	(5.09 ± 0.02)E+2	(1.854 ± 0.007)E+2	2.2
···	18677	51.91	+0.36	4	1.7	(3.00 ± 0.02)E+2	(7.31 ± 0.05)E+1	2.5
···	18679	51.64	+0.38	3	0.3	(2.12 ± 0.09)E+1	(5.6 ± 0.2)E+2	0.5
···	18681	51.67	+0.38	5	1.6	(2.08 ± 0.02)E+2	(6.07 ± 0.06)E+1	2.4
···	18682	51.78	+0.38	4	1.2	(2.71 ± 0.02)E+2	(1.79 ± 0.01)E+2	1.8
···	18688	51.71	+0.40	3	1.1	(1.10 ± 0.02)E+2	(8.4 ± 0.1)E+1	1.7
···	18695	51.85	+0.41	1	···	(6.2 ± 0.1)E+1	···	···
···	18702	51.76	+0.42	3	0.6	(1.00 ± 0.01)E+2	(5.14 ± 0.06)E+2	0.9

Continuation of Table B2

COHRS catalog #	Hi-GAL catalog #	ℓ (deg)	b (deg)	v_{LSR} (km s^{-1})	θ_{R} (arcmin)	M ($\mathrm{M}_\odot$)	n (cm^{-3})	R (pc)
···	18665	51.80	+0.35	···	1.7	(3.92 ± 0.02)E+2	(8.73 ± 0.05)E+1	2.6
···	18675	51.84	+0.37	···	1.1	(2.07 ± 0.01)E+2	(1.66 ± 0.01)E+2	1.7
···	18685	51.83	+0.39	···	0.8	(9.8 ± 0.1)E+1	(2.28 ± 0.03)E+2	1.2
···	18713	51.66	+0.43	···	···	(6.6 ± 0.7)E+0	···	···
···	18719	51.84	+0.44	···	1.0	(7.9 ± 0.1)E+1	(7.7 ± 0.1)E+1	1.6
···	18723	51.72	+0.45	···	1.2	(9.4 ± 0.2)E+1	(5.59 ± 0.09)E+1	1.9
···	18737	51.71	+0.48	···	0.9	(6.5 ± 0.1)E+1	(1.11 ± 0.02)E+2	1.3
···	18743	51.69	+0.50	···	1.1	(9.1 ± 0.1)E+1	(7.7 ± 0.1)E+1	1.7
4962	17416	51.26	−0.48	56	0.5	(4.2 ± 0.1)E+1	(3.7 ± 0.1)E+2	0.8
···	17434	51.20	−0.46	53	···	(3.9 ± 0.1)E+1	···	···
···	17453	51.23	−0.43	56	1.0	(8.9 ± 0.2)E+1	(7.6 ± 0.2)E+1	1.7
···	17465	51.21	−0.41	57	0.4	(2.7 ± 0.1)E+1	(2.9 ± 0.1)E+2	0.7
···	17433	51.26	−0.46	···	0.3	(2.3 ± 0.1)E+1	(1.20 ± 0.06)E+3	0.4
···	17439	51.22	−0.46	···	0.9	(7.6 ± 0.2)E+1	(8.1 ± 0.2)E+1	1.6
4993	17619	51.35	−0.08	56	0.8	(3.56 ± 0.02)E+2	(6.26 ± 0.03)E+2	1.3
···	17622	51.58	−0.07	53	1.1	(2.54 ± 0.02)E+2	(1.47 ± 0.01)E+2	1.9
···	17637	51.57	−0.05	52	1.8	(4.49 ± 0.03)E+2	(7.09 ± 0.05)E+1	2.9
···	17648	51.61	−0.02	59	1.5	(2.11 ± 0.03)E+2	(4.93 ± 0.07)E+1	2.6
···	17653	51.38	−0.02	54	1.8	(6.813 ± 0.004)E+3	(9.553 ± 0.006)E+2	3.1
···	17660	51.49	+0.00	55	0.5	(1.80 ± 0.01)E+2	(1.30 ± 0.01)E+3	0.8
···	17661	51.46	+0.00	55	0.7	(3.94 ± 0.02)E+2	(8.13 ± 0.04)E+2	1.3
···	18450	51.79	−0.10	55	0.9	(1.08 ± 0.01)E+2	(1.33 ± 0.02)E+2	1.5
···	18471	51.68	−0.07	54	1.4	(1.92 ± 0.02)E+2	(5.92 ± 0.07)E+1	2.4
···	18480	51.65	−0.07	55	1.0	(1.26 ± 0.02)E+2	(9.7 ± 0.1)E+1	1.7
···	18515	51.60	+0.00	60	0.8	(6.4 ± 0.1)E+1	(1.08 ± 0.02)E+2	1.3
···	18525	51.63	+0.03	53	0.7	(9.9 ± 0.2)E+1	(2.29 ± 0.04)E+2	1.2
···	18399	51.74	−0.20	···	1.4	(8.7 ± 0.2)E+1	(2.48 ± 0.06)E+1	2.4
···	18457	51.75	−0.09	···	1.8	(2.60 ± 0.02)E+2	(3.85 ± 0.04)E+1	3.0
···	18458	51.63	−0.10	···	1.9	(3.17 ± 0.03)E+2	(3.98 ± 0.04)E+1	3.2
···	18470	51.84	−0.08	···	0.8	(1.54 ± 0.01)E+2	(2.33 ± 0.02)E+2	1.4
···	18476	51.79	−0.07	···	2.2	(4.55 ± 0.03)E+2	(3.78 ± 0.02)E+1	3.6
5087	18416	51.96	−0.18	60	1.0	(1.02 ± 0.02)E+2	(9.5 ± 0.2)E+1	1.6
···	18423	52.00	−0.16	59	···	(3.6 ± 0.1)E+1	···	···
5253	18294	51.73	−0.46	48	1.1	(1.35 ± 0.02)E+2	(8.5 ± 0.1)E+1	1.9
···	18298	51.67	−0.45	48	1.4	(2.57 ± 0.02)E+2	(7.81 ± 0.07)E+1	2.4
5281	18528	51.97	+0.03	57	1.4	(2.74 ± 0.02)E+2	(8.35 ± 0.07)E+1	2.4
···	18560	51.94	+0.12	50	1.3	(2.38 ± 0.02)E+2	(8.49 ± 0.08)E+1	2.2
···	18578	51.94	+0.16	53	1.7	(1.95 ± 0.02)E+2	(3.52 ± 0.04)E+1	2.8
···	18598	51.82	+0.20	54	1.9	(1.87 ± 0.03)E+2	(2.23 ± 0.03)E+1	3.2
···	18576	51.90	+0.15	···	1.0	(1.47 ± 0.02)E+2	(1.16 ± 0.01)E+2	1.7
···	18586	51.87	+0.18	···	1.1	(8.9 ± 0.2)E+1	(5.0 ± 0.1)E+1	1.9
5359	17753	51.51	+0.19	57	0.5	(2.4 ± 0.1)E+1	(1.8 ± 0.1)E+2	0.8
···	17770	51.54	+0.21	57	1.5	(6.7 ± 0.2)E+1	(1.76 ± 0.06)E+1	2.5
···	17788	51.49	+0.26	50	1.1	(5.6 ± 0.2)E+1	(4.1 ± 0.1)E+1	1.8
···	17803	51.51	+0.29	51	1.2	(5.5 ± 0.2)E+1	(2.9 ± 0.1)E+1	2.0
···	17809	51.55	+0.30	52	0.6	(2.6 ± 0.1)E+1	(1.01 ± 0.06)E+2	1.0
···	18623	51.67	+0.25	53	1.9	(5.60 ± 0.03)E+2	(6.83 ± 0.04)E+1	3.2
···	18628	51.63	+0.26	54	0.6	(3.6 ± 0.1)E+1	(1.62 ± 0.05)E+2	1.0
···	18641	51.62	+0.30	54	2.5	(4.31 ± 0.03)E+2	(2.43 ± 0.02)E+1	4.1
···	18593	51.59	+0.20	···	0.8	(4.7 ± 0.1)E+1	(6.7 ± 0.2)E+1	1.4
5423	17754	51.00	+0.19	47	1.0	(2.32 ± 0.01)E+2	(4.16 ± 0.02)E+2	1.3
···	17766	51.08	+0.21	45	1.3	(3.29 ± 0.02)E+2	(2.48 ± 0.01)E+2	1.7
···	17767	50.98	+0.21	47	1.0	(2.55 ± 0.01)E+2	(5.08 ± 0.02)E+2	1.3
···	17777	50.96	+0.23	43	···	(5.64 ± 0.07)E+1	···	···
···	17781	50.92	+0.24	42	1.2	(2.64 ± 0.02)E+2	(2.51 ± 0.02)E+2	1.6
···	17791	50.98	+0.26	50	0.7	(3.90 ± 0.09)E+1	(1.83 ± 0.04)E+2	1.0
···	17780	51.02	+0.23	···	2.0	(9.09 ± 0.02)E+2	(2.044 ± 0.005)E+2	2.6
5428	17645	50.80	−0.03	44	0.9	(1.73 ± 0.01)E+2	(5.02 ± 0.03)E+2	1.1
···	17646	50.75	−0.03	44	2.1	(6.55 ± 0.02)E+2	(1.341 ± 0.005)E+2	2.7
···	17657	50.69	−0.00	47	···	(1.95 ± 0.08)E+1	···	···
···	17658	50.62	−0.01	43	0.9	(2.4 ± 0.1)E+1	(5.9 ± 0.3)E+1	1.2
···	17670	50.82	+0.01	42	1.3	(3.12 ± 0.01)E+2	(2.65 ± 0.01)E+2	1.7
···	17682	50.81	+0.05	41	0.9	(1.92 ± 0.01)E+2	(4.12 ± 0.02)E+2	1.2
···	17702	50.79	+0.08	44	2.2	(7.41 ± 0.02)E+2	(1.265 ± 0.004)E+2	2.9
···	17715	50.75	+0.11	44	0.8	(9.1 ± 0.1)E+1	(3.70 ± 0.04)E+2	1.0
···	17725	50.80	+0.12	44	···	(1.06 ± 0.06)E+1	···	···
···	17740	50.77	+0.15	42	1.2	(5.50 ± 0.02)E+2	(5.81 ± 0.02)E+2	1.6
···	17748	50.92	+0.17	46	0.8	(3.6 ± 0.1)E+1	(1.10 ± 0.03)E+2	1.1
···	17751	50.90	+0.19	47	···	(5.7 ± 0.5)E+0	···	···
···	17752	50.78	+0.18	42	1.7	(4.42 ± 0.02)E+2	(1.538 ± 0.007)E+2	2.3
···	17771	50.74	+0.23	43	0.8	(4.9 ± 0.1)E+1	(1.65 ± 0.04)E+2	1.1
···	17772	50.65	+0.22	43	0.9	(8.3 ± 0.1)E+1	(1.83 ± 0.02)E+2	1.2
···	17782	50.86	+0.24	43	1.0	(4.2 ± 0.1)E+1	(7.4 ± 0.2)E+1	1.3
···	17784	50.78	+0.25	44	···	(3.67 ± 0.07)E+1	···	···
···	17786	50.81	+0.25	44	1.9	(5.16 ± 0.02)E+2	(1.268 ± 0.005)E+2	2.5
···	17789	50.84	+0.27	44	1.3	(2.89 ± 0.02)E+2	(2.15 ± 0.01)E+2	1.8
···	17778	50.68	+0.24	···	1.7	(2.05 ± 0.02)E+2	(7.89 ± 0.07)E+1	2.2
···	17618	50.66	−0.07	···	1.0	(5.8 ± 0.1)E+1	(1.05 ± 0.02)E+2	1.3
···	17680	50.79	+0.04	···	1.1	(1.24 ± 0.01)E+2	(1.81 ± 0.02)E+2	1.4
···	17629	50.74	−0.07	···	1.5	(3.67 ± 0.02)E+2	(1.843 ± 0.008)E+2	2.0
5451	17587	50.89	−0.14	51	1.2	(6.1 ± 0.1)E+1	(5.8 ± 0.1)E+1	1.6
···	17593	50.84	−0.13	50	1.5	(2.11 ± 0.02)E+2	(1.197 ± 0.009)E+2	1.9
···	17606	50.81	−0.10	50	0.5	(2.58 ± 0.09)E+1	(3.0 ± 0.1)E+2	0.7
···	17575	50.90	−0.18	···	1.3	(1.15 ± 0.01)E+2	(9.1 ± 0.1)E+1	1.7

Continuation of Table B2

COHRS catalog #	Hi-GAL catalog #	ℓ (deg)	b (deg)	$v_{\rm LSR}$ (km s^{-1})	$\theta_{\rm R}$ (arcmin)	M (M$_\odot$)	n (cm^{-3})	R (pc)
5634	17487	51.05	−0.37	52	2.2	(1.95 ± 0.02)E+2	(3.49 ± 0.04)E+1	2.8
···	17490	50.99	−0.35	56	0.4	(9.2 ± 0.7)E+0	(3.4 ± 0.3)E+2	0.5
···	17525	50.99	−0.28	55	1.8	(1.71 ± 0.02)E+2	(5.17 ± 0.06)E+1	2.4
···	17470	51.08	−0.39	···	1.6	(1.27 ± 0.02)E+2	(5.56 ± 0.08)E+1	2.1
···	17521	51.02	−0.28	···	0.5	(2.08 ± 0.08)E+1	(2.50 ± 0.09)E+2	0.7
5637	17506	51.14	−0.31	54	1.1	(7.7 ± 0.1)E+1	(9.5 ± 0.2)E+1	1.5
···	17507	51.09	−0.31	53	0.8	(2.9 ± 0.1)E+1	(8.9 ± 0.3)E+1	1.1
···	17537	51.13	−0.27	54	1.6	(1.24 ± 0.02)E+2	(5.31 ± 0.07)E+1	2.1
···	17555	51.02	−0.23	54	···	(2.35 ± 0.06)E+1	···	···
···	17557	51.16	−0.22	54	1.6	(1.51 ± 0.02)E+2	(6.42 ± 0.07)E+1	2.1
···	17561	50.86	−0.22	65	0.9	(4.9 ± 0.1)E+1	(1.06 ± 0.02)E+2	1.2
···	17563	50.99	−0.21	52	0.7	(2.02 ± 0.01)E+2	(8.86 ± 0.05)E+2	1.0
···	17564	51.10	−0.21	55	1.1	(7.5 ± 0.1)E+1	(1.08 ± 0.02)E+2	1.4
···	17570	51.16	−0.19	55	1.4	(1.29 ± 0.02)E+2	(8.7 ± 0.1)E+1	1.8
···	17579	51.06	−0.16	58	···	(1.19 ± 0.06)E+1	···	···
···	17581	51.10	−0.15	57	1.1	(7.7 ± 0.1)E+1	(9.4 ± 0.2)E+1	1.5
···	17592	51.19	−0.14	54	0.7	(5.6 ± 0.1)E+1	(3.15 ± 0.05)E+2	0.9
···	17594	51.13	−0.13	53	0.9	(6.1 ± 0.1)E+1	(1.52 ± 0.03)E+2	1.2
···	17601	51.04	−0.12	56	1.5	(1.21 ± 0.02)E+2	(6.01 ± 0.08)E+1	2.0
···	17602	51.00	−0.12	57	1.1	(6.5 ± 0.1)E+1	(9.7 ± 0.2)E+1	1.4
···	17604	51.09	−0.11	57	1.4	(1.90 ± 0.02)E+2	(1.18 ± 0.01)E+2	1.9
···	17624	50.91	−0.08	59	1.4	(2.26 ± 0.02)E+2	(1.42 ± 0.01)E+2	1.9
···	17630	51.10	−0.07	57	1.8	(2.57 ± 0.02)E+2	(8.58 ± 0.06)E+1	2.3
···	17638	51.16	−0.05	53	0.7	(6.2 ± 0.1)E+1	(3.77 ± 0.06)E+2	0.9
···	17701	51.19	+0.08	55	0.7	(3.96 ± 0.09)E+1	(1.96 ± 0.05)E+2	0.9
···	17706	51.16	+0.11	56	1.9	(3.10 ± 0.02)E+2	(8.23 ± 0.05)E+1	2.5
···	17739	51.25	+0.16	54	2.7	(2.44 ± 0.02)E+2	(2.36 ± 0.02)E+1	3.5
···	17741	51.31	+0.16	54	1.9	(3.22 ± 0.02)E+2	(8.97 ± 0.05)E+1	2.4
···	17759	51.29	+0.20	···	1.3	(8.4 ± 0.1)E+1	(7.6 ± 0.1)E+1	1.6
···	17582	50.86	−0.16	···	1.7	(3.03 ± 0.02)E+2	(1.058 ± 0.007)E+2	2.3
···	17721	51.19	+0.13	···	0.8	(5.5 ± 0.1)E+1	(1.63 ± 0.03)E+2	1.1
···	17738	51.17	+0.14	···	0.7	(3.2 ± 0.1)E+1	(1.46 ± 0.05)E+2	1.0
5703	17428	50.53	−0.46	63	0.6	(2.50 ± 0.09)E+1	(2.11 ± 0.08)E+2	0.8
···	17442	50.46	−0.45	64	···	(3.05 ± 0.08)E+1	···	···
···	17457	50.57	−0.43	63	0.8	(7.1 ± 0.1)E+1	(3.02 ± 0.05)E+2	1.0
···	17461	50.60	−0.42	62	1.0	(5.3 ± 0.1)E+1	(8.7 ± 0.2)E+1	1.4
···	17448	50.49	−0.44	···	···	(3.79 ± 0.09)E+1	···	···
···	17489	50.36	−0.35	···	0.6	(1.12 ± 0.01)E+2	(8.00 ± 0.08)E+2	0.8
5838	17711	50.52	+0.10	59	1.4	(8.7 ± 0.1)E+1	(5.57 ± 0.09)E+1	1.8
5850	17520	50.03	−0.28	62	2.1	(4.17 ± 0.02)E+2	(8.22 ± 0.04)E+1	2.7
···	17534	50.08	−0.27	61	0.5	(5.29 ± 0.09)E+1	(6.7 ± 0.1)E+2	0.7
···	17538	50.05	−0.26	62	0.9	(7.4 ± 0.1)E+1	(1.99 ± 0.03)E+2	1.1
···	17547	50.01	−0.24	···	···	(1.01 ± 0.06)E+1	···	···
6127	17566	50.25	−0.21	41	1.8	(1.72 ± 0.02)E+2	(5.61 ± 0.06)E+1	2.3
···	17565	50.29	−0.20	···	1.3	(1.69 ± 0.01)E+2	(1.47 ± 0.01)E+2	1.7
6275	17531	50.42	−0.27	49	0.6	(3.86 ± 0.09)E+1	(3.31 ± 0.08)E+2	0.8
···	17558	50.41	−0.22	49	0.6	(4.18 ± 0.09)E+1	(3.26 ± 0.07)E+2	0.8
···	17640	50.42	−0.04	54	2.0	(2.67 ± 0.02)E+2	(6.21 ± 0.05)E+1	2.6
···	17556	50.50	−0.22	···	1.0	(3.2 ± 0.1)E+1	(5.3 ± 0.2)E+1	1.3
···	17567	50.44	−0.20	···	2.2	(3.59 ± 0.02)E+2	(6.55 ± 0.04)E+1	2.8
···	17607	50.55	−0.10	···	1.0	(5.3 ± 0.1)E+1	(8.8 ± 0.2)E+1	1.3
···	17625	50.54	−0.05	···	2.5	(2.29 ± 0.02)E+2	(2.68 ± 0.03)E+1	3.3
6349	17746	50.62	+0.17	55	1.1	(1.43 ± 0.01)E+2	(1.98 ± 0.02)E+2	1.4
···	17756	50.64	+0.19	55	1.4	(1.59 ± 0.02)E+2	(9.6 ± 0.1)E+1	1.9
···	17750	50.56	+0.20	···	2.6	(3.61 ± 0.03)E+2	(3.90 ± 0.03)E+1	3.3
6377	17449	50.27	−0.45	16	1.1	(2.280 ± 0.009)E+1	(2.149 ± 0.008)E+3	0.3
···	17469	50.29	−0.39	16	0.8	(5.005 ± 0.009)E+1	(1.089 ± 0.002)E+4	0.3
···	17420	50.26	−0.48	···	1.2	(1.679 ± 0.007)E+1	(1.141 ± 0.005)E+3	0.4
6403	17877	50.24	+0.46	24	1.9	(3.99 ± 0.03)E+2	(5.63 ± 0.04)E+1	3.1
···	17875	50.29	+0.45	···	0.2	(3.1 ± 0.1)E+1	(9.0 ± 0.3)E+3	0.2
6427	17712	49.92	+0.11	10	2.1	(3.03 ± 0.03)E+2	(3.29 ± 0.03)E+1	3.3
···	17724	49.96	+0.11	10	1.3	(1.66 ± 0.02)E+2	(8.4 ± 0.1)E+1	2.0
···	17763	49.94	+0.20	8	1.1	(1.44 ± 0.02)E+2	(1.02 ± 0.01)E+2	1.8
···	17776	49.94	+0.23	8	1.0	(8.5 ± 0.2)E+1	(8.1 ± 0.2)E+1	1.6
···	17799	49.97	+0.27	8	1.7	(3.07 ± 0.03)E+2	(6.41 ± 0.06)E+1	2.7
6440	17834	50.33	+0.35	4	1.1	(2.63 ± 0.02)E+2	(1.92 ± 0.02)E+2	1.8
···	17840	50.41	+0.38	4	1.6	(2.10 ± 0.03)E+2	(5.82 ± 0.07)E+1	2.4
···	17841	50.51	+0.38	4	···	(2.25 ± 0.09)E+1	···	···
···	17846	50.35	+0.39	4	1.9	(2.87 ± 0.03)E+2	(4.03 ± 0.04)E+1	3.1
···	17860	50.50	+0.42	7	2.1	(5.31 ± 0.03)E+2	(5.78 ± 0.03)E+1	3.3
···	17866	50.66	+0.44	5	1.8	(2.33 ± 0.03)E+2	(4.32 ± 0.05)E+1	2.8
···	17869	50.40	+0.44	5	2.2	(8.33 ± 0.04)E+2	(8.54 ± 0.04)E+1	3.4
···	17898	50.65	+0.49	5	0.9	(4.3 ± 0.1)E+1	(6.0 ± 0.2)E+1	1.4
···	17861	50.61	+0.42	···	0.7	(5.0 ± 0.1)E+1	(1.66 ± 0.05)E+2	1.1
···	17863	50.69	+0.42	···	1.0	(9.3 ± 0.2)E+1	(1.09 ± 0.02)E+2	1.5
6538	17792	50.41	+0.26	44	1.5	(1.24 ± 0.02)E+2	(3.66 ± 0.07)E+1	2.4
···	17806	50.30	+0.29	42	0.8	(6.4 ± 0.1)E+1	(1.21 ± 0.03)E+2	1.3
···	17812	50.35	+0.30	43	1.8	(2.83 ± 0.03)E+2	(5.08 ± 0.05)E+1	2.8
6589	17488	50.64	−0.35	54	2.3	(1.86 ± 0.03)E+2	(1.56 ± 0.02)E+1	3.6
···	17497	50.69	−0.35	47	1.9	(2.54 ± 0.03)E+2	(3.89 ± 0.04)E+1	3.0
6694	17576	49.88	−0.18	48	0.7	(4.1 ± 0.1)E+1	(2.27 ± 0.05)E+2	0.9
···	17583	49.93	−0.16	···	0.8	(6.9 ± 0.1)E+1	(2.07 ± 0.03)E+2	1.1
···	17584	49.88	−0.15	···	···	(4.3 ± 0.5)E+0	···	···
6709	17787	50.09	+0.25	54	0.8	(5.1 ± 0.1)E+1	(2.17 ± 0.04)E+2	1.0

Continuation of Table B2

COHRS catalog #	Hi-GAL catalog #	ℓ (deg)	b (deg)	v_{LSR} (km s^{-1})	θ_{R} (arcmin)	M (M$_{\odot}$)	n (cm^{-3})	R (pc)
···	17793	50.00	+0.26	56	···	(2.52 ± 0.06)E+1	···	···
···	17794	50.13	+0.28	56	2.0	(2.39 ± 0.02)E+2	(5.16 ± 0.04)E+1	2.7
···	17796	50.05	+0.27	53	1.7	(5.91 ± 0.02)E+2	(2.378 ± 0.008)E+2	2.2
···	17774	50.09	+0.23	···	0.7	(4.63 ± 0.09)E+1	(2.88 ± 0.05)E+2	0.9
6744	17666	50.56	+0.01	66	1.1	(1.01 ± 0.01)E+2	(1.37 ± 0.02)E+2	1.4
···	17675	50.53	+0.03	66	···	(3.02 ± 0.09)E+1	···	···
···	17676	50.50	+0.03	64	···	(1.79 ± 0.08)E+1	···	···
···	17697	50.21	+0.07	57	1.2	(5.4 ± 0.1)E+1	(5.7 ± 0.1)E+1	1.6
···	17705	50.46	+0.08	65	2.2	(2.08 ± 0.02)E+2	(3.68 ± 0.04)E+1	2.8
···	17708	50.42	+0.10	65	1.7	(1.44 ± 0.02)E+2	(4.90 ± 0.07)E+1	2.3
···	17709	50.30	+0.10	64	2.2	(1.41 ± 0.02)E+2	(2.36 ± 0.03)E+1	2.9
···	17716	50.26	+0.12	58	2.3	(1.29 ± 0.02)E+2	(1.84 ± 0.03)E+1	3.0
···	17734	50.31	+0.14	64	1.4	(7.3 ± 0.2)E+1	(4.6 ± 0.1)E+1	1.9
···	17736	50.36	+0.15	66	1.1	(2.9 ± 0.1)E+1	(4.5 ± 0.2)E+1	1.4
···	17717	50.22	+0.11	···	1.4	(8.2 ± 0.1)E+1	(5.5 ± 0.1)E+1	1.8
···	17726	50.19	+0.12	···	···	(8.2 ± 0.6)E+0	···	···
6990	17673	49.92	+0.03	46	···	(1.02 ± 0.06)E+1	···	···
···	17684	49.90	+0.06	45	1.0	(4.9 ± 0.1)E+1	(9.2 ± 0.2)E+1	1.3
···	17687	49.97	+0.06	44	0.4	(2.12 ± 0.07)E+1	(5.4 ± 0.2)E+2	0.5
···	17690	49.94	+0.06	45	···	(7.4 ± 0.6)E+0	···	···
7046	17536	50.72	−0.26	59	0.5	(1.48 ± 0.08)E+1	(2.6 ± 0.1)E+2	0.6
···	17551	50.73	−0.23	60	0.9	(2.7 ± 0.1)E+1	(6.6 ± 0.3)E+1	1.2
···	17569	50.73	−0.19	60	1.9	(1.67 ± 0.02)E+2	(4.30 ± 0.05)E+1	2.5
7055	17591	49.99	−0.13	47	1.8	(1.485 ± 0.002)E+3	(4.426 ± 0.007)E+2	2.4
···	17597	50.04	−0.12	47	···	(7.83 ± 0.09)E+1	···	···
···	17608	49.98	−0.09	46	0.6	(2.52 ± 0.09)E+1	(2.7 ± 0.1)E+2	0.7
···	17652	50.02	−0.02	55	0.8	(9.8 ± 0.1)E+1	(3.73 ± 0.04)E+2	1.0
···	17655	49.99	−0.01	55	1.1	(2.69 ± 0.01)E+2	(3.75 ± 0.02)E+2	1.4
···	17662	50.06	+0.00	56	0.5	(1.137 ± 0.009)E+2	(2.06 ± 0.02)E+3	0.6
···	17664	50.02	+0.01	55	1.2	(1.97 ± 0.01)E+2	(2.16 ± 0.01)E+2	1.5
···	17689	50.05	+0.05	54	1.9	(1.542 ± 0.002)E+3	(3.824 ± 0.006)E+2	2.5
···	17727	50.04	+0.13	56	0.9	(7.5 ± 0.1)E+1	(1.71 ± 0.03)E+2	1.2
7119	17413	50.27	−0.49	41	1.0	(2.70 ± 0.01)E+2	(4.31 ± 0.02)E+2	1.4
···	17417	50.30	−0.48	41	···	(4.10 ± 0.07)E+1	···	···
···	17459	50.40	−0.40	40	2.0	(1.502 ± 0.002)E+3	(3.438 ± 0.005)E+2	2.6
···	17462	50.38	−0.41	41	0.8	(4.17 ± 0.01)E+2	(1.324 ± 0.004)E+3	1.1
···	17464	50.36	−0.41	40	1.0	(2.66 ± 0.01)E+2	(5.42 ± 0.03)E+2	1.3
···	17468	50.46	−0.40	49	1.3	(1.65 ± 0.02)E+2	(1.31 ± 0.01)E+2	1.7
···	17519	50.37	−0.29	···	···	(4.4 ± 0.5)E+0	···	···
7466	17699	49.82	+0.08	64	0.4	(7.6 ± 0.2)E+1	(5.4 ± 0.1)E+2	0.8
···	17720	49.67	+0.11	59	1.6	(3.61 ± 0.04)E+2	(5.19 ± 0.06)E+1	3.0
···	17722	49.87	+0.11	···	1.6	(1.42 ± 0.03)E+2	(2.02 ± 0.05)E+1	3.0
···	17700	49.72	+0.08	···	0.7	(9.3 ± 0.2)E+1	(1.63 ± 0.04)E+2	1.3
7632	17572	49.67	−0.18	45	1.3	(3.05 ± 0.03)E+2	(7.77 ± 0.08)E+1	2.5
···	17598	49.80	−0.13	42	1.2	(1.63 ± 0.03)E+2	(5.31 ± 0.09)E+1	2.3
···	17621	49.76	−0.08	43	1.1	(1.99 ± 0.03)E+2	(8.0 ± 0.1)E+1	2.2
···	17654	49.73	−0.01	48	1.6	(2.795 ± 0.004)E+3	(4.514 ± 0.007)E+2	2.9
···	17667	49.75	+0.02	50	1.3	(6.65 ± 0.03)E+2	(1.745 ± 0.008)E+2	2.5
···	17679	49.71	+0.03	48	1.1	(3.99 ± 0.03)E+2	(1.70 ± 0.01)E+2	2.1
···	17685	49.73	+0.05	48	0.6	(9.6 ± 0.2)E+1	(2.50 ± 0.05)E+2	1.2
···	17694	49.77	+0.06	47	0.6	(1.73 ± 0.02)E+2	(4.13 ± 0.05)E+2	1.2
···	17704	49.76	+0.09	47	0.5	(4.3 ± 0.2)E+1	(2.06 ± 0.08)E+2	0.9
···	17603	49.75	−0.11	···	1.3	(3.69 ± 0.03)E+2	(1.042 ± 0.008)E+2	2.4
···	17599	49.72	−0.13	···	1.2	(2.62 ± 0.03)E+2	(9.3 ± 0.1)E+1	2.3
8017	16722	49.29	−0.05	59	1.4	(1.926 ± 0.003)E+3	(4.948 ± 0.008)E+2	2.5
···	16756	49.23	+0.01	53	1.8	(1.905 ± 0.004)E+3	(2.167 ± 0.004)E+2	3.3
···	16777	49.19	+0.06	53	0.9	(3.91 ± 0.02)E+2	(3.43 ± 0.02)E+2	1.7
8079	16652	49.38	−0.26	51	0.6	(2.884 ± 0.002)E+3	(7.268 ± 0.005)E+3	1.2
···	16688	49.37	−0.16	48	1.2	(1.752 ± 0.003)E+3	(7.50 ± 0.01)E+2	2.1
···	17529	49.56	−0.27	54	0.9	(2.827 ± 0.003)E+3	(2.610 ± 0.002)E+3	1.6
···	17544	49.60	−0.25	57	0.7	(1.008 ± 0.002)E+3	(1.992 ± 0.005)E+3	1.3
···	17553	49.56	−0.23	55	···	(5.9 ± 0.1)E+1	···	···
···	17560	49.40	−0.22	48	1.3	(3.591 ± 0.003)E+3	(1.137 ± 0.001)E+3	2.3
···	17573	49.52	−0.18	56	···	(9.9 ± 0.8)E+0	···	···
···	17586	49.53	−0.15	55	1.2	(7.00 ± 0.03)E+2	(2.47 ± 0.01)E+2	2.3
···	16658	49.31	−0.24	···	···	(9.0 ± 0.1)E+1	···	···
···	17550	49.48	−0.23	···	···	(3.01 ± 0.02)E+2	···	···
8099	16721	49.07	−0.06	47	0.9	(1.75 ± 0.02)E+2	(1.75 ± 0.02)E+2	1.6
···	16734	49.10	−0.03	47	1.1	(2.18 ± 0.02)E+2	(1.04 ± 0.01)E+2	2.0
···	16704	49.07	−0.12	···	0.8	(1.65 ± 0.02)E+2	(1.89 ± 0.02)E+2	1.5
···	16714	49.06	−0.08	···	0.9	(1.65 ± 0.02)E+2	(1.33 ± 0.01)E+2	1.7
8191	16711	48.92	−0.08	55	1.2	(5.03 ± 0.02)E+2	(1.800 ± 0.008)E+2	2.2
···	16725	48.93	−0.05	55	0.8	(1.60 ± 0.02)E+2	(2.02 ± 0.02)E+2	1.5
···	16736	48.94	−0.03	54	0.8	(2.17 ± 0.02)E+2	(2.70 ± 0.02)E+2	1.5
···	16765	48.96	+0.03	65	0.6	(1.08 ± 0.01)E+2	(3.39 ± 0.05)E+2	1.1
···	16793	48.93	+0.08	55	1.5	(3.48 ± 0.03)E+2	(6.31 ± 0.05)E+1	2.8
···	16803	48.96	+0.09	55	0.7	(5.1 ± 0.1)E+1	(1.19 ± 0.03)E+2	1.2
···	16829	48.94	+0.13	55	0.5	(7.8 ± 0.1)E+1	(5.4 ± 0.1)E+2	0.8
···	16883	49.11	+0.23	53	0.7	(3.7 ± 0.1)E+1	(8.8 ± 0.3)E+1	1.2
···	16893	48.91	+0.26	46	1.5	(6.27 ± 0.03)E+2	(1.187 ± 0.006)E+2	2.8
···	16868	48.93	+0.21	···	1.0	(3.67 ± 0.02)E+2	(2.59 ± 0.01)E+2	1.8
8289	16523	48.70	−0.49	62	···	(1.50 ± 0.09)E+1	···	···
···	16547	48.73	−0.45	70	0.5	(7.36 ± 0.09)E+1	(6.55 ± 0.08)E+2	0.8
···	16569	48.70	−0.41	60	0.7	(7.9 ± 0.1)E+1	(2.09 ± 0.04)E+2	1.2

Continuation of Table B2

COHRS catalog #	Hi-GAL catalog #	ℓ (deg)	b (deg)	v_{LSR} (km s^{-1})	θ_{R} (arcmin)	M (M$_{\odot}$)	n (cm^{-3})	R (pc)
···	16586	48.71	−0.38	63	1.3	(4.13 ± 0.02)E+2	(1.558 ± 0.008)E+2	2.2
···	16534	48.72	−0.47	···	0.7	(1.65 ± 0.01)E+2	(4.09 ± 0.04)E+2	1.2
···	16553	48.75	−0.43	···	1.3	(2.56 ± 0.02)E+2	(1.106 ± 0.009)E+2	2.1
8330	16641	49.11	−0.28	63	1.0	(1.183 ± 0.002)E+3	(7.12 ± 0.01)E+2	1.9
···	16645	49.08	−0.27	67	0.8	(1.262 ± 0.002)E+3	(1.637 ± 0.002)E+3	1.5
···	16654	49.10	−0.26	66	1.4	(2.458 ± 0.003)E+3	(5.794 ± 0.006)E+2	2.6
···	16671	49.17	−0.20	62	1.5	(5.765 ± 0.004)E+3	(1.0388 ± 0.0006)E+3	2.8
8393	16723	49.36	−0.05	51	0.5	(1.55 ± 0.01)E+2	(9.56 ± 0.09)E+2	0.9
···	17613	49.41	−0.09	50	···	(4.90 ± 0.09)E+1	···	···
···	16710	49.40	−0.08	···	···	(7.81 ± 0.09)E+1	···	···
8526	16706	48.96	−0.10	16	1.3	(1.83 ± 0.02)E+2	(7.41 ± 0.07)E+1	2.1
8761	16686	48.66	−0.15	16	···	(7.2 ± 0.2)E+1	···	···
···	16696	48.63	−0.14	16	0.5	(3.21 ± 0.03)E+2	(4.98 ± 0.05)E+2	1.4
···	16697	48.60	−0.14	16	1.4	(5.03 ± 0.05)E+2	(4.96 ± 0.05)E+1	3.4
8801	16938	48.61	+0.35	37	1.0	(5.13 ± 0.03)E+1	(4.91 ± 0.03)E+2	0.7
···	16947	48.68	+0.38	38	0.4	(1.19 ± 0.02)E+1	(2.31 ± 0.04)E+3	0.3
9226	17728	49.53	+0.12	63	1.1	(2.59 ± 0.03)E+2	(1.27 ± 0.01)E+2	2.0
···	17743	49.54	+0.16	···	1.5	(4.45 ± 0.03)E+2	(8.25 ± 0.06)E+1	2.8
···	17757	49.56	+0.19	···	0.6	(6.3 ± 0.2)E+1	(1.59 ± 0.04)E+2	1.2
9428	16838	48.43	+0.15	48	1.1	(4.70 ± 0.06)E+1	(1.70 ± 0.02)E+2	1.0
···	16842	48.58	+0.16	49	0.2	(7.8 ± 0.3)E+0	(3.9 ± 0.1)E+3	0.2
···	16851	48.56	+0.18	51	0.3	(1.33 ± 0.04)E+1	(3.6 ± 0.1)E+3	0.2
···	16778	48.74	+0.06	···	0.9	(1.038 ± 0.006)E+2	(5.42 ± 0.03)E+2	0.9
···	16822	48.48	+0.12	···	0.7	(3.74 ± 0.04)E+1	(4.12 ± 0.05)E+2	0.7
···	16828	48.45	+0.13	···	0.5	(3.03 ± 0.04)E+1	(8.8 ± 0.1)E+2	0.5
···	16831	48.60	+0.14	···	···	(1.67 ± 0.04)E+1	···	···
···	16808	48.51	+0.10	···	0.8	(4.66 ± 0.05)E+1	(4.11 ± 0.04)E+2	0.8
···	16834	48.47	+0.14	···	0.9	(3.83 ± 0.04)E+1	(2.77 ± 0.03)E+2	0.8
···	16841	48.72	+0.15	···	1.8	(2.251 ± 0.009)E+2	(1.814 ± 0.007)E+2	1.7
···	16789	48.72	+0.06	···	1.0	(1.076 ± 0.005)E+2	(4.49 ± 0.02)E+2	1.0
9429	16602	48.73	−0.34	63	0.8	(5.17 ± 0.06)E+1	(3.81 ± 0.04)E+2	0.8
···	16644	48.45	−0.28	57	1.4	(7.30 ± 0.08)E+1	(1.07 ± 0.01)E+2	1.4
···	16679	48.60	−0.18	56	···	(2.91 ± 0.04)E+1	···	···
9444	16857	48.66	+0.19	11	···	(9.9 ± 0.2)E+1	···	···
···	16864	48.71	+0.20	11	0.9	(4.37 ± 0.04)E+2	(1.38 ± 0.01)E+2	2.3
···	16873	48.62	+0.22	8	0.6	(1.156 ± 0.003)E+3	(1.448 ± 0.004)E+3	1.5
···	16875	48.74	+0.21	12	0.9	(6.59 ± 0.03)E+2	(2.35 ± 0.01)E+2	2.2
···	16878	48.66	+0.22	12	1.1	(1.781 ± 0.004)E+3	(3.352 ± 0.008)E+2	2.8
···	16882	48.64	+0.23	15	1.0	(2.164 ± 0.004)E+3	(5.82 ± 0.01)E+2	2.5
···	16885	48.60	+0.25	10	1.5	(3.719 ± 0.006)E+3	(2.450 ± 0.004)E+2	3.9
···	16908	48.66	+0.29	10	···	(3.07 ± 0.03)E+2	···	···
···	16977	48.66	+0.43	5	0.2	(3.6 ± 0.2)E+1	(1.06 ± 0.06)E+3	0.5
···	16978	48.63	+0.42	4	0.8	(2.27 ± 0.03)E+2	(1.06 ± 0.02)E+2	2.0
···	16989	48.61	+0.44	5	1.1	(4.73 ± 0.04)E+2	(9.12 ± 0.08)E+1	2.8
···	16935	48.64	+0.36	···	···	(1.91 ± 0.03)E+2	···	···
9446	16759	48.61	+0.01	18	1.9	(1.7965 ± 0.0008)E+4	(6.524 ± 0.003)E+2	4.8
···	16771	48.54	+0.04	16	···	(4.72 ± 0.02)E+2	···	···
···	16779	48.58	+0.05	16	1.2	(6.266 ± 0.005)E+3	(9.418 ± 0.008)E+2	3.0
···	16802	48.62	+0.09	17	0.5	(1.133 ± 0.003)E+3	(1.715 ± 0.005)E+3	1.4
···	16811	48.63	+0.11	18	1.1	(1.021 ± 0.004)E+3	(2.029 ± 0.008)E+2	2.7
···	16816	48.66	+0.12	19	1.0	(1.298 ± 0.004)E+3	(3.38 ± 0.01)E+2	2.5
···	16738	48.71	−0.03	···	0.4	(9.8 ± 0.2)E+1	(2.68 ± 0.06)E+2	1.1
···	16797	48.71	+0.08	···	0.7	(3.01 ± 0.03)E+2	(2.66 ± 0.02)E+2	1.7
···	16790	48.68	+0.07	···	···	(1.23 ± 0.02)E+2	···	···
9450	16588	48.48	−0.37	40	···	(7.4 ± 0.4)E+0	···	···
···	16591	48.64	−0.38	33	1.2	(3.75 ± 0.07)E+1	(9.5 ± 0.2)E+1	1.2
···	16593	48.54	−0.36	33	0.4	(7.7 ± 0.4)E+0	(7.5 ± 0.3)E+2	0.3
···	16614	48.57	−0.34	33	0.8	(5.82 ± 0.06)E+1	(4.26 ± 0.04)E+2	0.8
···	16624	48.65	−0.32	34	1.0	(6.95 ± 0.06)E+1	(3.47 ± 0.03)E+2	0.9
···	16626	48.58	−0.31	34	0.9	(2.80 ± 0.05)E+1	(2.01 ± 0.04)E+2	0.8
···	16628	48.66	−0.29	34	1.3	(2.888 ± 0.007)E+2	(6.56 ± 0.02)E+2	1.2
···	16640	48.55	−0.28	37	1.6	(6.74 ± 0.08)E+1	(7.60 ± 0.09)E+1	1.5
···	16643	48.61	−0.27	35	1.4	(3.63 ± 0.07)E+1	(5.8 ± 0.1)E+1	1.4
···	16659	48.67	−0.24	35	1.4	(2.075 ± 0.007)E+2	(3.38 ± 0.01)E+2	1.4
···	16669	48.68	−0.22	34	0.5	(4.85 ± 0.04)E+1	(2.37 ± 0.02)E+3	0.4
···	16599	48.66	−0.35	···	···	(4.5 ± 0.2)E+0	···	···
···	16603	48.51	−0.35	···	···	(7.3 ± 0.4)E+0	···	···
9452	16524	48.61	−0.49	31	···	(3.7 ± 0.2)E+0	···	···
···	16543	48.63	−0.46	30	1.3	(1.225 ± 0.007)E+2	(2.23 ± 0.01)E+2	1.3
···	16550	48.68	−0.44	30	1.4	(1.311 ± 0.007)E+2	(2.18 ± 0.01)E+2	1.3
···	16551	48.54	−0.42	31	1.2	(1.67 ± 0.06)E+1	(4.1 ± 0.1)E+1	1.2
10122	15689	47.12	−0.27	66	1.3	(2.02 ± 0.02)E+2	(8.48 ± 0.08)E+1	2.1
···	15700	47.15	−0.25	65	0.7	(3.0 ± 0.1)E+1	(6.7 ± 0.3)E+1	1.2
10353	15898	47.06	+0.11	40	1.5	(1.38 ± 0.02)E+2	(3.55 ± 0.05)E+1	2.5
···	15911	46.94	+0.13	41	···	(1.26 ± 0.08)E+1	···	···
10427	15929	46.76	+0.16	17	1.8	(3.99 ± 0.02)E+2	(5.33 ± 0.03)E+1	3.1
···	15970	46.78	+0.23	13	0.9	(2.08 ± 0.02)E+2	(2.25 ± 0.02)E+2	1.6
···	16000	46.79	+0.28	13	1.0	(1.73 ± 0.02)E+2	(1.60 ± 0.02)E+2	1.6
···	15916	46.74	+0.14	···	0.6	(6.0 ± 0.1)E+1	(2.32 ± 0.04)E+2	1.0
10433	15704	46.84	−0.25	17	···	(4.7 ± 0.5)E+0	···	···
···	15729	46.80	−0.21	14	···	(2.97 ± 0.08)E+1	···	···
···	15759	46.89	−0.14	19	2.4	(2.47 ± 0.03)E+2	(1.48 ± 0.02)E+1	4.1
···	15782	46.84	−0.10	22	1.3	(1.08 ± 0.02)E+2	(4.30 ± 0.07)E+1	2.2
···	15802	46.60	−0.08	15	0.6	(5.3 ± 0.1)E+1	(2.29 ± 0.05)E+2	1.0

Continuation of Table B2

COHRS catalog #	Hi-GAL catalog #	ℓ (deg)	b (deg)	$v_{\rm LSR}$ (km s^{-1})	$\theta_{\rm R}$ (arcmin)	M (M$_\odot$)	n (cm^{-3})	R (pc)
···	15810	46.72	−0.05	13	1.5	(1.81 ± 0.02)E+2	(4.54 ± 0.05)E+1	2.5
···	15820	46.77	−0.04	15	1.3	(1.32 ± 0.02)E+2	(5.08 ± 0.07)E+1	2.2
···	15831	46.64	−0.02	15	0.8	(1.62 ± 0.01)E+2	(2.29 ± 0.02)E+2	1.4
···	15801	46.62	−0.08	···	1.1	(1.80 ± 0.02)E+2	(1.09 ± 0.01)E+2	1.9
···	15837	46.68	−0.02	···	1.2	(1.71 ± 0.02)E+2	(7.75 ± 0.08)E+1	2.1
10443	15936	46.46	+0.17	8	1.0	(1.05 ± 0.01)E+2	(7.9 ± 0.1)E+1	1.7
···	15947	46.60	+0.20	8	0.9	(1.00 ± 0.01)E+2	(1.02 ± 0.02)E+2	1.6
···	15986	46.56	+0.26	9	1.2	(2.22 ± 0.02)E+2	(1.044 ± 0.009)E+2	2.0
···	15957	46.49	+0.19	···	2.0	(2.73 ± 0.03)E+2	(2.85 ± 0.03)E+1	3.4
···	15982	46.52	+0.25	···	2.2	(4.98 ± 0.03)E+2	(3.86 ± 0.02)E+1	3.7
10606	15790	47.00	−0.09	55	1.3	(9.6 ± 0.1)E+1	(6.38 ± 0.08)E+1	1.8
···	15804	46.96	−0.07	59	1.0	(6.7 ± 0.1)E+1	(1.19 ± 0.02)E+2	1.3
···	15813	47.04	−0.05	58	0.8	(3.47 ± 0.08)E+1	(1.17 ± 0.03)E+2	1.1
···	15818	46.99	−0.05	58	1.6	(1.16 ± 0.01)E+2	(4.51 ± 0.05)E+1	2.2
···	15881	46.70	+0.07	61	0.4	(2.49 ± 0.07)E+1	(5.0 ± 0.1)E+2	0.6
···	15908	46.60	+0.13	59	1.3	(1.34 ± 0.01)E+2	(9.22 ± 0.09)E+1	1.8
···	15919	46.70	+0.15	58	2.4	(2.47 ± 0.02)E+2	(3.02 ± 0.02)E+1	3.2
···	15933	46.67	+0.17	57	0.8	(3.44 ± 0.08)E+1	(1.09 ± 0.03)E+2	1.1
···	15948	46.52	+0.19	58	0.9	(8.05 ± 0.09)E+1	(1.85 ± 0.02)E+2	1.2
···	15965	46.95	+0.22	58	0.9	(1.196 ± 0.009)E+2	(2.28 ± 0.02)E+2	1.3
···	15977	46.93	+0.24	57	1.2	(1.57 ± 0.01)E+2	(1.48 ± 0.01)E+2	1.6
···	15980	47.03	+0.24	55	2.0	(2.237 ± 0.002)E+3	(4.511 ± 0.004)E+2	2.7
···	15991	46.93	+0.27	60	1.1	(6.7 ± 0.1)E+1	(8.4 ± 0.1)E+1	1.5
···	15809	46.93	−0.06	···	···	(1.21 ± 0.06)E+1	···	···
···	15822	46.88	−0.04	···	0.7	(3.02 ± 0.09)E+1	(1.30 ± 0.04)E+2	1.0
···	15893	46.64	+0.11	···	1.3	(1.81 ± 0.01)E+2	(1.49 ± 0.01)E+2	1.7
···	15930	46.51	+0.16	···	0.4	(1.82 ± 0.06)E+1	(5.4 ± 0.2)E+2	0.5
···	15941	46.54	+0.18	···	1.0	(9.8 ± 0.1)E+1	(1.67 ± 0.02)E+2	1.3
···	15990	47.09	+0.26	···	1.1	(3.34 ± 0.01)E+2	(4.05 ± 0.01)E+2	1.5
10699	15866	46.39	+0.03	60	1.7	(9.2 ± 0.1)E+1	(3.14 ± 0.05)E+1	2.3
···	15873	46.29	+0.05	56	0.9	(6.3 ± 0.1)E+1	(1.33 ± 0.02)E+2	1.2
···	15922	46.25	+0.14	···	1.7	(1.38 ± 0.01)E+2	(4.30 ± 0.04)E+1	2.3
10924	15701	46.50	−0.25	54	1.2	(2.26 ± 0.01)E+2	(2.13 ± 0.01)E+2	1.6
···	15708	46.35	−0.24	53	···	(4.88 ± 0.07)E+1	···	···
···	15709	46.42	−0.24	53	1.5	(8.42 ± 0.01)E+2	(4.404 ± 0.008)E+2	2.0
···	15710	46.38	−0.23	53	1.2	(3.21 ± 0.01)E+2	(2.91 ± 0.01)E+2	1.6
···	15715	46.30	−0.24	53	2.1	(1.419 ± 0.002)E+3	(2.658 ± 0.003)E+2	2.8
···	15719	46.51	−0.22	54	1.8	(6.27 ± 0.01)E+2	(1.888 ± 0.005)E+2	2.4
···	15723	46.37	−0.21	55	0.5	(1.133 ± 0.007)E+2	(1.78 ± 0.01)E+3	0.6
···	15730	46.24	−0.20	58	1.4	(1.43 ± 0.01)E+2	(8.59 ± 0.07)E+1	1.9
···	15736	46.54	−0.20	54	1.9	(5.69 ± 0.02)E+2	(1.378 ± 0.004)E+2	2.6
···	15737	46.42	−0.20	53	0.9	(1.187 ± 0.009)E+2	(3.08 ± 0.02)E+2	1.2
···	15738	46.27	−0.19	57	1.0	(1.156 ± 0.009)E+2	(1.77 ± 0.01)E+2	1.4
···	15740	46.46	−0.19	54	1.5	(4.41 ± 0.01)E+2	(2.176 ± 0.007)E+2	2.0
···	15750	46.34	−0.16	56	···	(2.69 ± 0.05)E+1	···	···
···	15752	46.25	−0.16	56	0.6	(4.29 ± 0.08)E+1	(3.50 ± 0.07)E+2	0.8
···	15754	46.57	−0.15	54	···	(1.61 ± 0.05)E+1	···	···
···	15755	46.41	−0.15	50	0.2	(1.257 ± 0.006)E+2	(1.340 ± 0.007)E+4	0.3
···	15769	46.58	−0.12	53	0.8	(3.89 ± 0.08)E+1	(1.11 ± 0.02)E+2	1.1
···	15774	46.61	−0.12	52	0.9	(1.04 ± 0.01)E+2	(2.41 ± 0.02)E+2	1.2
···	15685	46.47	−0.28	···	0.5	(4.50 ± 0.07)E+1	(7.7 ± 0.1)E+2	0.6
···	15724	46.31	−0.21	···	1.3	(4.84 ± 0.01)E+2	(3.276 ± 0.008)E+2	1.8
···	15727	46.35	−0.20	···	0.7	(7.59 ± 0.08)E+1	(2.99 ± 0.03)E+2	1.0
10942	15739	46.78	−0.18	47	1.7	(8.9 ± 0.1)E+1	(2.94 ± 0.04)E+1	2.3
···	15779	46.90	−0.11	46	0.6	(3.46 ± 0.07)E+1	(2.81 ± 0.06)E+2	0.8
···	15799	46.89	−0.08	46	0.7	(2.03 ± 0.07)E+1	(1.18 ± 0.04)E+2	0.9
···	15830	46.82	−0.02	49	3.1	(4.12 ± 0.02)E+2	(2.28 ± 0.01)E+1	4.2
···	15856	46.69	+0.02	48	1.3	(1.25 ± 0.01)E+2	(9.69 ± 0.09)E+1	1.7
···	15863	46.81	+0.04	48	1.5	(1.12 ± 0.01)E+2	(5.15 ± 0.06)E+1	2.1
11021	15838	46.47	−0.01	49	0.8	(1.612 ± 0.009)E+2	(5.97 ± 0.04)E+2	1.0
···	15844	46.56	−0.00	46	1.2	(1.49 ± 0.01)E+2	(1.30 ± 0.01)E+2	1.7
···	15854	46.50	+0.01	46	1.6	(4.14 ± 0.01)E+2	(1.635 ± 0.006)E+2	2.2
···	15816	46.59	−0.05	···	0.5	(1.23 ± 0.06)E+1	(1.89 ± 0.09)E+2	0.6
···	15859	46.54	+0.02	···	0.7	(2.48 ± 0.08)E+1	(1.33 ± 0.04)E+2	0.9
···	15864	46.58	+0.04	···	1.0	(3.2 ± 0.1)E+1	(5.6 ± 0.2)E+1	1.3
11178	15775	46.14	−0.12	56	0.9	(1.009 ± 0.009)E+2	(2.14 ± 0.02)E+2	1.2
···	15817	46.21	−0.05	61	···	(2.23 ± 0.07)E+1	···	···
···	15824	46.03	−0.03	60	0.4	(1.072 ± 0.008)E+2	(1.98 ± 0.01)E+3	0.6
···	15825	45.96	−0.03	63	0.3	(1.83 ± 0.06)E+1	(1.79 ± 0.06)E+3	0.3
···	15832	45.99	−0.02	61	···	(3.21 ± 0.07)E+1	···	···
···	15834	46.11	−0.02	60	0.9	(7.6 ± 0.1)E+1	(1.72 ± 0.02)E+2	1.2
···	15847	45.94	−0.00	61	0.6	(5.74 ± 0.08)E+1	(3.82 ± 0.06)E+2	0.8
···	15852	46.19	+0.00	57	0.9	(1.02 ± 0.01)E+2	(2.19 ± 0.02)E+2	1.2
···	15865	46.04	+0.03	60	1.0	(6.2 ± 0.1)E+1	(9.4 ± 0.2)E+1	1.4
···	15867	46.12	+0.04	61	0.3	(2.28 ± 0.06)E+1	(1.51 ± 0.04)E+3	0.4
···	15853	46.12	+0.01	···	0.4	(2.14 ± 0.06)E+1	(6.4 ± 0.2)E+2	0.5
···	15829	46.20	−0.03	···	0.6	(1.83 ± 0.07)E+1	(1.27 ± 0.05)E+2	0.8
···	15840	46.30	−0.01	···	1.1	(6.4 ± 0.1)E+1	(7.3 ± 0.1)E+1	1.5
11195	15915	45.87	+0.14	19	0.3	(1.47 ± 0.03)E+2	(6.3 ± 0.1)E+2	1.0
···	15924	45.72	+0.16	13	0.3	(9.3 ± 0.3)E+1	(4.1 ± 0.1)E+2	1.0
···	15927	45.83	+0.16	···	1.3	(2.60 ± 0.06)E+2	(1.91 ± 0.04)E+1	3.8
···	15972	45.81	+0.23	···	···	(5.1 ± 0.3)E+1	···	···
···	15979	45.73	+0.24	···	0.9	(3.87 ± 0.05)E+2	(6.77 ± 0.09)E+1	2.8
···	15984	45.89	+0.25	···	1.2	(3.80 ± 0.05)E+2	(2.92 ± 0.04)E+1	3.7

Continuation of Table B2

COHRS catalog #	Hi-GAL catalog #	ℓ (deg)	b (deg)	$v_{\rm LSR}$ (km s^{-1})	$\theta_{\rm R}$ (arcmin)	M (M$_\odot$)	n (cm^{-3})	R (pc)
11202	15749	45.97	−0.17	16	···	(7.9 ± 0.3)E+1	···	···
···	15753	45.77	−0.15	18	0.5	(9.4 ± 0.3)E+1	(1.42 ± 0.05)E+2	1.4
···	15764	45.89	−0.14	13	1.1	(2.38 ± 0.05)E+2	(2.67 ± 0.06)E+1	3.3
···	15778	45.81	−0.11	14	1.6	(6.17 ± 0.07)E+2	(2.41 ± 0.03)E+1	4.7
···	15781	45.99	−0.11	17	1.3	(6.67 ± 0.06)E+2	(5.08 ± 0.05)E+1	3.8
···	15783	45.77	−0.10	13	0.6	(1.18 ± 0.04)E+2	(8.5 ± 0.3)E+1	1.8
···	15793	45.95	−0.09	16	1.4	(7.08 ± 0.06)E+2	(3.78 ± 0.03)E+1	4.2
···	15812	45.95	−0.06	17	0.8	(4.88 ± 0.04)E+2	(1.32 ± 0.01)E+2	2.5
···	15763	45.96	−0.14	···	0.7	(1.36 ± 0.04)E+2	(5.5 ± 0.2)E+1	2.2
···	15711	45.84	−0.24	···	···	(9.3 ± 0.3)E+1	···	···
···	15748	46.03	−0.17	···	1.4	(1.564 ± 0.006)E+3	(8.71 ± 0.03)E+1	4.2
···	15758	45.78	−0.14	···	···	(3.0 ± 0.2)E+1	···	···
···	15794	45.84	−0.08	···	1.1	(5.38 ± 0.05)E+2	(5.53 ± 0.06)E+1	3.4
11203	15787	46.18	−0.11	15	1.3	(2.823 ± 0.007)E+3	(1.732 ± 0.004)E+2	4.0
11207	15706	46.10	−0.24	53	0.4	(1.51 ± 0.06)E+1	(5.4 ± 0.2)E+2	0.5
···	15742	46.05	−0.19	51	1.5	(4.06 ± 0.01)E+2	(1.740 ± 0.006)E+2	2.1
···	15760	46.05	−0.14	48	1.3	(2.47 ± 0.01)E+2	(1.717 ± 0.008)E+2	1.8
···	15771	46.06	−0.12	49	1.6	(2.63 ± 0.01)E+2	(9.98 ± 0.05)E+1	2.2
···	15788	46.11	−0.10	50	1.6	(3.20 ± 0.01)E+2	(1.203 ± 0.005)E+2	2.2
···	15807	46.06	−0.06	50	1.1	(1.41 ± 0.01)E+2	(1.53 ± 0.01)E+2	1.5
11504	15743	45.22	−0.18	55	0.9	(9.7 ± 0.2)E+1	(9.5 ± 0.2)E+1	1.6
···	15768	45.20	−0.13	58	0.3	(4.2 ± 0.1)E+1	(9.3 ± 0.2)E+2	0.6
···	15785	45.24	−0.10	59	2.0	(5.31 ± 0.03)E+2	(4.01 ± 0.03)E+1	3.8
···	15747	45.25	−0.17	···	1.3	(2.20 ± 0.02)E+2	(6.55 ± 0.07)E+1	2.4
···	15756	45.21	−0.15	···	0.5	(9.5 ± 0.1)E+1	(3.55 ± 0.05)E+2	1.0
11516	15672	45.58	−0.30	50	1.6	(3.32 ± 0.03)E+2	(4.93 ± 0.04)E+1	3.0
···	15696	45.51	−0.26	52	1.2	(6.34 ± 0.02)E+2	(2.012 ± 0.007)E+2	2.3
···	15707	45.48	−0.24	54	1.5	(3.69 ± 0.03)E+2	(6.95 ± 0.05)E+1	2.8
11577	15646	45.29	−0.34	58	2.3	(7.68 ± 0.04)E+2	(3.75 ± 0.02)E+1	4.4
···	15617	45.31	−0.38	···	0.8	(7.3 ± 0.1)E+1	(9.8 ± 0.2)E+1	1.4
···	15642	45.26	−0.34	···	0.9	(1.81 ± 0.02)E+2	(1.39 ± 0.01)E+2	1.7
11618	14840	45.04	−0.09	69	1.2	(9.3 ± 0.2)E+1	(4.15 ± 0.08)E+1	2.1
···	15773	45.12	−0.12	59	0.7	(1.14 ± 0.01)E+2	(2.59 ± 0.03)E+2	1.2
···	15826	45.10	−0.04	···	1.9	(1.92 ± 0.02)E+2	(2.06 ± 0.03)E+1	3.4
11626	15776	45.48	−0.12	59	1.3	(4.29 ± 0.02)E+2	(1.289 ± 0.006)E+2	2.4
···	15780	45.44	−0.11	60	1.5	(1.006 ± 0.002)E+3	(1.851 ± 0.004)E+2	2.8
···	15784	45.42	−0.10	61	0.6	(2.56 ± 0.02)E+2	(6.18 ± 0.04)E+2	1.2
···	15797	45.46	−0.07	58	1.4	(9.11 ± 0.03)E+2	(1.905 ± 0.005)E+2	2.7
···	15849	45.48	+0.00	58	···	(1.26 ± 0.01)E+2	···	···
···	15870	45.54	+0.05	61	···	(1.74 ± 0.02)E+2	···	···
···	15872	45.46	+0.04	64	1.6	(1.0544 ± 0.0004)E+4	(1.4978 ± 0.0005)E+3	3.1
···	15876	45.44	+0.07	57	1.5	(7.287 ± 0.003)E+3	(1.3280 ± 0.0005)E+3	2.8
···	15878	45.52	+0.06	56	···	(8.04 ± 0.09)E+1	···	···
···	15902	45.54	+0.12	58	1.0	(9.53 ± 0.02)E+2	(6.22 ± 0.01)E+2	1.8
···	15912	45.47	+0.13	63	0.7	(3.839 ± 0.002)E+3	(5.757 ± 0.003)E+3	1.4
···	15918	45.53	+0.14	59	0.7	(6.35 ± 0.02)E+2	(1.145 ± 0.003)E+3	1.3
···	15935	45.49	+0.16	58	···	(2.09 ± 0.09)E+1	···	···
···	15907	45.50	+0.13	···	0.8	(3.278 ± 0.002)E+3	(3.689 ± 0.002)E+3	1.5
11627	15888	45.17	+0.09	59	0.9	(5.37 ± 0.02)E+2	(4.63 ± 0.02)E+2	1.7
···	15900	45.28	+0.11	59	···	(1.37 ± 0.08)E+1	···	···
···	15901	45.24	+0.12	57	1.0	(2.64 ± 0.02)E+2	(1.70 ± 0.01)E+2	1.8
···	15910	45.12	+0.13	59	1.0	(8.775 ± 0.003)E+3	(5.327 ± 0.002)E+3	1.9
···	15913	45.07	+0.13	60	0.9	(5.479 ± 0.003)E+3	(4.020 ± 0.002)E+3	1.8
···	15905	45.19	+0.12	···	0.4	(1.17 ± 0.01)E+2	(8.04 ± 0.09)E+2	0.8
···	15959	45.10	+0.21	···	1.2	(5.28 ± 0.02)E+2	(1.892 ± 0.008)E+2	2.2
11822	15615	45.54	−0.39	58	0.5	(1.87 ± 0.01)E+2	(7.62 ± 0.05)E+2	1.0
···	15627	45.52	−0.35	60	2.2	(1.221 ± 0.004)E+3	(6.98 ± 0.02)E+1	4.1
11911	15553	45.61	−0.48	62	1.1	(1.72 ± 0.02)E+2	(7.64 ± 0.09)E+1	2.1
···	15558	45.57	−0.47	60	1.5	(5.16 ± 0.03)E+2	(9.38 ± 0.05)E+1	2.8
···	15570	45.53	−0.46	57	1.6	(2.53 ± 0.03)E+2	(4.05 ± 0.04)E+1	2.9
11938	16016	45.70	+0.31	18	···	(2.71 ± 0.08)E+1	···	···
···	16032	45.69	+0.33	18	1.1	(5.4 ± 0.2)E+1	(3.4 ± 0.1)E+1	1.9
···	16060	45.54	+0.37	17	0.8	(5.9 ± 0.1)E+1	(7.7 ± 0.2)E+1	1.5
···	16025	45.59	+0.32	···	2.1	(4.84 ± 0.03)E+2	(3.96 ± 0.02)E+1	3.7
···	16050	45.56	+0.34	···	0.8	(4.4 ± 0.1)E+1	(8.0 ± 0.2)E+1	1.3
···	16020	45.63	+0.31	···	···	(1.14 ± 0.07)E+1	···	···
···	16024	45.66	+0.31	···	0.7	(1.52 ± 0.01)E+2	(4.26 ± 0.03)E+2	1.1
···	16044	45.66	+0.35	···	1.6	(2.03 ± 0.02)E+2	(3.61 ± 0.04)E+1	2.8
12064	15808	45.10	−0.07	26	1.2	(1.03 ± 0.02)E+2	(3.76 ± 0.07)E+1	2.2
···	15842	45.16	−0.02	26	1.9	(2.41 ± 0.03)E+2	(2.26 ± 0.03)E+1	3.5
···	15928	45.29	+0.16	···	0.7	(7.3 ± 0.2)E+1	(1.18 ± 0.03)E+2	1.4
···	15800	45.06	−0.07	···	1.7	(2.40 ± 0.03)E+2	(2.84 ± 0.03)E+1	3.2
12071	15772	45.56	−0.12	5	1.1	(1.708 ± 0.006)E+3	(1.462 ± 0.005)E+2	3.6
···	15789	45.56	−0.09	6	0.6	(3.03 ± 0.04)E+2	(1.67 ± 0.02)E+2	1.9
···	15823	45.62	−0.04	8	0.7	(1.407 ± 0.005)E+3	(5.07 ± 0.02)E+2	2.2
···	15836	45.64	−0.01	7	1.5	(5.155 ± 0.009)E+3	(1.780 ± 0.003)E+2	4.9
12231	15643	45.77	−0.35	57	1.5	(1.175 ± 0.002)E+3	(1.946 ± 0.004)E+2	2.9
···	15654	45.74	−0.33	56	0.7	(3.98 ± 0.02)E+2	(6.77 ± 0.03)E+2	1.3
···	15662	45.77	−0.32	59	···	(8.0 ± 0.1)E+1	···	···
···	15671	45.71	−0.29	50	···	(1.11 ± 0.08)E+1	···	···
···	15681	45.83	−0.29	61	1.0	(1.690 ± 0.002)E+3	(1.135 ± 0.001)E+3	1.8
···	15693	45.92	−0.26	61	1.5	(3.42 ± 0.02)E+2	(6.79 ± 0.05)E+1	2.7
···	15695	45.88	−0.27	60	1.1	(2.65 ± 0.02)E+2	(1.092 ± 0.009)E+2	2.1
···	15702	45.76	−0.25	60	1.2	(1.480 ± 0.002)E+3	(4.995 ± 0.008)E+2	2.3

Continuation of Table B2

COHRS catalog #	Hi-GAL catalog #	ℓ (deg)	b (deg)	$v_{\rm LSR}$ (km s^{-1})	$\theta_{\rm R}$ (arcmin)	M (M$_\odot$)	n (cm^{-3})	R (pc)
···	15705	45.89	−0.25	60	1.0	(2.22 ± 0.02)E+2	(1.56 ± 0.01)E+2	1.8
···	15712	45.81	−0.23	61	···	(4.7 ± 0.1)E+1	···	···
···	15746	45.74	−0.18	58	1.3	(2.10 ± 0.02)E+2	(5.41 ± 0.06)E+1	2.5
···	15679	45.74	−0.29	···	0.8	(2.32 ± 0.02)E+2	(3.08 ± 0.02)E+2	1.4
···	15684	45.64	−0.28	···	0.7	(1.23 ± 0.01)E+2	(2.07 ± 0.02)E+2	1.3
···	15716	45.70	−0.23	···	2.3	(2.523 ± 0.004)E+3	(1.304 ± 0.002)E+2	4.3
···	15725	45.68	−0.21	···	1.1	(2.78 ± 0.02)E+2	(1.289 ± 0.009)E+2	2.1
12462	15835	45.74	−0.01	69	0.8	(1.19 ± 0.02)E+2	(1.44 ± 0.02)E+2	1.5
···	15848	45.77	+0.00	70	0.7	(3.8 ± 0.1)E+1	(7.4 ± 0.3)E+1	1.3
···	15868	45.76	+0.04	71	0.8	(5.5 ± 0.2)E+1	(6.3 ± 0.2)E+1	1.5
12981	15998	45.79	+0.27	63	1.0	(1.80 ± 0.02)E+2	(1.09 ± 0.01)E+2	1.9
···	16003	45.86	+0.28	64	1.8	(8.04 ± 0.03)E+2	(8.96 ± 0.03)E+1	3.3
···	16009	45.82	+0.28	62	1.9	(5.14 ± 0.03)E+2	(4.48 ± 0.03)E+1	3.6
13109	14987	44.84	+0.16	68	0.5	(8.3 ± 0.1)E+1	(4.79 ± 0.08)E+2	0.9
···	14994	44.88	+0.18	68	1.9	(5.41 ± 0.03)E+2	(4.91 ± 0.03)E+1	3.5
···	15006	44.91	+0.19	69	0.9	(1.11 ± 0.02)E+2	(1.05 ± 0.01)E+2	1.6
···	15009	45.02	+0.20	65	···	(9.3 ± 0.1)E+1	···	···
···	15946	44.97	+0.19	64	0.5	(7.6 ± 0.1)E+1	(4.02 ± 0.06)E+2	0.9
···	15954	45.00	+0.20	65	0.7	(1.10 ± 0.01)E+2	(2.19 ± 0.03)E+2	1.3
···	15973	45.02	+0.23	65	0.9	(1.35 ± 0.02)E+2	(1.06 ± 0.01)E+2	1.7
···	15999	45.06	+0.28	67	0.7	(8.2 ± 0.1)E+1	(1.53 ± 0.03)E+2	1.3
···	14969	44.94	+0.12	···	···	(4.8 ± 0.7)E+0	···	···
13159	14908	44.65	+0.00	41	1.2	(2.14 ± 0.02)E+2	(8.24 ± 0.08)E+1	2.2
···	14872	44.48	−0.05	···	1.3	(1.42 ± 0.02)E+2	(4.51 ± 0.07)E+1	2.3
13183	14912	44.39	+0.01	17	0.7	(5.7 ± 0.1)E+1	(1.14 ± 0.03)E+2	1.3
···	14937	44.10	+0.07	12	0.9	(1.21 ± 0.01)E+2	(1.37 ± 0.02)E+2	1.5
···	14945	44.55	+0.08	22	0.6	(4.8 ± 0.1)E+1	(1.55 ± 0.04)E+2	1.1
···	14939	44.44	+0.07	···	0.6	(9.1 ± 0.1)E+1	(2.66 ± 0.04)E+2	1.1
···	14914	44.82	+0.01	···	1.5	(1.96 ± 0.02)E+2	(4.38 ± 0.05)E+1	2.6
···	14918	44.86	+0.03	···	0.7	(5.2 ± 0.1)E+1	(9.6 ± 0.3)E+1	1.3
···	14951	44.59	+0.08	···	2.7	(9.93 ± 0.04)E+2	(3.86 ± 0.01)E+1	4.7
···	15018	44.11	+0.22	···	0.8	(2.65 ± 0.02)E+2	(3.68 ± 0.02)E+2	1.4
13267	14770	44.72	−0.26	63	1.9	(3.72 ± 0.03)E+2	(3.51 ± 0.03)E+1	3.5
···	14774	44.69	−0.25	62	0.8	(9.8 ± 0.2)E+1	(1.22 ± 0.02)E+2	1.5
···	14797	44.66	−0.19	60	0.8	(5.2 ± 0.2)E+1	(6.3 ± 0.2)E+1	1.5
···	14823	44.69	−0.12	51	1.5	(5.14 ± 0.03)E+2	(1.008 ± 0.005)E+2	2.7
···	14836	44.71	−0.11	51	0.9	(1.09 ± 0.02)E+2	(9.7 ± 0.2)E+1	1.7
···	14858	44.66	−0.08	52	0.6	(1.07 ± 0.01)E+2	(3.69 ± 0.05)E+2	1.1
···	14859	44.63	−0.08	52	1.3	(2.61 ± 0.02)E+2	(6.82 ± 0.06)E+1	2.5
···	14879	44.65	−0.04	52	0.6	(5.1 ± 0.1)E+1	(1.33 ± 0.04)E+2	1.2
···	14928	44.61	+0.03	53	1.3	(1.72 ± 0.02)E+2	(5.03 ± 0.07)E+1	2.4
···	14957	44.67	+0.10	55	0.6	(1.74 ± 0.02)E+2	(5.00 ± 0.05)E+2	1.1
···	14964	44.62	+0.11	52	0.5	(3.9 ± 0.1)E+1	(1.69 ± 0.06)E+2	1.0
···	14973	44.67	+0.12	54	1.6	(2.80 ± 0.03)E+2	(4.18 ± 0.04)E+1	3.0
···	14768	44.77	−0.26	···	1.7	(1.78 ± 0.03)E+2	(2.43 ± 0.04)E+1	3.1
···	14853	44.73	−0.10	···	0.7	(5.5 ± 0.2)E+1	(8.9 ± 0.3)E+1	1.4
···	14863	44.75	−0.07	···	0.9	(6.4 ± 0.2)E+1	(4.6 ± 0.1)E+1	1.8
···	14864	44.70	−0.07	···	···	(4.3 ± 0.1)E+1	···	···
13614	14929	44.07	+0.04	60	1.5	(7.60 ± 0.03)E+2	(1.161 ± 0.005)E+2	3.0
···	14949	44.13	+0.09	61	1.4	(4.78 ± 0.03)E+2	(9.61 ± 0.06)E+1	2.7
···	14956	44.17	+0.10	59	1.1	(1.97 ± 0.02)E+2	(8.07 ± 0.09)E+1	2.1
···	14958	44.11	+0.11	61	0.7	(1.27 ± 0.02)E+2	(2.14 ± 0.03)E+2	1.3
···	14985	44.11	+0.15	55	1.7	(9.54 ± 0.03)E+2	(1.071 ± 0.004)E+2	3.3
···	14946	44.09	+0.08	···	0.3	(9.2 ± 0.1)E+1	(1.43 ± 0.02)E+3	0.6
13648	14905	43.99	−0.02	66	2.3	(3.008 ± 0.005)E+3	(1.199 ± 0.002)E+2	4.7
···	14873	44.03	−0.05	···	0.8	(2.76 ± 0.02)E+2	(2.69 ± 0.02)E+2	1.6
13723	14989	43.96	+0.16	57	1.0	(1.12 ± 0.02)E+2	(6.3 ± 0.1)E+1	1.9
···	15014	43.96	+0.20	58	1.4	(2.51 ± 0.03)E+2	(4.65 ± 0.05)E+1	2.8
···	15021	43.92	+0.22	58	1.7	(5.47 ± 0.03)E+2	(5.95 ± 0.04)E+1	3.3
···	14996	43.93	+0.17	···	1.0	(1.65 ± 0.02)E+2	(8.1 ± 0.1)E+1	2.0
13761	14648	43.71	−0.50	59	1.7	(3.32 ± 0.03)E+2	(3.24 ± 0.03)E+1	3.5
···	14649	43.66	−0.49	61	1.6	(3.29 ± 0.03)E+2	(3.99 ± 0.04)E+1	3.2
···	14659	43.74	−0.46	60	1.0	(1.41 ± 0.02)E+2	(6.9 ± 0.1)E+1	2.0
···	14663	43.77	−0.45	62	1.2	(1.14 ± 0.02)E+2	(3.34 ± 0.06)E+1	2.4
···	14674	43.64	−0.44	54	···	(1.3 ± 0.1)E+1	···	···
···	14717	43.72	−0.36	59	0.8	(2.67 ± 0.02)E+2	(2.32 ± 0.02)E+2	1.7
···	14704	43.75	−0.38	···	0.2	(5.2 ± 0.1)E+1	(1.72 ± 0.04)E+3	0.5
14044	14684	43.60	−0.42	65	2.1	(4.57 ± 0.04)E+2	(2.42 ± 0.02)E+1	4.2
14251	14760	44.54	−0.28	63	1.4	(9.20 ± 0.03)E+2	(1.829 ± 0.006)E+2	2.7
···	14762	44.34	−0.28	67	1.7	(4.45 ± 0.03)E+2	(4.63 ± 0.03)E+1	3.4
···	14763	44.59	−0.28	63	1.0	(1.50 ± 0.02)E+2	(8.8 ± 0.1)E+1	1.9
···	14765	44.53	−0.27	64	0.9	(6.87 ± 0.02)E+2	(5.01 ± 0.01)E+2	1.8
···	14786	44.57	−0.21	62	1.2	(5.13 ± 0.03)E+2	(1.649 ± 0.009)E+2	2.3
···	14810	44.50	−0.16	59	1.2	(1.787 ± 0.003)E+3	(5.040 ± 0.008)E+2	2.4
···	14811	44.44	−0.15	61	0.3	(7.8 ± 0.1)E+1	(1.23 ± 0.02)E+3	0.6
···	14818	44.48	−0.13	61	1.2	(1.220 ± 0.003)E+3	(3.812 ± 0.009)E+2	2.3
···	14824	44.41	−0.13	63	···	(8.0 ± 0.2)E+1	···	···
···	14848	44.52	−0.09	60	0.8	(7.8 ± 0.2)E+1	(7.7 ± 0.2)E+1	1.6
···	14925	44.30	+0.04	58	1.5	(5.772 ± 0.004)E+3	(9.208 ± 0.007)E+2	2.9
···	14960	44.27	+0.12	59	1.4	(4.26 ± 0.03)E+2	(7.47 ± 0.05)E+1	2.8
···	14980	44.25	+0.16	58	1.5	(8.57 ± 0.03)E+2	(1.393 ± 0.005)E+2	2.9
···	14766	44.50	−0.27	···	1.5	(1.073 ± 0.003)E+3	(1.734 ± 0.005)E+2	2.9
···	14771	44.34	−0.25	···	1.0	(2.29 ± 0.02)E+2	(1.15 ± 0.01)E+2	2.0
···	14789	44.34	−0.22	···	2.5	(1.557 ± 0.005)E+3	(4.98 ± 0.01)E+1	5.0

Continuation of Table B2

COHRS catalog #	Hi-GAL catalog #	ℓ (deg)	b (deg)	$v_{\rm LSR}$ (km s^{-1})	$\theta_{\rm R}$ (arcmin)	M (M$_\odot$)	n (cm^{-3})	R (pc)
···	14795	44.30	−0.19	···	1.6	(6.17 ± 0.03)E+2	(7.55 ± 0.04)E+1	3.2
···	14798	44.52	−0.19	···	0.8	(4.00 ± 0.02)E+2	(3.70 ± 0.02)E+2	1.6
···	14826	44.26	−0.12	···	1.3	(3.85 ± 0.03)E+2	(9.06 ± 0.07)E+1	2.6
···	14837	44.53	−0.11	···	0.4	(6.5 ± 0.1)E+1	(4.3 ± 0.1)E+2	0.8
···	14950	44.28	+0.09	···	0.8	(2.32 ± 0.02)E+2	(2.73 ± 0.02)E+2	1.5
14266	14755	43.96	−0.28	69	1.7	(6.22 ± 0.04)E+2	(6.29 ± 0.04)E+1	3.4
···	14793	43.92	−0.22	60	2.3	(1.028 ± 0.005)E+3	(4.14 ± 0.02)E+1	4.6
···	14799	43.90	−0.19	60	1.1	(4.17 ± 0.02)E+2	(1.65 ± 0.01)E+2	2.2
14326	14976	43.70	+0.13	61	0.9	(1.99 ± 0.02)E+2	(1.54 ± 0.02)E+2	1.7
···	15012	43.66	+0.20	66	1.2	(2.98 ± 0.03)E+2	(8.55 ± 0.08)E+1	2.4
···	15029	43.69	+0.24	72	···	(7.5 ± 0.2)E+1	···	···
···	15037	43.75	+0.27	71	···	(5.7 ± 0.1)E+1	···	···
···	15038	43.70	+0.27	72	0.8	(7.1 ± 0.2)E+1	(5.9 ± 0.2)E+1	1.7
···	15046	43.73	+0.27	70	0.7	(9.8 ± 0.2)E+1	(1.21 ± 0.02)E+2	1.5
···	15054	43.75	+0.30	72	0.8	(1.46 ± 0.02)E+2	(1.34 ± 0.02)E+2	1.6
···	15061	43.76	+0.33	71	1.6	(1.91 ± 0.03)E+2	(2.57 ± 0.04)E+1	3.1
···	14975	43.64	+0.13	···	0.4	(9.9 ± 0.2)E+1	(9.3 ± 0.1)E+2	0.8
14529	15032	43.58	+0.25	17	1.2	(3.45 ± 0.03)E+2	(1.085 ± 0.009)E+2	2.3
···	15058	43.69	+0.31	7	1.7	(2.93 ± 0.03)E+2	(3.16 ± 0.04)E+1	3.3
···	15090	43.71	+0.39	17	1.4	(1.33 ± 0.03)E+2	(2.27 ± 0.05)E+1	2.9
···	15114	43.69	+0.43	18	0.8	(4.9 ± 0.2)E+1	(5.8 ± 0.2)E+1	1.5
···	15055	43.63	+0.30	···	1.5	(1.92 ± 0.03)E+2	(2.78 ± 0.04)E+1	3.0
···	15066	43.64	+0.33	···	0.9	(1.01 ± 0.02)E+2	(8.3 ± 0.2)E+1	1.7
···	15115	43.57	+0.43	···	1.2	(1.26 ± 0.02)E+2	(3.81 ± 0.07)E+1	2.4
···	15126	43.59	+0.45	···	0.6	(4.9 ± 0.2)E+1	(1.38 ± 0.04)E+2	1.1
14531	15015	43.35	+0.19	15	1.8	(2.83 ± 0.03)E+2	(3.19 ± 0.03)E+1	3.3
···	15003	43.44	+0.18	···	1.6	(1.58 ± 0.02)E+2	(2.87 ± 0.04)E+1	2.8
···	15033	43.48	+0.26	···	1.4	(1.80 ± 0.02)E+2	(4.82 ± 0.06)E+1	2.5
14584	14778	43.61	−0.23	15	1.1	(8.1 ± 0.2)E+1	(4.5 ± 0.1)E+1	1.9
14587	14896	43.66	−0.02	18	1.0	(1.97 ± 0.02)E+2	(1.10 ± 0.01)E+2	1.9
···	14920	43.68	+0.02	12	0.7	(8.8 ± 0.2)E+1	(1.25 ± 0.03)E+2	1.4
···	15019	43.73	+0.21	13	···	(8.2 ± 0.1)E+1	···	···
···	15023	43.81	+0.22	12	1.6	(2.24 ± 0.03)E+2	(2.63 ± 0.04)E+1	3.3
···	15031	43.75	+0.24	12	1.1	(3.38 ± 0.02)E+2	(1.135 ± 0.008)E+2	2.3
···	14865	43.66	−0.07	···	0.4	(3.7 ± 0.1)E+1	(3.0 ± 0.1)E+2	0.8
···	15028	43.88	+0.24	···	1.2	(3.59 ± 0.03)E+2	(1.015 ± 0.007)E+2	2.4
···	15040	43.78	+0.26	···	1.0	(7.6 ± 0.2)E+1	(3.8 ± 0.1)E+1	2.0
15030	14806	43.70	−0.17	66	0.8	(4.97 ± 0.02)E+2	(5.76 ± 0.03)E+2	1.5
···	14828	43.80	−0.13	45	0.8	(5.482 ± 0.003)E+3	(5.061 ± 0.003)E+3	1.6
···	14843	43.98	−0.10	44	1.2	(6.85 ± 0.03)E+2	(1.901 ± 0.009)E+2	2.4
···	14882	43.80	−0.04	60	···	(9 ± 1)E+0	···	···
···	14812	43.72	−0.15	···	0.7	(1.30 ± 0.02)E+2	(2.04 ± 0.03)E+2	1.4
···	14860	43.81	−0.08	···	1.4	(1.085 ± 0.003)E+3	(1.870 ± 0.006)E+2	2.9
15167	15024	43.53	+0.23	57	0.6	(3.2 ± 0.2)E+1	(8.3 ± 0.4)E+1	1.2
···	15025	43.39	+0.23	57	2.0	(4.20 ± 0.04)E+2	(2.77 ± 0.02)E+1	3.9
···	15026	43.46	+0.23	57	1.2	(1.85 ± 0.03)E+2	(5.90 ± 0.08)E+1	2.3
···	15034	43.44	+0.25	57	1.1	(1.10 ± 0.02)E+2	(3.69 ± 0.08)E+1	2.3
···	15082	43.50	+0.37	58	1.4	(1.41 ± 0.03)E+2	(2.87 ± 0.05)E+1	2.7
···	15002	43.54	+0.18	···	0.5	(3.5 ± 0.1)E+1	(1.48 ± 0.06)E+2	1.0
···	15109	43.39	+0.42	···	0.9	(3.5 ± 0.2)E+1	(2.2 ± 0.1)E+1	1.8
15380	14916	44.46	+0.01	69	···	(5.5 ± 0.1)E+1	···	···
···	14919	44.44	+0.04	69	1.4	(3.00 ± 0.03)E+2	(5.71 ± 0.05)E+1	2.8
···	14932	44.48	+0.06	69	0.9	(2.89 ± 0.02)E+2	(2.19 ± 0.02)E+2	1.7
···	14940	44.51	+0.07	69	1.8	(3.01 ± 0.03)E+2	(2.83 ± 0.03)E+1	3.5
···	14952	44.52	+0.09	70	0.5	(3.4 ± 0.1)E+1	(1.47 ± 0.06)E+2	1.0
···	14953	44.41	+0.09	···	1.2	(3.93 ± 0.03)E+2	(1.116 ± 0.007)E+2	2.4
15544	14941	42.91	+0.08	70	1.4	(3.84 ± 0.05)E+2	(2.89 ± 0.04)E+1	3.8
···	14991	43.10	+0.17	···	0.5	(5.4 ± 0.3)E+1	(7.8 ± 0.4)E+1	1.4
···	14992	43.07	+0.17	···	0.4	(7.1 ± 0.2)E+1	(2.33 ± 0.08)E+2	1.1
···	15004	43.18	+0.19	···	2.0	(4.11 ± 0.06)E+2	(9.4 ± 0.1)E+0	5.6
···	15000	42.99	+0.18	···	1.2	(1.75 ± 0.05)E+2	(2.14 ± 0.06)E+1	3.2
15615	14667	43.26	−0.45	62	0.7	(6.16 ± 0.04)E+2	(3.16 ± 0.02)E+2	2.0
···	14678	43.29	−0.43	63	0.4	(3.84 ± 0.03)E+2	(1.024 ± 0.008)E+3	1.1
···	14692	43.31	−0.41	63	0.6	(4.68 ± 0.03)E+2	(3.76 ± 0.03)E+2	1.7
···	14701	43.32	−0.39	63	1.2	(7.99 ± 0.05)E+2	(9.61 ± 0.06)E+1	3.2
···	14707	43.28	−0.37	64	1.6	(1.259 ± 0.006)E+3	(5.84 ± 0.03)E+1	4.4
···	14713	43.31	−0.36	63	1.5	(1.238 ± 0.005)E+3	(6.82 ± 0.03)E+1	4.2
···	14715	43.41	−0.36	60	0.8	(8.16 ± 0.04)E+2	(2.69 ± 0.01)E+2	2.3
···	14718	43.48	−0.36	59	0.9	(2.31 ± 0.04)E+2	(5.4 ± 0.1)E+1	2.6
···	14719	43.35	−0.36	62	1.2	(8.11 ± 0.05)E+2	(7.87 ± 0.05)E+1	3.5
···	14728	43.45	−0.34	58	0.5	(6.4 ± 0.3)E+1	(1.24 ± 0.05)E+2	1.3
···	14736	43.30	−0.33	62	1.1	(4.04 ± 0.04)E+2	(6.53 ± 0.07)E+1	2.9
···	14749	43.29	−0.31	62	0.9	(3.84 ± 0.04)E+2	(9.1 ± 0.1)E+1	2.6
···	14764	43.39	−0.27	62	···	(2.5 ± 0.2)E+1	···	···
···	14732	43.48	−0.33	···	1.3	(4.46 ± 0.05)E+2	(3.95 ± 0.04)E+1	3.6
···	14741	43.36	−0.31	···	···	(4.2 ± 0.2)E+1	···	···
···	14742	43.34	−0.31	···	···	(3.9 ± 0.3)E+1	···	···
···	14748	43.31	−0.30	···	0.5	(1.37 ± 0.03)E+2	(2.79 ± 0.06)E+2	1.3
15717	14833	43.48	−0.11	55	0.9	(5.85 ± 0.05)E+2	(1.58 ± 0.01)E+2	2.5
···	14856	43.60	−0.10	55	2.2	(1.724 ± 0.008)E+3	(2.91 ± 0.01)E+1	6.2
···	14817	43.46	−0.14	···	0.7	(3.03 ± 0.03)E+2	(1.65 ± 0.02)E+2	1.9
···	14830	43.63	−0.13	···	0.4	(8.6 ± 0.3)E+1	(1.83 ± 0.06)E+2	1.2
···	14844	43.56	−0.10	···	0.4	(3.04 ± 0.03)E+2	(9.5 ± 0.1)E+2	1.1
16267	14756	43.15	−0.29	46	···	(6.1 ± 0.3)E+1	···	···

Continuation of Table B2

COHRS catalog #	Hi-GAL catalog #	ℓ (deg)	b (deg)	$v_{\rm LSR}$ (km s^{-1})	$\theta_{\rm R}$ (arcmin)	M (M$_\odot$)	n (cm^{-3})	R (pc)
···	14769	43.16	−0.26	44	0.7	(2.32 ± 0.04)E+2	(1.43 ± 0.02)E+2	1.9
···	14852	43.03	−0.10	41	···	(7.4 ± 0.2)E+1	···	···
16500	13824	42.64	−0.20	58	···	(2.65 ± 0.02)E+2	···	···
···	13854	42.57	−0.17	66	1.2	(1.199 ± 0.005)E+3	(1.922 ± 0.008)E+2	2.9
···	13875	42.60	−0.15	65	0.8	(4.39 ± 0.04)E+2	(2.55 ± 0.02)E+2	1.9
···	13880	42.50	−0.15	68	1.6	(6.60 ± 0.05)E+2	(4.59 ± 0.04)E+1	3.9
···	13903	42.50	−0.11	69	0.8	(2.51 ± 0.04)E+2	(1.32 ± 0.02)E+2	2.0
···	13838	42.51	−0.18	···	0.6	(1.68 ± 0.03)E+2	(2.68 ± 0.04)E+2	1.4
16541	13891	42.03	−0.12	70	2.3	(2.848 ± 0.008)E+3	(6.53 ± 0.02)E+1	5.6
···	13930	41.98	−0.08	60	0.3	(1.55 ± 0.03)E+2	(1.49 ± 0.03)E+3	0.7
···	13932	42.05	−0.07	60	1.0	(3.79 ± 0.04)E+2	(1.16 ± 0.01)E+2	2.4
···	13944	42.01	−0.06	56	1.5	(7.26 ± 0.05)E+2	(6.41 ± 0.04)E+1	3.6
···	13956	41.99	−0.03	57	2.3	(3.082 ± 0.009)E+3	(6.66 ± 0.02)E+1	5.7
···	13970	42.04	−0.01	58	···	(3.4 ± 0.2)E+1	···	···
···	13915	42.22	−0.10	···	1.6	(5.28 ± 0.05)E+2	(3.74 ± 0.04)E+1	3.8
···	13927	42.09	−0.09	···	1.7	(9.06 ± 0.06)E+2	(4.68 ± 0.03)E+1	4.3
···	13954	42.12	−0.03	···	0.7	(1.43 ± 0.03)E+2	(9.7 ± 0.2)E+1	1.8
16562	13811	42.08	−0.23	64	1.6	(3.88 ± 0.05)E+2	(2.52 ± 0.03)E+1	4.0
16587	13766	42.73	−0.28	60	1.9	(8.46 ± 0.06)E+2	(3.58 ± 0.03)E+1	4.6
···	13825	42.76	−0.20	67	0.9	(4.01 ± 0.04)E+2	(1.32 ± 0.01)E+2	2.3
···	13837	42.73	−0.18	68	0.8	(2.47 ± 0.04)E+2	(1.46 ± 0.02)E+2	1.9
···	13858	42.72	−0.15	63	0.7	(1.39 ± 0.03)E+2	(1.20 ± 0.03)E+2	1.7
···	13870	42.70	−0.15	63	0.5	(3.64 ± 0.03)E+2	(1.028 ± 0.008)E+3	1.1
···	13898	42.77	−0.12	65	0.9	(1.29 ± 0.03)E+2	(5.5 ± 0.1)E+1	2.1
···	13902	42.69	−0.11	66	1.8	(4.274 ± 0.007)E+3	(1.846 ± 0.003)E+2	4.5
···	13907	42.72	−0.11	67	1.1	(7.56 ± 0.04)E+2	(1.77 ± 0.01)E+2	2.6
···	13910	42.82	−0.11	61	0.9	(2.75 ± 0.04)E+2	(1.14 ± 0.02)E+2	2.1
···	13937	42.64	−0.06	65	1.8	(7.42 ± 0.06)E+2	(3.58 ± 0.03)E+1	4.4
···	14780	42.91	−0.22	64	0.8	(1.55 ± 0.03)E+2	(8.5 ± 0.2)E+1	1.9
···	14796	42.84	−0.19	65	0.8	(2.95 ± 0.03)E+2	(1.47 ± 0.01)E+2	2.0
···	14801	42.88	−0.19	65	2.0	(1.572 ± 0.006)E+3	(5.45 ± 0.02)E+1	4.9
···	14803	42.80	−0.18	66	1.2	(4.73 ± 0.04)E+2	(7.79 ± 0.07)E+1	2.9
···	14816	42.82	−0.14	61	1.4	(1.524 ± 0.005)E+3	(1.404 ± 0.004)E+2	3.5
···	14820	42.92	−0.14	58	0.7	(2.41 ± 0.03)E+2	(2.34 ± 0.03)E+2	1.6
···	14835	42.95	−0.11	62	1.3	(4.12 ± 0.04)E+2	(4.58 ± 0.04)E+1	3.3
···	14845	42.91	−0.10	58	0.6	(1.89 ± 0.03)E+2	(2.57 ± 0.04)E+2	1.4
···	14808	42.85	−0.17	···	0.8	(3.40 ± 0.03)E+2	(1.73 ± 0.02)E+2	2.0
16598	14036	42.83	+0.09	71	1.2	(2.49 ± 0.05)E+2	(3.75 ± 0.07)E+1	3.0
···	14071	42.66	+0.16	64	0.9	(4.37 ± 0.04)E+2	(1.80 ± 0.02)E+2	2.1
···	14085	42.69	+0.18	64	···	(8.0 ± 0.3)E+1	···	···
···	14089	42.75	+0.20	64	1.0	(1.51 ± 0.04)E+2	(3.85 ± 0.09)E+1	2.5
···	14100	42.67	+0.22	64	2.3	(1.256 ± 0.008)E+3	(2.93 ± 0.02)E+1	5.6
···	14138	42.74	+0.29	63	1.8	(6.23 ± 0.06)E+2	(3.09 ± 0.03)E+1	4.3
···	14979	42.85	+0.15	66	1.5	(6.21 ± 0.05)E+2	(5.51 ± 0.05)E+1	3.6
···	14108	42.77	+0.22	···	2.0	(4.14 ± 0.06)E+2	(1.44 ± 0.02)E+1	4.9
···	15011	42.82	+0.19	···	···	(2.4 ± 0.2)E+1	···	···
16950	13899	42.35	−0.12	61	1.4	(4.43 ± 0.05)E+2	(4.53 ± 0.05)E+1	3.4
···	13958	42.32	−0.03	54	1.4	(5.27 ± 0.06)E+2	(4.75 ± 0.05)E+1	3.6
···	13966	42.24	−0.01	57	1.1	(5.08 ± 0.05)E+2	(1.09 ± 0.01)E+2	2.7
···	13989	42.34	+0.02	54	···	(1.12 ± 0.03)E+2	···	···
···	14002	42.23	+0.04	56	1.6	(8.67 ± 0.06)E+2	(6.25 ± 0.04)E+1	3.8
···	13871	42.30	−0.14	···	1.5	(8.40 ± 0.06)E+2	(6.29 ± 0.04)E+1	3.8
···	13934	42.37	−0.06	···	1.4	(3.78 ± 0.05)E+2	(3.97 ± 0.06)E+1	3.4
···	13941	42.23	−0.06	···	0.7	(1.79 ± 0.03)E+2	(1.60 ± 0.03)E+2	1.7
16971	13773	42.48	−0.28	65	···	(1.02 ± 0.03)E+2	···	···
···	13784	42.43	−0.27	66	2.0	(7.758 ± 0.009)E+3	(2.573 ± 0.003)E+2	5.0
···	13798	42.39	−0.25	65	0.8	(4.39 ± 0.04)E+2	(1.98 ± 0.02)E+2	2.1
···	13815	42.33	−0.21	56	0.8	(5.52 ± 0.04)E+2	(3.10 ± 0.02)E+2	1.9
17346	14867	42.94	−0.07	7	0.6	(2.04 ± 0.03)E+2	(2.08 ± 0.03)E+2	1.6
···	14884	42.93	−0.04	7	1.6	(1.120 ± 0.005)E+3	(7.95 ± 0.03)E+1	3.8
···	14894	43.02	−0.02	7	···	(1.93 ± 0.02)E+2	···	···
···	14895	42.91	−0.03	7	0.5	(1.14 ± 0.02)E+2	(2.69 ± 0.05)E+2	1.2
···	14906	42.90	−0.01	9	0.7	(1.93 ± 0.03)E+2	(1.53 ± 0.02)E+2	1.7
···	14911	43.01	−0.00	6	0.7	(2.87 ± 0.03)E+2	(2.52 ± 0.02)E+2	1.7
17437	13757	42.37	−0.30	29	0.6	(1.04 ± 0.02)E+2	(2.96 ± 0.05)E+2	1.1
···	13781	42.29	−0.27	31	0.3	(6.9 ± 0.1)E+1	(1.15 ± 0.02)E+3	0.6
···	13807	42.21	−0.24	32	1.0	(1.75 ± 0.02)E+2	(1.11 ± 0.02)E+2	1.9
···	13855	42.34	−0.16	22	···	(4.2 ± 0.1)E+1	···	···
···	13782	42.22	−0.27	···	0.9	(1.17 ± 0.02)E+2	(1.03 ± 0.02)E+2	1.7
···	13783	42.27	−0.25	···	1.8	(5.04 ± 0.04)E+2	(5.36 ± 0.04)E+1	3.4
···	13839	42.36	−0.19	···	0.5	(8.7 ± 0.2)E+1	(5.7 ± 0.1)E+2	0.8
···	13886	42.46	−0.12	···	0.8	(9.6 ± 0.2)E+1	(1.47 ± 0.03)E+2	1.4
17862	13777	41.64	−0.27	69	0.3	(3.0 ± 0.1)E+1	(4.8 ± 0.2)E+2	0.6
···	13799	41.72	−0.24	70	1.9	(9.16 ± 0.04)E+2	(9.27 ± 0.04)E+1	3.4
···	13808	41.67	−0.23	60	···	(2.6 ± 0.1)E+1	···	···
···	13820	41.69	−0.22	60	0.6	(4.9 ± 0.2)E+1	(1.81 ± 0.06)E+2	1.0
···	13794	41.64	−0.25	···	···	(2.0 ± 0.1)E+1	···	···
···	13803	41.62	−0.24	···	0.8	(7.1 ± 0.2)E+1	(8.6 ± 0.3)E+1	1.5
17887	13973	41.66	−0.01	14	0.6	(2.53 ± 0.06)E+2	(1.58 ± 0.04)E+2	1.9
···	13992	41.84	+0.02	15	1.3	(1.64 ± 0.01)E+3	(9.22 ± 0.06)E+1	4.2
···	14005	41.92	+0.05	16	0.5	(3.53 ± 0.05)E+2	(2.81 ± 0.04)E+2	1.7
···	14010	41.83	+0.06	16	0.4	(4.61 ± 0.05)E+2	(7.25 ± 0.08)E+2	1.4
···	14024	41.71	+0.07	16	1.3	(1.050 ± 0.008)E+3	(5.37 ± 0.04)E+1	4.3
···	14026	41.93	+0.07	20	···	(1.00 ± 0.04)E+2	···	···

Continuation of Table B2

COHRS catalog #	Hi-GAL catalog #	ℓ (deg)	b (deg)	$v_{\rm LSR}$ (km s^{-1})	$\theta_{\rm R}$ (arcmin)	M ($M_\odot$)	n (cm^{-3})	R (pc)
···	14032	41.86	+0.09	18	0.5	(1.76 ± 0.05)E+2	(1.99 ± 0.06)E+2	1.5
···	14037	41.74	+0.10	13	1.2	(3.11 ± 0.01)E+3	(2.091 ± 0.006)E+2	3.9
···	14044	41.81	+0.09	15	1.7	(2.62 ± 0.01)E+3	(6.50 ± 0.03)E+1	5.5
···	14058	41.90	+0.12	15	1.1	(1.55 ± 0.06)E+2	(1.22 ± 0.05)E+1	3.7
···	14059	41.75	+0.13	15	1.5	(1.89 ± 0.01)E+3	(6.73 ± 0.04)E+1	4.8
···	13990	41.81	+0.02	···	···	(2.30 ± 0.05)E+2	···	···
18040	13817	41.54	−0.21	61	1.3	(2.00 ± 0.03)E+2	(6.63 ± 0.08)E+1	2.3
···	13857	41.46	−0.16	61	1.2	(1.54 ± 0.02)E+2	(5.86 ± 0.09)E+1	2.2
···	13877	41.51	−0.16	62	2.6	(9.46 ± 0.05)E+2	(3.95 ± 0.02)E+1	4.6
···	13911	41.51	−0.11	62	1.0	(3.32 ± 0.02)E+2	(2.68 ± 0.02)E+2	1.7
···	13905	41.47	−0.11	···	0.9	(1.39 ± 0.02)E+2	(1.26 ± 0.02)E+2	1.6
18143	13887	41.02	−0.13	37	0.6	(5.3 ± 0.2)E+1	(1.83 ± 0.06)E+2	1.1
···	13909	41.12	−0.11	38	0.9	(4.96 ± 0.02)E+2	(4.80 ± 0.02)E+2	1.6
···	13939	40.96	−0.06	40	0.8	(8.8 ± 0.2)E+1	(1.31 ± 0.02)E+2	1.4
···	13959	41.03	−0.03	37	0.3	(3.8 ± 0.1)E+1	(1.02 ± 0.03)E+3	0.5
18295	14040	41.17	+0.09	38	1.4	(4.73 ± 0.02)E+2	(1.130 ± 0.006)E+2	2.6
···	14051	41.39	+0.11	37	0.7	(8.1 ± 0.2)E+1	(1.61 ± 0.03)E+2	1.3
···	14056	41.19	+0.12	38	1.1	(5.21 ± 0.02)E+2	(2.73 ± 0.01)E+2	2.0
···	14070	41.21	+0.14	38	1.1	(1.97 ± 0.02)E+2	(9.6 ± 0.1)E+1	2.0
···	14101	41.21	+0.22	42	···	(3.4 ± 0.1)E+1	···	···
···	14112	41.23	+0.25	42	1.0	(1.73 ± 0.02)E+2	(1.26 ± 0.01)E+2	1.8
···	14119	41.26	+0.26	42	0.7	(7.8 ± 0.2)E+1	(1.89 ± 0.04)E+2	1.2
···	14129	41.28	+0.28	···	0.8	(9.0 ± 0.2)E+1	(1.37 ± 0.03)E+2	1.4
18347	13797	40.91	−0.25	26	1.1	(7.46 ± 0.02)E+2	(4.56 ± 0.02)E+2	1.9
···	13809	40.88	−0.23	27	1.3	(5.56 ± 0.03)E+2	(1.898 ± 0.009)E+2	2.3
···	13819	40.79	−0.22	24	1.0	(4.06 ± 0.02)E+2	(3.33 ± 0.02)E+2	1.7
···	13826	40.91	−0.20	27	1.2	(2.33 ± 0.02)E+2	(9.8 ± 0.1)E+1	2.1
···	13827	40.81	−0.20	24	0.7	(1.46 ± 0.02)E+2	(3.42 ± 0.04)E+2	1.2
···	13847	40.88	−0.17	23	1.4	(4.93 ± 0.03)E+2	(1.326 ± 0.007)E+2	2.5
···	13889	40.70	−0.13	20	1.5	(9.60 ± 0.03)E+2	(2.272 ± 0.008)E+2	2.6
···	13918	40.79	−0.09	21	0.9	(7.8 ± 0.2)E+1	(6.8 ± 0.2)E+1	1.7
···	13787	40.75	−0.26	···	0.7	(1.49 ± 0.02)E+2	(2.67 ± 0.03)E+2	1.3
···	13802	40.81	−0.24	···	1.4	(6.53 ± 0.03)E+2	(1.856 ± 0.007)E+2	2.4
···	13816	40.84	−0.22	···	0.7	(1.82 ± 0.02)E+2	(4.21 ± 0.04)E+2	1.2
···	13818	40.86	−0.21	···	1.0	(3.02 ± 0.02)E+2	(2.01 ± 0.01)E+2	1.8
···	13848	40.73	−0.18	···	0.9	(1.49 ± 0.02)E+2	(1.41 ± 0.02)E+2	1.6
···	13852	40.76	−0.18	···	1.5	(2.93 ± 0.03)E+2	(6.29 ± 0.06)E+1	2.7
···	13867	40.85	−0.16	···	1.4	(3.81 ± 0.03)E+2	(9.69 ± 0.07)E+1	2.5
···	13869	40.74	−0.15	···	1.3	(4.13 ± 0.02)E+2	(1.329 ± 0.008)E+2	2.3
18359	13968	40.68	−0.01	21	0.5	(3.1 ± 0.1)E+1	(1.93 ± 0.09)E+2	0.9
···	13976	40.77	−0.00	22	1.0	(1.53 ± 0.02)E+2	(9.2 ± 0.1)E+1	1.9
···	14013	40.75	+0.05	23	1.4	(2.33 ± 0.03)E+2	(5.12 ± 0.06)E+1	2.6
···	14021	40.73	+0.07	23	0.9	(2.27 ± 0.02)E+2	(1.75 ± 0.02)E+2	1.7
···	14034	40.74	+0.09	22	1.9	(5.17 ± 0.04)E+2	(4.66 ± 0.03)E+1	3.6
···	14045	40.79	+0.10	20	1.4	(1.87 ± 0.03)E+2	(4.19 ± 0.06)E+1	2.6
···	14060	40.79	+0.12	21	1.1	(1.31 ± 0.02)E+2	(6.4 ± 0.1)E+1	2.0
···	14079	40.74	+0.17	18	1.4	(4.30 ± 0.03)E+2	(9.21 ± 0.07)E+1	2.7
···	14072	40.77	+0.16	···	0.9	(8.9 ± 0.2)E+1	(8.8 ± 0.2)E+1	1.6
18403	13994	41.07	+0.02	12	1.5	(3.49 ± 0.03)E+2	(7.51 ± 0.06)E+1	2.7
···	14008	40.96	+0.05	15	···	(2.42 ± 0.09)E+1	···	···
···	14029	40.86	+0.08	19	1.3	(9.5 ± 0.2)E+1	(3.34 ± 0.08)E+1	2.3
···	14065	41.28	+0.13	18	0.8	(1.15 ± 0.02)E+2	(1.37 ± 0.02)E+2	1.5
···	14082	41.12	+0.16	15	1.4	(1.92 ± 0.02)E+2	(4.94 ± 0.06)E+1	2.5
···	14083	41.23	+0.17	19	1.3	(5.80 ± 0.03)E+2	(1.842 ± 0.008)E+2	2.3
···	14033	40.95	+0.09	···	1.7	(3.20 ± 0.03)E+2	(4.53 ± 0.05)E+1	3.1
18462	13884	40.63	−0.14	33	1.3	(1.108 ± 0.001)E+4	(7.785 ± 0.007)E+2	3.9
···	12826	40.57	−0.16	···	1.4	(5.54 ± 0.09)E+2	(2.90 ± 0.05)E+1	4.3
18629	13993	41.54	+0.02	61	1.9	(1.148 ± 0.003)E+3	(1.244 ± 0.004)E+2	3.3
···	13996	41.50	+0.03	64	1.8	(8.89 ± 0.03)E+2	(1.160 ± 0.004)E+2	3.1
···	13999	41.57	+0.03	61	1.3	(3.72 ± 0.03)E+2	(1.218 ± 0.008)E+2	2.3
···	13961	41.58	−0.02	···	0.8	(1.60 ± 0.02)E+2	(2.47 ± 0.03)E+2	1.4
···	13991	41.61	+0.01	···	1.9	(7.36 ± 0.04)E+2	(7.68 ± 0.04)E+1	3.4
18631	14000	41.38	+0.03	59	1.1	(9.50 ± 0.03)E+2	(4.98 ± 0.01)E+2	2.0
···	14006	41.18	+0.05	58	···	(1.80 ± 0.01)E+2	···	···
···	14012	41.35	+0.05	61	1.0	(1.55 ± 0.02)E+2	(1.15 ± 0.02)E+2	1.8
···	14017	41.29	+0.06	60	0.5	(1.68 ± 0.01)E+2	(7.70 ± 0.07)E+2	1.0
···	14019	41.32	+0.06	61	1.1	(3.23 ± 0.02)E+2	(1.73 ± 0.01)E+2	2.0
···	14020	41.19	+0.07	58	0.9	(3.30 ± 0.02)E+2	(3.45 ± 0.02)E+2	1.6
···	14039	41.23	+0.09	57	···	(2.7 ± 0.1)E+1	···	···
···	14046	41.25	+0.11	58	···	(7.4 ± 0.1)E+1	···	···
···	14054	41.32	+0.11	61	3.0	(2.303 ± 0.005)E+3	(6.01 ± 0.01)E+1	5.4
···	14064	41.13	+0.13	60	1.4	(2.96 ± 0.03)E+2	(8.32 ± 0.07)E+1	2.4
···	14069	41.36	+0.15	61	0.9	(9.7 ± 0.2)E+1	(1.10 ± 0.02)E+2	1.5
···	14028	41.14	+0.07	···	1.5	(5.70 ± 0.03)E+2	(1.180 ± 0.006)E+2	2.7
18865	13768	41.31	−0.29	60	0.9	(1.41 ± 0.02)E+2	(1.45 ± 0.02)E+2	1.6
···	13771	41.28	−0.29	60	1.5	(2.75 ± 0.03)E+2	(5.49 ± 0.05)E+1	2.7
···	13786	41.29	−0.27	59	0.9	(1.13 ± 0.02)E+2	(1.12 ± 0.02)E+2	1.6
···	13793	41.25	−0.25	59	1.1	(2.79 ± 0.02)E+2	(1.48 ± 0.01)E+2	2.0
···	13795	41.04	−0.25	65	1.8	(1.915 ± 0.003)E+3	(2.560 ± 0.004)E+2	3.1
···	13804	41.10	−0.24	60	1.1	(1.438 ± 0.002)E+3	(7.06 ± 0.01)E+2	2.0
···	13814	41.13	−0.23	60	1.4	(2.472 ± 0.003)E+3	(6.517 ± 0.008)E+2	2.5
···	13828	41.23	−0.21	59	1.2	(1.084 ± 0.003)E+3	(4.96 ± 0.01)E+2	2.1
···	13830	41.20	−0.20	54	0.6	(1.47 ± 0.02)E+2	(5.54 ± 0.06)E+2	1.0
···	13831	41.13	−0.19	61	0.9	(8.75 ± 0.02)E+2	(9.99 ± 0.02)E+2	1.5

Continuation of Table B2

COHRS catalog #	Hi-GAL catalog #	ℓ (deg)	b (deg)	v_{LSR} (km s^{-1})	θ_{R} (arcmin)	M ($\mathrm{M}_{\odot}$)	n (cm^{-3})	R (pc)
···	13834	41.33	−0.20	58	0.3	(4.65 ± 0.02)E+2	(1.285 ± 0.005)E+4	0.5
···	13841	41.26	−0.19	56	···	(3.1 ± 0.1)E+1	···	···
···	13843	41.16	−0.18	60	1.9	(3.041 ± 0.004)E+3	(3.314 ± 0.004)E+2	3.3
···	13850	41.31	−0.17	57	1.1	(1.178 ± 0.003)E+3	(7.28 ± 0.02)E+2	1.9
···	13851	41.21	−0.17	54	0.4	(2.16 ± 0.01)E+2	(3.12 ± 0.02)E+3	0.7
···	13879	41.16	−0.14	52	0.8	(4.38 ± 0.02)E+2	(7.24 ± 0.03)E+2	1.3
···	13897	41.08	−0.12	64	1.2	(1.014 ± 0.002)E+3	(4.22 ± 0.01)E+2	2.1
···	13916	41.17	−0.11	51	1.5	(7.81 ± 0.03)E+2	(1.540 ± 0.006)E+2	2.7
···	13923	41.06	−0.10	63	0.6	(2.27 ± 0.02)E+2	(9.33 ± 0.07)E+2	1.0
···	13762	41.34	−0.30	···	0.4	(7.9 ± 0.1)E+1	(9.0 ± 0.1)E+2	0.7
···	13763	41.04	−0.29	···	0.7	(8.3 ± 0.2)E+1	(1.87 ± 0.03)E+2	1.2
···	13862	41.20	−0.15	···	1.2	(4.63 ± 0.02)E+2	(1.907 ± 0.009)E+2	2.1
···	13901	41.31	−0.12	···	1.5	(8.89 ± 0.03)E+2	(2.045 ± 0.007)E+2	2.6
19020	13979	41.02	+0.00	75	0.5	(6.1 ± 0.2)E+1	(2.74 ± 0.07)E+2	1.0
···	14018	40.99	+0.06	74	1.0	(1.45 ± 0.02)E+2	(9.5 ± 0.2)E+1	1.8
···	14004	41.00	+0.03	···	0.8	(1.40 ± 0.02)E+2	(1.46 ± 0.02)E+2	1.6
···	13995	40.97	+0.03	···	···	(1.08 ± 0.08)E+1	···	···
19174	14113	40.73	+0.25	48	1.2	(1.52 ± 0.03)E+2	(5.10 ± 0.08)E+1	2.3
···	14133	40.76	+0.27	48	2.3	(3.98 ± 0.04)E+2	(1.98 ± 0.02)E+1	4.3
···	14091	40.69	+0.20	···	1.9	(4.06 ± 0.04)E+2	(3.37 ± 0.03)E+1	3.6
···	14104	40.72	+0.22	···	0.4	(6.2 ± 0.2)E+1	(6.8 ± 0.2)E+2	0.7
19208	13027	40.51	+0.21	82	1.5	(1.20 ± 0.03)E+2	(2.01 ± 0.06)E+1	2.9
···	13057	40.39	+0.26	80	1.3	(2.70 ± 0.03)E+2	(7.46 ± 0.09)E+1	2.4
19241	12886	40.37	−0.06	72	1.2	(6.68 ± 0.05)E+2	(1.41 ± 0.01)E+2	2.7
···	12897	40.44	−0.05	68	1.2	(4.71 ± 0.04)E+2	(1.029 ± 0.009)E+2	2.6
···	12938	40.38	+0.02	74	0.8	(8.5 ± 0.3)E+1	(6.5 ± 0.2)E+1	1.7
···	12871	40.37	−0.09	···	1.1	(4.69 ± 0.04)E+2	(1.18 ± 0.01)E+2	2.5
···	12918	40.39	−0.01	···	0.5	(8.7 ± 0.3)E+1	(3.0 ± 0.1)E+2	1.1
19251	12732	40.21	−0.28	65	0.8	(2.23 ± 0.04)E+2	(1.45 ± 0.02)E+2	1.8
···	12741	40.12	−0.27	···	0.8	(1.21 ± 0.03)E+2	(7.9 ± 0.2)E+1	1.8
19544	12808	39.37	−0.18	62	1.0	(2.05 ± 0.01)E+2	(3.99 ± 0.03)E+2	1.3
···	12839	39.39	−0.14	66	1.1	(9.63 ± 0.02)E+2	(1.243 ± 0.003)E+3	1.5
···	12873	39.37	−0.09	67	···	(2.02 ± 0.07)E+1	···	···
···	12755	39.43	−0.24	···	···	(5.88 ± 0.08)E+1	···	···
19604	12853	40.02	−0.12	84	1.9	(4.80 ± 0.02)E+2	(1.135 ± 0.006)E+2	2.6
19910	12736	38.98	−0.26	48	1.8	(6.06 ± 0.02)E+2	(1.864 ± 0.007)E+2	2.4
···	12738	38.81	−0.27	43	0.8	(9.9 ± 0.1)E+1	(3.06 ± 0.03)E+2	1.1
···	12762	38.94	−0.24	43	1.4	(1.82 ± 0.02)E+2	(1.12 ± 0.01)E+2	1.9
···	12727	38.88	−0.29	···	···	(6.6 ± 0.5)E+0	···	···
···	12801	38.95	−0.19	···	0.7	(4.5 ± 0.1)E+1	(2.03 ± 0.05)E+2	1.0
20135	12935	38.98	+0.01	19	···	(4.39 ± 0.07)E+2	···	···
···	12937	38.93	+0.00	20	0.5	(1.50 ± 0.06)E+2	(1.11 ± 0.04)E+2	1.8
···	12941	38.96	+0.02	19	0.7	(4.37 ± 0.07)E+2	(1.17 ± 0.02)E+2	2.5
···	12950	38.95	+0.04	20	0.4	(1.69 ± 0.05)E+2	(2.43 ± 0.08)E+2	1.4
···	12963	38.87	+0.07	20	1.1	(7.14 ± 0.09)E+2	(5.88 ± 0.08)E+1	3.7
···	12951	38.92	+0.04	···	···	(4.0 ± 0.3)E+1	···	···
···	12955	38.90	+0.05	···	···	(4.8 ± 0.3)E+1	···	···
20221	12888	39.26	−0.06	24	2.0	(1.994 ± 0.002)E+4	(3.133 ± 0.003)E+2	6.4
···	12814	39.25	−0.18	···	0.3	(3.05 ± 0.05)E+2	(8.8 ± 0.1)E+2	1.1
···	12916	39.13	−0.02	···	0.8	(7.27 ± 0.07)E+2	(1.58 ± 0.02)E+2	2.6
···	12948	39.06	+0.03	···	2.4	(2.49 ± 0.02)E+3	(2.00 ± 0.01)E+1	7.9
20288	12754	39.52	−0.24	61	0.7	(5.6 ± 0.1)E+1	(3.29 ± 0.06)E+2	0.9
···	12777	39.55	−0.22	71	0.7	(1.29 ± 0.01)E+2	(6.36 ± 0.05)E+2	0.9
···	12790	39.59	−0.20	65	1.7	(1.055 ± 0.002)E+3	(3.314 ± 0.007)E+2	2.3
···	12792	39.50	−0.20	56	1.0	(4.95 ± 0.01)E+2	(8.20 ± 0.02)E+2	1.3
···	12794	39.53	−0.20	52	1.3	(5.79 ± 0.02)E+2	(4.22 ± 0.01)E+2	1.8
···	12807	39.48	−0.18	50	1.0	(2.66 ± 0.02)E+2	(4.05 ± 0.02)E+2	1.4
···	12764	39.58	−0.24	···	1.7	(3.73 ± 0.02)E+2	(1.287 ± 0.007)E+2	2.3
···	12825	39.67	−0.16	···	1.9	(5.14 ± 0.03)E+2	(1.193 ± 0.006)E+2	2.6
20469	12724	39.92	−0.29	55	···	(1.45 ± 0.07)E+1	···	···
···	12745	39.84	−0.25	58	···	(2.71 ± 0.08)E+1	···	···
···	12760	39.81	−0.24	57	1.1	(1.75 ± 0.02)E+2	(1.99 ± 0.02)E+2	1.5
···	12763	39.83	−0.23	58	0.6	(1.08 ± 0.01)E+2	(7.47 ± 0.07)E+2	0.8
···	12768	39.95	−0.24	56	1.3	(8.7 ± 0.1)E+1	(6.8 ± 0.1)E+1	1.7
···	12771	39.92	−0.23	59	···	(3.18 ± 0.08)E+1	···	···
···	12781	39.85	−0.21	56	1.4	(9.27 ± 0.02)E+2	(5.86 ± 0.01)E+2	1.9
···	12811	39.91	−0.18	57	···	(1.24 ± 0.07)E+1	···	···
···	12812	39.88	−0.17	56	0.7	(1.94 ± 0.01)E+2	(9.86 ± 0.06)E+2	0.9
···	12823	39.93	−0.17	58	0.7	(1.54 ± 0.01)E+2	(8.12 ± 0.06)E+2	0.9
···	12838	39.96	−0.14	57	1.6	(2.70 ± 0.02)E+2	(1.181 ± 0.008)E+2	2.1
···	12719	39.94	−0.29	···	0.3	(5.59 ± 0.09)E+1	(5.9 ± 0.1)E+3	0.3
20640	12769	38.67	−0.23	69	1.6	(7.93 ± 0.02)E+2	(3.688 ± 0.009)E+2	2.1
···	12784	38.60	−0.22	66	0.9	(3.71 ± 0.01)E+2	(1.046 ± 0.004)E+3	1.1
···	12789	38.63	−0.20	66	1.0	(3.66 ± 0.01)E+2	(6.92 ± 0.03)E+2	1.3
···	12806	38.60	−0.18	67	1.3	(2.32 ± 0.01)E+2	(1.74 ± 0.01)E+2	1.7
···	12851	38.60	−0.12	63	1.3	(1.36 ± 0.02)E+2	(1.00 ± 0.01)E+2	1.8
···	12852	38.56	−0.12	62	1.1	(1.02 ± 0.01)E+2	(1.38 ± 0.02)E+2	1.4
···	12734	38.66	−0.28	···	0.9	(1.95 ± 0.01)E+2	(4.33 ± 0.03)E+2	1.2
···	12748	38.66	−0.25	···	0.7	(1.93 ± 0.01)E+2	(1.127 ± 0.006)E+3	0.9
20881	11708	38.35	−0.30	68	1.9	(8.55 ± 0.06)E+2	(6.03 ± 0.04)E+1	3.9
···	11715	38.41	−0.29	69	···	(6.9 ± 0.2)E+1	···	···
···	11717	38.18	−0.29	57	1.4	(5.98 ± 0.05)E+2	(1.102 ± 0.009)E+2	2.8
···	11741	38.31	−0.27	68	1.0	(3.32 ± 0.03)E+2	(1.63 ± 0.02)E+2	2.0
···	11767	38.28	−0.23	53	1.5	(1.050 ± 0.005)E+3	(1.376 ± 0.007)E+2	3.1

Continuation of Table B2

COHRS catalog #	Hi-GAL catalog #	ℓ (deg)	b (deg)	v_{LSR} (km s^{-1})	θ_R (arcmin)	M ($M_\odot$)	n (cm^{-3})	R (pc)
···	11785	38.26	−0.20	66	···	(3.12 ± 0.03)E+2	···	···
···	11802	38.19	−0.16	63	1.6	(2.034 ± 0.006)E+3	(2.559 ± 0.007)E+2	3.2
···	11812	38.07	−0.14	58	0.9	(5.24 ± 0.04)E+2	(3.72 ± 0.03)E+2	1.8
···	11821	38.24	−0.13	63	1.1	(7.00 ± 0.04)E+2	(2.83 ± 0.02)E+2	2.2
···	11826	38.05	−0.12	58	0.9	(4.09 ± 0.04)E+2	(2.75 ± 0.03)E+2	1.8
···	11751	38.32	−0.24	···	0.9	(4.02 ± 0.03)E+2	(2.25 ± 0.02)E+2	1.9
···	11758	38.21	−0.23	···	0.9	(5.27 ± 0.03)E+2	(3.85 ± 0.03)E+2	1.8
···	11777	38.18	−0.21	···	1.1	(4.23 ± 0.04)E+2	(1.62 ± 0.01)E+2	2.2
···	11885	38.35	−0.06	···	···	(1.02 ± 0.03)E+2	···	···
···	12739	38.42	−0.27	···	0.6	(1.49 ± 0.03)E+2	(3.66 ± 0.07)E+2	1.2
···	12770	38.48	−0.23	···	1.1	(4.42 ± 0.04)E+2	(1.39 ± 0.01)E+2	2.3
···	12799	38.45	−0.20	···	1.3	(8.29 ± 0.04)E+2	(1.80 ± 0.01)E+2	2.6
···	12860	38.41	−0.11	···	0.8	(2.73 ± 0.03)E+2	(2.83 ± 0.03)E+2	1.6
20979	11981	38.21	+0.11	40	1.7	(6.48 ± 0.06)E+2	(6.00 ± 0.05)E+1	3.5
···	11994	38.20	+0.14	41	1.0	(2.59 ± 0.04)E+2	(1.14 ± 0.02)E+2	2.1
···	12031	37.75	+0.20	45	0.7	(6.07 ± 0.04)E+2	(7.88 ± 0.05)E+2	1.5
···	12044	38.07	+0.21	43	1.1	(5.00 ± 0.04)E+2	(1.73 ± 0.01)E+2	2.3
···	12047	38.03	+0.23	43	1.5	(4.40 ± 0.05)E+2	(6.11 ± 0.07)E+1	3.1
···	12053	37.77	+0.25	48	···	(7.4 ± 0.2)E+1	···	···
···	12058	38.07	+0.25	43	1.5	(5.12 ± 0.05)E+2	(6.98 ± 0.07)E+1	3.1
···	12060	37.96	+0.25	47	0.7	(1.09 ± 0.03)E+2	(1.65 ± 0.05)E+2	1.4
···	12061	37.78	+0.26	47	···	(5.9 ± 0.2)E+1	···	···
···	12065	37.83	+0.26	47	1.1	(3.96 ± 0.05)E+2	(1.35 ± 0.02)E+2	2.3
···	12066	37.93	+0.27	48	···	(5.8 ± 0.3)E+1	···	···
···	11998	38.16	+0.15	···	1.3	(2.68 ± 0.04)E+2	(6.3 ± 0.1)E+1	2.6
···	12040	38.15	+0.21	···	1.3	(1.04 ± 0.04)E+2	(2.31 ± 0.09)E+1	2.6
21042	11888	37.68	−0.05	40	1.5	(1.454 ± 0.006)E+3	(1.945 ± 0.008)E+2	3.1
···	11908	37.53	−0.02	41	0.4	(1.08 ± 0.03)E+2	(9.6 ± 0.2)E+2	0.8
···	11938	37.54	+0.04	41	0.6	(2.00 ± 0.03)E+2	(3.57 ± 0.05)E+2	1.3
···	11966	37.53	+0.08	42	1.7	(8.91 ± 0.06)E+2	(8.81 ± 0.06)E+1	3.4
···	11996	37.44	+0.14	40	1.6	(1.650 ± 0.006)E+3	(1.835 ± 0.007)E+2	3.3
···	12002	37.56	+0.15	42	···	(9.5 ± 0.2)E+1	···	···
···	11932	37.40	+0.03	···	0.5	(9.9 ± 0.3)E+1	(4.1 ± 0.1)E+2	1.0
21151	11957	38.31	+0.09	39	···	(4.6 ± 0.4)E+1	···	···
···	11979	38.43	+0.12	24	1.7	(1.85 ± 0.02)E+3	(4.33 ± 0.04)E+1	5.6
···	12000	38.40	+0.14	22	0.8	(6.98 ± 0.08)E+2	(1.39 ± 0.02)E+2	2.7
···	12996	38.52	+0.13	21	1.2	(8.80 ± 0.09)E+2	(5.69 ± 0.06)E+1	4.0
···	13004	38.55	+0.16	30	0.7	(2.837 ± 0.009)E+3	(9.26 ± 0.03)E+2	2.3
···	13007	38.59	+0.17	21	1.0	(7.36 ± 0.09)E+2	(7.8 ± 0.1)E+1	3.4
···	13040	38.66	+0.22	29	1.3	(1.93 ± 0.01)E+3	(9.36 ± 0.05)E+1	4.4
···	13069	38.56	+0.30	38	1.0	(4.35 ± 0.08)E+2	(4.39 ± 0.08)E+1	3.4
···	11907	38.34	−0.02	···	0.4	(4.80 ± 0.06)E+2	(8.0 ± 0.1)E+2	1.3
···	11913	38.36	−0.01	···	0.5	(3.91 ± 0.06)E+2	(3.42 ± 0.06)E+2	1.7
···	12977	38.47	+0.10	···	1.3	(1.25 ± 0.01)E+3	(6.55 ± 0.05)E+1	4.3
···	12994	38.57	+0.13	···	0.6	(1.34 ± 0.06)E+2	(6.2 ± 0.3)E+1	2.1
···	13009	38.52	+0.17	···	0.9	(7.76 ± 0.08)E+2	(1.33 ± 0.01)E+2	2.9
···	13023	38.63	+0.19	···	0.1	(1.74 ± 0.05)E+2	(9.4 ± 0.3)E+3	0.4
···	13043	38.38	+0.24	···	···	(1.24 ± 0.05)E+2	···	···
21387	11709	38.04	−0.30	63	1.5	(1.157 ± 0.006)E+3	(1.706 ± 0.008)E+2	3.0
···	11739	38.06	−0.27	···	1.4	(7.15 ± 0.05)E+2	(1.36 ± 0.01)E+2	2.8
21395	11844	37.47	−0.10	59	0.8	(1.354 ± 0.004)E+3	(1.266 ± 0.004)E+3	1.6
···	11865	37.38	−0.08	58	···	(3.17 ± 0.02)E+2	···	···
···	11884	37.35	−0.06	56	1.2	(2.453 ± 0.005)E+3	(7.38 ± 0.01)E+2	2.4
···	11886	37.40	−0.06	57	0.6	(6.62 ± 0.03)E+2	(1.446 ± 0.007)E+3	1.2
···	11889	37.45	−0.06	58	1.7	(2.204 ± 0.006)E+3	(2.228 ± 0.006)E+2	3.4
···	11896	37.48	−0.04	56	0.7	(1.53 ± 0.03)E+2	(2.57 ± 0.05)E+2	1.3
21672	11776	37.76	−0.21	61	1.3	(7.652 ± 0.006)E+3	(1.643 ± 0.001)E+3	2.7
···	11792	37.78	−0.18	···	···	(1.30 ± 0.03)E+2	···	···
21685	11752	37.65	−0.25	49	1.3	(3.74 ± 0.04)E+2	(9.1 ± 0.1)E+1	2.6
···	11786	37.63	−0.19	47	0.5	(1.39 ± 0.02)E+2	(6.7 ± 0.1)E+2	0.9
···	11790	37.58	−0.19	46	0.2	(7.3 ± 0.2)E+1	(2.77 ± 0.09)E+3	0.5
···	11797	37.59	−0.17	47	0.7	(1.09 ± 0.03)E+2	(1.46 ± 0.04)E+2	1.4
···	11815	37.58	−0.14	44	0.5	(1.43 ± 0.03)E+2	(5.2 ± 0.1)E+2	1.0
···	11834	37.74	−0.11	44	1.4	(3.694 ± 0.006)E+3	(6.19 ± 0.01)E+2	2.9
···	11835	37.55	−0.11	53	1.5	(3.085 ± 0.006)E+3	(4.451 ± 0.009)E+2	3.0
···	11843	37.64	−0.10	46	1.0	(7.40 ± 0.04)E+2	(3.60 ± 0.02)E+2	2.0
···	11845	37.89	−0.10	52	0.8	(6.09 ± 0.03)E+2	(5.89 ± 0.03)E+2	1.6
···	11853	37.92	−0.09	53	1.8	(2.000 ± 0.006)E+3	(1.697 ± 0.005)E+2	3.6
···	11856	37.67	−0.09	49	1.0	(6.35 ± 0.04)E+2	(3.28 ± 0.02)E+2	2.0
···	11858	37.70	−0.09	47	0.7	(2.07 ± 0.03)E+2	(2.84 ± 0.04)E+2	1.4
···	11867	37.95	−0.08	55	1.3	(7.75 ± 0.05)E+2	(1.89 ± 0.01)E+2	2.5
···	11868	37.76	−0.08	46	0.7	(2.52 ± 0.03)E+2	(2.90 ± 0.04)E+2	1.5
···	11872	37.99	−0.08	54	0.6	(1.53 ± 0.03)E+2	(4.26 ± 0.07)E+2	1.1
···	11880	37.61	−0.07	47	···	(1.18 ± 0.02)E+2	···	···
···	11881	37.64	−0.07	49	1.0	(8.70 ± 0.04)E+2	(3.87 ± 0.02)E+2	2.1
···	11909	38.03	−0.01	62	1.4	(1.529 ± 0.005)E+3	(2.559 ± 0.009)E+2	2.9
···	11798	37.65	−0.16	···	1.7	(7.95 ± 0.06)E+2	(7.99 ± 0.06)E+1	3.4
···	11827	37.59	−0.12	···	···	(8.9 ± 0.2)E+1	···	···
22111	12885	38.47	−0.07	24	···	(3.95 ± 0.04)E+2	···	···
22317	13014	38.64	+0.17	82	0.9	(1.53 ± 0.03)E+2	(9.7 ± 0.2)E+1	1.9
···	13022	38.68	+0.19	81	1.2	(1.054 ± 0.004)E+3	(3.06 ± 0.01)E+2	2.4
22474	11999	37.86	+0.14	−1	1.6	(1.242 ± 0.006)E+3	(1.726 ± 0.008)E+2	3.1
···	12030	37.95	+0.20	4	1.0	(1.52 ± 0.04)E+2	(8.0 ± 0.2)E+1	2.0
···	12048	37.98	+0.22	4	1.5	(2.16 ± 0.05)E+2	(3.69 ± 0.08)E+1	2.9

Continuation of Table B2

COHRS catalog #	Hi-GAL catalog #	ℓ (deg)	b (deg)	$v_{\rm LSR}$ (km s^{-1})	$\theta_{\rm R}$ (arcmin)	M ($\rm M_{\odot}$)	n (cm^{-3})	R (pc)
···	12021	37.98	+0.18	···	···	(2.4 ± 0.2)E+1	···	···
22490	12004	37.48	+0.15	18	0.7	(3.20 ± 0.03)E+2	(3.78 ± 0.04)E+2	1.5
···	11765	37.53	−0.23	···	···	(7.6 ± 0.2)E+1	···	···
···	11958	37.83	+0.09	···	1.2	(3.92 ± 0.05)E+2	(1.17 ± 0.01)E+2	2.4
···	12059	37.48	+0.26	···	0.5	(1.64 ± 0.03)E+2	(6.6 ± 0.1)E+2	1.0
···	12063	37.31	+0.25	···	1.0	(7.1 ± 0.3)E+1	(3.6 ± 0.2)E+1	2.0
23387	12921	38.65	−0.02	76	1.4	(6.55 ± 0.04)E+2	(1.162 ± 0.007)E+2	2.8
···	12928	38.62	−0.01	77	1.2	(2.88 ± 0.03)E+2	(7.77 ± 0.09)E+1	2.5
···	12985	38.50	+0.12	84	0.9	(2.76 ± 0.03)E+2	(2.04 ± 0.02)E+2	1.8
···	12900	38.60	−0.04	···	···	(1.36 ± 0.02)E+2	···	···
···	12984	38.43	+0.12	···	2.0	(8.12 ± 0.05)E+2	(5.01 ± 0.03)E+1	4.0
23448	11863	38.10	−0.09	80	···	(3.16 ± 0.02)E+2	···	···
···	11871	38.16	−0.07	83	0.6	(5.34 ± 0.03)E+2	(1.047 ± 0.006)E+3	1.3
···	11879	38.20	−0.07	83	0.8	(1.714 ± 0.004)E+3	(1.908 ± 0.005)E+3	1.5
···	11883	38.10	−0.06	80	0.8	(5.66 ± 0.03)E+2	(5.44 ± 0.03)E+2	1.6
···	11894	38.09	−0.04	80	1.4	(8.46 ± 0.05)E+2	(1.453 ± 0.009)E+2	2.9
···	11803	38.10	−0.16	···	0.9	(2.76 ± 0.04)E+2	(1.80 ± 0.02)E+2	1.8
···	11824	38.10	−0.13	···	···	(3.8 ± 0.2)E+1	···	···
···	11833	38.28	−0.11	···	0.9	(7.0 ± 0.3)E+1	(5.3 ± 0.2)E+1	1.7
23617	11759	38.12	−0.23	83	1.0	(1.308 ± 0.005)E+3	(6.49 ± 0.02)E+2	2.0
···	11788	38.20	−0.20	86	0.9	(3.97 ± 0.03)E+2	(2.65 ± 0.02)E+2	1.8
···	11806	38.41	−0.15	80	1.4	(1.581 ± 0.005)E+3	(2.908 ± 0.009)E+2	2.8
···	11809	38.38	−0.15	81	1.8	(3.788 ± 0.007)E+3	(3.131 ± 0.006)E+2	3.7
···	11906	38.37	−0.03	82	2.4	(2.262 ± 0.008)E+3	(7.36 ± 0.03)E+1	5.0
···	12905	38.42	−0.04	81	1.1	(4.03 ± 0.03)E+2	(1.51 ± 0.01)E+2	2.2
···	12779	38.42	−0.22	···	1.7	(5.99 ± 0.04)E+2	(6.19 ± 0.05)E+1	3.4
23816	11893	37.85	−0.05	84	1.1	(1.288 ± 0.005)E+3	(4.06 ± 0.01)E+2	2.3
···	11897	37.90	−0.04	82	0.6	(8.3 ± 0.3)E+1	(1.71 ± 0.05)E+2	1.3
···	11911	37.97	−0.00	80	2.0	(3.220 ± 0.007)E+3	(1.833 ± 0.004)E+2	4.1
···	11918	37.72	+0.01	86	0.4	(1.83 ± 0.03)E+2	(1.39 ± 0.02)E+3	0.8
···	11924	37.88	+0.03	82	···	(4.1 ± 0.2)E+1	···	···
···	11930	37.70	+0.03	87	···	(1.25 ± 0.02)E+2	···	···
···	11936	37.84	+0.04	92	···	(7.1 ± 0.2)E+1	···	···
···	11944	37.83	+0.06	93	0.9	(2.99 ± 0.04)E+2	(1.71 ± 0.02)E+2	1.9
···	11946	37.88	+0.06	92	1.1	(5.49 ± 0.05)E+2	(1.84 ± 0.02)E+2	2.3
···	11950	38.04	+0.08	82	1.1	(9.28 ± 0.04)E+2	(3.54 ± 0.02)E+2	2.2
···	11969	37.70	+0.09	86	0.6	(2.35 ± 0.03)E+2	(6.28 ± 0.08)E+2	1.1
···	11973	38.07	+0.10	85	···	(2.5 ± 0.1)E+1	···	···
···	11976	37.78	+0.11	92	0.8	(3.44 ± 0.04)E+2	(3.57 ± 0.04)E+2	1.6
···	11982	38.01	+0.12	83	···	(5.4 ± 0.2)E+1	···	···
···	11983	37.60	+0.12	81	1.6	(9.94 ± 0.06)E+2	(1.272 ± 0.007)E+2	3.2
···	11987	37.73	+0.12	84	1.5	(8.22 ± 0.05)E+2	(1.180 ± 0.007)E+2	3.0
···	11991	37.70	+0.13	83	0.7	(3.43 ± 0.03)E+2	(5.48 ± 0.05)E+2	1.4
···	11995	37.67	+0.12	85	2.1	(4.073 ± 0.008)E+3	(2.001 ± 0.004)E+2	4.3
···	11927	37.99	+0.03	···	···	(1.5 ± 0.2)E+1	···	···
···	11953	37.61	+0.07	···	0.9	(2.91 ± 0.03)E+2	(1.66 ± 0.02)E+2	1.9
···	11988	38.06	+0.13	···	1.2	(3.49 ± 0.04)E+2	(1.03 ± 0.01)E+2	2.4
23933	11746	37.26	−0.26	38	0.6	(4.49 ± 0.04)E+2	(6.95 ± 0.06)E+2	1.4
···	11753	37.23	−0.24	38	2.1	(3.29 ± 0.01)E+3	(1.173 ± 0.004)E+2	4.8
···	11756	37.38	−0.24	40	1.5	(4.780 ± 0.009)E+3	(4.221 ± 0.008)E+2	3.6
···	11760	37.29	−0.23	38	1.4	(9.43 ± 0.07)E+2	(1.188 ± 0.008)E+2	3.2
···	11770	37.32	−0.23	36	0.6	(1.48 ± 0.04)E+2	(2.57 ± 0.06)E+2	1.3
23935	12014	37.32	+0.17	92	0.6	(9.19 ± 0.05)E+2	(1.353 ± 0.007)E+3	1.4
···	12032	37.55	+0.20	85	1.3	(8.610 ± 0.009)E+3	(1.364 ± 0.001)E+3	2.9
···	12038	37.50	+0.21	82	···	(7.3 ± 0.3)E+1	···	···
···	12042	37.61	+0.22	86	1.3	(1.937 ± 0.006)E+3	(2.813 ± 0.009)E+2	3.0
···	12054	37.65	+0.25	84	1.3	(8.06 ± 0.06)E+2	(1.111 ± 0.008)E+2	3.1
···	12055	37.39	+0.25	88	0.8	(2.18 ± 0.04)E+2	(1.49 ± 0.03)E+2	1.8
···	12062	37.69	+0.26	89	0.8	(4.32 ± 0.04)E+2	(3.20 ± 0.03)E+2	1.8
···	12067	37.71	+0.28	89	1.0	(4.59 ± 0.05)E+2	(1.38 ± 0.02)E+2	2.4
···	12033	37.41	+0.20	···	0.6	(1.56 ± 0.04)E+2	(2.02 ± 0.05)E+2	1.5
···	12050	37.46	+0.24	···	0.6	(1.36 ± 0.04)E+2	(2.12 ± 0.06)E+2	1.4
24101	11796	37.22	−0.17	42	···	(1.07 ± 0.03)E+2	···	···
···	11816	37.24	−0.15	47	1.2	(1.09 ± 0.05)E+2	(2.07 ± 0.09)E+1	2.8
···	11851	37.18	−0.10	41	···	(1.16 ± 0.03)E+2	···	···
···	11869	37.26	−0.08	44	1.3	(1.606 ± 0.007)E+3	(2.41 ± 0.01)E+2	3.0
···	11840	37.30	−0.11	···	0.4	(2.04 ± 0.04)E+2	(7.1 ± 0.1)E+2	1.0
···	11850	37.40	−0.10	···	0.3	(9.1 ± 0.3)E+1	(1.65 ± 0.06)E+3	0.6
···	11852	37.09	−0.10	···	0.5	(1.15 ± 0.04)E+2	(2.53 ± 0.08)E+2	1.2
24119	11901	37.22	−0.02	90	0.7	(5.95 ± 0.05)E+2	(4.71 ± 0.04)E+2	1.7
···	11912	37.17	+0.00	88	0.8	(3.26 ± 0.04)E+2	(2.01 ± 0.03)E+2	1.9
···	11919	37.19	+0.01	90	0.6	(2.13 ± 0.04)E+2	(3.22 ± 0.05)E+2	1.4
···	11929	37.20	+0.03	91	0.3	(1.27 ± 0.03)E+2	(1.42 ± 0.04)E+3	0.7
···	11939	37.47	+0.05	82	1.5	(1.118 ± 0.007)E+3	(1.150 ± 0.007)E+2	3.4
···	11940	37.44	+0.05	83	0.3	(1.12 ± 0.03)E+2	(8.7 ± 0.2)E+2	0.8
···	11954	37.27	+0.08	90	1.2	(5.177 ± 0.008)E+3	(8.90 ± 0.01)E+2	2.9
···	11961	37.32	+0.09	91	0.7	(9.31 ± 0.05)E+2	(9.20 ± 0.05)E+2	1.6
···	11970	37.17	+0.09	92	1.7	(2.267 ± 0.008)E+3	(1.537 ± 0.006)E+2	3.9
···	11974	37.50	+0.09	82	1.0	(4.37 ± 0.05)E+2	(1.41 ± 0.02)E+2	2.3
···	11916	37.14	+0.01	···	···	(4.1 ± 0.3)E+1	···	···
···	11955	37.36	+0.08	···	1.2	(1.438 ± 0.007)E+3	(2.51 ± 0.01)E+2	2.8
···	11960	37.40	+0.09	···	0.6	(2.42 ± 0.04)E+2	(4.42 ± 0.07)E+2	1.3
24187	12005	36.24	+0.15	54	0.7	(1.28 ± 0.03)E+2	(1.76 ± 0.04)E+2	1.4
···	12007	36.29	+0.16	···	···	(4.9 ± 0.2)E+1	···	···

Continuation of Table B2

COHRS catalog #	Hi-GAL catalog #	ℓ (deg)	b (deg)	$v_{\rm LSR}$ (km s^{-1})	$\theta_{\rm R}$ (arcmin)	M (M$_\odot$)	n (cm^{-3})	R (pc)
24211	10944	36.35	−0.22	58	···	(4.4 ± 0.2)E+1	···	···
···	10964	35.92	−0.20	60	1.2	(2.07 ± 0.04)E+2	(7.4 ± 0.2)E+1	2.2
···	10994	35.98	−0.15	56	···	(1.00 ± 0.02)E+2	···	···
···	11001	35.95	−0.14	53	1.7	(1.503 ± 0.007)E+3	(2.14 ± 0.01)E+2	3.0
···	11006	36.07	−0.14	59	2.2	(7.34 ± 0.07)E+2	(4.24 ± 0.04)E+1	4.1
···	11035	36.10	−0.10	59	0.8	(4.33 ± 0.04)E+2	(5.71 ± 0.05)E+2	1.5
···	11731	36.62	−0.28	55	1.3	(3.29 ± 0.04)E+2	(1.05 ± 0.01)E+2	2.3
···	11742	36.58	−0.28	57	1.7	(7.92 ± 0.05)E+2	(1.016 ± 0.006)E+2	3.2
···	11784	36.30	−0.21	60	1.7	(4.91 ± 0.05)E+2	(7.03 ± 0.07)E+1	3.0
···	11800	36.26	−0.17	57	1.8	(4.81 ± 0.05)E+2	(5.30 ± 0.05)E+1	3.3
···	11808	36.75	−0.16	55	1.4	(7.01 ± 0.04)E+2	(1.71 ± 0.01)E+2	2.5
···	11831	36.67	−0.12	53	1.8	(2.002 ± 0.005)E+3	(2.276 ± 0.006)E+2	3.3
···	11841	36.64	−0.11	52	1.1	(8.38 ± 0.03)E+2	(3.85 ± 0.01)E+2	2.1
···	11842	36.59	−0.10	52	2.3	(1.875 ± 0.006)E+3	(1.007 ± 0.003)E+2	4.2
···	11862	36.18	−0.08	61	0.8	(1.22 ± 0.03)E+2	(1.38 ± 0.03)E+2	1.5
···	11728	36.46	−0.28	···	0.5	(1.00 ± 0.03)E+2	(4.5 ± 0.1)E+2	1.0
···	11733	36.54	−0.27	···	···	(5.3 ± 0.2)E+1	···	···
···	11748	36.40	−0.26	···	0.7	(1.17 ± 0.03)E+2	(2.69 ± 0.06)E+2	1.2
···	11762	36.64	−0.23	···	···	(6.1 ± 0.2)E+1	···	···
···	11772	36.51	−0.22	···	0.5	(3.9 ± 0.2)E+1	(2.5 ± 0.1)E+2	0.9
···	11805	36.22	−0.15	···	0.7	(9.4 ± 0.3)E+1	(1.94 ± 0.05)E+2	1.2
24457	10914	36.16	−0.27	41	1.5	(2.52 ± 0.06)E+2	(3.79 ± 0.09)E+1	3.0
24513	11962	37.04	+0.08	53	1.2	(2.19 ± 0.04)E+2	(5.9 ± 0.1)E+1	2.5
···	11980	36.84	+0.11	59	···	(1.93 ± 0.02)E+2	···	···
···	11984	36.90	+0.12	58	0.6	(2.82 ± 0.03)E+2	(7.23 ± 0.08)E+2	1.2
···	12001	36.92	+0.14	58	···	(1.97 ± 0.02)E+2	···	···
···	12009	37.06	+0.16	47	0.3	(3.0 ± 0.2)E+1	(3.8 ± 0.3)E+2	0.7
···	12015	37.02	+0.17	44	···	(1.7 ± 0.2)E+1	···	···
···	12026	36.94	+0.18	60	0.9	(4.89 ± 0.04)E+2	(3.85 ± 0.03)E+2	1.7
···	12068	36.94	+0.27	60	1.0	(1.72 ± 0.04)E+2	(8.9 ± 0.2)E+1	2.0
···	11986	37.03	+0.13	···	1.7	(3.50 ± 0.05)E+2	(3.78 ± 0.05)E+1	3.3
···	12003	37.03	+0.15	···	0.7	(1.00 ± 0.03)E+2	(1.59 ± 0.04)E+2	1.4
···	12006	36.98	+0.16	···	1.0	(1.15 ± 0.03)E+2	(6.1 ± 0.2)E+1	2.0
24528	11819	36.38	−0.13	30	···	(6.4 ± 0.2)E+1	···	···
···	11861	36.35	−0.08	32	1.1	(4.42 ± 0.03)E+2	(2.43 ± 0.02)E+2	1.9
···	11878	36.39	−0.06	30	1.6	(5.15 ± 0.04)E+2	(8.50 ± 0.07)E+1	2.9
···	11905	36.38	−0.02	30	1.5	(6.17 ± 0.04)E+2	(1.146 ± 0.008)E+2	2.8
···	10931	36.37	−0.24	···	1.0	(1.10 ± 0.04)E+2	(6.5 ± 0.2)E+1	1.9
24881	11722	36.71	−0.29	82	0.9	(1.81 ± 0.03)E+2	(1.75 ± 0.03)E+2	1.6
···	11783	36.63	−0.20	75	0.1	(1.06 ± 0.02)E+2	(2.66 ± 0.05)E+4	0.3
···	11723	36.64	−0.28	···	1.3	(3.77 ± 0.04)E+2	(1.14 ± 0.01)E+2	2.4
24892	11020	36.27	−0.12	84	1.4	(2.97 ± 0.05)E+2	(6.6 ± 0.1)E+1	2.6
···	11032	36.31	−0.10	83	1.0	(1.79 ± 0.04)E+2	(1.09 ± 0.02)E+2	1.9
···	11811	36.30	−0.15	83	0.7	(1.13 ± 0.02)E+2	(2.27 ± 0.05)E+2	1.3
···	11829	36.30	−0.12	83	0.7	(1.43 ± 0.02)E+2	(2.30 ± 0.04)E+2	1.4
···	10972	36.12	−0.17	···	2.6	(6.98 ± 0.08)E+2	(2.77 ± 0.03)E+1	4.7
25264	11941	36.69	+0.05	62	1.5	(3.28 ± 0.04)E+2	(5.99 ± 0.07)E+1	2.8
···	11968	36.70	+0.09	60	1.3	(7.06 ± 0.04)E+2	(2.07 ± 0.01)E+2	2.4
···	11971	36.61	+0.07	···	2.2	(7.15 ± 0.06)E+2	(4.17 ± 0.03)E+1	4.1
25514	10940	36.42	−0.23	76	···	(6.8 ± 0.3)E+1	···	···
···	11738	36.48	−0.27	75	···	(5.3 ± 0.2)E+1	···	···
···	11757	36.83	−0.23	79	0.6	(3.42 ± 0.02)E+2	(1.178 ± 0.008)E+3	1.1
···	11763	36.54	−0.23	77	···	(5.4 ± 0.2)E+1	···	···
···	11766	36.91	−0.21	80	1.9	(6.25 ± 0.05)E+2	(6.21 ± 0.05)E+1	3.4
···	11780	36.79	−0.20	78	1.7	(2.183 ± 0.005)E+3	(3.125 ± 0.007)E+2	3.0
···	11782	36.84	−0.20	78	1.8	(1.016 ± 0.005)E+3	(1.130 ± 0.005)E+2	3.3
···	11789	36.46	−0.19	75	1.2	(9.10 ± 0.04)E+2	(3.32 ± 0.01)E+2	2.2
···	11799	36.42	−0.17	77	2.2	(3.459 ± 0.007)E+3	(2.202 ± 0.005)E+2	4.0
···	11801	37.12	−0.16	80	···	(1.6 ± 0.1)E+1	···	···
···	11807	37.08	−0.15	78	1.1	(4.88 ± 0.04)E+2	(2.21 ± 0.02)E+2	2.1
···	11817	36.90	−0.13	79	0.4	(4.17 ± 0.03)E+2	(3.03 ± 0.02)E+3	0.8
···	11818	36.86	−0.13	79	0.6	(5.35 ± 0.03)E+2	(2.08 ± 0.01)E+3	1.0
···	11823	36.50	−0.14	76	1.9	(2.183 ± 0.006)E+3	(2.019 ± 0.005)E+2	3.5
···	11828	36.55	−0.12	76	1.4	(6.24 ± 0.04)E+2	(1.578 ± 0.009)E+2	2.5
···	11830	36.88	−0.12	79	···	(1.59 ± 0.02)E+2	···	···
···	11859	36.99	−0.08	80	0.7	(1.81 ± 0.03)E+2	(4.07 ± 0.06)E+2	1.2
···	11874	37.05	−0.08	81	1.0	(4.63 ± 0.04)E+2	(2.69 ± 0.02)E+2	1.9
···	11875	36.75	−0.07	82	0.2	(1.25 ± 0.02)E+2	(6.19 ± 0.08)E+3	0.4
···	11876	36.72	−0.07	82	1.0	(3.42 ± 0.03)E+2	(2.02 ± 0.02)E+2	1.9
···	11882	36.77	−0.06	82	1.4	(2.90 ± 0.03)E+2	(6.54 ± 0.07)E+1	2.6
···	11899	37.05	−0.03	82	1.8	(3.286 ± 0.006)E+3	(3.899 ± 0.007)E+2	3.2
···	11900	36.88	−0.04	79	1.4	(8.04 ± 0.04)E+2	(1.77 ± 0.01)E+2	2.6
···	11745	36.89	−0.26	···	···	(1.4 ± 0.1)E+1	···	···
···	11794	37.05	−0.18	···	1.1	(2.81 ± 0.03)E+2	(1.37 ± 0.02)E+2	2.0
···	11854	36.63	−0.09	···	1.4	(8.13 ± 0.04)E+2	(2.16 ± 0.01)E+2	2.5
···	11892	36.93	−0.05	···	1.7	(4.07 ± 0.04)E+2	(5.73 ± 0.06)E+1	3.1
25555	11123	36.12	+0.06	76	1.7	(7.30 ± 0.06)E+2	(1.052 ± 0.008)E+2	3.0
···	11193	36.22	+0.19	78	1.4	(2.59 ± 0.05)E+2	(5.7 ± 0.1)E+1	2.6
···	11210	36.16	+0.22	80	1.3	(1.58 ± 0.05)E+2	(4.8 ± 0.1)E+1	2.4
···	11978	36.18	+0.10	75	1.2	(4.70 ± 0.04)E+2	(1.75 ± 0.01)E+2	2.2
···	12036	36.19	+0.21	···	1.3	(1.46 ± 0.03)E+2	(4.3 ± 0.1)E+1	2.4
25866	11152	35.60	+0.12	86	0.5	(2.79 ± 0.03)E+2	(1.55 ± 0.01)E+3	0.9
···	11164	35.43	+0.13	75	0.9	(1.106 ± 0.004)E+3	(1.180 ± 0.004)E+3	1.6
···	11170	35.47	+0.14	77	1.2	(5.878 ± 0.005)E+3	(2.968 ± 0.003)E+3	2.0

Continuation of Table B2

COHRS catalog #	Hi-GAL catalog #	ℓ (deg)	b (deg)	$v_{\rm LSR}$ (km s^{-1})	$\theta_{\rm R}$ (arcmin)	M (M$_\odot$)	n (cm^{-3})	R (pc)
···	11171	34.98	+0.15	76	0.7	(1.29 ± 0.03)E+2	(2.96 ± 0.07)E+2	1.2
···	11173	35.59	+0.15	83	0.8	(1.75 ± 0.03)E+2	(3.09 ± 0.05)E+2	1.3
···	11175	35.75	+0.15	85	1.3	(2.345 ± 0.005)E+3	(9.21 ± 0.02)E+2	2.2
···	11176	35.56	+0.15	83	0.5	(1.99 ± 0.03)E+2	(1.56 ± 0.02)E+3	0.8
···	11180	34.95	+0.17	73	1.5	(5.41 ± 0.04)E+2	(1.47 ± 0.01)E+2	2.5
···	11219	35.31	+0.26	71	0.4	(1.17 ± 0.02)E+2	(1.92 ± 0.03)E+3	0.6
···	11227	35.11	+0.28	84	0.7	(1.28 ± 0.03)E+2	(2.76 ± 0.06)E+2	1.2
···	11229	35.34	+0.29	70	0.8	(1.07 ± 0.03)E+2	(1.67 ± 0.04)E+2	1.4
···	11239	35.12	+0.30	84	1.5	(2.29 ± 0.04)E+2	(6.3 ± 0.1)E+1	2.4
···	11203	35.17	+0.21	···	···	(5.9 ± 0.3)E+1	···	···
···	11086	35.29	+0.00	···	1.9	(4.55 ± 0.05)E+2	(6.15 ± 0.07)E+1	3.1
···	11190	35.31	+0.19	···	1.1	(1.65 ± 0.03)E+2	(1.13 ± 0.02)E+2	1.8
···	11198	35.34	+0.20	···	···	(4.5 ± 0.2)E+1	···	···
···	11156	35.81	+0.12	···	0.6	(7.0 ± 0.2)E+1	(2.48 ± 0.08)E+2	1.0
25964	10910	35.45	−0.29	55	0.7	(6.72 ± 0.03)E+2	(1.422 ± 0.007)E+3	1.2
···	10911	35.36	−0.29	54	1.5	(6.92 ± 0.04)E+2	(1.88 ± 0.01)E+2	2.5
···	10913	35.42	−0.29	54	1.0	(6.32 ± 0.04)E+2	(5.12 ± 0.03)E+2	1.7
···	10926	35.32	−0.25	53	···	(4.5 ± 0.1)E+1	···	···
···	10945	35.32	−0.22	54	0.9	(4.40 ± 0.03)E+2	(5.28 ± 0.04)E+2	1.5
···	10932	35.33	−0.24	···	0.5	(9.9 ± 0.2)E+1	(9.1 ± 0.2)E+2	0.8
25983	11050	35.69	−0.06	51	1.7	(7.72 ± 0.05)E+2	(1.284 ± 0.008)E+2	2.9
···	11055	35.88	−0.05	52	0.4	(4.8 ± 0.2)E+1	(6.5 ± 0.3)E+2	0.7
···	11056	35.67	−0.05	50	0.4	(2.41 ± 0.02)E+2	(3.40 ± 0.03)E+3	0.7
···	11058	35.83	−0.04	52	0.7	(1.73 ± 0.03)E+2	(4.55 ± 0.07)E+2	1.2
···	11074	35.80	−0.01	52	0.8	(1.90 ± 0.03)E+2	(3.39 ± 0.05)E+2	1.3
···	11070	35.71	−0.01	···	0.9	(1.52 ± 0.03)E+2	(2.04 ± 0.04)E+2	1.4
···	11083	35.69	−0.01	···	1.1	(3.26 ± 0.04)E+2	(2.01 ± 0.02)E+2	1.9
···	11094	35.74	+0.00	···	0.9	(1.12 ± 0.03)E+2	(1.40 ± 0.04)E+2	1.5
26017	10909	35.48	−0.30	45	1.8	(2.816 ± 0.006)E+3	(4.466 ± 0.009)E+2	2.9
···	10917	35.53	−0.27	46	1.4	(1.093 ± 0.005)E+3	(3.44 ± 0.01)E+2	2.3
···	10929	35.60	−0.25	45	1.5	(1.150 ± 0.005)E+3	(3.09 ± 0.01)E+2	2.5
···	10955	35.60	−0.20	49	1.3	(8.42 ± 0.04)E+2	(3.34 ± 0.02)E+2	2.2
···	10975	35.63	−0.18	54	1.0	(1.75 ± 0.03)E+2	(1.43 ± 0.03)E+2	1.7
···	10985	35.57	−0.16	54	···	(3.7 ± 0.2)E+1	···	···
···	10997	35.51	−0.16	54	0.6	(2.21 ± 0.03)E+2	(8.0 ± 0.1)E+2	1.0
···	11003	35.62	−0.15	49	0.5	(3.1 ± 0.2)E+1	(2.5 ± 0.2)E+2	0.8
···	11008	35.52	−0.13	55	1.3	(6.95 ± 0.04)E+2	(3.09 ± 0.02)E+2	2.1
···	11009	35.46	−0.14	53	1.3	(5.14 ± 0.04)E+2	(2.20 ± 0.02)E+2	2.1
···	11025	35.59	−0.12	55	1.2	(7.18 ± 0.04)E+2	(3.27 ± 0.02)E+2	2.1
···	11028	35.50	−0.11	57	0.8	(1.37 ± 0.03)E+2	(2.71 ± 0.05)E+2	1.3
···	11029	35.53	−0.10	55	···	(1.14 ± 0.02)E+2	···	···
···	11030	35.48	−0.09	55	1.0	(6.73 ± 0.04)E+2	(5.64 ± 0.03)E+2	1.7
···	11039	35.51	−0.09	56	0.6	(1.65 ± 0.02)E+2	(7.4 ± 0.1)E+2	1.0
···	11059	35.31	−0.04	45	2.6	(1.102 ± 0.007)E+3	(5.84 ± 0.04)E+1	4.2
···	11061	35.52	−0.04	56	1.0	(8.96 ± 0.03)E+2	(7.31 ± 0.03)E+2	1.7
···	11062	35.58	−0.03	53	0.9	(3.055 ± 0.004)E+3	(3.600 ± 0.005)E+3	1.5
···	11071	35.50	−0.02	58	1.5	(1.733 ± 0.005)E+3	(4.18 ± 0.01)E+2	2.6
···	11090	35.58	+0.01	54	0.9	(2.097 ± 0.004)E+3	(2.198 ± 0.004)E+3	1.6
···	11095	35.63	+0.01	52	···	(3.9 ± 0.1)E+1	···	···
···	11127	35.58	+0.07	50	1.7	(6.243 ± 0.006)E+3	(1.027 ± 0.001)E+3	2.9
···	11161	35.52	+0.13	···	···	(5.6 ± 0.2)E+1	···	···
···	11015	35.38	−0.13	···	0.7	(9.9 ± 0.2)E+1	(2.94 ± 0.07)E+2	1.1
26268	11052	34.84	−0.05	49	0.6	(2.22 ± 0.03)E+2	(8.5 ± 0.1)E+2	1.0
26370	10915	35.26	−0.28	61	1.0	(2.50 ± 0.04)E+2	(2.09 ± 0.03)E+2	1.7
···	10934	35.25	−0.24	62	0.5	(2.22 ± 0.03)E+2	(1.54 ± 0.02)E+3	0.8
···	10938	35.14	−0.24	61	···	(2.1 ± 0.2)E+1	···	···
···	10943	35.22	−0.23	62	···	(1.32 ± 0.03)E+2	···	···
26608	11124	35.36	+0.09	52	1.9	(7.69 ± 0.05)E+2	(9.31 ± 0.06)E+1	3.2
···	11150	35.40	+0.11	···	0.7	(2.05 ± 0.03)E+2	(4.24 ± 0.06)E+2	1.2
26964	10983	35.23	−0.14	84	2.2	(4.13 ± 0.06)E+2	(3.25 ± 0.04)E+1	3.7
···	11021	35.36	−0.11	93	0.7	(2.76 ± 0.03)E+2	(6.28 ± 0.07)E+2	1.2
···	11079	35.44	−0.01	95	0.4	(2.61 ± 0.03)E+2	(2.84 ± 0.03)E+3	0.7
···	11104	35.39	+0.02	95	2.0	(1.645 ± 0.007)E+3	(1.673 ± 0.007)E+2	3.4
···	11120	35.45	+0.06	94	···	(7.6 ± 0.2)E+1	···	···
27150	10948	34.81	−0.22	79	1.0	(1.97 ± 0.03)E+2	(1.45 ± 0.02)E+2	1.8
···	10953	34.77	−0.21	73	1.7	(3.77 ± 0.05)E+2	(6.13 ± 0.07)E+1	2.9
···	10973	34.78	−0.18	74	0.6	(1.01 ± 0.03)E+2	(4.9 ± 0.1)E+2	0.9
···	10981	34.62	−0.18	79	0.6	(8.9 ± 0.2)E+1	(3.7 ± 0.1)E+2	1.0
···	10984	34.59	−0.17	79	0.9	(1.38 ± 0.03)E+2	(1.48 ± 0.03)E+2	1.6
···	11016	34.74	−0.13	79	1.3	(1.332 ± 0.005)E+3	(5.50 ± 0.02)E+2	2.1
···	11022	34.67	−0.11	85	···	(1.96 ± 0.03)E+2	···	···
···	11036	34.56	−0.10	96	0.9	(2.07 ± 0.04)E+2	(2.15 ± 0.04)E+2	1.6
···	11067	34.72	−0.02	90	0.5	(2.19 ± 0.02)E+2	(1.60 ± 0.02)E+3	0.8
···	11085	34.57	−0.00	76	0.4	(4.24 ± 0.03)E+2	(4.47 ± 0.03)E+3	0.7
···	11103	34.68	+0.02	91	1.2	(5.09 ± 0.04)E+2	(2.29 ± 0.02)E+2	2.1
···	11105	34.75	+0.02	76	1.8	(2.089 ± 0.006)E+3	(2.877 ± 0.008)E+2	3.1
···	11129	34.52	+0.07	79	1.2	(3.77 ± 0.04)E+2	(1.91 ± 0.02)E+2	2.0
···	11004	34.56	−0.15	···	···	(2.0 ± 0.2)E+1	···	···
···	11066	34.76	−0.02	···	1.2	(5.37 ± 0.04)E+2	(2.31 ± 0.02)E+2	2.1
···	11122	34.66	+0.07	···	0.5	(7.7 ± 0.2)E+1	(6.0 ± 0.2)E+2	0.8
···	11128	34.73	+0.07	···	2.0	(2.079 ± 0.007)E+3	(2.023 ± 0.006)E+2	3.5
···	11135	34.56	+0.08	···	0.8	(1.02 ± 0.03)E+2	(1.77 ± 0.05)E+2	1.3
27530	11167	34.56	+0.14	61	0.9	(1.83 ± 0.03)E+2	(2.21 ± 0.04)E+2	1.5
27741	11076	34.89	−0.01	29	1.7	(6.71 ± 0.05)E+2	(1.181 ± 0.009)E+2	2.8

Continuation of Table B2

COHRS catalog #	Hi-GAL catalog #	ℓ (deg)	b (deg)	v_{LSR} (km s^{-1})	θ_{R} (arcmin)	M ($\mathrm{M}_\odot$)	n (cm^{-3})	R (pc)
27779	10015	34.19	−0.13	88	···	(2.5 ± 0.1)E+1	···	···
···	10032	34.14	−0.12	88	2.1	(1.157 ± 0.004)E+3	(9.79 ± 0.04)E+1	3.6
···	10920	34.24	−0.27	90	1.3	(3.15 ± 0.04)E+2	(1.12 ± 0.02)E+2	2.2
···	11091	34.46	+0.01	88	1.6	(1.564 ± 0.005)E+3	(3.37 ± 0.01)E+2	2.7
···	11107	34.43	+0.02	89	0.4	(1.44 ± 0.02)E+2	(1.66 ± 0.02)E+3	0.7
···	11143	34.40	+0.09	89	0.6	(1.67 ± 0.03)E+2	(7.8 ± 0.1)E+2	1.0
···	11151	34.42	+0.11	90	···	(1.31 ± 0.03)E+2	···	···
28338	10952	35.04	−0.21	90	1.4	(6.77 ± 0.05)E+2	(1.95 ± 0.01)E+2	2.4
···	10990	35.00	−0.16	···	0.7	(8.4 ± 0.3)E+1	(1.95 ± 0.06)E+2	1.2
28618	10149	34.04	+0.06	36	1.3	(9.40 ± 0.03)E+2	(3.52 ± 0.01)E+2	2.2
···	10180	34.07	+0.13	35	1.0	(3.61 ± 0.02)E+2	(3.33 ± 0.02)E+2	1.6
···	10246	34.02	+0.24	35	···	(4.0 ± 0.1)E+1	···	···
29052	10923	34.97	−0.27	44	1.8	(5.60 ± 0.05)E+2	(8.30 ± 0.08)E+1	3.0
···	10935	35.17	−0.24	49	1.7	(4.43 ± 0.05)E+2	(7.92 ± 0.09)E+1	2.8
···	10965	34.53	−0.20	54	0.5	(4.8 ± 0.2)E+1	(2.9 ± 0.1)E+2	0.9
···	10968	35.19	−0.20	50	1.5	(3.29 ± 0.04)E+2	(8.2 ± 0.1)E+1	2.5
···	10969	35.12	−0.19	42	···	(5.8 ± 0.1)E+1	···	···
···	10977	34.48	−0.17	53	1.1	(2.89 ± 0.04)E+2	(1.66 ± 0.02)E+2	1.9
···	10978	34.43	−0.18	54	0.8	(1.68 ± 0.03)E+2	(3.10 ± 0.06)E+2	1.3
···	10982	34.96	−0.17	44	···	(4.1 ± 0.2)E+1	···	···
···	10989	35.06	−0.16	42	0.5	(9.3 ± 0.2)E+1	(5.4 ± 0.1)E+2	0.9
···	11034	34.75	−0.09	52	1.3	(8.71 ± 0.05)E+2	(3.37 ± 0.02)E+2	2.2
···	11057	34.99	−0.05	47	0.7	(5.23 ± 0.03)E+2	(1.126 ± 0.007)E+3	1.2
···	11064	35.05	−0.01	46	0.8	(1.79 ± 0.03)E+2	(3.16 ± 0.05)E+2	1.3
···	11075	35.02	−0.00	47	1.7	(5.97 ± 0.05)E+2	(1.065 ± 0.009)E+2	2.8
···	11080	34.36	−0.01	36	0.7	(1.11 ± 0.03)E+2	(3.08 ± 0.07)E+2	1.1
···	11098	34.55	+0.02	48	0.7	(4.32 ± 0.03)E+2	(9.86 ± 0.06)E+2	1.2
···	11117	35.10	+0.05	48	1.9	(3.06 ± 0.05)E+2	(3.87 ± 0.06)E+1	3.2
···	11125	34.82	+0.07	49	0.9	(2.46 ± 0.03)E+2	(2.69 ± 0.03)E+2	1.5
···	11134	34.49	+0.07	47	1.3	(3.66 ± 0.04)E+2	(1.31 ± 0.01)E+2	2.2
···	11163	34.91	+0.13	42	0.9	(3.44 ± 0.04)E+2	(4.22 ± 0.05)E+2	1.5
···	11109	34.65	+0.03	···	0.8	(3.58 ± 0.03)E+2	(5.02 ± 0.04)E+2	1.4
···	11110	34.62	+0.02	···	1.6	(6.93 ± 0.05)E+2	(1.44 ± 0.01)E+2	2.7
···	11136	34.85	+0.08	···	0.5	(1.18 ± 0.02)E+2	(9.4 ± 0.2)E+2	0.8
···	10912	35.07	−0.29	···	0.7	(1.33 ± 0.03)E+2	(3.75 ± 0.08)E+2	1.1
···	10918	35.22	−0.29	···	1.8	(2.96 ± 0.05)E+2	(4.30 ± 0.07)E+1	3.0
···	10924	34.81	−0.26	···	2.2	(6.43 ± 0.05)E+2	(5.08 ± 0.04)E+1	3.7
···	10927	34.57	−0.24	···	1.1	(1.08 ± 0.03)E+2	(7.5 ± 0.2)E+1	1.8
···	10950	34.38	−0.21	···	0.9	(2.92 ± 0.03)E+2	(3.36 ± 0.04)E+2	1.5
···	10957	35.00	−0.22	···	1.7	(5.12 ± 0.05)E+2	(8.73 ± 0.09)E+1	2.9
···	10966	34.39	−0.20	···	1.4	(4.51 ± 0.04)E+2	(1.47 ± 0.01)E+2	2.3
···	11060	34.54	−0.05	···	1.1	(2.03 ± 0.04)E+2	(1.38 ± 0.02)E+2	1.8
···	11063	35.07	−0.03	···	0.9	(9.4 ± 0.3)E+1	(9.5 ± 0.3)E+1	1.6
···	11096	34.84	+0.02	···	···	(2.7 ± 0.2)E+1	···	···
···	11220	34.93	+0.24	···	1.9	(1.187 ± 0.006)E+3	(1.522 ± 0.008)E+2	3.2
···	11231	34.98	+0.29	···	1.3	(2.55 ± 0.04)E+2	(1.06 ± 0.02)E+2	2.1
29208	9909	33.65	−0.30	52	0.8	(1.39 ± 0.02)E+2	(2.12 ± 0.04)E+2	1.4
···	9939	33.67	−0.26	53	1.6	(6.21 ± 0.04)E+2	(1.024 ± 0.006)E+2	2.9
···	9940	33.50	−0.26	54	0.8	(2.60 ± 0.02)E+2	(3.48 ± 0.03)E+2	1.4
···	9953	33.48	−0.24	54	1.0	(1.70 ± 0.02)E+2	(1.12 ± 0.01)E+2	1.8
···	9958	33.64	−0.23	62	1.1	(1.320 ± 0.003)E+3	(7.16 ± 0.02)E+2	2.0
···	9965	33.82	−0.21	48	···	(2.99 ± 0.01)E+2	···	···
···	9968	33.48	−0.22	52	1.1	(4.64 ± 0.03)E+2	(2.08 ± 0.01)E+2	2.1
···	9970	33.61	−0.21	59	0.5	(6.2 ± 0.1)E+1	(3.90 ± 0.09)E+2	0.9
···	9971	33.59	−0.21	61	0.4	(7.0 ± 0.2)E+1	(6.0 ± 0.1)E+2	0.8
···	9983	33.81	−0.19	46	1.1	(1.912 ± 0.003)E+3	(9.76 ± 0.02)E+2	2.0
···	9992	33.78	−0.17	52	1.1	(5.16 ± 0.03)E+2	(2.83 ± 0.01)E+2	1.9
···	9996	33.65	−0.16	53	···	(7.7 ± 0.1)E+1	···	···
···	9998	33.56	−0.16	48	0.7	(2.38 ± 0.02)E+2	(5.67 ± 0.05)E+2	1.2
···	10001	33.81	−0.16	52	1.4	(1.174 ± 0.003)E+3	(2.830 ± 0.008)E+2	2.6
···	10003	33.67	−0.16	54	···	(7.8 ± 0.2)E+1	···	···
···	10020	33.75	−0.12	50	···	(5.3 ± 0.2)E+1	···	···
···	10021	33.73	−0.12	51	···	(6.3 ± 0.1)E+1	···	···
···	10028	33.83	−0.12	50	···	(8.2 ± 0.2)E+1	···	···
···	10036	33.73	−0.10	51	···	(5.1 ± 0.1)E+1	···	···
···	9923	33.77	−0.29	···	1.1	(1.78 ± 0.03)E+2	(8.0 ± 0.1)E+1	2.1
···	9941	33.63	−0.26	···	1.1	(2.14 ± 0.02)E+2	(1.20 ± 0.01)E+2	1.9
···	9961	33.44	−0.22	···	0.4	(6.6 ± 0.2)E+1	(9.4 ± 0.2)E+2	0.7
···	9977	33.67	−0.20	···	0.6	(4.3 ± 0.2)E+1	(1.50 ± 0.06)E+2	1.0
29247	10207	33.91	+0.17	59	···	(1.10 ± 0.02)E+2	···	···
···	10226	33.81	+0.20	···	0.8	(2.57 ± 0.03)E+2	(3.30 ± 0.03)E+2	1.5
29256	10089	33.98	−0.02	61	1.1	(1.358 ± 0.003)E+3	(7.42 ± 0.02)E+2	1.9
···	10109	33.99	−0.01	61	1.6	(1.337 ± 0.004)E+3	(2.256 ± 0.007)E+2	2.9
···	10128	33.85	+0.01	61	1.2	(9.88 ± 0.03)E+2	(3.94 ± 0.01)E+2	2.2
···	10033	33.94	−0.11	···	2.3	(1.093 ± 0.005)E+3	(6.15 ± 0.03)E+1	4.2
···	10048	34.01	−0.08	···	0.3	(5.5 ± 0.2)E+1	(1.13 ± 0.03)E+3	0.6
···	10087	34.03	−0.02	···	0.6	(1.15 ± 0.02)E+2	(3.84 ± 0.06)E+2	1.1
···	10098	33.92	−0.02	···	1.1	(4.28 ± 0.03)E+2	(2.00 ± 0.01)E+2	2.0
29302	9918	34.01	−0.29	12	1.2	(6.19 ± 0.04)E+2	(1.599 ± 0.009)E+2	2.5
···	9951	33.74	−0.24	11	1.9	(6.39 ± 0.05)E+2	(4.48 ± 0.04)E+1	3.9
···	9927	33.98	−0.28	···	0.4	(8.4 ± 0.2)E+1	(5.6 ± 0.1)E+2	0.8
···	9928	33.82	−0.28	···	0.6	(1.91 ± 0.03)E+2	(3.31 ± 0.04)E+2	1.3
29322	10144	33.68	+0.04	38	0.5	(3.49 ± 0.02)E+2	(2.49 ± 0.01)E+3	0.8
···	10146	33.66	+0.05	38	1.1	(4.98 ± 0.03)E+2	(2.23 ± 0.01)E+2	2.1

Continuation of Table B2

COHRS catalog #	Hi-GAL catalog #	ℓ (deg)	b (deg)	$v_{\rm LSR}$ (km s^{-1})	$\theta_{\rm R}$ (arcmin)	M (M$_\odot$)	n (cm^{-3})	R (pc)
29325	9911	34.19	−0.31	56	1.5	(2.46 ± 0.03)E+2	(4.93 ± 0.06)E+1	2.7
···	10086	34.10	−0.03	56	···	(1.6 ± 0.1)E+1	···	···
···	10127	34.09	+0.01	58	1.4	(3.431 ± 0.004)E+3	(9.17 ± 0.01)E+2	2.5
···	10165	34.13	+0.07	57	1.7	(1.246 ± 0.004)E+3	(1.594 ± 0.005)E+2	3.2
···	10169	34.17	+0.09	57	···	(1.81 ± 0.01)E+2	···	···
···	10237	34.00	+0.21	59	1.1	(2.89 ± 0.03)E+2	(1.31 ± 0.01)E+2	2.1
···	10243	34.25	+0.23	59	···	(7.1 ± 0.1)E+1	···	···
···	10276	34.19	+0.29	60	···	(4.6 ± 0.2)E+1	···	···
···	10922	34.21	−0.26	52	···	(4.0 ± 0.2)E+1	···	···
···	10951	34.26	−0.20	51	1.1	(1.082 ± 0.005)E+3	(5.96 ± 0.02)E+2	1.9
···	10967	34.23	−0.19	51	···	(1.12 ± 0.02)E+2	···	···
···	10998	34.28	−0.15	49	0.8	(6.74 ± 0.04)E+2	(1.043 ± 0.006)E+3	1.4
···	10999	34.31	−0.15	45	0.6	(1.04 ± 0.03)E+2	(2.95 ± 0.08)E+2	1.1
···	11093	34.21	+0.01	40	1.0	(5.78 ± 0.04)E+2	(4.00 ± 0.03)E+2	1.8
···	11162	34.24	+0.13	58	1.4	(1.1247 ± 0.0005)E+4	(2.714 ± 0.001)E+3	2.6
···	11177	34.26	+0.16	57	1.1	(5.3100 ± 0.0006)E+4	(2.8687 ± 0.0003)E+4	2.0
···	11212	34.40	+0.23	57	1.1	(1.5604 ± 0.0007)E+4	(6.892 ± 0.003)E+3	2.1
···	11218	34.45	+0.25	59	1.0	(2.278 ± 0.005)E+3	(1.558 ± 0.003)E+3	1.8
···	11232	34.49	+0.29	59	0.3	(2.04 ± 0.03)E+2	(6.8 ± 0.1)E+3	0.5
···	11031	34.18	−0.11	···	1.2	(1.51 ± 0.04)E+2	(6.5 ± 0.2)E+1	2.1
···	10131	34.14	+0.03	···	0.5	(1.09 ± 0.02)E+2	(4.65 ± 0.09)E+2	1.0
···	10212	34.01	+0.17	···	1.4	(3.48 ± 0.03)E+2	(8.36 ± 0.07)E+1	2.6
···	10936	34.21	−0.24	···	0.8	(2.18 ± 0.03)E+2	(3.25 ± 0.05)E+2	1.4
···	10970	34.29	−0.18	···	1.0	(2.45 ± 0.04)E+2	(1.49 ± 0.02)E+2	1.9
29360	10022	33.51	−0.12	112	1.0	(3.97 ± 0.03)E+2	(2.58 ± 0.02)E+2	1.8
···	10051	33.45	−0.09	109	1.0	(9.94 ± 0.03)E+2	(6.94 ± 0.02)E+2	1.8
···	10079	33.59	−0.04	104	···	(2.32 ± 0.02)E+2	···	···
···	10080	33.55	−0.03	103	1.1	(5.43 ± 0.03)E+2	(2.77 ± 0.01)E+2	2.0
···	10088	33.65	−0.03	104	1.8	(6.396 ± 0.005)E+3	(6.905 ± 0.005)E+2	3.3
···	10090	33.73	−0.01	105	1.8	(4.660 ± 0.004)E+3	(5.584 ± 0.005)E+2	3.2
···	10092	33.29	−0.02	99	1.3	(1.376 ± 0.003)E+3	(3.780 ± 0.009)E+2	2.4
···	10093	33.23	−0.02	100	0.9	(2.378 ± 0.003)E+3	(1.872 ± 0.002)E+3	1.7
···	10102	33.49	−0.02	102	0.8	(9.43 ± 0.02)E+2	(1.064 ± 0.003)E+3	1.5
···	10107	33.20	+0.01	101	1.6	(3.534 ± 0.004)E+3	(5.403 ± 0.006)E+2	3.0
···	10120	33.39	+0.00	104	1.3	(4.349 ± 0.003)E+3	(1.442 ± 0.001)E+3	2.3
···	10130	33.52	+0.02	104	0.5	(5.46 ± 0.02)E+2	(3.87 ± 0.01)E+3	0.8
···	10137	33.42	+0.04	104	1.0	(7.96 ± 0.03)E+2	(5.80 ± 0.02)E+2	1.8
···	10142	33.15	+0.04	105	0.2	(1.53 ± 0.02)E+2	(7.39 ± 0.08)E+3	0.4
···	10154	33.54	+0.07	104	1.1	(4.42 ± 0.03)E+2	(2.45 ± 0.01)E+2	1.9
···	10175	33.92	+0.11	108	1.0	(8.335 ± 0.004)E+3	(5.657 ± 0.002)E+3	1.8
···	10189	33.89	+0.14	107	1.0	(4.43 ± 0.03)E+2	(3.11 ± 0.02)E+2	1.8
···	10198	33.85	+0.15	108	0.7	(7.0 ± 0.2)E+1	(1.55 ± 0.04)E+2	1.2
···	10071	33.31	−0.05	···	···	(1.81 ± 0.01)E+2	···	···
···	10151	33.79	+0.06	···	0.6	(1.20 ± 0.02)E+2	(3.28 ± 0.06)E+2	1.1
···	10147	33.57	+0.05	···	0.6	(1.89 ± 0.02)E+2	(4.94 ± 0.05)E+2	1.2
29361	10200	33.65	+0.17	41	1.6	(8.60 ± 0.04)E+2	(1.479 ± 0.006)E+2	2.9
···	10205	33.75	+0.17	40	0.6	(3.27 ± 0.02)E+2	(1.200 ± 0.006)E+3	1.0
···	10244	33.61	+0.23	42	1.1	(7.97 ± 0.03)E+2	(3.90 ± 0.01)E+2	2.0
···	10251	33.57	+0.25	43	1.3	(4.43 ± 0.03)E+2	(1.323 ± 0.008)E+2	2.4
···	10262	33.71	+0.26	36	0.2	(4.42 ± 0.02)E+2	(3.82 ± 0.01)E+4	0.4
···	10267	33.55	+0.27	44	1.6	(2.93 ± 0.03)E+2	(4.54 ± 0.05)E+1	3.0
···	10278	33.70	+0.28	37	1.0	(9.31 ± 0.03)E+2	(6.74 ± 0.02)E+2	1.8
···	10231	33.68	+0.20	···	1.1	(6.00 ± 0.03)E+2	(2.86 ± 0.02)E+2	2.0
···	10279	33.59	+0.28	···	1.4	(1.60 ± 0.03)E+2	(3.92 ± 0.07)E+1	2.5
29368	10013	33.45	−0.13	89	···	(2.4 ± 0.1)E+1	···	···
···	10016	33.35	−0.13	88	1.0	(2.61 ± 0.03)E+2	(1.68 ± 0.02)E+2	1.8
···	10067	33.52	−0.04	85	1.0	(1.358 ± 0.003)E+3	(1.042 ± 0.002)E+3	1.7
···	10116	33.82	+0.01	90	0.4	(2.30 ± 0.02)E+2	(1.72 ± 0.01)E+3	0.8
···	10004	33.27	−0.15	···	0.7	(8.5 ± 0.2)E+1	(1.67 ± 0.04)E+2	1.3
···	10117	33.60	+0.01	···	0.3	(1.42 ± 0.02)E+2	(2.78 ± 0.03)E+3	0.6
···	10124	33.90	+0.01	···	0.8	(2.81 ± 0.02)E+2	(3.13 ± 0.03)E+2	1.5
···	10133	33.77	+0.03	···	0.6	(2.14 ± 0.02)E+2	(7.95 ± 0.08)E+2	1.0
···	10159	33.73	+0.07	···	0.4	(1.79 ± 0.02)E+2	(1.43 ± 0.02)E+3	0.8
29435	9954	33.95	−0.23	89	0.4	(7.1 ± 0.2)E+1	(1.06 ± 0.03)E+3	0.6
···	10011	34.01	−0.14	92	1.2	(3.29 ± 0.03)E+2	(1.36 ± 0.01)E+2	2.1
29444	10191	33.62	+0.15	94	0.5	(2.62 ± 0.02)E+2	(1.309 ± 0.009)E+3	0.9
···	10250	33.90	+0.25	96	0.4	(8.0 ± 0.2)E+1	(7.7 ± 0.2)E+2	0.7
···	10241	33.56	+0.22	···	1.2	(4.63 ± 0.03)E+2	(1.78 ± 0.01)E+2	2.2
29561	10139	32.99	+0.04	83	1.0	(3.615 ± 0.005)E+3	(1.788 ± 0.002)E+3	2.0
···	10157	33.11	+0.07	83	1.9	(4.064 ± 0.006)E+3	(3.083 ± 0.004)E+2	3.8
···	10160	33.04	+0.08	83	0.8	(5.45 ± 0.03)E+2	(4.95 ± 0.03)E+2	1.6
29564	10184	32.96	+0.14	77	0.9	(4.55 ± 0.03)E+2	(3.61 ± 0.02)E+2	1.7
···	10195	33.00	+0.16	72	1.7	(1.736 ± 0.005)E+3	(1.922 ± 0.005)E+2	3.3
29629	9980	32.41	−0.20	83	1.1	(1.63 ± 0.03)E+2	(6.3 ± 0.1)E+1	2.2
···	10023	32.52	−0.13	79	1.3	(6.09 ± 0.03)E+2	(1.630 ± 0.009)E+2	2.5
···	10038	32.46	−0.10	81	···	(7.6 ± 0.2)E+1	···	···
···	10041	32.41	−0.10	80	1.4	(8.78 ± 0.04)E+2	(1.708 ± 0.008)E+2	2.7
···	10049	32.36	−0.08	80	0.3	(7.0 ± 0.2)E+1	(9.4 ± 0.3)E+2	0.7
···	10099	32.45	−0.01	77	0.9	(2.00 ± 0.03)E+2	(1.53 ± 0.02)E+2	1.7
···	10119	32.48	+0.00	76	1.7	(6.90 ± 0.04)E+2	(7.45 ± 0.05)E+1	3.3
···	9972	32.47	−0.21	···	0.8	(3.3 ± 0.2)E+1	(3.9 ± 0.2)E+1	1.5
···	10024	32.41	−0.13	···	1.3	(7.55 ± 0.04)E+2	(1.804 ± 0.008)E+2	2.6
···	10025	32.32	−0.12	···	0.8	(1.31 ± 0.02)E+2	(1.57 ± 0.03)E+2	1.5
···	10043	32.50	−0.09	···	0.7	(1.50 ± 0.02)E+2	(2.51 ± 0.04)E+2	1.3

Continuation of Table B2

COHRS catalog #	Hi-GAL catalog #	ℓ (deg)	b (deg)	$v_{\rm LSR}$ (km s^{-1})	$\theta_{\rm R}$ (arcmin)	M (M$_\odot$)	n (cm^{-3})	R (pc)
...	10118	32.53	+0.01	...	...	(4.6 ± 0.2)E+1	...	...
29740	10268	33.02	+0.27	33	0.9	(1.56 ± 0.03)E+2	(9.9 ± 0.2)E+1	1.9
...	10269	32.90	+0.27	...	1.5	(2.91 ± 0.04)E+2	(4.17 ± 0.06)E+1	3.0
29806	9932	32.55	−0.28	45	0.7	(2.18 ± 0.03)E+1	(5.15 ± 0.08)E+2	0.6
...	9933	32.53	−0.28	44	0.9	(3.59 ± 0.04)E+1	(3.61 ± 0.04)E+2	0.7
...	9945	32.51	−0.25	44	1.7	(1.112 ± 0.006)E+2	(2.01 ± 0.01)E+2	1.3
...	9973	32.52	−0.19	43	1.6	(9.25 ± 0.07)E+1	(1.82 ± 0.01)E+2	1.3
...	9978	32.65	−0.20	51	0.7	(2.81 ± 0.04)E+1	(7.8 ± 0.1)E+2	0.5
29832	10162	32.32	+0.07	40	...	(1.04 ± 0.03)E+2	...	...
...	10166	32.42	+0.09	42	1.0	(1.985 ± 0.005)E+3	(4.81 ± 0.01)E+2	2.6
...	10167	32.37	+0.08	43	1.1	(1.260 ± 0.005)E+3	(2.65 ± 0.01)E+2	2.7
...	10185	32.31	+0.14	44	0.7	(2.46 ± 0.03)E+2	(2.33 ± 0.03)E+2	1.6
...	10187	32.34	+0.15	44	1.1	(6.45 ± 0.05)E+2	(1.38 ± 0.01)E+2	2.7
...	10190	32.59	+0.15	53	1.0	(2.72 ± 0.04)E+2	(7.8 ± 0.1)E+1	2.4
...	10199	32.45	+0.14	44	1.2	(1.791 ± 0.006)E+3	(2.569 ± 0.008)E+2	3.0
...	10202	32.41	+0.17	46	0.4	(3.65 ± 0.03)E+2	(1.24 ± 0.01)E+3	1.1
...	10203	32.38	+0.16	45	...	(3.43 ± 0.03)E+2	...	...
...	10229	32.62	+0.20	51	0.2	(1.42 ± 0.03)E+2	(3.82 ± 0.07)E+3	0.5
...	10230	32.55	+0.20	52	...	(1.29 ± 0.03)E+2	...	...
...	10234	32.58	+0.19	33	2.0	(1.481 ± 0.008)E+3	(4.92 ± 0.03)E+1	5.0
...	10235	32.47	+0.20	49	2.0	(7.21 ± 0.01)E+3	(2.479 ± 0.003)E+2	4.9
...	10248	32.39	+0.24	51	0.8	(2.20 ± 0.04)E+2	(1.02 ± 0.02)E+2	2.1
...	10254	32.42	+0.24	41	0.6	(9.4 ± 0.3)E+1	(1.52 ± 0.05)E+2	1.4
...	10264	32.51	+0.25	50	1.2	(1.191 ± 0.006)E+3	(1.893 ± 0.009)E+2	2.9
...	10270	32.47	+0.27	52	...	(1.22 ± 0.03)E+2	...	...
...	10179	32.57	+0.12	...	...	(7.7 ± 0.3)E+1	...	...
...	10261	32.56	+0.25	...	...	(1.59 ± 0.03)E+2	...	...
...	10263	32.60	+0.26	...	0.4	(5.2 ± 0.3)E+1	(3.1 ± 0.2)E+2	0.9
29908	10206	33.39	+0.16	10	0.6	(2.54 ± 0.01)E+3	(1.135 ± 0.004)E+3	2.1
...	10156	33.23	+0.07	...	...	(4.6 ± 0.4)E+1	...	...
...	10173	33.26	+0.10	...	0.7	(1.31 ± 0.01)E+3	(2.69 ± 0.02)E+2	2.7
...	10208	33.25	+0.17	...	0.9	(1.20 ± 0.01)E+3	(1.21 ± 0.01)E+2	3.4
...	10223	33.35	+0.20	...	1.1	(1.74 ± 0.01)E+3	(1.075 ± 0.007)E+2	4.0
29910	10216	32.70	+0.19	19	1.3	(5.39 ± 0.05)E+2	(6.73 ± 0.07)E+1	3.2
...	10220	32.80	+0.19	14	0.9	(1.5260 ± 0.0007)E+4	(5.009 ± 0.002)E+3	2.3
...	10221	32.74	+0.19	19	1.1	(3.222 ± 0.006)E+3	(6.96 ± 0.01)E+2	2.7
29959	10005	32.76	−0.15	37	1.3	(2.28 ± 0.01)E+3	(1.120 ± 0.005)E+2	4.3
...	10037	32.63	−0.10	33	1.0	(1.516 ± 0.009)E+3	(1.453 ± 0.008)E+2	3.5
...	10057	32.75	−0.07	37	0.6	(1.2615 ± 0.0009)E+4	(7.199 ± 0.005)E+3	1.9
...	10061	32.63	−0.07	33	0.8	(8.73 ± 0.07)E+2	(1.77 ± 0.02)E+2	2.7
...	10065	32.77	−0.06	38	...	(5.77 ± 0.05)E+2	...	...
...	10075	32.80	−0.05	40	0.6	(3.40 ± 0.06)E+2	(1.73 ± 0.03)E+2	2.0
...	10081	32.87	−0.04	40	1.7	(2.21 ± 0.01)E+3	(4.96 ± 0.03)E+1	5.6
...	10010	33.02	−0.14	...	...	(1.80 ± 0.05)E+2	...	...
30096	10017	33.18	−0.13	77	1.1	(2.61 ± 0.03)E+2	(1.16 ± 0.01)E+2	2.1
...	10042	33.13	−0.10	76	2.2	(8.364 ± 0.007)E+3	(4.414 ± 0.004)E+2	4.2
...	10106	33.35	−0.01	72	1.2	(1.271 ± 0.004)E+3	(4.01 ± 0.01)E+2	2.3
...	10110	33.43	−0.01	75	1.8	(5.290 ± 0.005)E+3	(4.609 ± 0.004)E+2	3.6
...	10129	33.55	+0.02	72	0.6	(6.76 ± 0.02)E+2	(2.150 ± 0.006)E+3	1.1
...	10192	33.48	+0.14	68	1.7	(1.067 ± 0.005)E+3	(1.097 ± 0.005)E+2	3.4
...	10215	33.51	+0.18	66	0.6	(3.79 ± 0.03)E+2	(9.25 ± 0.07)E+2	1.2
...	10077	33.45	−0.04	...	0.9	(5.96 ± 0.02)E+2	(4.45 ± 0.02)E+2	1.8
...	10152	33.52	+0.06	...	0.6	(4.04 ± 0.03)E+2	(1.032 ± 0.007)E+3	1.2
30821	9999	32.91	−0.16	98	1.4	(4.53 ± 0.04)E+2	(8.52 ± 0.07)E+1	2.8
...	10029	32.92	−0.12	98	0.6	(3.26 ± 0.02)E+2	(6.63 ± 0.05)E+2	1.3
...	10030	32.89	−0.12	98	1.3	(6.82 ± 0.04)E+2	(1.600 ± 0.009)E+2	2.6
...	10034	32.97	−0.11	88	1.1	(6.77 ± 0.04)E+2	(2.57 ± 0.01)E+2	2.2
...	10035	32.70	−0.11	93	...	(1.40 ± 0.02)E+2	...	...
...	10047	32.87	−0.09	84	0.6	(3.08 ± 0.02)E+2	(6.77 ± 0.05)E+2	1.2
...	10053	32.83	−0.08	99	0.8	(7.04 ± 0.03)E+2	(7.11 ± 0.03)E+2	1.6
...	10060	32.97	−0.07	89	1.4	(7.91 ± 0.04)E+2	(1.393 ± 0.007)E+2	2.8
...	10066	32.71	−0.06	100	0.4	(8.87 ± 0.02)E+2	(8.02 ± 0.02)E+3	0.8
...	10078	32.72	−0.04	101	0.8	(3.43 ± 0.03)E+2	(3.89 ± 0.03)E+2	1.5
...	10096	33.00	−0.01	96	1.3	(7.49 ± 0.04)E+2	(1.833 ± 0.009)E+2	2.5
...	10097	32.85	−0.02	99	1.0	(4.71 ± 0.03)E+2	(2.42 ± 0.01)E+2	2.0
...	10114	32.84	+0.00	100	1.0	(3.04 ± 0.03)E+2	(1.80 ± 0.02)E+2	1.9
...	10121	32.66	+0.00	100	1.3	(5.70 ± 0.04)E+2	(1.286 ± 0.008)E+2	2.6
...	10125	32.80	+0.02	100	0.8	(4.64 ± 0.03)E+2	(4.30 ± 0.02)E+2	1.6
...	10145	32.69	+0.05	97	1.2	(6.98 ± 0.04)E+2	(1.93 ± 0.01)E+2	2.4
...	10148	32.75	+0.05	88	0.4	(1.99 ± 0.02)E+2	(1.37 ± 0.02)E+3	0.8
...	10158	32.82	+0.05	88	2.3	(2.826 ± 0.006)E+3	(1.293 ± 0.003)E+2	4.4
...	10161	32.85	+0.08	99	1.2	(7.65 ± 0.03)E+2	(2.47 ± 0.01)E+2	2.3
...	10174	32.70	+0.10	95	1.0	(9.04 ± 0.03)E+2	(5.03 ± 0.02)E+2	1.9
...	10176	32.74	+0.11	95	0.5	(5.83 ± 0.02)E+2	(1.954 ± 0.008)E+3	1.1
...	9995	33.01	−0.17	...	0.8	(1.72 ± 0.02)E+2	(2.10 ± 0.03)E+2	1.5
...	10018	32.67	−0.13	...	0.7	(3.11 ± 0.02)E+2	(4.77 ± 0.04)E+2	1.4
...	10019	33.10	−0.13	...	1.5	(5.59 ± 0.04)E+2	(8.87 ± 0.06)E+1	2.9
...	10052	32.95	−0.08	...	...	(7.5 ± 0.1)E+1	...	...
...	10104	32.96	−0.01	...	0.5	(2.86 ± 0.02)E+2	(1.107 ± 0.009)E+3	1.0
...	10122	32.94	+0.01	...	1.4	(6.05 ± 0.04)E+2	(1.271 ± 0.008)E+2	2.7
...	10168	32.73	+0.08	...	...	(9.0 ± 0.2)E+1	...	...
...	10178	32.77	+0.12	...	...	(1.6 ± 0.1)E+1	...	...
30901	10224	33.23	+0.20	100	0.6	(1.08 ± 0.02)E+2	(3.01 ± 0.06)E+2	1.1
...	10228	33.20	+0.21	100	0.6	(1.65 ± 0.02)E+2	(3.25 ± 0.05)E+2	1.3

Continuation of Table B2

COHRS catalog #	Hi-GAL catalog #	ℓ (deg)	b (deg)	v_{LSR} (km s^{-1})	θ_{R} (arcmin)	M (M$_{\odot}$)	n (cm^{-3})	R (pc)
⋯	10232	33.14	+0.21	101	2.2	(8.55 ± 0.05)E+2	(4.58 ± 0.03)E+1	4.2
⋯	10240	33.06	+0.22	⋯	0.5	(1.10 ± 0.02)E+2	(5.8 ± 0.1)E+2	0.9
30971	10181	33.42	+0.13	83	1.0	(8.10 ± 0.03)E+2	(4.63 ± 0.02)E+2	1.9
⋯	10183	33.34	+0.13	85	⋯	(6.7 ± 0.2)E+1	⋯	⋯
⋯	10201	33.34	+0.17	85	1.4	(1.804 ± 0.004)E+3	(3.761 ± 0.008)E+2	2.7
⋯	10227	33.39	+0.20	85	0.5	(6.95 ± 0.03)E+2	(3.20 ± 0.01)E+3	1.0
31071	9922	32.80	−0.29	90	0.1	(9.8 ± 0.2)E+1	(1.87 ± 0.04)E+4	0.3
⋯	9943	32.61	−0.25	90	1.4	(1.876 ± 0.004)E+3	(3.397 ± 0.007)E+2	2.8
⋯	9944	32.65	−0.25	89	1.5	(1.117 ± 0.004)E+3	(1.944 ± 0.007)E+2	2.9
⋯	9919	32.77	−0.30	⋯	0.8	(2.36 ± 0.03)E+2	(2.55 ± 0.03)E+2	1.5
⋯	9942	32.70	−0.26	⋯	⋯	(2.4 ± 0.1)E+1	⋯	⋯
⋯	9956	32.70	−0.24	⋯	⋯	(4.3 ± 0.2)E+1	⋯	⋯
⋯	9959	32.87	−0.23	⋯	0.6	(2.03 ± 0.02)E+2	(5.76 ± 0.06)E+2	1.1
⋯	9962	32.91	−0.22	⋯	⋯	(8.5 ± 0.2)E+1	⋯	⋯
⋯	9981	32.89	−0.19	⋯	⋯	(6.4 ± 0.1)E+1	⋯	⋯
⋯	9982	32.71	−0.19	⋯	0.6	(1.05 ± 0.02)E+2	(2.20 ± 0.05)E+2	1.2
31380	9411	31.87	−0.16	100	⋯	(3.8 ± 0.2)E+1	⋯	⋯
⋯	9420	31.85	−0.13	102	1.2	(6.85 ± 0.04)E+2	(3.08 ± 0.02)E+2	2.1
⋯	9434	31.87	−0.10	102	0.7	(2.50 ± 0.03)E+2	(4.96 ± 0.05)E+2	1.3
⋯	9947	31.94	−0.25	93	1.3	(2.25 ± 0.02)E+2	(6.56 ± 0.07)E+1	2.4
⋯	9976	32.00	−0.20	97	0.6	(5.33 ± 0.02)E+2	(1.360 ± 0.005)E+3	1.2
⋯	9402	31.86	−0.22	⋯	1.7	(2.81 ± 0.04)E+2	(3.68 ± 0.06)E+1	3.1
⋯	9913	31.98	−0.30	⋯	1.4	(8.36 ± 0.03)E+2	(2.105 ± 0.008)E+2	2.5
⋯	9938	31.96	−0.28	⋯	1.9	(9.57 ± 0.04)E+2	(8.98 ± 0.04)E+1	3.5
⋯	9967	32.19	−0.22	⋯	0.8	(5.3 ± 0.2)E+1	(6.7 ± 0.2)E+1	1.5
31384	9466	31.58	+0.08	96	1.0	(4.120 ± 0.005)E+3	(2.734 ± 0.003)E+3	1.8
⋯	9470	31.66	+0.09	111	0.9	(1.87 ± 0.03)E+2	(1.59 ± 0.03)E+2	1.7
⋯	9472	31.81	+0.10	94	0.6	(2.68 ± 0.02)E+2	(1.009 ± 0.008)E+3	1.0
⋯	9484	31.80	+0.14	94	2.3	(2.348 ± 0.007)E+3	(1.288 ± 0.004)E+2	4.2
⋯	9485	31.61	+0.14	97	1.3	(1.179 ± 0.004)E+3	(3.88 ± 0.01)E+2	2.3
⋯	9488	31.75	+0.15	106	1.4	(7.30 ± 0.04)E+2	(1.73 ± 0.01)E+2	2.6
⋯	9490	31.72	+0.17	107	1.6	(8.32 ± 0.04)E+2	(1.466 ± 0.008)E+2	2.8
⋯	9495	31.61	+0.17	105	1.1	(3.75 ± 0.03)E+2	(1.81 ± 0.02)E+2	2.0
⋯	9503	31.59	+0.20	115	⋯	(2.64 ± 0.02)E+2	⋯	⋯
⋯	9506	31.58	+0.23	116	1.1	(5.08 ± 0.04)E+2	(2.36 ± 0.02)E+2	2.1
⋯	10153	32.03	+0.06	95	1.6	(1.4217 ± 0.0005)E+4	(2.1946 ± 0.0007)E+3	3.0
⋯	10170	32.25	+0.09	96	⋯	(9.0 ± 0.1)E+1	⋯	⋯
⋯	10171	32.12	+0.09	97	0.8	(2.311 ± 0.003)E+3	(3.190 ± 0.004)E+3	1.4
⋯	10186	32.15	+0.13	94	1.3	(5.467 ± 0.004)E+3	(1.769 ± 0.001)E+3	2.3
⋯	9491	31.67	+0.15	⋯	1.8	(1.066 ± 0.005)E+3	(1.179 ± 0.006)E+2	3.3
⋯	9473	31.60	+0.10	⋯	0.6	(1.96 ± 0.03)E+2	(7.18 ± 0.09)E+2	1.0
⋯	9479	31.55	+0.12	⋯	1.4	(3.25 ± 0.04)E+2	(7.87 ± 0.09)E+1	2.6
31417	9453	31.46	+0.02	103	1.3	(3.66 ± 0.04)E+2	(1.26 ± 0.01)E+2	2.3
⋯	9461	31.44	+0.05	⋯	1.4	(3.71 ± 0.04)E+2	(9.1 ± 0.1)E+1	2.5
31476	9984	32.34	−0.19	44	⋯	(1.81 ± 0.06)E+1	⋯	⋯
⋯	9987	32.30	−0.18	42	⋯	(2.30 ± 0.07)E+1	⋯	⋯
⋯	10006	32.26	−0.15	43	⋯	(1.84 ± 0.08)E+1	⋯	⋯
⋯	10026	32.27	−0.12	45	1.2	(1.04 ± 0.01)E+2	(1.20 ± 0.02)E+2	1.5
⋯	10044	32.33	−0.09	45	0.8	(3.9 ± 0.1)E+1	(1.59 ± 0.04)E+2	1.0
⋯	10045	32.29	−0.09	⋯	1.1	(7.2 ± 0.1)E+1	(9.8 ± 0.2)E+1	1.4
31505	10002	32.11	−0.16	42	1.5	(4.02 ± 0.02)E+2	(2.30 ± 0.01)E+2	1.9
⋯	10058	32.10	−0.07	48	1.1	(5.64 ± 0.01)E+2	(8.34 ± 0.02)E+2	1.4
⋯	10062	32.20	−0.08	42	1.1	(5.1 ± 0.1)E+1	(7.9 ± 0.2)E+1	1.4
⋯	10063	32.14	−0.08	39	1.8	(3.25 ± 0.02)E+2	(1.177 ± 0.006)E+2	2.2
⋯	10074	32.12	−0.05	40	1.2	(3.03 ± 0.01)E+2	(3.85 ± 0.02)E+2	1.5
⋯	10072	32.20	−0.05	⋯	⋯	(1.13 ± 0.07)E+1	⋯	⋯
31508	10085	32.18	−0.03	84	⋯	(1.0 ± 0.1)E+1	⋯	⋯
⋯	10112	32.22	−0.01	83	1.3	(2.21 ± 0.03)E+2	(6.64 ± 0.08)E+1	2.4
⋯	10126	32.22	+0.01	84	0.3	(1.20 ± 0.02)E+2	(3.00 ± 0.04)E+3	0.5
⋯	10108	32.31	−0.00	⋯	1.1	(9.1 ± 0.2)E+1	(5.3 ± 0.1)E+1	1.9
⋯	10225	32.16	+0.20	⋯	⋯	(4.9 ± 0.2)E+1	⋯	⋯
⋯	10257	32.20	+0.25	⋯	1.0	(1.56 ± 0.02)E+2	(1.20 ± 0.02)E+2	1.7
31567	9391	31.65	−0.26	44	⋯	(2.65 ± 0.02)E+2	⋯	⋯
⋯	9398	31.67	−0.24	45	0.7	(2.15 ± 0.03)E+2	(3.99 ± 0.05)E+2	1.3
⋯	9404	31.59	−0.20	43	1.3	(1.085 ± 0.004)E+3	(3.41 ± 0.01)E+2	2.3
⋯	9408	31.52	−0.18	44	0.3	(1.55 ± 0.02)E+2	(2.55 ± 0.03)E+3	0.6
⋯	9409	31.51	−0.16	47	1.3	(5.85 ± 0.04)E+2	(1.74 ± 0.01)E+2	2.4
⋯	9440	31.68	−0.05	40	1.5	(1.261 ± 0.005)E+3	(2.35 ± 0.01)E+2	2.8
⋯	9442	31.54	−0.04	45	1.2	(5.41 ± 0.04)E+2	(2.12 ± 0.02)E+2	2.2
⋯	9458	31.41	+0.05	45	0.3	(1.52 ± 0.02)E+2	(5.04 ± 0.07)E+3	0.5
⋯	9446	31.45	−0.02	⋯	1.8	(6.89 ± 0.05)E+2	(8.25 ± 0.06)E+1	3.2
31930	8655	30.79	−0.29	49	2.2	(1.319 ± 0.007)E+3	(8.27 ± 0.04)E+1	4.0
⋯	8728	30.86	−0.16	⋯	0.9	(1.024 ± 0.004)E+3	(1.016 ± 0.004)E+3	1.6
32092	8787	30.95	−0.07	34	0.7	(4.66 ± 0.03)E+2	(9.19 ± 0.06)E+2	1.3
⋯	8844	31.04	+0.02	39	1.3	(1.134 ± 0.005)E+3	(3.05 ± 0.01)E+2	2.5
⋯	8884	30.96	+0.08	40	0.4	(1.229 ± 0.003)E+3	(9.45 ± 0.02)E+3	0.8
⋯	8898	30.87	+0.11	40	0.5	(2.307 ± 0.003)E+3	(1.129 ± 0.001)E+4	0.9
⋯	8915	30.83	+0.13	38	1.3	(1.545 ± 0.005)E+3	(4.35 ± 0.01)E+2	2.4
⋯	9415	31.34	−0.15	42	0.4	(1.87 ± 0.02)E+2	(2.18 ± 0.03)E+3	0.7
⋯	9416	31.15	−0.15	42	0.9	(7.76 ± 0.03)E+2	(7.96 ± 0.04)E+2	1.6
⋯	9419	31.31	−0.13	43	1.3	(9.51 ± 0.04)E+2	(2.65 ± 0.01)E+2	2.4
⋯	9422	31.11	−0.12	42	0.9	(3.15 ± 0.03)E+2	(2.80 ± 0.03)E+2	1.7
⋯	9437	31.24	−0.06	46	0.7	(9.75 ± 0.03)E+2	(1.998 ± 0.006)E+3	1.3
⋯	9443	31.23	−0.04	45	0.9	(6.09 ± 0.03)E+2	(5.58 ± 0.03)E+2	1.6

Continuation of Table B2

COHRS catalog #	Hi-GAL catalog #	ℓ (deg)	b (deg)	$v_{\rm LSR}$ (km s^{-1})	$\theta_{\rm R}$ (arcmin)	M (M$_\odot$)	n (cm^{-3})	R (pc)
⋯	9447	31.24	−0.01	44	⋯	(1.35 ± 0.01)E+2	⋯	⋯
⋯	9451	31.13	−0.00	38	1.7	(1.316 ± 0.005)E+3	(1.919 ± 0.007)E+2	3.0
⋯	9456	31.12	+0.02	37	0.8	(7.31 ± 0.03)E+2	(9.99 ± 0.04)E+2	1.4
⋯	9459	31.16	+0.05	39	1.3	(3.038 ± 0.005)E+3	(8.26 ± 0.01)E+2	2.5
⋯	9460	31.07	+0.05	39	0.7	(7.49 ± 0.03)E+2	(1.496 ± 0.006)E+3	1.3
⋯	9463	31.13	+0.06	42	1.1	(9.31 ± 0.03)E+2	(4.63 ± 0.02)E+2	2.0
⋯	8727	30.90	−0.16	⋯	⋯	(4.0 ± 0.2)E+1	⋯	⋯
⋯	8918	30.90	+0.13	⋯	1.5	(4.032 ± 0.005)E+3	(8.52 ± 0.01)E+2	2.7
⋯	9412	31.25	−0.15	⋯	0.6	(4.22 ± 0.03)E+2	(1.012 ± 0.006)E+3	1.2
⋯	9417	31.18	−0.15	⋯	0.8	(9.45 ± 0.03)E+2	(1.011 ± 0.003)E+3	1.6
⋯	9427	31.04	−0.11	⋯	0.7	(1.49 ± 0.02)E+2	(2.92 ± 0.05)E+2	1.3
⋯	9457	31.09	+0.03	⋯	0.7	(2.27 ± 0.03)E+2	(4.34 ± 0.05)E+2	1.3
⋯	9465	31.10	+0.07	⋯	1.3	(1.065 ± 0.004)E+3	(3.07 ± 0.01)E+2	2.4
⋯	9468	31.15	+0.08	⋯	0.8	(3.21 ± 0.03)E+2	(4.89 ± 0.04)E+2	1.4
32180	8932	30.90	+0.16	106	1.5	(4.545 ± 0.006)E+3	(8.33 ± 0.01)E+2	2.8
⋯	8973	30.98	+0.21	108	0.5	(1.084 ± 0.003)E+3	(6.99 ± 0.02)E+3	0.9
⋯	8977	30.95	+0.22	103	⋯	(1.08 ± 0.02)E+2	⋯	⋯
⋯	8991	31.00	+0.23	108	0.8	(1.094 ± 0.003)E+3	(1.367 ± 0.004)E+3	1.5
32327	9410	31.23	−0.16	24	⋯	(2.79 ± 0.02)E+2	⋯	⋯
⋯	9425	31.24	−0.12	21	1.6	(3.327 ± 0.006)E+3	(5.355 ± 0.009)E+2	2.9
32345	9504	31.39	+0.20	18	⋯	(1.86 ± 0.02)E+2	⋯	⋯
⋯	9496	31.36	+0.17	⋯	⋯	(1.17 ± 0.02)E+2	⋯	⋯
⋯	9510	31.32	+0.25	⋯	⋯	(3.5 ± 0.2)E+1	⋯	⋯
32439	9423	31.83	−0.11	40	0.7	(6.87 ± 0.03)E+2	(1.071 ± 0.005)E+3	1.4
⋯	9433	31.81	−0.09	38	1.1	(4.92 ± 0.04)E+2	(2.14 ± 0.02)E+2	2.1
32932	8750	30.87	−0.13	101	0.8	(1.116 ± 0.003)E+3	(1.376 ± 0.004)E+3	1.5
⋯	8760	30.85	−0.11	98	⋯	(8.89 ± 0.02)E+2	⋯	⋯
⋯	8768	30.88	−0.10	101	⋯	(4.36 ± 0.02)E+2	⋯	⋯
⋯	8773	30.78	−0.09	94	⋯	(3.28 ± 0.02)E+2	⋯	⋯
⋯	8778	30.85	−0.08	96	0.6	(2.169 ± 0.003)E+3	(7.56 ± 0.01)E+3	1.0
⋯	8784	30.70	−0.06	89	1.7	(3.8689 ± 0.0006)E+4	(5.4414 ± 0.0009)E+3	3.1
⋯	8791	30.74	−0.06	96	1.4	(2.1812 ± 0.0005)E+4	(5.110 ± 0.001)E+3	2.6
⋯	8792	30.97	−0.05	90	⋯	(2.81 ± 0.02)E+2	⋯	⋯
⋯	8793	30.82	−0.06	96	0.7	(2.2547 ± 0.0004)E+4	(3.7073 ± 0.0007)E+4	1.3
⋯	8810	30.81	−0.03	95	0.7	(7.217 ± 0.003)E+3	(1.4453 ± 0.0006)E+4	1.3
⋯	8814	30.79	−0.03	97	1.0	(9.670 ± 0.004)E+3	(5.697 ± 0.002)E+3	1.9
⋯	8817	30.84	−0.02	92	⋯	(5.08 ± 0.02)E+2	⋯	⋯
⋯	8831	30.75	+0.00	92	0.8	(1.771 ± 0.003)E+3	(2.159 ± 0.004)E+3	1.5
33035	9393	31.10	−0.27	102	0.7	(1.26 ± 0.03)E+2	(2.14 ± 0.05)E+2	1.3
⋯	9405	31.13	−0.20	101	1.6	(1.222 ± 0.005)E+3	(1.998 ± 0.008)E+2	2.9
⋯	9394	31.07	−0.26	⋯	0.8	(2.27 ± 0.03)E+2	(2.46 ± 0.03)E+2	1.5
33079	9462	31.27	+0.07	108	2.1	(1.4111 ± 0.0008)E+4	(1.0341 ± 0.0006)E+3	3.8
⋯	9464	31.33	+0.07	104	1.1	(8.88 ± 0.04)E+2	(4.63 ± 0.02)E+2	2.0
⋯	9474	31.20	+0.09	108	1.2	(9.94 ± 0.04)E+2	(3.50 ± 0.01)E+2	2.3
⋯	9480	31.43	+0.14	⋯	1.3	(3.10 ± 0.04)E+2	(8.5 ± 0.1)E+1	2.4
33232	9483	31.11	+0.13	110	⋯	(1.27 ± 0.02)E+2	⋯	⋯
⋯	9489	31.18	+0.15	109	⋯	(1.52 ± 0.02)E+2	⋯	⋯
⋯	9492	31.13	+0.16	109	1.3	(1.076 ± 0.004)E+3	(3.29 ± 0.01)E+2	2.4
⋯	9500	31.16	+0.18	108	⋯	(1.09 ± 0.02)E+2	⋯	⋯
⋯	9516	31.11	+0.27	97	0.9	(6.78 ± 0.04)E+2	(6.22 ± 0.03)E+2	1.6
⋯	9517	31.15	+0.27	103	1.0	(1.391 ± 0.004)E+3	(8.04 ± 0.02)E+2	1.9
⋯	9519	31.08	+0.28	98	0.6	(2.80 ± 0.03)E+2	(8.39 ± 0.08)E+2	1.1
⋯	9521	31.06	+0.27	⋯	⋯	(3.03 ± 0.03)E+2	⋯	⋯
⋯	9523	31.13	+0.29	⋯	1.7	(7.66 ± 0.05)E+2	(1.119 ± 0.007)E+2	3.0
33263	9392	31.80	−0.28	104	1.7	(1.005 ± 0.005)E+3	(1.368 ± 0.007)E+2	3.1
⋯	9399	31.77	−0.25	105	1.1	(6.79 ± 0.04)E+2	(3.24 ± 0.02)E+2	2.0
⋯	9406	31.70	−0.18	104	2.1	(3.244 ± 0.007)E+3	(2.417 ± 0.005)E+2	3.8
⋯	9407	31.74	−0.19	99	1.1	(8.37 ± 0.04)E+2	(4.56 ± 0.02)E+2	1.9
⋯	9429	31.69	−0.10	104	1.4	(1.078 ± 0.005)E+3	(2.34 ± 0.01)E+2	2.6
⋯	9400	31.74	−0.23	⋯	0.8	(1.87 ± 0.03)E+2	(2.86 ± 0.04)E+2	1.4
33391	9389	31.56	−0.27	99	0.7	(3.20 ± 0.03)E+2	(5.08 ± 0.05)E+2	1.4
⋯	9395	31.40	−0.26	87	1.2	(4.795 ± 0.006)E+3	(1.684 ± 0.002)E+3	2.3
⋯	9396	31.35	−0.27	88	1.4	(4.10 ± 0.05)E+2	(9.0 ± 0.1)E+1	2.6
⋯	9430	31.44	−0.10	90	0.8	(3.57 ± 0.03)E+2	(4.23 ± 0.04)E+2	1.5
⋯	9401	31.44	−0.24	⋯	0.7	(1.16 ± 0.03)E+2	(2.02 ± 0.05)E+2	1.3
⋯	9424	31.46	−0.11	⋯	⋯	(1.31 ± 0.02)E+2	⋯	⋯
33476	9432	31.55	−0.10	86	2.0	(2.394 ± 0.006)E+3	(2.008 ± 0.005)E+2	3.6
⋯	9436	31.60	−0.08	85	1.4	(4.95 ± 0.04)E+2	(1.22 ± 0.01)E+2	2.5
33502	8865	30.88	+0.05	75	1.2	(2.082 ± 0.004)E+3	(8.56 ± 0.02)E+2	2.1
33530	8652	30.95	−0.28	83	1.6	(9.46 ± 0.05)E+2	(1.648 ± 0.009)E+2	2.8
⋯	8670	30.98	−0.25	87	⋯	(6.2 ± 0.2)E+1	⋯	⋯
⋯	9413	31.21	−0.15	78	0.2	(2.89 ± 0.02)E+2	(1.342 ± 0.009)E+4	0.4
⋯	9426	31.20	−0.11	78	1.1	(2.31 ± 0.03)E+2	(1.15 ± 0.02)E+2	2.0
⋯	9454	31.23	+0.02	76	0.5	(5.10 ± 0.02)E+2	(2.81 ± 0.01)E+3	0.9
⋯	9397	31.04	−0.26	⋯	1.6	(7.58 ± 0.05)E+2	(1.167 ± 0.007)E+2	3.0
⋯	9428	31.08	−0.10	⋯	0.8	(2.59 ± 0.03)E+2	(3.55 ± 0.05)E+2	1.4
33772	9385	31.14	−0.29	87	0.9	(2.80 ± 0.03)E+2	(2.29 ± 0.03)E+2	1.7
⋯	9390	31.15	−0.27	90	⋯	(1.21 ± 0.02)E+2	⋯	⋯
33826	8902	30.58	+0.12	95	1.2	(1.195 ± 0.004)E+3	(4.58 ± 0.02)E+2	2.2
⋯	8992	30.62	+0.24	95	1.0	(6.87 ± 0.04)E+2	(4.47 ± 0.03)E+2	1.8
⋯	9006	30.59	+0.26	94	0.7	(1.64 ± 0.03)E+2	(2.75 ± 0.05)E+2	1.3
⋯	9013	30.63	+0.27	94	0.8	(1.66 ± 0.03)E+2	(2.32 ± 0.04)E+2	1.4
34131	8862	30.29	+0.05	108	0.8	(1.857 ± 0.005)E+3	(1.380 ± 0.003)E+3	1.8
34159	8806	30.58	−0.05	42	1.3	(7.722 ± 0.007)E+3	(1.661 ± 0.001)E+3	2.7

Continuation of Table B2

COHRS catalog #	Hi-GAL catalog #	ℓ (deg)	b (deg)	$v_{\rm LSR}$ (km s^{-1})	$\theta_{\rm R}$ (arcmin)	M (M$_\odot$)	n (cm^{-3})	R (pc)
⋯	8812	30.45	−0.03	45	0.9	(1.007 ± 0.005)E+3	(5.81 ± 0.03)E+2	1.9
⋯	8818	30.48	−0.02	44	⋯	(2.37 ± 0.03)E+2	⋯	⋯
⋯	8828	30.38	−0.01	43	0.3	(3.24 ± 0.03)E+2	(7.04 ± 0.06)E+3	0.6
⋯	8841	30.38	+0.02	40	0.8	(5.05 ± 0.04)E+2	(3.56 ± 0.03)E+2	1.8
⋯	8845	30.53	+0.02	48	0.8	(1.978 ± 0.005)E+3	(1.932 ± 0.005)E+3	1.6
⋯	8858	30.35	+0.04	42	1.0	(5.29 ± 0.05)E+2	(2.50 ± 0.02)E+2	2.0
⋯	8875	30.32	+0.07	45	1.5	(3.358 ± 0.007)E+3	(3.927 ± 0.009)E+2	3.3
⋯	8937	30.50	+0.17	39	0.5	(4.13 ± 0.03)E+2	(1.47 ± 0.01)E+3	1.0
⋯	8941	30.21	+0.18	43	1.8	(1.502 ± 0.008)E+3	(1.033 ± 0.006)E+2	3.9
⋯	8965	30.62	+0.21	40	⋯	(1.43 ± 0.03)E+2	⋯	⋯
⋯	8967	30.31	+0.21	46	⋯	(1.02 ± 0.03)E+2	⋯	⋯
⋯	8982	30.18	+0.22	45	1.1	(3.53 ± 0.05)E+2	(1.29 ± 0.02)E+2	2.2
⋯	8779	30.55	−0.09	⋯	0.9	(6.32 ± 0.04)E+2	(3.90 ± 0.03)E+2	1.9
⋯	8866	30.68	+0.06	⋯	1.0	(1.009 ± 0.005)E+3	(4.43 ± 0.02)E+2	2.1
⋯	8903	30.32	+0.12	⋯	2.2	(4.43 ± 0.01)E+3	(1.871 ± 0.004)E+2	4.6
⋯	8908	30.55	+0.12	⋯	1.1	(7.03 ± 0.05)E+2	(2.20 ± 0.02)E+2	2.3
⋯	8921	30.66	+0.14	⋯	⋯	(3.06 ± 0.03)E+2	⋯	⋯
⋯	8953	30.49	+0.19	⋯	0.8	(3.37 ± 0.04)E+2	(2.92 ± 0.03)E+2	1.7
⋯	8960	30.12	+0.20	⋯	1.7	(9.92 ± 0.07)E+2	(8.56 ± 0.06)E+1	3.6
⋯	8978	30.49	+0.22	⋯	1.3	(6.03 ± 0.06)E+2	(1.11 ± 0.01)E+2	2.8
34198	8894	30.37	+0.11	96	1.5	(5.016 ± 0.007)E+3	(5.825 ± 0.009)E+2	3.3
⋯	8832	30.34	+0.00	⋯	⋯	(1.24 ± 0.03)E+2	⋯	⋯
34216	8646	30.31	−0.30	100	2.0	(1.959 ± 0.009)E+3	(1.004 ± 0.005)E+2	4.3
⋯	8657	30.34	−0.28	101	1.3	(7.20 ± 0.06)E+2	(1.50 ± 0.01)E+2	2.7
⋯	8701	30.30	−0.22	104	2.1	(5.285 ± 0.009)E+3	(2.514 ± 0.004)E+2	4.4
⋯	8710	30.22	−0.18	105	1.7	(8.216 ± 0.009)E+3	(7.054 ± 0.008)E+2	3.6
34249	8756	30.35	−0.12	112	1.5	(2.847 ± 0.007)E+3	(3.475 ± 0.008)E+2	3.2
⋯	8796	30.40	−0.05	114	⋯	(1.16 ± 0.03)E+2	⋯	⋯
⋯	8854	30.46	+0.03	106	0.9	(1.405 ± 0.006)E+3	(8.76 ± 0.04)E+2	1.9
34614	7703	29.31	−0.29	96	0.6	(3.18 ± 0.03)E+2	(8.85 ± 0.09)E+2	1.1
⋯	7732	29.39	−0.25	96	⋯	(1.0 ± 0.1)E+1	⋯	⋯
⋯	7750	29.43	−0.22	93	⋯	(3.7 ± 0.2)E+1	⋯	⋯
⋯	7777	29.49	−0.18	105	1.7	(2.349 ± 0.006)E+3	(2.621 ± 0.007)E+2	3.3
⋯	7801	29.50	−0.15	102	0.4	(1.68 ± 0.03)E+2	(1.11 ± 0.02)E+3	0.8
⋯	7818	29.46	−0.11	104	0.8	(2.13 ± 0.03)E+2	(2.70 ± 0.04)E+2	1.5
⋯	7830	29.40	−0.09	106	0.8	(1.484 ± 0.004)E+3	(1.997 ± 0.005)E+3	1.4
⋯	8746	29.37	−0.14	104	1.4	(9.28 ± 0.05)E+2	(1.881 ± 0.009)E+2	2.7
⋯	8759	29.43	−0.12	103	0.5	(1.01 ± 0.03)E+2	(4.0 ± 0.1)E+2	1.0
⋯	8775	29.47	−0.09	98	1.0	(4.36 ± 0.04)E+2	(2.57 ± 0.02)E+2	1.9
⋯	8805	29.42	−0.05	97	1.0	(3.55 ± 0.04)E+2	(2.00 ± 0.02)E+2	1.9
⋯	8748	29.33	−0.13	⋯	0.9	(5.62 ± 0.04)E+2	(4.93 ± 0.03)E+2	1.7
⋯	7696	29.39	−0.30	⋯	0.5	(6.9 ± 0.2)E+1	(3.8 ± 0.1)E+2	0.9
⋯	7843	29.40	−0.06	⋯	1.0	(3.88 ± 0.03)E+2	(2.62 ± 0.02)E+2	1.8
34629	8882	29.48	+0.08	27	1.0	(1.65 ± 0.04)E+2	(9.5 ± 0.2)E+1	1.9
⋯	8901	29.50	+0.11	⋯	0.8	(1.29 ± 0.03)E+2	(1.37 ± 0.03)E+2	1.6
⋯	7803	29.44	−0.14	⋯	0.7	(1.42 ± 0.03)E+2	(2.34 ± 0.05)E+2	1.3
⋯	7945	29.52	+0.09	⋯	0.7	(1.02 ± 0.03)E+2	(1.59 ± 0.04)E+2	1.4
34703	7961	29.58	+0.12	25	0.9	(2.65 ± 0.03)E+2	(2.43 ± 0.03)E+2	1.6
⋯	8981	29.46	+0.22	41	1.0	(3.05 ± 0.05)E+2	(1.64 ± 0.02)E+2	2.0
⋯	8948	29.50	+0.18	⋯	1.1	(5.11 ± 0.04)E+2	(2.49 ± 0.02)E+2	2.0
⋯	8998	29.43	+0.25	⋯	⋯	(3.4 ± 0.2)E+1	⋯	⋯
⋯	8006	29.62	+0.17	⋯	1.0	(1.95 ± 0.04)E+2	(1.01 ± 0.02)E+2	2.0
⋯	8030	29.42	+0.20	⋯	⋯	(9.7 ± 0.2)E+1	⋯	⋯
35524	8877	30.10	+0.08	36	0.6	(2.08 ± 0.01)E+3	(8.87 ± 0.05)E+2	2.1
⋯	8956	29.85	+0.19	38	1.0	(1.11 ± 0.01)E+3	(1.19 ± 0.01)E+2	3.3
⋯	8955	29.99	+0.19	⋯	0.6	(3.20 ± 0.09)E+2	(1.47 ± 0.04)E+2	2.1
⋯	8974	29.87	+0.21	⋯	1.2	(1.15 ± 0.01)E+3	(6.00 ± 0.07)E+1	4.3
⋯	8980	29.96	+0.23	⋯	1.5	(1.11 ± 0.02)E+3	(3.33 ± 0.05)E+1	5.1
⋯	7994	29.85	+0.15	⋯	⋯	(3.01 ± 0.08)E+2	⋯	⋯
35552	7720	29.78	−0.27	100	1.0	(8.64 ± 0.04)E+2	(5.63 ± 0.03)E+2	1.8
⋯	8656	29.82	−0.28	97	⋯	(1.03 ± 0.02)E+2	⋯	⋯
⋯	8665	29.83	−0.26	96	⋯	(8.8 ± 0.2)E+1	⋯	⋯
⋯	8696	29.89	−0.22	103	1.4	(1.536 ± 0.006)E+3	(3.50 ± 0.01)E+2	2.6
⋯	8679	29.91	−0.25	⋯	1.0	(2.40 ± 0.03)E+2	(1.35 ± 0.02)E+2	1.9
35564	7923	28.76	+0.06	36	⋯	(2.05 ± 0.02)E+2	⋯	⋯
⋯	8860	28.81	+0.04	49	0.9	(5.57 ± 0.04)E+2	(4.50 ± 0.03)E+2	1.7
⋯	7899	28.87	+0.02	⋯	⋯	(4.3 ± 0.2)E+1	⋯	⋯
35719	7772	28.77	−0.18	35	0.6	(4.60 ± 0.03)E+2	(1.199 ± 0.007)E+3	1.2
35752	7932	29.74	+0.07	45	0.9	(3.10 ± 0.04)E+2	(1.87 ± 0.02)E+2	1.9
⋯	8886	29.77	+0.09	⋯	1.1	(3.98 ± 0.05)E+2	(1.33 ± 0.02)E+2	2.3
⋯	7960	29.75	+0.11	⋯	0.5	(1.17 ± 0.03)E+2	(4.6 ± 0.1)E+2	1.0
⋯	7972	29.78	+0.13	⋯	⋯	(1.03 ± 0.03)E+2	⋯	⋯
35844	8813	29.53	−0.02	49	2.0	(1.123 ± 0.007)E+3	(8.21 ± 0.05)E+1	3.8
⋯	8807	29.63	−0.04	⋯	⋯	(3.2 ± 0.2)E+1	⋯	⋯
⋯	8850	29.41	+0.04	⋯	2.3	(1.568 ± 0.008)E+3	(7.63 ± 0.04)E+1	4.4
⋯	7841	29.55	−0.08	⋯	1.7	(6.39 ± 0.05)E+2	(7.07 ± 0.06)E+1	3.3
36382	8022	29.80	+0.19	83	1.6	(1.379 ± 0.005)E+3	(1.892 ± 0.007)E+2	3.1
⋯	8062	29.80	+0.26	83	0.8	(1.03 ± 0.03)E+2	(1.15 ± 0.03)E+2	1.5
36544	7785	29.76	−0.17	101	⋯	(3.4 ± 0.2)E+1	⋯	⋯
⋯	7842	29.83	−0.06	100	0.9	(6.16 ± 0.03)E+2	(4.58 ± 0.02)E+2	1.8
⋯	7877	29.71	−0.02	101	1.1	(2.30 ± 0.04)E+2	(9.0 ± 0.1)E+1	2.2
⋯	8739	30.00	−0.15	97	0.8	(7.99 ± 0.04)E+2	(9.45 ± 0.04)E+2	1.5
⋯	8753	30.01	−0.13	99	0.5	(5.25 ± 0.03)E+2	(2.41 ± 0.01)E+3	1.0
⋯	8765	29.84	−0.10	99	0.5	(3.91 ± 0.03)E+2	(2.48 ± 0.02)E+3	0.9

Continuation of Table B2

COHRS catalog #	Hi-GAL catalog #	ℓ (deg)	b (deg)	v_{LSR} (km s^{-1})	θ_R (arcmin)	M (M$_\odot$)	n (cm^{-3})	R (pc)
···	8771	29.82	−0.09	98	···	(3.78 ± 0.03)E+2	···	···
···	8788	29.94	−0.06	99	1.0	(7.648 ± 0.004)E+3	(4.641 ± 0.002)E+3	1.9
···	8798	30.02	−0.05	93	1.2	(4.302 ± 0.005)E+3	(1.534 ± 0.002)E+3	2.2
···	8799	29.97	−0.05	102	1.0	(5.169 ± 0.004)E+3	(3.325 ± 0.003)E+3	1.8
···	8802	29.92	−0.05	100	1.4	(1.1598 ± 0.0006)E+4	(2.360 ± 0.001)E+3	2.7
···	8803	29.86	−0.05	100	0.7	(3.401 ± 0.004)E+3	(5.174 ± 0.006)E+3	1.4
···	8808	29.84	−0.04	100	0.5	(6.19 ± 0.03)E+2	(2.56 ± 0.01)E+3	1.0
···	8821	29.96	−0.02	98	1.0	(1.2487 ± 0.0005)E+4	(7.165 ± 0.003)E+3	1.9
···	8823	29.92	−0.01	96	0.5	(1.641 ± 0.003)E+3	(6.94 ± 0.01)E+3	1.0
···	8834	29.85	+0.00	99	0.5	(5.82 ± 0.03)E+2	(2.30 ± 0.01)E+3	1.0
···	8839	30.02	+0.00	105	···	(1.20 ± 0.02)E+2	···	···
···	8842	29.94	+0.02	98	···	(2.00 ± 0.02)E+2	···	···
···	8853	29.86	+0.03	103	0.7	(1.050 ± 0.004)E+3	(1.678 ± 0.006)E+3	1.4
···	8861	30.10	+0.05	106	0.2	(2.32 ± 0.02)E+2	(1.78 ± 0.02)E+4	0.4
···	8869	30.12	+0.06	106	1.1	(7.52 ± 0.04)E+2	(3.51 ± 0.02)E+2	2.1
···	8889	29.91	+0.09	106	···	(8.4 ± 0.2)E+1	···	···
···	8891	30.06	+0.10	98	1.1	(1.255 ± 0.004)E+3	(5.78 ± 0.02)E+2	2.1
···	8895	30.03	+0.10	106	1.5	(2.828 ± 0.006)E+3	(5.08 ± 0.01)E+2	2.8
···	8833	29.89	−0.01	···	1.0	(2.301 ± 0.005)E+3	(1.321 ± 0.003)E+3	1.9
···	8876	29.94	+0.07	···	0.6	(1.02 ± 0.03)E+2	(2.75 ± 0.07)E+2	1.1
37312	7734	29.46	−0.25	77	1.8	(1.112 ± 0.006)E+3	(1.058 ± 0.005)E+2	3.5
···	8648	29.47	−0.28	78	···	(2.4 ± 0.2)E+1	···	···
···	8651	29.45	−0.29	···	···	(5.0 ± 0.3)E+1	···	···
37387	7990	29.49	+0.15	77	···	(6.5 ± 0.1)E+1	···	···
···	8036	29.60	+0.21	77	0.6	(2.54 ± 0.03)E+2	(8.43 ± 0.09)E+2	1.1
···	8050	29.59	+0.23	78	0.7	(1.93 ± 0.03)E+2	(2.92 ± 0.04)E+2	1.4
···	8063	29.62	+0.25	77	1.2	(9.21 ± 0.05)E+2	(2.84 ± 0.01)E+2	2.4
···	8923	29.41	+0.14	81	1.3	(3.80 ± 0.05)E+2	(1.03 ± 0.01)E+2	2.5
···	8936	29.45	+0.17	80	1.1	(1.43 ± 0.04)E+2	(6.2 ± 0.2)E+1	2.1
···	8947	29.55	+0.18	80	1.8	(1.447 ± 0.007)E+3	(1.586 ± 0.007)E+2	3.3
···	8971	29.18	+0.21	79	0.4	(1.22 ± 0.03)E+2	(8.1 ± 0.2)E+2	0.8
···	8983	29.57	+0.23	79	···	(3.9 ± 0.2)E+1	···	···
···	8892	29.28	+0.10	···	1.0	(6.53 ± 0.04)E+2	(4.44 ± 0.03)E+2	1.8
···	8924	29.34	+0.15	···	1.7	(9.45 ± 0.06)E+2	(1.129 ± 0.007)E+2	3.2
···	8015	29.39	+0.18	···	1.3	(4.24 ± 0.04)E+2	(1.02 ± 0.01)E+2	2.6
37849	7727	28.01	−0.26	100	0.2	(4.5 ± 0.2)E+1	(4.1 ± 0.2)E+3	0.4
···	7748	27.84	−0.22	95	1.6	(1.581 ± 0.005)E+3	(1.818 ± 0.006)E+2	3.3
···	7759	27.97	−0.20	96	0.6	(2.74 ± 0.03)E+2	(7.14 ± 0.08)E+2	1.2
···	7760	27.93	−0.19	96	1.4	(4.01 ± 0.05)E+2	(6.88 ± 0.09)E+1	2.9
···	7763	27.99	−0.20	98	1.1	(3.00 ± 0.04)E+2	(1.27 ± 0.02)E+2	2.1
···	7764	27.90	−0.20	96	0.6	(1.93 ± 0.03)E+2	(4.64 ± 0.07)E+2	1.2
···	7765	27.82	−0.20	90	···	(2.76 ± 0.02)E+2	···	···
···	7773	27.81	−0.18	89	0.8	(5.67 ± 0.04)E+2	(4.69 ± 0.03)E+2	1.7
···	7783	28.13	−0.17	97	1.0	(3.35 ± 0.04)E+2	(1.48 ± 0.02)E+2	2.1
···	7784	27.84	−0.18	95	0.8	(2.60 ± 0.03)E+2	(2.70 ± 0.03)E+2	1.6
···	7817	28.04	−0.13	98	2.1	(3.437 ± 0.008)E+3	(1.881 ± 0.004)E+2	4.2
···	7845	28.04	−0.07	93	1.1	(1.000 ± 0.005)E+3	(3.38 ± 0.02)E+2	2.3
···	7847	28.01	−0.06	94	0.9	(7.56 ± 0.04)E+2	(5.05 ± 0.03)E+2	1.8
···	7853	28.20	−0.05	97	1.2	(1.2686 ± 0.0006)E+4	(3.608 ± 0.002)E+3	2.4
···	7857	27.85	−0.04	99	0.7	(2.26 ± 0.03)E+2	(3.25 ± 0.05)E+2	1.4
···	7874	27.90	−0.02	98	1.3	(3.253 ± 0.006)E+3	(7.13 ± 0.01)E+2	2.6
···	7876	28.32	−0.01	100	0.6	(1.875 ± 0.003)E+3	(3.616 ± 0.007)E+3	1.3
···	7880	28.15	−0.01	99	1.2	(3.114 ± 0.005)E+3	(9.64 ± 0.02)E+2	2.4
···	7881	28.05	−0.00	100	1.0	(7.90 ± 0.04)E+2	(3.68 ± 0.02)E+2	2.1
···	7891	28.24	+0.01	106	1.0	(2.154 ± 0.004)E+3	(9.81 ± 0.02)E+2	2.1
···	7893	28.12	+0.01	98	0.5	(2.14 ± 0.03)E+2	(9.1 ± 0.1)E+2	1.0
···	7897	28.33	+0.02	100	···	(1.46 ± 0.02)E+2	···	···
···	7927	28.24	+0.06	108	1.6	(5.208 ± 0.007)E+3	(6.716 ± 0.009)E+2	3.2
···	7937	28.17	+0.08	101	0.5	(2.20 ± 0.03)E+2	(7.38 ± 0.09)E+2	1.1
···	7716	28.05	−0.26	···	0.9	(2.33 ± 0.04)E+2	(1.64 ± 0.03)E+2	1.8
···	7747	27.92	−0.22	···	···	(9.9 ± 0.2)E+1	···	···
···	7751	27.88	−0.21	···	1.1	(7.85 ± 0.04)E+2	(3.27 ± 0.02)E+2	2.1
···	7908	28.16	+0.03	···	0.8	(3.50 ± 0.04)E+2	(3.94 ± 0.04)E+2	1.5
38663	7887	28.70	+0.01	97	···	(3.3 ± 0.2)E+1	···	···
···	7896	28.60	+0.02	103	1.7	(7.090 ± 0.007)E+3	(7.466 ± 0.007)E+2	3.4
···	7902	29.22	+0.02	96	0.6	(8.56 ± 0.04)E+2	(1.632 ± 0.007)E+3	1.3
···	7903	29.00	+0.03	98	1.3	(1.692 ± 0.005)E+3	(3.400 ± 0.009)E+2	2.7
···	7904	28.65	+0.03	103	1.0	(5.418 ± 0.005)E+3	(2.464 ± 0.002)E+3	2.1
···	7907	28.68	+0.03	97	0.7	(9.84 ± 0.03)E+2	(1.356 ± 0.005)E+3	1.4
···	7918	28.71	+0.05	99	1.2	(1.580 ± 0.005)E+3	(4.06 ± 0.01)E+2	2.5
···	7928	29.19	+0.06	95	0.7	(4.73 ± 0.03)E+2	(7.98 ± 0.05)E+2	1.3
···	7955	28.76	+0.11	97	0.5	(4.88 ± 0.03)E+2	(2.59 ± 0.02)E+3	0.9
···	7975	29.19	+0.12	99	1.2	(8.04 ± 0.05)E+2	(2.19 ± 0.01)E+2	2.5
···	8004	28.78	+0.17	106	1.2	(1.778 ± 0.004)E+3	(5.53 ± 0.01)E+2	2.3
···	8026	28.78	+0.20	106	···	(3.39 ± 0.02)E+2	···	···
···	8028	28.55	+0.20	99	1.2	(6.29 ± 0.05)E+2	(1.83 ± 0.01)E+2	2.4
···	8054	28.77	+0.25	108	2.1	(4.356 ± 0.008)E+3	(2.217 ± 0.004)E+2	4.3
···	8819	28.88	−0.02	101	0.6	(1.267 ± 0.004)E+3	(3.66 ± 0.01)E+3	1.1
···	8820	28.80	−0.01	101	1.3	(1.761 ± 0.006)E+3	(3.96 ± 0.01)E+2	2.6
···	8836	29.23	+0.00	97	···	(1.02 ± 0.02)E+2	···	···
···	8851	29.12	+0.03	98	2.3	(5.587 ± 0.009)E+3	(2.373 ± 0.004)E+2	4.6
···	8888	29.12	+0.09	92	1.5	(2.390 ± 0.007)E+3	(3.66 ± 0.01)E+2	3.0
···	8917	29.28	+0.13	95	2.2	(3.006 ± 0.008)E+3	(1.334 ± 0.004)E+2	4.5
···	8938	28.81	+0.18	105	1.5	(7.688 ± 0.007)E+3	(1.138 ± 0.001)E+3	3.0

Continuation of Table B2

COHRS catalog #	Hi-GAL catalog #	ℓ (deg)	b (deg)	v_{LSR} (km s^{-1})	θ_{R} (arcmin)	M (M$_\odot$)	n (cm^{-3})	R (pc)
···	8976	29.04	+0.21	97	0.9	(3.25 ± 0.04)E+2	(2.01 ± 0.03)E+2	1.9
···	8912	29.15	+0.12	···	0.8	(3.77 ± 0.04)E+2	(3.18 ± 0.03)E+2	1.7
···	7931	28.55	+0.07	···	0.6	(3.72 ± 0.03)E+2	(7.76 ± 0.07)E+2	1.2
···	7862	29.29	−0.03	···	···	(1.4 ± 0.2)E+1	···	···
···	7871	28.71	−0.01	···	···	(6.8 ± 0.2)E+1	···	···
···	7886	29.19	+0.00	···	1.1	(9.37 ± 0.04)E+2	(3.56 ± 0.02)E+2	2.2
···	7912	28.90	+0.04	···	···	(1.9 ± 0.2)E+1	···	···
···	7914	28.56	+0.04	···	1.3	(8.25 ± 0.05)E+2	(1.75 ± 0.01)E+2	2.7
···	7936	29.25	+0.08	···	1.2	(7.44 ± 0.04)E+2	(2.09 ± 0.01)E+2	2.4
···	7995	28.63	+0.16	···	0.3	(2.15 ± 0.03)E+2	(3.45 ± 0.04)E+3	0.6
···	8017	28.59	+0.18	···	0.6	(1.07 ± 0.03)E+2	(2.65 ± 0.07)E+2	1.2
39046	7821	28.08	−0.09	45	1.3	(1.027 ± 0.005)E+3	(2.29 ± 0.01)E+2	2.6
···	7849	28.09	−0.06	45	0.2	(2.55 ± 0.03)E+2	(2.01 ± 0.02)E+4	0.4
···	7860	28.32	−0.04	34	1.4	(3.175 ± 0.005)E+3	(6.28 ± 0.01)E+2	2.7
···	7868	28.60	−0.03	44	1.4	(2.490 ± 0.006)E+3	(4.257 ± 0.009)E+2	2.9
···	7889	28.29	+0.01	47	0.6	(1.110 ± 0.003)E+3	(2.304 ± 0.007)E+3	1.2
···	7996	28.33	+0.16	26	···	(2.98 ± 0.02)E+2	···	···
···	8058	28.30	+0.25	36	1.2	(3.37 ± 0.04)E+2	(8.7 ± 0.1)E+1	2.5
···	7832	28.05	−0.09	···	1.0	(5.93 ± 0.04)E+2	(3.32 ± 0.02)E+2	1.9
···	7762	28.19	−0.20	···	1.5	(1.855 ± 0.006)E+3	(2.816 ± 0.008)E+2	3.0
···	7780	28.24	−0.18	···	1.5	(1.194 ± 0.005)E+3	(1.613 ± 0.007)E+2	3.1
···	7970	28.41	+0.13	···	0.5	(2.61 ± 0.03)E+2	(8.18 ± 0.09)E+2	1.1
···	8060	28.34	+0.25	···	···	(5.4 ± 0.2)E+1	···	···
···	8073	28.27	+0.25	···	0.7	(2.52 ± 0.03)E+2	(3.46 ± 0.04)E+2	1.4
···	8077	28.18	+0.26	···	1.2	(6.61 ± 0.05)E+2	(1.74 ± 0.01)E+2	2.5
39731	7698	28.72	−0.29	88	1.6	(3.610 ± 0.006)E+3	(4.553 ± 0.007)E+2	3.2
···	7706	28.69	−0.28	90	0.7	(2.138 ± 0.004)E+3	(2.640 ± 0.004)E+3	1.5
···	7708	28.54	−0.28	89	1.1	(1.620 ± 0.005)E+3	(5.47 ± 0.02)E+2	2.3
···	7718	28.78	−0.27	90	0.5	(1.78 ± 0.03)E+2	(7.0 ± 0.1)E+2	1.0
···	7724	28.83	−0.25	88	1.1	(7.325 ± 0.006)E+3	(3.111 ± 0.002)E+3	2.1
···	7738	28.57	−0.23	86	2.1	(1.1948 ± 0.0009)E+4	(6.785 ± 0.005)E+2	4.1
···	7743	28.92	−0.23	97	1.4	(1.978 ± 0.006)E+3	(3.300 ± 0.009)E+2	2.9
···	7756	29.09	−0.20	98	0.3	(3.07 ± 0.03)E+2	(8.88 ± 0.09)E+3	0.5
···	7775	28.73	−0.18	102	1.4	(7.73 ± 0.05)E+2	(1.47 ± 0.01)E+2	2.8
···	7778	29.01	−0.18	96	0.9	(1.183 ± 0.004)E+3	(7.61 ± 0.03)E+2	1.8
···	7805	28.88	−0.14	95	1.3	(3.85 ± 0.04)E+2	(8.4 ± 0.1)E+1	2.6
···	7835	28.89	−0.08	89	1.9	(1.092 ± 0.007)E+3	(7.66 ± 0.05)E+1	3.9
···	8642	29.11	−0.29	95	1.7	(2.588 ± 0.008)E+3	(2.780 ± 0.008)E+2	3.3
···	8699	28.84	−0.21	86	1.2	(1.882 ± 0.006)E+3	(5.39 ± 0.02)E+2	2.4
···	8705	28.96	−0.21	96	0.7	(5.37 ± 0.04)E+2	(8.67 ± 0.06)E+2	1.4
···	8689	28.86	−0.23	···	1.3	(2.133 ± 0.005)E+3	(4.41 ± 0.01)E+2	2.7
···	8677	28.75	−0.24	···	···	(3.95 ± 0.04)E+2	···	···
···	7713	29.06	−0.27	···	0.9	(8.5 ± 0.3)E+1	(4.9 ± 0.2)E+1	1.9
···	7721	28.96	−0.26	···	···	(6.7 ± 0.2)E+1	···	···
···	7723	29.01	−0.25	···	···	(8.7 ± 0.3)E+1	···	···
···	7774	28.83	−0.18	···	0.6	(6.8 ± 0.3)E+1	(1.76 ± 0.07)E+2	1.2
···	7776	28.57	−0.18	···	···	(4.1 ± 0.2)E+1	···	···
···	7846	28.67	−0.06	···	···	(4.4 ± 0.2)E+1	···	···
39826	7884	28.82	+0.00	80	0.4	(1.69 ± 0.03)E+2	(1.50 ± 0.03)E+3	0.8
···	7985	28.78	+0.14	86	0.8	(7.21 ± 0.04)E+2	(7.84 ± 0.04)E+2	1.5
···	7992	28.74	+0.15	86	0.7	(3.79 ± 0.03)E+2	(4.47 ± 0.04)E+2	1.5
···	8007	28.69	+0.18	84	···	(3.34 ± 0.02)E+2	···	···
···	8012	28.73	+0.18	83	···	(5.5 ± 0.2)E+1	···	···
···	9010	28.80	+0.27	82	1.7	(7.91 ± 0.06)E+2	(8.35 ± 0.06)E+1	3.4
40422	7709	27.80	−0.28	46	1.0	(2.235 ± 0.005)E+3	(8.53 ± 0.02)E+2	2.2
···	7717	27.75	−0.27	45	0.6	(3.04 ± 0.03)E+2	(5.12 ± 0.05)E+2	1.3
···	7728	27.60	−0.25	37	0.5	(4.8 ± 0.3)E+1	(1.8 ± 0.1)E+2	1.0
···	7766	27.64	−0.20	35	0.7	(1.11 ± 0.04)E+2	(1.49 ± 0.05)E+2	1.4
···	7800	27.59	−0.15	47	0.6	(1.85 ± 0.03)E+2	(3.24 ± 0.06)E+2	1.3
···	7710	27.61	−0.27	···	0.5	(1.09 ± 0.03)E+2	(4.4 ± 0.1)E+2	1.0
40478	7946	27.87	+0.09	105	1.2	(6.73 ± 0.05)E+2	(1.64 ± 0.01)E+2	2.5
···	8059	28.08	+0.24	108	0.6	(1.93 ± 0.04)E+2	(2.86 ± 0.05)E+2	1.4
41092	7978	28.12	+0.13	92	0.5	(1.52 ± 0.03)E+2	(6.5 ± 0.1)E+2	1.0
···	8001	28.16	+0.15	90	2.1	(3.467 ± 0.008)E+3	(1.432 ± 0.003)E+2	4.6
···	8013	28.22	+0.19	88	0.8	(4.11 ± 0.04)E+2	(3.05 ± 0.03)E+2	1.8
···	8034	28.07	+0.21	87	0.5	(2.12 ± 0.03)E+2	(7.6 ± 0.1)E+2	1.0
···	8038	28.10	+0.21	91	···	(4.7 ± 0.2)E+1	···	···
···	8045	28.23	+0.23	88	1.5	(1.511 ± 0.006)E+3	(1.937 ± 0.008)E+2	3.2
···	8053	28.27	+0.23	89	1.1	(4.88 ± 0.05)E+2	(1.51 ± 0.01)E+2	2.4
41160	6760	27.03	−0.16	104	1.1	(9.69 ± 0.05)E+2	(2.70 ± 0.02)E+2	2.4
···	6796	27.06	−0.12	103	1.3	(6.75 ± 0.05)E+2	(1.32 ± 0.01)E+2	2.7
···	6750	27.08	−0.18	···	0.5	(1.20 ± 0.03)E+2	(4.4 ± 0.1)E+2	1.0
···	6787	27.04	−0.13	···	1.0	(6.79 ± 0.05)E+2	(2.67 ± 0.02)E+2	2.2
41990	6688	27.41	−0.30	107	1.8	(1.405 ± 0.008)E+3	(8.81 ± 0.05)E+1	4.0
···	6693	27.50	−0.29	···	···	(6.3 ± 0.2)E+1	···	···
42120	7704	27.84	−0.29	105	0.9	(3.09 ± 0.04)E+2	(1.54 ± 0.02)E+2	2.0
···	7722	27.80	−0.26	104	1.9	(3.647 ± 0.008)E+3	(2.209 ± 0.005)E+2	4.1
···	7741	27.75	−0.24	97	1.1	(9.04 ± 0.05)E+2	(2.45 ± 0.01)E+2	2.5
43140	6805	27.17	−0.12	47	1.3	(1.215 ± 0.006)E+3	(2.08 ± 0.01)E+2	2.9
···	6845	26.99	−0.06	49	···	(1.43 ± 0.03)E+2	···	···
···	6793	27.11	−0.12	···	···	(9.8 ± 0.3)E+1	···	···
···	6817	27.06	−0.10	···	0.7	(1.95 ± 0.03)E+2	(2.18 ± 0.04)E+2	1.5
···	6789	27.13	−0.12	···	0.4	(1.26 ± 0.03)E+2	(9.1 ± 0.2)E+2	0.8
43337	7739	27.87	−0.24	18	1.4	(1.171 ± 0.006)E+3	(1.543 ± 0.008)E+2	3.1

Continuation of Table B2

COHRS catalog #	Hi-GAL catalog #	ℓ (deg)	b (deg)	$v_{\rm LSR}$ (km s^{-1})	$\theta_{\rm R}$ (arcmin)	M (M$_\odot$)	n (cm^{-3})	R (pc)
43455	7885	28.45	−0.00	−13	1.0	(8.62 ± 0.02)E+3	(3.76 ± 0.01)E+2	4.5
···	7879	28.41	−0.02	···	1.7	(1.197 ± 0.003)E+4	(1.043 ± 0.003)E+2	7.7
43988	6987	27.28	+0.15	31	1.5	(9.536 ± 0.008)E+3	(1.182 ± 0.001)E+3	3.2
···	6997	27.35	+0.17	34	1.4	(1.952 ± 0.006)E+3	(2.605 ± 0.008)E+2	3.1
···	7008	27.32	+0.17	34	0.8	(1.760 ± 0.004)E+3	(1.174 ± 0.003)E+3	1.8
···	6959	27.05	+0.11	···	0.5	(1.35 ± 0.03)E+2	(5.2 ± 0.1)E+2	1.0
···	6968	27.17	+0.13	···	0.7	(1.09 ± 0.03)E+2	(1.38 ± 0.04)E+2	1.5
···	6982	27.15	+0.15	···	0.3	(2.44 ± 0.03)E+2	(4.67 ± 0.06)E+3	0.6
···	7000	27.12	+0.16	···	0.9	(7.52 ± 0.05)E+2	(4.22 ± 0.03)E+2	1.9
···	7042	27.24	+0.23	···	1.0	(2.45 ± 0.04)E+2	(9.8 ± 0.2)E+1	2.2
···	7066	27.23	+0.26	···	1.9	(1.003 ± 0.007)E+3	(6.18 ± 0.04)E+1	4.0
44021	7057	27.55	+0.26	40	1.3	(5.85 ± 0.05)E+2	(1.12 ± 0.01)E+2	2.8
···	7083	27.55	+0.29	40	1.2	(7.53 ± 0.06)E+2	(1.54 ± 0.01)E+2	2.7
···	7863	27.92	−0.04	48	0.7	(5.61 ± 0.03)E+2	(7.76 ± 0.05)E+2	1.4
···	7965	27.75	+0.11	51	···	(3.49 ± 0.03)E+2	···	···
···	8035	27.93	+0.20	42	1.4	(4.176 ± 0.007)E+3	(6.13 ± 0.01)E+2	3.0
···	8067	27.79	+0.26	31	0.8	(2.53 ± 0.04)E+2	(1.86 ± 0.03)E+2	1.8
···	7044	27.45	+0.23	···	0.8	(9.2 ± 0.4)E+1	(8.6 ± 0.4)E+1	1.6
···	7949	28.02	+0.09	···	0.7	(2.83 ± 0.04)E+2	(3.74 ± 0.05)E+2	1.5
···	7959	28.07	+0.11	···	1.3	(8.76 ± 0.06)E+2	(1.67 ± 0.01)E+2	2.8
···	8010	27.95	+0.17	···	0.6	(3.83 ± 0.04)E+2	(5.95 ± 0.06)E+2	1.4
···	8020	28.00	+0.19	···	0.5	(2.25 ± 0.03)E+2	(5.50 ± 0.08)E+2	1.2
···	8055	27.84	+0.24	···	0.7	(1.57 ± 0.04)E+2	(1.60 ± 0.04)E+2	1.6
···	8061	27.92	+0.25	···	1.1	(2.82 ± 0.05)E+2	(8.9 ± 0.1)E+1	2.3
···	8070	27.59	+0.26	···	0.6	(2.83 ± 0.04)E+2	(4.49 ± 0.06)E+2	1.4
···	8074	27.85	+0.26	···	···	(2.5 ± 0.2)E+1	···	···
44031	7794	27.66	−0.15	75	2.9	(2.24 ± 0.01)E+3	(3.63 ± 0.02)E+1	6.3
···	7815	27.72	−0.12	76	1.4	(1.088 ± 0.006)E+3	(1.67 ± 0.01)E+2	3.0
···	7758	27.55	−0.21	···	0.8	(1.64 ± 0.04)E+2	(1.46 ± 0.03)E+2	1.7
···	7808	27.57	−0.13	···	0.5	(1.92 ± 0.03)E+2	(4.73 ± 0.07)E+2	1.2
44090	7749	28.25	−0.22	78	···	(7.0 ± 0.2)E+1	···	···
···	7768	28.29	−0.19	75	0.9	(7.16 ± 0.04)E+2	(3.78 ± 0.02)E+2	2.0
···	7790	28.28	−0.15	80	1.7	(5.398 ± 0.008)E+3	(4.590 ± 0.007)E+2	3.6
···	7910	28.43	+0.03	83	0.7	(5.68 ± 0.04)E+2	(6.59 ± 0.04)E+2	1.5
···	7920	28.37	+0.05	78	0.6	(1.806 ± 0.003)E+3	(3.347 ± 0.006)E+3	1.3
···	7926	28.34	+0.06	78	1.6	(5.750 ± 0.007)E+3	(5.467 ± 0.006)E+2	3.5
···	7939	28.40	+0.08	80	1.2	(1.0517 ± 0.0007)E+4	(2.721 ± 0.002)E+3	2.5
···	7963	28.34	+0.11	81	1.0	(2.795 ± 0.005)E+3	(1.073 ± 0.002)E+3	2.2
···	7971	28.37	+0.12	81	0.5	(5.17 ± 0.04)E+2	(1.269 ± 0.009)E+3	1.2
···	7982	28.34	+0.14	80	···	(1.26 ± 0.02)E+2	···	···
···	7925	28.43	+0.06	···	···	(1.11 ± 0.02)E+2	···	···
···	7954	28.46	+0.10	···	0.7	(3.13 ± 0.04)E+2	(4.51 ± 0.05)E+2	1.4
44151	7989	27.80	+0.15	83	0.9	(6.12 ± 0.04)E+2	(3.32 ± 0.02)E+2	2.0
···	8005	27.74	+0.18	78	0.9	(8.92 ± 0.05)E+2	(5.14 ± 0.03)E+2	1.9
44337	7694	28.37	−0.30	48	0.8	(2.15 ± 0.04)E+2	(1.41 ± 0.03)E+2	1.8
···	7705	28.46	−0.28	49	1.8	(1.628 ± 0.007)E+3	(1.149 ± 0.005)E+2	3.9
44587	6749	27.22	−0.18	92	0.4	(1.24 ± 0.03)E+2	(6.5 ± 0.2)E+2	0.9
···	6759	27.24	−0.17	93	1.1	(4.10 ± 0.05)E+2	(1.34 ± 0.02)E+2	2.3
···	6762	27.37	−0.17	91	1.1	(1.2009 ± 0.0008)E+4	(3.985 ± 0.003)E+3	2.3
···	6767	27.30	−0.15	91	0.3	(4.22 ± 0.03)E+2	(5.00 ± 0.04)E+3	0.7
···	6772	27.47	−0.15	89	1.4	(9.26 ± 0.06)E+2	(1.287 ± 0.009)E+2	3.1
···	6777	27.42	−0.14	91	1.1	(3.90 ± 0.05)E+2	(1.04 ± 0.01)E+2	2.5
···	6799	27.50	−0.12	94	0.9	(2.25 ± 0.04)E+2	(1.38 ± 0.02)E+2	1.9
···	6800	27.47	−0.11	95	···	(1.60 ± 0.03)E+2	···	···
···	6840	27.48	−0.06	98	0.7	(4.81 ± 0.04)E+2	(5.83 ± 0.05)E+2	1.5
···	6864	27.55	−0.04	94	···	(2.43 ± 0.03)E+2	···	···
···	6867	27.49	−0.04	98	0.8	(3.70 ± 0.04)E+2	(2.51 ± 0.03)E+2	1.8
···	6873	27.37	−0.02	98	···	(5.1 ± 0.2)E+1	···	···
···	6876	27.53	−0.02	95	1.0	(5.83 ± 0.05)E+2	(2.38 ± 0.02)E+2	2.1
···	6880	27.28	−0.01	94	1.1	(7.84 ± 0.05)E+2	(2.06 ± 0.01)E+2	2.5
···	6887	27.39	+0.01	90	0.5	(1.98 ± 0.03)E+2	(8.4 ± 0.1)E+2	1.0
···	6889	27.07	+0.01	96	1.0	(1.084 ± 0.005)E+3	(4.41 ± 0.02)E+2	2.1
···	6891	27.04	+0.02	102	0.6	(2.45 ± 0.04)E+2	(3.69 ± 0.06)E+2	1.4
···	6896	27.34	+0.02	90	1.9	(3.298 ± 0.009)E+3	(1.784 ± 0.005)E+2	4.2
···	6897	27.11	+0.02	97	1.1	(8.68 ± 0.05)E+2	(2.69 ± 0.02)E+2	2.4
···	6904	27.58	+0.03	88	0.8	(6.64 ± 0.04)E+2	(4.37 ± 0.03)E+2	1.8
···	6931	27.07	+0.07	107	0.5	(2.02 ± 0.03)E+2	(6.7 ± 0.1)E+2	1.1
···	6936	27.51	+0.08	85	···	(2.04 ± 0.03)E+2	···	···
···	6941	27.56	+0.08	84	0.9	(5.512 ± 0.006)E+3	(2.779 ± 0.003)E+3	2.0
···	6947	27.50	+0.09	85	···	(1.47 ± 0.03)E+2	···	···
···	6948	27.35	+0.09	105	···	(7.5 ± 0.3)E+1	···	···
···	6951	27.65	+0.11	100	1.7	(2.313 ± 0.007)E+3	(2.027 ± 0.006)E+2	3.6
···	6954	27.42	+0.09	99	2.2	(4.60 ± 0.01)E+3	(1.772 ± 0.004)E+2	4.7
···	6961	27.25	+0.11	90	0.4	(4.44 ± 0.03)E+2	(2.96 ± 0.02)E+3	0.8
···	6973	27.47	+0.12	100	1.4	(4.899 ± 0.007)E+3	(7.83 ± 0.01)E+2	2.9
···	7882	27.72	−0.00	96	1.4	(1.302 ± 0.006)E+3	(1.95 ± 0.01)E+2	3.0
···	7905	27.61	+0.02	90	1.3	(1.106 ± 0.006)E+3	(2.14 ± 0.01)E+2	2.8
···	7919	27.76	+0.06	100	1.2	(3.138 ± 0.005)E+3	(8.09 ± 0.01)E+2	2.5
···	7924	27.78	+0.06	101	1.0	(3.609 ± 0.005)E+3	(1.274 ± 0.002)E+3	2.3
···	7938	27.63	+0.08	83	1.1	(9.83 ± 0.05)E+2	(3.05 ± 0.02)E+2	2.4
···	7950	27.68	+0.10	101	2.0	(4.785 ± 0.008)E+3	(2.428 ± 0.004)E+2	4.3
···	8003	27.60	+0.17	97	1.1	(2.36 ± 0.05)E+2	(6.6 ± 0.1)E+1	2.4
···	6911	27.40	+0.03	···	1.2	(1.098 ± 0.006)E+3	(2.48 ± 0.01)E+2	2.6
···	6933	27.43	+0.07	···	0.3	(3.65 ± 0.03)E+2	(4.06 ± 0.03)E+3	0.7

Continuation of Table B2

COHRS catalog #	Hi-GAL catalog #	ℓ (deg)	b (deg)	v_{LSR} (km s^{-1})	θ_{R} (arcmin)	M (M$_{\odot}$)	n (cm^{-3})	R (pc)
44699	6877	27.05	−0.02	81	0.5	(3.53 ± 0.04)E+2	(1.04 ± 0.01)E+3	1.1
44901	6775	27.18	−0.15	26	1.1	(8.88 ± 0.05)E+2	(2.45 ± 0.01)E+2	2.4
···	6810	27.22	−0.10	28	1.4	(2.027 ± 0.007)E+3	(2.656 ± 0.009)E+2	3.1
···	6822	27.19	−0.08	26	1.3	(3.516 ± 0.007)E+3	(6.86 ± 0.01)E+2	2.7
···	6743	27.16	−0.18	···	0.8	(2.90 ± 0.04)E+2	(2.31 ± 0.03)E+2	1.7
45016	6811	26.98	−0.10	−15	1.5	(1.586 ± 0.007)E+3	(1.779 ± 0.008)E+2	3.3
···	6797	26.93	−0.12	···	1.4	(1.010 ± 0.006)E+3	(1.329 ± 0.008)E+2	3.1
45022	6754	26.77	−0.17	80	···	(1.52 ± 0.04)E+2	···	···
···	6784	26.86	−0.13	81	0.6	(8.7 ± 0.3)E+1	(1.44 ± 0.06)E+2	1.3
···	6823	26.83	−0.08	80	···	(2.50 ± 0.03)E+2	···	···
···	6829	26.96	−0.08	83	1.3	(2.273 ± 0.006)E+3	(3.247 ± 0.009)E+2	3.0
···	6830	26.86	−0.08	78	1.5	(5.37 ± 0.07)E+2	(5.49 ± 0.07)E+1	3.4
···	6831	26.66	−0.07	61	···	(1.13 ± 0.03)E+2	···	···
···	6851	26.61	−0.05	65	···	(2.48 ± 0.03)E+2	···	···
···	6724	27.00	−0.22	···	0.9	(4.39 ± 0.05)E+2	(2.13 ± 0.02)E+2	2.0
···	6768	26.75	−0.15	···	0.8	(4.62 ± 0.04)E+2	(3.28 ± 0.03)E+2	1.8
45091	6815	26.11	−0.10	25	0.9	(9.40 ± 0.06)E+2	(4.64 ± 0.03)E+2	2.0
···	6853	26.09	−0.06	28	1.7	(3.900 ± 0.009)E+3	(2.784 ± 0.006)E+2	3.8
45156	6728	26.31	−0.21	29	···	(4.6 ± 0.3)E+1	···	···
···	6739	26.25	−0.20	27	0.7	(1.44 ± 0.04)E+2	(1.72 ± 0.05)E+2	1.5
···	6769	26.57	−0.16	26	0.8	(2.45 ± 0.04)E+2	(1.53 ± 0.03)E+2	1.9
···	6814	26.58	−0.10	35	0.2	(5.35 ± 0.04)E+2	(1.36 ± 0.01)E+4	0.5
···	6827	26.55	−0.09	33	0.5	(1.00 ± 0.03)E+2	(3.3 ± 0.1)E+2	1.1
···	6869	26.44	−0.03	29	0.5	(1.27 ± 0.04)E+2	(4.2 ± 0.1)E+2	1.1
···	6872	26.59	−0.05	24	2.5	(6.32 ± 0.01)E+3	(1.325 ± 0.003)E+2	5.8
···	6900	26.88	+0.03	25	0.7	(2.20 ± 0.04)E+2	(1.97 ± 0.04)E+2	1.7
···	6922	26.59	+0.05	28	1.6	(2.451 ± 0.008)E+3	(2.014 ± 0.006)E+2	3.7
···	6940	26.58	+0.07	29	1.1	(2.142 ± 0.005)E+3	(5.58 ± 0.01)E+2	2.5
···	6943	26.70	+0.09	25	···	(8.6 ± 0.3)E+1	···	···
···	6949	26.58	+0.09	26	1.2	(2.112 ± 0.006)E+3	(4.65 ± 0.01)E+2	2.6
···	7006	26.71	+0.17	32	1.3	(1.434 ± 0.007)E+3	(2.34 ± 0.01)E+2	2.9
···	6991	26.66	+0.15	···	···	(5.5 ± 0.3)E+1	···	···
···	6727	26.58	−0.21	···	···	(1.78 ± 0.03)E+2	···	···
···	6746	26.43	−0.19	···	1.2	(5.79 ± 0.06)E+2	(1.24 ± 0.01)E+2	2.7
···	6886	26.53	+0.01	···	···	(9.5 ± 0.3)E+1	···	···
···	7014	26.77	+0.18	···	···	(3.9 ± 0.3)E+1	···	···
···	7030	26.78	+0.21	···	0.5	(3.57 ± 0.04)E+2	(8.9 ± 0.1)E+2	1.2
···	7062	26.54	+0.26	···	···	(1.63 ± 0.03)E+2	···	···
···	6738	26.27	−0.19	···	···	(6.2 ± 0.2)E+1	···	···
···	6785	26.55	−0.13	···	1.1	(4.95 ± 0.06)E+2	(1.24 ± 0.01)E+2	2.5
45225	6773	26.82	−0.15	96	···	(1.07 ± 0.03)E+2	···	···
···	6809	26.78	−0.11	98	1.9	(2.184 ± 0.009)E+3	(1.058 ± 0.005)E+2	4.4
···	6812	26.71	−0.09	99	1.2	(7.78 ± 0.06)E+2	(1.61 ± 0.01)E+2	2.7
···	6846	26.80	−0.07	98	2.3	(2.45 ± 0.01)E+3	(7.10 ± 0.03)E+1	5.2
···	6858	26.74	−0.04	107	0.6	(4.97 ± 0.05)E+2	(6.24 ± 0.06)E+2	1.5
···	6866	26.66	−0.04	103	0.3	(1.55 ± 0.04)E+2	(2.76 ± 0.06)E+3	0.6
···	6874	26.76	−0.02	106	1.3	(1.249 ± 0.007)E+3	(1.80 ± 0.01)E+2	3.0
···	6892	26.74	+0.02	99	···	(6.9 ± 0.3)E+1	···	···
···	6898	26.78	+0.03	99	···	(4.6 ± 0.2)E+1	···	···
···	6906	26.69	+0.04	96	0.7	(1.171 ± 0.005)E+3	(1.136 ± 0.005)E+3	1.6
···	6907	26.55	+0.04	94	···	(5.78 ± 0.03)E+2	···	···
···	6969	26.55	+0.12	96	1.6	(1.728 ± 0.007)E+3	(1.525 ± 0.006)E+2	3.6
···	6790	26.70	−0.12	···	1.3	(1.455 ± 0.006)E+3	(2.42 ± 0.01)E+2	2.9
···	6807	26.54	−0.11	···	0.4	(9.1 ± 0.3)E+1	(5.1 ± 0.2)E+2	0.9
···	6971	26.51	+0.13	···	1.0	(5.53 ± 0.05)E+2	(2.00 ± 0.02)E+2	2.2
45264	6718	26.02	−0.25	111	1.6	(1.013 ± 0.006)E+3	(1.369 ± 0.008)E+2	3.1
···	6752	26.03	−0.18	115	0.8	(1.76 ± 0.03)E+2	(2.05 ± 0.04)E+2	1.5
···	6721	25.99	−0.23	···	···	(1.6 ± 0.2)E+1	···	···
···	6702	26.14	−0.28	···	1.0	(4.05 ± 0.04)E+2	(2.06 ± 0.02)E+2	2.0
···	6736	26.01	−0.20	···	1.3	(3.87 ± 0.05)E+2	(9.8 ± 0.1)E+1	2.5
45483	6962	25.86	+0.11	100	2.2	(2.333 ± 0.008)E+3	(1.190 ± 0.004)E+2	4.3
···	7011	25.70	+0.18	103	1.5	(1.244 ± 0.005)E+3	(1.861 ± 0.007)E+2	3.0
···	7031	25.73	+0.21	110	1.6	(5.016 ± 0.006)E+3	(6.877 ± 0.008)E+2	3.1
···	7036	25.61	+0.23	113	1.7	(3.606 ± 0.007)E+3	(3.881 ± 0.007)E+2	3.3
···	7046	25.87	+0.24	107	0.5	(7.0 ± 0.3)E+1	(2.30 ± 0.09)E+2	1.1
···	7049	25.81	+0.26	110	2.1	(6.895 ± 0.007)E+3	(3.812 ± 0.004)E+2	4.2
···	7050	25.74	+0.25	109	1.6	(3.587 ± 0.006)E+3	(4.649 ± 0.007)E+2	3.1
···	7068	25.76	+0.27	112	0.8	(7.72 ± 0.04)E+2	(7.90 ± 0.04)E+2	1.6
···	6984	26.01	+0.14	···	0.8	(6.7 ± 0.3)E+1	(7.1 ± 0.3)E+1	1.6
···	7073	25.49	+0.28	···	0.5	(5.5 ± 0.3)E+1	(2.5 ± 0.1)E+2	1.0
···	7082	25.65	+0.29	···	···	(5.7 ± 0.2)E+1	···	···
45506	6683	26.48	−0.30	107	0.3	(2.69 ± 0.02)E+2	(5.99 ± 0.05)E+3	0.6
···	6695	26.68	−0.29	109	1.1	(3.46 ± 0.04)E+2	(1.29 ± 0.02)E+2	2.2
···	6696	26.51	−0.29	107	1.1	(1.561 ± 0.004)E+3	(5.73 ± 0.02)E+2	2.2
···	6697	26.54	−0.29	108	0.7	(2.090 ± 0.004)E+3	(2.994 ± 0.005)E+3	1.4
···	6706	26.53	−0.27	106	0.7	(1.020 ± 0.003)E+3	(1.823 ± 0.006)E+3	1.3
···	6709	26.64	−0.27	109	1.8	(1.599 ± 0.006)E+3	(1.470 ± 0.006)E+2	3.5
···	6725	26.60	−0.22	108	0.3	(8.01 ± 0.03)E+2	(1.018 ± 0.004)E+4	0.7
45622	6978	26.37	+0.15	108	1.3	(3.37 ± 0.04)E+2	(8.8 ± 0.1)E+1	2.5
···	6979	26.33	+0.14	112	1.1	(3.353 ± 0.005)E+3	(1.194 ± 0.002)E+3	2.2
···	7015	26.45	+0.18	100	1.4	(1.253 ± 0.006)E+3	(2.65 ± 0.01)E+2	2.7
···	7032	26.40	+0.22	108	0.3	(1.41 ± 0.02)E+2	(3.66 ± 0.06)E+3	0.5
···	7053	26.38	+0.25	105	0.8	(4.84 ± 0.04)E+2	(4.46 ± 0.03)E+2	1.6
···	6952	26.37	+0.10	···	0.9	(2.30 ± 0.03)E+2	(1.90 ± 0.03)E+2	1.7

Continuation of Table B2

COHRS catalog #	Hi-GAL catalog #	ℓ (deg)	b (deg)	$v_{\rm LSR}$ (km s^{-1})	$\theta_{\rm R}$ (arcmin)	M (M$_{\odot}$)	n (cm^{-3})	R (pc)
···	7043	26.53	+0.24	···	···	(4.5 ± 0.2)E+1	···	···
45919	6729	26.34	−0.21	113	1.0	(1.73 ± 0.04)E+2	(1.01 ± 0.02)E+2	1.9
···	6744	26.37	−0.18	112	···	(5.6 ± 0.2)E+1	···	···
···	6855	26.28	−0.05	114	1.3	(1.624 ± 0.005)E+3	(4.05 ± 0.01)E+2	2.5
···	6870	26.33	−0.04	113	0.9	(9.74 ± 0.04)E+2	(7.66 ± 0.03)E+2	1.7
···	6820	26.35	−0.09	···	0.9	(1.93 ± 0.03)E+2	(1.56 ± 0.02)E+2	1.7
···	6824	26.37	−0.08	···	0.6	(1.17 ± 0.03)E+2	(3.10 ± 0.08)E+2	1.1
45974	7086	26.23	+0.29	71	0.6	(1.68 ± 0.03)E+2	(3.24 ± 0.05)E+2	1.3
···	7001	26.11	+0.17	···	0.8	(2.48 ± 0.04)E+2	(2.33 ± 0.04)E+2	1.6
···	7025	26.31	+0.21	···	1.1	(3.17 ± 0.04)E+2	(1.28 ± 0.02)E+2	2.2
46051	6753	25.83	−0.18	93	1.2	(7.548 ± 0.007)E+3	(2.179 ± 0.002)E+3	2.4
···	6758	25.72	−0.16	94	···	(6.14 ± 0.04)E+2	···	···
···	6763	25.89	−0.17	93	···	(4.84 ± 0.03)E+2	···	···
···	6764	25.66	−0.16	92	1.4	(2.350 ± 0.005)E+3	(4.57 ± 0.01)E+2	2.7
···	6766	25.80	−0.16	95	0.7	(2.477 ± 0.004)E+3	(3.573 ± 0.006)E+3	1.4
···	6771	25.69	−0.15	94	0.9	(8.33 ± 0.04)E+2	(6.63 ± 0.03)E+2	1.7
···	6778	25.92	−0.14	108	···	(3.55 ± 0.03)E+2	···	···
···	6779	25.39	−0.14	94	1.3	(1.4055 ± 0.0006)E+4	(3.561 ± 0.002)E+3	2.5
···	6782	25.62	−0.14	94	0.6	(1.053 ± 0.003)E+3	(2.624 ± 0.007)E+3	1.2
···	6795	25.67	−0.12	92	0.9	(1.361 ± 0.004)E+3	(8.81 ± 0.03)E+2	1.8
···	6798	25.98	−0.12	107	···	(1.66 ± 0.02)E+2	···	···
···	6801	25.64	−0.12	94	1.5	(2.512 ± 0.005)E+3	(4.034 ± 0.008)E+2	2.9
···	6802	25.54	−0.12	95	0.8	(2.01 ± 0.04)E+2	(1.80 ± 0.03)E+2	1.7
···	6803	25.94	−0.11	98	0.7	(1.81 ± 0.03)E+2	(2.64 ± 0.05)E+2	1.4
···	6816	25.57	−0.10	95	···	(1.21 ± 0.02)E+2	···	···
···	6819	25.55	−0.09	94	0.2	(1.18 ± 0.03)E+2	(6.3 ± 0.1)E+3	0.4
···	6821	25.63	−0.09	94	0.5	(1.97 ± 0.03)E+2	(7.8 ± 0.1)E+2	1.0
···	6838	25.60	−0.07	95	···	(1.33 ± 0.03)E+2	···	···
···	6842	25.62	−0.07	95	0.4	(1.94 ± 0.03)E+2	(1.85 ± 0.03)E+3	0.7
···	6861	25.63	−0.04	96	···	(6.8 ± 0.2)E+1	···	···
···	6863	25.61	−0.04	95	···	(7.5 ± 0.3)E+1	···	···
···	6899	25.62	+0.02	89	1.3	(1.361 ± 0.005)E+3	(3.32 ± 0.01)E+2	2.5
···	6707	25.60	−0.26	···	0.5	(1.45 ± 0.03)E+2	(4.57 ± 0.09)E+2	1.1
···	6719	25.92	−0.23	···	0.3	(9.9 ± 0.3)E+1	(2.37 ± 0.06)E+3	0.6
···	6781	25.89	−0.15	···	0.6	(2.91 ± 0.03)E+2	(6.00 ± 0.06)E+2	1.3
46449	6794	26.07	−0.12	104	1.1	(6.06 ± 0.04)E+2	(2.50 ± 0.02)E+2	2.1
···	6825	26.27	−0.08	99	1.6	(2.142 ± 0.006)E+3	(2.528 ± 0.007)E+2	3.2
···	6832	26.32	−0.07	100	1.2	(1.705 ± 0.005)E+3	(4.62 ± 0.01)E+2	2.5
···	6834	26.16	−0.07	105	0.5	(3.66 ± 0.03)E+2	(1.61 ± 0.01)E+3	1.0
···	6852	26.14	−0.06	104	1.4	(2.209 ± 0.005)E+3	(4.12 ± 0.01)E+2	2.8
···	6875	26.30	−0.03	104	0.9	(5.59 ± 0.04)E+2	(4.22 ± 0.03)E+2	1.7
···	6878	26.08	−0.01	104	2.0	(1.683 ± 0.007)E+3	(1.068 ± 0.004)E+2	4.0
···	6883	26.32	−0.00	104	···	(6.6 ± 0.2)E+1	···	···
···	6884	26.27	+0.00	111	1.4	(6.62 ± 0.05)E+2	(1.28 ± 0.01)E+2	2.8
···	6893	26.19	+0.03	103	1.7	(1.678 ± 0.006)E+3	(1.721 ± 0.006)E+2	3.4
···	6917	26.09	+0.04	102	1.0	(3.60 ± 0.04)E+2	(2.00 ± 0.02)E+2	1.9
···	6950	26.15	+0.10	101	···	(1.96 ± 0.03)E+2	···	···
···	6955	26.24	+0.10	97	0.7	(7.72 ± 0.04)E+2	(1.364 ± 0.007)E+3	1.3
···	6980	26.17	+0.14	113	1.1	(2.361 ± 0.005)E+3	(9.49 ± 0.02)E+2	2.2
···	6983	26.29	+0.14	113	0.8	(1.369 ± 0.004)E+3	(1.255 ± 0.004)E+3	1.6
···	6995	26.16	+0.16	112	1.1	(1.642 ± 0.005)E+3	(6.73 ± 0.02)E+2	2.1
···	6999	26.23	+0.15	114	1.1	(4.46 ± 0.04)E+2	(1.54 ± 0.01)E+2	2.3
···	6871	26.25	−0.04	···	0.9	(3.35 ± 0.04)E+2	(2.68 ± 0.03)E+2	1.7
···	6974	26.25	+0.13	···	0.4	(2.51 ± 0.03)E+2	(1.44 ± 0.02)E+3	0.9
···	7016	26.20	+0.19	···	···	(9.7 ± 0.3)E+1	···	···
47282	6722	25.54	−0.23	116	1.1	(1.643 ± 0.005)E+3	(6.40 ± 0.02)E+2	2.2
···	6731	25.46	−0.21	120	0.6	(2.860 ± 0.004)E+3	(5.445 ± 0.007)E+3	1.3
···	6735	25.56	−0.21	117	0.6	(1.97 ± 0.03)E+2	(4.12 ± 0.06)E+2	1.2
···	6741	25.62	−0.20	121	1.6	(1.874 ± 0.006)E+3	(2.468 ± 0.008)E+2	3.1
···	6761	25.64	−0.17	···	1.0	(1.493 ± 0.004)E+3	(7.95 ± 0.02)E+2	2.0
47343	5938	25.39	+0.04	−13	1.3	(1.800 ± 0.003)E+4	(3.886 ± 0.007)E+2	5.7
47571	6937	25.80	+0.07	30	···	(4.06 ± 0.02)E+2	···	···
···	6990	25.63	+0.15	31	···	(1.38 ± 0.03)E+2	···	···
···	7041	25.55	+0.23	31	1.8	(1.887 ± 0.007)E+3	(1.780 ± 0.006)E+2	3.5
···	6923	25.59	+0.06	···	1.0	(4.54 ± 0.04)E+2	(2.69 ± 0.03)E+2	1.9
···	6885	25.59	−0.00	···	1.0	(1.48 ± 0.04)E+2	(8.2 ± 0.2)E+1	1.9
···	6903	25.57	+0.03	···	0.2	(1.59 ± 0.03)E+2	(5.6 ± 0.1)E+3	0.5
47799	5735	25.16	−0.28	64	1.7	(7.113 ± 0.009)E+3	(7.41 ± 0.01)E+2	3.4
···	5746	25.19	−0.26	64	1.0	(6.16 ± 0.05)E+2	(3.44 ± 0.03)E+2	1.9
···	5763	25.24	−0.22	63	0.9	(8.85 ± 0.05)E+2	(6.39 ± 0.04)E+2	1.8
···	5780	25.34	−0.20	62	1.4	(6.263 ± 0.008)E+3	(1.147 ± 0.001)E+3	2.8
···	5793	25.41	−0.18	64	1.0	(3.228 ± 0.005)E+3	(1.747 ± 0.003)E+3	2.0
···	6714	25.40	−0.26	63	···	(2.41 ± 0.02)E+2	···	···
···	6748	25.38	−0.18	64	0.8	(4.725 ± 0.004)E+3	(4.250 ± 0.004)E+3	1.6
···	6909	25.68	+0.03	52	1.4	(2.577 ± 0.005)E+3	(5.011 ± 0.009)E+2	2.7
···	6836	25.57	−0.07	···	···	(2.7 ± 0.2)E+1	···	···
···	5800	25.25	−0.16	···	···	(1.27 ± 0.03)E+2	···	···
···	5812	25.22	−0.15	···	0.3	(5.2 ± 0.3)E+1	(1.09 ± 0.06)E+3	0.6
···	6685	25.38	−0.30	···	···	(1.87 ± 0.03)E+2	···	···
···	6691	25.44	−0.30	···	···	(4.6 ± 0.2)E+1	···	···
···	6723	25.48	−0.23	···	···	(6.5 ± 0.2)E+1	···	···
···	6839	25.50	−0.07	···	0.6	(2.17 ± 0.03)E+2	(4.14 ± 0.06)E+2	1.3
47871	7070	25.93	+0.27	71	0.7	(2.24 ± 0.03)E+2	(2.91 ± 0.04)E+2	1.5
···	7040	25.91	+0.23	···	···	(7.1 ± 0.2)E+1	···	···

Continuation of Table B2

COHRS catalog #	Hi-GAL catalog #	ℓ (deg)	b (deg)	v_{LSR} (km s^{-1})	θ_{R} (arcmin)	M (M$_\odot$)	n (cm^{-3})	R (pc)
47974	6908	26.36	+0.04	57	1.0	(6.68 ± 0.04)E+2	(3.19 ± 0.02)E+2	2.0
…	6916	26.31	+0.05	55	0.9	(1.711 ± 0.004)E+3	(1.042 ± 0.003)E+3	1.9
…	7023	26.40	+0.20	…	0.5	(1.35 ± 0.03)E+2	(4.6 ± 0.1)E+2	1.1
…	7024	26.33	+0.20	…	1.4	(4.51 ± 0.05)E+2	(8.80 ± 0.09)E+1	2.7
48215	6080	25.39	+0.24	40	0.8	(3.41 ± 0.04)E+2	(3.48 ± 0.04)E+2	1.6
…	6084	25.35	+0.24	41	1.3	(1.779 ± 0.006)E+3	(4.69 ± 0.02)E+2	2.5
…	6116	25.32	+0.28	41	1.6	(1.859 ± 0.007)E+3	(2.343 ± 0.009)E+2	3.2
…	6996	25.46	+0.16	42	1.3	(4.95 ± 0.05)E+2	(1.10 ± 0.01)E+2	2.6
48361	5964	25.16	+0.06	46	0.9	(1.515 ± 0.005)E+3	(1.055 ± 0.004)E+3	1.8
…	5982	25.16	+0.10	45	1.2	(1.792 ± 0.006)E+3	(5.82 ± 0.02)E+2	2.3
…	6018	25.28	+0.14	56	1.6	(4.38 ± 0.06)E+2	(5.80 ± 0.08)E+1	3.1
…	5969	25.31	+0.08	…	…	(3.7 ± 0.2)E+1	…	…
…	5990	25.23	+0.11	…	…	(1.89 ± 0.03)E+2	…	…
…	6015	25.32	+0.13	…	1.1	(2.69 ± 0.05)E+2	(9.2 ± 0.2)E+1	2.3
48386	5738	24.33	−0.27	54	1.5	(4.85 ± 0.06)E+2	(7.9 ± 0.1)E+1	2.9
…	5756	24.44	−0.23	57	1.2	(6.782 ± 0.007)E+3	(2.082 ± 0.002)E+3	2.4
…	5771	24.37	−0.21	54	1.7	(1.477 ± 0.006)E+3	(1.739 ± 0.008)E+2	3.2
…	5782	24.40	−0.19	59	0.6	(1.454 ± 0.004)E+3	(4.39 ± 0.01)E+3	1.1
…	5785	25.04	−0.18	46	1.2	(7.22 ± 0.06)E+2	(2.02 ± 0.02)E+2	2.4
…	5786	25.01	−0.18	46	0.9	(8.10 ± 0.04)E+2	(7.00 ± 0.04)E+2	1.7
…	5787	24.53	−0.18	42	…	(2.22 ± 0.03)E+2	…	…
…	5801	24.98	−0.17	45	1.3	(1.023 ± 0.006)E+3	(2.40 ± 0.01)E+2	2.6
…	5803	24.93	−0.16	47	0.9	(1.380 ± 0.005)E+3	(9.11 ± 0.03)E+2	1.8
…	5805	24.36	−0.16	56	1.4	(2.058 ± 0.006)E+3	(4.51 ± 0.01)E+2	2.6
…	5814	25.05	−0.14	50	1.1	(2.88 ± 0.05)E+2	(1.03 ± 0.02)E+2	2.2
…	5822	24.91	−0.14	48	1.0	(1.208 ± 0.005)E+3	(7.44 ± 0.03)E+2	1.9
…	5832	24.32	−0.13	53	1.1	(1.237 ± 0.006)E+3	(4.61 ± 0.02)E+2	2.2
…	5847	24.86	−0.12	50	1.2	(9.58 ± 0.05)E+2	(2.74 ± 0.02)E+2	2.4
…	5855	24.81	−0.10	49	1.6	(1.592 ± 0.007)E+3	(2.021 ± 0.008)E+2	3.2
…	5862	24.65	−0.08	50	0.6	(5.58 ± 0.04)E+2	(1.55 ± 0.01)E+3	1.1
…	5863	24.29	−0.08	55	1.2	(3.49 ± 0.05)E+2	(1.13 ± 0.02)E+2	2.3
…	5866	24.58	−0.07	52	…	(2.14 ± 0.03)E+2	…	…
…	5868	24.16	−0.07	54	0.4	(2.54 ± 0.03)E+2	(1.86 ± 0.02)E+3	0.8
…	5895	24.19	−0.04	53	0.7	(2.85 ± 0.04)E+2	(4.76 ± 0.06)E+2	1.3
…	5923	24.91	+0.01	44	0.4	(2.55 ± 0.03)E+2	(1.85 ± 0.02)E+3	0.8
…	5937	24.05	+0.02	59	1.3	(1.060 ± 0.006)E+3	(2.52 ± 0.01)E+2	2.6
…	5968	23.86	+0.08	54	0.6	(3.54 ± 0.03)E+2	(9.02 ± 0.08)E+2	1.2
…	5970	24.94	+0.08	41	…	(1.058 ± 0.002)E+3	…	…
…	5978	24.92	+0.08	43	1.0	(4.295 ± 0.007)E+3	(2.341 ± 0.004)E+3	1.9
…	5983	24.96	+0.09	42	0.7	(3.43 ± 0.04)E+2	(6.34 ± 0.07)E+2	1.3
…	5999	24.63	+0.10	40	1.1	(3.88 ± 0.05)E+2	(1.41 ± 0.02)E+2	2.2
…	6064	24.55	+0.21	39	…	(1.19 ± 0.03)E+2	…	…
…	6102	24.91	+0.27	45	1.3	(5.06 ± 0.06)E+2	(1.22 ± 0.01)E+2	2.6
…	5799	24.25	−0.17	…	…	(9.6 ± 0.2)E+1	…	…
…	5806	24.18	−0.16	…	0.9	(3.87 ± 0.04)E+2	(2.82 ± 0.03)E+2	1.8
…	5858	24.07	−0.09	…	0.5	(1.17 ± 0.03)E+2	(5.3 ± 0.1)E+2	1.0
…	5884	24.58	−0.05	…	0.6	(1.37 ± 0.03)E+2	(3.51 ± 0.09)E+2	1.2
…	5888	24.70	−0.04	…	…	(5.0 ± 0.2)E+1	…	…
…	5894	24.95	−0.05	…	1.4	(1.418 ± 0.007)E+3	(2.68 ± 0.01)E+2	2.8
…	5909	24.67	−0.01	…	…	(1.13 ± 0.02)E+2	…	…
…	5933	24.66	+0.02	…	0.7	(3.36 ± 0.04)E+2	(5.10 ± 0.06)E+2	1.4
…	6050	24.81	+0.19	…	0.5	(1.08 ± 0.03)E+2	(4.4 ± 0.1)E+2	1.0
…	5749	24.95	−0.25	…	0.8	(2.22 ± 0.04)E+2	(2.53 ± 0.05)E+2	1.5
48393	5951	25.37	+0.06	110	1.2	(9.74 ± 0.05)E+2	(2.83 ± 0.02)E+2	2.4
…	6005	25.19	+0.12	105	0.8	(7.47 ± 0.05)E+2	(8.11 ± 0.05)E+2	1.5
…	6019	25.18	+0.14	104	1.1	(1.392 ± 0.006)E+3	(5.10 ± 0.02)E+2	2.2
…	6022	25.24	+0.15	108	0.5	(2.91 ± 0.04)E+2	(1.21 ± 0.02)E+3	1.0
…	6042	25.15	+0.17	97	1.0	(1.266 ± 0.005)E+3	(7.12 ± 0.03)E+2	1.9
…	6049	25.18	+0.19	99	0.5	(3.62 ± 0.03)E+2	(1.61 ± 0.01)E+3	1.0
…	6063	25.18	+0.22	99	1.3	(1.506 ± 0.006)E+3	(3.98 ± 0.02)E+2	2.5
…	6069	25.10	+0.22	103	1.0	(3.34 ± 0.05)E+2	(1.96 ± 0.03)E+2	1.9
…	6075	25.14	+0.23	103	1.3	(1.194 ± 0.006)E+3	(2.79 ± 0.01)E+2	2.6
…	6960	25.41	+0.11	96	0.9	(1.472 ± 0.005)E+3	(1.125 ± 0.003)E+3	1.7
…	6966	25.49	+0.12	97	0.7	(1.96 ± 0.03)E+2	(3.33 ± 0.06)E+2	1.3
…	6981	25.51	+0.14	108	…	(2.10 ± 0.02)E+2	…	…
…	7020	25.51	+0.20	98	…	(1.06 ± 0.02)E+2	…	…
…	6006	25.09	+0.12	…	0.8	(8.4 ± 0.3)E+1	(9.5 ± 0.4)E+1	1.5
48404	5854	25.10	−0.10	90	1.5	(7.67 ± 0.06)E+2	(1.23 ± 0.01)E+2	2.9
…	5881	25.13	−0.06	97	0.8	(2.49 ± 0.04)E+2	(2.86 ± 0.05)E+2	1.5
…	5893	25.10	−0.05	105	1.3	(4.87 ± 0.05)E+2	(1.20 ± 0.01)E+2	2.5
…	5903	25.13	−0.02	97	1.1	(2.63 ± 0.05)E+2	(1.20 ± 0.02)E+2	2.1
…	5906	25.06	−0.01	102	0.5	(1.37 ± 0.04)E+2	(6.6 ± 0.2)E+2	0.9
…	5916	25.02	+0.00	105	0.8	(4.26 ± 0.04)E+2	(4.97 ± 0.05)E+2	1.5
…	5944	25.08	+0.03	105	1.1	(7.16 ± 0.05)E+2	(2.82 ± 0.02)E+2	2.2
…	5852	25.14	−0.09	…	1.0	(2.35 ± 0.04)E+2	(1.39 ± 0.02)E+2	1.9
48409	5860	24.76	−0.09	111	0.8	(5.74 ± 0.04)E+2	(5.40 ± 0.04)E+2	1.6
…	5899	24.87	−0.02	105	…	(9.0 ± 0.2)E+1	…	…
…	5900	24.85	−0.03	105	0.6	(3.74 ± 0.04)E+2	(8.53 ± 0.08)E+2	1.2
…	5921	24.86	+0.01	109	1.0	(9.77 ± 0.05)E+2	(5.93 ± 0.03)E+2	1.9
…	5939	24.85	+0.04	107	0.8	(8.39 ± 0.04)E+2	(7.72 ± 0.04)E+2	1.6
…	5942	24.81	+0.04	108	0.8	(8.95 ± 0.04)E+2	(9.87 ± 0.05)E+2	1.5
…	5957	24.76	+0.06	110	…	(3.70 ± 0.02)E+2	…	…
…	5979	24.85	+0.08	109	…	(6.19 ± 0.03)E+2	…	…
…	5980	24.73	+0.09	110	…	(2.08 ± 0.03)E+2	…	…

Continuation of Table B2

COHRS catalog #	Hi-GAL catalog #	ℓ (deg)	b (deg)	$v_{\rm LSR}$ (km s^{-1})	$\theta_{\rm R}$ (arcmin)	M ($M_\odot$)	n (cm^{-3})	R (pc)
···	5984	24.76	+0.09	109	0.6	(2.261 ± 0.004)E+3	(4.938 ± 0.009)E+3	1.2
···	6001	24.73	+0.11	108	···	(1.30 ± 0.02)E+2	···	···
···	6016	24.82	+0.13	110	···	(4.72 ± 0.03)E+2	···	···
···	6024	24.73	+0.15	110	···	(8.74 ± 0.03)E+2	···	···
···	6032	24.75	+0.17	108	1.1	(1.954 ± 0.005)E+3	(8.14 ± 0.02)E+2	2.1
···	6040	24.63	+0.17	115	1.1	(2.242 ± 0.006)E+3	(1.014 ± 0.003)E+3	2.1
···	6048	24.60	+0.19	115	···	(3.8 ± 0.2)E+1	···	···
···	5877	24.77	−0.06	···	0.3	(1.26 ± 0.03)E+2	(1.65 ± 0.04)E+3	0.7
···	5936	24.70	+0.02	···	1.0	(5.08 ± 0.05)E+2	(3.15 ± 0.03)E+2	1.9
···	5974	24.79	+0.09	···	1.2	(2.4348 ± 0.0007)E+4	(6.904 ± 0.002)E+3	2.4
···	6076	24.78	+0.23	···	0.6	(2.22 ± 0.04)E+2	(4.59 ± 0.07)E+2	1.2
48878	5723	23.85	−0.30	56	0.8	(5.14 ± 0.04)E+2	(6.83 ± 0.05)E+2	1.4
···	5731	23.91	−0.28	57	2.4	(4.48 ± 0.01)E+3	(1.994 ± 0.004)E+2	4.5
···	5734	23.86	−0.28	56	0.6	(3.10 ± 0.03)E+2	(7.67 ± 0.08)E+2	1.2
···	5825	23.91	−0.13	···	···	(1.17 ± 0.03)E+2	···	···
49673	5725	23.32	−0.30	102	0.9	(3.630 ± 0.005)E+3	(3.159 ± 0.004)E+3	1.7
···	5728	23.37	−0.29	78	···	(1.639 ± 0.003)E+3	···	···
···	5740	23.36	−0.26	102	1.0	(2.063 ± 0.005)E+3	(1.265 ± 0.003)E+3	1.9
···	5747	23.27	−0.25	82	1.5	(6.432 ± 0.007)E+3	(1.208 ± 0.001)E+3	2.8
···	5748	23.44	−0.26	104	0.6	(1.097 ± 0.003)E+3	(2.490 ± 0.008)E+3	1.2
···	5755	23.32	−0.22	82	1.3	(1.516 ± 0.005)E+3	(4.27 ± 0.01)E+2	2.4
···	5757	23.46	−0.23	103	···	(8.94 ± 0.03)E+2	···	···
···	5758	23.41	−0.23	104	2.2	(1.9981 ± 0.0009)E+4	(1.0509 ± 0.0005)E+3	4.2
···	5770	23.28	−0.21	79	1.2	(2.995 ± 0.006)E+3	(9.51 ± 0.02)E+2	2.3
···	5773	23.44	−0.20	106	0.7	(2.153 ± 0.004)E+3	(3.422 ± 0.006)E+3	1.4
···	5792	23.46	−0.18	99	0.6	(1.632 ± 0.003)E+3	(3.901 ± 0.008)E+3	1.2
···	5809	23.46	−0.15	100	1.1	(2.099 ± 0.005)E+3	(8.76 ± 0.02)E+2	2.1
···	5821	23.35	−0.14	97	0.9	(1.396 ± 0.004)E+3	(1.104 ± 0.003)E+3	1.7
···	5830	23.38	−0.13	99	1.0	(1.795 ± 0.005)E+3	(9.78 ± 0.02)E+2	1.9
···	5850	23.43	−0.10	110	···	(2.54 ± 0.03)E+2	···	···
···	5869	23.46	−0.07	83	···	(1.39 ± 0.03)E+2	···	···
···	5879	23.53	−0.06	96	0.3	(6.27 ± 0.03)E+2	(1.026 ± 0.004)E+4	0.6
···	5885	23.56	−0.05	96	1.0	(6.26 ± 0.05)E+2	(3.29 ± 0.02)E+2	2.0
···	5886	23.52	−0.05	95	0.8	(8.03 ± 0.04)E+2	(8.52 ± 0.04)E+2	1.6
···	5902	23.45	−0.02	79	1.2	(1.561 ± 0.005)E+3	(5.27 ± 0.02)E+2	2.3
···	5904	23.51	−0.02	93	···	(3.96 ± 0.03)E+2	···	···
···	5924	23.51	+0.01	93	0.5	(2.95 ± 0.03)E+2	(1.06 ± 0.01)E+3	1.0
···	5927	23.57	+0.02	107	0.9	(3.926 ± 0.006)E+3	(3.011 ± 0.004)E+3	1.7
···	5953	23.53	+0.05	104	···	(1.03 ± 0.02)E+2	···	···
···	6007	23.68	+0.12	87	0.7	(2.56 ± 0.04)E+2	(5.19 ± 0.07)E+2	1.3
···	6008	23.57	+0.12	83	1.2	(1.100 ± 0.005)E+3	(3.50 ± 0.02)E+2	2.3
···	6031	23.57	+0.16	90	1.1	(7.46 ± 0.04)E+2	(3.52 ± 0.02)E+2	2.0
···	6045	23.60	+0.17	87	1.9	(2.460 ± 0.007)E+3	(2.189 ± 0.006)E+2	3.6
···	6053	23.65	+0.19	87	0.5	(2.98 ± 0.03)E+2	(1.13 ± 0.01)E+3	1.0
···	6061	23.55	+0.20	82	1.2	(1.195 ± 0.005)E+3	(4.46 ± 0.02)E+2	2.2
···	6071	23.53	+0.22	82	1.3	(1.416 ± 0.005)E+3	(3.80 ± 0.01)E+2	2.5
···	6079	23.47	+0.24	108	0.9	(3.66 ± 0.04)E+2	(2.66 ± 0.03)E+2	1.8
···	6083	23.52	+0.25	82	1.1	(1.217 ± 0.005)E+3	(4.97 ± 0.02)E+2	2.1
···	6085	23.55	+0.25	83	1.0	(9.53 ± 0.04)E+2	(5.60 ± 0.03)E+2	1.9
···	5729	23.30	−0.29	···	1.1	(2.724 ± 0.005)E+3	(1.220 ± 0.002)E+3	2.1
···	5788	23.43	−0.18	···	1.8	(1.4025 ± 0.0007)E+4	(1.4681 ± 0.0007)E+3	3.4
···	5802	23.51	−0.17	···	···	(1.69 ± 0.04)E+2	···	···
···	5874	23.43	−0.07	···	0.4	(8.5 ± 0.3)E+1	(5.8 ± 0.2)E+2	0.8
···	5896	23.46	−0.04	···	0.5	(6.32 ± 0.03)E+2	(2.88 ± 0.02)E+3	1.0
···	6003	23.60	+0.11	···	1.2	(1.051 ± 0.005)E+3	(3.67 ± 0.02)E+2	2.3
···	6115	23.52	+0.29	···	1.6	(1.392 ± 0.007)E+3	(1.99 ± 0.01)E+2	3.0
50188	4961	23.20	+0.00	78	1.8	(6.662 ± 0.009)E+3	(7.119 ± 0.009)E+2	3.4
···	5925	23.24	+0.01	77	0.6	(7.55 ± 0.04)E+2	(1.700 ± 0.009)E+3	1.2
···	5971	23.27	+0.08	78	0.6	(2.802 ± 0.004)E+3	(8.21 ± 0.01)E+3	1.1
···	5973	23.35	+0.07	85	1.1	(3.96 ± 0.04)E+2	(1.73 ± 0.02)E+2	2.1
···	5994	23.37	+0.10	83	0.7	(4.31 ± 0.04)E+2	(6.83 ± 0.06)E+2	1.4
···	5995	23.25	+0.10	77	0.4	(5.40 ± 0.03)E+2	(3.94 ± 0.03)E+3	0.8
···	5985	23.30	+0.09	···	···	(7.5 ± 0.3)E+1	···	···
50208	5739	24.06	−0.27	82	···	(4.0 ± 0.2)E+1	···	···
···	5760	24.09	−0.23	81	1.2	(2.85 ± 0.04)E+2	(9.8 ± 0.1)E+1	2.3
···	5797	24.12	−0.17	81	1.5	(2.795 ± 0.008)E+3	(4.44 ± 0.01)E+2	2.9
···	5813	24.26	−0.14	90	0.5	(2.82 ± 0.04)E+2	(1.00 ± 0.01)E+3	1.0
···	5882	24.21	−0.06	92	1.6	(1.775 ± 0.006)E+3	(2.736 ± 0.009)E+2	3.0
···	5889	24.23	−0.04	90	1.1	(1.155 ± 0.005)E+3	(5.27 ± 0.02)E+2	2.1
···	6026	23.99	+0.15	82	1.0	(2.475 ± 0.005)E+3	(1.430 ± 0.003)E+3	1.9
···	6027	23.96	+0.16	80	1.5	(8.425 ± 0.007)E+3	(1.413 ± 0.001)E+3	2.9
···	5872	24.13	−0.07	···	1.0	(6.21 ± 0.04)E+2	(3.44 ± 0.02)E+2	1.9
···	5911	24.27	−0.01	···	1.9	(8.56 ± 0.05)E+2	(7.82 ± 0.05)E+1	3.5
50299	5741	24.20	−0.26	94	1.3	(5.71 ± 0.05)E+2	(1.57 ± 0.01)E+2	2.4
···	5790	24.26	−0.18	···	···	(4.9 ± 0.2)E+1	···	···
···	5781	24.34	−0.20	···	1.0	(4.30 ± 0.04)E+2	(2.53 ± 0.03)E+2	1.9
50336	5730	24.53	−0.28	97	1.5	(2.918 ± 0.006)E+3	(4.74 ± 0.01)E+2	2.9
···	5732	24.60	−0.28	96	0.5	(1.58 ± 0.03)E+2	(6.2 ± 0.1)E+2	1.0
···	5733	24.45	−0.28	96	1.0	(7.66 ± 0.05)E+2	(4.08 ± 0.02)E+2	2.0
···	5737	24.58	−0.27	97	0.9	(8.06 ± 0.04)E+2	(6.01 ± 0.03)E+2	1.8
···	5750	24.55	−0.25	100	0.8	(3.079 ± 0.005)E+3	(3.676 ± 0.005)E+3	1.5
···	5764	24.51	−0.22	99	1.1	(3.308 ± 0.006)E+3	(1.401 ± 0.002)E+3	2.1
···	5766	24.55	−0.21	101	0.8	(1.185 ± 0.005)E+3	(1.196 ± 0.005)E+3	1.6
···	5789	24.85	−0.18	90	1.1	(4.82 ± 0.05)E+2	(2.21 ± 0.02)E+2	2.1

Continuation of Table B2

COHRS catalog #	Hi-GAL catalog #	ℓ (deg)	b (deg)	v_{LSR} (km s^{-1})	θ_{R} (arcmin)	M ($\mathrm{M}_{\odot}$)	n (cm^{-3})	R (pc)
···	5804	24.77	−0.15	82	0.9	(6.14 ± 0.04)E+2	(4.66 ± 0.03)E+2	1.7
···	5823	24.54	−0.13	94	1.2	(2.558 ± 0.006)E+3	(9.42 ± 0.02)E+2	2.2
···	5839	24.52	−0.11	95	···	(2.19 ± 0.03)E+2	···	···
···	5871	24.70	−0.07	93	0.5	(3.20 ± 0.04)E+2	(1.37 ± 0.01)E+3	1.0
···	5815	24.82	−0.15	···	2.3	(3.568 ± 0.009)E+3	(1.737 ± 0.004)E+2	4.4
···	5752	24.72	−0.24	···	0.7	(1.91 ± 0.04)E+2	(3.48 ± 0.07)E+2	1.3
···	5765	24.74	−0.21	···	···	(1.22 ± 0.03)E+2	···	···
···	5774	24.82	−0.20	···	0.3	(6.7 ± 0.2)E+1	(1.05 ± 0.04)E+3	0.6
···	5776	24.75	−0.20	···	···	(7.4 ± 0.3)E+1	···	···
51146	5890	24.49	−0.04	109	1.1	(8.205 ± 0.007)E+3	(4.132 ± 0.003)E+3	2.0
···	5891	24.29	−0.04	117	0.9	(4.35 ± 0.04)E+2	(3.69 ± 0.03)E+2	1.7
···	5901	24.26	−0.03	121	1.1	(5.85 ± 0.04)E+2	(2.74 ± 0.02)E+2	2.1
···	5910	24.33	−0.01	117	···	(9.2 ± 0.2)E+1	···	···
···	5917	24.48	−0.00	110	···	(9.2 ± 0.3)E+1	···	···
···	5928	24.39	+0.02	118	0.7	(7.17 ± 0.04)E+2	(1.161 ± 0.006)E+3	1.4
···	5940	24.35	+0.03	117	1.2	(3.614 ± 0.006)E+3	(1.281 ± 0.002)E+3	2.2
···	5948	24.20	+0.04	110	0.7	(4.06 ± 0.04)E+2	(6.69 ± 0.07)E+2	1.3
···	5949	24.01	+0.05	111	0.6	(1.396 ± 0.004)E+3	(4.66 ± 0.01)E+3	1.1
···	5956	24.39	+0.05	118	0.8	(1.150 ± 0.004)E+3	(1.203 ± 0.004)E+3	1.6
···	5961	24.35	+0.06	117	1.2	(2.670 ± 0.005)E+3	(1.005 ± 0.002)E+3	2.2
···	5967	24.41	+0.07	112	0.5	(1.313 ± 0.004)E+3	(6.84 ± 0.02)E+3	0.9
···	5981	24.31	+0.09	113	1.7	(3.259 ± 0.007)E+3	(3.986 ± 0.008)E+2	3.2
···	5991	24.42	+0.11	113	1.5	(6.980 ± 0.007)E+3	(1.114 ± 0.001)E+3	2.9
···	5993	24.26	+0.10	99	···	(1.43 ± 0.02)E+2	···	···
···	5997	24.03	+0.11	106	1.7	(1.853 ± 0.007)E+3	(2.272 ± 0.008)E+2	3.2
···	6011	24.18	+0.12	114	0.4	(1.392 ± 0.004)E+3	(1.515 ± 0.004)E+4	0.7
···	6017	23.82	+0.13	111	0.5	(6.17 ± 0.03)E+2	(3.40 ± 0.02)E+3	0.9
···	6020	24.33	+0.15	114	0.9	(5.741 ± 0.006)E+3	(4.924 ± 0.005)E+3	1.7
···	6029	24.49	+0.16	118	0.3	(4.25 ± 0.03)E+2	(6.17 ± 0.04)E+3	0.7
···	6038	24.16	+0.16	107	0.8	(8.68 ± 0.04)E+2	(1.078 ± 0.005)E+3	1.5
···	6041	23.71	+0.17	113	1.6	(8.094 ± 0.008)E+3	(1.107 ± 0.001)E+3	3.1
···	6044	24.48	+0.18	120	···	(2.03 ± 0.02)E+2	···	···
···	6054	24.45	+0.19	119	1.1	(3.784 ± 0.005)E+3	(1.707 ± 0.002)E+3	2.1
···	6055	24.02	+0.21	105	1.1	(2.802 ± 0.004)E+3	(1.310 ± 0.002)E+3	2.1
···	6059	24.24	+0.21	114	1.3	(2.045 ± 0.005)E+3	(6.13 ± 0.02)E+2	2.4
···	6060	24.05	+0.20	114	2.1	(3.955 ± 0.008)E+3	(2.410 ± 0.005)E+2	4.0
···	6065	24.29	+0.21	113	···	(1.97 ± 0.03)E+2	···	···
···	6074	24.45	+0.22	121	1.6	(6.377 ± 0.006)E+3	(9.706 ± 0.009)E+2	3.0
···	6081	24.21	+0.24	115	1.2	(1.254 ± 0.006)E+3	(3.83 ± 0.02)E+2	2.4
···	6082	24.02	+0.25	96	1.6	(2.475 ± 0.006)E+3	(3.380 ± 0.009)E+2	3.1
···	6089	24.43	+0.26	116	1.4	(4.877 ± 0.006)E+3	(1.026 ± 0.001)E+3	2.7
···	6090	23.97	+0.25	114	···	(8.4 ± 0.2)E+1	···	···
···	6093	24.12	+0.25	113	0.6	(6.70 ± 0.04)E+2	(1.494 ± 0.008)E+3	1.2
···	6097	24.47	+0.26	119	···	(6.00 ± 0.03)E+2	···	···
···	6098	24.29	+0.26	114	0.8	(6.04 ± 0.04)E+2	(5.87 ± 0.04)E+2	1.6
···	6112	24.46	+0.28	121	0.4	(6.16 ± 0.03)E+2	(4.58 ± 0.02)E+3	0.8
···	6113	24.35	+0.28	114	2.0	(5.494 ± 0.008)E+3	(3.899 ± 0.006)E+2	3.8
···	5929	24.16	+0.02	···	1.1	(5.62 ± 0.05)E+2	(2.46 ± 0.02)E+2	2.1
···	5915	24.11	+0.01	···	2.0	(2.174 ± 0.007)E+3	(1.565 ± 0.005)E+2	3.8
···	5926	24.32	+0.01	···	0.4	(1.98 ± 0.03)E+2	(2.24 ± 0.03)E+3	0.7
···	5987	24.56	+0.10	···	···	(1.84 ± 0.03)E+2	···	···
···	5992	24.36	+0.10	···	0.5	(4.70 ± 0.03)E+2	(1.93 ± 0.01)E+3	1.0
···	6030	23.75	+0.16	···	1.0	(1.433 ± 0.004)E+3	(7.78 ± 0.02)E+2	2.0
···	6033	23.79	+0.18	···	2.3	(4.398 ± 0.009)E+3	(2.061 ± 0.004)E+2	4.4
···	6078	24.65	+0.23	···	0.7	(3.19 ± 0.04)E+2	(6.72 ± 0.08)E+2	1.2
···	6087	24.57	+0.25	···	1.4	(9.98 ± 0.06)E+2	(2.25 ± 0.01)E+2	2.6
···	6106	24.09	+0.27	···	0.8	(4.08 ± 0.04)E+2	(4.86 ± 0.04)E+2	1.5
···	6107	24.06	+0.27	···	1.2	(7.12 ± 0.05)E+2	(2.52 ± 0.02)E+2	2.2
···	6114	24.03	+0.28	···	0.6	(2.38 ± 0.03)E+2	(5.37 ± 0.07)E+2	1.2
···	6125	24.48	+0.30	···	0.5	(6.31 ± 0.03)E+2	(2.29 ± 0.01)E+3	1.0
51220	5742	23.94	−0.25	97	1.6	(1.480 ± 0.006)E+3	(2.202 ± 0.009)E+2	3.0
51607	5962	23.89	+0.06	40	2.0	(5.013 ± 0.008)E+3	(3.881 ± 0.006)E+2	3.7
51644	5878	23.57	−0.06	54	0.8	(6.22 ± 0.04)E+2	(7.95 ± 0.05)E+2	1.5
···	5908	23.61	−0.01	54	1.5	(3.880 ± 0.007)E+3	(6.27 ± 0.01)E+2	2.9
···	5943	23.63	+0.04	51	···	(1.97 ± 0.02)E+2	···	···
···	5954	23.33	+0.05	55	0.6	(4.97 ± 0.03)E+2	(1.43 ± 0.01)E+3	1.1
···	5955	23.30	+0.05	55	0.6	(4.93 ± 0.04)E+2	(1.065 ± 0.008)E+3	1.2
···	5965	23.43	+0.07	48	···	(2.46 ± 0.02)E+2	···	···
···	5838	23.19	−0.12	···	0.8	(1.51 ± 0.03)E+2	(1.82 ± 0.04)E+2	1.5
···	5880	23.25	−0.06	···	0.6	(4.92 ± 0.04)E+2	(1.110 ± 0.008)E+3	1.2
···	5864	23.41	−0.08	···	···	(3.3 ± 0.1)E+1	···	···
···	5947	23.36	+0.04	···	0.6	(9.4 ± 0.3)E+1	(2.25 ± 0.07)E+2	1.2
52418	4874	23.02	−0.12	104	1.6	(1.631 ± 0.006)E+3	(2.96 ± 0.01)E+2	2.8
···	4888	23.08	−0.11	···	···	(9.0 ± 0.2)E+1	···	···
52427	5043	23.03	+0.12	108	0.6	(5.79 ± 0.03)E+2	(1.632 ± 0.008)E+3	1.1
···	5085	23.08	+0.16	104	0.9	(5.41 ± 0.03)E+2	(5.43 ± 0.03)E+2	1.6
···	5089	23.11	+0.17	103	1.2	(8.79 ± 0.05)E+2	(4.28 ± 0.02)E+2	2.0
···	5097	23.04	+0.17	105	1.0	(1.017 ± 0.004)E+3	(8.75 ± 0.04)E+2	1.7
···	5114	23.05	+0.20	106	0.2	(3.36 ± 0.03)E+2	(2.40 ± 0.02)E+4	0.4
···	5042	23.14	+0.12	···	0.6	(2.04 ± 0.03)E+2	(5.73 ± 0.09)E+2	1.1
···	5068	23.06	+0.14	···	0.9	(4.42 ± 0.04)E+2	(3.98 ± 0.03)E+2	1.6
···	5092	22.97	+0.16	···	1.1	(4.66 ± 0.04)E+2	(2.71 ± 0.02)E+2	1.9
···	5110	23.00	+0.19	···	0.4	(1.14 ± 0.03)E+2	(1.17 ± 0.03)E+3	0.7
52494	6111	23.23	+0.28	88	0.9	(1.73 ± 0.03)E+2	(1.65 ± 0.03)E+2	1.6

Continuation of Table B2

COHRS catalog #	Hi-GAL catalog #	ℓ (deg)	b (deg)	v_{LSR} (km s^{-1})	θ_R (arcmin)	M ($M_\odot$)	n (cm^{-3})	R (pc)
52918	4771	22.72	−0.28	73	0.7	(1.446 ± 0.003)E+3	(3.466 ± 0.008)E+3	1.2
···	4777	22.79	−0.26	72	1.6	(1.457 ± 0.005)E+3	(2.85 ± 0.01)E+2	2.7
···	4785	22.84	−0.25	72	0.4	(2.71 ± 0.03)E+2	(2.30 ± 0.03)E+3	0.8
···	4782	22.91	−0.26	···	1.2	(8.72 ± 0.05)E+2	(3.55 ± 0.02)E+2	2.1
53025	4859	23.12	−0.15	65	0.5	(1.32 ± 0.03)E+2	(9.0 ± 0.2)E+2	0.8
···	4887	23.11	−0.11	67	···	(1.66 ± 0.03)E+2	···	···
···	4914	23.09	−0.07	69	1.7	(2.283 ± 0.007)E+3	(3.51 ± 0.01)E+2	3.0
53035	4805	22.95	−0.23	69	···	(1.48 ± 0.02)E+2	···	···
···	4843	22.92	−0.17	66	0.9	(5.90 ± 0.04)E+2	(5.56 ± 0.04)E+2	1.6
···	4855	22.96	−0.17	64	1.7	(1.840 ± 0.006)E+3	(2.89 ± 0.01)E+2	2.9
···	4892	22.95	−0.11	65	0.7	(7.28 ± 0.04)E+2	(1.354 ± 0.007)E+3	1.3
···	5761	23.15	−0.22	68	1.1	(5.00 ± 0.04)E+2	(2.96 ± 0.02)E+2	1.9
···	4788	22.93	−0.25	···	0.6	(4.13 ± 0.03)E+2	(1.41 ± 0.01)E+3	1.1
···	4809	23.01	−0.21	···	1.9	(2.153 ± 0.006)E+3	(2.381 ± 0.007)E+2	3.3
···	4824	22.91	−0.20	···	···	(6.8 ± 0.2)E+1	···	···
···	4925	22.93	−0.05	···	0.8	(1.36 ± 0.03)E+2	(2.37 ± 0.05)E+2	1.3
53168	5031	21.60	+0.11	118	0.5	(3.22 ± 0.04)E+2	(1.16 ± 0.01)E+3	1.0
···	5081	21.71	+0.15	115	1.2	(3.93 ± 0.05)E+2	(1.29 ± 0.02)E+2	2.3
···	5083	21.75	+0.16	110	0.4	(1.34 ± 0.04)E+2	(9.7 ± 0.3)E+2	0.8
···	5102	21.67	+0.17	114	1.8	(1.087 ± 0.008)E+3	(1.051 ± 0.007)E+2	3.5
54855	4936	21.74	−0.03	23	1.7	(1.785 ± 0.007)E+3	(1.869 ± 0.008)E+2	3.4
···	4943	21.70	−0.03	23	2.2	(1.722 ± 0.009)E+3	(8.72 ± 0.05)E+1	4.3
···	4954	21.82	−0.02	23	0.3	(2.31 ± 0.04)E+2	(4.06 ± 0.07)E+3	0.6
···	4964	21.65	−0.00	22	1.3	(7.35 ± 0.07)E+2	(1.80 ± 0.02)E+2	2.5
···	4968	21.83	−0.00	24	0.9	(2.29 ± 0.04)E+2	(1.96 ± 0.04)E+2	1.7
···	4971	21.88	+0.01	21	1.1	(2.432 ± 0.007)E+3	(1.045 ± 0.003)E+3	2.1
···	5061	21.63	+0.14	24	···	(4.2 ± 0.2)E+1	···	···
···	5074	21.66	+0.15	24	0.4	(2.80 ± 0.04)E+2	(2.74 ± 0.03)E+3	0.7
···	5106	21.54	+0.18	24	···	(1.8 ± 0.2)E+1	···	···
55007	5117	22.34	+0.21	16	0.8	(1.24 ± 0.02)E+1	(1.61 ± 0.02)E+3	0.3
···	5132	22.46	+0.24	17	0.9	(1.06 ± 0.02)E+1	(9.6 ± 0.2)E+2	0.4
···	5105	22.24	+0.18	···	1.4	(1.75 ± 0.02)E+1	(4.24 ± 0.06)E+2	0.5
···	5130	22.30	+0.23	···	0.9	(1.32 ± 0.02)E+1	(1.01 ± 0.01)E+3	0.4
55153	4870	21.57	−0.13	120	1.2	(1.966 ± 0.006)E+3	(6.13 ± 0.02)E+2	2.3
···	4944	21.56	−0.04	114	1.6	(2.385 ± 0.008)E+3	(2.87 ± 0.01)E+2	3.2
···	4901	21.72	−0.09	···	0.9	(2.32 ± 0.04)E+2	(1.95 ± 0.04)E+2	1.7
···	4902	21.63	−0.08	···	1.8	(8.22 ± 0.08)E+2	(7.45 ± 0.07)E+1	3.5
···	4912	21.59	−0.07	···	0.6	(1.24 ± 0.03)E+2	(2.48 ± 0.07)E+2	1.3
55611	5029	22.02	+0.10	52	0.6	(1.89 ± 0.03)E+2	(4.76 ± 0.08)E+2	1.2
···	5078	22.15	+0.16	56	0.8	(9.7 ± 0.4)E+1	(1.11 ± 0.05)E+2	1.5
···	5123	22.05	+0.21	51	1.9	(6.02 ± 0.01)E+3	(4.413 ± 0.007)E+2	3.8
···	5149	22.16	+0.26	53	1.2	(5.40 ± 0.05)E+2	(1.82 ± 0.02)E+2	2.3
···	5150	22.04	+0.27	50	1.2	(4.21 ± 0.05)E+2	(1.21 ± 0.02)E+2	2.4
···	5141	21.87	+0.25	···	0.7	(1.18 ± 0.04)E+2	(1.58 ± 0.06)E+2	1.4
55828	4837	22.41	−0.18	38	0.8	(8.34 ± 0.05)E+2	(7.54 ± 0.04)E+2	1.6
···	4846	22.43	−0.17	28	1.4	(2.168 ± 0.007)E+3	(3.91 ± 0.01)E+2	2.8
···	4856	22.33	−0.16	30	1.2	(1.137 ± 0.007)E+3	(3.27 ± 0.02)E+2	2.4
···	4885	22.27	−0.12	32	···	(7.4 ± 0.3)E+1	···	···
55855	4951	22.48	−0.02	110	0.7	(4.39 ± 0.04)E+2	(6.33 ± 0.05)E+2	1.4
···	4952	22.46	−0.02	114	1.4	(1.130 ± 0.006)E+3	(2.29 ± 0.01)E+2	2.7
···	4953	22.41	−0.02	116	2.4	(2.79 ± 0.01)E+3	(1.124 ± 0.004)E+2	4.6
···	4967	22.42	+0.01	118	0.8	(5.11 ± 0.04)E+2	(5.06 ± 0.04)E+2	1.6
···	5005	22.44	+0.06	117	1.0	(3.04 ± 0.05)E+2	(1.42 ± 0.02)E+2	2.1
···	4998	22.54	+0.04	···	0.9	(1.35 ± 0.04)E+2	(1.07 ± 0.03)E+2	1.7
56137	5075	21.50	+0.14	51	1.9	(1.29 ± 0.01)E+3	(5.99 ± 0.05)E+1	4.4
56420	4833	22.26	−0.19	77	0.7	(1.23 ± 0.04)E+2	(2.05 ± 0.06)E+2	1.3
···	4857	22.20	−0.15	70	1.7	(7.23 ± 0.07)E+2	(8.46 ± 0.08)E+1	3.3
···	4884	22.37	−0.12	85	1.6	(4.22 ± 0.06)E+2	(5.39 ± 0.08)E+1	3.2
···	4945	22.36	−0.03	87	0.8	(4.06 ± 0.04)E+2	(3.69 ± 0.04)E+2	1.6
···	4963	22.34	−0.00	85	1.0	(2.42 ± 0.05)E+2	(1.17 ± 0.02)E+2	2.0
···	4973	22.23	+0.01	88	0.9	(4.13 ± 0.04)E+2	(2.71 ± 0.03)E+2	1.8
···	4989	22.25	+0.04	83	1.1	(9.69 ± 0.06)E+2	(3.65 ± 0.02)E+2	2.2
···	5000	22.32	+0.05	81	1.7	(2.055 ± 0.008)E+3	(2.193 ± 0.009)E+2	3.4
···	5007	22.35	+0.07	84	1.0	(3.208 ± 0.006)E+3	(1.719 ± 0.003)E+3	2.0
···	5016	22.26	+0.08	81	···	(5.2 ± 0.3)E+1	···	···
···	5051	22.36	+0.12	85	0.6	(1.53 ± 0.04)E+2	(3.28 ± 0.08)E+2	1.2
···	4868	22.27	−0.14	···	···	(6.6 ± 0.3)E+1	···	···
···	4872	22.16	−0.13	···	0.8	(1.99 ± 0.04)E+2	(1.73 ± 0.03)E+2	1.7
···	4999	22.42	+0.05	···	0.4	(2.05 ± 0.03)E+2	(2.28 ± 0.03)E+3	0.7
···	5057	22.26	+0.13	···	0.8	(1.48 ± 0.04)E+2	(1.76 ± 0.04)E+2	1.5
···	5077	22.31	+0.15	···	···	(8.4 ± 0.3)E+1	···	···
56572	4763	22.74	−0.30	107	1.4	(1.992 ± 0.007)E+3	(3.57 ± 0.01)E+2	2.8
···	4773	22.75	−0.27	104	1.0	(2.373 ± 0.005)E+3	(1.161 ± 0.002)E+3	2.0
···	4796	22.74	−0.24	105	1.2	(2.276 ± 0.006)E+3	(6.17 ± 0.02)E+2	2.5
···	4814	22.70	−0.21	109	0.6	(3.17 ± 0.04)E+2	(6.71 ± 0.08)E+2	1.2
···	4819	22.67	−0.21	109	0.8	(3.85 ± 0.04)E+2	(3.98 ± 0.04)E+2	1.6
···	4811	22.72	−0.22	···	0.7	(3.41 ± 0.04)E+2	(4.57 ± 0.05)E+2	1.4
56737	5039	21.87	+0.12	70	0.7	(9.3 ± 0.4)E+1	(1.71 ± 0.07)E+2	1.3
···	5046	21.94	+0.12	76	1.3	(1.586 ± 0.007)E+3	(3.86 ± 0.02)E+2	2.5
···	5026	21.99	+0.10	···	0.9	(3.07 ± 0.04)E+2	(2.60 ± 0.03)E+2	1.7
···	5045	22.01	+0.12	···	0.6	(1.85 ± 0.04)E+2	(3.62 ± 0.08)E+2	1.3
56817	4794	22.43	−0.25	82	0.5	(1.32 ± 0.03)E+2	(7.2 ± 0.2)E+2	0.9
···	4812	22.46	−0.22	76	1.5	(1.214 ± 0.006)E+3	(1.749 ± 0.009)E+2	3.0
···	4813	22.57	−0.22	78	1.4	(1.973 ± 0.006)E+3	(4.08 ± 0.01)E+2	2.7

Continuation of Table B2

COHRS catalog #	Hi-GAL catalog #	ℓ (deg)	b (deg)	$v_{\rm LSR}$ (km s^{-1})	$\theta_{\rm R}$ (arcmin)	M ($M_\odot$)	n (cm^{-3})	R (pc)
···	4820	22.59	−0.21	77	0.9	(1.020 ± 0.004)E+3	(8.52 ± 0.03)E+2	1.7
···	4825	22.50	−0.20	76	1.2	(1.196 ± 0.005)E+3	(3.82 ± 0.02)E+2	2.3
···	4827	22.53	−0.19	76	1.1	(1.460 ± 0.005)E+3	(6.50 ± 0.02)E+2	2.1
···	4847	22.49	−0.17	77	0.8	(4.21 ± 0.04)E+2	(3.95 ± 0.04)E+2	1.6
56827	5133	22.92	+0.24	72	1.2	(2.49 ± 0.05)E+2	(7.1 ± 0.2)E+1	2.4
···	5144	22.88	+0.27	73	1.5	(6.81 ± 0.07)E+2	(1.11 ± 0.01)E+2	2.9
···	5049	23.00	+0.13	···	1.1	(1.230 ± 0.005)E+3	(4.30 ± 0.02)E+2	2.3
56934	4882	22.78	−0.13	64	2.0	(1.809 ± 0.008)E+3	(1.117 ± 0.005)E+2	4.0
···	4918	22.75	−0.07	71	2.1	(2.680 ± 0.009)E+3	(1.612 ± 0.005)E+2	4.1
···	4940	22.80	−0.03	74	0.9	(3.35 ± 0.04)E+2	(2.29 ± 0.03)E+2	1.8
···	4950	22.82	−0.02	72	···	(6.0 ± 0.2)E+1	···	···
···	5004	22.88	+0.06	74	···	(8.8 ± 0.3)E+1	···	···
···	4915	22.72	−0.07	···	···	(1.33 ± 0.02)E+2	···	···
···	4985	22.74	+0.03	···	0.7	(1.30 ± 0.04)E+2	(1.93 ± 0.06)E+2	1.4
56950	5129	21.51	+0.23	76	1.7	(1.466 ± 0.008)E+3	(1.609 ± 0.009)E+2	3.3
···	5145	21.63	+0.26	80	0.5	(2.07 ± 0.04)E+2	(1.05 ± 0.02)E+3	0.9
···	5134	21.59	+0.24	···	1.0	(2.57 ± 0.05)E+2	(1.40 ± 0.03)E+2	1.9
···	5155	21.61	+0.27	···	0.8	(2.66 ± 0.04)E+2	(2.57 ± 0.04)E+2	1.6
57240	4787	21.39	−0.25	92	1.0	(3.798 ± 0.007)E+3	(2.067 ± 0.004)E+3	1.9
···	4806	21.38	−0.23	91	0.9	(1.553 ± 0.005)E+3	(1.094 ± 0.004)E+3	1.8
···	4817	21.42	−0.21	80	0.8	(2.59 ± 0.05)E+2	(2.24 ± 0.04)E+2	1.7
···	4842	21.36	−0.18	91	0.6	(8.67 ± 0.04)E+2	(1.92 ± 0.01)E+3	1.2
57409	4779	21.82	−0.26	78	0.4	(1.28 ± 0.03)E+2	(9.0 ± 0.2)E+2	0.8
···	4783	22.05	−0.26	76	0.9	(1.44 ± 0.04)E+2	(1.12 ± 0.03)E+2	1.7
···	4800	21.98	−0.24	67	0.9	(4.26 ± 0.04)E+2	(3.59 ± 0.04)E+2	1.7
···	4801	21.87	−0.23	79	0.8	(4.98 ± 0.04)E+2	(6.12 ± 0.05)E+2	1.5
···	4803	21.80	−0.23	81	···	(2.1 ± 0.2)E+1	···	···
···	4815	22.02	−0.21	88	0.6	(2.15 ± 0.03)E+2	(5.94 ± 0.09)E+2	1.1
···	4822	21.96	−0.20	78	0.8	(4.19 ± 0.04)E+2	(4.13 ± 0.04)E+2	1.6
···	4834	21.99	−0.20	69	1.5	(1.066 ± 0.007)E+3	(1.61 ± 0.01)E+2	3.0
···	4836	22.02	−0.19	88	1.0	(5.44 ± 0.05)E+2	(3.24 ± 0.03)E+2	1.9
···	4839	21.89	−0.19	78	1.1	(3.25 ± 0.05)E+2	(1.22 ± 0.02)E+2	2.2
···	4844	22.06	−0.19	76	1.4	(2.52 ± 0.06)E+2	(4.6 ± 0.1)E+1	2.8
···	4798	21.85	−0.25	···	1.3	(8.86 ± 0.06)E+2	(2.38 ± 0.02)E+2	2.5
···	4850	22.02	−0.16	···	1.0	(3.72 ± 0.05)E+2	(1.94 ± 0.03)E+2	2.0
···	4864	21.75	−0.15	···	0.7	(8.1 ± 0.4)E+1	(1.45 ± 0.07)E+2	1.3
57439	4761	21.70	−0.28	85	1.3	(6.61 ± 0.06)E+2	(1.69 ± 0.02)E+2	2.5
···	4786	21.67	−0.26	71	0.9	(3.46 ± 0.05)E+2	(2.16 ± 0.03)E+2	1.9
···	4804	21.76	−0.23	63	0.6	(2.96 ± 0.04)E+2	(6.04 ± 0.08)E+2	1.3
57792	3914	20.77	−0.22	53	1.4	(1.130 ± 0.008)E+3	(1.47 ± 0.01)E+2	3.1
···	3928	20.70	−0.18	55	···	(6.5 ± 0.2)E+1	···	···
···	3932	20.89	−0.18	58	1.1	(1.900 ± 0.007)E+3	(5.68 ± 0.02)E+2	2.4
···	3941	20.80	−0.17	51	···	(1.68 ± 0.03)E+2	···	···
···	3954	20.73	−0.16	56	···	(2.15 ± 0.03)E+2	···	···
···	3955	20.67	−0.17	55	1.6	(1.419 ± 0.008)E+3	(1.390 ± 0.008)E+2	3.5
···	3966	20.65	−0.14	57	1.6	(2.909 ± 0.009)E+3	(2.789 ± 0.008)E+2	3.5
···	3985	20.66	−0.11	57	0.5	(2.16 ± 0.04)E+2	(5.7 ± 0.1)E+2	1.2
···	3993	20.79	−0.11	57	0.9	(6.28 ± 0.05)E+2	(3.07 ± 0.03)E+2	2.0
···	3996	20.75	−0.10	59	1.3	(6.591 ± 0.009)E+3	(1.041 ± 0.001)E+3	2.9
···	4004	20.80	−0.08	57	0.9	(3.32 ± 0.05)E+2	(1.99 ± 0.03)E+2	1.9
···	4024	20.72	−0.07	55	1.6	(6.353 ± 0.009)E+3	(5.773 ± 0.008)E+2	3.5
···	4040	20.77	−0.04	58	1.7	(6.624 ± 0.009)E+3	(4.858 ± 0.007)E+2	3.8
···	4062	20.72	−0.01	61	1.2	(1.064 ± 0.007)E+3	(2.56 ± 0.02)E+2	2.6
···	4877	20.94	−0.11	66	0.6	(1.59 ± 0.04)E+2	(3.5 ± 0.1)E+2	1.2
···	4020	20.63	−0.07	···	···	(5.9 ± 0.3)E+1	···	···
···	4042	20.94	−0.04	···	1.0	(1.91 ± 0.05)E+2	(8.0 ± 0.2)E+1	2.1
···	4055	20.74	−0.03	···	0.6	(6.86 ± 0.04)E+2	(1.097 ± 0.007)E+3	1.4
57819	4866	21.33	−0.14	67	2.4	(6.19 ± 0.01)E+3	(1.727 ± 0.004)E+2	5.2
···	4871	21.49	−0.12	73	0.6	(1.64 ± 0.05)E+2	(3.5 ± 0.1)E+2	1.2
···	4903	21.55	−0.09	68	2.1	(2.05 ± 0.01)E+3	(8.45 ± 0.04)E+1	4.6
···	4907	21.50	−0.09	73	···	(7.2 ± 0.3)E+1	···	···
···	4906	21.75	−0.09	···	···	(8.7 ± 0.3)E+1	···	···
···	4911	21.77	−0.07	···	0.8	(2.07 ± 0.05)E+2	(1.58 ± 0.04)E+2	1.7
···	4921	21.38	−0.07	···	0.7	(2.17 ± 0.05)E+2	(2.48 ± 0.05)E+2	1.5
···	4982	21.53	+0.02	···	1.1	(5.69 ± 0.06)E+2	(1.69 ± 0.02)E+2	2.4
···	5030	21.70	+0.10	···	0.5	(2.66 ± 0.04)E+2	(7.6 ± 0.1)E+2	1.1
57885	5095	21.38	+0.17	25	0.8	(2.65 ± 0.04)E+2	(3.34 ± 0.05)E+2	1.5
···	5100	21.32	+0.18	25	···	(1.11 ± 0.03)E+2	···	···
···	5113	21.24	+0.20	25	0.9	(9.70 ± 0.05)E+2	(9.89 ± 0.05)E+2	1.6
···	5151	21.25	+0.27	39	1.6	(7.97 ± 0.05)E+2	(1.43 ± 0.01)E+2	2.8
···	5041	21.20	+0.12	···	1.1	(4.38 ± 0.04)E+2	(2.86 ± 0.02)E+2	1.8
···	5143	21.28	+0.25	···	1.0	(2.09 ± 0.03)E+2	(1.53 ± 0.02)E+2	1.8
57988	4873	21.19	−0.13	65	2.3	(3.22 ± 0.01)E+3	(1.015 ± 0.004)E+2	5.0
58032	4909	21.41	−0.08	76	1.3	(6.60 ± 0.08)E+2	(1.04 ± 0.01)E+2	2.9
···	4932	21.35	−0.04	74	1.5	(4.76 ± 0.08)E+2	(5.50 ± 0.09)E+1	3.3
···	4956	21.40	−0.01	77	1.0	(8.97 ± 0.07)E+2	(2.92 ± 0.02)E+2	2.3
···	4957	21.24	−0.00	75	1.0	(3.47 ± 0.06)E+2	(1.23 ± 0.02)E+2	2.3
···	4975	21.27	+0.02	75	···	(1.70 ± 0.05)E+2	···	···
···	4977	21.23	+0.02	75	···	(1.57 ± 0.04)E+2	···	···
···	4987	21.41	+0.02	76	2.1	(2.75 ± 0.01)E+3	(1.146 ± 0.005)E+2	4.6
···	5003	21.31	+0.06	79	···	(8.9 ± 0.3)E+1	···	···
···	4958	21.07	−0.01	···	1.1	(3.32 ± 0.06)E+2	(1.03 ± 0.02)E+2	2.3
58080	4821	21.18	−0.20	93	0.9	(4.25 ± 0.06)E+2	(1.85 ± 0.03)E+2	2.1
···	4853	21.25	−0.15	91	1.7	(3.063 ± 0.009)E+3	(2.419 ± 0.007)E+2	3.7

Continuation of Table B2

COHRS catalog #	Hi-GAL catalog #	ℓ (deg)	b (deg)	v_{LSR} (km s^{-1})	θ_{R} (arcmin)	M ($\mathrm{M}_{\odot}$)	n (cm^{-3})	R (pc)
58292	3951	20.54	−0.17	51	0.8	(5.54 ± 0.06)E+2	(3.82 ± 0.04)E+2	1.8
···	3962	20.44	−0.16	73	0.9	(9.13 ± 0.07)E+2	(4.34 ± 0.03)E+2	2.0
···	3969	20.55	−0.13	49	1.4	(1.015 ± 0.008)E+3	(1.29 ± 0.01)E+2	3.2
···	4025	20.44	−0.06	52	0.6	(3.56 ± 0.04)E+2	(6.45 ± 0.07)E+2	1.3
···	3956	20.39	−0.18	···	1.4	(8.84 ± 0.08)E+2	(1.031 ± 0.009)E+2	3.3
···	3967	20.47	−0.14	···	0.3	(9.0 ± 0.4)E+1	(1.10 ± 0.05)E+3	0.7
···	4008	20.52	−0.08	···	0.8	(1.65 ± 0.05)E+2	(1.29 ± 0.04)E+2	1.7
···	4009	20.45	−0.08	···	0.9	(4.87 ± 0.06)E+2	(2.12 ± 0.03)E+2	2.1
58875	3883	19.70	−0.25	42	1.3	(5.80 ± 0.01)E+3	(8.31 ± 0.01)E+2	3.0
···	3891	19.61	−0.26	43	0.8	(4.315 ± 0.006)E+3	(2.664 ± 0.004)E+3	1.9
···	3901	19.61	−0.23	41	0.6	(1.3551 ± 0.0007)E+4	(1.969 ± 0.001)E+4	1.4
···	3957	19.81	−0.16	39	0.6	(1.17 ± 0.04)E+2	(1.74 ± 0.06)E+2	1.4
···	3958	19.64	−0.16	36	1.3	(2.185 ± 0.007)E+3	(3.85 ± 0.01)E+2	2.8
59293	4026	21.00	−0.05	31	1.7	(1.43 ± 0.01)E+3	(9.40 ± 0.06)E+1	3.9
···	4039	20.93	−0.05	30	···	(9.8 ± 0.3)E+1	···	···
···	4810	20.93	−0.22	40	···	(4.4 ± 0.3)E+1	···	···
···	4890	21.10	−0.11	35	···	(2.5 ± 0.3)E+1	···	···
···	4913	20.97	−0.08	31	1.5	(1.89 ± 0.01)E+3	(1.82 ± 0.01)E+2	3.5
···	4923	21.07	−0.07	33	1.1	(6.85 ± 0.07)E+2	(1.87 ± 0.02)E+2	2.5
···	3899	20.83	−0.23	···	0.4	(1.61 ± 0.04)E+2	(9.7 ± 0.2)E+2	0.9
···	3919	20.87	−0.21	···	0.5	(1.53 ± 0.04)E+2	(3.53 ± 0.09)E+2	1.2
···	3931	20.97	−0.18	···	···	(6.7 ± 0.3)E+1	···	···
···	3964	20.92	−0.14	···	1.6	(9.01 ± 0.08)E+2	(8.32 ± 0.07)E+1	3.5
···	4023	21.02	−0.06	···	···	(3.02 ± 0.04)E+2	···	···
···	4095	20.49	+0.03	···	0.7	(1.42 ± 0.05)E+2	(1.70 ± 0.06)E+2	1.5
···	4830	21.01	−0.20	···	1.1	(3.25 ± 0.07)E+2	(8.6 ± 0.2)E+1	2.5
···	4875	21.07	−0.12	···	1.2	(3.91 ± 0.07)E+2	(8.3 ± 0.1)E+1	2.7
60338	4129	20.82	+0.09	58	···	(1.11 ± 0.04)E+2	···	···
···	4143	20.79	+0.11	58	2.6	(1.84 ± 0.01)E+3	(3.88 ± 0.03)E+1	5.8
···	4166	20.91	+0.17	58	0.6	(1.58 ± 0.05)E+2	(2.43 ± 0.07)E+2	1.4
···	4173	20.86	+0.17	58	1.6	(1.96 ± 0.01)E+3	(1.569 ± 0.008)E+2	3.7
60612	4036	20.40	−0.05	77	···	(7.6 ± 0.3)E+1	···	···
···	4049	20.44	−0.04	76	1.6	(1.746 ± 0.009)E+3	(1.610 ± 0.008)E+2	3.5
···	4084	20.57	+0.02	81	1.0	(3.53 ± 0.05)E+2	(1.43 ± 0.02)E+2	2.1
···	4094	20.59	+0.03	79	0.8	(1.94 ± 0.05)E+2	(1.55 ± 0.04)E+2	1.7
···	4100	20.67	+0.05	82	0.8	(2.69 ± 0.05)E+2	(1.67 ± 0.03)E+2	1.9
···	4101	20.35	+0.05	72	0.5	(3.16 ± 0.05)E+2	(9.8 ± 0.1)E+2	1.1
···	4109	20.28	+0.05	70	0.9	(6.19 ± 0.06)E+2	(2.72 ± 0.03)E+2	2.1
···	4115	20.24	+0.07	71	0.3	(1.831 ± 0.005)E+3	(1.531 ± 0.004)E+4	0.8
···	4120	20.32	+0.08	67	1.3	(3.373 ± 0.009)E+3	(4.91 ± 0.01)E+2	3.0
···	4125	20.52	+0.08	78	0.8	(1.46 ± 0.05)E+2	(9.7 ± 0.3)E+1	1.8
···	4127	20.24	+0.09	73	1.1	(1.746 ± 0.007)E+3	(4.73 ± 0.02)E+2	2.5
···	4074	20.58	+0.00	···	0.5	(2.60 ± 0.04)E+2	(6.9 ± 0.1)E+2	1.2
···	4079	20.17	+0.01	···	1.4	(6.03 ± 0.08)E+2	(8.0 ± 0.1)E+1	3.1
···	4126	20.28	+0.08	···	1.0	(4.66 ± 0.05)E+2	(1.85 ± 0.02)E+2	2.2
61310	3888	19.93	−0.26	65	0.9	(4.794 ± 0.008)E+3	(2.159 ± 0.003)E+3	2.1
···	3897	19.91	−0.24	66	1.0	(1.281 ± 0.006)E+3	(4.75 ± 0.02)E+2	2.2
···	3906	19.87	−0.22	55	0.5	(2.29 ± 0.05)E+2	(8.6 ± 0.2)E+2	1.0
···	3912	19.98	−0.22	45	0.8	(1.075 ± 0.006)E+3	(6.43 ± 0.04)E+2	1.9
···	3915	19.77	−0.21	67	···	(7.0 ± 0.3)E+1	···	···
···	3920	19.91	−0.20	63	1.3	(1.683 ± 0.008)E+3	(2.66 ± 0.01)E+2	2.9
···	3929	19.85	−0.19	55	1.4	(5.69 ± 0.08)E+2	(7.2 ± 0.1)E+1	3.2
···	3942	19.76	−0.17	65	1.7	(1.938 ± 0.009)E+3	(1.429 ± 0.007)E+2	3.8
···	3943	19.70	−0.17	56	···	(1.60 ± 0.02)E+2	···	···
···	3945	20.03	−0.17	56	1.1	(1.052 ± 0.006)E+3	(3.12 ± 0.02)E+2	2.4
···	3946	20.00	−0.17	55	1.4	(1.501 ± 0.007)E+3	(1.805 ± 0.009)E+2	3.2
···	3947	19.72	−0.17	66	0.7	(7.51 ± 0.05)E+2	(6.69 ± 0.04)E+2	1.7
···	3965	19.98	−0.14	57	0.9	(4.86 ± 0.06)E+2	(2.26 ± 0.03)E+2	2.1
···	3970	19.61	−0.13	57	0.9	(4.300 ± 0.007)E+3	(2.291 ± 0.004)E+3	2.0
···	3972	19.56	−0.14	62	0.6	(3.43 ± 0.05)E+2	(5.98 ± 0.08)E+2	1.3
···	3977	19.69	−0.13	57	0.8	(1.549 ± 0.006)E+3	(1.111 ± 0.004)E+3	1.8
···	3984	19.73	−0.12	60	1.3	(3.142 ± 0.008)E+3	(4.62 ± 0.01)E+2	3.0
···	3991	19.97	−0.10	68	0.9	(9.65 ± 0.06)E+2	(5.20 ± 0.03)E+2	2.0
···	3994	19.58	−0.10	64	0.7	(1.557 ± 0.005)E+3	(1.390 ± 0.005)E+3	1.7
···	4003	19.52	−0.08	67	1.1	(7.83 ± 0.06)E+2	(2.36 ± 0.02)E+2	2.4
···	4013	19.60	−0.07	61	1.9	(4.80 ± 0.01)E+3	(2.379 ± 0.005)E+2	4.3
···	4071	19.95	−0.00	74	2.8	(3.66 ± 0.01)E+3	(5.57 ± 0.02)E+1	6.4
···	4044	19.94	−0.05	···	1.1	(6.38 ± 0.06)E+2	(1.56 ± 0.02)E+2	2.5
···	4077	20.10	+0.01	···	0.7	(2.47 ± 0.05)E+2	(2.16 ± 0.05)E+2	1.7
···	4180	20.05	+0.19	···	1.1	(7.93 ± 0.07)E+2	(1.87 ± 0.02)E+2	2.6
61476	3926	19.27	−0.20	38	1.1	(1.051 ± 0.006)E+3	(3.82 ± 0.02)E+2	2.2
61609	3988	19.44	−0.11	27	1.5	(9.75 ± 0.06)E+2	(1.50 ± 0.01)E+2	3.0
···	4116	19.31	+0.06	27	1.2	(2.527 ± 0.006)E+3	(7.50 ± 0.02)E+2	2.4
···	4124	19.28	+0.07	27	1.4	(2.124 ± 0.007)E+3	(3.55 ± 0.01)E+2	2.9
···	4161	19.25	+0.15	26	1.0	(2.29 ± 0.05)E+2	(1.23 ± 0.03)E+2	2.0
···	4021	19.48	−0.08	···	1.2	(8.80 ± 0.06)E+2	(2.28 ± 0.01)E+2	2.5
···	4032	19.49	−0.06	···	0.9	(5.31 ± 0.05)E+2	(3.74 ± 0.03)E+2	1.8
···	4217	19.20	+0.28	···	···	(7.1 ± 0.3)E+1	···	···
···	4091	19.24	+0.03	···	1.2	(9.25 ± 0.06)E+2	(2.88 ± 0.02)E+2	2.3
···	4102	19.56	+0.04	···	0.9	(4.27 ± 0.04)E+2	(3.11 ± 0.03)E+2	1.8
···	4121	19.72	+0.08	···	0.5	(4.3 ± 0.3)E+1	(2.0 ± 0.1)E+2	1.0
···	4156	19.69	+0.14	···	1.4	(4.77 ± 0.06)E+2	(8.3 ± 0.1)E+1	2.9
···	4157	19.93	+0.15	···	1.6	(3.68 ± 0.06)E+2	(4.10 ± 0.07)E+1	3.3
···	4216	19.75	+0.29	···	2.0	(2.118 ± 0.009)E+3	(1.286 ± 0.006)E+2	4.0

Continuation of Table B2

COHRS catalog #	Hi-GAL catalog #	ℓ (deg)	b (deg)	$v_{\rm LSR}$ (km s^{-1})	$\theta_{\rm R}$ (arcmin)	M ($\rm M_{\odot}$)	n (cm^{-3})	R (pc)
62233	2972	18.41	−0.29	68	1.8	(1.709 ± 0.008)E+3	(2.63 ± 0.01)E+2	3.0
···	2980	18.35	−0.28	67	0.9	(1.112 ± 0.004)E+3	(1.544 ± 0.006)E+3	1.4
···	2984	18.29	−0.26	68	1.4	(2.708 ± 0.006)E+3	(8.46 ± 0.02)E+2	2.3
62313	2879	18.66	−0.50	71	1.3	(7.69 ± 0.05)E+2	(2.98 ± 0.02)E+2	2.2
···	2917	18.69	−0.38	67	1.6	(1.355 ± 0.007)E+3	(2.77 ± 0.01)E+2	2.7
···	2948	18.71	−0.33	67	···	(9.4 ± 0.3)E+1	···	···
···	3812	18.71	−0.43	···	0.7	(1.44 ± 0.03)E+2	(4.35 ± 0.08)E+2	1.1
62708	3139	17.96	−0.01	52	1.0	(5.43 ± 0.09)E+2	(1.64 ± 0.03)E+2	2.4
···	3145	17.91	−0.00	52	1.2	(1.25 ± 0.01)E+3	(2.17 ± 0.02)E+2	2.9
···	3149	18.01	+0.00	···	0.3	(7.9 ± 0.5)E+1	(8.0 ± 0.5)E+2	0.7
···	3188	17.86	+0.07	···	1.2	(2.10 ± 0.01)E+3	(3.72 ± 0.02)E+2	2.8
62744	3142	17.51	−0.01	36	0.9	(3.89 ± 0.08)E+2	(1.70 ± 0.04)E+2	2.1
···	3183	17.70	+0.07	36	···	(9.8 ± 0.6)E+1	···	···
···	3121	17.64	−0.06	···	0.7	(2.27 ± 0.07)E+2	(2.50 ± 0.07)E+2	1.5
···	3185	17.78	+0.06	···	2.1	(1.30 ± 0.02)E+3	(4.26 ± 0.05)E+1	5.0
···	3189	17.48	+0.07	···	0.7	(5.63 ± 0.07)E+2	(4.52 ± 0.06)E+2	1.7
···	3203	17.50	+0.10	···	0.7	(2.17 ± 0.07)E+2	(2.07 ± 0.06)E+2	1.6
62785	3123	18.17	−0.06	50	0.9	(8.3 ± 0.4)E+1	(9.8 ± 0.4)E+1	1.5
···	3169	18.32	+0.04	53	0.9	(3.92 ± 0.04)E+2	(4.09 ± 0.05)E+2	1.6
···	3178	18.10	+0.05	52	0.9	(7.85 ± 0.04)E+2	(9.01 ± 0.05)E+2	1.5
···	3191	18.17	+0.07	55	0.9	(3.26 ± 0.04)E+2	(3.73 ± 0.05)E+2	1.5
···	3211	18.18	+0.11	54	1.5	(8.54 ± 0.06)E+2	(2.26 ± 0.01)E+2	2.5
···	3098	18.10	−0.08	···	2.0	(7.06 ± 0.08)E+2	(7.39 ± 0.08)E+1	3.4
···	3155	18.25	+0.01	···	0.5	(1.25 ± 0.03)E+2	(7.4 ± 0.2)E+2	0.9
···	3159	18.35	+0.02	···	1.4	(5.05 ± 0.06)E+2	(1.75 ± 0.02)E+2	2.3
···	3163	18.29	+0.01	···	1.4	(4.43 ± 0.05)E+2	(1.55 ± 0.02)E+2	2.3
···	3173	18.28	+0.04	···	1.1	(3.16 ± 0.05)E+2	(1.83 ± 0.03)E+2	1.9
···	3201	18.16	+0.09	···	0.3	(2.95 ± 0.02)E+2	(6.74 ± 0.06)E+3	0.6
62805	2895	18.57	−0.43	46	1.3	(7.57 ± 0.06)E+2	(2.67 ± 0.02)E+2	2.3
···	2957	18.57	−0.32	47	1.0	(2.25 ± 0.04)E+2	(1.91 ± 0.03)E+2	1.7
···	2974	18.56	−0.29	47	···	(1.20 ± 0.03)E+2	···	···
···	3003	18.69	−0.23	45	1.6	(2.776 ± 0.007)E+3	(5.99 ± 0.02)E+2	2.7
···	3904	18.73	−0.23	40	1.0	(4.855 ± 0.004)E+3	(3.751 ± 0.003)E+3	1.7
···	2983	18.62	−0.26	···	···	(7.0 ± 0.3)E+1	···	···
···	2996	18.64	−0.24	···	···	(5.4 ± 0.2)E+1	···	···
62885	2883	18.24	−0.47	50	0.8	(5.43 ± 0.04)E+2	(8.97 ± 0.07)E+2	1.3
···	2886	18.01	−0.47	50	1.2	(5.73 ± 0.05)E+2	(3.09 ± 0.03)E+2	2.0
···	2897	18.06	−0.44	51	1.0	(2.56 ± 0.04)E+2	(2.23 ± 0.03)E+2	1.7
···	2900	18.03	−0.44	40	1.2	(3.35 ± 0.05)E+2	(1.56 ± 0.02)E+2	2.1
···	2906	18.18	−0.41	48	0.3	(8.2 ± 0.3)E+1	(3.7 ± 0.1)E+3	0.4
···	2909	18.14	−0.40	47	1.6	(1.899 ± 0.007)E+3	(3.69 ± 0.01)E+2	2.7
···	2918	18.37	−0.38	45	1.3	(1.452 ± 0.007)E+3	(5.82 ± 0.03)E+2	2.2
···	2923	18.23	−0.37	49	···	(2.61 ± 0.03)E+2	···	···
···	2925	18.16	−0.37	46	···	(1.64 ± 0.03)E+2	···	···
···	2926	18.06	−0.37	42	···	(3.0 ± 0.2)E+1	···	···
···	2927	18.02	−0.37	41	0.9	(4.05 ± 0.04)E+2	(4.92 ± 0.05)E+2	1.5
···	2942	18.00	−0.35	42	1.1	(7.45 ± 0.05)E+2	(4.31 ± 0.03)E+2	1.9
···	2943	17.97	−0.35	41	1.1	(2.57 ± 0.04)E+2	(1.64 ± 0.03)E+2	1.8
···	2945	18.22	−0.34	47	1.1	(2.849 ± 0.005)E+3	(1.702 ± 0.003)E+3	1.9
···	2953	18.11	−0.32	56	···	(1.210 ± 0.003)E+3	···	···
···	2962	18.06	−0.30	47	1.0	(1.334 ± 0.004)E+3	(1.043 ± 0.003)E+3	1.7
···	2966	18.09	−0.30	51	1.2	(3.838 ± 0.005)E+3	(2.137 ± 0.003)E+3	1.9
···	2968	18.18	−0.30	50	0.9	(2.084 ± 0.005)E+3	(2.292 ± 0.006)E+3	1.5
···	2975	18.14	−0.30	56	1.6	(7.998 ± 0.007)E+3	(1.742 ± 0.002)E+3	2.6
···	2999	17.97	−0.23	53	···	(4.4 ± 0.2)E+1	···	···
···	3010	18.22	−0.22	56	0.8	(7.95 ± 0.04)E+2	(1.370 ± 0.007)E+3	1.3
···	3022	18.44	−0.20	52	1.7	(1.046 ± 0.006)E+3	(1.73 ± 0.01)E+2	2.9
···	3024	18.49	−0.18	45	2.1	(2.266 ± 0.007)E+3	(2.000 ± 0.007)E+2	3.6
···	3033	18.24	−0.19	52	···	(9.9 ± 0.2)E+1	···	···
···	3041	18.26	−0.16	52	···	(1.61 ± 0.03)E+2	···	···
···	3046	18.52	−0.17	52	1.0	(6.69 ± 0.04)E+2	(5.63 ± 0.03)E+2	1.7
···	3050	18.56	−0.16	51	1.2	(8.95 ± 0.05)E+2	(4.60 ± 0.03)E+2	2.0
···	3057	18.53	−0.13	45	1.0	(2.61 ± 0.05)E+2	(2.12 ± 0.04)E+2	1.7
···	3073	18.24	−0.12	50	0.8	(3.06 ± 0.04)E+2	(5.55 ± 0.08)E+2	1.3
···	3092	18.57	−0.09	46	1.0	(5.34 ± 0.05)E+2	(5.03 ± 0.04)E+2	1.6
···	3105	18.52	−0.08	45	···	(6.9 ± 0.2)E+1	···	···
···	3107	18.61	−0.08	45	0.8	(1.541 ± 0.005)E+3	(2.358 ± 0.008)E+3	1.4
···	3117	18.65	−0.06	45	1.3	(3.859 ± 0.007)E+3	(1.357 ± 0.002)E+3	2.3
···	3061	18.69	−0.14	···	···	(1.13 ± 0.03)E+2	···	···
···	2914	18.11	−0.39	···	0.5	(2.03 ± 0.03)E+2	(1.87 ± 0.03)E+3	0.8
62971	3820	18.86	−0.41	26	0.8	(8.45 ± 0.06)E+2	(4.99 ± 0.03)E+2	1.9
63606	3176	18.87	+0.05	49	0.3	(4.63 ± 0.04)E+2	(1.46 ± 0.01)E+4	0.5
···	3788	18.82	−0.48	65	1.6	(8.244 ± 0.005)E+3	(1.688 ± 0.001)E+3	2.7
···	3792	18.89	−0.48	66	1.7	(9.918 ± 0.006)E+3	(1.6050 ± 0.0009)E+3	2.9
···	3793	18.76	−0.46	68	1.1	(4.85 ± 0.04)E+2	(3.45 ± 0.03)E+2	1.8
···	3837	18.84	−0.38	61	0.9	(1.278 ± 0.004)E+3	(1.416 ± 0.004)E+3	1.5
···	3879	18.90	−0.28	64	1.9	(2.404 ± 0.006)E+3	(2.921 ± 0.007)E+2	3.2
···	3894	19.08	−0.24	66	1.5	(2.002 ± 0.005)E+3	(4.88 ± 0.01)E+2	2.5
···	3898	18.87	−0.24	65	0.3	(5.2 ± 0.2)E+1	(1.97 ± 0.08)E+3	0.5
···	3907	18.90	−0.23	67	1.1	(5.08 ± 0.04)E+2	(3.50 ± 0.02)E+2	1.8
···	3916	19.06	−0.20	63	1.3	(1.945 ± 0.005)E+3	(7.42 ± 0.02)E+2	2.2
···	3917	18.91	−0.20	59	0.7	(2.16 ± 0.03)E+2	(6.35 ± 0.08)E+2	1.1
···	3918	18.89	−0.20	66	0.9	(3.14 ± 0.03)E+2	(3.27 ± 0.03)E+2	1.6
···	3924	18.84	−0.20	64	1.3	(3.92 ± 0.03)E+2	(1.66 ± 0.01)E+2	2.1

Continuation of Table B2

COHRS catalog #	Hi-GAL catalog #	ℓ (deg)	b (deg)	v_{LSR} (km s^{-1})	θ_{R} (arcmin)	M ($M_\odot$)	n (cm^{-3})	R (pc)
⋯	3948	19.05	−0.16	63	0.6	(1.73 ± 0.03)E+2	(8.4 ± 0.1)E+2	0.9
⋯	3952	19.08	−0.17	60	1.2	(5.43 ± 0.04)E+2	(2.53 ± 0.02)E+2	2.1
⋯	3983	18.92	−0.12	66	⋯	(5.7 ± 0.2)E+1	⋯	⋯
⋯	3992	18.94	−0.10	64	⋯	(1.04 ± 0.02)E+2	⋯	⋯
⋯	4001	18.98	−0.09	63	⋯	(2.36 ± 0.01)E+2	⋯	⋯
⋯	4011	19.01	−0.08	62	1.1	(1.552 ± 0.004)E+3	(8.87 ± 0.02)E+2	1.9
⋯	4019	18.92	−0.07	47	⋯	(1.47 ± 0.02)E+2	⋯	⋯
⋯	4045	18.99	−0.05	62	1.6	(3.576 ± 0.004)E+3	(7.84 ± 0.01)E+2	2.6
⋯	4052	19.01	−0.02	61	1.3	(3.976 ± 0.005)E+3	(1.436 ± 0.002)E+3	2.2
⋯	4081	18.82	+0.01	49	1.2	(2.28 ± 0.04)E+2	(1.26 ± 0.02)E+2	1.9
⋯	4099	18.95	+0.04	49	0.5	(4.90 ± 0.03)E+2	(4.18 ± 0.02)E+3	0.8
⋯	4117	19.09	+0.06	46	1.6	(7.69 ± 0.04)E+2	(1.69 ± 0.01)E+2	2.6
⋯	3801	18.94	−0.45	⋯	1.0	(3.16 ± 0.03)E+2	(3.08 ± 0.03)E+2	1.6
⋯	3843	18.82	−0.37	⋯	0.3	(1.02 ± 0.02)E+2	(3.06 ± 0.06)E+3	0.5
⋯	3939	18.92	−0.18	⋯	⋯	(8.1 ± 0.2)E+1	⋯	⋯
⋯	3949	18.97	−0.17	⋯	⋯	(1.5 ± 0.1)E+1	⋯	⋯
⋯	3953	18.84	−0.17	⋯	0.5	(1.89 ± 0.02)E+2	(1.40 ± 0.02)E+3	0.8
⋯	3961	18.99	−0.15	⋯	⋯	(5.2 ± 0.2)E+1	⋯	⋯
⋯	4000	18.90	−0.09	⋯	⋯	(2.26 ± 0.02)E+2	⋯	⋯
⋯	3800	19.01	−0.45	⋯	⋯	(5.8 ± 0.2)E+1	⋯	⋯
63718	3020	17.87	−0.21	53	1.6	(3.50 ± 0.06)E+2	(6.9 ± 0.1)E+1	2.7
⋯	3058	17.77	−0.14	52	0.8	(1.77 ± 0.04)E+2	(3.53 ± 0.07)E+2	1.3
⋯	3059	17.70	−0.14	51	1.6	(7.97 ± 0.06)E+2	(1.84 ± 0.01)E+2	2.6
⋯	3099	17.79	−0.10	47	1.0	(2.28 ± 0.05)E+2	(1.91 ± 0.04)E+2	1.7
⋯	3067	17.76	−0.12	⋯	⋯	(1.27 ± 0.03)E+2	⋯	⋯
⋯	3076	17.78	−0.12	⋯	0.5	(2.11 ± 0.03)E+2	(1.33 ± 0.02)E+3	0.9
⋯	3082	17.72	−0.11	⋯	0.6	(1.48 ± 0.03)E+2	(6.4 ± 0.1)E+2	1.0
63783	2933	17.39	−0.35	51	1.8	(7.35 ± 0.08)E+2	(7.95 ± 0.09)E+1	3.3
⋯	2949	17.26	−0.34	43	⋯	(4.5 ± 0.2)E+1	⋯	⋯
⋯	2955	17.25	−0.34	43	1.4	(2.82 ± 0.06)E+2	(6.2 ± 0.1)E+1	2.6
⋯	2965	17.16	−0.30	55	0.9	(2.06 ± 0.04)E+2	(2.05 ± 0.04)E+2	1.6
⋯	2981	17.27	−0.27	45	⋯	(1.14 ± 0.03)E+2	⋯	⋯
⋯	2993	17.31	−0.25	45	1.1	(4.02 ± 0.06)E+2	(1.76 ± 0.03)E+2	2.1
⋯	2994	17.28	−0.24	47	0.8	(1.86 ± 0.05)E+2	(2.80 ± 0.07)E+2	1.4
⋯	3007	17.25	−0.22	44	0.8	(1.09 ± 0.04)E+2	(1.51 ± 0.05)E+2	1.4
⋯	3012	17.47	−0.23	52	1.5	(1.578 ± 0.007)E+3	(3.26 ± 0.02)E+2	2.7
⋯	3013	17.22	−0.22	43	0.8	(1.24 ± 0.05)E+2	(1.63 ± 0.06)E+2	1.5
⋯	3015	17.10	−0.22	45	1.0	(2.86 ± 0.05)E+2	(1.58 ± 0.03)E+2	1.9
⋯	3023	17.28	−0.21	42	0.9	(5.62 ± 0.06)E+2	(5.32 ± 0.05)E+2	1.6
⋯	3028	17.45	−0.20	53	1.4	(1.836 ± 0.008)E+3	(3.87 ± 0.02)E+2	2.7
⋯	3044	17.31	−0.17	48	1.2	(5.78 ± 0.06)E+2	(2.02 ± 0.02)E+2	2.3
⋯	3047	17.15	−0.18	43	2.3	(2.22 ± 0.01)E+3	(1.221 ± 0.006)E+2	4.2
⋯	3103	16.92	−0.08	41	⋯	(6.93 ± 0.04)E+2	⋯	⋯
⋯	3119	16.87	−0.07	41	1.2	(6.53 ± 0.06)E+2	(2.26 ± 0.02)E+2	2.3
⋯	2919	17.33	−0.38	⋯	0.7	(1.91 ± 0.04)E+2	(2.98 ± 0.07)E+2	1.4
⋯	2956	17.16	−0.33	⋯	1.7	(6.56 ± 0.08)E+2	(8.2 ± 0.1)E+1	3.2
⋯	3034	17.21	−0.18	⋯	1.5	(1.272 ± 0.008)E+3	(2.21 ± 0.01)E+2	2.9
⋯	2928	17.36	−0.38	⋯	1.8	(5.81 ± 0.08)E+2	(6.35 ± 0.09)E+1	3.3
⋯	3049	17.39	−0.16	⋯	0.4	(4.0 ± 0.3)E+1	(4.5 ± 0.4)E+2	0.7
⋯	3052	17.06	−0.15	⋯	0.8	(2.65 ± 0.05)E+2	(3.35 ± 0.06)E+2	1.5
⋯	3108	16.95	−0.08	⋯	1.7	(2.186 ± 0.009)E+3	(2.94 ± 0.01)E+2	3.1
63972	2437	16.70	+0.23	26	1.2	(2.20 ± 0.05)E+2	(8.0 ± 0.2)E+1	2.2
⋯	3196	16.88	+0.08	26	⋯	(7.2 ± 0.3)E+1	⋯	⋯
⋯	3222	16.89	+0.14	24	2.2	(2.35 ± 0.01)E+3	(1.462 ± 0.007)E+2	4.0
⋯	3260	16.92	+0.22	24	1.4	(2.395 ± 0.008)E+3	(5.30 ± 0.02)E+2	2.6
⋯	3270	16.93	+0.26	25	1.5	(3.299 ± 0.008)E+3	(5.69 ± 0.01)E+2	2.9
⋯	3278	17.03	+0.28	23	0.9	(5.11 ± 0.05)E+2	(4.34 ± 0.04)E+2	1.7
⋯	3279	16.99	+0.28	23	1.7	(9.66 ± 0.08)E+2	(1.30 ± 0.01)E+2	3.1
⋯	3287	16.96	+0.30	23	0.4	(1.59 ± 0.04)E+2	(1.62 ± 0.04)E+3	0.7
⋯	3289	17.03	+0.30	23	0.7	(2.75 ± 0.04)E+2	(4.60 ± 0.07)E+2	1.3
⋯	3298	17.03	+0.35	23	0.6	(4.35 ± 0.05)E+2	(1.46 ± 0.02)E+3	1.1
⋯	3303	16.91	+0.33	25	2.0	(3.41 ± 0.01)E+3	(2.718 ± 0.008)E+2	3.7
⋯	3313	16.93	+0.37	26	0.8	(3.06 ± 0.05)E+2	(3.36 ± 0.05)E+2	1.5
⋯	3316	16.76	+0.39	23	1.1	(1.50 ± 0.05)E+2	(7.9 ± 0.3)E+1	2.0
⋯	3323	17.09	+0.40	23	0.6	(4.25 ± 0.05)E+2	(1.01 ± 0.01)E+3	1.2
⋯	3328	17.06	+0.42	24	1.8	(2.073 ± 0.008)E+3	(2.45 ± 0.01)E+2	3.2
⋯	3329	17.00	+0.41	26	0.5	(3.45 ± 0.04)E+2	(2.33 ± 0.03)E+3	0.8
⋯	3332	16.77	+0.43	26	1.3	(1.78 ± 0.06)E+2	(5.2 ± 0.2)E+1	2.4
⋯	3333	17.03	+0.42	25	1.5	(1.443 ± 0.007)E+3	(2.59 ± 0.01)E+2	2.8
⋯	3337	16.92	+0.46	25	1.5	(5.28 ± 0.07)E+2	(1.07 ± 0.01)E+2	2.7
⋯	3340	17.09	+0.46	23	1.3	(1.014 ± 0.007)E+3	(2.72 ± 0.02)E+2	2.5
⋯	3344	16.89	+0.48	24	1.4	(7.01 ± 0.07)E+2	(1.77 ± 0.02)E+2	2.5
⋯	3312	17.11	+0.37	⋯	⋯	(2.5 ± 0.3)E+1	⋯	⋯
⋯	3325	16.84	+0.41	⋯	1.9	(4.35 ± 0.07)E+2	(3.85 ± 0.07)E+1	3.6
⋯	3345	16.83	+0.48	⋯	⋯	(3.6 ± 0.3)E+1	⋯	⋯
64017	3175	17.52	+0.05	23	1.0	(2.72 ± 0.05)E+2	(1.85 ± 0.03)E+2	1.8
⋯	3186	17.51	+0.07	22	1.2	(7.79 ± 0.06)E+2	(2.64 ± 0.02)E+2	2.3
⋯	3228	17.64	+0.16	23	1.4	(9.35 ± 0.01)E+3	(2.401 ± 0.002)E+3	2.5
⋯	3254	17.64	+0.20	23	⋯	(5.4 ± 0.3)E+1	⋯	⋯
⋯	3264	17.58	+0.23	24	1.3	(2.90 ± 0.06)E+2	(8.4 ± 0.2)E+1	2.4
⋯	3283	17.68	+0.29	23	0.8	(9.1 ± 0.4)E+1	(1.17 ± 0.06)E+2	1.5
⋯	3294	17.43	+0.32	23	⋯	(3.6 ± 0.3)E+1	⋯	⋯
⋯	3342	17.39	+0.47	23	1.0	(2.04 ± 0.06)E+2	(1.13 ± 0.03)E+2	1.9
⋯	3179	17.63	+0.04	⋯	2.6	(2.05 ± 0.01)E+3	(7.31 ± 0.05)E+1	4.8

Continuation of Table B2

COHRS catalog #	Hi-GAL catalog #	ℓ (deg)	b (deg)	$v_{\rm LSR}$ (km s^{-1})	$\theta_{\rm R}$ (arcmin)	M (M$_\odot$)	n (cm^{-3})	R (pc)
···	3263	17.77	+0.24	···	1.4	(4.17 ± 0.07)E+2	(9.7 ± 0.2)E+1	2.6
···	3200	17.59	+0.09	···	0.3	(5.70 ± 0.04)E+2	(1.89 ± 0.01)E+4	0.5
···	3207	17.58	+0.11	···	1.1	(2.85 ± 0.05)E+2	(1.21 ± 0.02)E+2	2.1
···	3221	17.54	+0.14	···	1.3	(6.08 ± 0.06)E+2	(1.98 ± 0.02)E+2	2.3
···	3236	17.55	+0.17	···	1.0	(6.71 ± 0.06)E+2	(4.30 ± 0.04)E+2	1.8
···	3255	17.78	+0.20	···	0.9	(2.25 ± 0.05)E+2	(2.09 ± 0.05)E+2	1.6
···	3257	17.91	+0.22	···	1.8	(4.02 ± 0.08)E+2	(4.45 ± 0.09)E+1	3.3
···	3261	17.98	+0.25	···	1.5	(7.47 ± 0.08)E+2	(1.49 ± 0.02)E+2	2.7
···	3268	17.74	+0.25	···	0.8	(1.31 ± 0.04)E+2	(1.64 ± 0.06)E+2	1.5
···	3217	17.44	+0.13	···	2.0	(1.12 ± 0.01)E+3	(8.34 ± 0.07)E+1	3.8
64271	2165	15.94	−0.21	27	1.1	(1.66 ± 0.04)E+2	(1.19 ± 0.03)E+2	1.8
···	2193	15.91	−0.18	27	1.5	(1.96 ± 0.05)E+2	(5.3 ± 0.1)E+1	2.5
···	2216	15.91	−0.14	27	0.6	(1.63 ± 0.03)E+2	(9.1 ± 0.1)E+2	0.9
···	2230	15.88	−0.12	26	1.7	(6.11 ± 0.06)E+2	(1.17 ± 0.01)E+2	2.8
···	2255	15.86	−0.10	26	1.2	(2.48 ± 0.04)E+2	(1.55 ± 0.02)E+2	1.9
···	2264	15.88	−0.07	26	2.0	(3.99 ± 0.06)E+2	(5.06 ± 0.07)E+1	3.2
···	2338	15.94	+0.05	25	1.9	(5.49 ± 0.06)E+2	(7.89 ± 0.08)E+1	3.0
···	2364	15.95	+0.09	23	2.2	(4.82 ± 0.07)E+2	(4.51 ± 0.06)E+1	3.5
···	2330	15.91	+0.02	···	1.1	(2.88 ± 0.04)E+2	(2.07 ± 0.03)E+2	1.8
···	2361	15.88	+0.08	···	1.9	(2.53 ± 0.05)E+2	(3.79 ± 0.08)E+1	3.0
64385	2451	16.61	+0.28	45	2.3	(2.72 ± 0.06)E+2	(2.16 ± 0.05)E+1	3.7
64405	2396	15.91	+0.15	21	0.9	(1.29 ± 0.03)E+2	(2.06 ± 0.05)E+2	1.4
···	2453	15.97	+0.29	20	1.7	(6.44 ± 0.06)E+2	(1.20 ± 0.01)E+2	2.8
···	2470	16.04	+0.35	19	1.2	(1.86 ± 0.04)E+2	(1.10 ± 0.02)E+2	1.9
···	2477	16.26	+0.38	28	1.0	(4.83 ± 0.03)E+2	(4.23 ± 0.03)E+2	1.7
···	2485	16.31	+0.40	27	1.0	(2.48 ± 0.03)E+2	(2.36 ± 0.03)E+2	1.6
···	2489	16.28	+0.41	27	1.9	(1.173 ± 0.006)E+3	(1.638 ± 0.008)E+2	3.1
···	2495	16.14	+0.44	28	2.8	(1.623 ± 0.008)E+3	(7.61 ± 0.04)E+1	4.4
···	2496	15.93	+0.43	28	1.6	(1.90 ± 0.05)E+2	(5.0 ± 0.1)E+1	2.5
···	2497	16.22	+0.44	27	2.2	(1.462 ± 0.007)E+3	(1.329 ± 0.006)E+2	3.5
···	2509	16.10	+0.47	19	1.5	(4.21 ± 0.05)E+2	(1.19 ± 0.01)E+2	2.4
···	2436	16.08	+0.23	···	0.8	(9.6 ± 0.3)E+1	(1.66 ± 0.05)E+2	1.3
···	2441	16.01	+0.25	···	1.1	(1.04 ± 0.04)E+2	(7.5 ± 0.3)E+1	1.8
···	2446	16.09	+0.27	···	···	(3.3 ± 0.2)E+1	···	···
···	2452	16.00	+0.29	···	0.6	(9.0 ± 0.3)E+1	(5.3 ± 0.1)E+2	0.9
···	2455	15.92	+0.30	···	1.9	(7.26 ± 0.06)E+2	(9.99 ± 0.08)E+1	3.1
···	2475	16.08	+0.36	···	1.6	(4.43 ± 0.05)E+2	(9.8 ± 0.1)E+1	2.6
···	2486	16.09	+0.40	···	1.0	(1.60 ± 0.03)E+2	(1.66 ± 0.03)E+2	1.6
···	2488	16.05	+0.40	···	1.4	(2.62 ± 0.04)E+2	(1.02 ± 0.02)E+2	2.2
···	2501	16.33	+0.45	···	0.7	(8.8 ± 0.3)E+1	(2.23 ± 0.07)E+2	1.2
···	2508	16.35	+0.47	···	0.6	(4.8 ± 0.2)E+1	(2.3 ± 0.1)E+2	0.9
···	2514	16.06	+0.49	···	1.2	(1.64 ± 0.04)E+2	(1.03 ± 0.02)E+2	1.9
···	2511	16.37	+0.49	···	0.9	(1.37 ± 0.03)E+2	(2.11 ± 0.05)E+2	1.4
···	2513	16.20	+0.49	···	0.6	(5.4 ± 0.3)E+1	(2.3 ± 0.1)E+2	1.0
64461	2899	16.85	−0.43	50	1.2	(2.53 ± 0.05)E+2	(1.52 ± 0.03)E+2	1.9
64896	2055	16.39	−0.45	48	1.8	(7.81 ± 0.05)E+2	(1.257 ± 0.007)E+2	2.9
···	2069	16.36	−0.43	48	1.4	(6.03 ± 0.04)E+2	(2.00 ± 0.01)E+2	2.3
···	2070	16.42	−0.42	48	1.6	(3.01 ± 0.05)E+2	(7.5 ± 0.1)E+1	2.5
···	2089	16.45	−0.38	47	1.1	(5.59 ± 0.04)E+2	(3.91 ± 0.03)E+2	1.8
···	2104	16.37	−0.36	47	1.4	(4.58 ± 0.05)E+2	(1.68 ± 0.02)E+2	2.2
···	2115	16.48	−0.33	46	1.5	(4.08 ± 0.04)E+2	(1.31 ± 0.01)E+2	2.3
···	2166	16.36	−0.21	50	1.5	(6.139 ± 0.006)E+3	(1.780 ± 0.002)E+3	2.4
···	2177	16.30	−0.19	50	···	(1.40 ± 0.02)E+2	···	···
···	2190	16.40	−0.19	45	0.8	(6.55 ± 0.03)E+2	(1.066 ± 0.006)E+3	1.4
···	2212	16.33	−0.15	50	1.5	(2.464 ± 0.005)E+3	(7.20 ± 0.01)E+2	2.4
···	2213	16.30	−0.14	50	1.4	(1.335 ± 0.005)E+3	(5.24 ± 0.02)E+2	2.2
···	2259	16.35	−0.09	47	···	(1.10 ± 0.02)E+2	···	···
···	2267	16.36	−0.07	47	0.8	(7.21 ± 0.04)E+2	(1.212 ± 0.006)E+3	1.3
···	2268	16.31	−0.07	46	1.8	(1.196 ± 0.006)E+3	(1.930 ± 0.009)E+2	2.9
···	2903	16.63	−0.42	47	0.9	(2.54 ± 0.04)E+2	(3.81 ± 0.06)E+2	1.4
···	2905	16.58	−0.41	47	0.7	(3.80 ± 0.04)E+2	(9.7 ± 0.1)E+2	1.2
···	2912	16.68	−0.39	45	1.1	(1.92 ± 0.04)E+2	(1.60 ± 0.03)E+2	1.7
···	2921	16.55	−0.38	42	0.9	(4.08 ± 0.03)E+2	(6.08 ± 0.05)E+2	1.4
···	2946	16.67	−0.34	47	0.5	(2.53 ± 0.03)E+2	(1.66 ± 0.02)E+3	0.8
···	2952	16.50	−0.33	46	0.9	(2.71 ± 0.04)E+2	(3.83 ± 0.05)E+2	1.4
···	2959	16.53	−0.32	45	1.3	(6.04 ± 0.05)E+2	(2.83 ± 0.02)E+2	2.0
···	2960	16.60	−0.31	42	1.3	(5.47 ± 0.05)E+2	(2.41 ± 0.02)E+2	2.1
···	2998	16.61	−0.24	44	1.1	(7.92 ± 0.05)E+2	(5.36 ± 0.03)E+2	1.8
···	3014	16.52	−0.21	48	0.7	(1.40 ± 0.03)E+2	(4.6 ± 0.1)E+2	1.1
···	2892	16.68	−0.46	···	1.2	(2.43 ± 0.04)E+2	(1.56 ± 0.03)E+2	1.8
···	2087	16.33	−0.39	···	···	(2.3 ± 0.2)E+1	···	···
64921	2419	15.44	+0.19	48	1.6	(1.816 ± 0.005)E+3	(4.68 ± 0.01)E+2	2.5
···	2438	15.47	+0.23	49	1.4	(6.52 ± 0.04)E+2	(2.16 ± 0.01)E+2	2.3
···	2442	15.50	+0.23	48	2.3	(1.544 ± 0.007)E+3	(1.191 ± 0.005)E+2	3.7
···	2449	15.52	+0.29	48	2.7	(1.169 ± 0.008)E+3	(6.08 ± 0.04)E+1	4.3
64989	2979	16.81	−0.29	40	1.6	(1.015 ± 0.006)E+3	(2.29 ± 0.01)E+2	2.6
···	3005	16.89	−0.23	42	···	(5.4 ± 0.2)E+1	···	···
65090	3195	16.83	+0.08	62	1.1	(9.88 ± 0.05)E+2	(6.54 ± 0.04)E+2	1.8
···	3226	16.76	+0.15	···	1.5	(2.49 ± 0.05)E+2	(6.7 ± 0.1)E+1	2.5
65257	2464	15.62	+0.34	50	2.1	(2.04 ± 0.05)E+2	(2.31 ± 0.06)E+1	3.3
···	2510	15.64	+0.48	49	2.3	(4.16 ± 0.07)E+2	(3.27 ± 0.05)E+1	3.7
65332	2447	16.42	+0.28	29	1.8	(3.26 ± 0.05)E+2	(5.96 ± 0.09)E+1	2.8
···	2479	16.48	+0.39	38	1.2	(3.45 ± 0.04)E+2	(1.82 ± 0.02)E+2	2.0
···	2490	16.51	+0.43	38	2.1	(2.48 ± 0.06)E+2	(2.78 ± 0.06)E+1	3.3

Continuation of Table B2

COHRS catalog #	Hi-GAL catalog #	ℓ (deg)	b (deg)	v_{LSR} (km s^{-1})	θ_{R} (arcmin)	M ($M_{\odot}$)	n (cm^{-3})	R (pc)
···	2458	16.39	+0.30	···	1.7	(2.19 ± 0.05)E+2	(4.04 ± 0.09)E+1	2.8
···	2463	16.53	+0.32	···	1.3	(9.3 ± 0.4)E+1	(3.9 ± 0.2)E+1	2.1
65506	2257	16.50	−0.09	39	0.9	(2.03 ± 0.03)E+2	(2.87 ± 0.05)E+2	1.4
···	2263	16.57	−0.08	40	1.5	(1.644 ± 0.006)E+3	(5.11 ± 0.02)E+2	2.3
···	3045	16.68	−0.17	37	0.6	(5.9 ± 0.3)E+1	(2.3 ± 0.1)E+2	1.0
65666	2073	15.50	−0.42	40	1.4	(1.560 ± 0.005)E+3	(5.20 ± 0.02)E+2	2.3
···	2083	15.53	−0.41	39	1.1	(1.119 ± 0.004)E+3	(7.56 ± 0.03)E+2	1.8
···	2093	15.64	−0.38	40	0.5	(1.42 ± 0.02)E+2	(9.6 ± 0.2)E+2	0.8
···	2033	15.61	−0.48	···	0.9	(2.32 ± 0.03)E+2	(3.72 ± 0.05)E+2	1.4
66032	2040	16.42	−0.47	22	···	(1.26 ± 0.02)E+2	···	···
···	2067	16.12	−0.43	22	1.4	(3.48 ± 0.05)E+2	(1.24 ± 0.02)E+2	2.2
···	2908	16.54	−0.41	21	1.9	(2.648 ± 0.007)E+3	(4.05 ± 0.01)E+2	3.0
···	2028	16.31	−0.48	···	1.2	(8.98 ± 0.04)E+2	(5.06 ± 0.02)E+2	1.9
···	2045	16.35	−0.47	···	···	(3.80 ± 0.03)E+2	···	···
···	2062	16.51	−0.44	···	1.2	(8.90 ± 0.04)E+2	(5.35 ± 0.03)E+2	1.9
···	2099	16.31	−0.37	···	1.4	(8.94 ± 0.05)E+2	(3.06 ± 0.02)E+2	2.3
···	2161	16.20	−0.22	···	0.8	(9.1 ± 0.3)E+1	(1.49 ± 0.05)E+2	1.3
···	2048	16.33	−0.45	···	1.0	(5.72 ± 0.04)E+2	(5.26 ± 0.03)E+2	1.6
66707	3161	17.11	+0.03	72	2.1	(2.66 ± 0.02)E+3	(8.26 ± 0.05)E+1	5.1
66998	3096	16.73	−0.09	69	1.3	(1.152 ± 0.006)E+3	(5.14 ± 0.02)E+2	2.1
···	3131	16.84	−0.03	69	···	(8.5 ± 0.2)E+1	···	···
67240	2382	15.57	+0.14	28	1.3	(1.97 ± 0.04)E+2	(8.1 ± 0.2)E+1	2.1
67670	2898	16.89	−0.43	23	···	(4.3 ± 0.3)E+1	···	···
···	2958	16.85	−0.32	24	0.5	(1.53 ± 0.03)E+2	(9.5 ± 0.2)E+2	0.9
···	3018	16.82	−0.21	26	0.7	(1.00 ± 0.03)E+2	(3.5 ± 0.1)E+2	1.1
···	3070	16.83	−0.12	23	0.8	(2.09 ± 0.03)E+2	(4.49 ± 0.07)E+2	1.2
···	2920	16.83	−0.38	···	···	(3.0 ± 0.2)E+1	···	···
···	2939	16.89	−0.36	···	1.3	(3.23 ± 0.05)E+2	(1.39 ± 0.02)E+2	2.1
···	2990	16.74	−0.25	···	0.5	(1.12 ± 0.03)E+2	(8.9 ± 0.2)E+2	0.8
···	2995	16.80	−0.24	···	0.9	(4.00 ± 0.04)E+2	(6.20 ± 0.06)E+2	1.4
···	2916	16.96	−0.39	···	1.3	(3.00 ± 0.05)E+2	(1.28 ± 0.02)E+2	2.1
···	2922	16.85	−0.38	···	···	(4.2 ± 0.2)E+1	···	···
···	2982	16.66	−0.26	···	···	(2.5 ± 0.2)E+1	···	···
···	3048	16.72	−0.16	···	1.4	(3.31 ± 0.05)E+2	(1.32 ± 0.02)E+2	2.2
68082	2304	16.19	−0.01	23	0.8	(2.24 ± 0.04)E+2	(4.52 ± 0.07)E+2	1.3
···	2354	16.28	+0.08	26	1.7	(2.67 ± 0.05)E+2	(5.8 ± 0.1)E+1	2.6
···	2294	16.26	−0.03	···	1.6	(3.11 ± 0.05)E+2	(7.5 ± 0.1)E+1	2.6
68117	2284	16.59	−0.05	59	0.7	(3.079 ± 0.004)E+3	(8.12 ± 0.01)E+3	1.2
···	3127	16.67	−0.05	59	1.3	(5.24 ± 0.05)E+2	(2.13 ± 0.02)E+2	2.1
···	2286	16.64	−0.05	···	0.9	(3.20 ± 0.03)E+2	(3.91 ± 0.04)E+2	1.5
69018	2385	15.98	+0.13	30	1.1	(6.9 ± 0.3)E+1	(5.7 ± 0.3)E+1	1.7
···	2416	16.17	+0.19	35	2.2	(3.87 ± 0.06)E+2	(3.51 ± 0.06)E+1	3.5
···	2428	15.79	+0.23	29	2.4	(3.19 ± 0.06)E+2	(2.41 ± 0.05)E+1	3.8
···	2478	15.75	+0.37	28	2.0	(1.90 ± 0.06)E+2	(2.19 ± 0.06)E+1	3.3
···	2480	15.69	+0.39	28	1.6	(1.95 ± 0.05)E+2	(4.6 ± 0.1)E+1	2.6
69166	3151	16.69	+0.00	28	0.6	(7.4 ± 0.3)E+1	(4.3 ± 0.2)E+2	0.9
···	3170	16.78	+0.04	34	1.5	(7.46 ± 0.06)E+2	(2.31 ± 0.02)E+2	2.4
···	3143	16.74	−0.00	···	1.8	(1.368 ± 0.007)E+3	(2.24 ± 0.01)E+2	2.9
···	3158	16.79	+0.01	···	···	(1.9 ± 0.1)E+1	···	···
69546	2130	16.11	−0.30	39	1.0	(3.79 ± 0.03)E+2	(5.22 ± 0.04)E+2	1.4
···	2132	16.21	−0.30	45	···	(4.4 ± 0.1)E+1	···	···
···	2135	16.17	−0.29	42	0.9	(1.81 ± 0.03)E+2	(3.09 ± 0.05)E+2	1.3
···	2137	16.15	−0.28	41	0.9	(1.78 ± 0.03)E+2	(3.93 ± 0.06)E+2	1.2
···	2122	16.09	−0.32	···	0.8	(1.59 ± 0.02)E+2	(3.75 ± 0.06)E+2	1.2
69572	2256	15.44	−0.10	50	1.4	(4.37 ± 0.03)E+2	(2.24 ± 0.02)E+2	2.0
···	2222	15.45	−0.13	···	0.9	(2.79 ± 0.03)E+2	(5.32 ± 0.05)E+2	1.3
···	2288	15.36	−0.05	···	1.6	(5.20 ± 0.04)E+2	(1.68 ± 0.01)E+2	2.3
69761	2066	15.78	−0.44	49	0.8	(1.38 ± 0.02)E+2	(4.63 ± 0.08)E+2	1.1
···	2079	15.79	−0.41	46	0.7	(2.67 ± 0.02)E+2	(1.17 ± 0.01)E+3	1.0
···	2082	15.95	−0.40	40	0.4	(5.1 ± 0.2)E+1	(8.0 ± 0.3)E+2	0.6
···	2086	16.04	−0.39	42	1.0	(9.0 ± 0.3)E+1	(1.41 ± 0.04)E+2	1.4
···	2091	15.97	−0.38	41	1.1	(1.87 ± 0.03)E+2	(1.83 ± 0.03)E+2	1.6
···	2105	16.01	−0.36	42	0.5	(3.2 ± 0.2)E+1	(3.8 ± 0.2)E+2	0.7
···	2108	15.70	−0.35	57	···	(1.15 ± 0.02)E+2	···	···
···	2113	15.62	−0.33	60	0.6	(1.24 ± 0.02)E+2	(9.1 ± 0.2)E+2	0.8
···	2124	15.75	−0.32	57	···	(5.2 ± 0.2)E+1	···	···
···	2128	15.94	−0.31	43	···	(4.1 ± 0.2)E+1	···	···
···	2131	15.59	−0.30	60	1.1	(4.32 ± 0.03)E+2	(4.25 ± 0.03)E+2	1.6
···	2139	15.77	−0.28	57	1.2	(1.53 ± 0.03)E+2	(1.24 ± 0.02)E+2	1.7
···	2144	15.75	−0.27	57	···	(7.9 ± 0.2)E+1	···	···
···	2152	15.76	−0.24	57	1.7	(3.31 ± 0.04)E+2	(9.7 ± 0.1)E+1	2.4
···	2154	15.60	−0.22	59	···	(4.3 ± 0.2)E+1	···	···
···	2157	15.71	−0.22	57	1.3	(3.68 ± 0.03)E+2	(2.50 ± 0.02)E+2	1.8
···	2158	15.50	−0.22	60	···	(5.9 ± 0.2)E+1	···	···
···	2160	15.65	−0.23	57	2.0	(1.186 ± 0.005)E+3	(2.149 ± 0.009)E+2	2.8
···	2179	15.49	−0.20	60	0.6	(3.9 ± 0.2)E+1	(2.5 ± 0.1)E+2	0.9
···	2214	15.67	−0.15	60	1.7	(6.79 ± 0.04)E+2	(1.99 ± 0.01)E+2	2.4
···	2221	15.70	−0.14	60	0.9	(3.03 ± 0.03)E+2	(5.65 ± 0.05)E+2	1.3
···	2051	15.88	−0.46	···	0.9	(2.23 ± 0.02)E+2	(4.07 ± 0.04)E+2	1.3
···	2058	15.90	−0.45	···	1.3	(4.25 ± 0.03)E+2	(2.56 ± 0.02)E+2	1.9
···	2107	15.83	−0.36	···	1.2	(2.07 ± 0.03)E+2	(1.59 ± 0.02)E+2	1.7
···	2134	15.87	−0.28	···	1.5	(1.86 ± 0.03)E+2	(7.4 ± 0.1)E+1	2.2
···	2138	15.83	−0.27	···	1.9	(3.83 ± 0.04)E+2	(8.4 ± 0.1)E+1	2.6
69835	2146	15.22	−0.26	18	1.0	(1.14 ± 0.03)E+2	(1.49 ± 0.04)E+2	1.5

Continuation of Table B2

COHRS catalog #	Hi-GAL catalog #	ℓ (deg)	b (deg)	v_{LSR} (km s^{-1})	θ_{R} (arcmin)	M (M$_{\odot}$)	n (cm^{-3})	R (pc)
...	2185	15.27	−0.19	...	1.4	(3.46 ± 0.03)E+2	(1.73 ± 0.02)E+2	2.0
...	2231	15.24	−0.12	...	1.3	(5.32 ± 0.04)E+2	(3.26 ± 0.02)E+2	1.9
...	2237	15.28	−0.12	...	2.1	(1.323 ± 0.005)E+3	(2.128 ± 0.008)E+2	2.9
...	2248	15.20	−0.11	...	1.1	(2.10 ± 0.03)E+2	(2.56 ± 0.03)E+2	1.5
69836	2027	15.13	−0.50	20	0.6	(4.69 ± 0.02)E+2	(3.82 ± 0.02)E+3	0.8
...	2037	15.18	−0.48	21	0.4	(8.3 ± 0.2)E+1	(2.73 ± 0.05)E+3	0.5
...	2038	15.15	−0.48	20	1.4	(9.53 ± 0.04)E+2	(5.49 ± 0.02)E+2	1.9
...	2059	15.21	−0.43	21	1.5	(1.929 ± 0.005)E+3	(8.42 ± 0.02)E+2	2.1
...	2032	15.38	−0.49	...	1.8	(4.23 ± 0.04)E+2	(1.12 ± 0.01)E+2	2.5
70160	2427	15.21	+0.21	25	1.0	(1.36 ± 0.03)E+2	(2.25 ± 0.05)E+2	1.3
...	2431	15.29	+0.23	21	0.4	(9.3 ± 0.2)E+1	(2.87 ± 0.06)E+3	0.5
...	2425	15.26	+0.22	...	0.9	(5.7 ± 0.2)E+1	(1.29 ± 0.05)E+2	1.2
70493	2457	14.63	+0.30	26	1.5	(1.506 ± 0.004)E+3	(7.97 ± 0.02)E+2	2.0
...	2459	14.72	+0.32	26	1.7	(3.08 ± 0.04)E+2	(1.01 ± 0.01)E+2	2.3
...	2465	14.62	+0.33	27	1.0	(4.38 ± 0.03)E+2	(7.92 ± 0.05)E+2	1.3
...	2474	14.77	+0.36	26	1.0	(6.6 ± 0.2)E+1	(1.22 ± 0.04)E+2	1.3
...	1559	14.42	+0.29	...	1.9	(2.68 ± 0.04)E+2	(6.9 ± 0.1)E+1	2.5
...	1570	14.36	+0.32	...	0.5	(6.3 ± 0.2)E+1	(1.01 ± 0.03)E+3	0.6
...	1583	14.42	+0.35	...	1.1	(1.71 ± 0.03)E+2	(2.02 ± 0.03)E+2	1.5
...	1592	14.36	+0.36	...	1.1	(1.44 ± 0.03)E+2	(1.85 ± 0.03)E+2	1.5
...	1597	14.33	+0.38	...	1.0	(8.5 ± 0.2)E+1	(1.59 ± 0.04)E+2	1.3
...	1600	14.32	+0.40	...	1.7	(1.80 ± 0.04)E+2	(6.5 ± 0.1)E+1	2.2
...	1601	14.37	+0.40	...	0.7	(7.5 ± 0.2)E+1	(3.6 ± 0.1)E+2	0.9
...	1611	14.29	+0.44	...	1.7	(3.25 ± 0.04)E+2	(1.17 ± 0.01)E+2	2.2
...	1618	14.34	+0.46	...	0.5	(1.9 ± 0.2)E+1	(3.0 ± 0.2)E+2	0.6
...	1632	14.38	+0.49	...	1.0	(6.2 ± 0.3)E+1	(9.7 ± 0.4)E+1	1.4
...	2440	14.61	+0.25	...	0.8	(1.00 ± 0.02)E+2	(3.15 ± 0.06)E+2	1.1
...	2450	14.58	+0.28	...	1.5	(4.06 ± 0.03)E+2	(2.23 ± 0.02)E+2	1.9
...	2454	14.50	+0.29	...	...	(9.8 ± 0.9)E+0	...	...
...	2460	14.48	+0.31	...	0.8	(4.6 ± 0.2)E+1	(1.59 ± 0.07)E+2	1.1
...	2482	14.69	+0.38	...	1.1	(1.04 ± 0.02)E+2	(1.53 ± 0.03)E+2	1.4
...	2484	14.76	+0.38	...	0.7	(6.5 ± 0.2)E+1	(3.0 ± 0.1)E+2	1.0
...	2493	14.64	+0.43	...	1.8	(1.69 ± 0.04)E+2	(5.5 ± 0.1)E+1	2.3
70825	1400	13.81	−0.00	48	1.6	(5.42 ± 0.04)E+2	(2.45 ± 0.02)E+2	2.1
...	1508	13.85	+0.19	46	1.8	(1.285 ± 0.005)E+3	(3.79 ± 0.01)E+2	2.4
...	1511	13.92	+0.20	48	0.7	(3.34 ± 0.02)E+2	(1.68 ± 0.01)E+3	0.9
...	1518	13.93	+0.22	48	0.9	(2.78 ± 0.02)E+2	(5.95 ± 0.05)E+2	1.2
...	1540	13.80	+0.26	50	...	(1.31 ± 0.02)E+2	...	...
...	1553	13.87	+0.28	48	1.2	(4.105 ± 0.004)E+3	(4.326 ± 0.004)E+3	1.6
...	1573	14.00	+0.33	46	1.2	(4.77 ± 0.03)E+2	(5.04 ± 0.03)E+2	1.6
...	1477	13.85	+0.14	...	...	(1.2 ± 0.1)E+1	...	...
...	1431	13.76	+0.05	...	0.8	(1.00 ± 0.02)E+2	(2.92 ± 0.06)E+2	1.1
...	1495	13.81	+0.18	...	0.5	(7.2 ± 0.2)E+1	(1.23 ± 0.03)E+3	0.6
...	1499	13.95	+0.17	...	1.2	(6.6 ± 0.3)E+1	(5.9 ± 0.2)E+1	1.6
...	1517	13.81	+0.22	...	1.0	(1.76 ± 0.03)E+2	(3.04 ± 0.04)E+2	1.3
...	1529	13.96	+0.23	...	1.3	(3.33 ± 0.03)E+2	(2.74 ± 0.03)E+2	1.7
...	1547	13.96	+0.27	...	...	(4.2 ± 0.1)E+1	...	...
...	1562	13.91	+0.30	...	1.0	(1.67 ± 0.02)E+2	(2.86 ± 0.04)E+2	1.3
...	1565	14.03	+0.30	...	1.7	(7.62 ± 0.04)E+2	(2.68 ± 0.01)E+2	2.3
...	1434	13.84	+0.06	...	1.1	(1.77 ± 0.03)E+2	(2.14 ± 0.03)E+2	1.5
71144	1086	13.90	−0.51	23	2.1	(2.382 ± 0.005)E+3	(4.47 ± 0.01)E+2	2.8
...	1101	13.85	−0.49	23	1.4	(7.08 ± 0.03)E+2	(4.66 ± 0.02)E+2	1.8
...	1103	13.79	−0.48	24	1.1	(3.38 ± 0.03)E+2	(4.47 ± 0.04)E+2	1.4
...	1116	14.00	−0.45	21	0.4	(1.46 ± 0.02)E+2	(5.65 ± 0.06)E+3	0.5
...	1121	13.96	−0.45	23	1.3	(5.74 ± 0.03)E+2	(4.49 ± 0.02)E+2	1.7
...	1122	13.91	−0.45	23	1.1	(3.81 ± 0.03)E+2	(5.63 ± 0.04)E+2	1.4
...	1131	13.98	−0.44	23	1.0	(4.44 ± 0.03)E+2	(7.37 ± 0.04)E+2	1.3
...	1144	14.00	−0.42	21	0.6	(2.17 ± 0.02)E+2	(2.14 ± 0.02)E+3	0.7
...	1147	13.96	−0.41	20	1.4	(1.210 ± 0.003)E+3	(8.60 ± 0.02)E+2	1.8
...	1159	13.99	−0.39	21	0.6	(3.59 ± 0.02)E+2	(2.35 ± 0.01)E+3	0.9
...	2030	14.30	−0.49	19	0.5	(1.58 ± 0.02)E+2	(2.43 ± 0.03)E+3	0.6
...	1095	13.76	−0.50	...	...	(1.10 ± 0.02)E+2	...	...
...	1170	13.89	−0.37	...	0.9	(4.03 ± 0.03)E+2	(8.46 ± 0.06)E+2	1.2
...	1180	14.20	−0.34	...	0.8	(7.3 ± 0.2)E+1	(2.30 ± 0.06)E+2	1.1
...	1168	14.25	−0.37	...	0.4	(7.7 ± 0.2)E+1	(1.62 ± 0.04)E+3	0.6
...	1183	13.92	−0.34	...	...	(3.4 ± 0.1)E+1	...	...
71167	1309	13.88	−0.14	18	0.9	(5.35 ± 0.03)E+2	(1.517 ± 0.008)E+3	1.1
...	1300	14.13	−0.15	...	...	(1.8 ± 0.1)E+1	...	...
71532	2223	14.60	−0.14	41	...	(1.16 ± 0.01)E+2	...	...
...	2233	14.59	−0.13	45	0.4	(8.9 ± 0.1)E+1	(3.21 ± 0.05)E+3	0.5
...	2245	14.64	−0.12	40	0.9	(5.86 ± 0.03)E+2	(1.219 ± 0.006)E+3	1.2
...	2290	14.68	−0.04	42	0.6	(1.74 ± 0.02)E+2	(1.35 ± 0.02)E+3	0.8
...	2316	14.65	−0.00	39	0.5	(3.10 ± 0.02)E+2	(4.04 ± 0.02)E+3	0.7
...	2270	14.68	−0.08	...	...	(8.1 ± 0.2)E+1	...	...
72525	1218	13.90	−0.29	40	1.4	(6.17 ± 0.04)E+2	(3.99 ± 0.02)E+2	1.8
...	1265	13.86	−0.20	38	1.1	(1.91 ± 0.03)E+2	(2.56 ± 0.04)E+2	1.4
...	1274	14.19	−0.20	41	2.1	(5.593 ± 0.005)E+3	(1.089 ± 0.001)E+3	2.7
...	1275	14.31	−0.18	39	1.5	(6.92 ± 0.03)E+2	(3.94 ± 0.02)E+2	1.9
...	1286	14.01	−0.17	42	1.3	(1.992 ± 0.003)E+3	(1.586 ± 0.003)E+3	1.7
...	1290	14.23	−0.17	38	1.1	(7.79 ± 0.03)E+2	(1.179 ± 0.004)E+3	1.4
...	1299	14.20	−0.14	38	1.4	(1.004 ± 0.003)E+3	(5.80 ± 0.02)E+2	1.9
...	1308	13.98	−0.15	40	1.7	(2.403 ± 0.004)E+3	(8.54 ± 0.01)E+2	2.2
...	1318	14.01	−0.13	41	1.2	(2.540 ± 0.003)E+3	(2.311 ± 0.003)E+3	1.6
...	1376	14.09	−0.04	35	1.6	(5.97 ± 0.04)E+2	(2.70 ± 0.02)E+2	2.1

Continuation of Table B2

COHRS catalog #	Hi-GAL catalog #	ℓ (deg)	b (deg)	$v_{\rm LSR}$ (km s^{-1})	$\theta_{\rm R}$ (arcmin)	M (M$_\odot$)	n (cm^{-3})	R (pc)
···	2169	14.52	−0.20	43	0.9	(3.96 ± 0.02)E+2	(8.56 ± 0.05)E+2	1.2
···	2183	14.49	−0.19	43	1.2	(6.64 ± 0.03)E+2	(6.56 ± 0.03)E+2	1.6
···	2184	14.46	−0.18	40	1.7	(7.87 ± 0.03)E+2	(2.67 ± 0.01)E+2	2.3
···	2192	14.39	−0.19	43	1.0	(3.12 ± 0.03)E+2	(4.86 ± 0.04)E+2	1.4
···	2201	14.42	−0.17	42	0.9	(5.65 ± 0.03)E+2	(1.407 ± 0.007)E+3	1.2
···	2217	14.49	−0.14	41	1.2	(2.678 ± 0.003)E+3	(2.458 ± 0.003)E+3	1.6
···	2252	14.46	−0.10	40	1.8	(5.445 ± 0.004)E+3	(1.554 ± 0.001)E+3	2.4
···	1207	13.93	−0.31	···	···	(8.3 ± 0.1)E+1	···	···
···	1250	14.06	−0.23	···	···	(7.9 ± 0.2)E+1	···	···
···	1264	14.05	−0.21	···	···	(3.3 ± 0.1)E+1	···	···
···	1268	14.02	−0.20	···	0.9	(2.83 ± 0.02)E+2	(6.90 ± 0.06)E+2	1.2
···	1271	14.34	−0.20	···	0.4	(1.05 ± 0.02)E+2	(2.56 ± 0.04)E+3	0.5
···	1307	14.32	−0.14	···	1.2	(3.71 ± 0.03)E+2	(3.58 ± 0.03)E+2	1.6
···	1354	13.86	−0.07	···	1.2	(1.53 ± 0.03)E+2	(1.60 ± 0.03)E+2	1.6
···	1364	14.10	−0.06	···	0.4	(1.39 ± 0.02)E+2	(4.28 ± 0.06)E+3	0.5
···	1372	13.97	−0.04	···	···	(3.4 ± 0.2)E+1	···	···
···	2148	14.46	−0.25	···	1.3	(5.34 ± 0.03)E+2	(3.98 ± 0.02)E+2	1.8
···	2172	14.44	−0.20	···	···	(3.49 ± 0.09)E+1	···	···
···	2176	14.36	−0.20	···	0.7	(1.06 ± 0.02)E+2	(5.9 ± 0.1)E+2	0.9
···	2253	14.36	−0.10	···	1.1	(2.51 ± 0.03)E+2	(3.27 ± 0.03)E+2	1.5
···	2277	14.42	−0.06	···	1.4	(1.206 ± 0.003)E+3	(8.52 ± 0.02)E+2	1.8
···	1236	14.06	−0.26	···	···	(4.4 ± 0.2)E+1	···	···
···	1241	14.04	−0.25	···	···	(2.7 ± 0.1)E+1	···	···
···	1276	13.88	−0.18	···	0.7	(1.25 ± 0.02)E+2	(6.2 ± 0.1)E+2	0.9
72909	2077	14.69	−0.42	60	1.6	(4.78 ± 0.04)E+2	(2.11 ± 0.02)E+2	2.1
···	2085	14.89	−0.40	62	1.1	(8.15 ± 0.03)E+2	(1.060 ± 0.004)E+3	1.5
···	2142	14.50	−0.27	60	1.9	(1.319 ± 0.004)E+3	(3.46 ± 0.01)E+2	2.5
···	2075	14.73	−0.42	···	0.5	(6.4 ± 0.2)E+1	(1.00 ± 0.02)E+3	0.6
···	2094	14.55	−0.38	···	1.2	(4.16 ± 0.03)E+2	(4.72 ± 0.03)E+2	1.5
···	2101	14.66	−0.38	···	1.5	(4.21 ± 0.03)E+2	(1.99 ± 0.01)E+2	2.0
···	2106	14.89	−0.36	···	1.6	(5.43 ± 0.04)E+2	(2.25 ± 0.01)E+2	2.1
···	2129	14.84	−0.31	···	0.3	(4.2 ± 0.1)E+1	(2.75 ± 0.09)E+3	0.4
···	2136	14.55	−0.28	···	0.6	(8.9 ± 0.2)E+1	(6.8 ± 0.1)E+2	0.8
···	2141	14.65	−0.28	···	0.4	(8.3 ± 0.2)E+1	(1.74 ± 0.03)E+3	0.6
···	2162	14.65	−0.21	···	1.4	(3.14 ± 0.03)E+2	(2.16 ± 0.02)E+2	1.8
···	2076	14.55	−0.42	···	···	(5.6 ± 0.1)E+1	···	···
74066	2035	14.78	−0.49	22	1.2	(7.05 ± 0.03)E+2	(7.39 ± 0.03)E+2	1.6
···	2049	14.78	−0.44	23	2.2	(1.195 ± 0.005)E+3	(1.947 ± 0.008)E+2	2.9
···	2084	14.59	−0.41	24	1.4	(7.12 ± 0.03)E+2	(4.24 ± 0.02)E+2	1.9
···	2053	14.65	−0.45	···	0.5	(8.7 ± 0.2)E+1	(9.4 ± 0.2)E+2	0.7
···	2098	14.45	−0.37	···	0.9	(6.4 ± 0.2)E+1	(1.84 ± 0.06)E+2	1.1
···	2156	14.68	−0.22	···	1.1	(1.092 ± 0.003)E+3	(1.393 ± 0.004)E+3	1.5
···	2171	14.61	−0.20	···	0.9	(2.12 ± 0.02)E+2	(5.91 ± 0.06)E+2	1.1
···	2097	14.58	−0.37	···	1.3	(3.31 ± 0.03)E+2	(2.46 ± 0.02)E+2	1.8
···	2118	14.62	−0.31	···	1.9	(9.79 ± 0.04)E+2	(2.36 ± 0.01)E+2	2.6
74969	1360	14.25	−0.07	60	0.7	(1.347 ± 0.003)E+3	(7.03 ± 0.02)E+3	0.9
···	2327	14.65	+0.02	···	1.1	(5.08 ± 0.02)E+2	(6.38 ± 0.03)E+2	1.5
···	2281	14.76	−0.06	···	0.6	(5.4 ± 0.2)E+1	(4.3 ± 0.1)E+2	0.8
···	2301	14.53	−0.03	···	···	(6.2 ± 0.2)E+1	···	···
···	2300	14.50	−0.03	···	0.4	(1.47 ± 0.01)E+2	(4.97 ± 0.05)E+3	0.5
74998	2269	14.91	−0.07	28	1.3	(7.12 ± 0.03)E+2	(5.79 ± 0.02)E+2	1.7
···	2289	14.91	−0.04	27	1.2	(4.14 ± 0.03)E+2	(3.72 ± 0.02)E+2	1.6
···	2306	14.99	−0.01	25	0.6	(3.60 ± 0.02)E+2	(2.49 ± 0.01)E+3	0.8
···	2307	14.85	−0.01	26	···	(1.14 ± 0.02)E+2	···	···
···	2323	15.01	+0.01	24	0.3	(2.50 ± 0.02)E+2	(1.78 ± 0.01)E+4	0.4
···	2325	15.03	+0.02	24	···	(3.0 ± 0.1)E+1	···	···
···	2333	14.94	+0.03	26	1.7	(1.115 ± 0.004)E+3	(4.17 ± 0.01)E+2	2.2
···	2352	14.92	+0.07	26	1.0	(1.042 ± 0.003)E+3	(1.804 ± 0.005)E+3	1.3
···	2355	14.82	+0.08	30	0.8	(1.41 ± 0.02)E+2	(5.11 ± 0.08)E+2	1.0
···	2273	14.81	−0.06	···	0.7	(1.15 ± 0.02)E+2	(5.09 ± 0.09)E+2	1.0
···	2321	14.87	+0.01	···	···	(4.9 ± 0.1)E+1	···	···
···	2326	14.84	+0.01	···	1.1	(3.63 ± 0.03)E+2	(5.06 ± 0.04)E+2	1.4
···	2202	15.03	−0.17	···	1.1	(7.8 ± 0.2)E+1	(9.2 ± 0.3)E+1	1.5
···	2261	15.03	−0.08	···	1.5	(2.71 ± 0.03)E+2	(1.51 ± 0.02)E+2	1.9
75133	1179	12.85	−0.35	38	1.2	(5.47 ± 0.03)E+2	(6.36 ± 0.03)E+2	1.5
···	1184	12.55	−0.35	36	1.5	(6.15 ± 0.03)E+2	(4.13 ± 0.02)E+2	1.8
···	1222	12.52	−0.29	35	1.3	(8.58 ± 0.03)E+2	(8.04 ± 0.03)E+2	1.6
···	1227	12.86	−0.27	36	···	(7.47 ± 0.01)E+2	···	···
···	1235	12.90	−0.26	35	2.0	(1.2580 ± 0.0005)E+4	(3.367 ± 0.001)E+3	2.5
···	1243	12.86	−0.25	36	···	(2.93 ± 0.01)E+2	···	···
···	1251	12.95	−0.24	34	1.4	(1.597 ± 0.003)E+3	(1.226 ± 0.002)E+3	1.7
···	1256	12.85	−0.23	37	···	(7.14 ± 0.01)E+2	···	···
···	1258	12.50	−0.22	36	0.9	(5.96 ± 0.03)E+2	(1.903 ± 0.008)E+3	1.1
···	1263	12.72	−0.22	34	0.5	(7.55 ± 0.02)E+2	(1.292 ± 0.003)E+4	0.6
···	1273	12.98	−0.19	34	0.8	(3.59 ± 0.02)E+2	(1.419 ± 0.007)E+3	1.0
···	1279	13.05	−0.19	36	0.4	(1.52 ± 0.01)E+2	(5.87 ± 0.05)E+3	0.5
···	1284	13.01	−0.17	34	1.6	(1.290 ± 0.003)E+3	(6.65 ± 0.02)E+2	2.0
···	1288	12.49	−0.18	36	0.8	(1.45 ± 0.02)E+2	(7.07 ± 0.09)E+2	0.9
···	1292	13.06	−0.17	37	1.1	(5.55 ± 0.02)E+2	(9.62 ± 0.04)E+2	1.3
···	1294	12.96	−0.16	35	1.2	(6.05 ± 0.02)E+2	(8.41 ± 0.03)E+2	1.4
···	1302	12.46	−0.14	34	0.7	(1.53 ± 0.02)E+2	(9.2 ± 0.1)E+2	0.9
···	1306	12.42	−0.14	33	1.5	(6.03 ± 0.03)E+2	(3.64 ± 0.02)E+2	1.9
···	1322	12.38	−0.12	33	1.7	(5.63 ± 0.03)E+2	(2.59 ± 0.02)E+2	2.1
···	1344	13.12	−0.10	36	1.0	(7.13 ± 0.03)E+2	(1.635 ± 0.006)E+3	1.2

Continuation of Table B2

COHRS catalog #	Hi-GAL catalog #	ℓ (deg)	b (deg)	v_{LSR} (km s^{-1})	θ_{R} (arcmin)	M ($\mathrm{M}_{\odot}$)	n (cm^{-3})	R (pc)
···	1349	13.24	−0.08	37	1.2	(1.335 ± 0.003)E+3	(1.658 ± 0.004)E+3	1.5
···	1355	13.16	−0.08	37	1.5	(8.88 ± 0.03)E+2	(5.87 ± 0.02)E+2	1.8
···	1359	12.93	−0.07	31	···	(1.14 ± 0.01)E+2	···	···
···	1397	12.56	−0.00	···	···	(6.9 ± 0.1)E+1	···	···
···	1173	12.73	−0.36	···	···	(2.22 ± 0.09)E+1	···	···
···	1196	12.58	−0.33	···	···	(2.0 ± 0.1)E+1	···	···
···	1269	12.81	−0.20	···	1.3	(3.1908 ± 0.0004)E+4	(2.8886 ± 0.0003)E+4	1.6
···	1315	12.64	−0.14	···	0.6	(1.17 ± 0.01)E+2	(1.36 ± 0.02)E+3	0.7
···	1352	12.63	−0.07	···	0.5	(1.72 ± 0.02)E+2	(2.98 ± 0.03)E+3	0.6
···	1358	13.21	−0.08	···	0.3	(2.02 ± 0.02)E+2	(1.57 ± 0.01)E+4	0.4
···	1166	12.56	−0.38	···	0.7	(8.7 ± 0.2)E+1	(5.0 ± 0.1)E+2	0.9
···	1260	12.62	−0.22	···	0.3	(6.1 ± 0.1)E+1	(4.7 ± 0.1)E+3	0.4
75161	1502	13.46	+0.18	18	1.8	(5.39 ± 0.04)E+2	(1.99 ± 0.01)E+2	2.2
···	1506	13.34	+0.20	18	1.1	(4.16 ± 0.03)E+2	(6.31 ± 0.04)E+2	1.4
···	1525	13.27	+0.23	17	0.8	(2.68 ± 0.02)E+2	(1.056 ± 0.008)E+3	1.0
···	1542	13.27	+0.26	18	1.5	(3.37 ± 0.03)E+2	(2.26 ± 0.02)E+2	1.8
···	1548	13.14	+0.27	20	···	(4.0 ± 0.1)E+1	···	···
···	1215	13.40	−0.30	···	1.0	(1.57 ± 0.02)E+2	(3.40 ± 0.04)E+2	1.2
···	1238	13.44	−0.25	···	0.9	(1.92 ± 0.02)E+2	(5.62 ± 0.06)E+2	1.1
···	1278	13.37	−0.18	···	0.8	(1.06 ± 0.02)E+2	(4.01 ± 0.08)E+2	1.0
···	1382	13.44	−0.03	···	2.1	(1.485 ± 0.005)E+3	(3.27 ± 0.01)E+2	2.6
···	1423	13.50	+0.05	···	0.9	(7.3 ± 0.2)E+1	(2.54 ± 0.07)E+2	1.0
···	1428	13.53	+0.05	···	0.7	(5.5 ± 0.2)E+1	(3.1 ± 0.1)E+2	0.9
···	1474	13.44	+0.12	···	0.9	(6.1 ± 0.2)E+1	(2.00 ± 0.07)E+2	1.1
···	1523	13.20	+0.22	···	1.4	(3.14 ± 0.03)E+2	(2.26 ± 0.02)E+2	1.8
···	1545	13.21	+0.27	···	1.8	(3.27 ± 0.04)E+2	(1.15 ± 0.01)E+2	2.3
···	1577	13.30	+0.34	···	0.4	(4.9 ± 0.1)E+1	(1.93 ± 0.06)E+3	0.5
···	1578	13.28	+0.34	···	0.4	(2.7 ± 0.1)E+1	(1.29 ± 0.06)E+3	0.4
···	1589	13.27	+0.36	···	0.6	(4.1 ± 0.2)E+1	(3.5 ± 0.1)E+2	0.8
75162	1296	13.75	−0.16	17	1.0	(1.84 ± 0.02)E+2	(4.07 ± 0.05)E+2	1.2
···	1148	13.74	−0.41	···	1.1	(9.7 ± 0.2)E+1	(1.68 ± 0.04)E+2	1.3
···	1149	13.69	−0.41	···	0.7	(4.9 ± 0.2)E+1	(2.69 ± 0.09)E+2	0.9
···	1160	13.69	−0.39	···	0.8	(6.2 ± 0.2)E+1	(2.75 ± 0.09)E+2	1.0
···	1169	13.69	−0.37	···	0.6	(5.1 ± 0.2)E+1	(5.0 ± 0.2)E+2	0.7
···	1186	13.64	−0.34	···	···	(3.5 ± 0.1)E+1	···	···
···	1214	13.74	−0.30	···	1.6	(2.67 ± 0.03)E+2	(1.34 ± 0.02)E+2	2.0
···	1237	13.64	−0.25	···	···	(1.8 ± 0.1)E+1	···	···
···	1163	13.72	−0.38	···	1.2	(8.1 ± 0.2)E+1	(1.14 ± 0.03)E+2	1.4
···	1224	13.56	−0.28	···	···	(9.4 ± 0.1)E+1	···	···
75208	1571	12.82	+0.32	20	1.8	(1.253 ± 0.004)E+3	(4.49 ± 0.01)E+2	2.2
···	1579	12.77	+0.34	18	1.9	(3.083 ± 0.004)E+3	(1.033 ± 0.001)E+3	2.3
···	1584	12.69	+0.35	18	0.9	(1.55 ± 0.02)E+2	(4.63 ± 0.06)E+2	1.1
···	1595	12.83	+0.39	19	···	(2.32 ± 0.02)E+2	···	···
···	1619	12.79	+0.46	20	0.9	(1.60 ± 0.02)E+2	(4.11 ± 0.05)E+2	1.2
···	1622	12.69	+0.48	19	2.0	(1.354 ± 0.004)E+3	(3.43 ± 0.01)E+2	2.5
···	1558	12.99	+0.30	···	0.9	(9.8 ± 0.2)E+1	(2.56 ± 0.05)E+2	1.2
···	1614	12.66	+0.45	···	···	(2.6 ± 0.1)E+1	···	···
75322	1126	13.31	−0.43	37	2.0	(1.168 ± 0.004)E+3	(3.01 ± 0.01)E+2	2.5
···	1150	13.26	−0.41	38	1.6	(1.335 ± 0.004)E+3	(6.89 ± 0.02)E+2	2.0
···	1191	13.27	−0.33	42	1.5	(1.628 ± 0.004)E+3	(1.110 ± 0.002)E+3	1.8
···	1192	13.23	−0.33	41	···	(8.3 ± 0.1)E+1	···	···
···	1193	13.18	−0.33	39	1.4	(6.76 ± 0.03)E+2	(5.55 ± 0.03)E+2	1.7
···	1208	13.32	−0.31	40	0.9	(3.66 ± 0.02)E+2	(1.027 ± 0.006)E+3	1.1
···	1231	13.34	−0.27	39	0.8	(2.88 ± 0.02)E+2	(1.109 ± 0.008)E+3	1.0
···	1242	13.37	−0.25	40	1.1	(4.51 ± 0.02)E+2	(7.17 ± 0.03)E+2	1.4
···	1247	13.32	−0.23	···	1.1	(2.25 ± 0.02)E+2	(4.16 ± 0.05)E+2	1.3
···	1172	13.34	−0.37	···	···	(1.66 ± 0.02)E+2	···	···
···	1205	13.23	−0.31	···	0.5	(8.6 ± 0.2)E+1	(1.43 ± 0.03)E+3	0.6
···	1219	13.28	−0.29	···	···	(2.5 ± 0.1)E+1	···	···
75375	1301	13.13	−0.15	45	0.7	(9.72 ± 0.02)E+2	(6.58 ± 0.02)E+3	0.8
···	1305	13.09	−0.15	44	1.0	(8.60 ± 0.03)E+2	(1.623 ± 0.005)E+3	1.3
···	1312	13.21	−0.14	52	1.0	(3.497 ± 0.003)E+3	(6.773 ± 0.006)E+3	1.3
···	1336	13.19	−0.11	54	1.1	(1.324 ± 0.003)E+3	(2.371 ± 0.005)E+3	1.3
···	1379	13.36	−0.04	55	1.5	(4.41 ± 0.03)E+2	(3.01 ± 0.02)E+2	1.8
···	1418	13.21	+0.04	50	2.0	(5.272 ± 0.004)E+3	(1.475 ± 0.001)E+3	2.4
···	1426	13.25	+0.05	51	0.6	(1.72 ± 0.02)E+2	(2.00 ± 0.02)E+3	0.7
···	1440	13.17	+0.07	49	1.2	(3.381 ± 0.003)E+3	(4.298 ± 0.004)E+3	1.5
···	1444	13.12	+0.06	53	0.5	(1.12 ± 0.02)E+2	(1.80 ± 0.03)E+3	0.6
···	1458	13.28	+0.09	53	0.7	(1.08 ± 0.02)E+2	(8.3 ± 0.1)E+2	0.8
···	1345	13.36	−0.09	···	···	(1.5 ± 0.1)E+1	···	···
···	1378	13.33	−0.05	···	1.4	(1.429 ± 0.003)E+3	(1.095 ± 0.003)E+3	1.7
···	1403	13.31	+0.01	···	1.3	(8.25 ± 0.03)E+2	(7.48 ± 0.03)E+2	1.6
···	1414	12.98	+0.02	···	1.1	(3.55 ± 0.02)E+2	(5.63 ± 0.04)E+2	1.4
···	1225	13.02	−0.27	···	1.5	(5.71 ± 0.03)E+2	(4.03 ± 0.02)E+2	1.8
75384	1217	12.12	−0.29	52	1.4	(3.50 ± 0.03)E+2	(2.07 ± 0.02)E+2	1.9
···	406	12.15	−0.27	···	1.1	(1.50 ± 0.03)E+2	(2.05 ± 0.03)E+2	1.4
···	1229	12.17	−0.27	···	0.6	(6.2 ± 0.2)E+1	(6.1 ± 0.2)E+2	0.7
···	1255	12.18	−0.23	···	0.7	(6.3 ± 0.2)E+1	(3.4 ± 0.1)E+2	0.9
···	1293	12.29	−0.17	···	···	(4.9 ± 0.2)E+1	···	···
···	1200	12.16	−0.32	···	1.4	(2.39 ± 0.03)E+2	(1.51 ± 0.02)E+2	1.9
76716	1380	12.20	−0.03	51	1.0	(1.176 ± 0.003)E+3	(1.999 ± 0.006)E+3	1.3
···	1385	12.15	−0.03	47	0.7	(1.02 ± 0.02)E+2	(4.5 ± 0.1)E+2	1.0
···	1392	12.44	−0.00	···	1.7	(4.77 ± 0.04)E+2	(1.81 ± 0.01)E+2	2.2
···	1398	12.25	−0.00	···	0.4	(1.58 ± 0.02)E+2	(4.19 ± 0.05)E+3	0.5

Continuation of Table B2

COHRS catalog #	Hi-GAL catalog #	ℓ (deg)	b (deg)	$v_{\rm LSR}$ (km s^{-1})	$\theta_{\rm R}$ (arcmin)	M (M$_\odot$)	n (cm^{-3})	R (pc)
···	1401	12.38	+0.01	···	0.3	(1.56 ± 0.02)E+2	(8.55 ± 0.09)E+3	0.4
···	1437	12.46	+0.05	···	1.1	(2.57 ± 0.03)E+2	(3.90 ± 0.04)E+2	1.4
77060	1383	12.90	−0.02	56	1.6	(2.249 ± 0.005)E+3	(8.87 ± 0.02)E+2	2.2
···	1415	12.88	+0.03	···	1.4	(2.73 ± 0.03)E+2	(1.78 ± 0.02)E+2	1.8
78512	1587	12.99	+0.36	31	0.6	(2.07 ± 0.03)E+2	(1.82 ± 0.02)E+3	0.8
···	1588	12.95	+0.34	32	1.5	(3.27 ± 0.04)E+2	(1.87 ± 0.02)E+2	1.9
···	1616	12.92	+0.45	32	1.1	(8.96 ± 0.03)E+2	(1.268 ± 0.004)E+3	1.4
···	1627	12.89	+0.50	33	1.9	(6.901 ± 0.005)E+3	(1.816 ± 0.001)E+3	2.5
···	1599	13.01	+0.39	···	···	(2.4 ± 0.1)E+1	···	···
78679	664	12.21	+0.14	40	1.6	(1.063 ± 0.004)E+3	(4.73 ± 0.02)E+2	2.1
···	1527	12.26	+0.23	···	1.0	(1.82 ± 0.02)E+2	(3.66 ± 0.04)E+2	1.3
···	651	12.09	+0.11	···	···	(3.8 ± 0.1)E+1	···	···
80328	1202	12.81	−0.32	14	0.8	(1.373 ± 0.003)E+3	(4.188 ± 0.009)E+3	1.1
···	1189	12.77	−0.34	···	···	(7.1 ± 0.1)E+1	···	···
···	1199	12.71	−0.33	···	1.3	(3.19 ± 0.03)E+2	(2.79 ± 0.03)E+2	1.7
82207	385	11.52	−0.33	48	1.8	(9.92 ± 0.05)E+2	(2.22 ± 0.01)E+2	2.6
···	459	11.94	−0.15	43	0.7	(1.241 ± 0.003)E+3	(4.98 ± 0.01)E+3	1.0
···	472	11.90	−0.14	37	1.1	(3.454 ± 0.004)E+3	(3.343 ± 0.004)E+3	1.6
···	480	12.11	−0.13	45	···	(4.07 ± 0.02)E+2	···	···
···	483	11.98	−0.13	43	1.1	(4.88 ± 0.04)E+2	(4.68 ± 0.03)E+2	1.6
···	545	11.94	−0.04	39	1.4	(1.279 ± 0.004)E+3	(5.54 ± 0.02)E+2	2.1
···	372	11.86	−0.33	···	1.1	(2.09 ± 0.03)E+2	(2.14 ± 0.03)E+2	1.6
···	376	11.46	−0.33	···	1.3	(2.40 ± 0.04)E+2	(1.51 ± 0.02)E+2	1.9
···	387	11.81	−0.31	···	0.5	(8.2 ± 0.2)E+1	(6.4 ± 0.2)E+2	0.8
···	407	11.99	−0.27	···	1.9	(1.615 ± 0.005)E+3	(3.20 ± 0.01)E+2	2.7
···	420	11.74	−0.24	···	0.8	(2.01 ± 0.03)E+2	(5.79 ± 0.08)E+2	1.1
···	430	11.86	−0.22	···	···	(4.1 ± 0.2)E+1	···	···
···	403	11.50	−0.27	···	0.8	(1.79 ± 0.03)E+2	(5.12 ± 0.08)E+2	1.1
···	412	11.94	−0.26	···	1.2	(8.68 ± 0.04)E+2	(7.22 ± 0.04)E+2	1.7
···	446	11.34	−0.20	···	1.6	(3.44 ± 0.04)E+2	(1.19 ± 0.01)E+2	2.3
···	506	11.94	−0.10	···	0.8	(2.70 ± 0.03)E+2	(7.76 ± 0.08)E+2	1.1
···	575	11.95	+0.00	···	···	(4.2 ± 0.2)E+1	···	···
···	393	11.50	−0.30	···	0.6	(1.62 ± 0.02)E+2	(1.06 ± 0.02)E+3	0.9
···	379	11.55	−0.33	···	0.3	(1.24 ± 0.02)E+2	(6.3 ± 0.1)E+3	0.4
82236	728	11.60	+0.26	30	1.2	(2.52 ± 0.04)E+2	(1.77 ± 0.03)E+2	1.8
···	730	11.55	+0.26	30	1.4	(6.91 ± 0.04)E+2	(3.12 ± 0.02)E+2	2.1
···	581	11.72	+0.01	···	···	(8.4 ± 0.2)E+1	···	···
···	706	11.38	+0.21	···	···	(9 ± 1)E+0	···	···
···	719	11.63	+0.23	···	0.6	(8.9 ± 0.2)E+1	(5.3 ± 0.1)E+2	0.9
···	738	11.49	+0.28	···	0.6	(9.3 ± 0.2)E+1	(5.3 ± 0.1)E+2	0.9
···	743	11.49	+0.31	···	1.5	(2.34 ± 0.04)E+2	(9.3 ± 0.2)E+1	2.2
···	751	11.29	+0.32	···	0.7	(1.67 ± 0.03)E+2	(5.58 ± 0.09)E+2	1.1
···	753	11.42	+0.33	···	1.1	(1.03 ± 0.03)E+2	(9.9 ± 0.3)E+1	1.6
···	762	11.37	+0.36	···	1.3	(1.00 ± 0.04)E+2	(5.4 ± 0.2)E+1	2.0
···	658	11.65	+0.13	···	1.2	(1.45 ± 0.04)E+2	(1.19 ± 0.03)E+2	1.7
···	641	11.68	+0.10	···	···	(3.1 ± 0.2)E+1	···	···
···	713	11.27	+0.22	···	1.4	(4.11 ± 0.04)E+2	(1.88 ± 0.02)E+2	2.1
···	739	11.27	+0.29	···	0.3	(7.5 ± 0.2)E+1	(4.8 ± 0.1)E+3	0.4
···	722	11.30	+0.24	···	1.4	(3.31 ± 0.04)E+2	(1.53 ± 0.02)E+2	2.1
···	768	11.34	+0.40	···	0.7	(4.9 ± 0.3)E+1	(1.58 ± 0.08)E+2	1.1
82293	497	11.86	−0.11	15	···	(1.31 ± 0.02)E+2	···	···
···	503	11.84	−0.10	15	0.8	(5.46 ± 0.03)E+2	(1.470 ± 0.009)E+3	1.1
···	435	11.79	−0.20	···	1.1	(1.39 ± 0.03)E+2	(1.19 ± 0.03)E+2	1.7
···	441	11.70	−0.21	···	1.3	(2.89 ± 0.04)E+2	(1.82 ± 0.02)E+2	1.9
···	525	11.72	−0.07	···	1.4	(9.86 ± 0.04)E+2	(4.76 ± 0.02)E+2	2.0
···	621	11.80	+0.06	···	···	(9 ± 1)E+0	···	···
···	625	11.82	+0.06	···	1.1	(5.3 ± 0.3)E+1	(5.8 ± 0.3)E+1	1.5
···	434	12.02	−0.21	···	1.2	(9.37 ± 0.04)E+2	(6.78 ± 0.03)E+2	1.8
···	436	11.66	−0.20	···	1.3	(2.44 ± 0.03)E+2	(1.59 ± 0.02)E+2	1.8
···	645	11.84	+0.11	···	1.5	(2.74 ± 0.04)E+2	(1.09 ± 0.02)E+2	2.2
···	531	11.82	−0.06	···	0.9	(3.21 ± 0.03)E+2	(5.77 ± 0.06)E+2	1.3
82671	630	10.27	+0.08	48	2.2	(2.55 ± 0.01)E+3	(1.391 ± 0.006)E+2	4.2
···	530	10.25	−0.06	···	···	(9.4 ± 0.3)E+1	···	···
···	537	10.37	−0.05	···	2.0	(2.828 ± 0.009)E+3	(2.022 ± 0.006)E+2	3.8
···	552	10.54	−0.03	···	0.6	(2.29 ± 0.04)E+2	(5.63 ± 0.09)E+2	1.2
···	560	10.57	−0.02	···	0.9	(6.08 ± 0.05)E+2	(5.80 ± 0.05)E+2	1.6
···	596	10.47	+0.03	···	0.9	(2.2436 ± 0.0007)E+4	(1.8022 ± 0.0006)E+4	1.7
···	536	10.57	−0.05	···	···	(5.3 ± 0.2)E+1	···	···
83048	302	11.28	−0.46	32	1.4	(8.64 ± 0.07)E+2	(1.82 ± 0.01)E+2	2.7
···	481	11.13	−0.13	30	1.1	(2.270 ± 0.006)E+3	(1.041 ± 0.003)E+3	2.1
···	493	11.11	−0.12	29	1.2	(3.002 ± 0.006)E+3	(1.010 ± 0.002)E+3	2.3
···	508	11.06	−0.10	29	1.7	(2.542 ± 0.008)E+3	(2.942 ± 0.009)E+2	3.3
···	310	11.23	−0.45	···	1.7	(4.01 ± 0.07)E+2	(4.77 ± 0.08)E+1	3.2
···	317	11.00	−0.43	···	···	(4.5 ± 0.3)E+1	···	···
···	437	11.07	−0.21	···	0.6	(6.5 ± 0.3)E+1	(2.1 ± 0.1)E+2	1.1
···	451	11.00	−0.17	···	1.0	(7.25 ± 0.05)E+2	(4.58 ± 0.03)E+2	1.9
···	464	10.98	−0.15	···	1.1	(5.95 ± 0.05)E+2	(2.94 ± 0.03)E+2	2.0
···	305	11.00	−0.46	···	1.4	(2.42 ± 0.06)E+2	(5.7 ± 0.1)E+1	2.6
84131	358	10.29	−0.35	11	0.4	(5.00 ± 0.04)E+2	(4.02 ± 0.03)E+3	0.8
···	374	10.25	−0.34	11	···	(4.46 ± 0.03)E+2	···	···
···	443	10.41	−0.21	11	1.8	(2.874 ± 0.008)E+3	(3.287 ± 0.009)E+2	3.3
···	457	10.32	−0.16	12	0.7	(7.445 ± 0.004)E+3	(1.3592 ± 0.0008)E+4	1.3
···	469	10.30	−0.15	14	0.8	(9.460 ± 0.005)E+3	(1.3726 ± 0.0007)E+4	1.4
···	471	10.35	−0.15	13	1.5	(1.0938 ± 0.0008)E+4	(1.805 ± 0.001)E+3	2.9

Continuation of Table B2

COHRS catalog #	Hi-GAL catalog #	ℓ (deg)	b (deg)	v_{LSR} (km s^{-1})	θ_R (arcmin)	M ($M_\odot$)	n (cm^{-3})	R (pc)
···	487	10.28	−0.12	13	1.1	(1.1848 ± 0.0006)E+4	(5.060 ± 0.003)E+3	2.1
···	527	10.34	−0.06	16	···	(2.03 ± 0.03)E+2	···	···
···	577	10.44	+0.00	···	0.9	(1.442 ± 0.005)E+3	(1.332 ± 0.004)E+3	1.6
84734	427	10.74	−0.23	30	1.0	(9.71 ± 0.06)E+2	(5.42 ± 0.03)E+2	1.9
···	433	10.67	−0.22	30	0.8	(1.792 ± 0.006)E+3	(1.984 ± 0.006)E+3	1.5
···	442	10.67	−0.20	28	1.0	(1.399 ± 0.005)E+3	(9.50 ± 0.04)E+2	1.8
···	445	10.76	−0.20	32	1.8	(2.507 ± 0.008)E+3	(2.863 ± 0.009)E+2	3.3
···	456	10.67	−0.16	30	0.9	(8.26 ± 0.05)E+2	(7.75 ± 0.04)E+2	1.6
···	482	10.74	−0.12	29	1.5	(3.128 ± 0.007)E+3	(6.29 ± 0.01)E+2	2.7
···	485	10.68	−0.13	31	1.0	(1.584 ± 0.005)E+3	(9.67 ± 0.03)E+2	1.9
···	486	10.65	−0.12	29	1.3	(1.301 ± 0.006)E+3	(3.68 ± 0.02)E+2	2.4
···	587	10.75	+0.02	32	1.3	(1.933 ± 0.007)E+3	(4.87 ± 0.02)E+2	2.5
···	591	10.70	+0.01	38	1.6	(2.156 ± 0.007)E+3	(3.31 ± 0.01)E+2	3.0
···	620	10.85	+0.06	38	1.5	(6.61 ± 0.07)E+2	(1.17 ± 0.01)E+2	2.8
···	634	10.67	+0.10	20	1.9	(2.898 ± 0.009)E+3	(2.428 ± 0.007)E+2	3.6
···	644	10.65	+0.11	19	1.2	(1.108 ± 0.005)E+3	(4.23 ± 0.02)E+2	2.2
···	389	10.80	−0.31	···	0.4	(1.63 ± 0.03)E+2	(2.06 ± 0.04)E+3	0.7
···	392	10.59	−0.30	···	0.6	(2.91 ± 0.04)E+2	(1.07 ± 0.01)E+3	1.0
···	466	10.71	−0.15	···	1.0	(1.063 ± 0.006)E+3	(5.74 ± 0.03)E+2	2.0
···	607	10.69	+0.04	···	1.4	(1.129 ± 0.006)E+3	(2.44 ± 0.01)E+2	2.7
···	660	10.58	+0.14	···	2.1	(1.000 ± 0.008)E+3	(6.68 ± 0.05)E+1	3.9
···	678	10.64	+0.15	···	1.2	(6.30 ± 0.06)E+2	(2.15 ± 0.02)E+2	2.3
···	723	10.63	+0.23	···	1.8	(7.92 ± 0.07)E+2	(7.95 ± 0.07)E+1	3.4
84999	512	10.98	−0.08	30	2.3	(6.33 ± 0.01)E+3	(3.312 ± 0.006)E+2	4.3
···	541	11.05	−0.04	30	···	(2.27 ± 0.04)E+2	···	···
···	589	10.96	+0.02	22	0.8	(2.968 ± 0.006)E+3	(3.033 ± 0.006)E+3	1.6
···	628	10.93	+0.07	19	0.6	(2.70 ± 0.04)E+2	(6.17 ± 0.08)E+2	1.2
···	559	10.97	−0.02	···	0.9	(4.08 ± 0.05)E+2	(3.84 ± 0.04)E+2	1.6
···	593	11.03	+0.03	···	0.3	(4.14 ± 0.04)E+2	(9.27 ± 0.08)E+3	0.6
···	639	10.92	+0.09	···	···	(1.06 ± 0.03)E+2	···	···
···	555	11.03	−0.03	···	···	(1.45 ± 0.03)E+2	···	···
···	615	10.93	+0.05	···	···	(2.16 ± 0.03)E+2	···	···

End of Table